Development of an Electrochemical Micromachining (µECM) machine

A Thesis Submitted for the Degree of doctor of Philosophy

By

Alexandre SPIESER

College of Engineering, Design and Physical Sciences

Brunel University

London, United Kingdom

March 2015

ABSTRACT

Electrochemical machining (ECM) and especially electrochemical micromachining (µECM) became an attractive area of research due to the fact that this process does not create any defective layer after machining and that there is a growing demand for better surface integrity on different micro applications such as microfluidics systems and stress-free drilled holes in the automotive and aerospace sectors.

Electrochemical machining is considered as a non-conventional machining process based on the phenomenon of electrolysis. This process requires maintaining a small gap - the interelectrode gap (IEG) - between the anode (workpiece) and the cathode (tool-electrode) in order to achieve acceptable machining results (i.e. accuracy, high aspect ratio with appropriate material removal rate and efficiency).

This work presents the design of a next generation µECM machine for the automotive, aerospace, medical and metrology sectors. It has 3 axes of motion (X, Y and Z) and a spindle allowing the tool-electrode to rotate during machining.

The linear slides for each axis use air bearings with linear DC brushless motors and 2nm-resolution encoders for ultra-precise motion. The control system is based on the Power PMAC motion controller from Delta Tau. The electrolyte tank is located at the rear of the machine and allows the electrolyte to be changed quickly.

A pulse power supply unit (PSU) and a special control algorithm have been implemented. The pulse power supply provides not only ultra-short pulses (50ns), but also plus and minus biases as well as a polarity switching functionality. It fulfils the requirements of tool preparation with reversed ECM on the machine. Moreover, the PSU is equipped with an ultrafast over current protection which prevents the tool-electrode from being damaged in case of short-circuits.

Two different process control algorithms were made: one is fuzzy logic based and the other is adapting the feed rate according to the position and time at which short-circuits were detected.

The developed machine is capable of drilling micro holes in hard-to-machine materials but also machine micro-styli and micro-needles for the metrology (micro CMM) and medical sectors. This work also presents drilling trials performed with the machine with an orbiting

tool. Machining experiments were also carried out using electrolytes made of a combination of HCl and $NaNO_3$ aqueous solutions.

The developed machine was used to fabricate micro tools out of 170µm WC-Co alloy shafts via micro electrochemical turning and drill deep holes via µECM in disks made of 18NiCr6 alloy.

Results suggest that this process can be used for industrial applications for hard-to-machine materials. The author also suggests that the developed machine can be used to manufacture micro-probes and micro-tools for metrology and micro-manufacturing purposes.

Keywords — Micro ECM, PECM, micromanufacturing, micro ECM machines, electrochemical micromachining (EMM)

ACKNOWLEDGEMENTS

I would like to express my deepest gratitude to the people who have helped and guided in working to realize this research project.

Firstly, I would like to thank my supervisor, Dr. Atanas IVANOV, for his guidance, assistance, time, effort and never ending patience to make this project a success.

Not forgetting Andreas Rohrmeier, Rebecca Leese, Martin Santl and Paul Yates for their support and help through one-on-one or group meetings.

I also would like to thank the Delta Tau support team who took the time to answer my questions.

I would like also thank Brunel University and the European Commission for financing my PhD studies. I am thankful to the EU FP7 Micro-ECM and EU FP7 MIDEMMA projects' partners for the constructive discussions.

I would also like to express my gratitude to my family for supporting me and providing me endless encouragement and my girlfriend for her support and motivation. Lastly, I would like to thank my friends and colleagues for all their help and support.

This project is dedicated to those mentioned above.

TABLE OF CONTENT

ABSTRACT .... **II**

ACKNOWLEDGEMENTS .... **IV**

TABLE OF CONTENT .... **V**

LIST OF FIGURES .... **XII**

LIST OF TABLES .... **XX**

LIST OF ABBREVIATIONS .... **XXI**

LIST OF SYMBOLS .... **XXIV**

CHAPTER 1: INTRODUCTION **1**

1.1. From ECM to µECM 1

1.2. Justification, Aims and Objectives 2
- 1.2.1. Justification 2
- 1.2.2. Aims 4
- 1.2.3. Objectives 4

1.3. Methodology 5
- 1.3.1. Identification of gaps in research and key requirements for µECM 5
- 1.3.2. Development of a simulation programme to investigate the µECM process behaviour . 7
- 1.3.3. Development of a novel pulse PSU architecture for the needs of µECM 7
- 1.3.4. Component selection and machine system integration 8
- 1.3.5. Development of an innovative control strategy for the µECM process 9
- 1.3.6. Development of an intelligent HMI 10
- 1.3.7. Experimental validation 10

1.4. Description of chapters 10

1.5. Key contributions 12

CHAPTER 2: LITERATURE REVIEW **15**

2.1. Introduction 15

2.2. ECM Fundamentals 17

2.2.1. Basic ECM setup 17
2.2.2. The chemical reaction 18
2.2.3. The material removal rate (MRR) 19
2.2.3.1. MRR for pure materials (non-alloy) 19
2.2.3.2. MRR for alloys in ECM 21

2.3. Machining process 21
2.3.1. Review and analysis of the ECM and µECM machines available on the market 21
2.3.2. Design requirements and constraints for µECM systems 23
2.3.2.1. Ultra-precision motion for tool-positioning 23
2.3.2.1. High dynamics and frictionless motion 24
2.3.2.2. Workpiece clamping and tool holder constraints 24
2.3.3. Process monitoring and control 25
2.3.3.1. Interelectrode gap control and optimization algorithms 26
2.3.3.2. The electrical double layer (EDL) effect in µECM 31
2.3.3.3. Control of the voltage at the electrodes 35
2.3.4. Machining strategies 36

2.4. Pulse power supply unit (PSU) considerations 38

2.5. Electrode and workpiece preparation 41
2.5.1. Tool design software 41
2.5.2. Off-Machine electrode fabrication 42
2.5.3. On-Machine electrode preparation 43
2.5.4. Electrical connections 45

2.6. Measurement 46
2.6.1. Measuring dimensions 46
2.6.2. Machine set-up 47
2.6.3. Surface roughness 48
2.6.3.1. Influence of the electrolyte 48
2.6.3.2. Material grain structure and composition 50
2.6.3.3. Influence of electrical parameters 50

2.7. Handling 51
2.7.1. Electrodes and workpiece 51
2.7.2. Electrolytes 51

2.8. Discussion and conclusions 54

CHAPTER 3: µECM PROCESS MODELLING AND SIMULATION 57

3.1. Inter-electrode gap behaviour without feed rate 57

3.2. Bin Wei's PECM gap model with constant feed rate 61
3.2.1. Mathematical formulation 61
3.2.2. Simulation 62
3.2.3. Concluding remarks regarding Bin Wei's model with constant feed rate 67

3.3. μECM model according to Marla et al. 67

3.4. The electrical double layer: study of existing models and simulation.................................. 69
3.4.1. Models of the electrical double layer effect on the gap voltage.................................. 69
3.4.2. Similarities with Zener diodes 71
3.4.3. More realistic model of the IEG.. 75

3.5. 2D Drilling simulation with simple electrical double layer (EDL) model............................ 77
3.5.1. Point to point inter-electrode gap (h) calculation method... 78
3.5.2. Modelling the influence of the EDL on the gap change 79
3.5.3. Simulation workflow 80

3.6. Influence of the pulse frequency on the localization and the machining time. 83

3.7. Summary.. 85

CHAPTER 4: AN INNOVATIVE PULSE POWER SUPPLY UNIT FOR μECM 86

4.1. An novel pulse PSU architecture 86

4.2. Previous prototypes 87
4.2.1. First prototype 88
4.2.2. Second prototype.. 88

4.3. Pulse PSU prototype modules.. 89
4.3.1. The control circuitry 89
4.3.1.1. Pulse generating module 89
4.3.1.2. Pulse shape selection... 91
4.3.1.3. 24V-logic isolated digital interface.. 93
4.3.2. The power stage 94
4.3.2.1. Configuration... 94
4.3.2.2. MOSFET selection... 95
4.3.2.3. Driver selection.. 96
4.3.2.4. Optimized layout for smaller footprint and reduced parasitics............................ 97
4.3.3. The over current protection (OCP) stage 98
4.3.1. PSU testing and mounting 100
4.3.1.1. On-board signals 105
4.3.1.2. OCP triggering trials 106
4.3.2. Operation of the third PSU prototype..109

4.4. Discussion and conclusion for Chapter 3 110

CHAPTER 5: MACHINE SYSTEM INTEGRATION 111

5.1. Granite base 112

5.2. X, Y and Z Slides 113
5.2.1. The linear DC brushless motor 114
5.2.2. Encoder system 115

5.2.3. The air bearings 116

5.3. The spindle 116

5.4. Electrical cabinet 119
5.4.1. Control components 119
5.4.1.1. Power PMAC motion controller 119
5.4.1.2. ACC24E-2 4 axes interface board 120
5.4.1.3. ACC36UK 16bit Analogue input board 121
5.4.1.4. ACC65E digital input/output board 123
5.4.1. GeoDrive direct PWM amplifiers 124
5.4.2. 24V logic and electrical Safety components 125
5.4.2.1. 24V logic components 125
5.4.2.2. Circuit breakers 126
5.4.3. Filtering and shielding 126

5.5. Electrochemical machining cell and electrical connections 126

5.6. Electrolyte circuit 129

5.7. Conclusions 130

CHAPTER 6: PROCESS CONTROL AND SUPERVISION 131

6.1. Servo loop tuning of the X, Y and Z axes 131

6.2. Orbiting motion 134

6.3. Machine initialization algorithms 135

6.4. Process control algorithms 136
6.4.1. The state machine 137
6.4.1. The gap initialisation algorithm 138
6.4.2. Machining process control algorithms 140
6.4.2.1. IEG control using fuzzy logic 140
6.4.2.2. Adaptive feed rate algorithm 146
6.4.2.3. Escape strategy 148

6.5. An intelligent Human Machine Interface (HMI) 151

6.6. Conclusions 156

CHAPTER 7: EXPERIMENTAL WORK AND RESULTS 157

7.1. Experimental work at Sonplas GmbH on the machine developed in 2013 (Germany) 157
7.1.1. Discussion on the setup 157
7.1.2. Experiments and results 159
7.1.2.1. Effect of frequency on the hole shape 159
7.1.2.2. Drilling with orbiting electrode 160

7.1.2.1. Gasoline injector drilling 163
7.1.2.1. Damaged electrodes due to sparking 165
7.1.3. Process behaviour with the fuzzy logic control algorithm 165

7.2. Drilling experiments with orbiting tool-electrode 166

7.3. Investigation on the effect of pulse frequency, duty cycle and voltage on the machining performance 171
7.3.1. Methodology 171
7.3.2. Results 172
7.3.3. Discussion on the effect of pulse frequency, duty cycle and voltage on the machining performance 177
7.3.4. Verification of the µECM LabVIEW simulation model 178

7.4. On-line tool fabrication followed by workpiece drilling 180

7.5. Micro-Tool fabrication 183

CHAPTER 8: CONCLUSIONS AND FUTURE WORK 186

8.1. Conclusions 186

8.2. Contributions to knowledge 189

8.3. Recommendations for future work 191

REFERENCES 192

LIST OF FIGURES IN APPENDICES 205

LIST OF TABLES IN APPENDICES 208

APPENDIX 1. LIST OF PUBLICATIONS 209

APPENDIX 2. CALCULATION OF Kv alloy FOR 100CR6 210

APPENDIX 3. POWER ELECTRONICS FUNDAMENTALS 211

Appendix 3.1. Structure of a pulse power supply unit 211
Appendix 3.1.1. Microcontroller 211
Appendix 3.1.1.1. On-board I2C communication 211
Appendix 3.1.1.2. On-board SPI communication 212
Appendix 3.1.1.3. Modulation 212
Appendix 3.1.2. The power part of a pulse power supply unit 213
Appendix 3.1.2.1. MOSFET basics 213
Appendix 3.1.2.2. Reducing ringing at the MOSFET switch nodes using snubbers 215
Appendix 3.1.3. Isolation between control and power parts 217

Appendix 3.1.4. Current sensing for over-current protection....217
Appendix 3.1.5. Board design considerations and assembly....218

APPENDIX 4. DEVELOPMENT OF THE FIRST PULSE PSU PROTOTYPE....221

Appendix 4.1. First prototype: General presentation....221

Appendix 4.2. First prototype: The control circuitry....221

Appendix 4.3. First prototype: The power stage....230
Appendix 4.3.1. Timing aspects of the control signals....230
Appendix 4.3.2. MOSFET selection....232
Appendix 4.3.3. Driver selection....233
Appendix 4.3.4. Power electronics board layout....234

Appendix 4.4. First prototype: The current sensing board....236
Appendix 4.4.1. Over current protection (OCP)....236
Appendix 4.4.2. The peak detector....237
Appendix 4.4.3. First prototype: firmware programming....238

Appendix 4.5. Tests and conclusion on first prototype....241
Appendix 4.5.1. Measuring the PSU output and the influence of cabling....241
Appendix 4.5.2. On-board signal measurement....243
Appendix 4.5.3. Conclusions regarding the first PSU prototype....244

APPENDIX 5. PULSE PSU SIMULATION WITH MATLAB/SIMULINK....245

Appendix 5.1. Basic model (ideal)....245

Appendix 5.2. Realistic model (including parasitics)....246

APPENDIX 6. SECOND PULSE PSU PROTOTYPE....248

Appendix 6.1. Second PSU prototype: control circuitry....248
Appendix 6.1.1. Pulse generating module....248
Appendix 6.1.2. Pulse shape selection....249
Appendix 6.1.3. Avoiding MOSFET cross conduction....252

Appendix 6.2. Second PSU prototype: power stage....253

Appendix 6.3. Second PSU prototype: over current protection (OCP) stage....262

APPENDIX 7. EXPERIMENTAL WORK AT BRUNEL USING A TEST STAND....264

Appendix 7.1. Planning of experiment and experimental setup....264
Appendix 7.1.1. Materials and equipment used....265
Appendix 7.1.2. Interelectrode gap (IEG) initialization....266
Appendix 7.1.3. Tool approach and gap initialization on the test stand....267

Appendix 7.2. Preliminary Experiments 268
Appendix 7.2.1. Trials 1 & 2 268
Appendix 7.2.2. Trials 3 & 4 269
Appendix 7.2.3. Trial 5 271
Appendix 7.2.4. Trial 6 271
Appendix 7.2.5. Trial 7 272
Appendix 7.2.6. Trial 8 273
Appendix 7.2.7. Conclusions and discussion for the preliminary experimental work at Brunel 273

APPENDIX 8. PSU MODES 280

LIST OF FIGURES

Figure 2-1: Schematic diagram of a μECM system (Zhang et al., 2007) 16
Figure 2-2: Diagram representing the Micro ECM problematic areas 16
Figure 2-3: Schematic diagram of an electrochemical drilling unit (IIT Kharagpur, 2014)........... 17
Figure 2-4: Schematic of the electrochemical machining (ECM) process 18
Figure 2-5: Typical ECM machine from Indec. Die sinking only. 23
Figure 2-6: Two typical machine configurations and their coordinate definitions. (a) Open frame, (b) closed frame, (c) Structural loop stiffness calculated for both configurations 24
Figure 2-7: Flow chart for a control of the gap (Yong et al., 2003).. 28
Figure 2-8: A system for μECM (Kim et al., 2005a) 30
Figure 2-9: Representation of the electrical double layer and its different characteristics (Spieser, 2011).. 32
Figure 2-10: The capacitance as a function of the charging voltage. The error bar shows maximum and minimum values in 3 measurements. (Fujii, Muramoto and Shimizu, 2010)................. 32
Figure 2-11: Scheme of an electrical cell, the double layer capacity (CDL) is charged via the electrolyte resistance (Schuster et al., 2000) 33
Figure 2-12: Electrical model of the interelectrode gap proposed for the μECM process(Kozak, Gulbinowicz and Gulbinowicz, 2008) 34
Figure 2-13: Charging and discharging waveforms during μECM machining (Mithu, Fantoni and Ciampi, 2011a) 34
Figure 2-14: Schematic diagram of the Micro ECM system using a potentiostat (Yang, Park and Chu, 2009) 36
Figure 2-15: Micro cavities machined by controlling dissolution time and pulse duration (Jo et al., 2008).. 37
Figure 2-16: Principle of pulse generator for micro-ECM (Zhang et al., 2009)............................ 39
Figure 2-17: Basic circuitry of pulse-unit (PU) for PECM in connection with gap via feeder. Switches SW carry the rising current $ifeed$ during the pulse on-time, diodes D carry the falling reverse-current $irev$ at beginning of the pulse off-time. PU is connected to supply-unit PS on the left side. (Burkert et al., 2009)... 40
Figure 2-18: Basic circuitry of simple μECM pulse-unit (PU) in push-pull topology with bipolar (two) power supply (PS) feeding. Switches SW may conduct in alternation for loading and reloading of the gap's double layer capacitance. (Burkert et al., 2009) 40
Figure 2-19: Scanning electron micrographs (a) the tool; (b) structure in Ni substrate (Trimmer et al., 2003) 43

Figure 2-20: 10 µm tungsten tool electrode machined using electrochemical etching (Zhang et al., 2007)........ 44
Figure 2-21: Schematic diagrams of the tool electrode fabrication: (a) cylindrical tool and (b) semi-cylindrical tool (Yang, Park and Chu, 2009) 44
Figure 2-22: Schematic diagram of µECM sequentially: (a) micro-tool machining, (b) micro-workpiece machining (Zhang et al., 2011) 44
Figure 2-23: Comparison of grooves profiles created with 2 electrolytes (Lee, Park and Moon, 2002) 49
Figure 2-24: Current efficiencies of the soft annealed steel 100Cr6 obtained by galvanostatic flow channel experiments with $NaCl$ (20%) and $NaNO3$ (40%). The corresponding values for Armco-Iron are given for comparison. Average flow velocity: 7m/s. (Haisch, Mittemeijer and Schultze, 2001)........ 49
Figure 3-1: Simulink model based on the model with stationary electrode 58
Figure 3-2: Variation of the gap (in µm) over time (in s) without any feed rate (Spieser, 2011)... 59
Figure 3-3: Matlab/Simulink submodel to obtain the variation of I over time 59
Figure 3-4: Variation of the current (A) over time (s)........ 60
Figure 3-5: Interelectrode gap change during pulse cycle (Wei, 1994) 61
Figure 3-6: Matlab/Simulink model developed to simulate Wei's PECM model (1994) with constant feed rate 63
Figure 3-7: Internal diagram of the system (1) calculating the variation of h and Rgap with respect to U and Vf 63
Figure 3-8: Simulation results for 0.01 sec and Vf = 5mm/min: (1) variation of the inter-electrode gap (m) over time (s); (2) variation of the inter-electrode gap resistance (Ohm) over time (s) 64
Figure 3-9: Simulation results for 0.01 sec and Vf = 5mm/min: (1) variation of the inter-electrode gap (m) over time (s); (2) variation of the inter-electrode gap resistance (Ohm) over time (s) 65
Figure 3-10: Scheme diagram of the Matlab model used to define the optimal theoretical feed rate 66
Figure 3-11: Measured variation of i (A) over time over time before and after the Zero-Order Hold block 66
Figure 3-12: Variation of the inter-electrode gap (m) over time (s) with a constant feed rate of $0.937 \times 10 - 4m/s$ 67
Figure 3-13: Schematic of the µECM process (Marla, Joshi and Mitra, 2008)........ 68
Figure 3-14: Evolution of the gap current with respect to the applied voltage, Urkt : activating potential (V) , Up : Pulse amplitude (V) (Schuster and Kirchner, 2004) 71

Figure 3-15: Evolution of the current (mA) in a diode with respect to its polarization voltage (V) (Technologyuk.net, 2011) ... 71
Figure 3-16: Proposed inter-electrode gap model (Spieser, 2011) ... 72
Figure 3-17: Variation of the current density passing through the EDL of the anode during its charge (Ica) in A/m² over time (s) (Spieser, 2011) ... 73
Figure 3-18: Variation of the faradaic current passing through the EDL of the anode (Ifa) in A/m² over time (s) (Spieser, 2011) ... 73
Figure 3-19: Variation of the total current density (ic + if) flowing through the system (A/m²) over time (s) (Spieser, 2011) ... 74
Figure 3-20: Variation of the applied voltage (Pulses) (V) over time (s) (Spieser, 2011) ... 74
Figure 3-21: Potential at the EDL of the anode (V) over time (s) (Spieser, 2011) ... 74
Figure 3-22: Picture of the more realistic model of the IEG ... 76
Figure 3-23: Voltage pulses measured across the gap in V and time in s ... 76
Figure 3-24: Faradaic current pulses, amplitude in A and time in seconds ... 77
Figure 3-25: Drawing illustrating the tool-workpiece geometrical configuration ... 78
Figure 3-26: VI creating the mesh for the simulation ... 81
Figure 3-27: Picture of the geometrical configuration created by the 'Create Mesh' VI ... 81
Figure 3-28: Simplified flowchart of the LabVIEW simulation programme ... 82
Figure 3-29: Simulation results after a 50µm drilling simulation in 2D, the tool surface is in red and the workpiece surface is in white. ... 83
Figure 3-30: Results of the simulation illustrating the influence of the pulse frequency at different electrolyte conductivities Y and X positions are in mm. ... 84
Figure 4-1: Schematic diagram of the first PSU prototype and its interfaces ... 87
Figure 4-2: Electrical schematic diagram of the oscillator and the pulse generator ... 89
Figure 4-4: Control circuitry of the second PSU prototype ... 91
Figure 4-5: Drawing representing the 4 different control signal used to change the pulse shape when Channel A is selected. ... 92
Figure 4-6: Drawing representing the 4 different control signal used to change the pulse shape when Channel B is selected. ... 92
Figure 4-7: Drawing of the different pulse shapes that can be obtained in the different configuration ... 93
Figure 4-8: Schematic of the MOSFETs switching between the PULSE and OFFSET voltages to be applied to the H-bridge ... 94
Figure 4-9: Schematic of the MOSFETs and their drivers in the H-bridge ... 95
Figure 4-10: CAD Model of the package (Power 56) and representation of the MOSFET FDMS7578 (Fairchild-Semiconductor, 2009) ... 96

Figure 4-11: PSU prototype layout to optimise the current path and reduce overall inductance. Arrows symbolise the direction of the current. 97
Figure 4-12: Electrical diagram of the current sensing part on the OCP stage of the second prototype: 98
Figure 4-13: C1: OCP threshold (380mV/A); C2: comparator output; C3: OCP signal (latched output); C4: current (380mV/A); 1MHz 25% duty cycle 99
Figure 4-14: C1: OCP threshold (380mV/A); C2: comparator output; C3: OCP signal (latched output); C4: current (380mV/A); 1MHz 25% duty cycle (20ns/div) 99
Figure 4-15: Picture of the PSU being tested with the 1Ohm load and current transformer 100
Figure 4-16: C1: current (1V/A), C2: voltage; PSU in pulse mode 1: 3V pulse, no offset; 750kHz 25% duty cycle..101
Figure 4-17: C2: voltage; PSU in pulse mode 2: 2VDC (positive)..101
Figure 4-18: C1: current (1V/A), C2: voltage; PSU in pulse mode 3: 3V pulse, 1 V negative offset; 750kHz 25% duty cycle..102
Figure 4-19: C1: current (1V/A), C2: voltage; PSU in pulse mode 4: 3V pulse, 1 V positive offset; 750kHz 25% duty cycle..102
Figure 4-20: C1: current (1V/A), C2: voltage; PSU in pulse mode 5: 3V negative pulse, no offset; 750kHz 25% duty cycle..103
Figure 4-21: C2: voltage; PSU in pulse mode 6: 2VDC (negative)..103
Figure 4-22: C1 current (1V/A), C2: voltage; PSU in pulse mode 7: negative 3V pulse, 1 V positive offset; 750kHz 25% duty cycle 104
Figure 4-23: C1 current (1V/A), C2: voltage; PSU in pulse mode 8: negative 3V pulse, 1 V negative offset; 750kHz 25% duty cycle 104
Figure 4-24: Oscilloscope screenshot of the measured signals on the PSU, 1MHz frequency, duty cycle of 25%, pulse amplitude of 3.2V and no offset during off-time 500ns/div. 106
Figure 4-25: Oscilloscope screenshot of the OCP signal delay 50ns/div. (C1: Measured gap current via commercial current sensor at 1V/div. and 1V/A; C2: OCP signal 1V/div; C3: OCP threshold level at 380mV/div. and 380mV/A; C4: Measured gap current via on-board current sensing circuitry at 380mV/A and 380mV/div.)..107
Figure 4-26: Graph representing the pulse amplitude at the IEG (mV) according to the frequency (in kHz). 107
Figure 4-27: Pictures of the PSU mounted on the µECM machine. 108
Figure 5-1: 3D-CAD models of the µECM machine. 112
Figure 5-2: Schematic diagram of the developed micro-ECM machine 112
Figure 5-3: Mechanical drawing of the assembled X slide and its cross-section.........................113
Figure 5-4: Mechanical drawing and specifications of the LEM-S-3-S linear motor (Anorad Linear Motor Division, 1999) 114

Figure 5-5: Mechanical drawing of the Renishaw encoder system 115
Figure 5-6: Picture of the groove pattern machined in the inner surface of the pressurized bearing to improve stability. The encoder read head can also be seen. 116
Figure 5-7: Cross section of the developed spindle for the µECM machine. For safety reasons, the mercury slip ring was later replaced by a ring with microfiber carbon brushes. 117
Figure 5-8: Schematic diagram showing the wiring of the stepper motor as well as its interface with the HMI 118
Figure 5-9: Picture of the electrical cabinet 119
Figure 5-10: A picture representing the UMAC rack as a modular system. Source: http://www.heason.com/catalogue/74/umac.html 120
Figure 5-11: Electrical schematic of the encoder wired to the Acc24E-2 (Delta Tau Data Systems, 2009) 121
Figure 5-12: Electrical schematic of the Hall effect sensor wired to the Acc24E-2 (Delta Tau Data Systems, 2009) 121
Figure 5-13: ACC36UK memory pointers setup in the global definitions.pmh file of the Power PMAC IDE 123
Figure 5-14: The function GetAcc36UKValue() using pointers to access the data acquired by the ACC36UK in C. 123
Figure 5-15: Electrical schematic of the wiring of the amplifiers 125
Figure 5-16: CAD View of the machining cell with the base, the workpiece and the cap 127
Figure 5-17: Picture of the workpiece (coin) being clamped by the cap and making electrical contact with a copper electrode. 127
Figure 5-18: Picture of the electrochemical cell with a wire installed for micro-probe machining 128
Figure 5-19: Picture of the 2 filters and the pump 129
Figure 6-1: Flow chart of the PID tuning method (Nor, 2010). 132
Figure 6-2: Plot of a step response step used to setup the PID gains of motor 2. 133
Figure 6-3: Plot of a parabolic move used to setup the feed forward gains of motor 2. 133
Figure 6-4: Plot of the tool trajectory in the X, Y plane when the orbiting motion program is executed, the position is in motor units, corresponding to 2nm/unit. The radius of the orbiting movement was therefore 100µm. 135
Figure 6-5: Flowchart describing the program to setup the motors at the power up of the machine 136
Figure 6-6: Flow chart of the main control programme running on the µECM machine 138
Figure 6-7: Flowchart describing the program to set the initial IEG 139
Figure 6-8: Gap initialization, tool trajectory in Z axis 140
Figure 6-9: Block diagram representation of the fuzzy logic controller on Matlab 142

Figure 6-10: Example of trapezoidal membership function (Mathworks, 2014a) 143
Figure 6-11: Example of triangular membership function (Mathworks, 2014b) 143
Figure 6-12: Defined membership functions for the input variable ‘Current’ 144
Figure 6-13: Defined membership functions for the input variable ‘PSUStatus’ 144
Figure 6-14: The machining current setup tab in which the current parameters can be entered.... 145
Figure 6-15: Illustration of the adaptive feed rate algorithm 147
Figure 6-16: Graph and code illustrating the tool retraction followed by the repositioning to reset the IEG 150
Figure 6-17: Screenshot of the self-developed HMI of the µECM machine 151
Figure 6-18: Picture of the ‘PPMAC System Terminal’ tab of the HMI 152
Figure 6-19: Picture of the 'Controller Terminal' tab of the HMI 153
Figure 6-20: Picture of the 'A/D IOs' tab of the HMI 153
Figure 6-21: Screenshot of the ‘Motion’ tab of the HMI 154
Figure 6-22: Picture of the 'Machining Current Setup' tab of the HMI 154
Figure 6-23: Picture of the 'Motion Parameter Setup' tab of the HMI 155
Figure 6-24: Picture of the Spindle and Orbiting tab of the HMI 156
Figure 7-1: Pulse PSU mounting and connection to the PCB ring with spring probes 158
Figure 7-2: Electrochemical cell configuration used at Sonplas and the different dimensions of each element 158
Figure 7-3: Pictures of the holes machined, only the frequency and the pulse width were varied, to preserve the same duty cycle value (25%), electrolyte $NaNO3$. 159
Figure 7-4: Profile of hole 4 160
Figure 7-5: 1) 607µm ∅ (right hole); 2) 596µm ∅ (middle hole); 3) 505µm ∅ (left hole).......... 161
Figure 7-6: Profiles of the holes 1, 2 and 3 162
Figure 7-7: Current and position charts for each of the holes drilled. 163
Figure 7-8: Picture of a part being machined 164
Figure 7-9: Picture of holes drilled in gasoline injectors (chromium-based alloy) 164
Figure 7-10: Picture and profile of a hole machined in a fuel injector with the sidewalls of the tool non-insulated. 164
Figure 7-11: A case of extreme tool-electrode wear when machining at 12V 165
Figure 7-12: Machining result with the fuzzy logic control algorithm. Machining current and tool position (Z) plotted over time (150ms per count) 166
Figure 7-13: Picture of the workpiece after the electrochemical drilling process (taken with a TESA Visio) 168
Figure 7-14: Evolution of the current peak value during the machining process. Each point represents an average of 50 data points 168
Figure 7-15: Evolution of the tool position during the machining process 169

Figure 7-16: Hole 5 diameter: Top: 0.432mm, Bottom: 0.221mm 170
Figure 7-17: Hole 7 diameter: 0.472mm 170
Figure 7-18: Hole 9, diameter: 0.394mm 170
Figure 7-19: Picture of the hole nr. 9 and the tool-electrode of a diameter of 175µm orbiting with 50µm radius 170
Figure 7-20: Array used to determine which type of experimental array to use (Woolf, 2014) 172
Figure 7-21: Graph representing the evolution of the peak value of the current during machining time 172
Figure 7-22: Graph representing the evolution of the tool position during machining 173
Figure 7-23: Overall picture of the workpiece used for the experiment 174
Figure 7-24: Experiment 1 174
Figure 7-25: Experiment 4 174
Figure 7-26: Experiment 6 175
Figure 7-27: Experiment 8 175
Figure 7-28: Experiment 3: Hole entry Radius: 290µm 176
Figure 7-29: Experiment 3: Hole exit Radius: 223µm 176
Figure 7-30: Experiment 5: Hole entry Radius: 248µm 176
Figure 7-31: Experiment 5: Hole exit Radius: 208µm 176
Figure 7-32: Experiment 9: Hole entry 176
Figure 7-33: Experiment 9: Hole exit Radius: 185µm 176
Figure 7-34: Experiment 2: Hole entry Radius: 255µm 177
Figure 7-35: Experiment 2: Hole exit Radius: 189µm 177
Figure 7-36: Experiment 7: Hole entry Radius: 196µm 177
Figure 7-37: Experiment 7: Hole exit Radius: 200µm 177
Figure 7-38: Screenshot of the resulting workpiece shape after the simulations. 179
Figure 7-39: (a) Tool in the tool holder (b) Picture of the micro tip etched via Wire µECM (electrochemical turning), a $NaNO3$ salt layer can be observed along the tool surface (WC-Co alloy, electrolyte 0.5M $NaNO3$+ 0.1M $H2SO4$, pulse amplitude: -7.5 V, pulse duration: 50 ns, pulse period: 500ns, feed rate: 0.3µm/s, diameter: 95µm). 181
Figure 7-40: Picture of the hole fabricated by ECM with the WC-Co etched tool. (a) hole entrance, (b) hole exit (18NiCr6 alloy, depth: 1.1mm, hole entrance diameter: 517µm, hole exit diameter: 414µm, electrolyte 0.5M $NaNO3$+ 0.1M $H2SO4$, pulse amplitude: 8V, pulse duration: 250 ns, pulse period: 1 µs, feed rate: 0.3µm/s). 181
Figure 7-41: Graphs representing (a) the evolution of the current peak value of the pulses (in A) and (b) the evolution of the tool position (in mm) throughout the machining time (in s) 182

Figure 7-42: Oscilloscope screenshot of the measured pulses at the IEG during workpiece machining, 1MHz frequency, duty cycle of 25%, pulse amplitude of 8V and no offset during off-time 500ns/div. 182
Figure 7-43: Tool of the shape of a needle made by micro electrochemical turning. A non-machined tool-electrode of 170μm is placed next to it for size comparison. (WC-Co alloy, electrolyte 0.5M $NaNO3$+ 0.1M $H2SO4$, pulse amplitude: -7.5 V, pulse duration: 50 ns, pulse period: 500ns, feed rate: 0.3μm/s, diameter: 95μm) 183
Figure 7-44: Micro-tool made by micro electrochemical turning. (WC-Co alloy, electrolyte 0.5M $NaNO3$+ 0.1M $H2SO4$, pulse amplitude: -7.5 V, pulse duration: 50 ns, pulse period: 500ns, feed rate: 0.2μm/s, diameter of tip: 57μm, smallest diameter measured: 46μm)..................184
Figure 7-45: Shaft surface picture Ra = 120nm...184
Figure 7-46: (a) Micro-styli, diameter of tip: 45μm, smallest diameter measured: 32μm (b) Micro-shaft of 95μm diameter. (both made of WC-Co alloy with electrolyte 0.5M $NaNO3$+ 0.1M $H2SO4$, pulse amplitude: -7.5 V, pulse duration: 50 ns, pulse period: 500ns, feed rate: 0.2μm/s)..185

LIST OF TABLES

Table 3-1: Simulation parameters used to obtain the shape shown in figure 24............................ 82
Table 3-2: Machining parameters used for the simulations... 84
Table 4-1: Table summarizing the main characteristics of the MOSFET FDMS7578.................. 96
Table 4-2: Specs of the developed pulse PSU 105
Table 4-3: Description of the signals measured in Figure 4-24. 106
Table 5-1: µECM machine specifications 111
Table 5-2: Summary of the components used in the encoder system 115
Table 5-3: Table of the DIP switch configuration used to set the address of the Acc36UK 122
Table 5-4: Summary of the specifications of the direct PWM drive GPL052 (Delta Tau Data Systems, 2006)...124
Table 7-1: The different pulse PSU parameters and their respective range of values...................167
Table 7-2: The different pulse PSU parameters and their respective range of values...................171
Table 7-3: Selected parameter values for the experiment 171
Table 7-4: L9 Table of experiments to evaluate the influence of frequency 172
Table 7-5: Table of the parameters considered as non-optimal for the drilling of 18NiCr6 under the test conditions 175
Table 7-6: Table of the parameters considered as optimal for the drilling of 18NiCr6 under the test conditions..175
Table 7-7: Table of the parameters considered as medium for the drilling of 18NiCr6 under the test conditions..177
Table 7-8: Comparison of the material removal rates (MRR) between the process simulations and the actual experiments 179

LIST OF ABBREVIATIONS

ANFIS – Adaptive Neuro Fuzzy Inference System

BEDG - Block Electrical Discharge Grinding

BEM - Boundary Elements method

CAD – Computer Aided Design

CAM – Computer Aided Manufacturing

CLD – Cutter Location Data

CMM – Coordinate Measuring Machines

CMOS – Complementary metal–oxide–semiconductor

CNC – Computer Numerical Control

CVD – Chemical vapour deposition

DAC – Digital to Analogue Converter

DADJ – Duty-cycle adjust input of the MAX038

DC – Direct Current

ECM – Electrochemical Machining

EDL – Electrical Double Layer

EDM – Electro-Discharge Machining

EMM or μECM – Electrochemical Micro Machining

FADJ – Frequency adjust input of the MAX038

FDM – Finite Difference Method

FEM – Finite element method

FET – Field Effect Transistor

FLC – Fuzzy Logic Controller

GaN – Gallium Nitride

GaN FET – Gallium Nitride Field Effect Transistor

GND – Electrical ground

HMI – Human Machine Interface

IC – Integrated circuit

IDE – Integrated Development Environment

IEG – Inter-electrode gap

IIN – Current Input for frequency control of the MAX038

LSB – Least significant bit

MCU – Microcontroller Unit

MEMS – Micro Electro-Mechanical Systems

MIDEMMA – Minimizing Defects in Micro-Manufacturing Applications

MISO – Master in Slave Out

MOSFET – Metal Oxide Semiconductor Field Effect Transistor

MOSI – Master Out Slave In

OCP – Over Current Protection

MRR – Material Removal Rate

PCB – Printed circuit board

PECM – Pulsed Electrochemical Machining

PID – Proportional-Integral-Derivative

PLC – Programmable Logic Controller (soft)

PMAC – Programmable Multi Axis Controller

PPMAC – Power Programmable Multi Axis Controller

PSU – Power Supply Unit

PTFE – Polytetrafluoroethylene

PWM – Pulse Width Modulation

RC – Resistor-Capacitor

RF – Radio Frequency

SMPS – Switch-Mode Power supply

SPI – Serial Peripheral Interface

STEM – Shaped Tube Electrolytic Machining

TTL – Transistor-Transistor Logic

USB – Universal Serial Bus

VCO – Voltage-Controlled Oscillator

WEDG – Wire Electro-Discharge Grinding

LIST OF SYMBOLS

Roman

A: Atomic weight of the material (amu)

A_c: Cross sectional area of the tool-electrode (m²)

$a_{Fe^{2+}}$: Activity of the ion Fe^{2+} (no units)

a_{OH^-}: Activity of the ion OH^- (no units)

a_{H^+} : Activity of the ion H^+ (no units)

$a_{Fe(OH)_2}$: Activity of iron hydroxyde (no units)

$c = \frac{K_v}{r}$: Constant used to symplify the expression of the IEG change

$c_{Fe^{2+}}$: Concentration of ion Fe^{2+} (mol/L)

C: Capacitance of a capacitor (F)

C_{DL}: Overall electrical double layer capacitance (F)

C_F: Capacitance setting the nominal frequency of the MAX038's oscillator (F)

C_{GS}: MOSFET Gate-Source Capacitance (F)

C_{iss}: MOSFET input capacitance

C1: MOSFET parasitic capacitance (F)

C2: MOSFET compensated parasitic capacitance (F)

E: Electrical field in (V/m)

E_a: Overpotential of the anode (V)

E_{a0} : Stationary value of the over-potential (V)

$E_{act.}$: Potential required to activate the dissolution reaction (V)

E_c: Overpotential of the cathode (V)

F: Faraday's constant (96500C)

F_0: Nominal frequency of the MAX038's output signal (Hz)

F1: Original MOSFET Ringing frequency (Hz)

F2: Second MOSFET Ringing frequency (Hz)

f_{cutoff}: Cut-off frequency of the RC network created by the electrolyte resistance and C_{DL} (Hz)

H: Gain of the lowpass filter created by the electrolyte resistance and C_{DL} (no unit)

H: Width of the inter-electrode gap (IEG)

h_{ij}: Gap between a point (X_i, Y_i) of the workpiece surface and a point (X_j, Y_j) of the tool surface (m)

h_f: Width of the equilibrium inter-electrode gap (m)

h_0: Width of the inter-electrode gap at $t = 0$ (initial IEG) (m)

I: Total current passing through the system (A)

i_a: Current density at the anode surface (A/m²)

i_c: Current density at the cathode surface (A/m²)

I_L: Current passing through the load (A)

J: Current density defined as $J = \kappa_0 \frac{\partial E}{\partial x}_{x=h} = \frac{I}{A_c}$ (A/m²)

$k = \frac{A}{Fz}$: constant and it is specific to the material

Kaff: Acceleration feed forward Gain of the servo control algorithm

Kd: Derivative Gain of the servo control algorithm

Ki: Integral Gain of the servo control algorithm

$K_v = \eta \frac{k}{\rho}$: Coefficient of electrochemical machinability

K_{valloy}: Coefficient of electrochemical machinability for alloys

Kvff: Velocity feed forward Gain of the servo control algorithm

Kp: Proportional Gain of the servo control algorithm

L: Cathode feed distance (m)

L1: MOSFET parasitic inductance (H)

m: Mass of material (kg)

n_d: Duty cycle of the pulses defined as $n_d = \frac{T_{on}}{T_{on}+T_{off}}$

n: Number of electrons (no units)

Q: Charge $Q = It$ in ($A.s$ or C)

R: Resistance of the gap (Ohm)

R_{AB}: Nominal resistance of the potentiometer

R_{cable}: Resistance of the cable connecting the PSU to the IEG (Ohm)

$R_{DS(ON)}$: MOSFET ON resistance (Ohm)

R_e: Resistance of the eletrolyte (Ohm)

R_{dla}: Resistance of the electrical double layer at anode (Ohm)

R_{dlc}: Resistance of the electrical double layer at cathode (Ohm)

R_{DL}: Resistance of the electrical double layer (Ohm)

R_{GATE}: MOSFET Gate resistance (external) (Ohm)

$R_{G,I}$: MOSFET Internal Gate resistance (Ohm)

R_{POT}: Resistance of the potentionmeter used to setup the MAX038 (Ohm)

R_S: Sensing resistor (Ohm)

R_{snub}: MOSFET snubber resistor (Ohm)

R_W: Resistance of the wiper of the potentiometer (Ohm)

R_{WA}: Resistance across the wiper and the A terminal (Ohm)

R_{WB}: Resistance across the wiper and the B terminal (Ohm)

r_0: The resistivity in ($Ohm.m$)

R_g: Gas constant ($J/(K.mol)$)

S: Area of the electrode (m^2)

T: Temperature of the electrolyte (K)

T_{tot}: Total time of machining including the on-times and off-times (s)

t_0: Time at the beginning of a pulse (s)

t_p: Time at the end of a pulse (s)

t_{off}: Pulse off-time (s)

t_{on}: Pulse on-time (s)

t: Time (s)

U_0: Amplitude of the pulses (V)

U_{0-in}: Amplitude of the pulse at the input of the lowpass filter (V)

U_{0-out}: Amplitude of the pulse at the output of the lowpass filter (V)

U: $U_0 - \Delta U$: potential applied to the inter-electrode gap (V)

V: Volume of dissolved material (m^3)

V_{DADJ}: Voltage used to adjust the duty cycle of the output of the MAX038 (V)

V_f: Cathode feed rate (m/s)

V_{GS}: MOSFET Gate-Source voltage (V)

V_S: Differential voltage amplified by the instrumentation amplifier (V)

V_{LOAD}: Voltage passing through the load (V)

V_{OUT}: Output voltage of the instrumentation amplifier (V)

X_L: Inductive reactance of the cabling $X_L(f) = 2\pi fL$ (Ohm)

Y_i: Y position of a point 'i' of the workpiece surface (m)

z: Valency of the workpiece material (no units)

Z: Impedance of the cabling (Ohm)

Z_{sys}: Impedance of the overall system (Ohm)

Greek

β: transfer coefficient used in the Tafel Equation

ΔT_p: Rise in temperature during 1 pulse (K)

ΔU: $E_a - E_c$ over-voltage (V)

Δh: Minimum step distance of the linear actuator (m)

κ: Conductivity of the electrolyte in (S/m)

κ_0: Initial conductivity of the electrolyte (S/m)

$\eta = \frac{current\ responsible\ for\ metal\ dissolution}{total\ current\ (I)} \times 100$: Current efficiency (in %)

ρ_e: Density of the electrolyte (kg/m^3)

ρ: Density of the material of the anode (kg/m^3)

τ: Charging constant of the electrical double layer (s)

Chapter 1: INTRODUCTION

1.1. From ECM to µECM

Electrochemical micromachining is a non-conventional manufacturing process used as an alternative to conventional mechanical machining and non-conventional manufacturing processes for electrically conductive materials. Electrochemical machining (ECM) is based on the process of electrolysis. It is very popular for material volume removal and shaping the anode using DC current with cathode electrodes of various shapes. The anode (workpiece) and the cathode (tool-electrode) are both submerged in a constantly renewed electrolytic solution and a voltage is applied. The resulting current passes through the system and a chemical reaction takes place. Anodic dissolution occurs, material is removed and the workpiece is shaped according to the features of the cathode (McGeough, 1974).

Recent developments in this area aim at the use of much smaller electrodes with a smaller inter-electrode gap (IEG) size for machining complex features. This requires improving severely the resolution of the anodic dissolution and respectively the achieved accuracy. These developments led to the appearance of a new area of ECM machining technology defined as 'Pulsed Electrochemical Machining' (PECM) (Wei, 1994; Rajurkar, Kozak, Wei and McGeough, 1993; Rajurkar, Wei, Kozak and McGeough, 1995). PECM uses voltage pulses instead of DC voltage in order to enable a better feature resolution (Rajurkar et al., 1993).

This new technology can nowadays be applied at a micrometre scale and is called 'Pulse Electrochemical Micromachining' (also referred to as µECM, µPECM, EMM, PECMM, PEMM) (Kozak, Rajurkar and Makkar, 2004b; a; Zhang, Zhu, Qu and Wang, 2007; Kamaraj and Sundaram, 2013). In most papers, the frequency and the pulse duration are respectively much higher and much shorter than in initial PECM (Cagnon et al., 2003; Schuster, Kirchner, Allongue and Ertl, 2000).

1.2. Justification, Aims and Objectives

1.2.1. Justification

Products are becoming smaller, lighter and more compact. Furthermore, standards and quality requirements are rising. Micro-machining is finding more applications in many products in the Aerospace, Automotive, Medical Device, Jewellery and Consumables industries. In order to stay competitive manufacturers have to produce parts that are less pricey, have better surface finishes and meet ever increasing product quality requirements. ECM is one of the processes gaining wider acceptance in this sector to machine parts more accurately.

The micro-machining sector is a very competitive sector, with many companies involved in newly developed technologies and trying to make it into the market place. Success in this market is difficult and requires a good, stable and robust product that an end-user can install in their shop floor and easily configure to rapidly start manufacturing. However in many cases the new products are still at a prototype stage and are relatively expensive due to the high development costs and at the same time there are many competing processes in the micro-machining sector.

Electro Chemical Machining (ECM) has been neglected as a micro-capable technology for many years. The process was used mainly for sinking processes, deburring, and was developed to work in the aerospace industry working on turbine blades in the form of Shaped Tube Electrolytic Machining (STEM) drilling. The major advantages of the process are the high removal rate (energy efficiency), simplicity of the process, there is also no associated electrode tool wear and there is no defective layer left after machining. The latter makes this process extremely desirable for aerospace, medical, MEMS and many other applications. In addition there is no debris left from the process which means that no post-processing of the workpiece is required. In the recent years Pulsed ECM has appeared where the removal of material in a specific area has become more controllable. However, the boundaries of the process are also not well known yet. This process, unlike mechanical processes, lies in the grey area of chemistry, electric pulses and mechanical structure of the machine tool capabilities.

With rising needs for miniaturisation, techniques for machining of components to achieve dimensions and tolerances in the order of 1μm and 10nm, with associated surface roughness

as fine as Ra 1nm are increasingly demanded. To that end, processes such as electrochemical (ECM) and electro-discharge (EDM) machining that have already been successfully employed in the aerospace, car, medical and other industries, for shaping, cutting and finishing, especially of hard alloys, are now receiving fresh attention for the fabrication of micro-components.

The ECM process needs to compete with these and it has an advantage over some of the processes in that there is no tool wear, material hardness is not an issue. The quality of the surface finish that can be achieved is very high; there is no re-cast layer - which can be obtained from EDM and laser machining. However there are issues such as the electrolyte that is used which can lead to oxidation of the part if it isn't protected or cleaned immediately after processing, the stability of the process which can lead to poor quality, and the end-users knowledge of the technology.

There are some ECM systems available on the market that can match the quality of some of the micro manufacturing processes however they are prohibitively expensive, typically between €350,000 and €500,000 for a granite-based machine and they are normally not production capable. Therefore it is important to promote the advantages of ECM by ensuring that a machine can be developed that can achieve the accuracy demanded by the market, that can work in a production environment and can do so consistently. The machine should be at a price point to compete with the other technologies in that space and to prove the quality of the process through the manufacture of µm accuracy parts and to do this consistently.

It is also important to educate the market about the ECM process and to show the advances that have been made in the process to bring it to the point where it is able to compete with the other technologies.

In spite of the accumulated knowledge and number of attempts to build test demonstrators there is still no commercially available system encompassing all the knowledge and offering new micro/nanotechnology with revolutionary capabilities. This is mainly due to the fact that the work on Micro ECM to date has been sporadic and not well organized.

1.2.2. Aims

The aim of this research is to develop an innovative Micro ECM (µECM) machine for the automotive, aerospace, metrology and medical sectors.

The ultimate goal is directed to the elaboration of an automated machining process which could then be used as a stable base for process optimisation and machining experiments with new materials and electrolytes. This work also aims to provide the scientific community with contributions to knowledge in the field of process modelling, interelectrode gap control strategies, pulse power supply design and experimental process analysis.

The relevant research subject, rationale and justification are presented in Chapter 2, 'Introduction', formulating the research gaps identified in the literature review.

1.2.3. Objectives

The subsequent particular objectives of this work are described below:

(1) To analytically review the state of the art technologies and methods developed in µECM in order to identify research gaps.

(2) To gain a solid knowledge of the µECM process and its theoretical behaviour by developing a simulation programme based on an extended mathematical model of pulsed ECM taking into account the electrical double layer effect.

(3) To develop a pulse power supply unit (PSU) that can be programmed and generate 50ns pulses at a frequency of 5MHz, while offering different pulse shapes and featuring over current protection.

(4) To develop an innovative control strategy for the process in order to achieve the best machining performance, while protecting the tool.

(5) To develop an intelligent Human Machine Interface (HMI) using fuzzy logic and data analytics to assist the operators in setting up, controlling and monitoring the µECM process.

(6) To validate the machine capabilities and applications through machining experiments including:

- Drilling hole in18NiCr6 disks
- Fabricating micro styli and micro shafts
- Fabricating micro needles

1.3. Methodology

This section presents the methods used to achieve the different objectives that have been previously listed.

1.3.1. Identification of gaps in research and key requirements for μECM

In order to find research gaps and identify key requirements, design considerations and specifications for an innovative μECM machine, a background review was necessary. This background review looked at the different aspects related to μECM and classified them into groups. In the case of μECM, these groups were:

- The design requirements for the mechanical structure and actuators (spindle and slides).
- Machining process: The work reported on the machining process, monitoring and control, a review of the existing ECM and μECM setups and the machining strategies used so far.
- Pulse PSU: The existing pulse power supplies developed for μECM, their weaknesses and which parts needed further research.
- The tooling used in μECM and the different methods used for electrode preparation.
- The metrology concepts used in μECM, including the process setup and gap initialization procedures.
- The reported ways to handle the electrode, the workpiece and the electrolyte.

From this review, the following specifications for the development of the machine were established:

(a) The mechanical structure had to be made out of material with a very low thermal expansion coefficient and high damping characteristics, such as granite. A gantry configuration was recommended, where the X axis supported the Z axis.

(b) Regarding the slides, air-bearings seemed to offer superior performance to ball-screw system because they provided frictionless motion and high dynamic response (more details are given in section 1.3.4). Combined with a direct-drive DC brushless linear motor setup and a high-resolution position feedback system,

it would allow the machine to provide sufficient stiffness for precision-machining applications.

(c) The spindle must allow the orientation of the tool to be precisely controlled, so a precision stepper motor was seen as a suitable actuation system. It was also read in the literature review that the tool would not need to be spinned at very high rpm, which reinforced the choice for a stepper motor. Regarding the connection of the pulse PSU to the spinning tool-electrode, two solutions were identified to deliver the high frequency pulses to the IEG: 1) the use of a slip ring in a liquid metal bath such as mercury or galinstan 2) the use of a ring with microfiber carbon brushes.

(d) The control of the µECM process would require a custom-made programme. Standard control algorithm such as PID or state-space representation were not adapted for this purpose, so the combination of state machine algorithm with a fuzzy logic controller was chosen. An open-architecture controller was chosen to implement this control strategy.

(e) An intelligent human machine interface would have to be developed to monitor the current and tool position during the machining process. It also had to be user friendly and guide the operator when setting up the machining parameters.

(f) The machine will require a custom-made pulse PSU which must be programmable, generate different pulse shape, reverse pulse polarity, and provide an ultrafast over current protection (more details are given in section 1.3.3).

(g) The tool holder shall allow the clamping of tool-electrodes with very small diameters (typically 170µm). Furthermore, since the tool is very brittle because of its small size, a highly reactive tool protection system must be integrated to the machining process. It was found that the manual handling of the cathode was a very delicate task and should be done only when absolutely necessary, so the on-line tool preparation should be preferred to the off-line one whenever possible.

(h) In µECM, the electrolyte can be highly corrosive and present health hazards, therefore the piping and the pump had to be resistant to corrosion.

1.3.2. Development of a simulation programme to investigate the μECM process behaviour

In order to assess the controllability of the interelectrode gap, the PECM and ECM process models from Wei (1994) and Hocheng et al. (2003) were extended. The simulation programme allowed to observe the influence of the electrical double layer on the inter-electrode gap and the influence of the machining parameters on the process performance. The first simulations were 'open loop' which meant the behaviour of the process was observed without the tool being moved to maintain the gap. Then a 'closed loop' simulation was performed to define the most appropriate control strategy to be employed.

To assess the reliability of the model, the simulation results were compared with the results from the experiment.

This simulation programme was then used to provide a theoretical validation for the machining parameter and the setup of the control system.

1.3.3. Development of a novel pulse PSU architecture for the needs of μECM

Requirements for the pulse PSU were identified in the literature review and it was concluded that the μECM process needed a specially designed power supply which must be programmable and able to supply ultra-short pulses with a possibility to change the shapes and polarity of the voltage pulses. Since short-circuits can occur during the process, an ultra-fast short-circuit protection has been developed.

The architectures of existing pulse PSUs was thoroughly studied and critically reviewed in order to develop an innovative pulse PSU providing new capabilities with respect to the existing devices.

The following requirements guided the design and implementation of this novel pulse PSU:

(a) Pulse shape and characteristics can be changed during the machining process
(b) Pulse durations ranging from 50ns to 1ms
(c) Pulse frequency ranging from 1kHz to 5MHz
(d) The pulse amplitude can range from 0V to 15V
(e) The pulse PSU must be able to supply current pulses up to 5A.

(f) The pulse PSU must have an ultrafast Over Current Protection to protect the tool in case short circuits occur in the inter-electrode gap.

(g) The pulse PSU must be able to reverse the polarity of the pulses to machine the tool-electrode without changing the cabling.

(h) The pulse PSU must have a small footprint to be mounted close to the tool on the Z axis in order to reduce the inductance of the cabling.

The PSU was designed in 3 different boards – one for each subsystem – allowing an easy and flexible prototyping process. Indeed, this modular strategy enabled the replacement of a defective or under-performing module without having to redesign and reassemble the rest of the PSU.

1.3.4. Component selection and machine system integration

The machine integration was performed to meet the requirements identified in the literature review:

(a) Mechanical structure: Granite was used for the base of the machine and for the slides. A gantry configuration was used, where the X axis supported the Z axis.

(b) Regarding the slides, precision air-bearings were used. DC brushless linear motors from Anorad were used as actuators and were controlled thanks to direct drive PWM amplifiers from Delta Tau. A 2-nm resolution position feedback system from Renishaw was interfaced with an ACC24E-2 motion control card. The tuning of the servo control guaranteed a maximum following error below 0.1µm on all axes.

(c) A purpose built spindle using precision bearings was used and the transmission of the pulses to the rotating tool-electrode was performed thanks to a ring with microfiber carbon brushes. This type of ring is normally used for shaft grounding and bearing protection, and is able to handle high current at high frequencies. The use of mercury slip ring, which was seen as the other solution, was seen as a potential health hazard.

A stepper motor was chosen to actuate the spindle and allow precise tool orientation. The stepper motor on the spindle is the model ST4218L1806-LC-NEU from Nanotec which can be controlled using a SMCI33-1 drive. The step angle of the motor is 1.8 degrees with an accuracy of +/- 5%. The drive communicates with the HMI using a USB port.

(d) The controller chosen for the machine is a Delta Tau Power PMAC in a UMAC rack. The Power PMAC was interfaced with other boards from Delta Tau such as an Acc24E-2 motion control board and an Acc65-E digital input/output board. A control algorithm consisting of a fuzzy logic control system embedded in state machine was written in C and downloaded to the controller and machining trials were performed.

(e) An intelligent human machine interface was developed using LabWindows/CVI and successfully interfaced with the Power PMAC motion controller (more details are given in section 1.3.6).

(f) A purpose-built tool holder was developed to clamp the tools with diameters down to 150µm. The preparation of the tool could be done on-line using the developed pulse PSU.

(g) The electrolyte circuit was made out of chemical resistant pipes, a chemically resistant pump was chosen, PTFE (polytetrafluoroethylene) and Polyether ether ketone (PEEK) components were used whenever possible. Two filter were installed in line in order to clean the electrolyte from the by-products of the machining process (sludge).

1.3.5. Development of an innovative control strategy for the µECM process

Considering that the current can be used as a sensing parameter to maintain the interelectrode gap, the fuzzy logic controller would monitor the machining current and adjust the tool position to maintain the gap constant.

In the experiments it was observed that the fuzzy logic controller needed to have his rules constantly updated, because the optimal machining current would change according to the depth of the hole being drilled when the sidewalls of the tool-electrode were not electrically insulated.

It was therefore decided to develop a more aggressive algorithm which would find the optimal tool feed-rate by doing a linear interpolation using the recorded time and position at which short-circuits occurred.

The control routine that would retract the tool in case of short-circuit could be customized with parameters set by the user such as the initial tool retraction distance and the dimension at which the gap had to be reset.

1.3.6. Development of an intelligent HMI

Because of software driver issues, the pulse PSU and the spindle drive could not be directly interfaced with the Power PMAC controller. Therefore, the HMI was fully integrated in the control process and would communicate with the pulse PSU and the spindle when the controller requested it.

The HMI communicated with the Power PMAC using the Telnet protocol. The HMI would assist the operator to configure the fuzzy logic controller by suggesting some starting values based on the machining current measured by the Power PMAC. It would also feature built-in error checking functions in order to prevent the tool from being damaged by untrained operators.

1.3.7. Experimental validation

The experimental validation consisted in using the machine to drill holes in materials used in the automotive industry such as 18NiCr6 and other chromium-based alloys.

The role of the drilling experiments was also to validate the simulated results with the experimental one. In order to compare the results, the materials removal rate obtained in simulations was compared to the real model.

To demonstrate the machine capabilities, holes have been machined with an orbiting tool.

Moreover, tool-fabrication followed by workpiece machining was performed the possibility to reverse the pulse polarity without changing the cabling.

Finally, micro-shafts, micro-tools and micro-needles have been machined to illustrate potential applications in the medical and metrology sectors.

1.4. Description of chapters

This section is an executive summary describing the content of the different chapters. This thesis follows logically the development of the machine.

1. The relevant research subject, rationale and justification are presented in 'Chapter 2: Literature Review', formulating the problematic areas identified in the literature. This topical review provides with a critical analysis of the progress achieved in the field of ECM and µECM so far. Information about essential concepts of the machine such as: process monitoring and control, machining strategies, pulse power supply design, electrode and workpiece preparation, machine setup and electrolyte influence are also evaluated.
2. 'Chapter 3: µECM process modelling and simulation' highlights the necessary in-depth theoretical calculation to simulate the behaviour of the µECM process. It starts with an overview of the fundamental concepts in electrochemical machining and micromachining and explains the importance of the electrical double layer (EDL) effect in µECM.
3. One of the core components of the machine is the pulse power supply unit (PSU) of which the detailed development is described in 'Chapter 4: An innovative pulse power supply unit for µECM'. Three prototypes have been made and their respective characteristics and working principles will be explained.
4. The assembly of the machine and its setup is an essential objective in this project. 'Chapter 5: Machine system integration' describes – as its title suggests – the development and assembly of the different machine subsystems. This part therefore aims to study the main components of the machine such as the X, Y and Z axes, the electrical cabinet, the spindle, the machining cell and the electrolyte circuitry.
5. Once the entire machine is assembled, the control software has to be developed and implemented. 'Chapter 6: Process control and supervision' presents in a logical order the development of the software running on the machine. This chapter describes the method used for tuning the position control algorithms of the X, Y and Z motors as well as the different workflows of each program. The control logic is explained in detail and the Human Machine Interface (HMI) is also presented.
6. The last objective is to gain a deeper understanding of what happens in the machining processes when nanosecond pulses are used. The machining experiments and their results are discussed in 'Chapter 7: Experimental work and results'. In this chapter machining experiments with orbiting tool and different materials are performed and analysed.

7. The last part of this thesis is a discussion of the work achieved and the results from the different experiments. This part also discussed the different applications that this machine can be used for as well as the future work.

1.5. Key contributions

As a result of this work, a novel µECM machine was developed. This machine is a first step towards the development of the µECM machine for commercial industrial application. Indeed, the machining tests performed on automotive parts as well as the fabrication of micro-tools and probes suggest the use of µECM machines for specific applications in the automotive, micro-machining and metrology (coordinate-measuring machines) sectors. This work has been funded by the European Commission in the frame of 2 European Research projects: 1) The Micro-ECM project and 2) The 'Minimizing Defects in Micro-Manufacturing Applications' (MIDEMMA) project.

The development of this machine is associated by the following contributions to knowledge in the µECM sector:

1) An analytical and thorough background research showing that the problems limiting full scale ECM are the same as those being highlighted for µECM (inter-electrode gap control, electrolyte and tool handling, etc...). This work identified the research challenges that the µECM and ECM sectors are facing today and by identifying the gaps where further research is needed. This research was published in the paper 'Recent developments and research challenges in electrochemical micromachining (µECM)' published in The International Journal of Advanced Manufacturing Technology (Spieser and Ivanov, 2013).
2) The µECM process modelling and simulation provide the µECM sector with a greater understanding of the process and is a step towards the development of an on-the-machine simulation step before machining. Key concepts introduced by (Hocheng et al., 2003) were extended to consider the electrical double layer effect and its influence was modelled using LabVIEW. The computation time of the programme does not depend on the frequency of the pulsed voltage and is therefore time efficient. The results obtained from the simulation illustrate the electrical double layer effect and are similar to the experimental results.

3) The research and development of a pulse power supply unit (PSU) for µECM were extensively reviewed and a novel pulse PSU architecture with ultra-fast over current protection was proposed. The PSU provides not only tens nanosecond order pulse duration, but also plus and minus biases as well as a polarity switching functionality. It fulfils the requirements of tool preparation with reversed ECM on the machine. The careful design, integration with MCU and implementation are of good references to the researchers and engineers who work in the µECM sector. This research was accepted for publication in the paper 'Design of a Pulse Power Supply Unit for Micro ECM' in The International Journal of Advanced Manufacturing Technology (Spieser and Ivanov, 2014a).
4) The machine configuration and PSU integration enabled an innovative and industry-capable machining strategy consisting of a 2-step sequential method: a fully automated on-line tool preparation followed by workpiece machining. Encoders with 2nm resolution enable moves with outstanding precision compared to machines currently found on the market, with a following error during motion. This research was accepted for publication in the paper 'Design of an Electrochemical Micromachining Machine' in The International Journal of Advanced Manufacturing Technology (Spieser and Ivanov, 2014b).
5) Two innovative inter-electrode gap (IEG) control strategies were presented. Both of these control approaches required the use of the developed pulse PSU featuring an ultra-fast Over Current Protection (OCP):
   i. The first control strategy is the use of a fuzzy logic controller to adjust the IEG according to a desired machining current. The use of this approach for the ECM processed was pointed out by Labib et al. (Labib, Keasberry, Atkinson and Frost, 2011) who highlighted the necessity for the controller to have decision making capabilities. This strategy has been adapted for the needs of µECM.

      The main findings resulting from the machining trials using this control strategy were:

      - The occurrence of sparking is efficiently prevented when using fuzzy logic control (FLC)
      - There is a need to constantly update the rules to change the targeted machining current when drilling with a tool-electrode of which the sidewalls are not insulated.

ii. The second control strategy consists in the use of an adaptive machining algorithm decreasing the tool-electrode feed rate according to the times and positions at which short circuits are detected. When drilling holes, the Z position of the tool and the machining time are stored in an array inside the motion controller and are used to calculate the material removal rate in the Z direction. A special algorithm filters out the short circuits which are not representative of the machining conditions in order to supply the controller with reliable data.

    The main findings resulting from the machining trials using this control strategy were:

    - The occurrence of sparking is efficiently prevented when the optimum tool-electrode feed rate in reached.
    - There is no machining underperformance linked to the tool feed rate, resulting in a more efficient machining process.

6) The experimental work described µECM drilling trials in 18NiCr6 alloys, which were never published before. The fabrication of micro-tools in tungsten carbide using wire µECM complements the rare literature describing this process. Results suggest that µECM provides an alternative solution for fabricating micro-probes and micro-tools.

Chapter 2: LITERATURE REVIEW

2.1. Introduction

μECM is being developed to meet the increasing demand driven by progress made in aerospace (aero-engine blades (Li and Ji, 2009) and gas turbine blade cooling system (Wang, Zhu, Qu and Zhang, 2007)), microelectronics (Datta and Landolt, 2000), automotive (requirement for smaller fuel injection nozzles in combustion engines), electronics (miniaturization of components), medical and biomedical fields (Kamaraj, Sundaram and Mathew, 2013; Lu and Leng, 2005; Bhattacharyya, Doloi and Sridhar, 2001). It enables the machining of micro-size features with high accuracy and high aspect ratio in materials with high hardness and stiffness (or in the materials that are very hard to machine conventionally because they are very brittle such as Indium Antimonite (InSb)).

This technique exploits the capacitive properties of the electrical double layer (EDL) at the electrode/electrolyte interfaces: it has been demonstrated that the electrical model of the electrochemical cell is a RC circuit (Schuster et al., 2000; Schuster, 2007; Schuster and Kirchner, 2004; Trimmer, Hudson, Kock and Schuster, 2003; Kock, Kirchner and Schuster, 2003). The charging constant ($\tau = RC_{DL}$, where C_{DL} is the overall capacitance of the cell and R is the electrolyte resistance) of the EDL depends on the distance between the tool and the workpiece (which actually corresponds to the charging current path): the further the tool is from the workpiece surface, the longer the charging time of the EDL will be. By using this property, the localisation of the material removal can be controlled very accurately by setting the pulse duration according to the charging time of the EDL.

This technology brings a new challenge to the research teams worldwide and it became a rapidly growing area because of the industrial interest and the attractive fields of application of the new μECM technology. However, the current state-of-the-art in electrochemical machining shows that further research is needed: the μECM process is very complex and requires knowledge in chemical, electrical, thermal, hydrodynamic phenomena and process control.

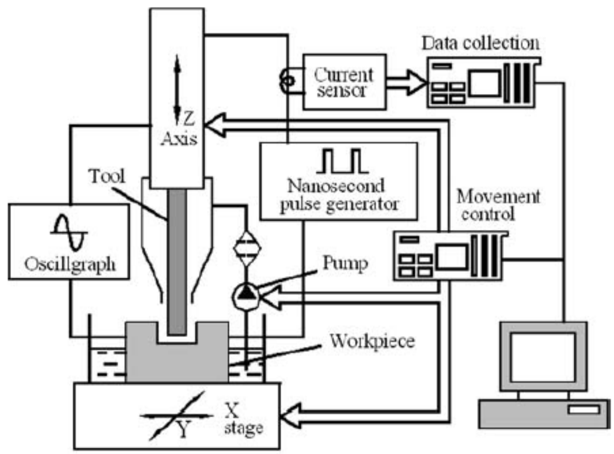

Figure 2-1: Schematic diagram of a μECM system (Zhang et al., 2007)

The last literature reviews were conducted several years ago (Bhattacharyya, Malapati and Munda, 2004; Landolt, Chauvy and Zinger, 2003; Rajurkar et al., 2006) and the progress that has been made to date redefines the new challenges the μECM process development is now facing.

In the schematic below (Figure 2-2) are given the identified problematic areas of the μECM process which will be discussed in this work as seen by the author.

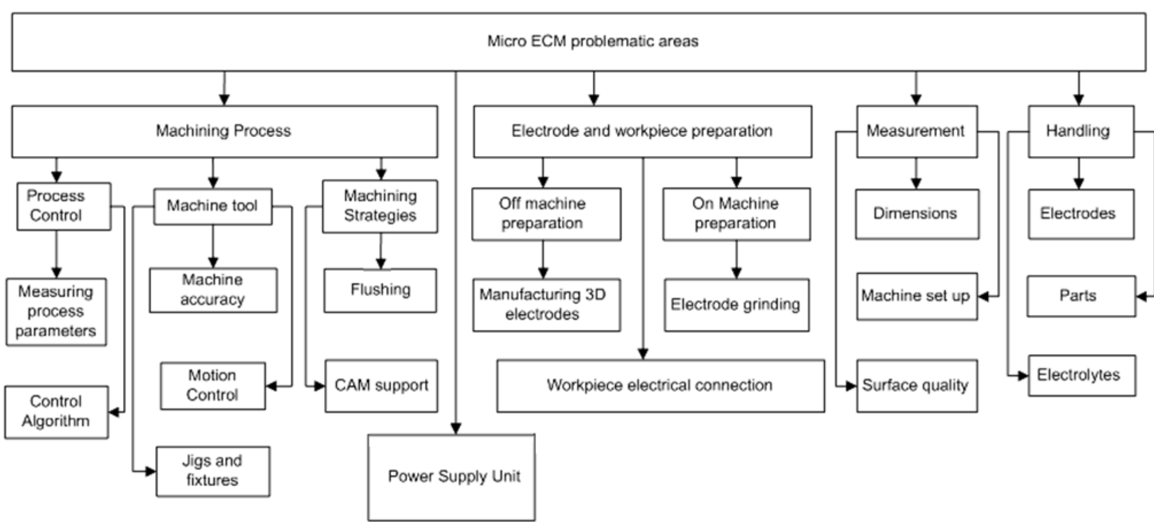

Figure 2-2: Diagram representing the Micro ECM problematic areas

2.2. ECM Fundamentals

2.2.1. Basic ECM setup

In order to be able to perform electrochemical machining, the tool (cathode) and the workpiece have to be made of conductive materials. The voltage applied on the tool-workpiece system is relatively low (0-20V) whereas the machining current is high (. During the machining process, the gap between the anode and the cathode has to be maintained in order to increase the process efficiency. Typically, sodium chloride ($NaCl$) water solution is used as the electrolyte for the ECM process. However, sodium nitrate ($NaNO_3$) can also be used (McGeough, 1974; Kozak, Rajurkar and Makkar, 2004b).
A schematic diagram of an electrochemical drilling unit is presented in Figure 2-3.

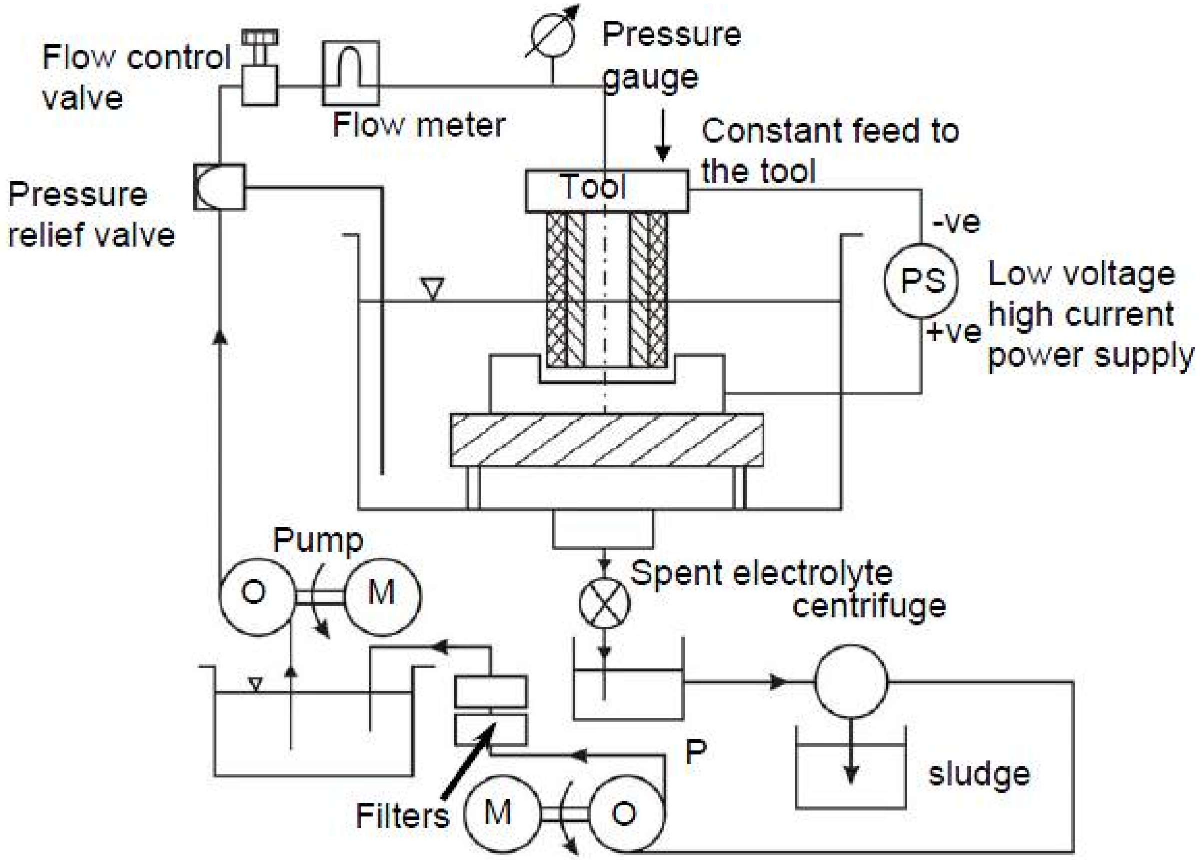

Figure 2-3: Schematic diagram of an electrochemical drilling unit (IIT Kharagpur, 2014)

An ideal model of ECM encompasses the following assumptions (Mukherjee, Kumar and Srivastava, 2007):

(a) *'Ohm's law holds the entire gap up to the surfaces of the electrodes;*

(b) The electrical conductivity of the electrolyte in the remains constant in both time and space

(c) At each electrode, the potential remains the same over the entire surface during the machining process

(d) The current efficiency of the anodic dissolution of the metal is the same at any point on the surface of the work piece'

2.2.2. The chemical reaction

In this particular process, the electrolyte employed for the ECM reaction is a sodium chloride ($NaCl$) aqueous solution.

$$NaCl \rightarrow Na^{+} + Cl^{-} \text{ and } H_2O \rightarrow H^{+} + OH^{-} \quad (2\text{-}1)$$

The H^{+} ions evolve to the cathode (tool-electrode) to gain 2 electrons, creating Hydrogen:

$$2H^{+} + 2e^{-} = H_2 \quad (2\text{-}2)$$

At the anode (workpiece) two reactions can be observed. The material of the workpiece (Fe^{3+} and Fe^{2+}) is removed and takes part into the reaction: iron hydroxide ($Fe(OH)_3/Fe(OH)_2$) is created:

$$Fe^{3+} + 3OH^{-} = Fe(OH)_3 \text{ and } Fe^{2+} + 2OH^{-} = Fe(OH)_2 \quad (2\text{-}3)$$

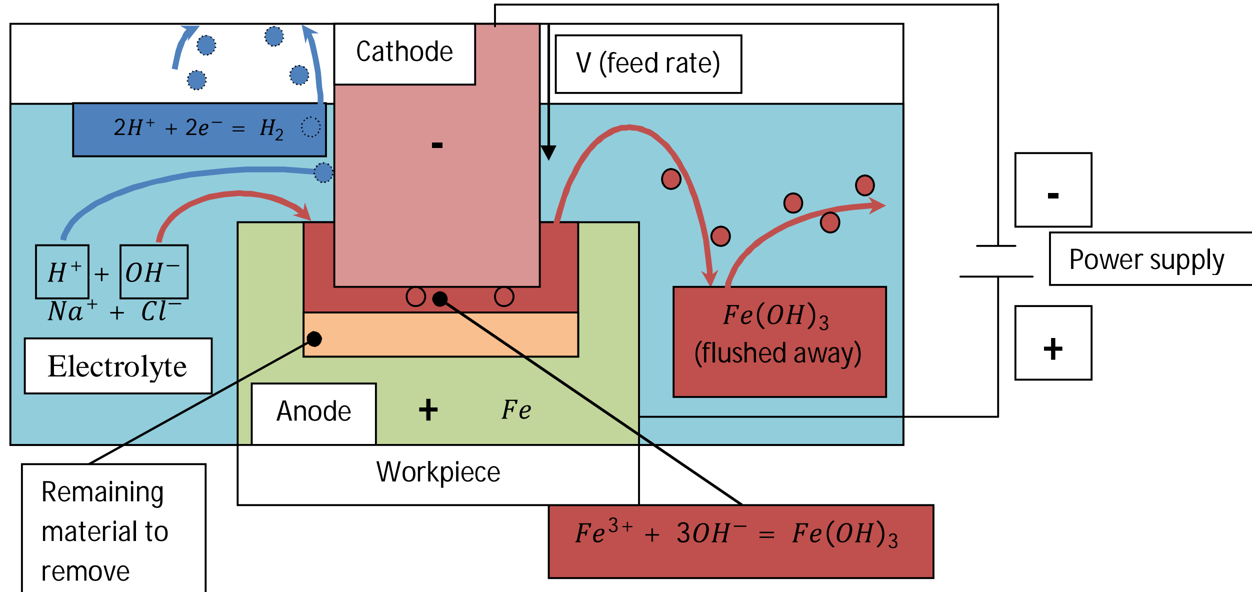

Figure 2-4: Schematic of the electrochemical machining (ECM) process

Note: It has been reported that the principal reaction in the ECM process is the divalent Fe (Fe^{2+}) dissolution (Haisch, Mittemeijer and Schultze, 2004). The authors only observed the

direct oxidation to Fe^{3+} at high current efficiencies ($\eta \approx 100\%$). Figure 2-4 illustrates the process.

The standard electrode potential for the reaction: $Fe^{2+} + 2e^- = Fe$ is $E_{a0} = -0.44V$ vs. a standard hydrogen electrode (SHE).

According to the Nernst equation, the potential required to activate the above reaction is:

$$E_{act.} = E_{a0} - \frac{R_g T}{2F} \ln(c_{Fe^{2+}}) \quad (2\text{-}4)$$

Where R_g is the gas constant, T is the temperature (in K), $c_{Fe^{2+}}$ is the concentration of ion Fe^{2+} in the solution and F is the Faraday constant.

However, $E_{act.}$ is also influenced by the pH. According to an electrochemistry course (EPFL, 2011),

$$K_1 = \frac{a_{Fe^{2+}} a_{OH^-}}{a_{Fe(OH)_2}} \approx 10^{-28} \frac{c_{Fe^{2+}}}{(a_{H^+})^2} \quad (2\text{-}5)$$

Where $a_{Fe^{2+}}, a_{OH^-}$ and $a_{Fe(OH)_2}$ are the activities of the different chemical species in the electrolyte. a_{H^+} is the activity of the ion H^+ in the solution.

With $c_{Fe^{2+}}$= 0.01M and at pH = 7.45, $K_1 = 10^{-15.1}$

At 25°C (298.15K), $\frac{R_g T}{F} = 2{,}5693.10^{-2}$

$$E_{act.} = E_{a0} - \frac{R_g T}{2F} \ln(c_{Fe^{2+}}) = E_{a0} - \frac{R_g T}{2F} \ln(K_1 . 10^{-28} . (a_{H^+})^2) \quad (2\text{-}6)$$

$$= -0.06 - 0.059pH$$

$$E_{act.} = -0.06 - 0.059pH$$

From the above equation it can be concluded that the activating potential of the dissolution reaction also depends on the pH of the solution (EPFL, 2011).

2.2.3. The material removal rate (MRR)

2.2.3.1. MRR for pure materials (non-alloy)

The material removal rate (MRR) corresponds to the amount of metal removed per time unit during the machining process. It is governed by Faraday's law stating that the 'amount of removed material is proportional to the amount of charge (Q)'.

Moreover, the amount of material removed m during a time t depends on the electrochemical equivalence (ECE) which is the ratio of the atomic weight A and the valence z (McGeough, 1974). This relation is expressed by:

$$m = \eta \frac{Q.A}{F.z} = \eta.k.Q = \eta.k.I.t \qquad (2\text{-}7)$$

where

- F is the Faraday's Constant ($F = 96500\ C$)
- I is the current
- t is the time
- Q is the charge $(Q = I.t)$.
- η is the current efficiency (in %) defined as.

$$\eta = \frac{\text{current responsible for metal dissolution}}{\text{total current }(I)}$$

- $k = \frac{A}{Fz}$ is a constant and it is specific to the material.

Expressing the dissolved mass dm in terms of removed material thickness dh over a time dt and across a surface dS, the following expression can be obtained:

$$dm = \rho.dh.dS \qquad (2\text{-}8)$$

Where ρ is the density of the material of the anode (workpiece).

Furthermore, it is known that $dm = \eta.k.I.dt = \eta.k.dQ$ so $\rho.dh.dS = \eta.k.I.dt$
So it can be deduced that:

$$dh = \eta k \frac{I.dt}{\rho.dS} = K_v \times \frac{I}{dS} \times dt = K_v.i_a.dt \qquad (2\text{-}9)$$

Where

- $K_v = \eta \frac{k}{\rho}$ is the coefficient of electrochemical machinability
- $i_a = \frac{I}{dS}$ is the current density at the surface of the anode

Finally the following equation is obtained:

$$MRR = \frac{m}{t\rho} = \frac{V}{t} = \eta \frac{Itk}{t\rho} = \eta \frac{Ik}{\rho} = I \times K_v \qquad (2\text{-}10)$$

However, the previous formula is only working when one particular type of metal is dissolved during the reaction. Since most of the manufacturing applications use alloys, it is needed to go further in the development of this expression.

2.2.3.2. *MRR for alloys in ECM*

The formula to calculate the MRR for alloys in ECM is different: the atomic weight A becomes A_i, the valence z becomes z_i and the mass fraction α_i is introduced. The index i designates a specific metal that is a component of the alloy to dissolve.

For a volume V_{alloy} removed by passing a current I over a period of time t, the following equation can be posed (ρ is the density of the alloy and m_i is the mass of one specific metal of the alloy):

$$m_i = V_{alloy}\rho\alpha_i \quad (2\text{-}11)$$

It is known that $m_i = \frac{Q_i A_i}{F z_i} = Q_i k_i$; so $Q_i = \frac{V_{alloy}\rho\alpha_i}{k_i}$ where Q_i is the amount of charge of one specific metal of the alloy.

All the Q_i's are summed to obtain the total charge in the system:

$$Q_{Total} = \sum Q_i = V_{alloy}\rho \sum\left(\frac{\alpha_i}{k_i}\right) = \eta I t \quad (2\text{-}12)$$

Finally:

$$MRR = \frac{V_{alloy}}{t} = \eta\frac{I}{\rho} \times \frac{1}{\sum\left(\frac{\alpha_i}{k_i}\right)} = I.K_{v\ alloy} \quad (2\text{-}13)$$

Where $K_{v\ alloy}$ is the coefficient of electrochemical machinability of the alloy.

2.3. Machining process

2.3.1. Review and analysis of the ECM and µECM machines available on the market

Most of the commercially available machines are ECM sinking machines and micro features are made by copying the shape of the tool-electrode. ECM manufacturers are 'Winbro Group' who offer stem drilling machines and die sinking machines (Winbro Group Technologies, 2012), EMAG also offer die sinking ECM machines (EMAG GmbH, 2014) and pECM systems (pECM Systems, 2014) provides the European market with a range of ECM sinking machines from Russia ('ET' series manufactured by Indec (Indec, 2014)).

There is no great deal of µECM machines on the market. The literature review reported two purpose-built machines able to perform µECM milling using simple shaped electrodes. The first one has been developed by ECMTEC (ECMTEC GmbH, 2012) (now part of EMAG

GmbH) and is commercially available in table-top and standard models (EMAG, 2012). The second machine has been reported in China and is a table-top machine developed for research purposes (Wang et al., 2010). This machine is able to perform on-line tool fabrication by Block Electrical Discharge Grinding (BEDG), whereas the EMAG machine does not seem to have this capability for electrode preparation. Such machines are usually developed and used in laboratory conditions mainly for research purposes and the available documentation regarding them is very limited.

Sequential on-line tool machining followed by workpiece machining has been reported in laboratory experiments but it seems that none of the commercially available machines have the capability to perform it (Zhang, Wang, Chen and Mao, 2011). The reported work used two different electrolytes: KOH to fabricate the tool and then HCl to machine the workpiece. Having to manage two different electrolytes is a big constraint in the design of a machine for industrial applications because the system has to be rinsed and different tanks must be used to avoid contamination.

Usually when a new technology appears, people use and adapt existing machines for the needs of the new technology. In this case the first attempts were to adapt EDM machines for the purpose of the ECM technology. A difference should be made between the development of simple die sinking machine (Figure 2-5) utilizing classical ECM removal mechanism and machines developed which can be used to work in writing mode (µECM milling) (Kirchner, Cagnon, Schuster and Ertl, 2001; Kim, Ryu, Choi and Chu, 2005b; Kozak, Rajurkar and Makkar, 2004b; Liu, Zhu and Zhu, 2012). Die sinking ECM machines use pre-shaped cathode electrodes and create the needed workpiece shape by copying the shape of the cathode electrode onto the workpiece. Writing (or µECM milling) mode is a term used to describe machining of complex shape features using tool-electrode with a simple shape (i.e. cylindrical) and in this case the final shape of the machined feature is created by consecutive movements of the simple-shaped electrode (Kozak, Gulbinowicz and Gulbinowicz, 2008).

Figure 2-5: Typical ECM machine from Indec. Die sinking only.
Source: http://www.indec-ecm.com/en/equipment/ET500/

2.3.2. Design requirements and constraints for µECM systems

2.3.2.1. Ultra-precision motion for tool-positioning

The accuracy required for the machine is directly linked to the accuracy required for the final product. In µECM, it is usually required to maintain a gap smaller than 10µm during machining (Cagnon et al., 2003; Schuster et al., 2000; Yong, Yunfei, Guang and Liangqiang, 2003). Therefore the resolution of the machine movement should be a fraction of that gap. Some developers in µECM even consider maintaining a gap size ranging from 1 to 5µm (Kirchner et al., 2001; Choi et al., 2013), the resolution of the machine movement would be expected to be better than 100nm or less.

Huo et al. reported that the use of a closed frame mechanical structure provided better stiffness (Figure 2-6) (Huo, Cheng and Wardle, 2010b). Their work provided *a 'bench-mark and systematic methodology for designing bench-top ultra-precision machines, especially those using direct-drive linear motors combined with aerostatic bearings'*. This methodology can therefore be used to satisfy the ultra-precision needs of the µECM technology.

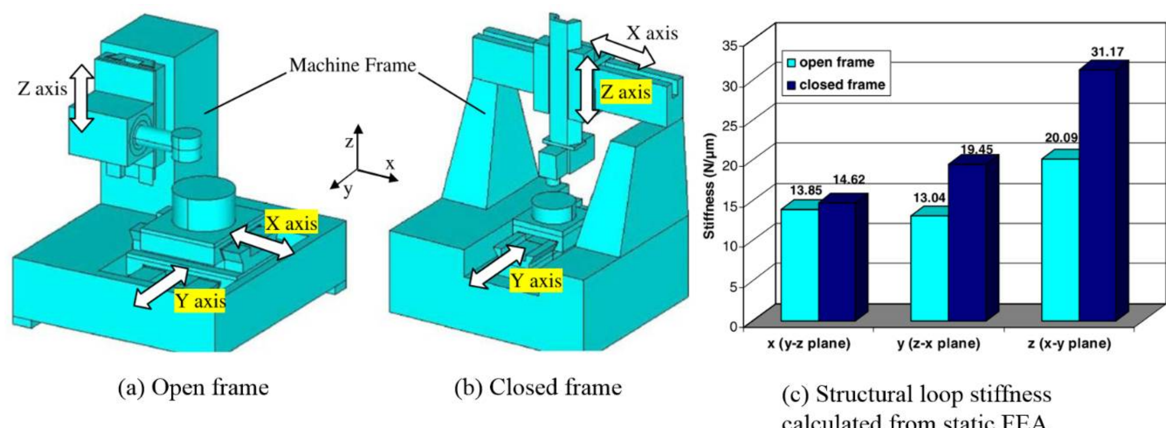

Figure 2-6: Two typical machine configurations and their coordinate definitions. (a) Open frame, (b) closed frame, (c) Structural loop stiffness calculated for both configurations

2.3.2.1. High dynamics and frictionless motion

The dynamics of the main axes (usually Z especially for die sinking operations) should be very high in order not to damage the electrode when a short circuit occurs and to save machining time when retracting and approaching the workpiece again (gap reset) (Yong et al., 2003; Bhattacharyya and Munda, 2003). A 50ms reaction time of the mechanical structure for the corresponding axes (usually Z) is a good example. In order to have high dynamics and precise motion, the machine design should be based on the use of frictionless slides like air-bearing stages (Luo, Cheng, Webb and Wardle, 2005; Wardle et al., 2010). Counterweights and frictionless pressurized air cylinders can be used to support the weight of the slides in order to improve the mechanical dynamics of the system (usually for the Z axis). Air cylinders shall also have mounted brakes on them in order to prevent the supported slides from being damaged in case of a pressure drop (Huo, Cheng and Wardle, 2010b). The averaging effect of the air film on local surface errors allows the air-bearings to have higher precision and better repeatability of motion compared to slide bearings or roller bearings with mechanical contact between elements (Gao et al., 2006).

2.3.2.2. Workpiece clamping and tool holder constraints

Electrical and chemical constraints are also applied to the jigs and fixtures holding the workpiece and the cathode electrode. During machining there is no physical contact between the cathode and the anode and therefore there is no stress involved in the machining process apart from the electrolyte flow causing some pressure onto the both electrodes.

For the workpiece, apart from removing the 6 degrees of freedom in an appropriate way for the achieved dimensions and applying a small clamping force, the fixture should be able to

provide electrical contact which would preferably not to be exposed to the electrolyte flow. This is needed to avoid the corrosion of the contact point and to make sure that the electrical affinity of metals will not cause problems with the current flow.

The cathode electrode should have a reliable electrical contact with the power supply and it should allow the flushing of the electrolyte through the cathode (hollow in that case) even with a small diameter cathode. In some cases the electrolyte pressure may reach very high values such as 70-100 bar if the diameter of the cathode electrode goes down to 80-100µm diameter in order to have sufficient electrolyte flow. For smaller diameter electrodes, side flushing is the only solution. Rotating cathodes should help the renewal of the electrolyte in the working zone which is highly desirable for the efficiency and accuracy of the process. The effect of the rotating tool on the electrolyte flushing could be enhanced using helical or semi-cylindrical tools (Zhang et al., 2007; Tsui, Hung, You and Yan, 2008).

The development of spindles capable of precision rotation and able to transmit the high frequency current pulses with minimized RF emissions is another challenge in order to complete the design of a µECM machine.

2.3.3. Process monitoring and control

Usually, in order to be able to control a process, the variation of a reliable parameter has to be measured and has to be significant enough in order to give a good representation of the current state of the process. The control of the µECM and ECM processes mainly refers to a constant adjustment of the process parameters in order to achieve better accuracy, productivity and prevent from occurrence of electrical discharges (sparks). It *'has been one of the main goals of ECM machine manufacturers and user industries such as turbine manufacturers'* (Rajurkar et al., 1995).

The control system of a PECM (µECM) machine is complex and is made of several subsystems controlling different machining parameters: the interelectrode gap, electrolyte flow, the voltage pulses and the temperature. The role of the electrolyte control subsystem is to maintain the electrolyte properties and the flow rate at the inlet of the interelectrode gap within a specified range.

2.3.3.1. Interelectrode gap control and optimization algorithms

Despite the progress made in Micro-ECM and PECM over the last 20 years, the controllability and monitoring of the Interelectrode gap (IEG) in the process is still a big issue. During the machining process, the motion control logic mainly depends on the variation of the interelectrode gap size. The dimension of this gap can vary from a few µm to 100µm depending on the application and has a dramatic influence on the machining accuracy. When drilling micro-holes, the feed rate of the tool-electrode should match the material removal rate of the process to maintain the gap size and reduce the chances for short circuits to occur (Mithu, Fantoni, Ciampi and Santochi, 2012). The interelectrode gap (IEG) is very hard to control because it cannot be measured directly.

The different issues influencing the IEG size that can be met during an ECM or PECM process have been summarized as follows (Wei, 1994; Kozak, Rajurkar and Makkar, 2004a):

1. Variation of the electrical conductivity in the inter-electrode gap caused by the appearance of bubbles in the electrolyte. This variation engenders a variation of the material removal rate (Shin, Kim and Chu, 2008)
2. Lack of understanding of the kinetics and stoichiometry of the anodic reactions, causing indeterminacy in the reaction modes (and then in the valence and electrochemical equivalent);
3. Difficulty in determining anodic overpotential changes;
4. Variation in local anodic current efficiency;
5. Complexity of the involved mass and energy transport conditions in the gap;
6. Non-uniformity in the distribution of the electric field in the gap region;
7. Presence of stray current lines;

By using the eddy current technique, under specified frequencies, Bignon et al. have created a measurement method of the IEG (Bignon, Bédrin and Weill, 1982). The authors claimed that they could correct the deviations of the IEG from the normal gap value, by adjusting one or several machining parameters (voltage, feed rate) and also claimed that this gave a better reproducibility of machined shapes. However, this control approach has only been applied to ECM and not to the PECM or µECM processes.

In 1984, Meijer et al. explained that *'due to the non-linearity of the process a detail transfer function, which is helpful in linear cases, cannot be used'* (Meijer and Veringa, 1984). The process can however be linearized around a specific point but this generates approximations error. In most cases binary logic control systems were used to control the interelectrode gap.

Based on the mathematical model of the interelectrode gap variation, Rajurkar et al. simulated a gap control approach using state space representation (Rajurkar, Schnacker and Packard, 1988). Nevertheless, no results were presented in their paper and no other work using this method has been reported later. The validity of this approach regarding the µECM process has therefore to be exploited further.

In 1996, Wei et al. proved that the current response of the PECM to a pulsed voltage could be used as a sensing parameter to evaluate the interelectrode gap (Wei, Rajurkar and Talpallikar, 1996). It was concluded that it is therefore possible to conceive an online gap measurement system that can be used to control this parameter in real-time - which confirmed the statements from (Rajurkar et al., 1995). This technique was used by Schuster et al. who monitored the distance between the tool and workpiece by measuring the current flowing through the cell (Schuster et al., 2000).

In 2000, De Silva et al. worked with Philips to model the process characteristics and increase the dimensional control of the process (De Silva, Altena and McGeough, 2000). The developed model managed to give a dimensional accuracy better than 5µm and a surface finish better than Ra 0.03µm. The use of shorter pulses to reduce the size of the side gap (Shin, Kim and Chu, 2008) – especially for non-side-insulated tools – is also recommended to avoid taper-shaped holes (Fan and Hourng, 2011).

Yong et al. developed a control system based on the measurement of the current passing through the system (Yong et al., 2003). To be able to control the gap during the machining process, they moved the tool towards the workpiece until a *'current jump-up'* and then retracted the tool by a few µm (Figure 2-7).

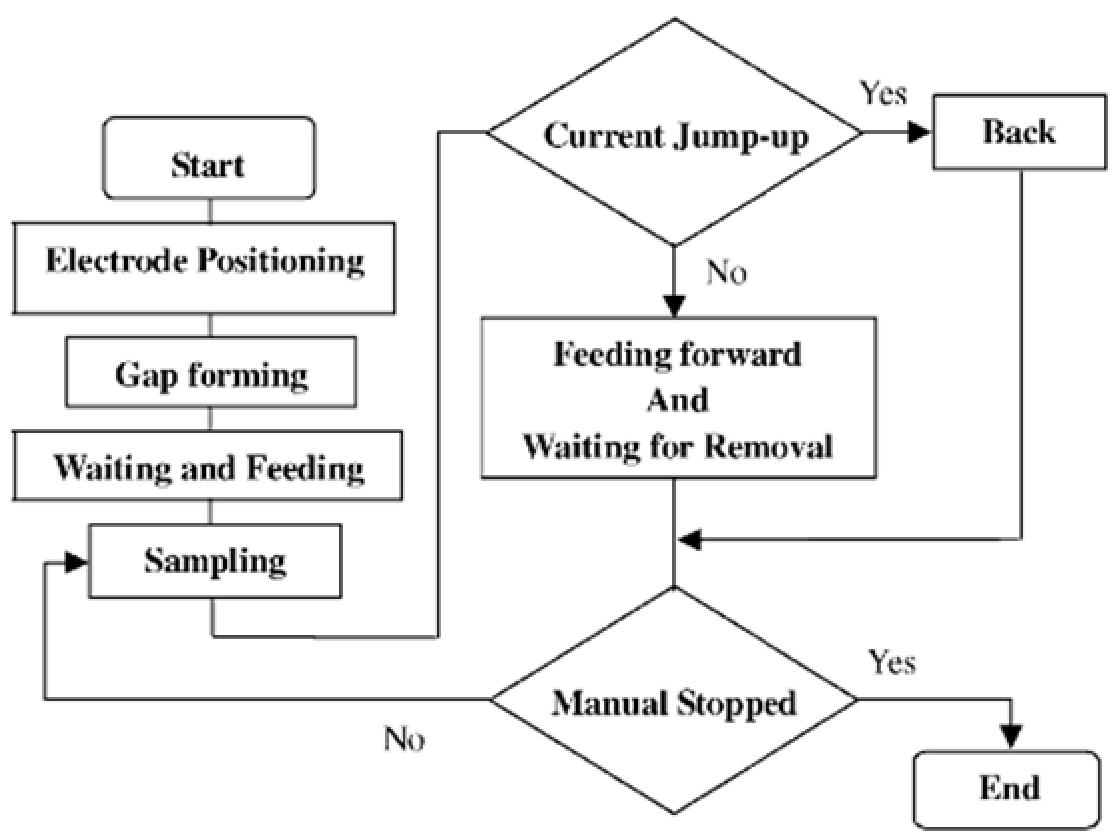

Figure 2-7: Flow chart for a control of the gap (Yong et al., 2003)

Mithu et al. used the same logic (Mithu et al., 2012). This control approach was based on binary logic. A similar approach has been adopted by Bhattacharyya et al. who controlled the interelectrode gap using an 'electrical conduction method': 1V was applied to the IEG and the resulting current was measured to check if there was electrical contact (short circuit) between the tool-electrode and the workpiece. This event then triggered the retraction of the tool (moved upwards) to break this contact (Bhattacharyya and Munda, 2003). Recently, Mithu et al. were able to determine the short situation by analysing the shape of the current during machining (Mithu, Fantoni and Ciampi, 2011b) which is an encouraging step to develop a process monitoring system.

Cagnon et al. and Choi et al. controlled the motion of the tool by using a shortcircuit detector: if a shortcircuit occurred during machining the tool was retracted until there was no more contact between the tool electrode and the workpiece to the initial value of the IEG (Cagnon et al., 2003; Choi et al., 2013).

In 2008, Ozkeskin also developed a binary logic approach to control the current and the position of the tool during the process (Ozkeskin, 2008). The current was used as the sensing parameter in the decision making process. The upper and lower limits of the current were experimentally determined to define a '*stable machining current interval*'.

In 2002, Clifton et al. demonstrated that the measurement of the IEG using ultrasonic waves can also be successfully applied to control the interelectrode gap (Clifton, Mount, Alder and Jardine, 2002). However the gap measured in the experiment were not smaller than 400µm which makes this method not very suitable for µECM. Wei et al. also proposed and patented a method to monitor electrochemical machining by generating ultrasonic waves towards the workpiece thanks to two ultrasonic transducers and then measuring arrival times (Wei, Li and Lamphere, 2005). Although, the smallest gap that could be measured using this technique is not mentioned in the patent. Muir et al. also reported the development of a similar system to measure the interelectrode gap (Muir et al., 2007). The dimensions of the gap did not correspond to the case of µECM: the machining area was around 600mm² and the initial gap was 1mm, which were much greater than the IEGs used in µECM.

In 2004, Schuster et al. proposed a patented *'method for electrochemically processing material'* (Schuster and Kirchner, 2004). They also presented a way to control the interelectrode gap within a 10µm range. The current peaks were measured via a current peak detector and their values were compared with the desired value. The output of the comparator was passed through a low pass filter (integrator) and a downstream amplifier. This amplifier controlled an electromagnetic mechanism that had a 10µm travel distance. The position of the workpiece was then adjusted with respect to the measured current peaks. The authors claimed that the gap was *'sufficiently small to obtain the desired local resolution'* and *'sufficiently high to avoid short circuits'*. However, no specific distances were mentioned.

In order to monitor the gap size, Kim et al. (Kim et al., 2005a) measured the potential drop between the tool and the workpiece (Figure 2-8). If the potential drop was equal to zero, this meant a short circuit was detected. This potential drop can therefore be used to control the feed rate of the tool electrode and also detect short circuits.

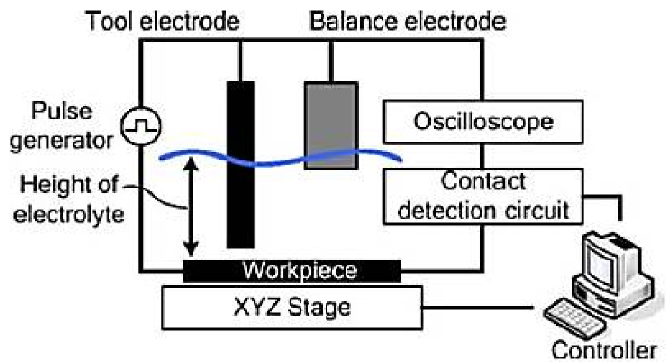

Figure 2-8: A system for μECM (Kim et al., 2005a)

Labib et al. pointed out the necessity for the controller to have decision making capabilities (Labib et al., 2011). Since the PECM process is very hard to mathematically model, conventional control approaches such as proportional-integral-derivative (PID) or state space controllers are limited and based on the linearisation of the process function (and therefore approximation). They observed that the occurrence of sparking was efficiently prevented when fuzzy logic control (FLC) was applied to the ECM process and encouraged further research to develop FLCs for the EMM process. Moreover, it is worth mentioning that fuzzy logic was also used to control the process in EDM, Wire-EDM (Çaydaş, Hasçalık and Ekici, 2009; Lin, Chung and Huang, 2001) and Electro-Chemical Discharge Machining (ECDM) (Mediliyegedara, Silva, Harrison and McGeough, 2005; Skrabalak, Zybura-Skrabalak and Ruszaj, 2004).

Labib et al. also suggested the association of FLC to another control method and claimed that the FLC would bring *'intelligent control'* to the process. They also mentioned that investigation in the area of adaptive neuro-fuzzy inference system (ANFIS) would provide the control system also with learning capabilities (Labib et al., 2011). The combination of an active control loop with neural networks or optimisation algorithms seems very promising as some authors have already used neural networks to tune the machining parameters in ECM (Abuzied, 2012; Li and Ji, 2009; Asokan, Ravi Kumar, Jeyapaul and Santhi, 2008; Zare Chavoshi, 2011). Recently, micro-herringbone grooves were machined in hydrodynamics bearings using a simulation-assisted μECM process (Chang et al., 2011). Fuzzy logic was also applied to control the gap during an ECM process using a 6D force sensor while measuring the machining current (Yonghua and Kai, 2010).

Finally, in 2010 a CNC system was developed for μECM using a soft-CNC architecture based on RT-Linux. This system used a real-time module to handle the motion, short-circuit

detection (the detection signal was coming from the pulse generator) and gap adjustment aspects (Wang et al., 2010). The authors managed to mill an hexagonal star and micro-stepped cavities at a feed rate of 6µm/min using G code generated from a standard CAD/CAM software.

The majority of the authors consider that the most reliable sensing parameter to control the IEG is the current (Yong et al., 2003; Schuster and Kirchner, 2004; Ozkeskin, 2008; Bhattacharyya and Munda, 2003; Mithu et al., 2012; Cagnon et al., 2003), so a good relationship between the current and the gap size must be defined. The only way to answer this demand is to create electrical model(s) of the interelectrode gap.

2.3.3.2. The electrical double layer (EDL) effect in µECM

The electrical double layer can be considered as an 'electrical barrier' located between the metal and the solution in which it is submerged. More precisely, it is a potential difference that is established by *'the transfer of the metal ions to the solution'* and *'the discharge on the ions from the solution'*. When this phenomenon reaches an equilibrium potential difference, a layer of metallic ions (+ at the anode) - whose charge is equal and opposite to those in the solution (-) - is formed at the metal-solution interface: the EDL is then fully established (McGeough, 1974). In PECM and ECM the electrical model of the inter-electrode gap is a variable resistance. However, in µPECM the effect of the electrical double layer is significant enough not to be neglected.

The EDL has several characteristic regions: (A) the Helmholtz double layer and (B) the Gouy-Chapman layer. Helmoltz highlighted that the double layer (A) could be treated as a capacitor since it consists of 2 plans parallel to each other and having opposite charges. On the other hand, over the Gouy-Chapman layer (B) – also called 'diffuse layer' –, the potential decreases exponentially when the distance from the metal surface increases: the potential drop over that layer is therefore non-linear. These layers can be represented the following way (Figure 2-9):

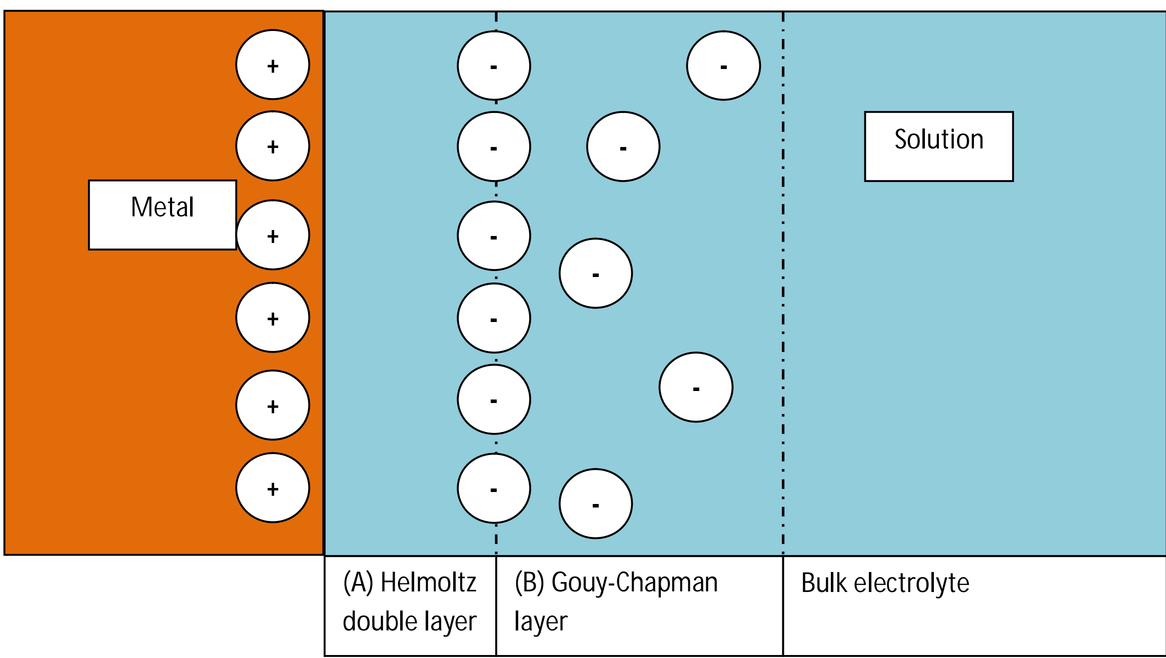

Figure 2-9: Representation of the electrical double layer and its different characteristics (Spieser, 2011)

These statements imply that in order to dissolve the metal in the solution, the energy necessary for the ions to pass across the double layer has to be supplied (McGeough, 1974).

Fujii et al. analyzed the EDL in a NaCl aqueous solution (Fujii, Muramoto and Shimizu, 2010). They applied an increasing voltage to an electrochemical cell with 2 electrodes made of the same material (2 experiments were conducted: one with SUS304 stainless steel electrodes and the other with gold electrodes). The electrodes were both submerged in a 5wt% NaCl solution. During the experiment an increase of the double layer capacitance has been observed: when the DC voltage was 0.3~0.5V the measured capacitance was about 10.6µF and for 1V, the capacitance was 34.6µF (Figure 2-10). They therefore concluded that the double layer capacitance was a function of the charging voltage.

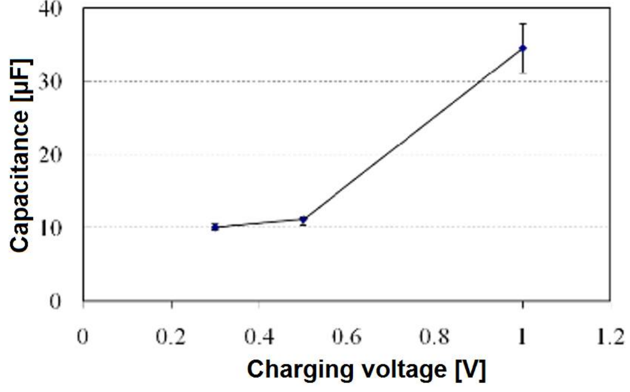

Figure 2-10: The capacitance as a function of the charging voltage. The error bar shows maximum and minimum values in 3 measurements. (Fujii, Muramoto and Shimizu, 2010)

Furthermore, they noticed that: *'Current started to flow through the cell at 0.6V and 1.1V for the SUS304 steel electrodes and the gold electrodes respectively'*. Fujii *et al.* explained the increase of the capacitance by the fact that when the voltage gets closer to the activating potential of the corrosion reaction, the density of ions in the electrical double layer increases: *'the distance between the layers of the EDL decreases and the number of ions participating in the EDL increases'*.

Furthermore, Schuster *et al.* claimed that the activating potential over the double layer was proportional to the electrolyte resistivity (Schuster and Kirchner, 2004).

It can be seen that the behaviour of the electrical double layer is very complex: its capacitance depends on the concentration of the electrolyte, the chemical species (type of ions) in the solution, on the applied voltage and on the material of the electrodes. The electrolyte has therefore to be chosen carefully according to properties of the material of the workpiece (Spieser, 2011).

In 2000, Schuster et al. experimented PECM with ultra-short pulses by taking into account the effect of the electrical double layer (Schuster et al., 2000; Kirchner et al., 2001). Studies showed that a capacitor was a suitable representation of the electrical double layer in this process (Schuster et al., 2000; Ahn, Ryu, Choi and Chu, 2004). The electrical model of the gap that they used is presented on Figure 2-11.

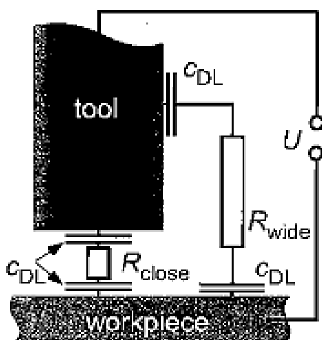

Figure 2-11: Scheme of an electrical cell, the double layer capacity (C_{DL}) is charged via the electrolyte resistance (Schuster et al., 2000)

Kozak (Kozak, Gulbinowicz and Gulbinowicz, 2008) and Marla et al. (Marla, Joshi and Mitra, 2008) improved this model by adding non-linear resistors (r_a and r_k) in parallel with the electrical double layers (Figure 2-12).

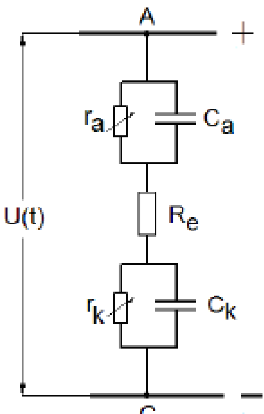

Figure 2-12: Electrical model of the interelectrode gap proposed for the μECM process(Kozak, Gulbinowicz and Gulbinowicz, 2008)

They claimed that the current going through the double layer was actually the sum of 2 different currents (Figure 2-13):

- *The charging current:* It is the current that flows through the double layer when the latter is getting charged.
- *The faradaic current: It is the current that causes the dissolution of the material when the electrical double layer is fully charged.*

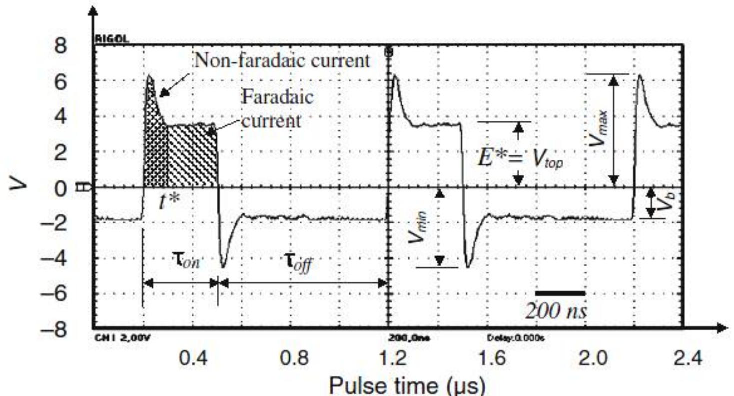

Figure 2-13: Charging and discharging waveforms during μECM machining (Mithu, Fantoni and Ciampi, 2011a)

It can be said that the current representing the gap size is the faradaic current because it only starts flowing through the cell when the electrical double layer is fully charged, and is therefore strongly related to the interelectrode gap resistance. The use of this model has been reported by other authors (Mithu, Fantoni and Ciampi, 2011a; Fan, Hourng and Lin, 2012; Ahn et al., 2004).

To increase the amount of faradaic current contained in each pulse, Kozak et al. made μECM trials by combining a DC voltage source and a pulsed voltage. The role of the DC voltage

was to polarise the electrical double layer to make sure that it would never discharge, then the voltage pulses would remove material more efficiently and at the same time, the tool would be protected from corrosion. The DC voltage was therefore relatively low and below the activating potential of the electrochemical reaction (Kozak, Rajurkar and Makkar, 2004b).

The current is mainly influenced by the conductivity of the electrolyte and the gap size. However, the conductivity of the electrolyte is influenced by several parameters including the ionic concentration (i.e. pH, Cl^-, NO_3^-) and the temperature.

Therefore, if the current is used as a sensing parameter, the properties of the electrolyte have to be carefully maintained constant within the IEG, otherwise the relationship between the measured current and the gap size changes.

In order to have a more accurate representation of the gap, the side walls of the cathode (tool electrode) should be insulated to prevent the current from flowing through them: only the current flowing through the front face of the cathode can be used to indirectly measure the IEG size unless a very complicated algorithm is created to compensate for the change of the active zone on the cathode electrode.

2.3.3.3. Control of the voltage at the electrodes

In some papers, a polarisation of the workpiece and the tool-electrode have been reported (Trimmer et al., 2003; Zemann, Reiss, Schörghofer and Bleicher, 2012; Schuster et al., 2000; Yang, Park and Chu, 2009; Park, Kim and Chu, 2006; Kirchner et al., 2001; Shin, Kim and Chu, 2008). Researchers employed a low-frequency bipotentiostat which was maintaining independently - with the aid of a platinum counterelectrode - specified base values of potentials of the tool and workpiece relative to a reference electrode (Figure 2-14). The potentials were selected so as to prevent the corrosion of the electrodes and to prevent the formation of an oxide layer on the surface of the workpiece (Park, Kim and Chu, 2006; Schuster et al., 2000). They applied a train of voltage pulses (pulse-on time 50 ns, pulse-off time 500 ns) coming from a pulse generator to the workpiece. Such short pulses did not interfere with the potentiostat operation, so the generator could polarize the workpiece precisely in the area to be dissolved (Davydov, Volgin and Lyubimov, 2004; Schuster et al., 2000).

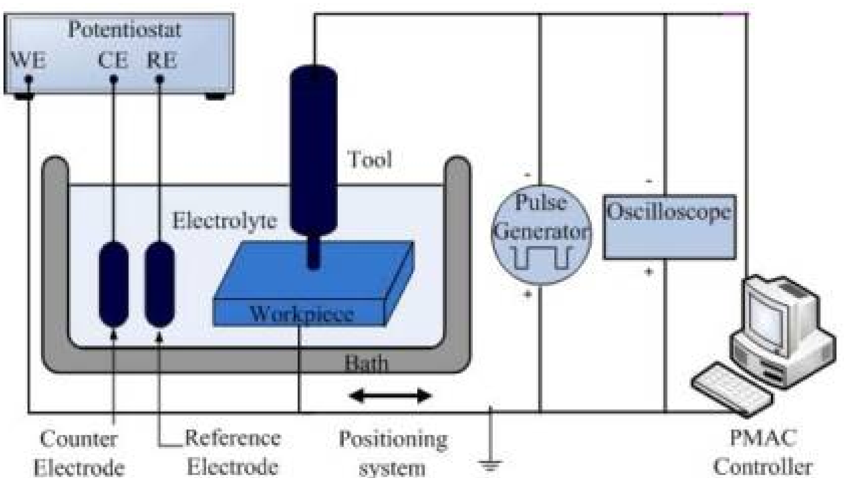

Figure 2-14: Schematic diagram of the Micro ECM system using a potentiostat (Yang, Park and Chu, 2009)

2.3.4. Machining strategies

The existing machining strategies described below are derived only from the very limited experience of people having such equipment. At present there is no theory supporting development of such strategies. The very high complexity of this task is due to the fact that many variables should be taking part in the process. Workpiece material properties are very important and formation of oxides on the surface and time for their re-appearance determines the machining strategy to a great extent.

In some cases, at the beginning of the machining, longer current pulses or higher voltage values are needed to break the oxide layer on the workpiece surface (Landolt, Chauvy and Zinger, 2003). Later the duration of the pulses can be shortened or the voltage lowered in order to improve the resolution and the accuracy of the etching process. Moreover it has been reported that in the case of micro electrochemical milling, the features were machined using two tool paths: during the first tool path, a long pulse duration (143ns) was used, in order to do a 'rough machining', then a short pulse on-time (50ns) was used for the second tool path at a slower tool feed rate, giving a better surface roughness to the machined structure (Cagnon et al., 2003). It can also be said that the pulse duration should be defined according to the EDL charging time ($\tau = RC_{DL}$) to ensure the localized removal of material. The larger the distance from the tool electrode is, the longer the charging time constant of the EDL will be. Moreover, Schuster *et al.* (2004) stated that the pulse duty cycle had to be adjusted so that the temporal mean value of the voltage remained below the activating potential of the anodic dissolution process (Schuster and Kirchner, 2004).

Recently, a simple shape tool has been used to 3D machine structures: the tool was moved along the workpiece surface like a milling cutter, locally removing material. This has been defined as micro electrochemical milling (Kim et al., 2005b; Cagnon et al., 2003; Kozak, Rajurkar and Makkar, 2004b; Yong et al., 2010). This kind of machining method does not yet have any software tool to calculate the tool path in order to machine a particular feature.

In some other cases, the pulse duration was increased when the tool reached a desired location, in order to create cavities (undercuts) into the workpiece and machine complex features (Figure 2-15) (Jo et al., 2008).

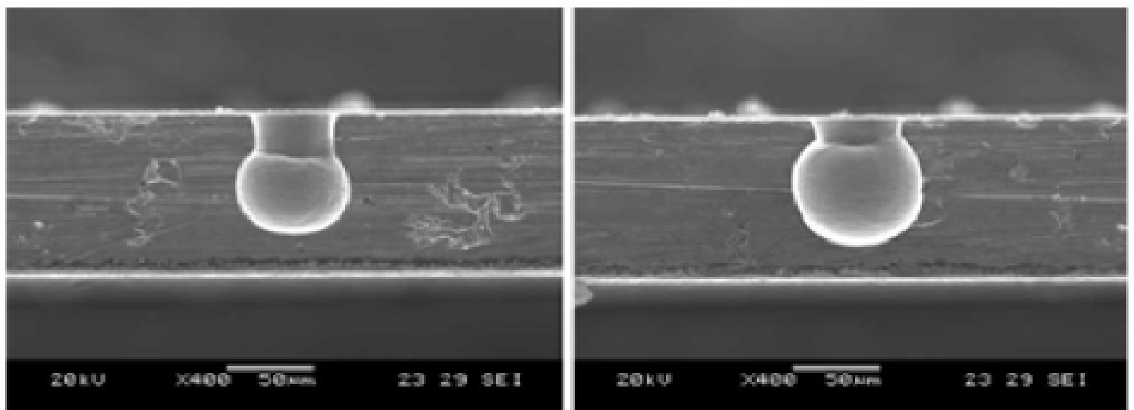

Figure 2-15: Micro cavities machined by controlling dissolution time and pulse duration (Jo et al., 2008)

It is a well-known fact that the renewal of the electrolyte in the working area is a very important factor for effective ECM machining. Hence, machining using rotating electrodes and vibrations have shown some increase in performance regarding machining accuracy and the flushing of the electrolyte, with a better prevention of short circuits events (Yang, Park and Chu, 2009; Bhattacharyya, Malapati, Munda and Sarkar, 2007; Fan and Hourng, 2011; Tsui et al., 2008; Ruszaj, Zybura, Żurek and Skrabalak, 2003).

For the moment, there is no CAD/CAM software offering automatic generation of the machining parameters (electrolyte composition, pulse duration, duty cycle, feed rate and tool path) as well as Cutter Location Data (CLD) file to produce 3D structures utilizing the ECM writing mode process.

Side flushing or flushing through the cathode is another problem. Usually it is considered that through flushing gives better results but this limits the size of the electrodes to be used and creates additional difficulties for μECM milling applications. If the electrolyte is flushed through the electrode, the pressure requirements increase when the electrode diameter decreases, leading to very expensive equipment and complex technical solutions.

Moreover, the gap size between the electrodes must be big enough to allow the electrolyte to circulate.

Side flushing does not require expensive equipment, but the electrolyte flow might apply a lateral force which could bend the tool and disturb the machining process especially when high aspect ratio is required.

2.4. Pulse power supply unit (PSU) considerations

In µECM, a special PSU is needed. It should be able to apply pulses with the following characteristics:

- Pulse amplitude : 1-10V (Bhattacharyya and Munda, 2003)
- Current : up to 5A (dependant of the cathode working area)
- Frequency : ranging from 1kHz up to 5MHz

This kind of device is hard to design mainly because it requires the MOSFETs to be switched at a very high frequency. Indeed, most of the silicon based power transistors commercially available are designed to work at a maximum switching frequency of 1 MHz and are limited by their turn-on and turn-off times. To make a MOSFET turn on in a few nanoseconds, a high current pulse (of several amps) has to be applied to quickly charge the capacitor at its gate (Oh, 2000; Balogh, 2001). Therefore in most cases a special gate driver needs to be developed (Tang and Burkhart, 2009). Although the design of single switch pulse generators has been reported (use of a RF MOSFET (Campbell, Harper, Natham, Vinodhkumar, Xiao and Sundararajan, 2008) and use of a thyristor (Bhattacharyya and Munda, 2003)), most of the µECM power supplies found in the litterature have a half bridge configuration (Zhang et al., 2009; Burkert, Schulze, Gmelin and Leone, 2009). The low side switch applies the voltage pulse to the gap when it is closed (pulse on-time), and the high side switch shorts the gap during the pulse off-time. Driving the high side switch at very high frequencies is another issue, since the conventional high side gate drive technique using a bootstrap diode and a bootstrap capacitor cannot be used (because of the relatively long charging/discharging time of the bootstrap capacitor). A solution to this problem is to completely isolate the high side using an isolated DC/DC converter. The DC/DC converter should be designed to supply the driver with enough current to drive the MOSFET at the required frequency.

Machining at a very small interelectrode gap dramatically increases the chances for short circuits to occur. Short circuits are strongly undesirable as they might damage the tool, alter the quality of the workpiece surface and even damage the pulse generator. Therefore, an ultra fast short circuit protection is necessary to be built into the PSU. Most of the solutions implemented for that purpose, measure the current flowing through the system via a sensing resistor in series with the gap. The potential accross this sensing resistor – whose value is usually a few mΩs – is measured with a differential amplifier and compared with a reference voltage corresponding to the maximum allowable voltage accross this resistor (the voltage proportionally represents the current going through the resistor according to Ohm's law). If the current increases over a preset value, the comparator triggers a logic signal that will switch off the power transistors (Zhang et al., 2009). This implies also that the pulse generator and the control system of the machine should communicate constantly in order to take appropriate actions when a short circuit situation is detected (i.e. switch off the pulses and retract the tool).

Zhang et al. proposed a power supply design and claimed they could achieve a pulse frequency of 20MHz using a MAX038 function generator to control the MOSFETs (see Figure 2-16). They also presented a fast short circuit protection, which basically consists of an over current protection where the current is measured through a sensing resistor (Zhang et al., 2009).

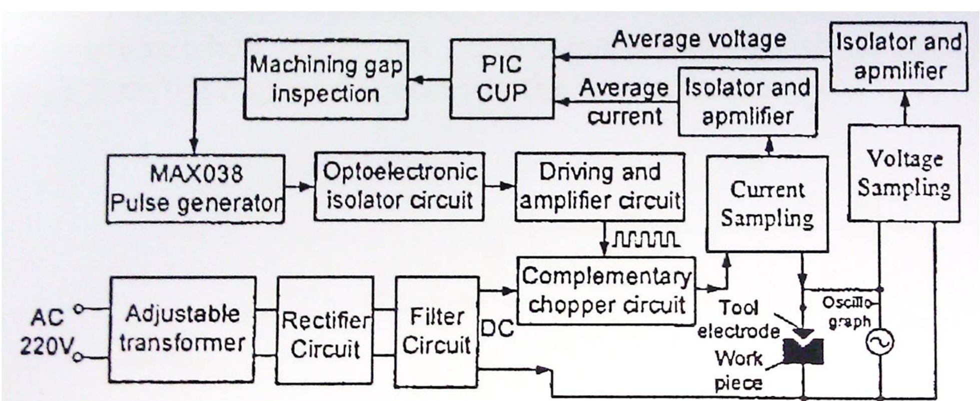

Figure 2-16: Principle of pulse generator for micro-ECM (Zhang et al., 2009)

Burkert et al. outlined the differences between the power supply units (PSU) in PECM and µECM (Burkert et al., 2009). The 'classic' PECM-pulse unit circuitry is shown on Figure 2-17.

The pulse unit for the µECM has to meet the requirements of the gap conditions during the micromachining. In order to improve the localization of the machining, Burkert et al.

claimed it is necessary to reload the double layer capacitances, which means both loading and unloading them. They presented a bipolar PSU enabling to load/unload the electrical double layer thanks to two power sources, as shown on Figure 2-18.

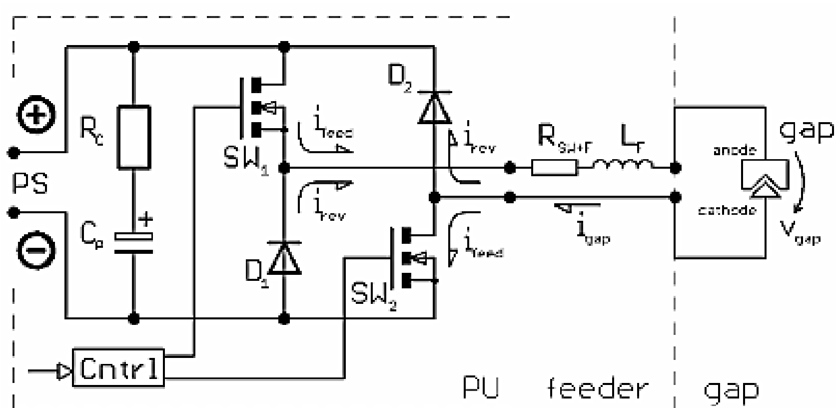

Figure 2-17: Basic circuitry of pulse-unit (PU) for PECM in connection with gap via feeder. Switches SW carry the rising current i_{feed} during the pulse on-time, diodes D carry the falling reverse-current i_{rev} at beginning of the pulse off-time. PU is connected to supply-unit PS on the left side. (Burkert et al., 2009)

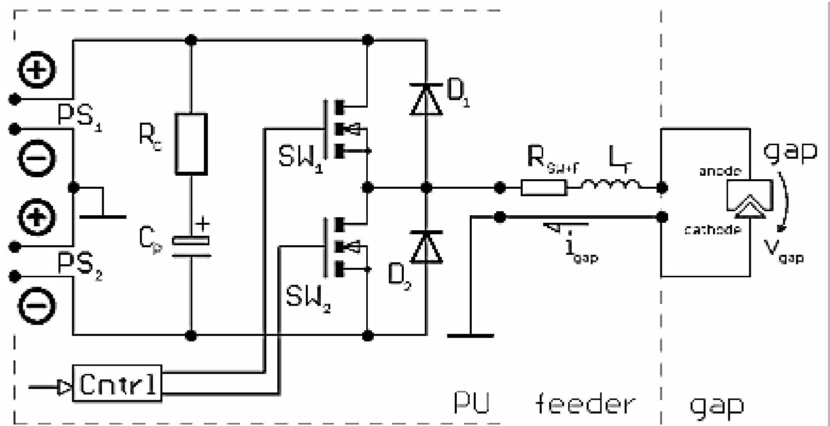

Figure 2-18: Basic circuitry of simple µECM pulse-unit (PU) in push-pull topology with bipolar (two) power supply (PS) feeding. Switches SW may conduct in alternation for loading and reloading of the gap's double layer capacitance. (Burkert et al., 2009)

The two supply voltages of the power supplies PS1 and PS2 are adjustable; the unloading/loading of the double layer capacitances can therefore be controlled and hence the current slope can be optimized for a more efficient metal dissolution. *'In this respect, the connecting of the gap to the necessary voltages takes place via the semiconductor switches SW1 for the positive PS1, and SW2 for the negative PS2. The diodes D serve the purpose of protecting the circuit.'* (Burkert et al., 2009).

A low cost power supply unit with satisfying performance will have to be developed in order to make the µECM technology fulfill the needs of the industry. Lots of further research is

therefore needed in this particular area. Schulze et al. outlined the specifications of an energy source that have to be developed in order to efficiently use ECM for micro-machining (Schulze, Borkenhagen and Burkert, 2008).

Recent developments in Gallium Nitride (GaN) power transistors (such as the eGaN FET from EPC Corporation) having a very high switching speed with a very small package inductance and resistance should make the development of this kind of power supply more feasible (Danilovic et al., 2011).

Since the pulses last about 20ns each, and that a very high current density is applied, an innovative power supply unit (PSU) has to be developed. In µECM, the EDL loading/unloading time can be controlled to improve anodic dissolution. For this reason, the PSU circuitry for PECM is not the same as in µECM.

2.5. Electrode and workpiece preparation

In µECM, the shape of the cathode electrode has a direct influence of the shape created on the anode electrode. Therefore, the accuracy of the tool shape has a direct effect on the workpiece accuracy (Bhattacharyya, Malapati and Munda, 2005). As mentioned before, the cathode electrode does not wear during the machining process, so the electrode does not have to be changed after the machining operation. It is also worth mentioning that the shape of the tool tip has an influence on the machining performance (Swain, 2010; Liu, Zhu, Zeng and Yu, 2011).

2.5.1. Tool design software

Tool design software tool chains have been developed to help define the shapes and feature sizes to be machined onto the cathode electrode for the desired application.

The methods and software that were used to design tools for ‘normal’ ECM and millisecond range PECM (Kozak et al., 2000; Purcar, Bortels, Vandenbossche and Deconinck, 2004) cannot be applied to the µECM because the effect of the electrical double layer is not considered in the normal ECM simulation. All these simulation tools use analytical numerical methods such as the boundary elements method (BEM) (Deconinck, 1992; Pattavanitch, Hinduja and Atkinson, 2010; Narayanan, Hinduja and Noble, 1986), the finite difference method (FDM) (Kozak, 2001) or the finite element method (FEM) (Jain and Pandey, 1981) to map the current density over the cathode and workpiece surfaces according to predefined parameters (electrolyte conductivity, geometrical configuration). The main

challenge is to take into account the variation of the electrical potential distribution (and therefore, of the current density distribution) when material is removed: the distribution of the electrical potential needs to be recalculated after each pulse. In most of the time, to simplify the system, the electrical double layer capacitance and the conductivity of the electrolyte within the IEG (depending on both temperature and electrolyte concentration) are considered constant throughout the machining time (Kozak, Gulbinowicz and Gulbinowicz, 2008; Marla, Joshi and Mitra, 2008). More recently, simulations have been performed taking into account the temperature distribution in the IEG and its influence on the shape evolution during machining (Deconinck, Van Damme and Deconinck, 2012a; b).

The current density is at its strongest value at the end surface of the electrode. However, when the workpiece is machined the sidewalls of the electrode also have an influence on the shaping process. In reality, µECM processes present a non-uniform current density distribution along the surface of the workpiece (Kock, Kirchner and Schuster, 2003; Floridor et al., 2004).

Kenney et al. and Chang et al. proposed simulation tools and procedures that could be used for future cathode tool design and process parameter study for the EMM process (Kenney, Hwang and Shin, 2004; Chang et al., 2011).

More recently, Hotoiu et al. have been working on the development of a software pack to simulate the µECM process by taking into account the effect of the electrical double layer (Hotoiu, Van Damme and Deconinck, 2011; Hotoiu et al., 2011; Van Damme et al., 2011).

2.5.2. Off-Machine electrode fabrication

In cases of die sinking operation the cathode electrode has to be machined in advance and there is a complex relationship between the shape of the final product and the shape of the cathode electrode, as explained above. The shape of the tool electrode is usually complex (Wang and Zhu, 2009; Trimmer et al., 2003). This process requires sometimes the combination of different machining technologies (such as milling, EDM and followed by electrochemical etching (Wang and Zhu, 2009)).

In these cases 3D micro features are machined on the cathode electrode which is then used to create the features onto the anode workpiece (Figure 2-19) (Chang et al., 2011; Trimmer et al., 2003).

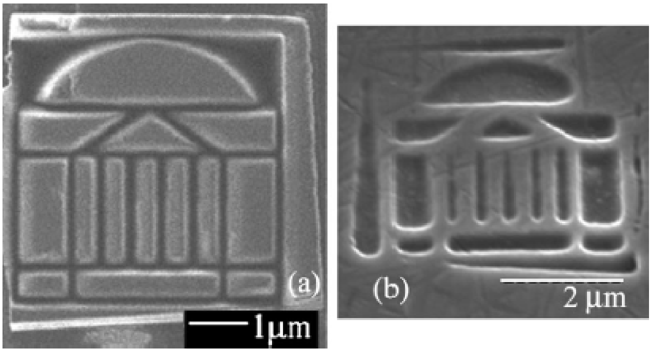

Figure 2-19: Scanning electron micrographs (a) the tool; (b) structure in Ni substrate (Trimmer et al., 2003)

To reduce the stray current, the sides of the tool can be insulated. When using insulated tools, '*the machining rate and the machining gap are uniform, regardless of the machining depth*'. Moreover, the taper shape of structures can be effectively prevented (Park, Kim and Chu, 2006).'*Insulated materials like SiC, Si_3N_4 can be coated on the side wall of the cathode by chemical vapour deposition (CVD) process.*' (Bhattacharyya and Munda, 2003; Bhattacharyya, Malapati and Munda, 2005). A dual pole tool would also help achieving a higher accuracy by making the current flow only through the front face of the electrode (Zhu and Xu, 2002). In µECM, the use of acid-based electrolyte implies that the insulation material should be resistant to corrosive chemicals. Jo et al. reported the use of '*polystyrene as an adhesive and tetrahydrofuran (THF) as a solvent*' to overcome corrosion problems (Jo et al., 2008).

All the above recommendations require the cathode to be prepared off the machine. Therefore - for such precise machining application - the clamping of the tool electrode is a very delicate step at machine setup procedure.

2.5.3. On-Machine electrode preparation

In drilling and milling operations, the cathodes usually have a simple shape (cylindrical or semi-cylindrical) and can be machined by electrochemical etching (Figure 2-20) (Zhang et al., 2007, 2011; Lee, Baek and Cho, 2007; Mathew and Sundaram, 2012; Liu, Zhu and Zhu, 2012; Choi, Ryu, Choi and Chu, 2007) or in a manner similar to the Wire Electro-Discharge Grinding devices (Figure 2-21) which allows to achieve very small sizes (diameters) (Yang, Park and Chu, 2009; Huang, Huang and Yan, 2004).

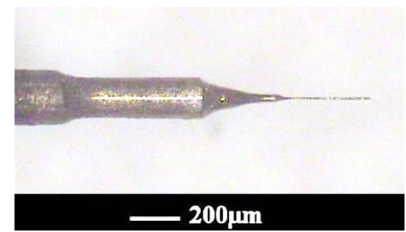

Figure 2-20: 10 µm tungsten tool electrode machined using electrochemical etching (Zhang et al., 2007)

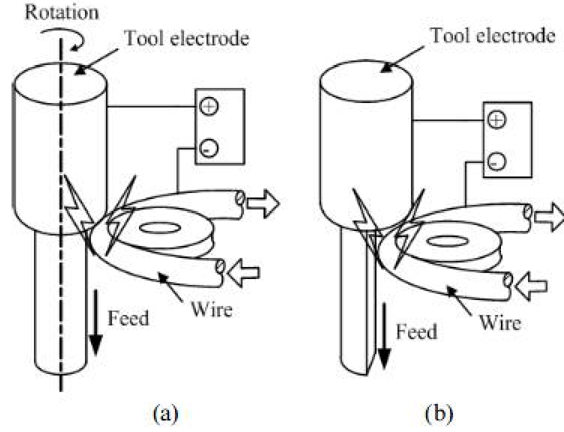

Figure 2-21: Schematic diagrams of the tool electrode fabrication: (a) cylindrical tool and (b) semi-cylindrical tool (Yang, Park and Chu, 2009)

The diagram in Figure 2-22 shows an example of a micro-tool being machined using electrochemical etching (anodic dissolution of the tool with a DC current) followed by the machining of the workpiece (anodic dissolution of the workpiece using the pulsed power supply unit). One of the major benefits of the on-the-machine electrode preparation is that the axis of rotation of the electrode and the electrode position and dimension(s) are known.

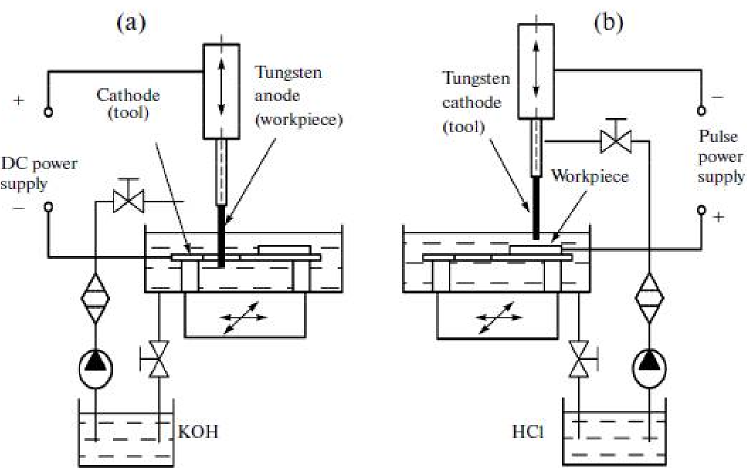

Figure 2-22: Schematic diagram of µECM sequentially: (a) micro-tool machining, (b) micro-workpiece machining (Zhang et al., 2011)

Once the tool is 'ground' and the required size is achieved, it can be used in the electrochemical micromachining process by reversing the polarity of the electrodes (Zhang et al., 2011).

In analogy with the micro EDM process, block wire and disk electrodes can be used for the on-the-machine electrode preparation (Pham et al., 2004).

Until now, no publications have been found to show which method of on-the-machine electrode preparation would be the most suitable for the µECM process. However, the modelling of the fabrication of micro tools using pulse electrochemical micromachining has been reported recently (Mathew and Sundaram, 2012; Kamaraj and Sundaram, 2013). This step is crucial in the development of the on-machine tool-electrode preparation and further developments are very likely to be seen in the coming years.

2.5.4. Electrical connections

Burkert et al. stated that one of the critical parameters of the µECM process circuitry is the inductance of the cables connecting the PSU to the electrodes (Burkert et al., 2009). This parasitic cable inductance increases the rise time of the voltage pulses especially for pulse durations below 1µs. At high frequency, the impedance of the cable gets so big that only a portion of the output power is delivered to the IEG and the pulses are distorted. The cabling therefore limits the frequency at which machining can occur and problems have been reported above 1MHz (Fan, Hourng and Lin, 2012). To solve this issue, special low inductance cables should be used and their length must be minimised. The use of coaxial cables to minimise cable inductance have also been reported (Park, Kim and Chu, 2006). This would mean that the PSU has to 'be positioned as close as possible at the gap connection' (Burkert et al., 2009). This task becomes even more difficult when additional device like the described above on-the machine grinding device should be considered for the wiring.

In µECM tool electrodes with simple shapes (cylindrical or semi-cylindrical) are used in most cases. The electrical connection of the cathode is complex to achieve because the tool is spinning: energy must be reliably transmitted to the rotating element (Zhang et al., 2009).

In the case of high frequency power supply and high current it is not suitable to use the traditional carbon or silver brushes because the transmission of high current has a detrimental effect on them and they do not work well at high frequency (parasitic

inductance). At the moment there is no good solution on the market such as a system transmitting high frequency signals and high current to a spinning electrode and at the same time to be located as close as possible to the IEG.

The electrical connection of the anode electrode (workpiece) is even more complicated and important as few rules have to be followed:

- Only the machined material has to be exposed to the electrolyte and the electrical connection.
- The cables should be special and with minimum length to minimize the inductance.
- In the best case the working zone should be in a structure acting like a Faraday cage to prevent RF emissions and reduce parasitic inductance.
- In the case of on-the-machine electrode preparation the power supply should be able to reverse the polarity of the pulses and the wiring should support this as well.

2.6. Measurement

Measuring the workpiece position in the coordinate system of the machine, the electrode dimensions, the achieved feature dimensions or the surface roughness of micro-features is not an easy task. All measurements have to be performed on the machine, because any off-machine measurement is linked with introducing more errors associated with removing and re-setting up either of the tool-electrode or the workpiece or both. On-the-machine measurement of the tool-electrode and feature dimensions is necessary in order to achieve good accuracy in a μECM machining process. This is mainly due to the fact that removing a machined part for measurement and resetting it up afterwards will create an error that will severely affect the final accuracy of the machined features.

2.6.1. Measuring dimensions

At present there is no accurate way to predict the achieved dimensions with the μECM process. There are not many machines available and all μECM machines are still in state where these new features are under development. In analogy with the micro EDM process where the electrode is used as a probe to perform measuring functions as well, in μECM machines it will be not that easy to adopt the same approach.

In μECM machines, similarly to the micro-EDM machines, the two electrodes are electrically insulated from each other. However regarding the micro-EDM process the

working medium used is dielectric which allows the use of the electrode for probing based on electrical contact between the electrode and the surfaces from the workpiece.

Regarding μECM machines the working medium is electrically conductive and such approach is not applicable unless further research and developments are done. At present the approach is to remove all electrolyte from the electrode and the workpiece and to use measuring cycles similar to the one used in micro-EDM machines based on the electrical contact between the electrode and workpiece surfaces. The dimensions are calculated using data from the encoders which register the exact moment of electrical contact, as suggested by (Bhattacharyya and Munda, 2003). Measuring algorithms are well developed and used for many years on coordinate-measuring machines (CMM) and all CNC-based machines utilising measuring cycles.

Different researchers communicate that repeatability of the process is very high but a test run is needed in order to establish the exact parameters of the process and to measure the achieved dimensions. The dimensions and the corresponding accuracy are directly related to the method used for achieving and maintaining the IEG. If the method of maintaining the IEG is accurate and the IEG variation is small then the machining accuracy from the pulsed μECM process is good.

2.6.2. Machine set-up

At present the development of μECM equipment is still at research level. Nearly all machines use one pre-set cathode electrode for one specific operation. Therefore the setting up of the machine will be considered only for one electrode which simplifies the machining set up procedure. As for all setting up procedures for CNC machines, the setup includes:

- Determining the position of the working coordinate system of the workpiece according to the machine coordinate system;
- Measuring the relative position of the cathode electrode according to the workpiece coordinate system.

The setting up procedure in this case will involve also positioning of the electrode to the IEG distance which has to be maintained during machining operation.

There are no reported machines with optical devices for setting up the position of the workpiece and therefore the described above measuring capabilities of the machine will be used to determine the position of the working coordinate system (workpiece coordinate

system) in the machine coordinate system and the position of the programmed point from the cathode electrode in two dimensions length (usually in Z direction) and diameter (usually X, Y direction).

To define the IEG, a similar approach is used. A small voltage is applied to the electrochemical cell and the tool is being moved towards the workpiece until a short circuit is detected. Then the tool is very slowly retracted until the electrical contact disappears. This method helps define the position of the workpiece surface. From this position, the tool is retracted by the initial gap distance. The accuracy of the above measurements will adversely affect the accuracy of the machined features and the position of these features onto the workpiece.

Still there is no solution to the problem of performing reliable set up measurements when very small electrodes are used (e.g. 20μm or below). The major difficulties come from the cleaning the surfaces of the workpiece which especially involves removing the electrolyte drops from the electrodes in order to reliably perform the measuring cycles.

2.6.3. Surface roughness

There is a lot of information in macro ECM and some in μECM on how the different components of the process influence the surface roughness.

2.6.3.1. Influence of the electrolyte

Lee et al. compared the surface profiles of microgrooves electrochemically machined with NaCl and $NaNO_3$ electrolytes (Lee, Park and Moon, 2002). They observed that the use of the NaCl electrolyte results in a rougher anode surface whereas the $NaNO_3$ electrolyte makes the machined surface smoother as shown on Figure 2-23.

Another interesting comparison between NaCl and $NaNO_3$ electrolytes has been made by Haisch et al. who measured current efficiency during the machining of a workpiece made of 100Cr6 alloy (Figure 2-24) (Haisch, Mittemeijer and Schultze, 2001). From their results they noticed a strong influence of the electrolyte on the process. Using the NaCl electrolyte seems to strongly increase the current efficiency compared to the $NaNO_3$. Moreover, during their study they observed that the dissolution of the metal starts at a lower overpotential for the NaCl electrolyte than for the $NaNO_3$ electrolyte.

Sample	Electrolyte	Groove Profiles
1	NaCl	10µm
2		10µm
3	$NaNO_3$	10µm
4		10µm

Figure 2-23: Comparison of grooves profiles created with 2 electrolytes (Lee, Park and Moon, 2002)

The electrolyte will also have an influence on the formation of a film on the surface of the anode. The adhesion of this surface film depends of the type of electrolyte being used. When machining the 100Cr6 alloy, NaCl electrolyte leads to a surface film which can easily be removed whereas the anodic surface film formed in $NaNO_3$ electrolytes is strongly attached to the workpiece (Haisch, Mittemeijer and Schultze, 2001; Haisch, 2002).

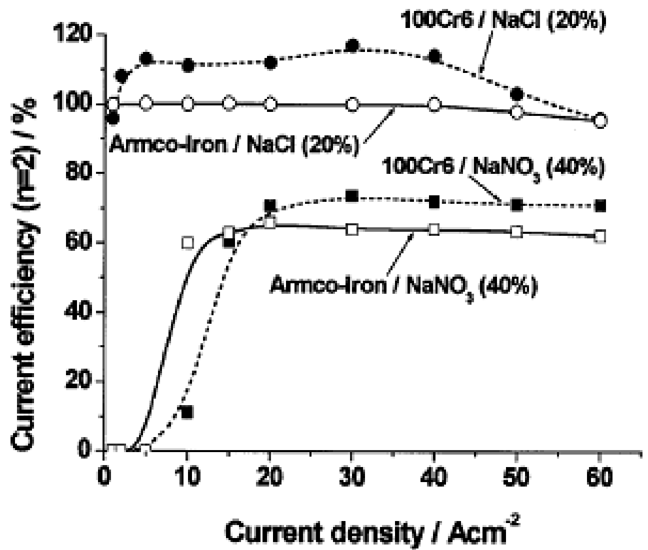

Figure 2-24: Current efficiencies of the soft annealed steel 100Cr6 obtained by galvanostatic flow channel experiments with $NaCl$ (20%) and $NaNO_3$ (40%). The corresponding values for Armco-Iron are given for comparison. Average flow velocity: 7m/s. (Haisch, Mittemeijer and Schultze, 2001)

The properties of the electrolyte and electrolyte flushing conditions (inlet pressure, temperature, concentration) influence severely the accuracy of the machined features,

surface topography, overpotential at the electrodes and the material removal rate (Rajurkar et al., 2006; Bähre, Weber and Rebschläger, 2013; Landolt, Chauvy and Zinger, 2003). Fan et al. also reported that the use of an electrolyte made of a combination of NaCl and HCl solutions is recommended to dissolve the byproducts of the machining but that the HCl concentration should not be too high (< 0.3M) otherwise the workpiece would start to corrode (Fan, Hourng and Lin, 2012).

Moreover, it has been reported that PECM at high pressure (4.44 bar) would improve the surface finish, as it would repress the formation of bubbles (which would lead to electrolyte disparities in the IEG) (Bähre, Weber and Rebschläger, 2013).

It can be concluded that the electrolyte has to be cautiously selected and its properties must be carefully (and actively) monitored and controlled.

2.6.3.2. Material grain structure and composition

It has been reported hat the grain size of the material had an influence on the material removal rate and the surface roughness: the smaller the grain, the faster it is dissolved. Moreover, a correlation between grain size and surface roughness has been identified: the bigger the grain, the rougher the surface (Rajurkar, Schnacker and Packard, 1988; Rajurkar et al., 2006).

The authors would expect a good correlation between the surface roughness and the grain structure of the material when using one electrolyte.

2.6.3.3. Influence of electrical parameters

According to some authors it seems like the current efficiency is an important parameter for surface roughness (De Silva, Altena and McGeough, 2000): *'The test results showed that it is the efficiency rather than the current density, which determined the final surface finish for precision ECM. […]The current density at which a smooth bright finish is achieved (at which the efficiency reaches maximum) is governed by the pulse time and the electrolyte concentration'.*

However, other researchers (Bähre, Weber and Rebschläger, 2013; Landolt, Chauvy and Zinger, 2003) did not mention that the current efficiency had a particular role in the surface roughness, but that high current density would lead to better surface quality (low Ra and bright surface). Bähre et al. (Bähre, Weber and Rebschläger, 2013) also reported that the

pulse on-time is the most influencial parameter on the surface roughness (Ra) because it has a critical influence on the formation of a *'polish film'* which could either improve or deteriorate the surface finish if the pulses are too short or too long: '*At optimal pulse lengths, a polish film grows on the anode surface in which the ionic transport is hindered, involving a preferred metal dissolution at short diffusion paths leading to a surface leveling'*. Moreover, application of pulses at high voltage values changes the way the film grows, which reduces the leveling effect and therefore increases surface roughness (Haisch, 2002). The influence of the pulse duration on the surface quality was also noticed by Cagnon et al. who machined features in two steps: *'the 'rough cut' was performed with 143 ns pulses and was followed by 'fine etching' with 50 ns pulses'* (Cagnon et al., 2003).

Of course, events implying very high current such as short circuits will damage the workpiece and the tool, which will have an influence on the surface roughness (Schulze, 2009).

2.7. Handling

2.7.1. Electrodes and workpiece

In all micro manufacturing processes, problems with handling of the parts and tools exist. µECM is not an exception: In µECM die-sinking, drilling or milling, different techniques and devices can be employed to help handling and manipulating small electrodes and parts. For instance, the electrodes mainly used for EDM drilling and milling are Copper (Cu), W (tungsten) or WC (tungsten carbide) rods or tubes, of diameters within the range 0.1–0.4 mm, and their handling is difficult as they can be easily damaged. There are available rods below 0.1mm diameter but handling them and clamping them on the machines have proved unreliable. Therefore, sub-systems must be incorporated into µECM machines for on-the-machine manufacture and holding of the required micro-electrodes as explained above. The most common sub-systems are ceramic guides for the electrodes and electrode dressing units as shown above which are very similar to the ones used in µEDM processes (Pham et al., 2004; Masuzawa et al., 1985).

2.7.2. Electrolytes

'The electrolyte not only closes the electric circuit between the tool and workpiece, but also allows the desired machining process to occur.'- (Bhattacharyya, Malapati and Munda, 2005)

Unlike the μEDM process where a dielectric medium (either pure water or oil-based) is used and the electrolyte is very rarely changed, in μECM there is a need to renew the electrolyte depending on the material properties of the workpiece material and required parameters of the machined surface topography.

The electrolyte flows in the interelectrode gap and flushes away the waste (i.e $Fe(OH)_3$) produced during the reaction. Clark et al. monitored the temperature of the electrolyte at different locations during the ECM process and observed that the temperature inside the interelectrode gap was higher than at the outside (Clark and McGeough, 1977). They also highlighted the fact that the electrolyte would rise to temperature close to the boiling point if the flow-rate was not high enough. Hence the electrolyte has to evacuate the heat generated by the high current passing through the gap and it is therefore supplied with a relatively high velocity (Yong et al., 2003). This may cause problems to control the electrolyte splashes, especially if dangerous chemicals are used. The use of Lacomit to protect the tool holder against the electrolyte has been reported (Zemann et al., 2012).

According to Clark et al. the $NaCl$ solution seems to rise in temperature more easily than the $NaNO_3$ solution (Clark and McGeough, 1977).

Mukherjee et al. studied the influence of the $NaCl$ electrolyte on the current carrying process in ECM. They concluded that the Na^+ and Cl^- ions only contribute to a fraction of the current-carrying process, whereas the H^+ and OH^- ions produced by the electrolysis of water play an important role in carrying the current (Mukherjee, Kumar and Srivastava, 2007).

According to Bhattacharyya et al., μECM electrolytes are basically classified into two categories (Bhattacharyya, Malapati and Munda, 2005):

- *'Passive electrolytes containing oxidizing anions, i.e. sodium nitrate ($NaNO_3$), sodium chlorate, etc. They are known to give better machining precision.'*
- *'Non-passive electrolytes containing aggressive anions, i.e. sodium chloride. Acidic electrolytes are advantageous due to formation of soluble reaction products, which can completely get swept clean from the narrow IEG during machining without micro-tool being affected.'*

De Silva et al. and Bhattacharyya et al. also claimed that decreasing the concentration of the electrolyte allows a smaller IEG to be maintained, which, as previously mentioned,

increases the machining accuracy (De Silva, Altena and McGeough, 2003; Bhattacharyya, Malapati and Munda, 2005). It was also pointed out that it is possible to use additives in the electrolytes to improve the dimensional accuracy (i.e. $NaHSO_4$). In another experiment, Bhattacharyya et al. confirmed the significant effect of the electrolyte concentration on the material removal rate (MRR) and accuracy: the higher the concentration, the higher the MRR and the lower the machining accuracy (Bhattacharyya et al., 2007).

Some materials are well machined with salt based electrolytes ($NaNO_3$, $NaCl$) but some would require acid based electrolytes (HCl, H_2SO_4) (Trimmer et al., 2003; Kim et al., 2005b; a; Lee, Baek and Cho, 2007; Landolt, Chauvy and Zinger, 2003). The use of highly concentrated 6M HF and 3M HCl electrolyte to machine stainless steel workpiece has been reported (Kirchner et al., 2001; Cagnon et al., 2003). It is has been claimed that the combination of Cl^- and F^- ions destabilize the oxide layer which therefore allows the dissolution process to occur (Kirchner et al., 2001). In µECM, electrolytes tend to be more aggressive in order to reduce the amount of insoluble sludge in the IEG. Obviously the use of such chemicals creates additional difficulties for manipulations of the electrolytes on the machine. However, some research is undergoing to avoid the use of such dangerous chemicals: recently, the use of complexing agents (EDTA-Na2) has been reported and provided encouraging results (Hui, Wang, Wang and Zhao, 2011).

In order to maintain the properties of the electrolyte, the solution must be filtered and treated to remove the iron and chromium compounds resulting from the electrochemical reaction. The filters must be able to remove the precipitated sludge from the electrolyte, which could cause short-circuit in the gap. For these reasons, filters with a fineness smaller than 5µm are recommended. However, filters cannot remove the very fine particles and the chromium ions - which are known for their high toxicity, especially Cr(VI) - when chromium-based alloys are machined (Owlad, Aroua, Daud and Baroutian, 2009).

Schuurman et al. developed a patented method for Philips for removing the iron and chromium compounds out of an aqueous solution in ECM. This method consists of the following steps (Schuurman and Faber, 1997; Altena, 2004):

1- Adding an excess of hydrogen peroxide based upon the amount of chromium present to the solution and, if necessary, adapting the acidity of the solution so that the pH value of the solution is ≥ 7;

2- Separating the iron hydroxide formed;

3- Adapting the acidity of the solution so that the pH value of the solution is < 4;

4- Adapting the acidity of the solution so that the pH value of the solution is ≥ 7;

5- Separating the chromium hydroxide formed.

Recently, other methods have been investigated to treat aqueous solutions contaminated by hexavalent chromium including adsorption, membrane filtration and ion exchange (Owlad et al., 2009).

The electrolyte system on the µECM machine should be able to allow easy and quick change of the electrolyte and at the same time this should be safe for the operator of the machine. The contact of the operator with the electrolyte should be minimized and the change of the electrolyte on the machine should be made a safe procedure.

2.8. Discussion and conclusions

From this review, the following specifications for the development of the machine can be established:

The mechanical structure has to be made out of material with a very low thermal expansion coefficient and high damping characteristics, such as granite. A gantry configuration was recommended, where the X axis supported the Z axis.

In µECM, it is usually required to maintain a gap smaller than 10µm during machining. Therefore the resolution of the machine movement should be a fraction of that gap, therefore the resolution of the machine movement would be expected to be better than 100nm or less.

Frictionless slides such as air-bearing shall be used to provide high-dynamics on all axis. These slides would also provide high-precision motion capabilities when coupled with direct PWM drives and a high-resolution encoder system. The averaging effect of the air film on local surface errors allows the air-bearings to have higher precision and better repeatability of motion compared to slide bearings or roller bearings with mechanical contact between elements. Regarding the slides, air-bearings seemed to offer superior performance to ball-screw system because they provided frictionless motion and high dynamic response. Combined with a direct-drive DC brushless linear motor setup and a high-resolution position feedback system, it would allow the machine to provide sufficient stiffness for precision-machining applications.

A constant adjustment of the tool position is essential to maintain the gap within an acceptable range for an efficient and accurate machining process. Measuring the variation of the machining current has been identified as a suitable way to measure the variation of the gap. Indeed, assuming that the conductivity of the electrolyte is maintained to a constant value, the variation of the current is the closest representation of the inter-electrode gap change.

The trend in µECM control systems seems to go towards fuzzy logic and neural networks, allowing manufacturers to put their knowledge into the system for a more efficient and accurate machining process. The control of the µECM process therefore requires a custom-made programme. Furthermore, since the tool is very brittle because of its small size, a highly reactive tool protection system must be integrated to the machining process.

An intelligent human machine interface will have to be developed to monitor the machining current and tool position during the machining process. It also had to be user friendly and guide the operator when setting up the machining parameters.

The machine will require a custom-made pulse PSU which must be programmable, generate different pulse shape and reverse pulse polarity. Furthermore, a protection system should be designed to protect the tool against undesired events occuring within the gap. The PSU should therefore provide an ultrafast over current protection.

It has been found in the review that the electrolyte has a severe influence on the µECM process and has to be chosen in accordance with the workpiece material. Moreover, if the properties of the electrolyte are not maintained the current cannot be used as a sensing parameter. The accuracy of the gap measurement therefore relies on a proper maintenance of the electrolyte properties. The electrolyte also directly influences the electrical double layer (capacitance and local resistance) whose effect has to be considered in µECM.

The electrical double layer can be loaded/unloaded with very short voltage pulses to confine the dissolution process into a very small area. As a result, the removal of material is localized and micro features can be machined with very high aspect ratio. It has been reported that the charging time of the double layer. Influences machining precision. This time constant can be approximately determined by assuming that the inter-electrode gap can be modeled as an RC circuit. It has been confirmed that a fine tuning of the pulse width and the scanning ratio would ensure the localization of the dissolution process. The design of a power supply capable of delivering ultrashort pulses and providing enough power to the IEG is needed in

order to progress in the development of µECM equipment. Over current protection is a must and should be integrated into the power supply. A quick communication protocol between the power supply and the control system is essential for the successful control of the µECM process.

Process improvements such as the use of vibrating and rotating tools have been discussed and experiments have to be undertaken to confirm the efficiency of these approaches. A first approach would be custom-made spindle capable of precision rotation and able to transmit the high frequency current pulses shall be developed in order to complete the design of a µECM machine. The need for this precise rotation suggests the use of a stepper motor to actuate the spindle. The literature review reported that high rpm had a detrimental effect on process so the tool would be spinned at a maximum of 1000rpm, which reinforces the choice for a stepper motor. Regarding the connection of the pulse PSU to the spinning tool-electrode, two solutions were identified to deliver the high frequency pulses to the IEG: 1) the use of a slip ring in a liquid metal bath such as mercury or galinstan 2) the use of a ring with microfiber carbon brushes.

Further research needs to be done to avoid the use of dangerous chemicals and strict safety measures have to be implemented on the equipment developed for µECM. It is also worth noticing that in µECM the electrolytes are generally more concentrated that in macro ECM processes and use dangerous chemicals such a strong acids (HF, H_2SO_4). Therefore the piping and the pump has to be resistant to corrosion: PTFE (polytetrafluoroethylene) and Polyether ether ketone (PEEK) components must be used whenever possible. Filters must be able to remove the precipitated sludge from the electrolyte, which could cause short-circuit in the gap. For these reasons, filters with a fineness smaller than 5µm shall be used.

Chapter 3: µECM PROCESS MODELLING AND SIMULATION

In this chapter, the µECM process is modelled and simulated.

In sections 3.1, 3.2 and 3.3 the models of Bin Wei (Wei, 1994) and Marla et al. (Marla, Joshi and Mitra, 2008) are first studied and compared using MATLAB. Then in section 3.4 the existing models of the electrical double layer effect on the voltage pulses are then developed based on models from (Cagnon et al., 2003; Kozak, Gulbinowicz and Gulbinowicz, 2008). In section 3.4.2 the author outlines the similarity between these models and an electrical model including Zener diodes is assessed and the current pulses are accurately simulated. A more realistic model is then established to take into account the parasitic inductance of the cabling and to assess its effect on the pulse shape.

A simplified version of these models allowing longer simulation times is proposed by assuming at the electrical double layer behaves like a low pass filter. This assumption is then utilized to perform a 2D drilling simulation of the µECM process.

3.1. Inter-electrode gap behaviour without feed rate

Wei investigated the behaviour of the IEG without a moving tool (Wei, 1994) and a MATLAB/Simulink simulation model was built from his work (Spieser, 2011).

In this model, it is assumed that a current I removed material over a time dt and that a volume of material equal to $S \times dh$ is dissolved (S is the cross section area of the tool electrode).

Ohm's law states that:

$$I = \frac{U}{R} = \frac{U}{r_0 \times \frac{h}{S}} = \frac{US}{r_0 h} \quad (3\text{-}1)$$

where U (V) is the potential, R is the gap resistance (Ohms) r_0 is the resistivity (Ohm.m) and h is the IEG size. It can also be noticed that:

$$MRR = dV/dt = IK_v = \frac{dh}{dt}S \quad (3\text{-}2)$$

Thanks to this analogy it can be said:

$$\frac{dh}{dt} = K_v\left(\frac{U.S}{r_0.h} \times \frac{1}{S}\right) = \frac{cU}{h} \text{ With } c = \frac{K_v}{r_0} = \kappa_0.K_v \quad (3\text{-}3)$$

From equation (3-3), the following analogy can be deduced and integrated:

$$h.dh = c.U.dt \quad (3\text{-}4)$$

$$\int_{h_0}^{h} h.dh = c.U\int_0^t dt \rightarrow h^2 - h_0^2 = 2cUt \rightarrow h = \sqrt{2cUt + h_0{}^2} \quad (3\text{-}5)$$

Where h_0 is the initial value of h , usually called the initial gap.

From that the dissolution rate is not linear and decreases over time when there is no feed rate (Spieser, 2011).

A MATLAB/Simulink model was developed to confirm the behaviour of the IEG and the machinining current without too feed rate. This model should also confirm the MRR dynamics model without any feed rate.

The simulation has been performed for 10sec with the following parameters:

- $K_v = 0.0281\ mm^3/As$
- $\kappa_0 = 2.43\ S.m^{-1}$
- $U = 10V$
- $T_{on} = 10ns$
- $T = 60ms$
- $h_0 = 5\mu m$

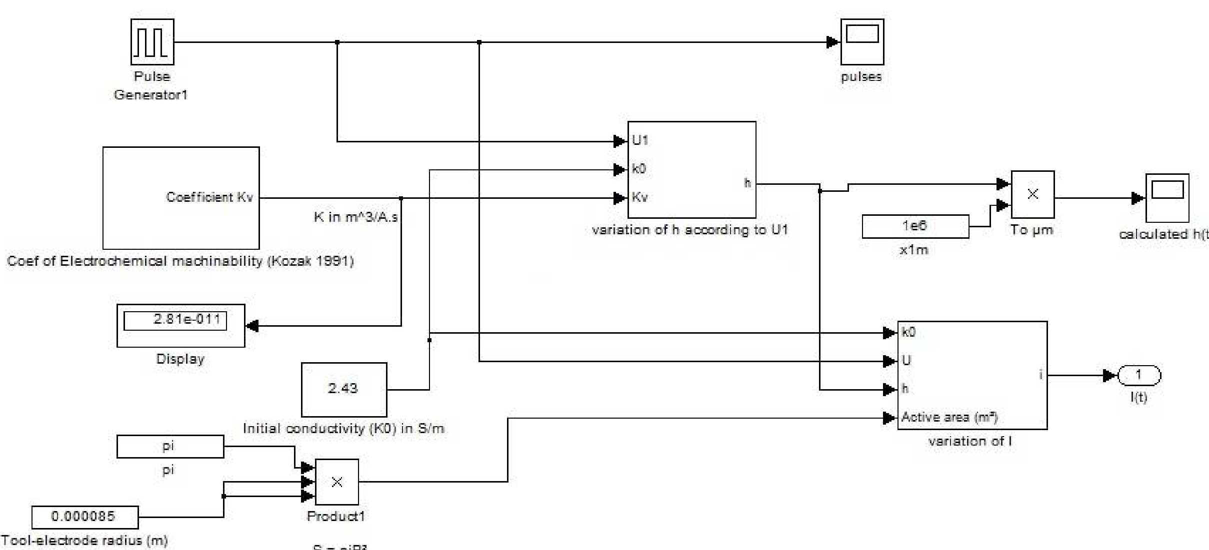

Figure 3-1: Simulink model based on the model with stationary electrode

The variation of the gap over time has been plotted on Figure 3-2.

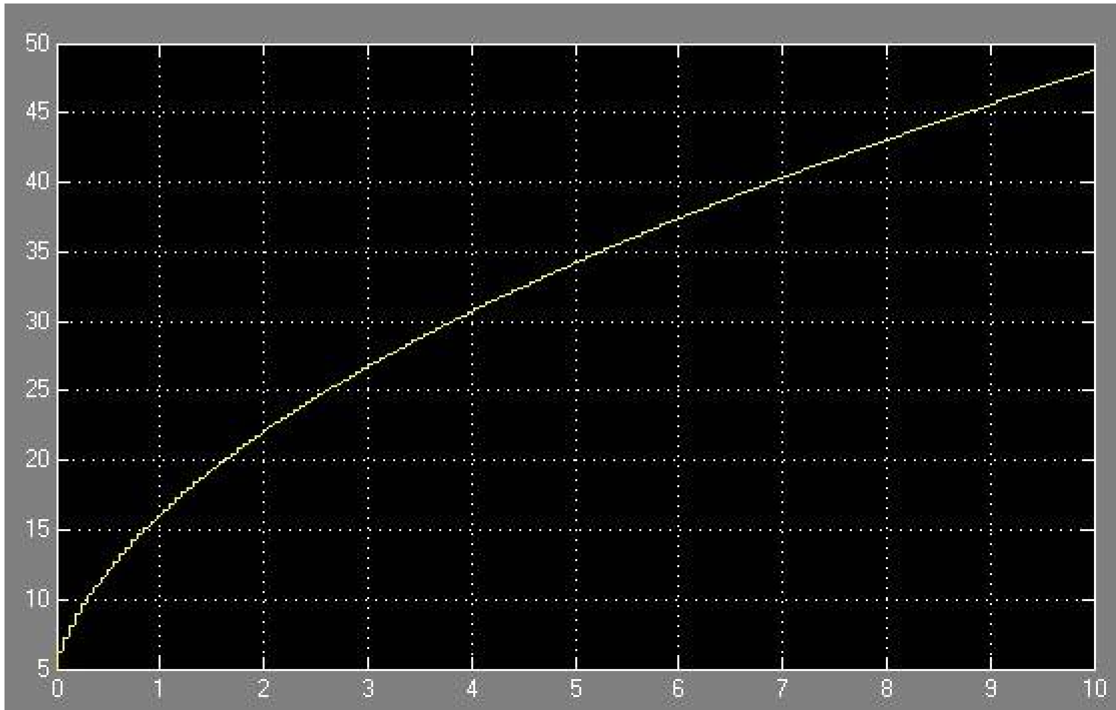

Figure 3-2: Variation of the gap (in µm) over time (in s) without any feed rate (Spieser, 2011)

As predicted, without any feed rate the material removal rate decreases over time, this is mainly related to the fact that the IEG becomes bigger and bigger, which increases the resistance and therefore reduces the current.

The electrode is considered to be a cylinder with a diameter of 170µm, which is an electrode diameter that will be used by the next generation µPECM machine.

The equation $I = \frac{\kappa_0 US}{h}$ has been implemented into the previous model to obtain the variation of the current over time (Figure 3-3).

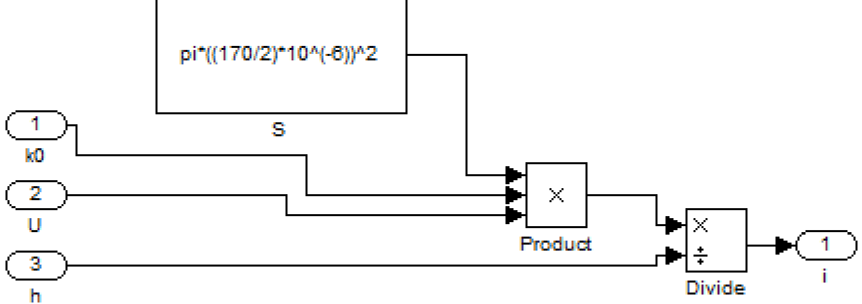

Figure 3-3: Matlab/Simulink submodel to obtain the variation of I over time

According to the previous equation and the MATLAB submodel, the variation of the IEG from Figure 3-2 gives the following current change over time (Figure 3-4):

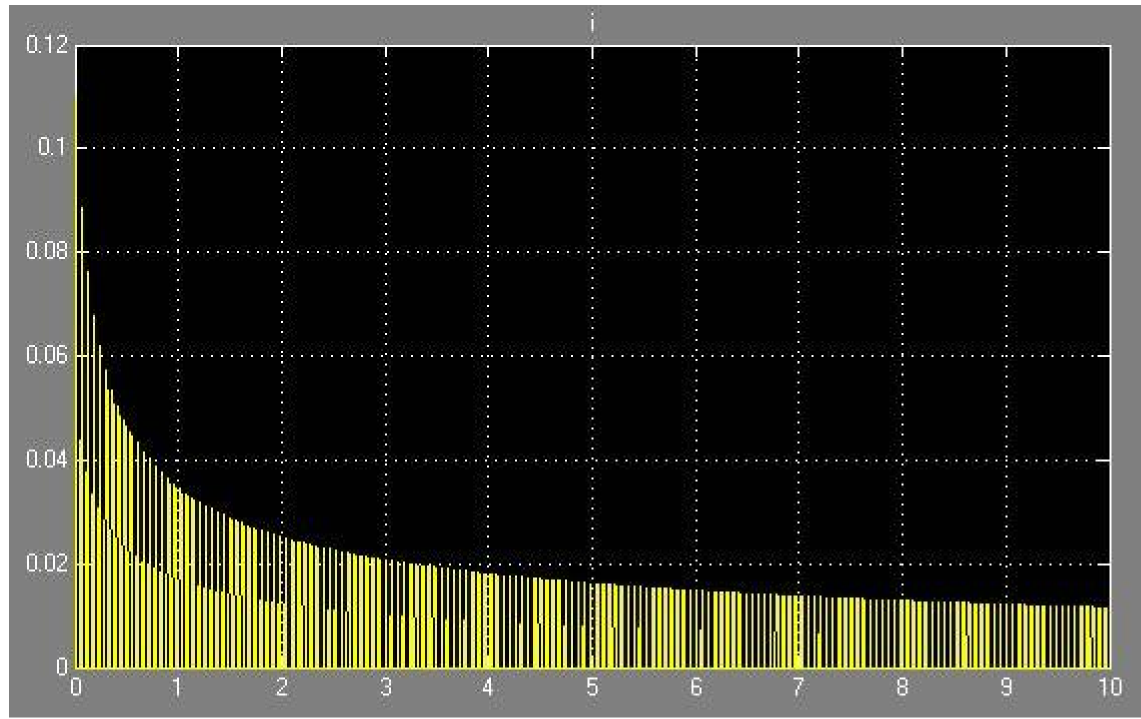

Figure 3-4: Variation of the current (A) over time (s)

A comparison between the different charts on Figure 3-2 and Figure 3-4 shows that at the end of the simulation (t = 0.25s) a gap size variation of 48 – 5 = 43µm has made the current decrease by around 0.11 – 0.01 = 0.1A. This illustrates the dramatic influence of the gap size on the current.

Since the IEG cannot be measured directly, measuring the variation of the current throughout the machining time can be an efficient way to monitor the inter-electrode gap behavior.

If the conductivity is assumed to be constant during the process, the inter-electrode gap can be calculated thanks to the measured value of the current. In reality, the current can be measured thanks to a current probe connected to an oscilloscope.

Assuming that the value of the IEG is unknown, it can be estimated thanks to the following expression: $I = \frac{\kappa_0 US}{h} ==> h = \frac{\kappa_0 US}{I}$

This means that according to the Bin Wei's model from 1994, the variation of the gap can theoretically be obtained by measuring the current.

The control system will therefore have to analyze the variation of the current over time and compute the variation of the IEG. It will then have to readjust the tool-position in order to maintain the IEG constant.

3.2. Bin Wei's PECM gap model with constant feed rate

3.2.1. Mathematical formulation

Bin Wei modelled the process of pulse electrochemical machining (Rajurkar et al., 1993; Wei, Rajurkar and Talpallikar, 1996) and his work is based on the model developed by Kozak et al. in 1991 (Kozak, Rajurkar and Ross, 1991).

In this model, the evolution of the interelectrode gap (IEG) can be represented in Figure 3-5.

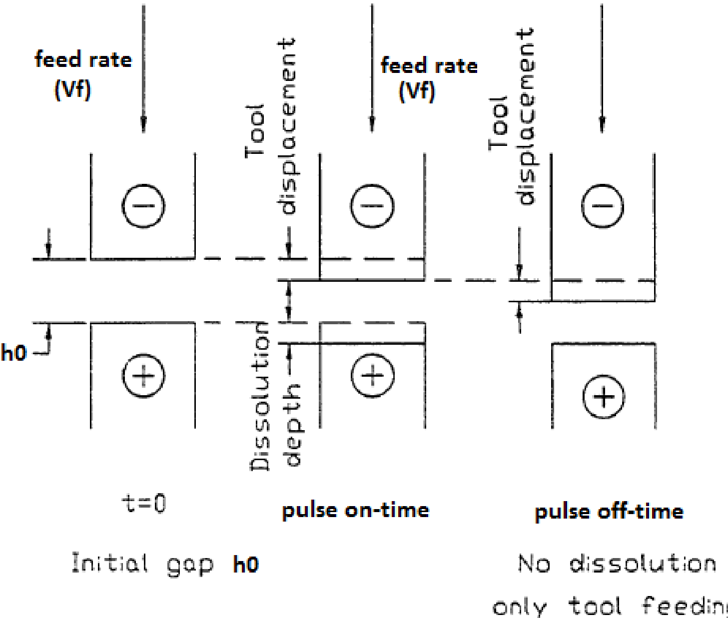

Figure 3-5: Interelectrode gap change during pulse cycle (Wei, 1994)

Assuming that (1) the electrolyte conductivity(κ_0); (2) the current efficiency; and (3) the over-voltage ΔU: $E_a - E_c$ (where E_a and E_c are respectively the anode and cathode overpotentials) are constant throughout the machining time, the Ohm's law can be applied in the IEG. From the conceptual equation:

Change in gap size = Anodic dissolution depth – Cathode feed distance

Wei developed a general IEG equation to model its behaviour during the machining process. From equation (2-10):

$$\text{Anodic dissolution depth} = i_a . K_v . dt = \frac{\kappa_0 . K_v . (U_0 - \Delta U)}{h} dt \qquad (3\text{-}6)$$

The cathode feed distance L can be calculated by:

$$L = V_f . dt \qquad (3\text{-}7)$$

Where V_f is the feed rate of the tool-electrode in m/s.

Then the change in gap size dh during machining when the tool is moving towards the workpiece at a constant feed rate can be expressed by:

$$dh = \left[\frac{\kappa_0 . K_v . (U_0 - \Delta U)}{h . V_f} - 1\right] \times V_f . dt \qquad (3\text{-}8)$$

Wei observed that:

$$\text{If } h = h_f = \frac{\kappa_0 . K_v (U_0 - \Delta U)}{V_f} \text{ then } \frac{dh}{dt} = 0. \ (\kappa_0 = \text{constant})$$

h_f is defined as the equilibrium gap size and is seen as a constant. Bin Wei (Wei, 1994) highlighted that even if h_f was a solution of (3-8), reaching $\frac{dh}{dt} = 0$ in PECM is impossible.

According to Wei the solution of equation (3-9) is given by the following expression:

$$h_f \times \ln\left(\frac{h_f - h_0}{h_f - h}\right) + (h_0 - h) - V_f . t = 0 \qquad (3\text{-}9)$$

Equation (3-9) describes the gap change considering the previous assumptions at any time t during the pulse on-time t_{on}.

3.2.2. Simulation

To simulate the µPECM process with constant feed rate, the following model (Figure 3-6) has been developed according to Wei's model (1994). Since Ohm's law can be applied according to the assumptions of the model, the gap can be represented as a variable resistor controlled by a signal that is function of the voltage (U) and the feed rate V_f.

The variation of h and the resistance of the gap (Rgap) have been computed over time through the subsystem (1) with the equation: $dh = \left[\frac{\kappa_0 . K_v (U_0 - \Delta U)}{h} - V_f\right] . dt$

The resistance of the IEG is obtained using the formula: $R_{gap} = r_0 \times \frac{h}{S} = \frac{h}{\kappa_0 S}$

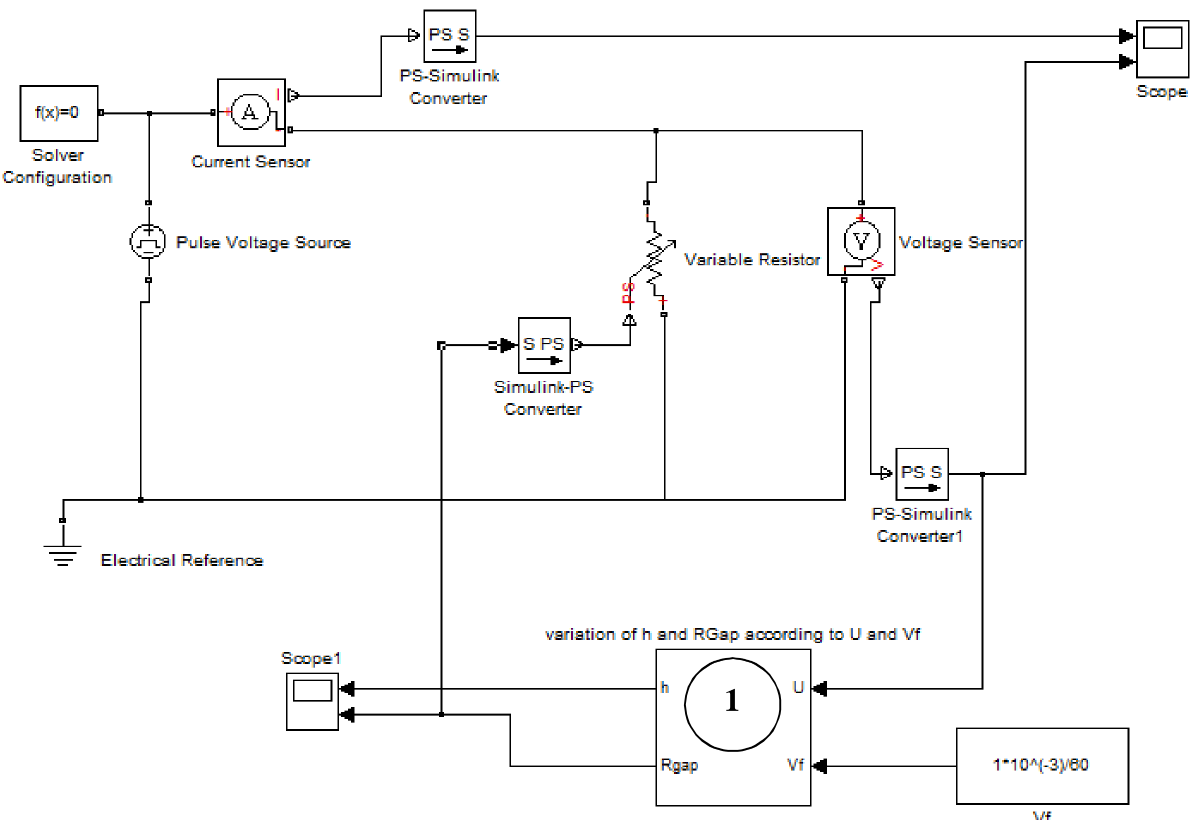

Figure 3-6: Matlab/Simulink model developed to simulate Wei's PECM model (1994) with constant feed rate

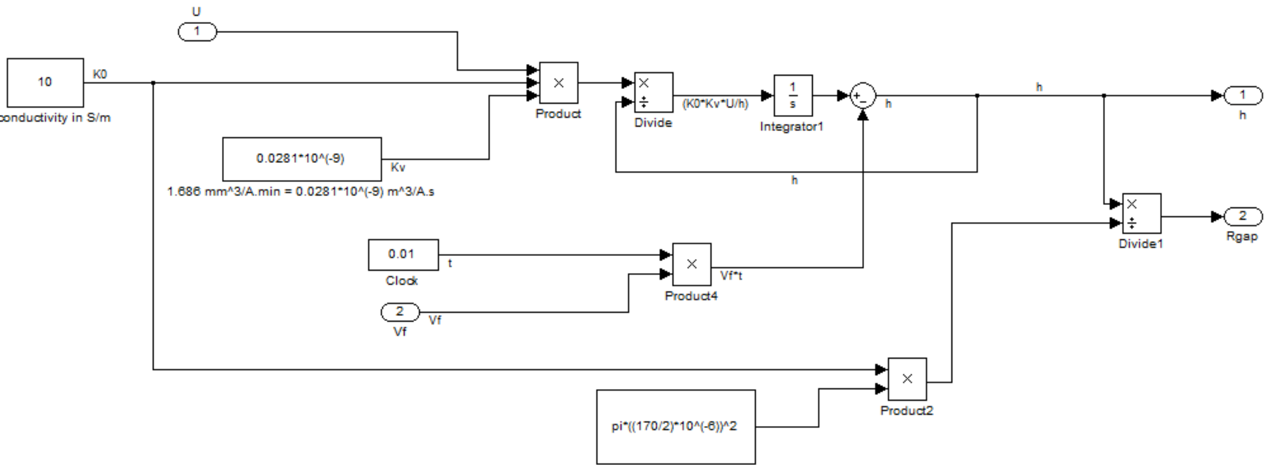

Figure 3-7: Internal diagram of the system (1) calculating the variation of h and Rgap with respect to U and Vf

With κ_0=10 S/m, the initial resistance of the gap is: $R_{gap} = \frac{h}{\kappa_0 S} \approx 22$ Ohms. A simulation for 0.01 sec gives the following results with a constant feed rate of 1mm/min (Figure 3-8).

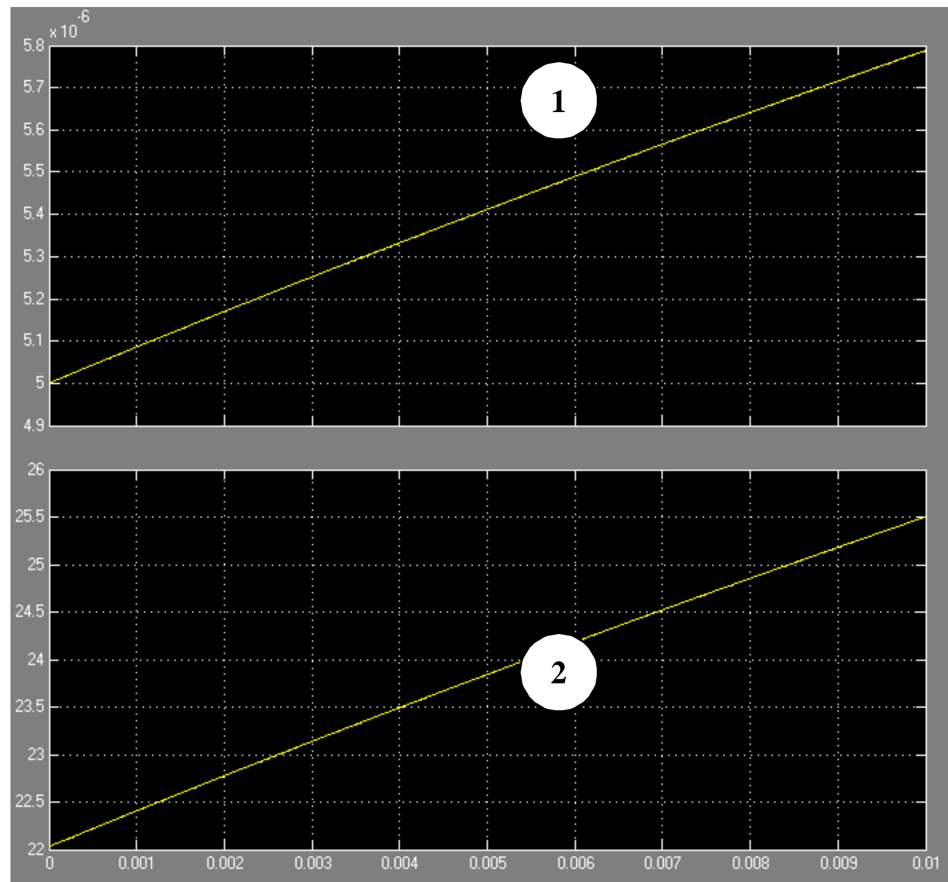

Figure 3-8: Simulation results for 0.01 sec and Vf = 5mm/min: (1) variation of the inter-electrode gap (m) over time (s); (2) variation of the inter-electrode gap resistance (Ohm) over time (s)

It can be noticed (Figure 3-8) that the gap is increasing over time, which means that the feed rate is not high enough to compensate for the dissolution of the material. Therefore it has to be increased.

A simulation for 0.01 sec gives the following results with a constant feed rate of 5mm/min (Figure 3-9).

Figure 3-9 shows that the inter-electrode gap increases at a much slower rate over time when the feed rate in this simulation. This means that the value of the velocity of the electrode is close to the dissolution rate of the workpiece.

Defining the optimal feed rate is important since it is the only mean to theoretically maintain the gap to a constant value.

The Wei's constant feedrate model and the steady state value of the inter-electrode equilibrium gap can be used to define the ideal feed rate.

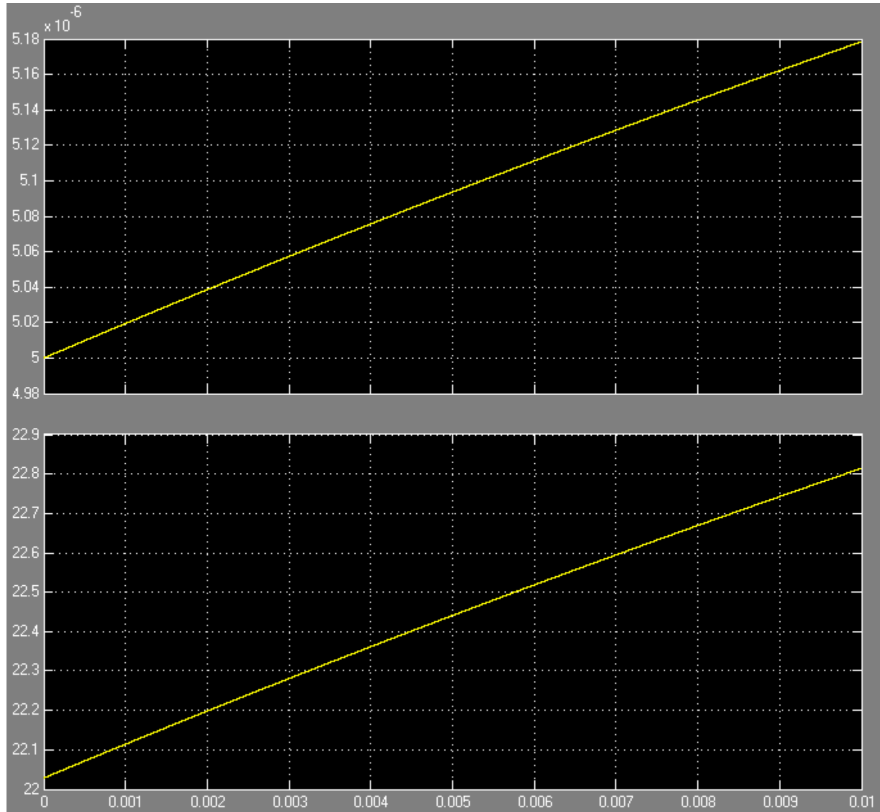

Figure 3-9: Simulation results for 0.01 sec and Vf = 5mm/min: (1) variation of the inter-electrode gap (m) over time (s); (2) variation of the inter-electrode gap resistance (Ohm) over time (s)

It has been seen previously that whatever the initial value of the gap is, the IEG will converge towards a constant value over time. The optimal feed rate can therefore be found with the following expression:

$$V_f = \frac{\kappa_0 . K_v (U_0 - \Delta U)}{h_f} \quad (3\text{-}10)$$

With the values from the previous model the optimal feed rate is:

$\kappa_0 = 10\ S/m;\ K_v = 0.0281.10^{-9} m^3/A.s;\ U_0 - \Delta U = 10V;\ h_f = 5.10^{-6} m$

$$V_f = \frac{10 \times 0.0281.10^{-9} \times 10}{5.10^{-6}} \cong 5.62.10^{-4}\ m/s$$

However, since the pulse on-time represents 1/6 of the pulse period, this result has to be divided by 6. Finally, $V_f = 0.936667 \times 10^{-4}\ m/s$.

The calculation time of the previous model was very long, another similar model has therefore been made without using P-SIM components (Figure 3-10). Thanks to this model the calculation time is reduced and the model can therefore be simulated for a longer period.

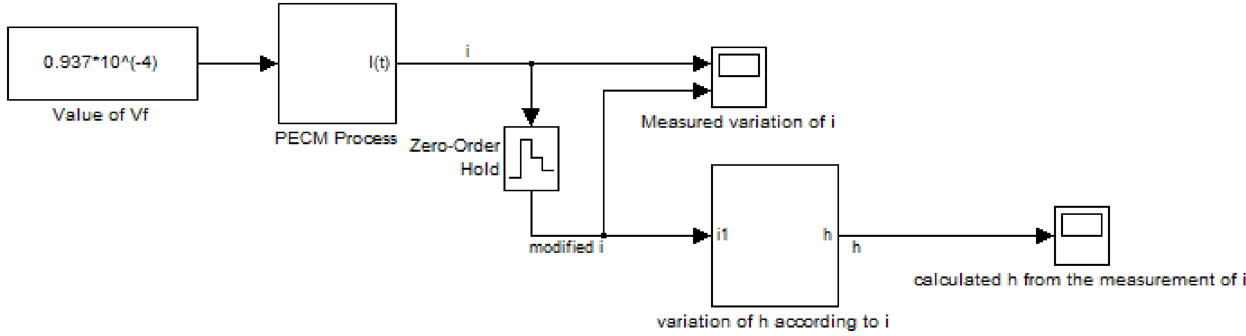

Figure 3-10: Scheme diagram of the Matlab model used to define the optimal theoretical feed rate

A simulation with the optimal feed rate value of the feed rate gives the results in Figure 3-11 and Figure 3-12.

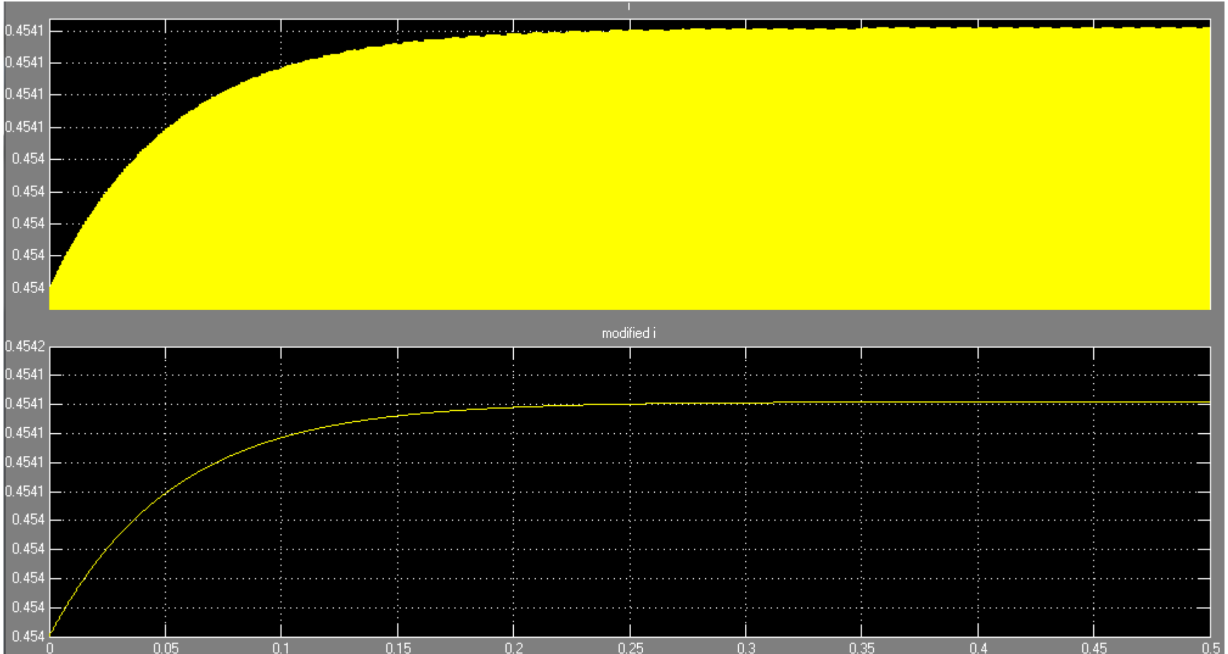

Figure 3-11: Measured variation of i (A) over time over time before and after the Zero-Order Hold block

It can be observed (Figure 3-12) that the inter-electrode gap slightly decreases over time before reaching the steady state value of the equilibrium gap. It is linked to the fact that the value of the constant feed rate has been rounded from $0{,}936667\ .10^{-4}$ m/s to $0{,}937\ .10^{-4}$ m/s approximating the equilibrium inter-electrode gap to:

$$h_f = \frac{10 \times 0.0281.\,10^{-9} \times 10}{0{,}937\ .10^{-4} \times 6} = 4.9982\ \mu\mathrm{m}$$

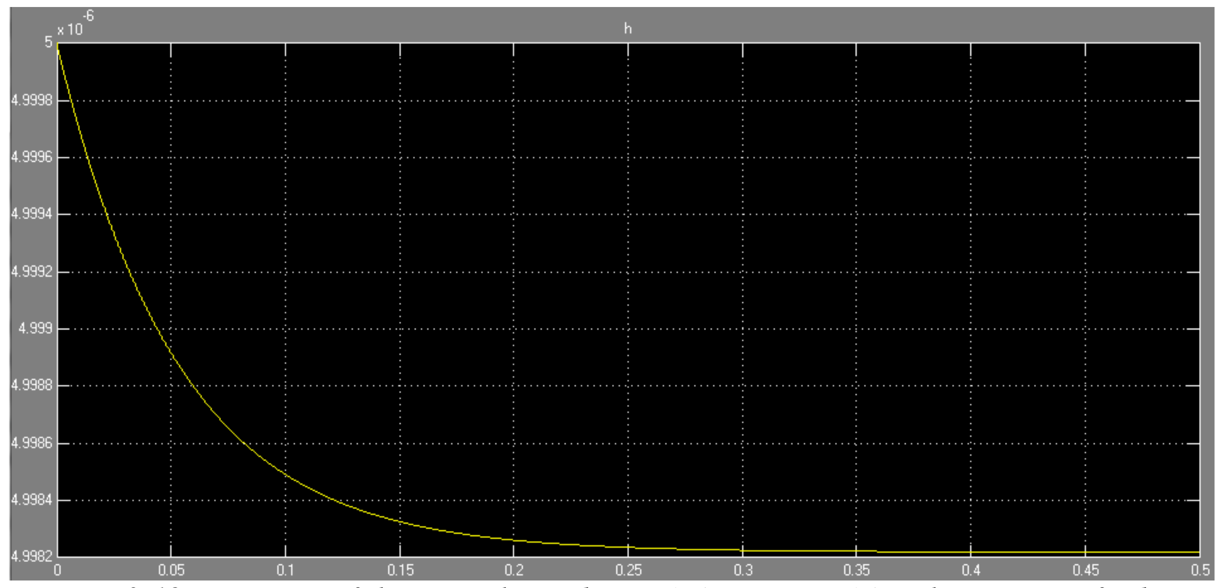

Figure 3-12: Variation of the inter-electrode gap (m) over time (s) with a constant feed rate of $0.937 \times 10^{-4} m/s$

The current is therefore maintained to the same value, throughout the machining time, guaranteeing a constant material removal rate.

3.2.3. Concluding remarks regarding Bin Wei's model with constant feed rate

The notion of equilibrium gap has been explained and a way to maintain the gap to a constant value was theoretically verified. The feed rate has been adjusted to obtain the desired inter-electrode gap. The simulations done in this part confirmed that an equilibrium gap could be reached and this model can be used to define the optimal feed rate value.

This is however very hard to reach an equilibrium state in real machining conditions: a short-circuit can occur and change the MRR within the gap. This leads to unstable behaviour. This model is particularly suited for PECM at high current densities and large machining gaps, but in µECM the gap and current densities are respectively much smaller and lower.

3.3. µECM model according to Marla et al.

Marla et al. (Marla, Joshi and Mitra, 2008) suggested that the removed material could be calculated according to the following equation:

$$m = \frac{A.S}{z.F} \kappa_0 \frac{\partial E}{\partial x}_{x=h} n_d T_{tot} = k.S.J.n_d.T_{tot} \qquad (3\text{-}11)$$

where:

- T_{tot} is the total time of machining including the on-time and off-time
- $k = \frac{A}{z.F}$ is a constant of electrochemical machinability.
- S is the cross sectional area of the tool-electrode
- n_d is the duty cycle of the pulses defined as:

$$n_d = \frac{T_{on}}{T_{on} + T_{off}}$$

- J is the current density defined as (Marla, Joshi and Mitra, 2008)

$$J = \kappa_0 \frac{\partial E}{\partial x}_{x=h} = \frac{I}{S}.$$

with a potential gradient in the x direction equal to $\frac{\partial E}{\partial x}_{x=h} = V$

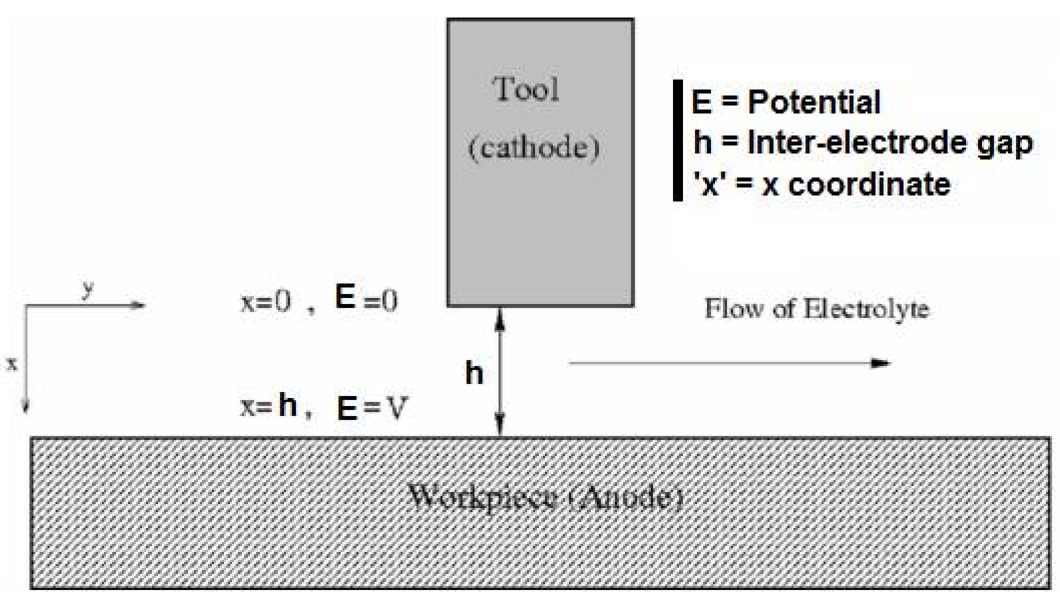

Figure 3-13: Schematic of the µECM process (Marla, Joshi and Mitra, 2008)

According to equation (2-10) and taking the current efficiency into account, the volume of material removed throughout the µECM process can be calculated as follows:

$$\frac{m}{\rho} = V = n_d . K_{valloy} . I . T_{tot} \qquad (3\text{-}12)$$

This model expression is in agreement with Bin Wei's model. However, the electrical double layer (EDL) effect is not taken into account in their model.

3.4. The electrical double layer: study of existing models and simulation

3.4.1. Models of the electrical double layer effect on the gap voltage

In ECM the electrical model of the inter-electrode gap is a variable resistance. However, in μECM the effect of the electrical double layer (EDL) is significant enough not to be neglected (Spieser, 2011).

If the EDL charging time is equal to the pulse on-time, the potential at the EDL is always varying, since the double layer capacitance is charged during each pulse. The expression of the anodic over-potential is therefore (Schuster and Kirchner, 2004; Kim et al., 2005a; b; Zhang et al., 2007):

$$E_a(t) = E_{a0}\left(1 - e^{-\frac{t}{\tau}}\right) \approx E_{a0}\frac{t}{\tau} \quad \text{(Taylor approx.)} \tag{3-13}$$

Where E_{a0} is the stationary value of the over-potential, t is the polarization time and $\tau = RC$ corresponds to the EDL charging time.

According to the Tafel equation, the expression of the current density during the charge of the EDL is the following (Schuster and Kirchner, 2004; Kim et al., 2005a; b; Zhang et al., 2007):

$$i_a(t) = i_{a0}e^{\frac{\beta nF}{R_gT}E_a(t)} \approx i_{a0}e^{\frac{\beta nF}{R_gT}\times E_{a0}\times\frac{t}{\tau}} \tag{3-14}$$

Where i_{a0} is the exchange current density, β is the transfer coefficient (usually equal to 0.5), n is the number of electrons (2 and 3 for respectively the ions Fe II and Fe III), F is the Faraday constant, R_g is the gas constant and T is the temperature (in °K).

The volume V of dissolved material after 1 pulse is therefore equal to:

$$V = K_v.\int_0^{t_{on}} i_a(t)\,dt = K_v.\int_0^{t_{on}} i_{a0}e^{\frac{\beta nF}{R_gT}\times E_{a0}\times\frac{t}{\tau}}\,dt$$

$$V = K_v.\,i_{a0}\frac{R_gT}{\beta nF}\frac{\tau}{E_{a0}}.\,[\,e^{\frac{\beta nF}{R_gT}\times E_{a0}\times\frac{t_{on}}{\tau}} - 1] \tag{3-15}$$

However, Kozak claimed (Kozak, Gulbinowicz and Gulbinowicz, 2008) that the current density going through the double layer was actually the sum of 2 different current densities:

- The charging current: it is the current density that flows through the double layer when it is getting charged
- The faradaic current: it is the current density that participates in the dissolution of the material when the electrical double layer is fully charged

The equation describing the evolution of the current during the charge of a capacitor is:

$$i(t) = C.\frac{dU(t)}{dt} \quad (3\text{-}16)$$

Where C is the capacitance of the capacitor (in F) and $U(t)$ is the potential applied to the capacitor (in V).

According to the Butler-equation the values of the Faraday current densities at the tool and at the workpiece are given by (Kozak, Gulbinowicz and Gulbinowicz, 2008):

$$\text{At the anode: } i_{fa} = i_{a0}\left(e^{\frac{(1-\beta)nF}{R_gT}E_a(t)} - e^{\frac{(-\beta)nF}{R_gT}E_a(t)}\right)$$
$$\text{At the cathode: } i_{fc} = i_{c0}\left(e^{\frac{(1-\beta)nF}{R_gT}E_c(t)} - e^{\frac{(-\beta)nF}{R_gT}E_c(t)}\right) \quad (3\text{-}17)$$

The total currents at the cathode i_c and at the anode i_a can be expressed as follows:

$$i_a(t) = i_{ca}(t) + i_{fa}(t) = C_a.\frac{dE_a(t)}{dt} + i_{a0}\left(e^{\frac{(1-\beta)nF}{R_gT}E_a(t)} - e^{\frac{(-\beta)nF}{R_gT}E_a(t)}\right)$$
$$i_c(t) = i_{cc}(t) + i_{fc}(t) = C_c.\frac{dE_c(t)}{dt} + i_{c0}\left(e^{\frac{(1-\beta)nF}{R_gT}E_c(t)} - e^{\frac{(-\beta)nF}{R_gT}E_c(t)}\right) \quad (3\text{-}18)$$

It has been previously seen that a certain activating voltage had to be applied for the dissolution to occur and that the resulting current density was non-linear. In their patent, Schuster et al. described the evolution of the EDL current density with respect to the polarization voltage thanks to the chart in Figure 3-14 (Schuster and Kirchner, 2004).

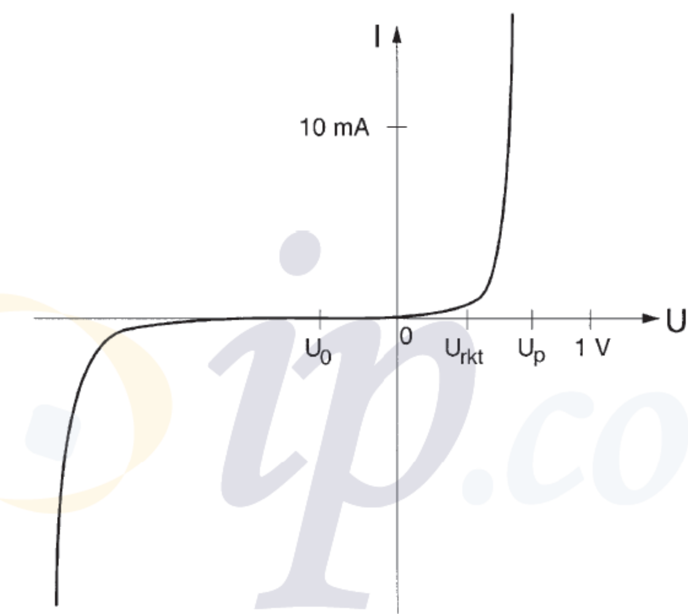

Figure 3-14: Evolution of the gap current with respect to the applied voltage, Urkt : activating potential (V) , Up : Pulse amplitude (V) (Schuster and Kirchner, 2004)

3.4.2. Similarities with Zener diodes

It can be noticed that this current/voltage non-linear relationship is very similar to the one of a Zener diode. Indeed, in a Zener diode, the current evolves with respect to a polarization voltage according to the characteristic graph (Figure 3-15):

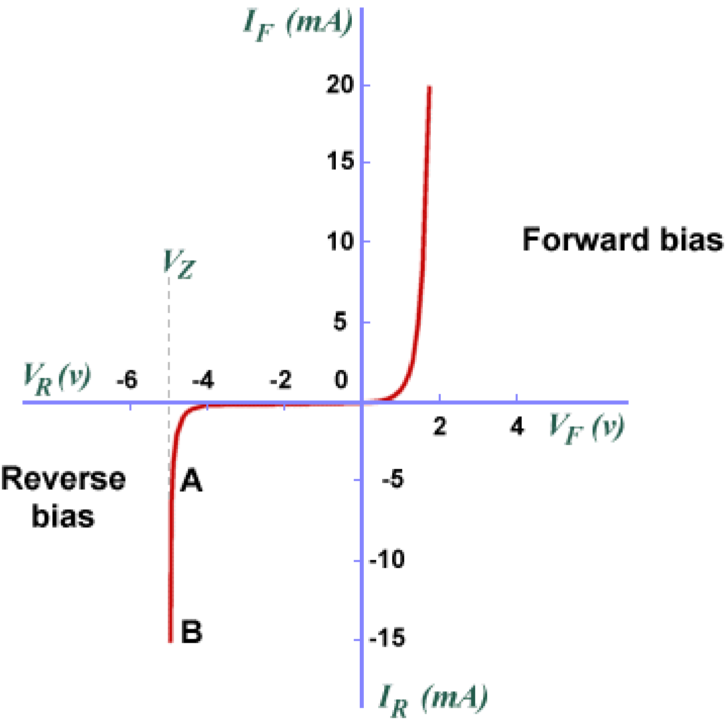

Figure 3-15: Evolution of the current (mA) in a diode with respect to its polarization voltage (V) (Technologyuk.net, 2011)

In the following model, the electrical double layer will therefore be represented in Figure 3-16.

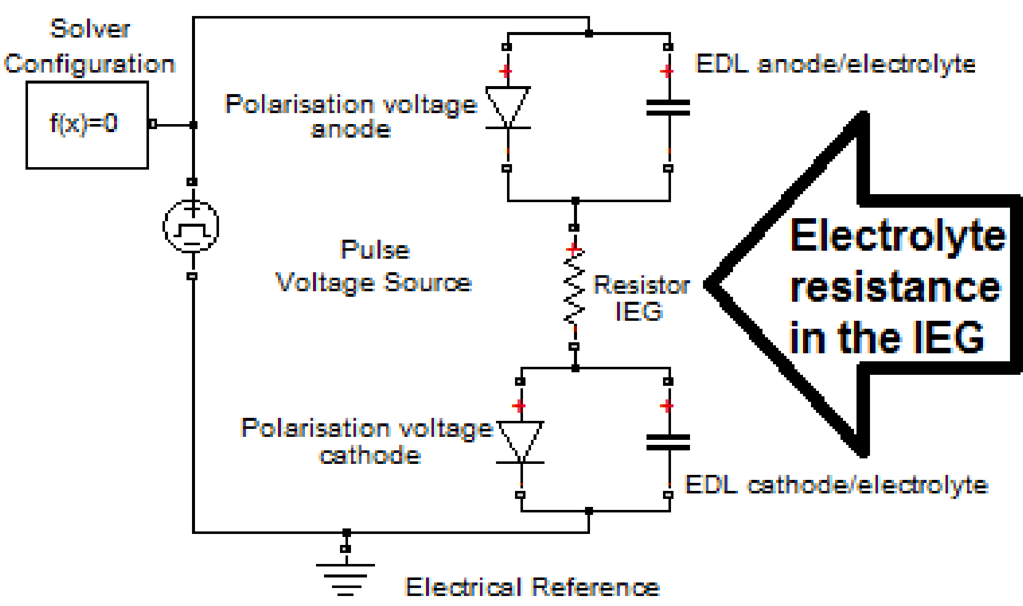

Figure 3-16: Proposed inter-electrode gap model (Spieser, 2011)

According to Kirchoff's law, in the proposed model, the current passing through the Zener diode will be added to the charging current of the capacitor. The faradaic current density is therefore represented by the current of the diode.

The model has been simulated with the following values:

Diode resistance of the double layers (diode): $R_{dla} = R_{dlc} = R_{DL} = 5.10^{-5}$ Ohm; Polarization voltage: 0,5V; Pulse width: 10ns; Pulse period: 60ns; Electrolyte Resistance: R_e 30.10^{-5} Ohm;

Capacitance of the EDLs: $C_a = C_c = C_{DL} = 10.10^{-6}F$

The time constant of the above circuit τ is equal to (Van Damme et al., 2011):

$$\tau = R_{eq.}C_{eq.} = \frac{1}{\frac{1}{C_{DL}R_e} + \frac{2}{C_{DL}R_{DL}}} \approx 2.3 \times 10^{-10}s \tag{3-19}$$

The following chart shows the value of the current passing through the anodic EDL during its charge (Figure 3-17):

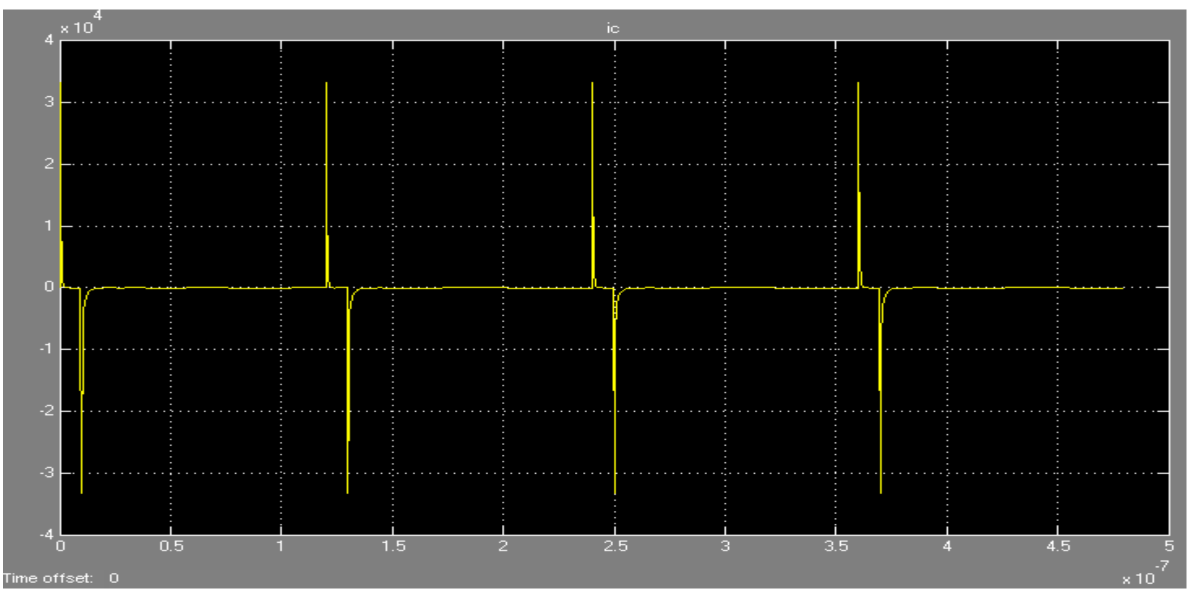

Figure 3-17: Variation of the current density passing through the EDL of the anode during its charge (I_{ca}) in A/m² over time (s) (Spieser, 2011)

The loading/unloading time constant is very small hence the curve representing the current is very sharp.

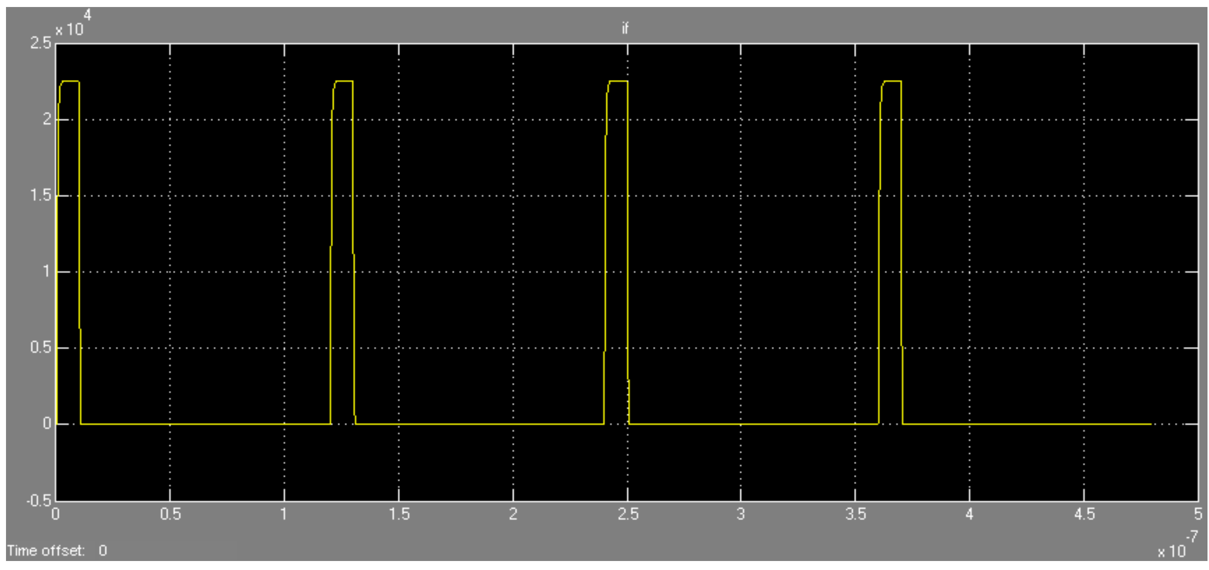

Figure 3-18: Variation of the faradaic current passing through the EDL of the anode (I_{fa}) in A/m² over time (s) (Spieser, 2011)

The above pulses (Figure 3-18) represent the faradaic current density that will take part in the dissolution process of the workpiece.

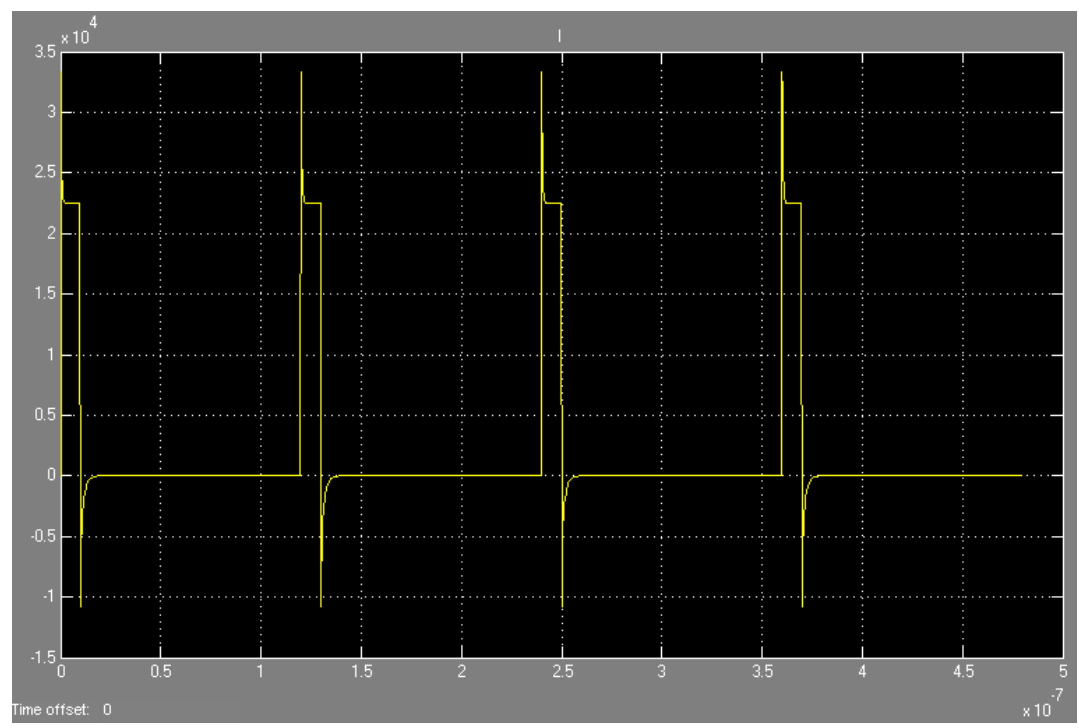

Figure 3-19: Variation of the total current density (ic + if) flowing through the system (A/m²) over time (s) (Spieser, 2011)

On the above graph (Figure 3-19), the total current density flowing through the system is represented. It can clearly be seen that the total current is the sum of the faradaic and charging ones.

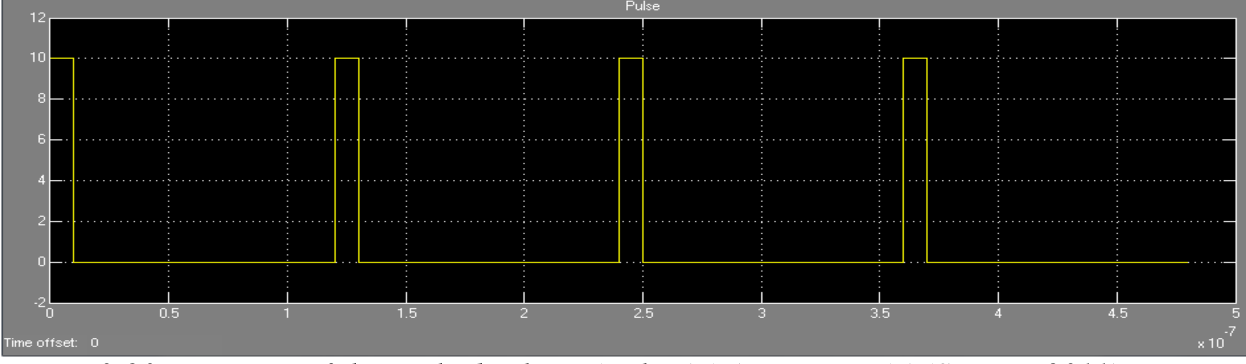

Figure 3-20: Variation of the applied voltage (Pulses) (V) over time (s) (Spieser, 2011)

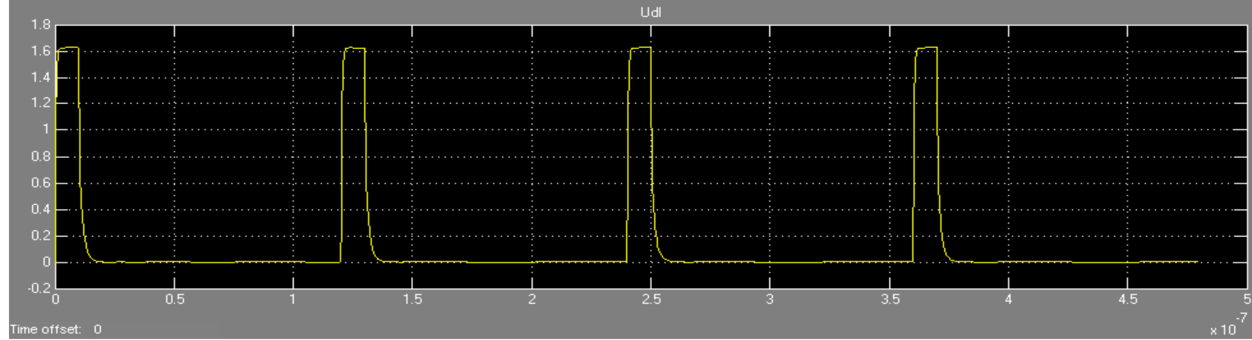

Figure 3-21: Potential at the EDL of the anode (V) over time (s) (Spieser, 2011)

By taking into account the electrical double layer, more realistic pulses have been obtained.

This part can be considered as a first exploration of the inter-electrode gap evolution. Pulses have been applied to the gap and the influence of the electrical double layer on the current response has been modelled. It has been confirmed that the current passing through the system is the sum of the faradaic current and the charging current of the EDL (Spieser, 2011).

3.4.3. More realistic model of the IEG

This model combines the gap model taking into the EDL and adds the effect of the cabling on the overall machining current. The following values are taken:

Influence of connection cables: these cables connect to pulse PSU to the machining cell. It is assume that the cables are made of copper which has an electrical resistivity of $\rho = 16.78\ n\Omega.m$. The cable is considered to be of length $l = 0.12m$ and to have a cross-sectional area of $S = 2 \times 10^{-6}m^2$.

The cable resistance can therefore be calculated as follows:

$$R_{cable} = \rho\frac{l}{S} = 16.78 \times 10^{-9}\frac{0.12}{2 \times 10^{-6}m^2} \cong 0.001\Omega \quad (3\text{-}20)$$

The cable inductance is modelled by a 75nH inductor.

The electrolyte resistance is considered to have a conductivty σ of 13S/m. Assuming a gap of 5µm and that the current flows only through the front face of a cylindrical cathode having a diameter of 170µm, the electrolyte resistance in the IEG can be expressed the following way:

$$R_e = \frac{h}{\sigma S} = \frac{5 \times 10^{-6}}{13 \times \pi \times (85 \times 10^{-6})^2} \cong 16.94\Omega \quad (3\text{-}21)$$

The pulse on-time is set to 150ns whereas the pulse period is set to 1µs.

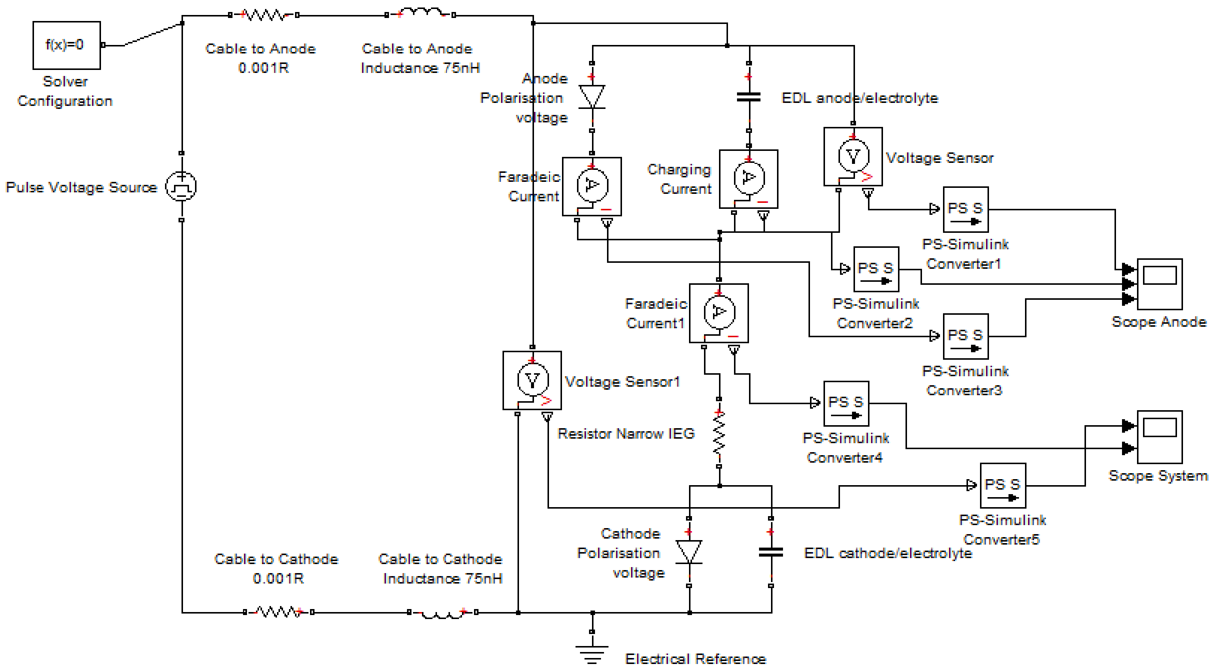

Figure 3-22: Picture of the more realistic model of the IEG

Using these values, the following results can be obtained:

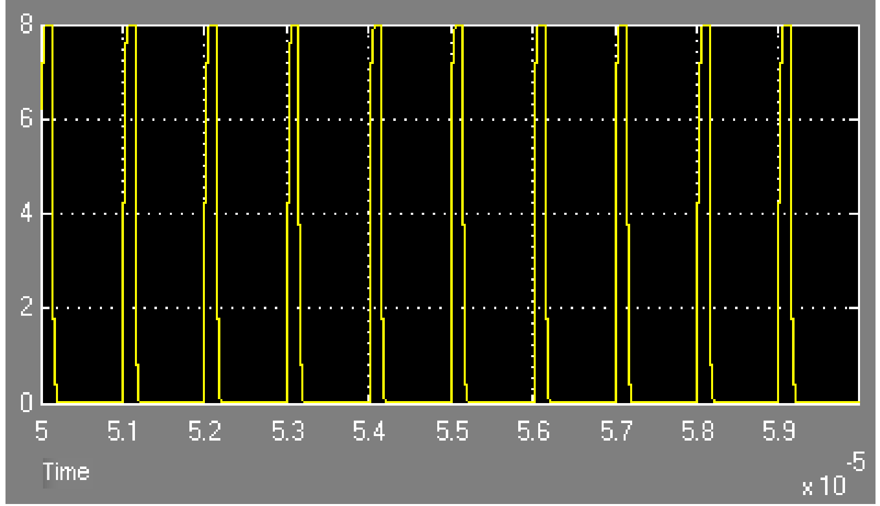

Figure 3-23: Voltage pulses measured across the gap in V and time in s

It can be observed that in µECM the total amount of current flowing through the system is not very high compared to conventional ECM. This is mainly due to the small size of the tool reducing the active area dramatically, and therefore increasing the resistance in the gap.

In µECM the dissolution will show a stochastic behavior due to the variation of material properties and composition as well as the variation of the electrical parameters of the continuum and if for any reason the dissolution rate changes during the process, the inter-electrode gap will not be maintained since the feed rate does not vary over time in the previous model.

To adjust the feed rate according to the variation of the dissolution rate, a control system has to be developed.

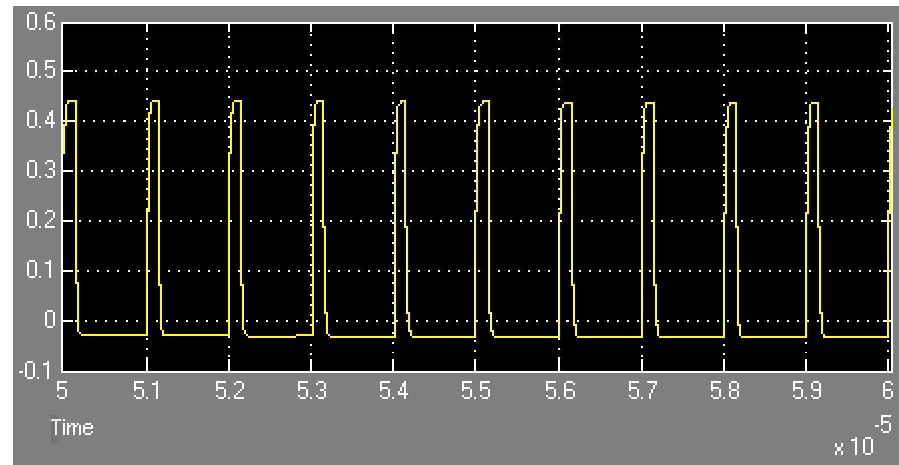

Figure 3-24: Faradaic current pulses, amplitude in A and time in seconds

3.5. 2D Drilling simulation with simple electrical double layer (EDL) model

Mathematical models have been developed to provide with a better insight of the ECM and PECM processes (McGeough, 1974; Datta and Landolt, 1981; Rajurkar et al., 1993, 1995; Floridor et al., 2004). However, in μECM these models cannot be applied anymore: the inter-electrode gap size is so small (less than 10μm) that factors that were neglected before (electrical double layer (EDL) effect, local electrolyte conductivity and electrical field distribution) are now significant enough to change the machining process (Davydov, Volgin and Lyubimov, 2004; Cagnon et al., 2003; Schuster et al., 2000; Kirchner et al., 2001; Marla, Joshi and Mitra, 2008; Kozak, Gulbinowicz and Gulbinowicz, 2008).

Most of the simulation models reviewed are very computationally intensive and do not allow simulations for a very long period of time (Hotoiu et al., 2011; Deconinck, Van Damme and Deconinck, 2012b; Van Damme et al., 2011).

In this section a simplified μECM process model is proposed by assuming that the EDL effect behaves like a low-pass filter that attenuates the pulses when either the frequency or the IEG increase. This model can be used to quickly setup a machining session and estimate the material removal rates for specific values of the machining parameters.

A simulation program has been developed using LabVIEW in order to study the influence of the different machining parameter and to predict the shape of the machined hole. This

program gives useful insights on how the process will behave and can be used to determine the machining parameters to achieve a desired shape.

3.5.1. Point to point inter-electrode gap (h) calculation method

If we suppose that electrical charges are uniformly distributed along the tool-electrode surface, it is possible to calculate the change in position of each point of the workpiece by calculating the local change in gap dh during a time dt. The distance h between a point of the tool and a point of the workpiece influences the value of dh (Figure 3-25).

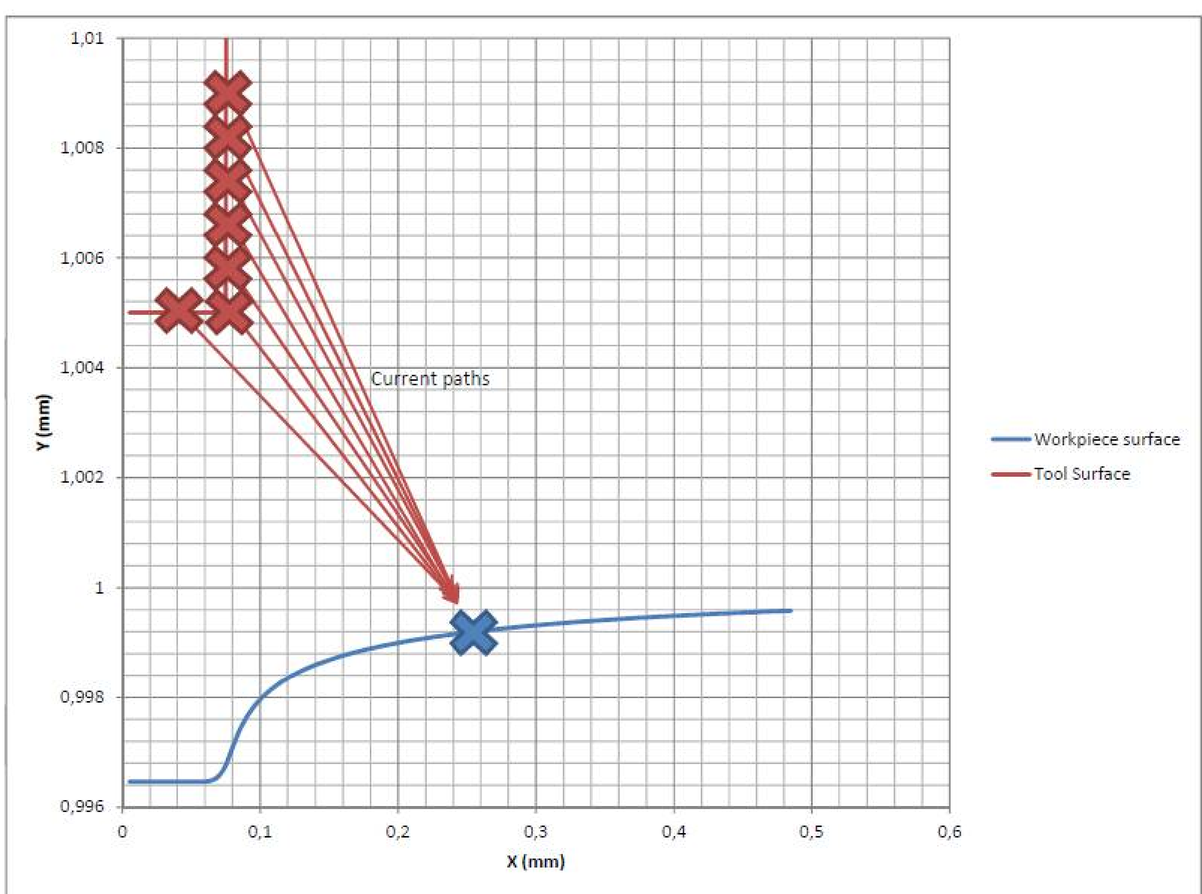

Figure 3-25: Drawing illustrating the tool-workpiece geometrical configuration

Therefore, before calculating dh, the shortest distance h between the tool surface and a point of the workpiece surface must be found. The distance h_{ij} between a point of the tool surface with coordinates (X_j, Y_j) and a point i of the workpiece surface with coordinates (X_i, Y_i) can be calculated as follows:

$$h_{ij} = \sqrt{(X_i - X_j)^2 + (Y_i - Y_j)^2} \quad (3\text{-}22)$$

The number of points (X_i, Y_i) and (X_j, Y_j) depends on the resolution chosen. The algorithm will calculate for each point (X_i, Y_i) all the possible gaps h_{ij} and will then take the smallest one.

3.5.2. Modelling the influence of the EDL on the gap change

The current density can be deduced thanks to Ohm's law:

$$J = \kappa_0 E \tag{3-23}$$

Where J is the current density (A/m², κ_0 is the conductivity (S/m) of the electrolyte and E is the intensity of the electric field in (V/m).

With $c = \kappa_0 . K_v$ (3-6) becomes:

$$dh = \frac{\kappa_0 . K_v (U_0 - \Delta U)}{h} dt = \frac{c(U_0 - \Delta U)}{h} dt \tag{3-24}$$

However, the above equation does not include the influence of the EDL on the process. Schuster et al. mentioned that the electrical double layer can be modelled as a RC circuit, which behaves like a low pass filter (Schuster and Kirchner, 2004; Schuster et al., 2000). According to their work, the charging constant τ of EDL would be calculated as follows:

$$\tau = \frac{h}{\kappa_0} C_{DL} \tag{3-25}$$

It is important to mention that C_{DL} is in µF/m². This equation respects the SI units because farads are also seen as seconds/Ω.

Assuming that the capacitance of the electrical double layer C_{DL} remains constant during the process, it is possible to calculate the cut-off frequency f_{cutoff} of the RC network:

$$f_{cutoff}(h) = \frac{1}{2\pi\tau(h)} = \frac{1}{2\pi R_e(h) C_{DL}} \tag{3-26}$$

Where R_e is the resistance of the electrolyte through which the current is flowing to charge the EDL and depends on the distance between the tool and the workpiece (IEG or h).

R_{el} is calculated as Wei and Marla suggested it, by considering that the conductive area of the tool is equal to its cross section S:

$$R_e(h) = \frac{h}{\kappa_0 S} \tag{3-27}$$

Following the properties of a low-pass filter, the amplitude of the pulses will decrease depending on the frequency and the resistance R_e. This decreasing effect can be modelled using the following formula to calculate the gain $H(f)$.

$$H(h,f) = \frac{U_{0-out}}{U_{0-in}} = \frac{1}{\sqrt{1 + (\frac{2\pi f}{2\pi f_{cutoff}(h)})^2}} \quad (3\text{-}28)$$

$H(f)$ is used to calculate the amplitude of the voltage pulse which will remove material, and the duty cycle n_d is added to the equation.

$$dh = c\frac{(n_d.U_0.H(h,f) - \Delta U)}{h}dt \quad (3\text{-}29)$$

Also, the impedance of the cabling has an influence on the process. The impedance of the cable increases along with the pulse frequency f because of its parasitic inductance L. The general formula to calculate the impedance Z is as follows:

$$Z(f) = \sqrt{R_{cable}^2 + (X_L(f))^2} \quad (3\text{-}30)$$

Where the inductive reactance of the cable is: $X_L(f) = 2\pi fL$

To include the impedance of the cables, the equation to calculate dh is changed the following way:

$$dh = K_v\frac{(n_d.U_0.H(h,f) - \Delta U)}{\left(R_e(h) + Z_{sys}(f)\right).S}dt \quad (3\text{-}31)$$

Where $Z_{sys}(f)$ is the impedance of the cabling as well as the resistance of the tool electrode (the 'sys' index is for system).

Also the current I can be calculated directly by applying the following formula:

$$I(h,f) = \frac{(n_d.U_0.H(h,f) - \Delta U)}{R_e(h) + Z_{sys}(f)} \quad (3\text{-}32)$$

3.5.3. Simulation workflow

The workpiece Y position $Y_i(t)$ can be calculated after each time step dt as followed:

$$Y_i(t) = Y_i(t - dt) - dh_{ij} \quad (3\text{-}33)$$

Where $Y_i(t)$ is the new Y position of the point of the workpiece is surface and $Y_i(t - dt)$ is the previously calculated Y_i surface position (at the simulation time t-dt).

The expression $P(U_i, h_i)$ can be described this way:

$$dh_{ij} = K_v \frac{(n_d . U_0 . H(h_{ij}, f) - \Delta U)}{\left(R_{el}(h_{ij}) + Z_{sys}(f)\right) . S} dt \qquad (3\text{-}34)$$

At the beginning of the simulation, a squared mesh (Figure 3-27) is created according to the geometrical configuration specified by the user.

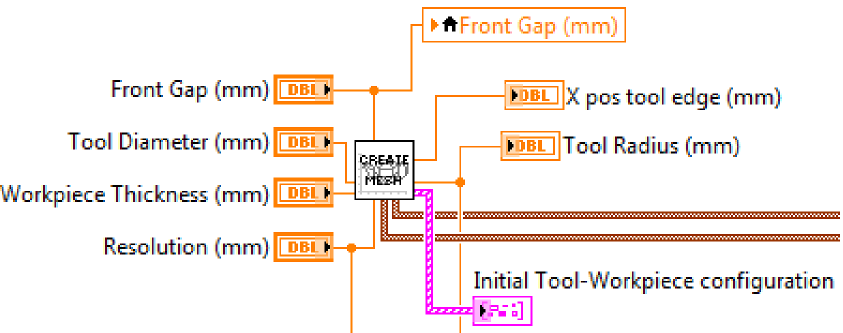

Figure 3-26: VI creating the mesh for the simulation

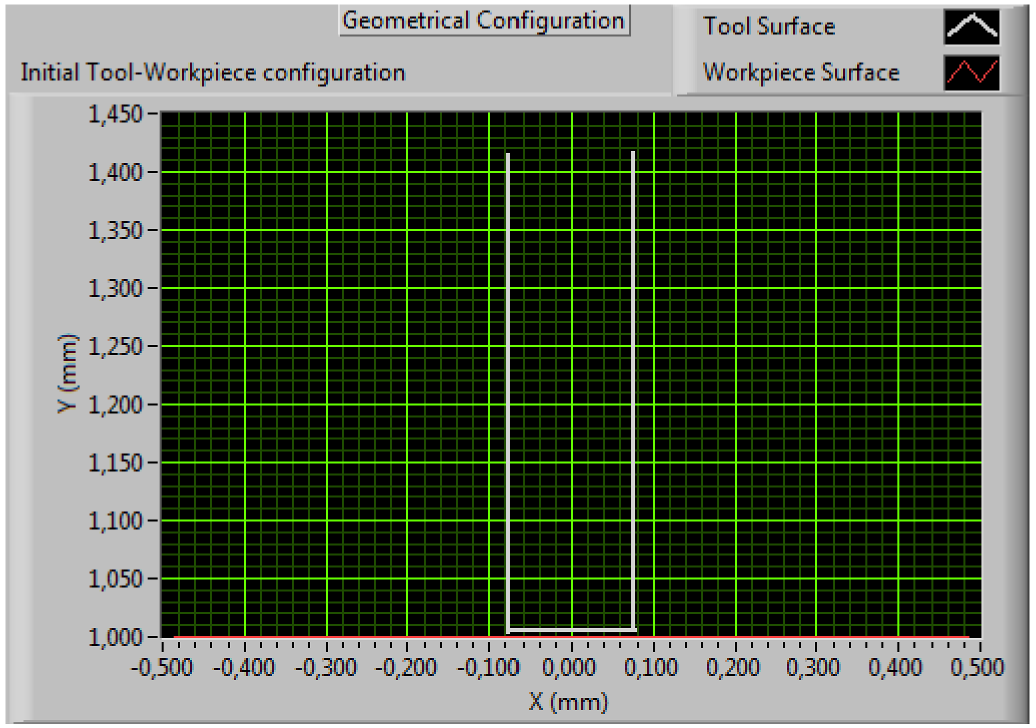

Figure 3-27: Picture of the geometrical configuration created by the 'Create Mesh' VI

The removed depth at each time step is calculated according to the following algorithm (Figure 3-28):

Every second during the simulation time, the position of the tool is updated and the new workpiece surface is plotted.

For each point (X_i, Y_i) of the workpiece surface do:

<table>
<tr><td>1</td><td>Generate an array of the temporal mean values of the voltage $n_d.U_0$ for each desired time step dt</td></tr>
<tr><td rowspan="5">2</td><td>For each cell of the created array, do:</td></tr>
<tr><td>Find the shortest tool-workpiece distance :
$h_{ij} = \sqrt{(X_i - X_j)^2 + (Y_i - Y_j)^2}$</td></tr>
<tr><td>Calculate $R_{el}(h_{ij})$, $H(h_{ij},f)$ and $Z_{sys}(f)$.</td></tr>
<tr><td>Calculate the gap change for one time step:
$dh_{ij} = K_v \frac{(n_d.U_0.H(h_{ij},f) - \Delta U)}{R_{el}(h_{ij}) + Z_{sys}(f)} dt$</td></tr>
<tr><td>Update the Y position of the workpiece surface point:
$Y_i(t) = Y_i(t - dt) - dh_{ij}$
And then jump to the next cell using this new Y position.</td></tr>
</table>

$Y_i(t)$

End of 'for each point (X_i, Y_i) of the workpiece surface do'

Figure 3-28: Simplified flowchart of the LabVIEW simulation programme

Figure 3-29 shows the final shape of the workpiece after a 50µm drilling session using parameters in Table 3-1.

Frequency (Hz)	60000
Duty Cycle (%)	25
Off-time Offset (V)	0
Pulse amplitude (V)	8
Kv (cubic mm/As)	0.0281
Conductivity (S/mm)	0.013
EDL Capacitance (F/mm²)	1.00E-07
Activation Potential (V)	0.92
Current efficiency (%)	50
Feed Rate (mm/s)	0.000624
Simulation Time (s)	35
System Resistance (Ωs)	0.001

Table 3-1: Simulation parameters used to obtain the shape shown in figure 24.

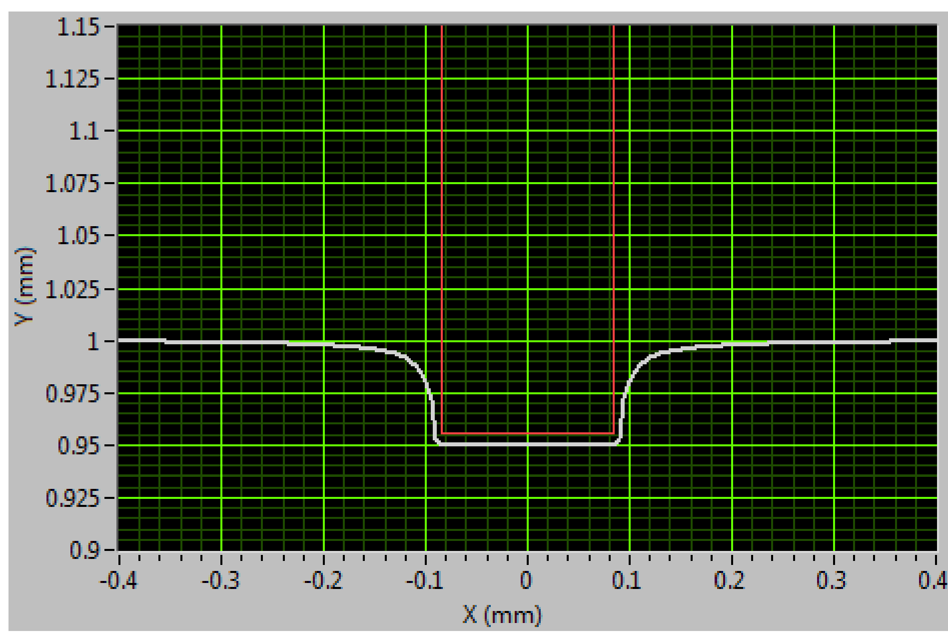

Figure 3-29: Simulation results after a 50µm drilling simulation in 2D, the tool surface is in red and the workpiece surface is in white.

The programme exports the machining results by creating a text file which can then be imported in Microsoft Office Excel to in order to compare the different workpiece shapes for different machining parameters.

3.6. Influence of the pulse frequency on the localization and the machining time.

In this simulation, the tool is fed towards the workpiece so that the IEG is maintained constant. All the parameters (Table 3-2) except the frequency remain the same for the trials. The machining is stopped as soon as a depth of 50µm is achieved.

From the results (Figure 3-30) it can be observed that the frequency has a dramatic influence on the localization of the machining: at low frequency, the electrical double layer has less effect and the current passing though the side walls of tool electrode removes material at long distances from the desired machining region. This results in a hole with a relatively big tapper angle and a greater diameter than the one of the tool electrode.

On the other hand, it can be noticed that when pulsing at high frequency the machining is much more localized and the edge of the hole entry becomes sharper.

Frequency (Hz)	from 60kHz to 1MHz
Duty Cycle (%)	25
Off-time Offset (V)	0
Pulse amplitude (V)	8
Kv (cubic mm/As) (100Cr6 alloy)	0.0281
Conductivity (S/mm)	0.0027 and 0.013
EDL Capacitance (F/mm²)	1E-07
Activation Potential (V)	0.92
Current efficiency (%)	50
Simulation Time (s)	from 35s to 267s
Current efficiency	50%

Table 3-2: Machining parameters used for the simulations

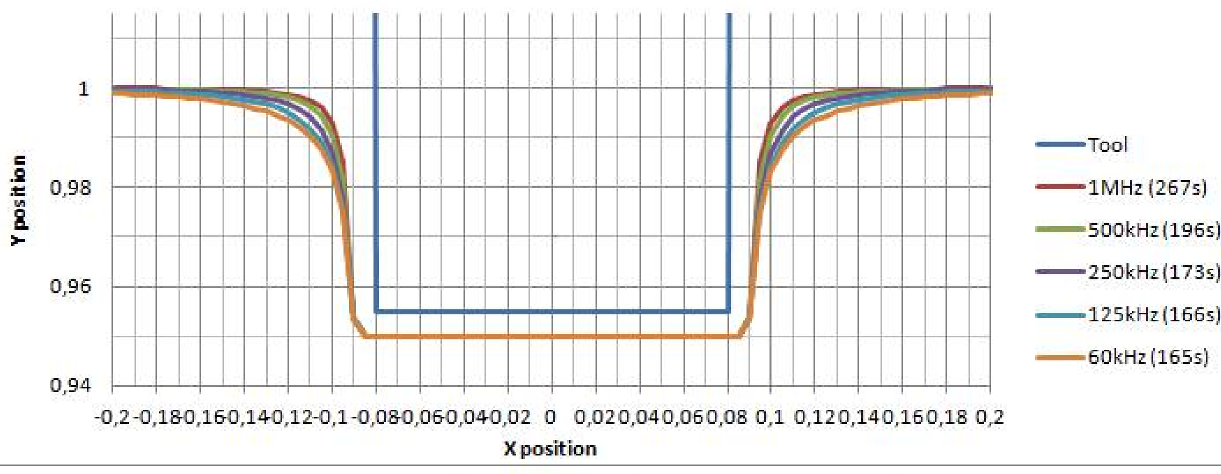

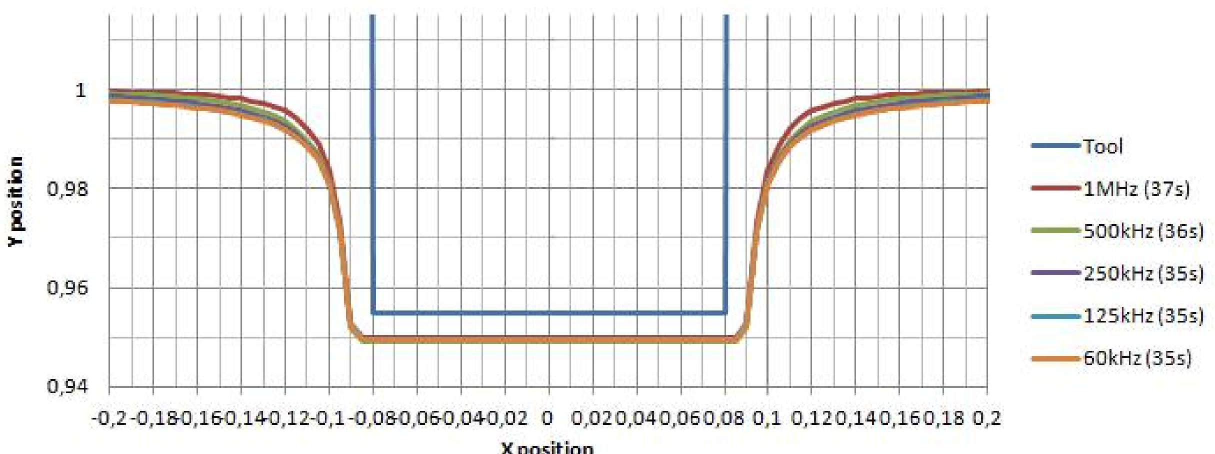

Figure 3-30: Results of the simulation illustrating the influence of the pulse frequency at different electrolyte conductivities Y and X positions are in mm.

However, at higher frequencies, the machining time to achieve the same depth is much longer because the charging time of the EDL takes a greater portion of the pulse on-time at higher frequencies and therefore the amount of faradaic current created during each pulse becomes smaller.

Moreover, it can be seen that when the conductivity of the electrolyte is low, the effect of the EDL is increased: the machining time becomes very long but the localization of the dissolution process is better than with a conductivity of 0.013 S/m. A trade-off must therefore be made in order to have an efficient and accurate machining process.

3.7. Summary

In this chapter, the behaviour of the µECM process and the influence of the electrical double layer have been modelled and simulated. The presented work is built over models found in the literature review and provides an enhanced version of what has been achieved.

The models and concepts of Marla (Marla, Joshi and Mitra, 2008), Wei (Wei, 1994), Schuster (Kozak, Gulbinowicz and Gulbinowicz, 2008) and Hocheng (Hocheng et al., 2003) have been studied, verified and combined in this work.

A simplified model assuming that the EDL effect is similar to the effect of low-pass filter was developed in order to simulate the µECM process for a long time.

The simulation programme provided realistic results and can be used to determine optimum machining parameters. The influence of conductivity and frequency on the localisation and the machining time were analysed. It was concluded that for a same frequency, the lower conductivity electrolyte exploited at best the EDL effect, providing an improved localization. However, a lower electrolyte conductivity and a higher pulse frequency will increase the machining time. Therefore, a trade-off must be made between the precision of the machining and the cycle time.

Chapter 4: AN INNOVATIVE PULSE POWER SUPPLY UNIT FOR µECM

It has been seen in the literature review that the power supply in µECM is a critical element. Different circuits have been studied and 3 prototypes have been built in order to conceive a pulse power supply meeting the requirements for µECM identified in the literature review:

- Pulse frequency: 1kHz to 5MHz
- Pulse width: 50ns to 1ms
- Ultra-fast over current protection to protect the tool
- Fully programmable with possibility to change parameters dynamically and during machining
- Possibility to reverse the pulse polarity to machine the tool without changing the cabling
- Possibility to create different pulse shapes to improve machining efficiency

This chapter presents an innovative pulse PSU for µECM. This prototype has been designed following the power electronics fundamentals explained in Appendix 3 as well as the development of two previous prototypes.

4.1. An novel pulse PSU architecture

PSU a new design of pulse power supply is proposed to be able to perform an on line machining of the cathode or to manufacture to or probes that are being clamped in the took holder without having to manually swap the polarity by changing the cabling.

Proposed pulse power supply concept:

To be able to quickly reverse the pulse polarity, an H bridge circuit has been identified as the most suitable circuit. It is composed of 4 N-type MOSFETs (SW1, SW2, SW3, and SW4):

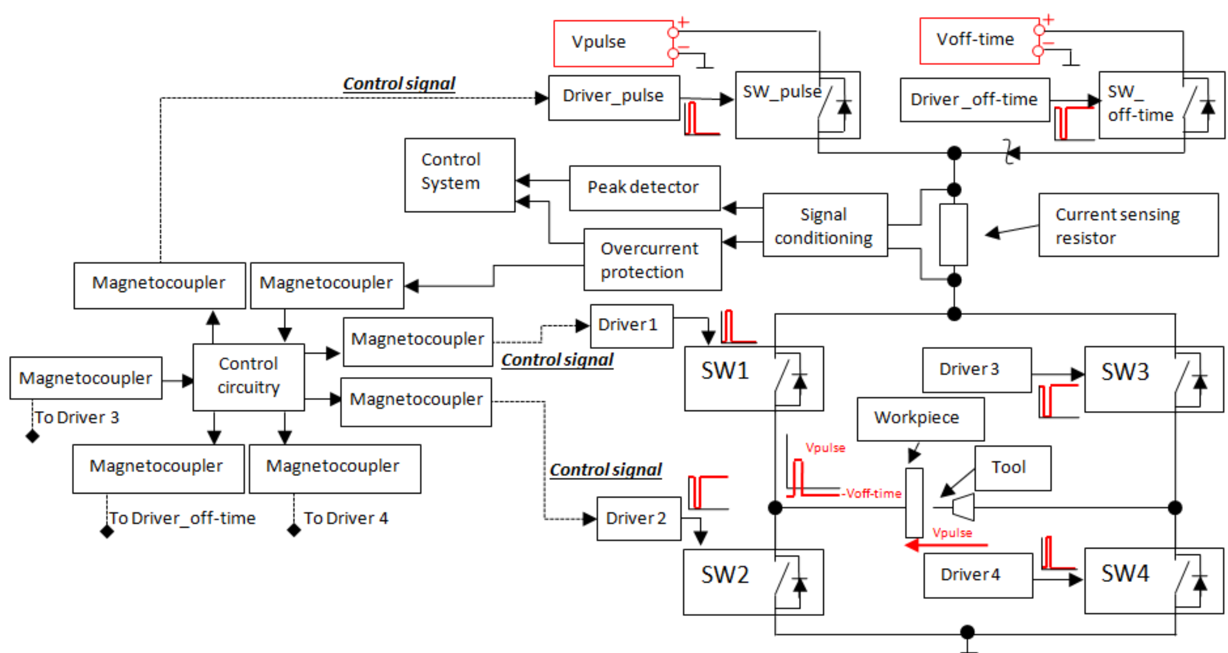

Figure 4-1: Schematic diagram of the first PSU prototype and its interfaces

When SW_pulse, SW1 and SW4 are turned on, a positive voltage is applied to the IEG and the workpiece is machined.

When SW_pulse, SW2 and SW3 are turned on, a negative voltage is applied to the IEG: the current will flow from the tool to the workpiece, which will machine the tool.

It is also possible to apply a positive voltage during the pulse on-time, followed by a negative or positive voltage set by the PSU VOff-time during the pulse off time. This configuration allows the creation of different pulse shapes to experiment the effect of the polarization voltage during the pulse off-time. The pulse shapes that can be created with this setup will be described in the section dedicated to the control circuitry.

4.2. Previous prototypes

To facilitate the testing of the developed circuits and their prototyping, each PSU prototype was separated in 3 parts:

- The control part: controlling the power components
- The power part: sending the voltage pulses to the gap
- The over-current protection part: preventing short circuits from damaging the PSU

4.2.1. First prototype

The first prototype delivered the expected results despite off the noise present in the sensing circuitry. However, some limitations have been observed:

- The way the function generator was configured prevented a wide range of frequency to be reached because a capacitance used with the oscillator could not be changed dynamically.
- There was no possibility to reverse to polarity in a programmed way. The only way to do so was to swap the cable connections.
- It was not possible to apply a negative or positive voltage offset voltage during the pulse off-time.
- The size of the board was too big and the footprint of the board needed optimization.

This prototype was mainly considered as a proof of concept to validate the choice for the core components and the 3-board modular architecture. It has been deduced that this concept would be a viable way to develop the other prototypes. The full research and development for this prototype can be read in Appendix 4.

4.2.2. Second prototype

The second prototype used an innovative architecture which was first simulated using MATLAB/Simulink (Appendix 5).

The second prototype can be seen as a proof of concept showing encouraging results (Appendix 6). The pulse polarity as well as the offset voltage during off-time worked as expected.

The new pulse generating module produced very accurate results and was a major improvement with respect to the first prototype: the pulse frequency was varied from 2kHz up to 5MHz. The drivers were drawing a lot of current at that frequency so the consumption was high and the drivers were heating up. Heat-sinks have been added to help them cool down.

This new prototype shall also offer more connectivity, with an isolated 24V digital input/output interface to efficiently communicate with the motion controller of the machine.

However, the size of the board and the layout of the PSU could be respectively smaller and more optimised. It was therefore decided to change the layout of the board, making a third prototype.

Overall, this prototype provided a solid and innovative proof of concept for a pulse PSU targeted for the µECM sector.

4.3. Pulse PSU prototype modules

4.3.1. The control circuitry

4.3.1.1. Pulse generating module

To control the switching of the MOSFETs a switching signal needs to be generated. The frequency needs to be variable over a range, 1 kHz to 5MHz, with a duty cycle changing from 5% to 100% (DC). Varying the frequency of the signal over such a large range is uncommon, pulse width modulating the resulting signal, even more so. This means that this part of the system becomes an important issue.

The solution adopted is shown in Figure 4-2 and uses two components: an oscillator and a pulse generator.

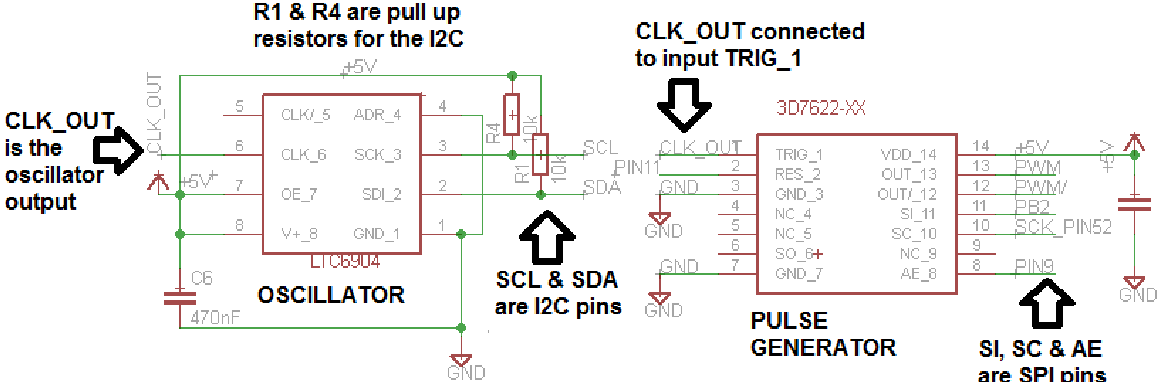

Figure 4-2: Electrical schematic diagram of the oscillator and the pulse generator

- **Oscillator**

The LTC6904 is a low power self-contained digital frequency source providing a precision frequency from set through a serial port. This programmable oscillator is capable of generating a 5V logic signal at a frequency varying from 1kHz to 68MHz. The LTC6904 requires no external components other than a power supply bypass capacitor, and it operates over a single wide supply range of 2.7V to 5.5V.

The frequency of the oscillator is set according to the following equation (Linear Technology, 2014):

$$f = 2^{OCT} . \frac{2078(Hz)}{(2 - \frac{DAC}{1024})} \quad (4\text{-}1)$$

OCT is a four-bit digital code and DAC is a ten-bit digital code. Evaluating this formula to calculate OCT and DAC from a required frequency f, gives the following statements:

$$OCT = 3.22\log_{10}\left(\frac{f}{1039}\right),$$
$$DAC = round\left(2048 - \frac{2078(Hz).2^{(10+OCT)}}{f}\right) \quad (4\text{-}2)$$

The output of the programmable oscillator LTC6904 is connected to the trigger input of the programmable pulse generator 3D7622-0.25 (Figure 4-2). The pulse generator will therefore output pulses at each rising edge of the signal coming from the LTC6904, thus creating a pulse train with adjustable frequency and duty cycle.

- **Modulation component**

The Data Delay Devices 3D7622-0.25 device is a twenty two bit serial programmable pulse generator that operates with either CMOS or TTL logic levels (Data Delay Devices, 2008).

A rising edge on the trigger input (TRIG) initiates a pulse, which is presented on the output pins (OUT, OUTB) and ends at a time determined by the address loaded into the device via SPI serial interface. The pulse width, programmed via the serial interface, can be varied over 4,194,303 equal steps of 0.25ns. The 3D7622-0.25 has a minimum pulse width of 14.0ns and a maximum pulse width of 1.05ms. The pulse width can be varied according to the formula (Data Delay Devices, 2008):

$$t_{PW} = t_{inh} + addr + t_{inc} \quad (4\text{-}3)$$

Where $addr$ is the programmed address, t_{inc} is the pulse width increment (equal to 0.25ns) and t_{inh} inherent pulse width (equal to 14ns). The device also offers a reset input (RES) to terminate the pulse before the programmed pulse duration has expired.

The Arduino compatible Max32 development board is directly interfaced with the human machine interface (HMI), which sends all the data necessary to configure the pulse PSU:

frequency, duty cycle, over current protection threshold and desired pulse shape. The microcontroller then sets the frequency by communicating with the programmable oscillator via I2C and also sets the duty cycle thanks to the pulse generator using the SPI communication protocol.

4.3.1.2. Pulse shape selection

A multiplexer defines the polarity of the pulsed voltage. Signals PWM and PWM/ correspond respectively to outputs OUT and OUTB of the pulse generator. OUT and OUTB generate signals that are logically inverted from each other: if OUT is HIGH (5V) then OUTB is LOW (0V) and vice versa (Figure 4-3).

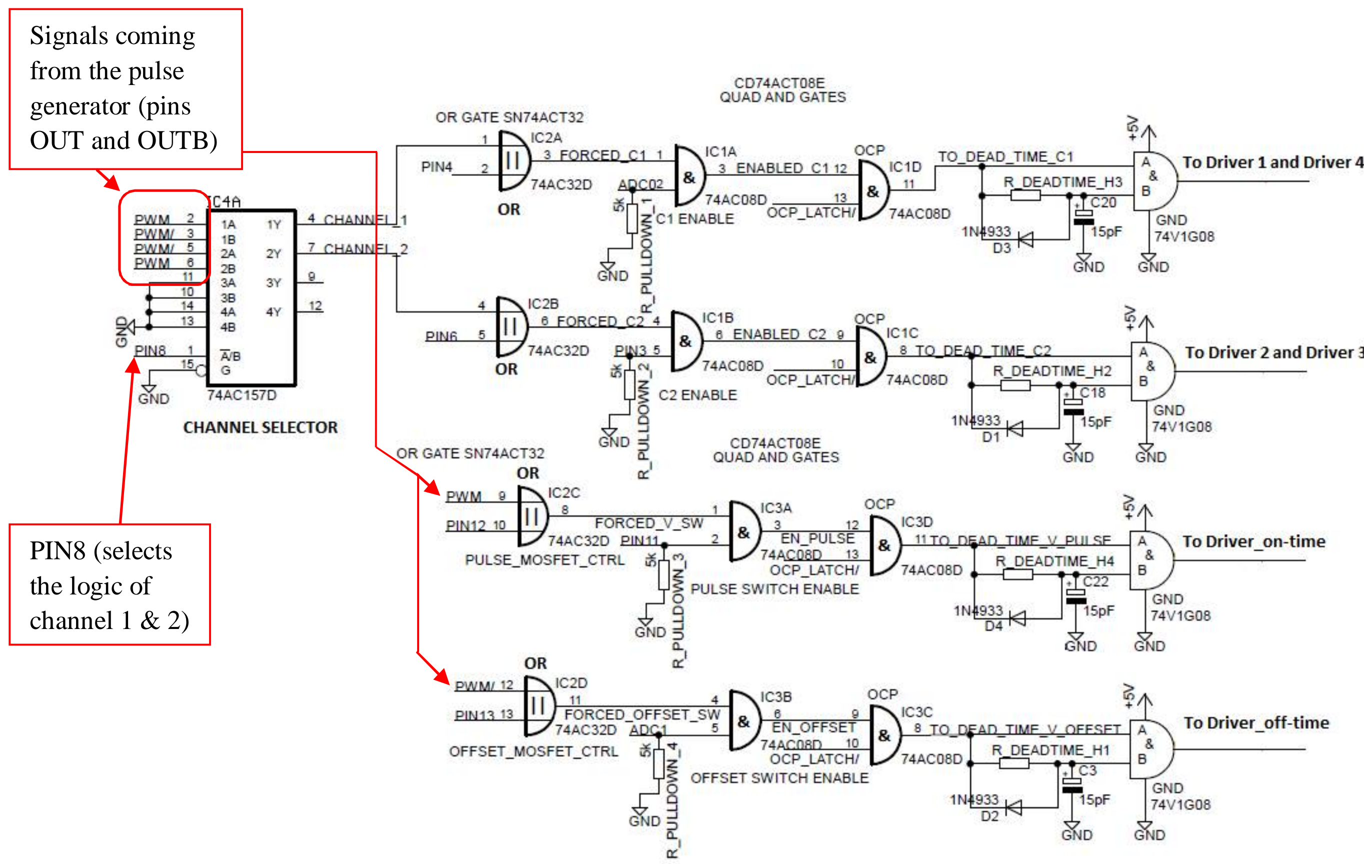

Figure 4-3: Control circuitry of the second PSU prototype

If PIN8 is LOW (0V), Channel A is selected, so SW1 and SW4 are synchronized with SW_pulse whereas SW2 and SW3 are synchronized with SW_offtime. This results in the configuration shown in Figure 4-4.

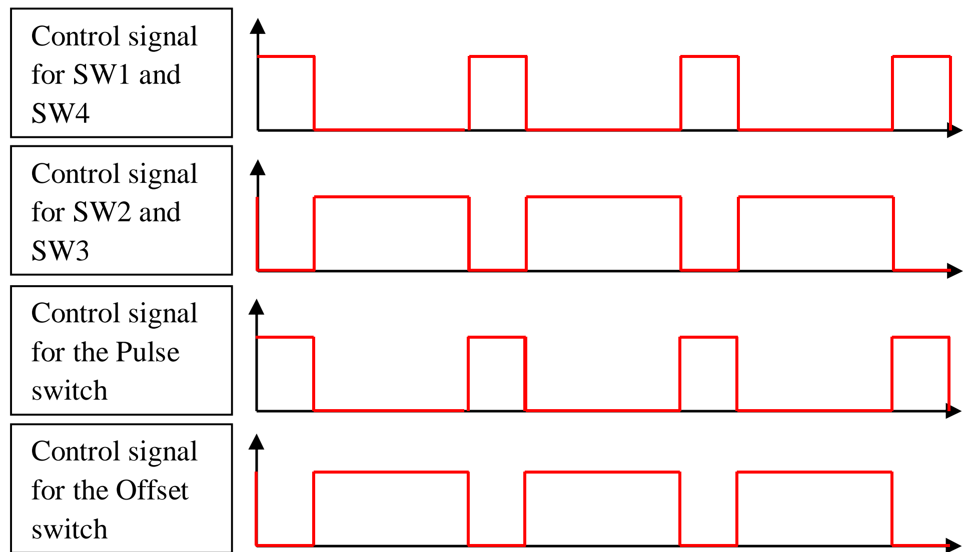

Figure 4-4: Drawing representing the 4 different control signal used to change the pulse shape when Channel A is selected.

If PIN8 is HIGH (5V), Channel B is selected, so SW2 and SW3 are synchronized with SW_pulse whereas SW1 and SW4 are synchronized with SW_offtime. The following signals are obtained (Figure 4-5):

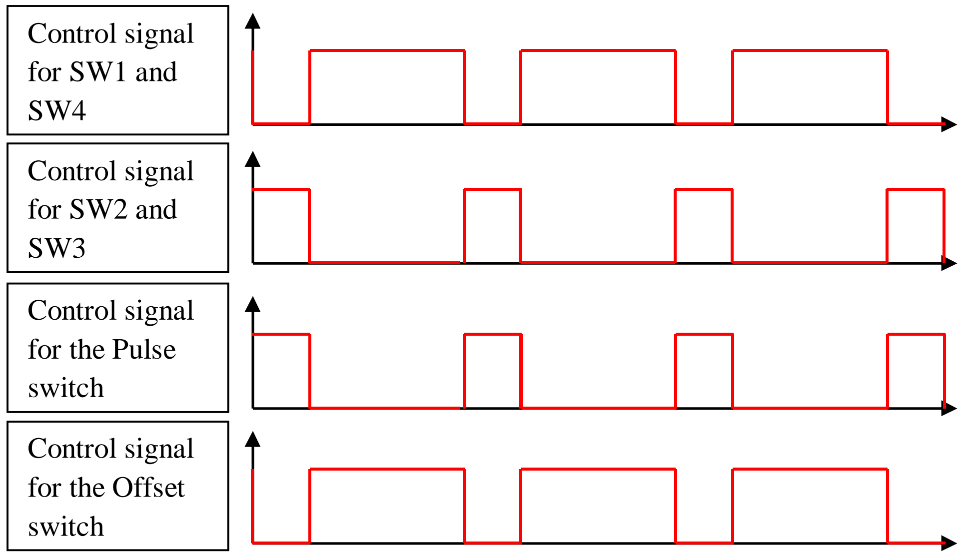

Figure 4-5: Drawing representing the 4 different control signal used to change the pulse shape when Channel B is selected

The following drawing (Figure 4-6) describes the different pulse shapes that can be obtained with the developed power supply:

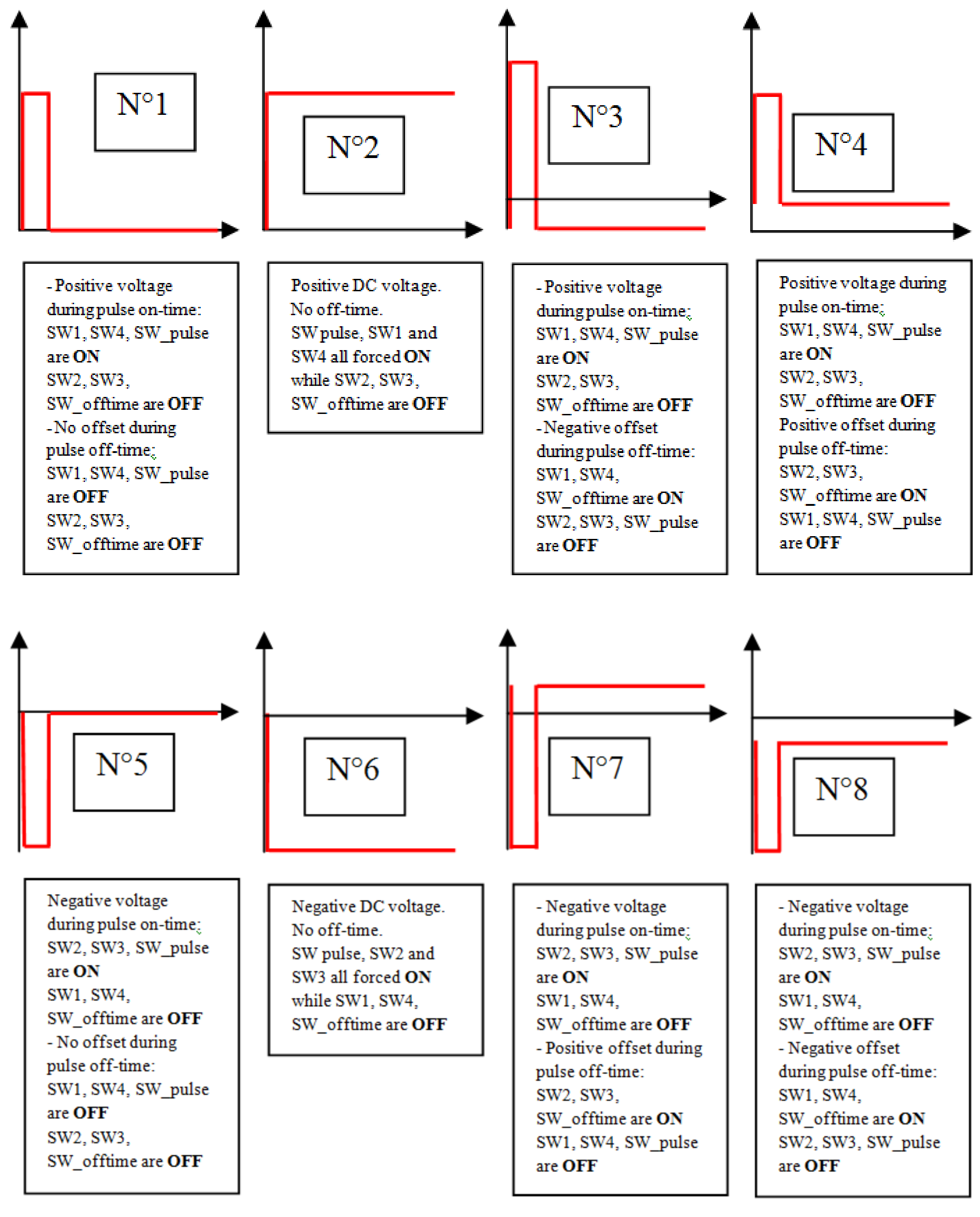

Figure 4-6: Drawing of the different pulse shapes that can be obtained in the different configuration

4.3.1.3. 24V-logic isolated digital interface

The PSU is interfaced with the Power PMAC using optocouplers to guarantee the protection of the microcontroller but also to shift the logic level from 3.3V (on the PSU side) to 24V (on the Power PMAC side).

4.3.2. The power stage

4.3.2.1. *Configuration*

Different voltages can be applied to the H-bridge thanks to two MOSFETs, allowing to apply a lower voltage during the pulse off-time. A Schottky barrier (D1) prevents current from flowing from V_PULSE to V_OFFSET (because V_PULSE is greater than V_OFFSET and the MOSFETs have built-in parallel diodes) (Figure 4-7).

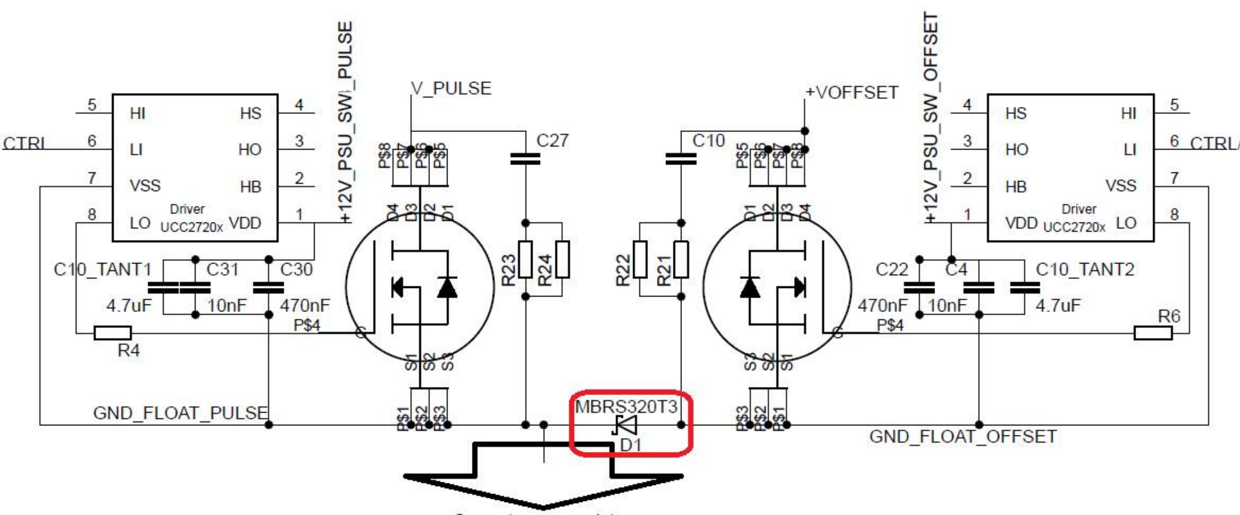

Figure 4-7: Schematic of the MOSFETs switching between the PULSE and OFFSET voltages to be applied to the H-bridge

The drivers of the MOSFETs SW_pulse, SW_offset, SW1 and SW3 are isolated from the ground thanks to 4 individual isolated DC-DC converters. This allows driving the MOSFETs at a very wide range of frequencies and duty cycles.

To optimise the layout of the power stages, it has been decided that the drivers would be powered by the control circuitry board. The isolated DC-DC converters are therefore not present on the power stage, but on the control stage.

A pin connector placed close to the current sensing resistors allows the current sensing circuitry board to be plugged onto the power stage. The output of the current sensing circuitry board is interfaced with the control stage in order to interrupt the pulsing when the over current protection is triggered.

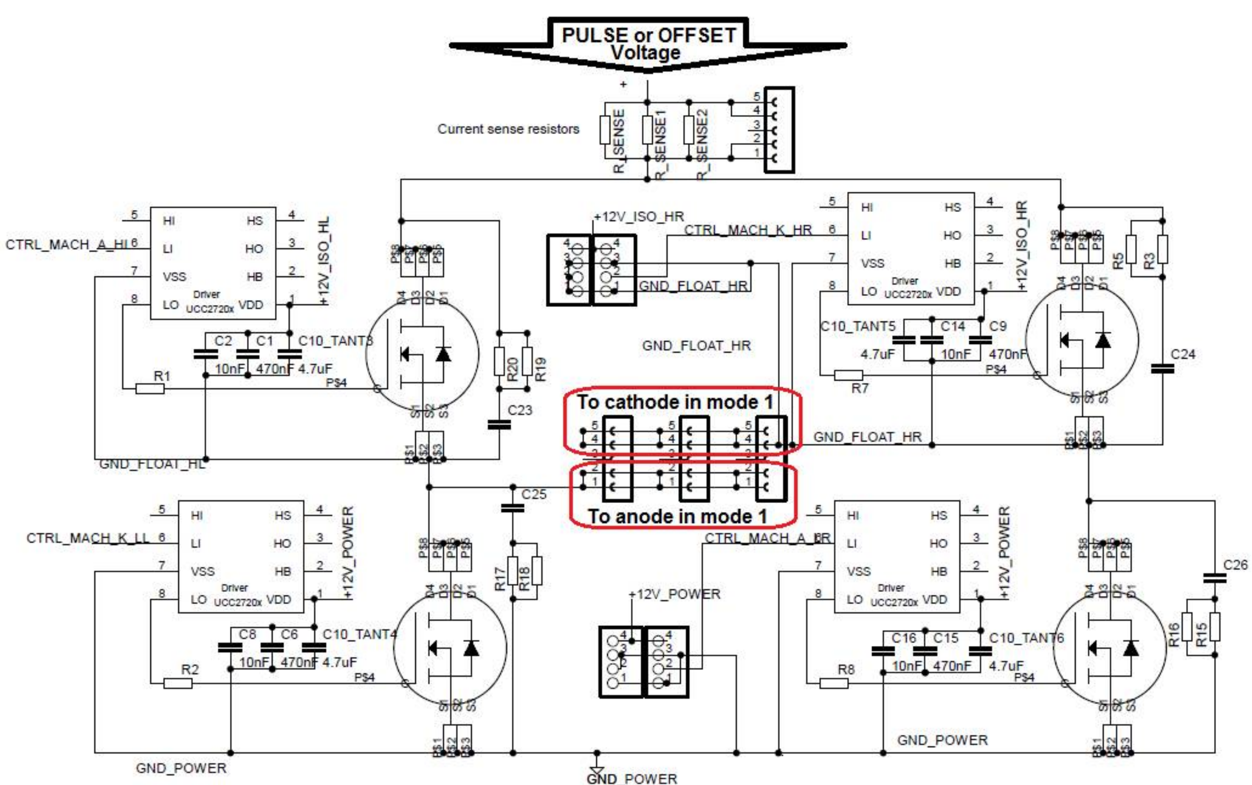

Figure 4-8: Schematic of the MOSFETs and their drivers in the H-bridge

4.3.2.2. MOSFET selection

The MOSFETs have been selected to the following criteria:

- Operating voltage
- Operating current
- Turn-on and turn off-time
- Package shall allow soldering by hand

The selected MOSFET is a FDMS7578 from Fairchild Semiconductors (Figure 4-9). This N-Channel MOSFET has been designed specifically to improve the overall efficiency and to minimize switch node ringing of DC/DC converters using either synchronous or conventional switching PWM controllers. It has been optimized for low gate charge, low ON resistance ($R_{DS(ON)}$), fast switching speed and body diode reverse recovery performance (Fairchild-Semiconductor, 2009).

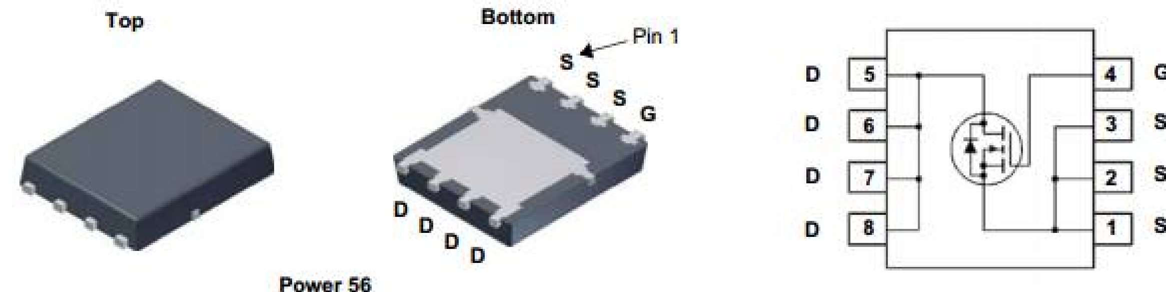

Figure 4-9: CAD Model of the package (Power 56) and representation of the MOSFET FDMS7578 (Fairchild-Semiconductor, 2009)

The main characteristics of the FDMS7578 are summarised below (Table 4-1):

Parameters	**Value**	**Unit**
Maximum drain to source voltage V_{DS}	25	V
Maximum drain current I_D	17 continuous 60 pulsed	A
Drain-source on resistance, $R_{DS(ON)}$	0.0058	Ω
Typical Turn-On Delay time	8	ns
Typical Rise Time	2.6	ns
Typical Turn-Off Delay time	20	ns
Typical Fall Time	2.2	ns
Maximum Gate-source voltage, V_{GS}	+/-20	V
Gate-source threshold voltage V_{TH}	1.6	V
Source ohmic resistance	0.0025	Ω
Drain ohmic resistance	0.0025	Ω
Input capacitance C_{iss}	1221	pF
Reverse transfer capacitance C_{rss}	54	pF

Table 4-1: Table summarizing the main characteristics of the MOSFET FDMS7578

4.3.2.3. Driver selection

The UCC27201DG4 high frequency N-Channel MOSFET driver includes a high-side/low-side driver with independent inputs for maximum control flexibility. This allows for N-Channel MOSFET control in half-bridge or full-bridge converters. The low-side and the high-side gate drivers are independently controlled and matched to 1-ns between the turn-on and turn-off of each other (TI, 2008).

In most cases, controlling the high-side MOSFET requires the use of a bootstrap diode and a bootstrap capacitor to create a floating reference at its source - allowing a gate-source voltage V_{GS} to be applied. However the desired switching frequency of the pulse power supply is too high to use such configuration. The high-side gate driver is therefore not used

and each MOSFET will have its own driver. A floating ground (GND_FLOAT) is provided to the high-side drivers using an isolated 12V DC-DC converter (Figure 4-8).

4.3.2.4. Optimized layout for smaller footprint and reduced parasitics

The layout of the power board (Figure 4-10) has been designed to reduce the overall current path across the PSU and a symmetrical configuration has been adopted to place the power switches. The new placement of the MOSFET reduces the parasitic inductance of the board and therefore reduces the amount of EMI generated (Jauregui, 2009).

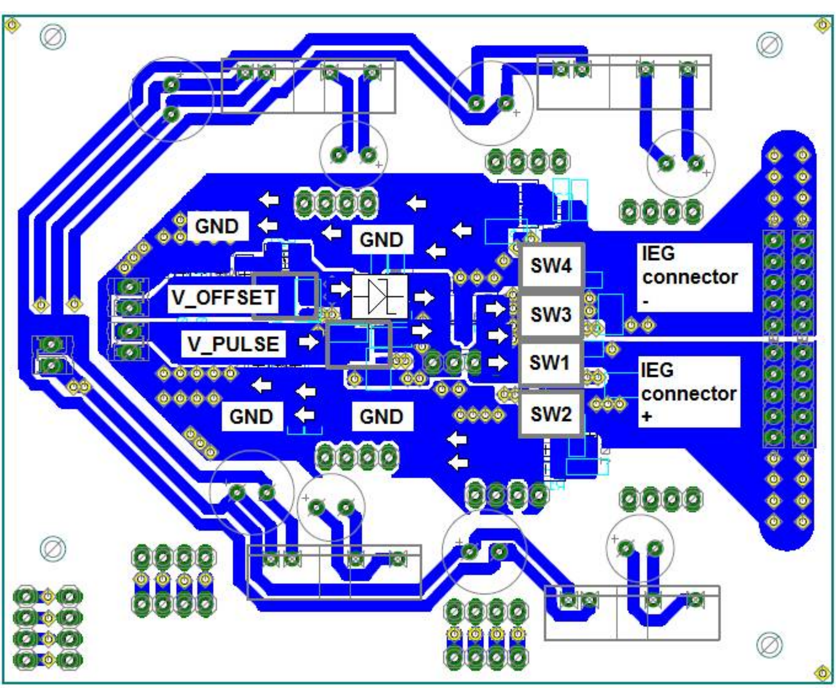

Figure 4-10: PSU prototype layout to optimise the current path and reduce overall inductance. Arrows symbolise the direction of the current.

The cabling of the 3rd PSU is also different: flat braided cables have been used to reduce the inductance of the cabling. The cables are directly soldered onto the board, to avoid the parasitic inductance from cable connectors.

Some heat sinks have been placed on the MOSFETs and their drivers to help them cool down when the pulse PSU is switching at high frequencies.

4.3.3. The over current protection (OCP) stage

The over current protection (Figure 4-11) on the second prototype is similar to the one on the first prototype: the current is measured via a sensing resistor and sent to a comparator as well as a peak detector. The comparator compares the measured current with a threshold set by the microcontroller. On the other hand, the peak detector provides the control system with a reliable current value.

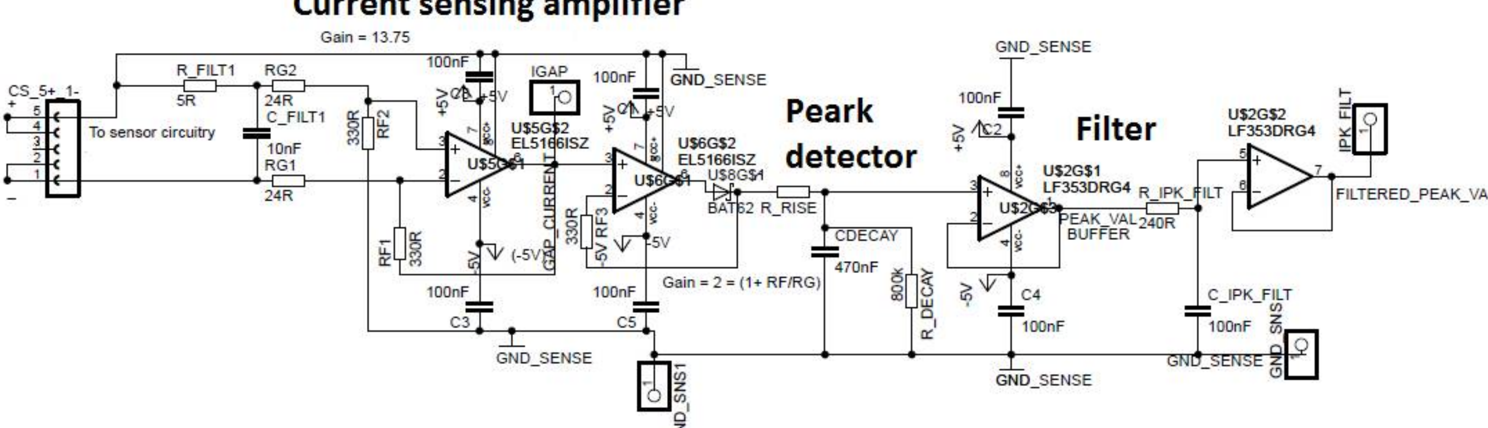

Figure 4-11: Electrical diagram of the current sensing part on the OCP stage of the second prototype:

- Testing of the OCP stage

The OCP stage is mounted on the top of the power stage, as shown on the picture below. The output of the PSU is connected to a 1Ω load.

On the Figure 4-12, the OCP can be seen triggering when the current goes above 3A. The comparator output goes HIGH for a very short amount of time, but this time is sufficient to make the SR flip-flop latch and stop the pulses.

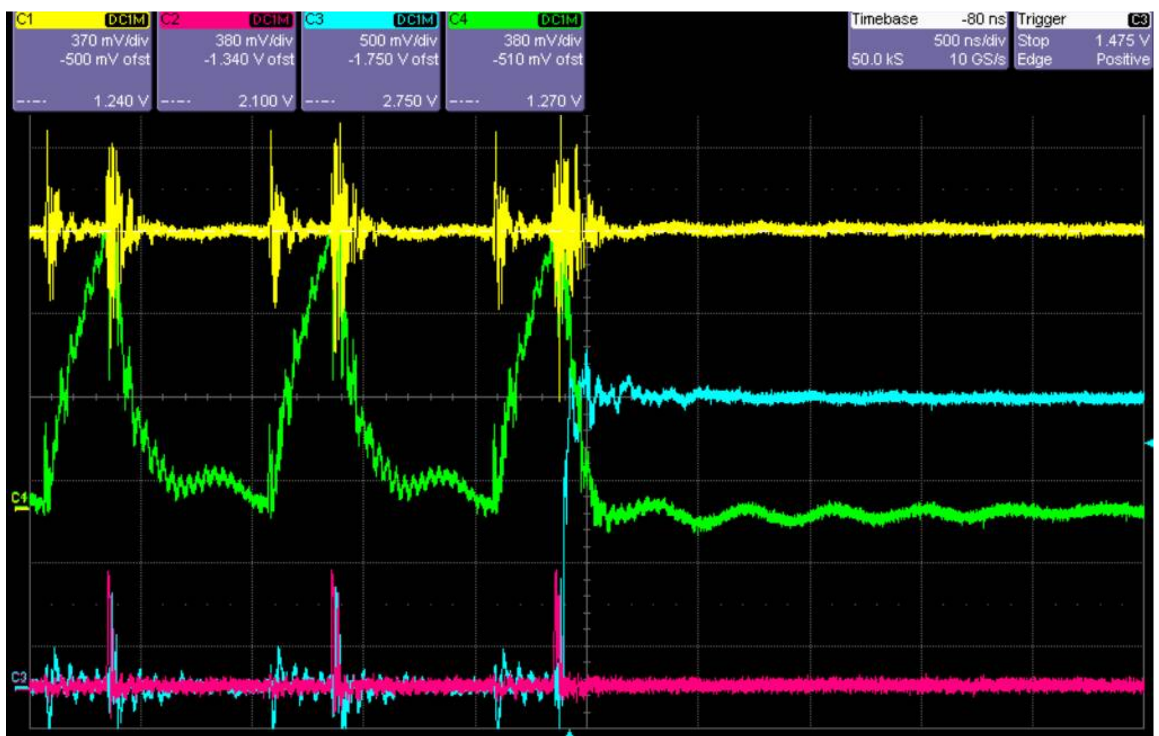

Figure 4-12: C1: OCP threshold (380mV/A); C2: comparator output; C3: OCP signal (latched output); C4: current (380mV/A); 1MHz 25% duty cycle

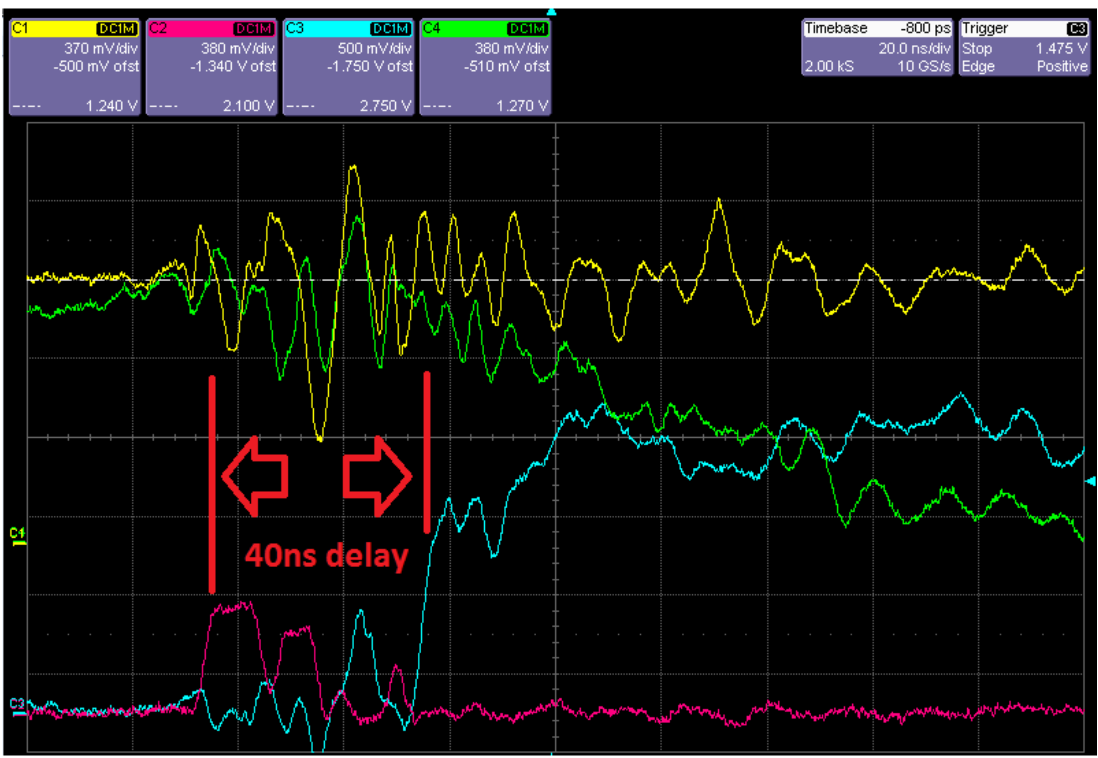

Figure 4-13: C1: OCP threshold (380mV/A); C2: comparator output; C3: OCP signal (latched output); C4: current (380mV/A); 1MHz 25% duty cycle (20ns/div)

From a timing perspective, the pulses are stopped approximately 40ns after the comparator triggers the over current protection signal (Figure 4-13).

4.3.1. PSU testing and mounting

In this section, the output of the PSU is connected to a 1Ω 50W resistor which simulates the gap and allows high current to flow through the PSU (as shown on Figure 4-14). Commands are then sent to the PSU via the developed HMI and the obtained pulse shapes are visualized with a scope. The current flowing though the resistor is measured thanks to a current transformer.

The presented results have been obtained by connecting the output of the PSU to a 1Ohm 50W resistor used as a test load which allows high current (up to 7A for 7VDC) to flow through the PSU (Figure 4-14). Commands are then sent to the PSU via the developed HMI and the obtained pulse shapes are visualized with a Wavepro 7300A Lecroy oscilloscope. The current flowing though the resistor is measured using a wide-band terminated current transformer with a rise time of 7ns and a bandwidth of 60MHz model 13G1000 from Lilco ltd.

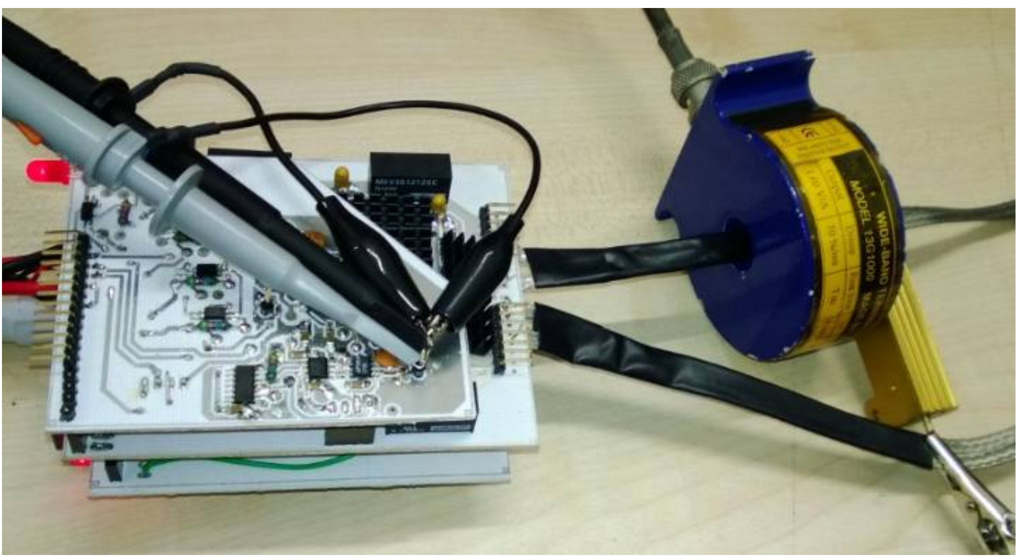

Figure 4-14: Picture of the PSU being tested with the 1Ohm load and current transformer

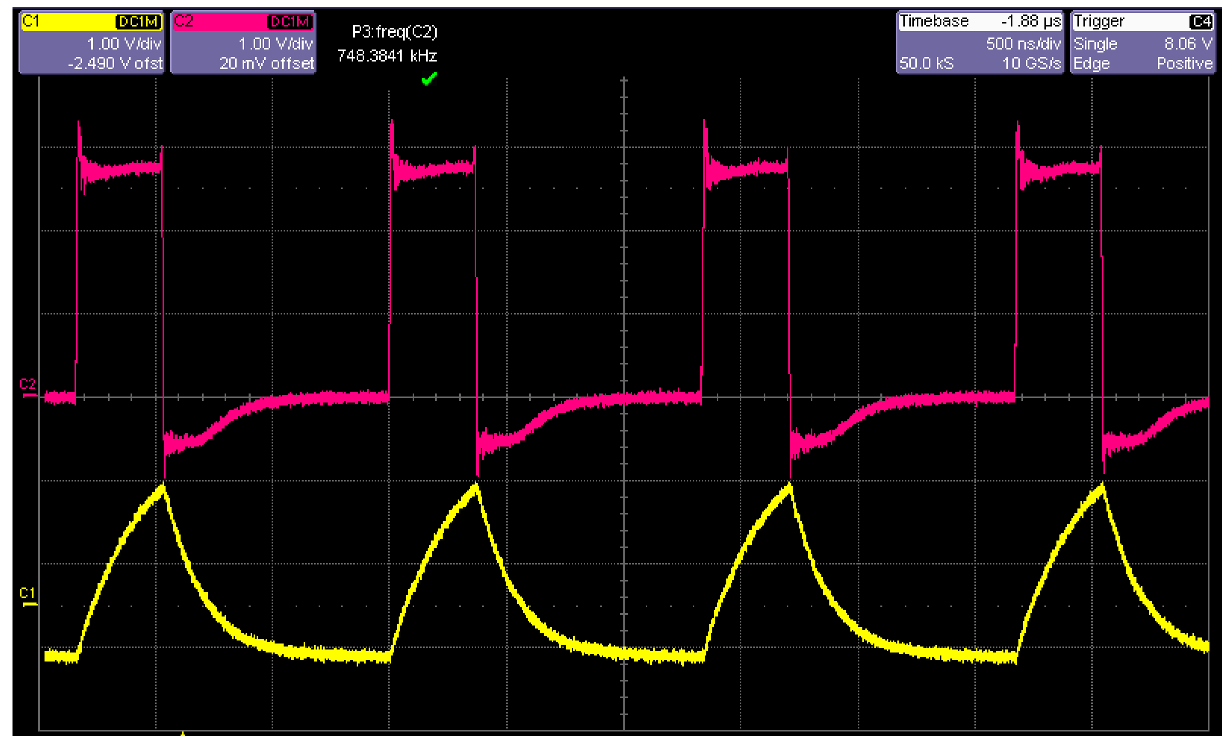

Figure 4-15: C1: current (1V/A), C2: voltage; PSU in pulse mode 1: 3V pulse, no offset; 750kHz 25% duty cycle

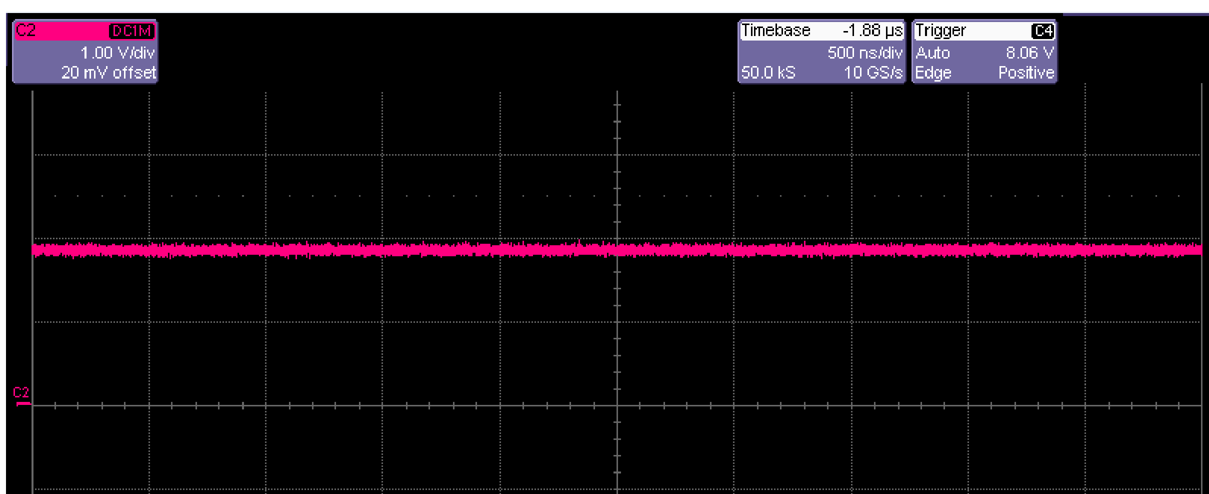

Figure 4-16: C2: voltage; PSU in pulse mode 2: 2VDC (positive)

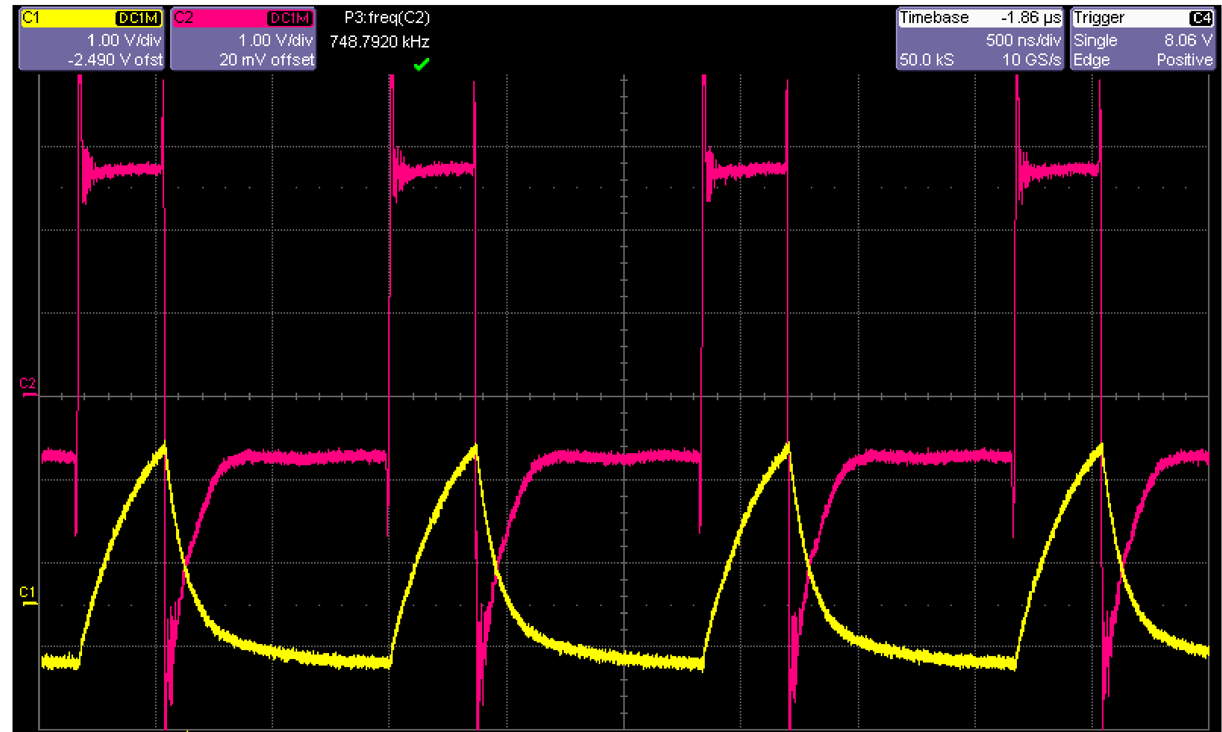

Figure 4-17: C1: current (1V/A), C2: voltage; PSU in pulse mode 3: 3V pulse, 1 V negative offset; 750kHz 25% duty cycle

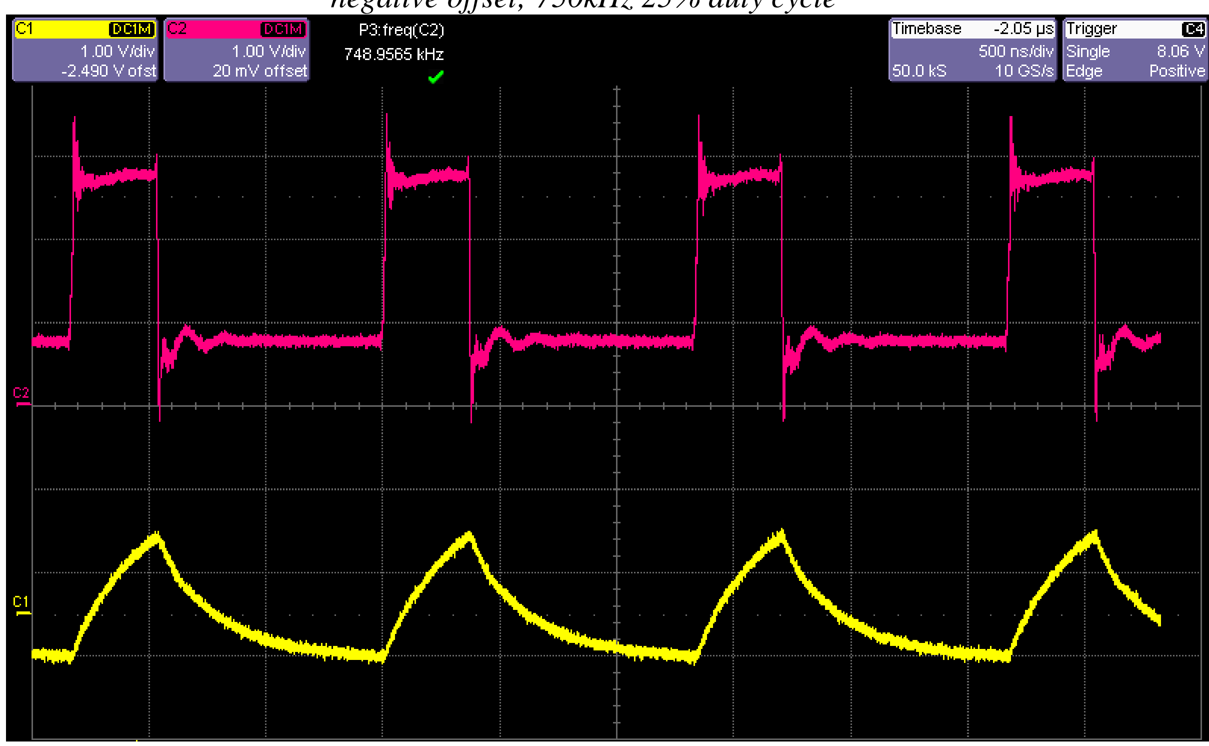

Figure 4-18: C1: current (1V/A), C2: voltage; PSU in pulse mode 4: 3V pulse, 1 V positive offset; 750kHz 25% duty cycle

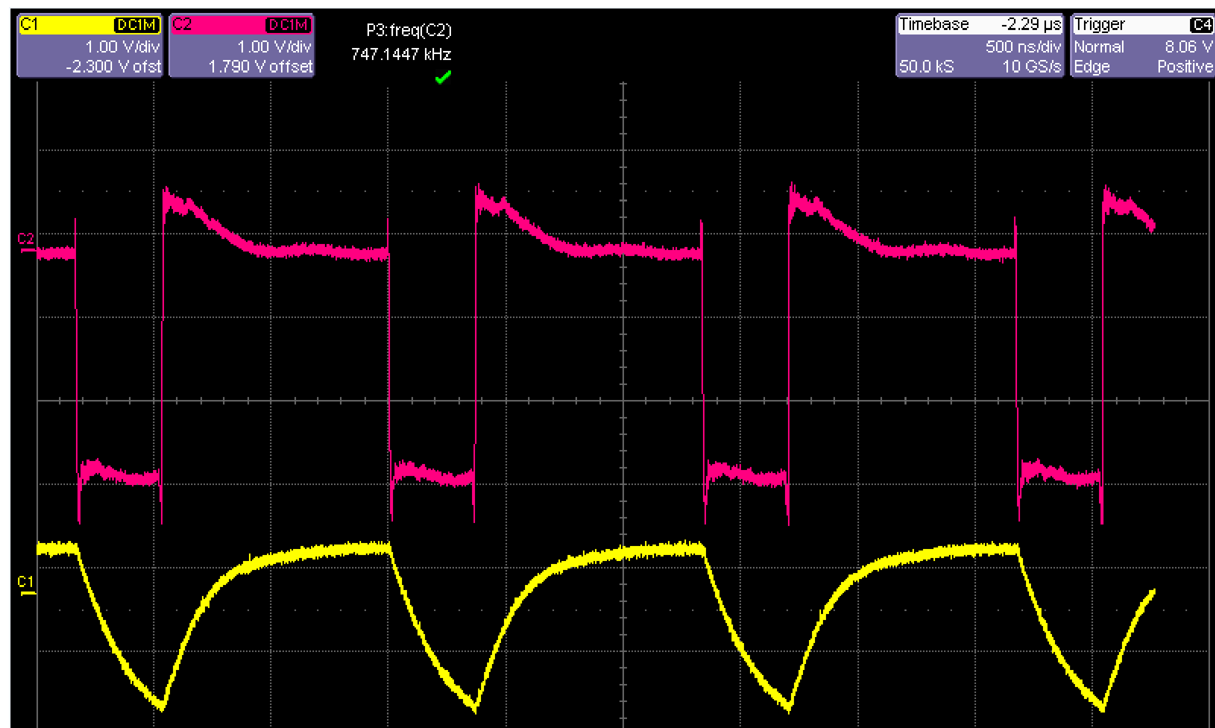

Figure 4-19: C1: current (1V/A), C2: voltage; PSU in pulse mode 5: 3V negative pulse, no offset; 750kHz 25% duty cycle

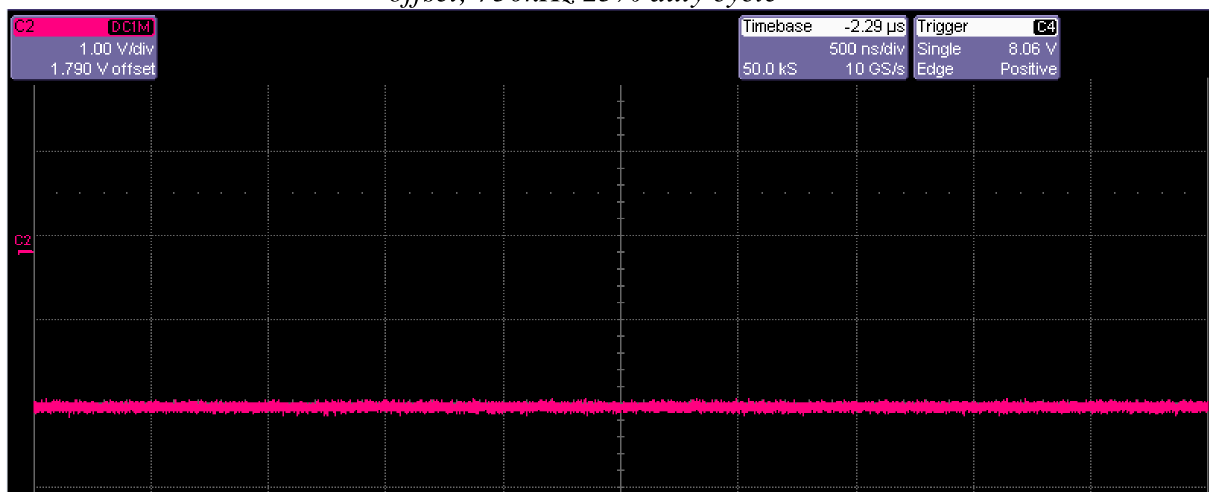

Figure 4-20: C2: voltage; PSU in pulse mode 6: 2VDC (negative)

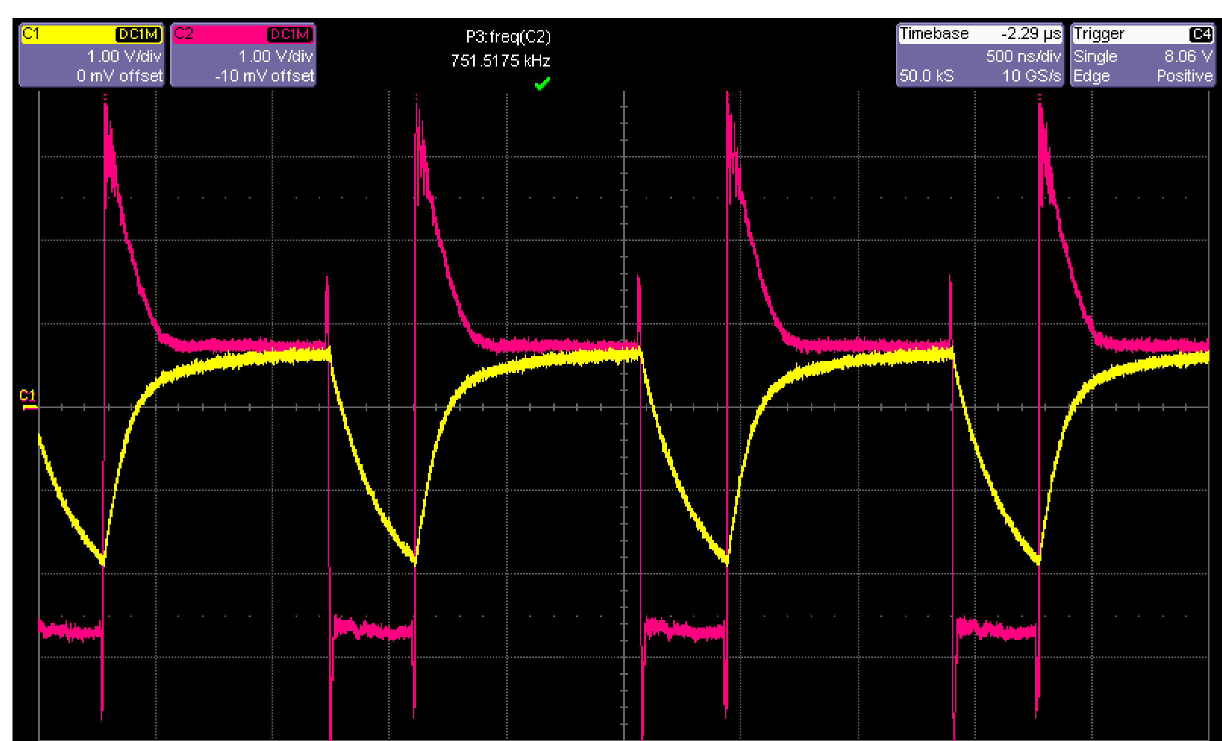

Figure 4-21: C1 current (1V/A), C2: voltage; PSU in pulse mode 7: negative 3V pulse, 1 V positive offset; 750kHz 25% duty cycle

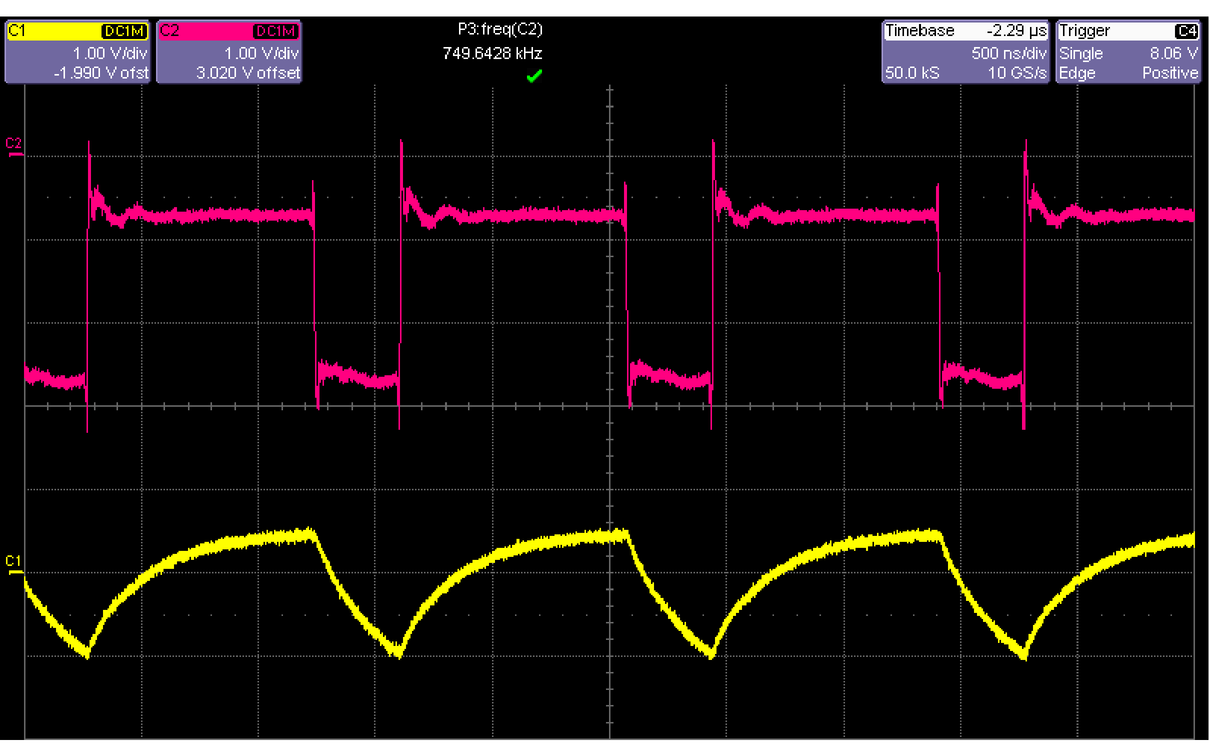

Figure 4-22: C1 current (1V/A), C2: voltage; PSU in pulse mode 8: negative 3V pulse, 1 V negative offset; 750kHz 25% duty cycle

- Conclusion from tests with standard power cables

From the previous results, it can be seen that the parasitic inductance of the standard cables is quite high as we can observe – particularly in mode 3 and 7 – a significant reverse voltage

peak after each pulse. This highlights the fact that low inductance cabling should be used to improve the pulse shape.

The developed pulse PSU will enable to experiment the effects of the offset voltage during the pulse off-time. Some papers advised a positive off-set during the pulse off time, which would maintain the EDL constantly charged, whereas other papers mentioned that a negative pulse off-time would enhance the machining process by accelerating the unloading/reloading process of the EDL.

A lot of noise was generated when the power MOSFETs were being turned on/off. The origin of this noise was mainly the high current transient across when the MOSFETs were turned on /off. To reduce these current transient, a resistor has been added between the output of the driver and the gate of the MOSFET. This resistor increases the turn on time of the switch and therefore reduces the di/dt across it. It is common practice to add a resistor between the driver and the semiconductor switch. The literature review and the experiments showed that at very high frequency the machining time dramatically increases (Mithu et al., 2012). Therefore it was decided to add a gate resistor (4.7Ω) which should increase the turn-on time but improve the quality of the output pulse as well as the current measuring board.

Since increasing the gate resistance also increases the turn off time, anti-parallel Schottky diodes have been added to bypass the gate resistor during the turn off time, allowing for the driver to sink the off time current in a faster way.

It was observed that when applying 6V pulses to the 1Ohm load at a frequency of 2.5MHz and a duty cycle of 20%, the impedance of the cables becomes so important that only half of the power is transmitted to the load. This highlights how essential a low inductance cabling is for the µECM technology. The electrical specifications of the pulse PSU can be found in Table 4-2.

Current Max	10A
Frequency range	2kHz-8MHz
Voltage max	15V
Smallest pulse duration	50ns

Table 4-2: Specs of the developed pulse PSU

4.3.1.1. On-board signals

Different on-board signals can be observed while the PSU is pulsing (Figure 4-23). The OCP level and measured current signals are constantly compared and as soon as the measured current goes above the OCP level, the pulses are shut down. The peak value of

the current is sent to a motion controller which controls the IEG and proceeds to the tool retraction when a short circuit is detected.

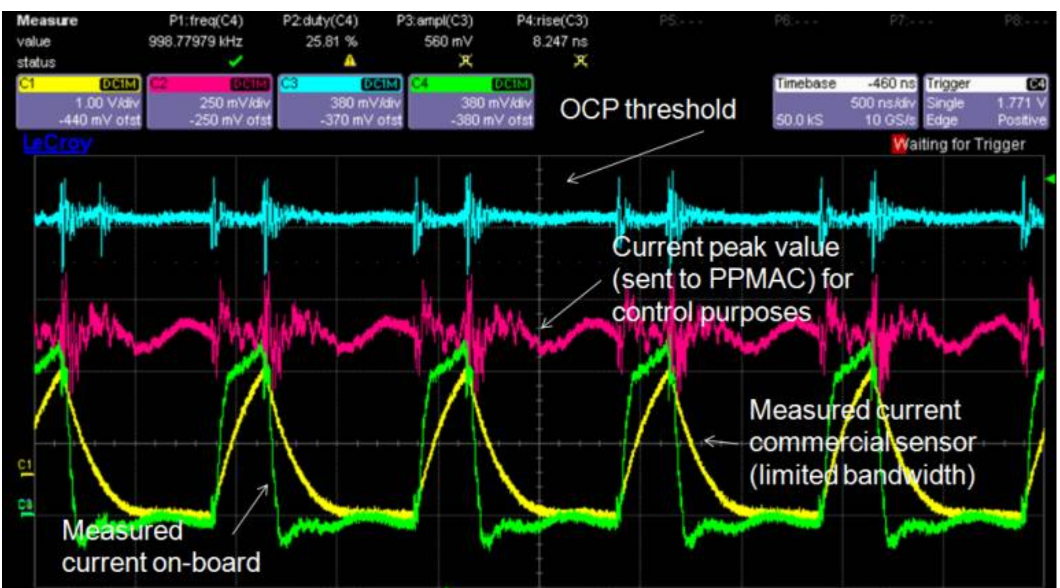

Figure 4-23: Oscilloscope screenshot of the measured signals on the PSU, 1MHz frequency, duty cycle of 25%, pulse amplitude of 3.2V and no offset during off-time 500ns/div.

Channel	Description	Scaling
C1	Measured gap current via commercial current sensor	1V/div., 1V/A
C2	Peak current value	250mV/div., 250mV/A
C3	OCP threshold level	380mV/div., 380mV/A
C4	Measured gap current via on-board current sensing circuitry	380mV/div., 380mV/A

Table 4-3: Description of the signals measured in Figure 4-23.

4.3.1.2. OCP triggering trials

An important feature of the developed PSU is the time it takes for the pulses to be stopped after the over current protection (OCP) has been triggered. This represents the time during which the tool is exposed to an electrical and mechanical stress. The presented results are obtained by short-circuiting the output of the pulse PSU and sending pulses (1MHz, 25% duty cycle, 2V pulse, 0V offset). The OCP signal triggered at the first pulse and the pulses were stopped (Figure 4-24).

It can be seen from Figure 4-24 that the delay between the OCP being triggered and the pulses being stopped is less than 50ns. The pulse duration is also reduced: instead of a 250ns pulse, a short pulse of 150ns is generated.

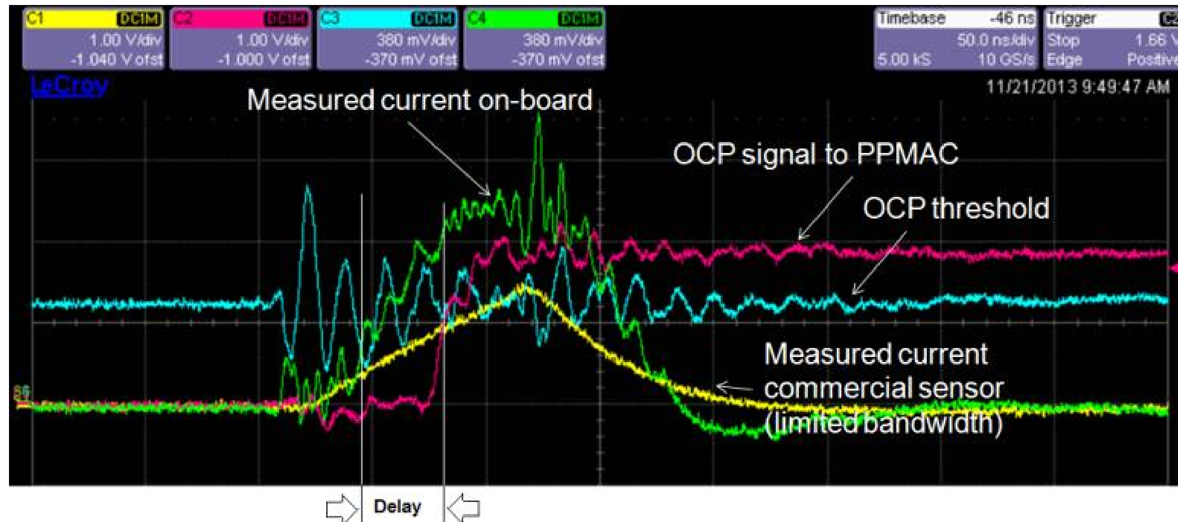

Figure 4-24: Oscilloscope screenshot of the OCP signal delay 50ns/div. (C1: Measured gap current via commercial current sensor at 1V/div. and 1V/A; C2: OCP signal 1V/div; C3: OCP threshold level at 380mV/div. and 380mV/A; C4: Measured gap current via on-board current sensing circuitry at 380mV/A and 380mV/div.)

The results given in Figure 4-25: Graph representing the pulse amplitude at the IEG (mV) according to the frequency (in kHz).show the variation of the pulse amplitude measured at the gap according to the applied pulse frequency. For this, a 450µm copper tool-electrode was used. The tool was moved towards the workpiece until electrical contact was made, the OCP was set to 2A, the duty cycle was set to 15% and the pulse shape was set to 1.58V during on-time and 0V during of time (referring to mode 1 in fig. 8). All the above parameters were maintained constant during the experiment, the spindle was not spinning and only the frequency was changed. The frequency was varied from 500kHz to 8MHz by steps of 250kHz and the following values of the pulse amplitude at the IEG were measured.

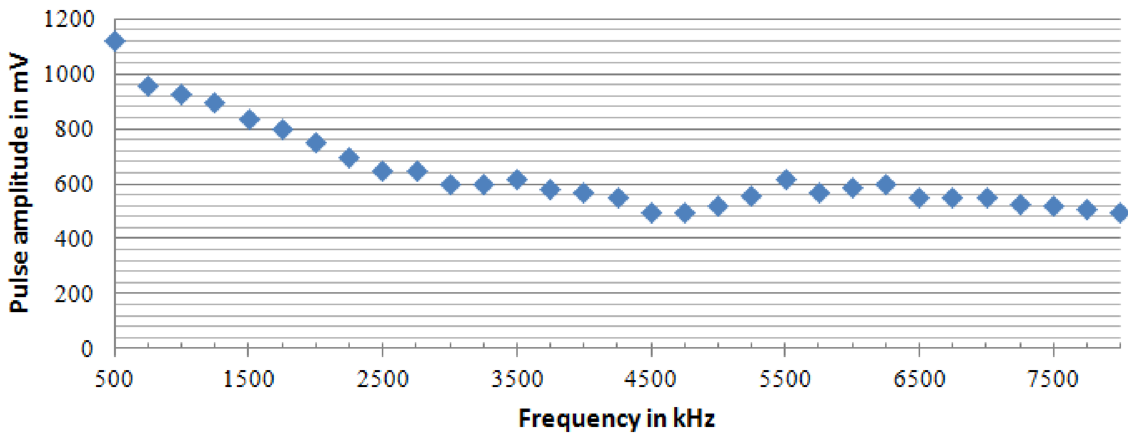

Figure 4-25: Graph representing the pulse amplitude at the IEG (mV) according to the frequency (in kHz).

It can be observed from the graph that the voltage applied to the IEG becomes smaller when the frequency increases. This phenomenon is due to the parasitic capacitance, resistance and inductance of the cables which increase the impedance of the cable when greater frequencies are applied.

It can be predicted from the graph (Figure 4-25) that significant material removal rate (MRR) can be achieved at frequencies up to 2MHz, past this frequency, the amount of power reaching the gap makes it hard to achieve an efficient machining process. This will have a dramatic influence on the MRR but will improve the resolution of the machining because of the higher frequencies (Mithu, Fantoni and Ciampi, 2011a).

The PSU has been installed on a self-developed µECM machine (Figure 4-26). A significant effort has been taken to make the cables as short as possible:

- The PSU is directly mounted on the Z axis very close to the tool-electrode;
- When the electrode mounted on the Z axis is close to the workpiece, a second shorter cable is connected to the machining cell in order to further reduce the length of the current path during machining (Figure 4-26 (c)).

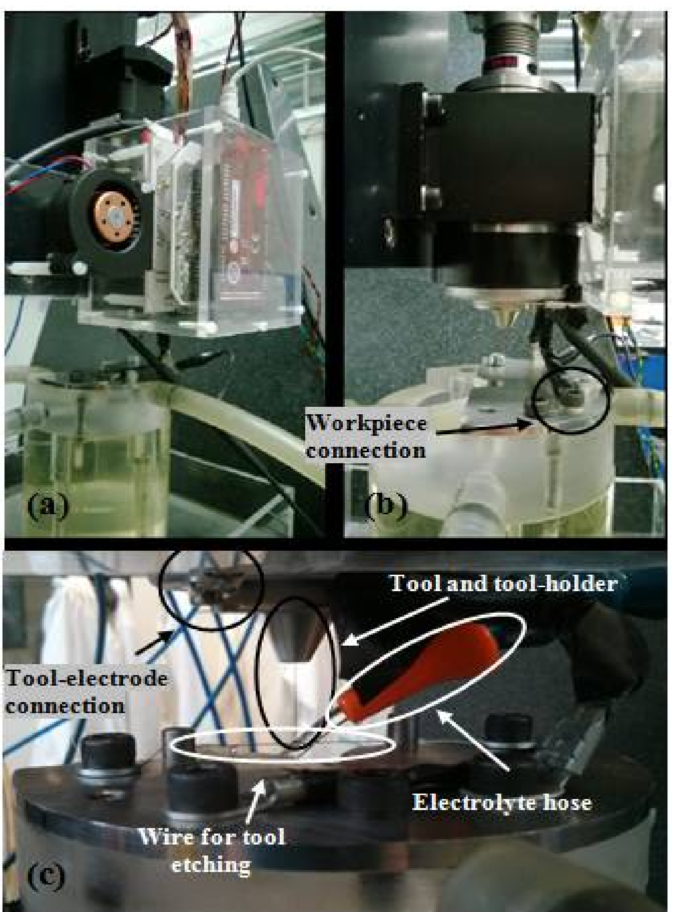

Figure 4-26: Pictures of the PSU mounted on the µECM machine.

4.3.2. Operation of the third PSU prototype

The firmware of the PSU has been programmed using the MPIDE developing environment. This IDE allows you to write a programme, compile it and the download it to the Max32 development board via an USB cable. The programme will start executing as soon as the Max32 is powered up, allowing it to run in standalone mode.

When the microcontroller receives the data from the HMI, it checks it the values for each of the parameters are within a correct range. If that is the case, the microcontroller will communicate with the following elements:

- The square wave oscillator: The oscillator sets the frequency of the pulses and outputs a square wave signal with the desired frequency. The communication protocol between the microcontroller and the oscillator is I2C. The default I2C communication library of the microcontroller is used to send the desired frequency to the oscillator.
- The pulse generator: The pulse generator outputs a pulse which has a programmed duration each time its trigger input goes high. The output of the square wave oscillator is directly wired to the trigger input of the pulse generator. The output of the pulse generator is therefore a train of pulses set with a specified duration (duty cycle) and frequency, which controls the on-times and off-times of the MOSFETs on the power board. The pulse generator has a SPI interface which is also compatible with the microcontroller and therefore the default SPI communication library can be used.

Once the microcontroller has set the duty cycle and the frequency, it will set the pulse shape and polarity using the AND logic gates and the multiplexer to select which channel with control the power board.

Finally the microcontroller sets the OCP level by using one of its PWM outputs which is sent to the low pass filter of which the output is connected to the negative input pin of an ultrafast comparator.

The microcontroller then enables the output on the control board - which actuates the power board - and starts polling on the serial communication for incoming messages (e.g. different setting required) and for the OCP to trigger. If the OCP is triggered, the controller will immediately reset the pulse generator and the disables the control channel. It is important to

mention that the OCP circuit has the power to disable the pulses on its own because the protection logic is designed using solid state components (logic gates and SR latch) to ensure the reliability and the deterministic timing of the protection.

Therefore, when the microcontroller detects that the OCP has triggered, pulses have been disabled earlier and the system is protected already.

4.4. Discussion and conclusion for Chapter 3

The experience acquired when developing the previous prototypes allowed for the optimization of the design in order to facilitate its integration in the machine. The small footprint of the PSU makes its mounting on the Z axis easy. The new layout provided better results at high frequency with less noise. The opto-isolated 24V logic interface made the communication with the Power PMAC motion controller simpler and more reliable. The reset of the OCP during machining was much faster because it was directly done using hardwired circuitry and did not require the intervention of the HMI, resulting in improved performance.

The design of a power supply capable of delivering ultra-short pulses and providing enough power to the IEG is essential in order to progress in the development of µECM equipment. In this Chapter, a device meeting the pulse PSU requirements for µECM has been designed, developed and tested. An over current protection (OCP) system has been implemented to protect the tool against undesired events occurring within the interelectrode gap during machining.

A quick communication protocol between the power supply and the motion controller is essential for the successful control of the µECM process. Therefore, the developed pulse PSU provides the control system with signals such as the current peak value as well as the OCP signal, in order to quickly react and adapt the motion of the tool.

In Sections 7.3, 7.4 and 7.5 of Chapter 7, the developed pulse PSU was used to produce micro tools of different tip diameters (95µm, 57µm and 5µm) and drill a deep hole (1.1mm) in 18NiCr6 with an on-line fabricated tool. The diameter (414µm) of the drilled hole was relatively greater than the tool diameter. This result is mainly linked to 2 parameters: 1) the tool run-out was quite significant 2) the machining time was very long so a bigger volume was machined by the active sidewalls of the tool-electrode.

Chapter 5: MACHINE SYSTEM INTEGRATION

This Chapter provides a detailed presentation of the µECM machine configuration. It has 3 axes of motion and a spindle allowing the tool-electrode to rotation during machining (Figure 5-1). The rotation of the tool-electrode eases flushing of by-product and guarantees that the holes drilled have a shape perfectly circular.

Description	**Value**
Slide Type	Air bearing slides (5bar pressure)
Accuracy (X, Y & Z axes)	<1.0µm over total travel
Stroke	X: 200mm, Y: 200mm, Z: 150mm
Resolution (X, Y & Z axes)	2nm
Drive system (X, Y & Z axes)	DC Brushless linear motor
Controller architecture	Open architecture motion controller
Maximum current	5A
Pulse frequency range	DC or 1kHz – 5MHz
Short circuit protection delay	50ns
Tool retraction strategies	Simple retraction mode Custom retraction mode
Process Control type	Fuzzy logic & custom adaptive algorithms
Machining operation	µECM drilling (for hole drilling) µECM turning (for micro-tool fabrication)

Table 5-1: µECM machine specifications

The linear slides for each axis use air bearings with linear DC brushless motors and 2nm-resolution encoders for ultra-precise motion. The control system is based on the Power PMAC motion controller from Delta Tau. The electrolyte tank is located at the rear of the machine and allows the electrolyte to be changed quickly.

A self-developed pulse generator has been mounted and interfaced with the machine and a wire ECM grinding device has been added. The pulse generator has the possibility to reverse the pulse polarity for on-line tool fabrication.

All the electrical components are located in a drawer under the machine, which makes the machine look similar to the µMill (Luo et al., 2005; Nor, 2010). The machine (Figure 5-2) consists of different subsystems which will be detailed below.

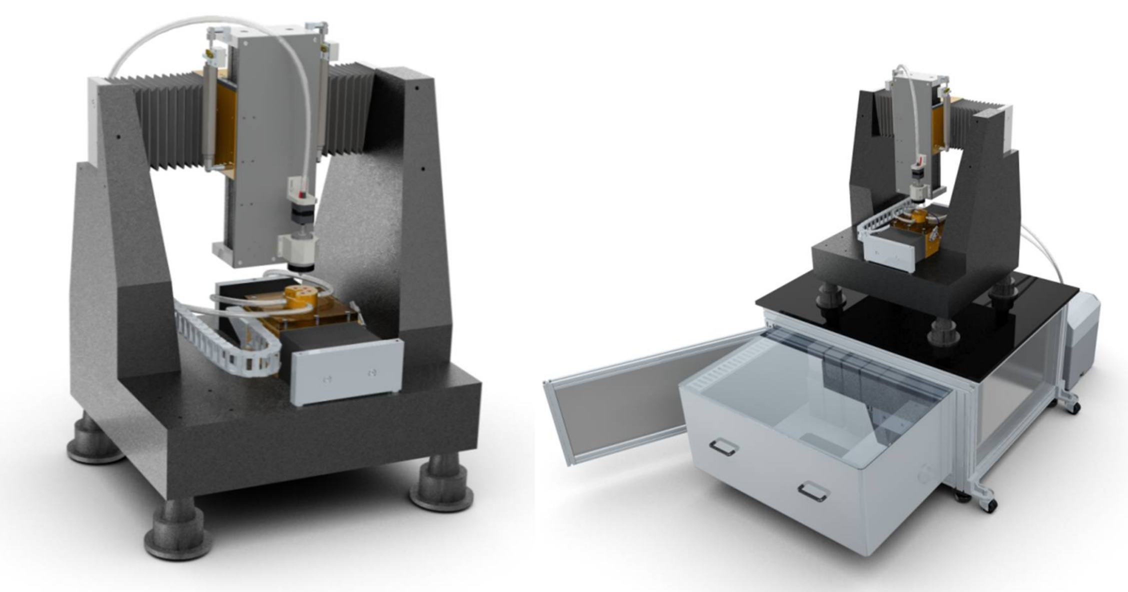

Figure 5-1: 3D-CAD models of the μECM machine.

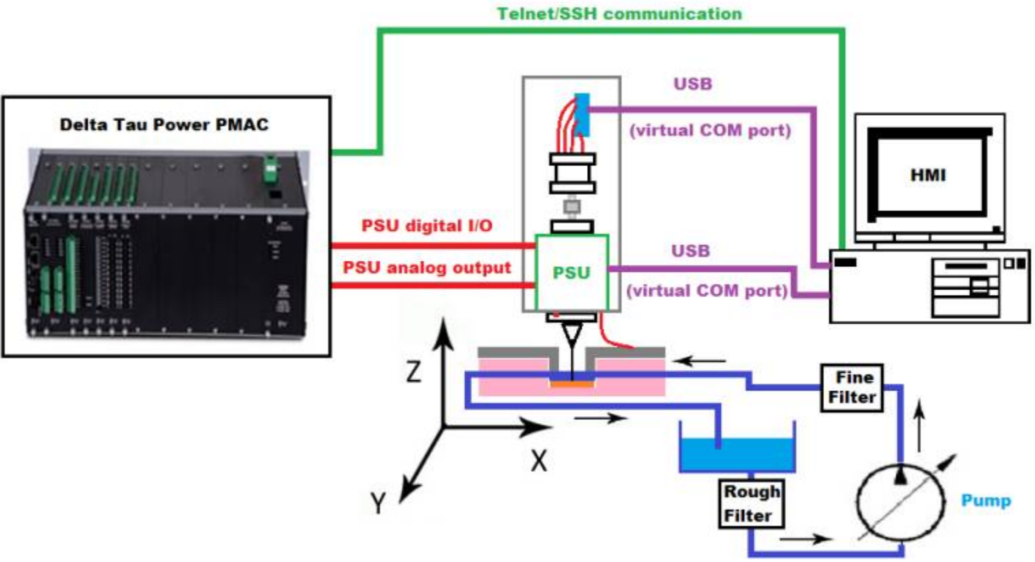

Figure 5-2: Schematic diagram of the developed micro-ECM machine

5.1. Granite base

In order to achieve ultraprecise motion to maintain the 5μm machining IEG, the material of the base on which the slides are mounted must be very carefully selected.

Granite was chosen for the base in accordance to the requirements for ultra-precision machines: it has a very low thermal expansion coefficient, good damping characteristics and

is very resistant to wear. Granite has always been a preferred material in the precision engineering sector.

The axes are arranged in a gantry configuration where the X axis supports the Z axis and the Y axis is directly mounted on the base (Figure 5-1). It was reported in the literature review that this gantry configuration enabled a better overall machine stiffness in static and dynamic conditions (Huo and Cheng, 2008; Cheng, 2008).

In order to isolate the machine from external vibrations, the base is mounted on four rubber feet.

5.2. X, Y and Z Slides

It has been identified in the literature review that the use of slides with aerostatic bearings are the best way to reach precise and accurate motion in micro manufacturing applications. Air bearings feature frictionless and backlash-free motion, high acceleration capabilities, high accuracy and easy maintenance. The X, Y and Z slides implement a direct drive system, which has proven to be the best choice in precision machining applications (Luo et al., 2005; Nor, 2010; Wardle et al., 2010; Cheng, 2008).

Custom aerostatic slides were designed to achieve the best performance (Figure 5-3). Each of the slides consists of a DC brushless linear motor with a trapezoidal hall sensor, a linear encoder readhead with its scale and an air bearing.

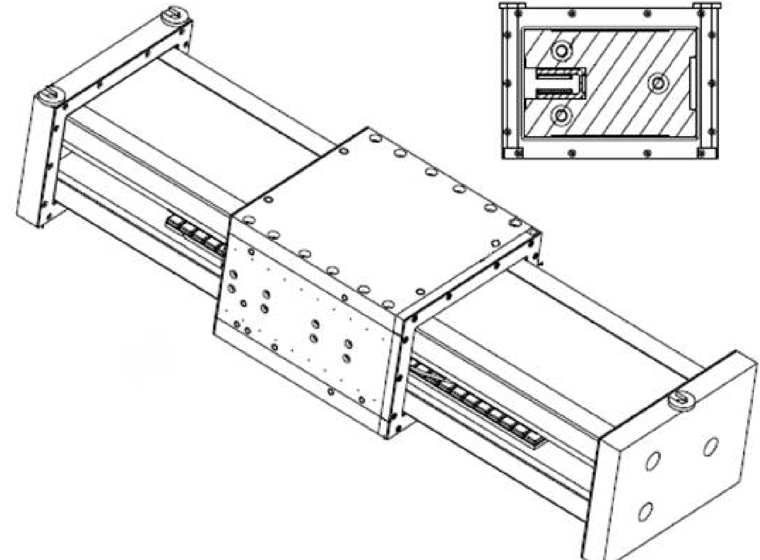

Figure 5-3: Mechanical drawing of the assembled X slide and its cross-section

5.2.1. The linear DC brushless motor

The linear motors models are LEM-S-3-S from Anorad. Figure 5-4 illustrates the typical assembly of the linear motor components. The coil assembly reflects the optional cooling and Hall Effect sensor. A trapezoidal hall effect sensor is used to find the phase at motor start up (Anorad Linear Motor Division, 1999). The motors therefore have two feedback sensors for control: 1) the trapezoidal Hall Effect sensor and 2) the linear position encoder.

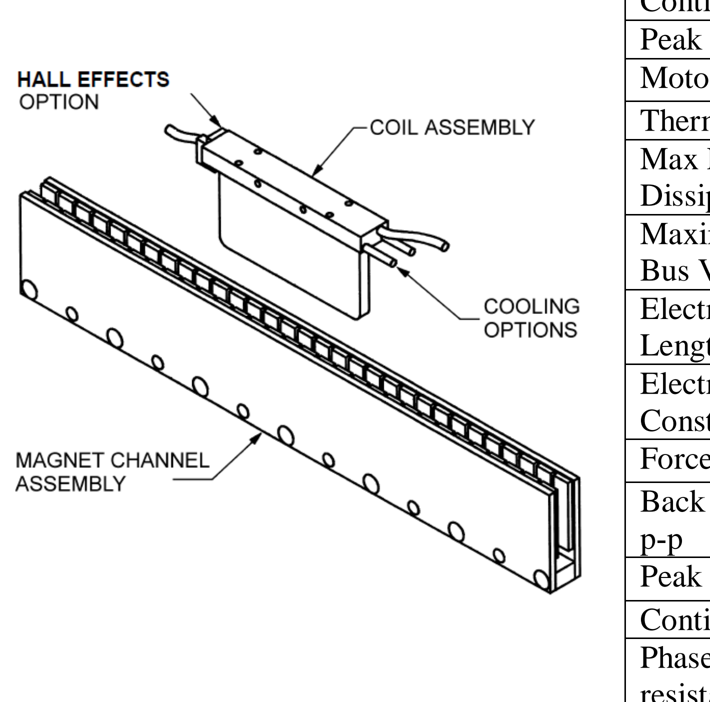

Parameters Model: LEM-S-3-S	**Value**
Continuous Force	75 N
Peak Force	238 N
Motor Constant	7.1 N/√W
Thermal Resistance	0.89 °C/W
Max Power Dissipation	113W
Maximum Applied Bus Voltage	325 Volts
Electrical Cycle Length	30mm
Electrical Time Constant	0.5msec
Force constant	16.7 N/A_{pk}
Back EMF constant p-p	V_p/m/s
Peak Current	14.3 A_{pk}
Continuous Current	4.5 A
Phase to phase resistance	5.3 Ω
Phase to phase inductance	2.7 mH

Figure 5-4: Mechanical drawing and specifications of the LEM-S-3-S linear motor (Anorad Linear Motor Division, 1999)

Linear motors have several advantages over screw driven systems:

- High Velocity
- High Acceleration
- Smoothness Of Motion
- High Accuracy and Repeatability
- High Stiffness
- Low Maintenance and high Life Expectancy
- Possibility for Clean Room And Vacuum Applications

Both of these feedback devices are interfaced with the motion control system via an interface board Delta Tau ACC24E-2, which can control up to 4 axes simultaneously.

For the Z axis, the linear motor is mounted vertically and the weight of the slide is supported by frictionless air cylinders. The weight of the Z slide is cancelled by adjusting the pressure into the air cylinders so that the force of the motor is only used to move the slide. This avoids motor overheating and prevents the tool from crashing into the workpiece in case of power loss. Brakes are also mounted onto the air cylinders and are activated if there is no air pressure, which prevents the Z slide from falling and being damaged.

5.2.2. Encoder system

The encoder system (Figure 5-5) is made of a readhead, an interpolator and a scale. The models of these components are summarised in Table 5-2.

Readhead	**Renishaw TONIC READHEAD 5m RELM/RSLM, Model T1011-50A.** Tonic, Linear, Standard Readhead, for RSLM/RELM Scales, all reference marks are output, cable length 5m. With standard mini connector to mate with Ti/TD interface.
Interpolator	**Renishaw TI 10KD A 20 A** Digital, Tonic (Ti), Interpolation factor/resolution: 2nm (10KD), Line driven E output; All alarms (A), Minimum receiver clock frequency (40 MHz), Options: A = P/Q limits – 'active high', standard reference mark.
Scale	**Renishaw Scale - RSLM-SS-20U3A-0430-A** Standard, high accuracy stainless steel scale, with a pitch of 20µm, a cross section of 15mm X 1.5mm and a spar length of 430mm.

Table 5-2: Summary of the components used in the encoder system

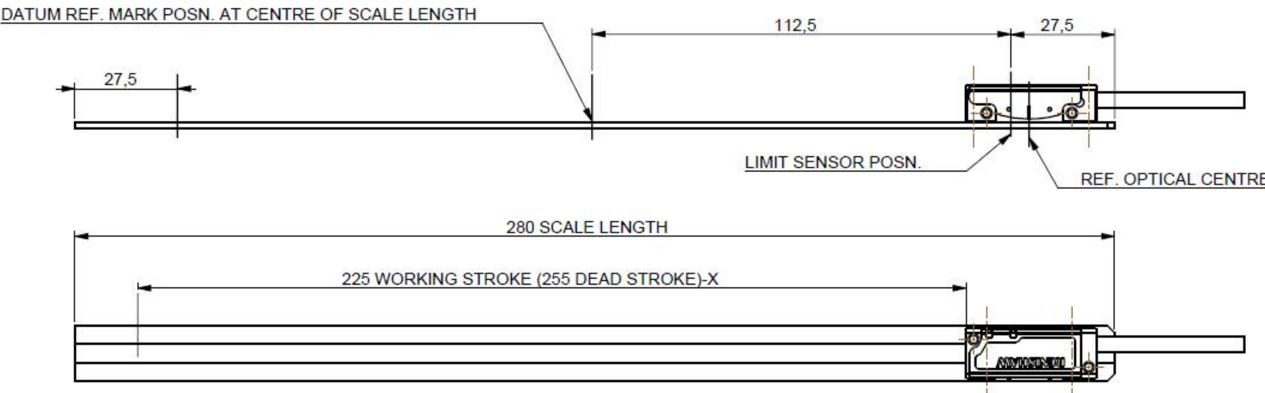

Figure 5-5: Mechanical drawing of the Renishaw encoder system

The encoder receiver frequency of the motion control system is set to 40MHz, which allows a maximum speed of 0.054m/s on each axis. This speed is more than sufficient because the tool feed rates during the machining process is very low. The 2nm encoder resolution of the position feedback system allows a very precise motion of the slides. A reference mark is

located in the middle of the scale and is used at initialization to setup the axis (during phase and home search).

5.2.3. The air bearings

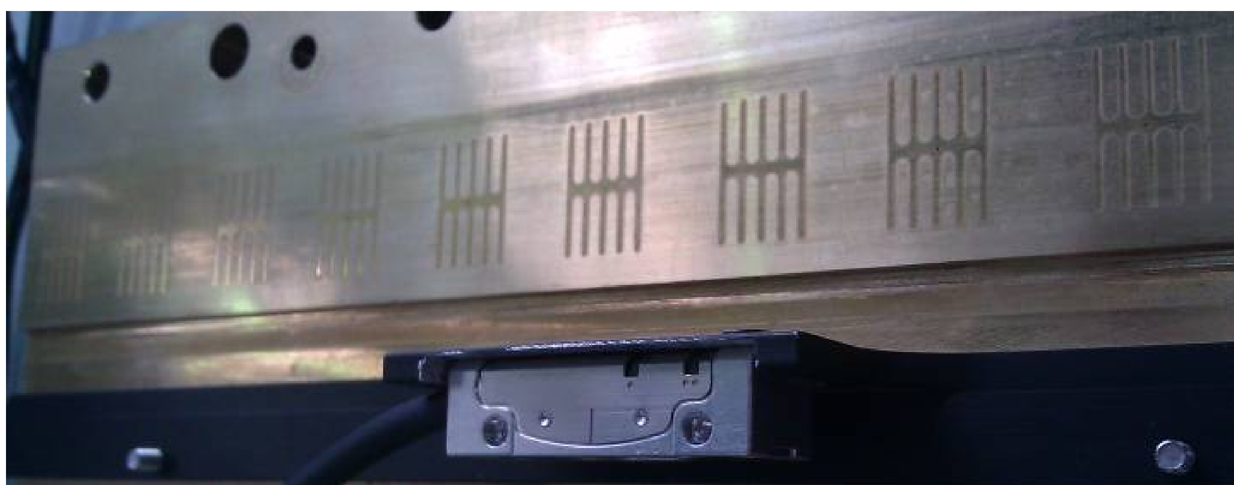

Figure 5-6: Picture of the groove pattern machined in the inner surface of the pressurized bearing to improve stability. The encoder read head can also be seen.

The air bearings play a crucial role in ultra-precision motion. One of the major features of the machine tool is that aerostatic bearings are used for all axes, which differs from the situation for all of the μECM machines in the market. The air bearings consist of a sliding cage which is made of brass assembled around a granite beam. The linear slides are based on new novel aerostatic bearing technology which improves the stiffness and load capability by 50% (Huo, Cheng and Wardle, 2010a). A very specific groove pattern (Figure 5-6) has been machined on the air bearing surface to improve stability as mentioned by Luo et al. (2005) and Stanev et al. (2004) (Luo et al., 2005; Stanev, Wardle and Corbett, 2004). Therefore, sub-micron motion accuracy is ensured by the above technologies. The clearance between the brass plates and the beam surface has been optimized for better performance of the slides.

5.3. The spindle

The spindle of the μECM machine is made of a stepper motor and a rotating part holding the tool-electrode.

The spindle (Figure 5-7) rotates the electrode during machining in order to reduce the influence of the asymmetric imperfections of the tool-electrode (run out). This spindle uses

a stepper motor, which allows precise positioning when tool-electrodes with different shapes are needed (triangle, square etc.).

In µECM, tool-electrodes with simple shapes (cylindrical or semi-cylindrical (Yang, Park and Chu, 2009)) are used in most cases. The electrical connection of the cathode is complex to achieve because the tool is spinning: energy must be reliably transmitted to the rotating element. In the case of high frequency power supply and high current it is not suitable to use the traditional carbon or silver brushes because the transmission of high current has a detrimental effect on them and they do not work well at high frequency (parasitic inductance).

At the moment there is no good solution on the market such as a system transmitting high frequency signals and high current to a spinning electrode and at the same time to be located as close as possible to the IEG (with a minimal length of metal conducting the pulses).

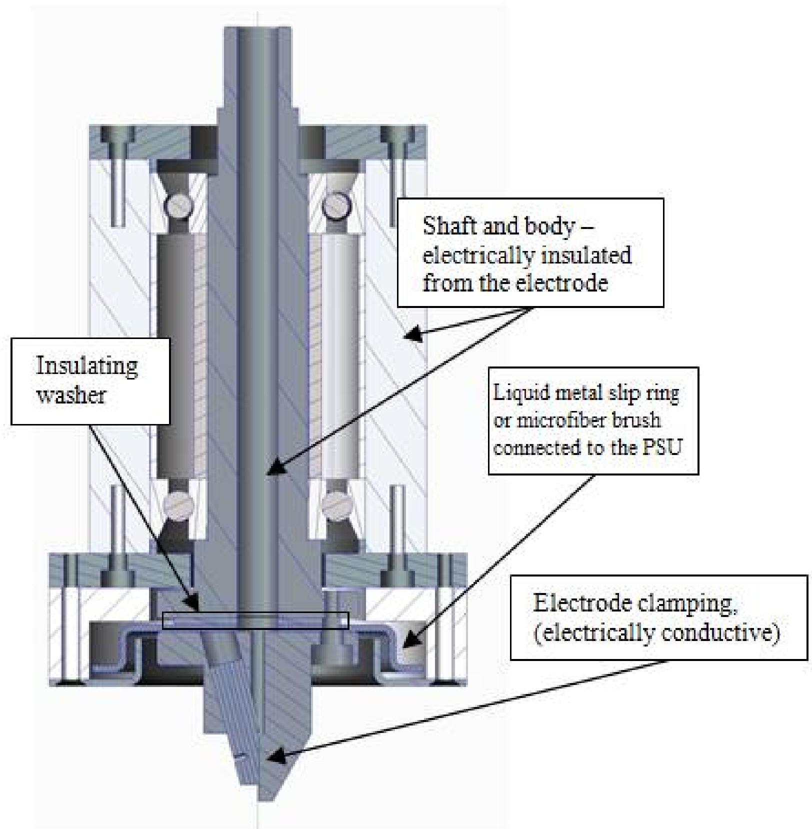

Figure 5-7: Cross section of the developed spindle for the µECM machine. For safety reasons, the mercury slip ring was later replaced by a ring with microfiber carbon brushes.

The solution adopted by the author was to develop a purpose built spindle (Figure 5-7) using precision bearings and to have the transmission of the signals to be done via a ring with

microfiber carbon brushes. This type of ring is normally used for shaft grounding and bearing protection, and is able to handle high current at high frequencies (Muetze and Oh, 2008).

To improve the electrical contact between the brushes and the tool-electrode, a silver coating was applied on the surface of the electrode-holder. This setup makes a reliable connection between the PSU and the rotating parts of the spindle which holds the tool-electrode.

The stepper motor on the spindle is the model ST4218L1806-LC-NEU from Nanotec which can be controlled using a SMCI33-1 drive. The step angle of the motor is 1.8 degrees with an accuracy of +/- 5%. The drive communicates with the HMI using a USB port (Figure 5-8).

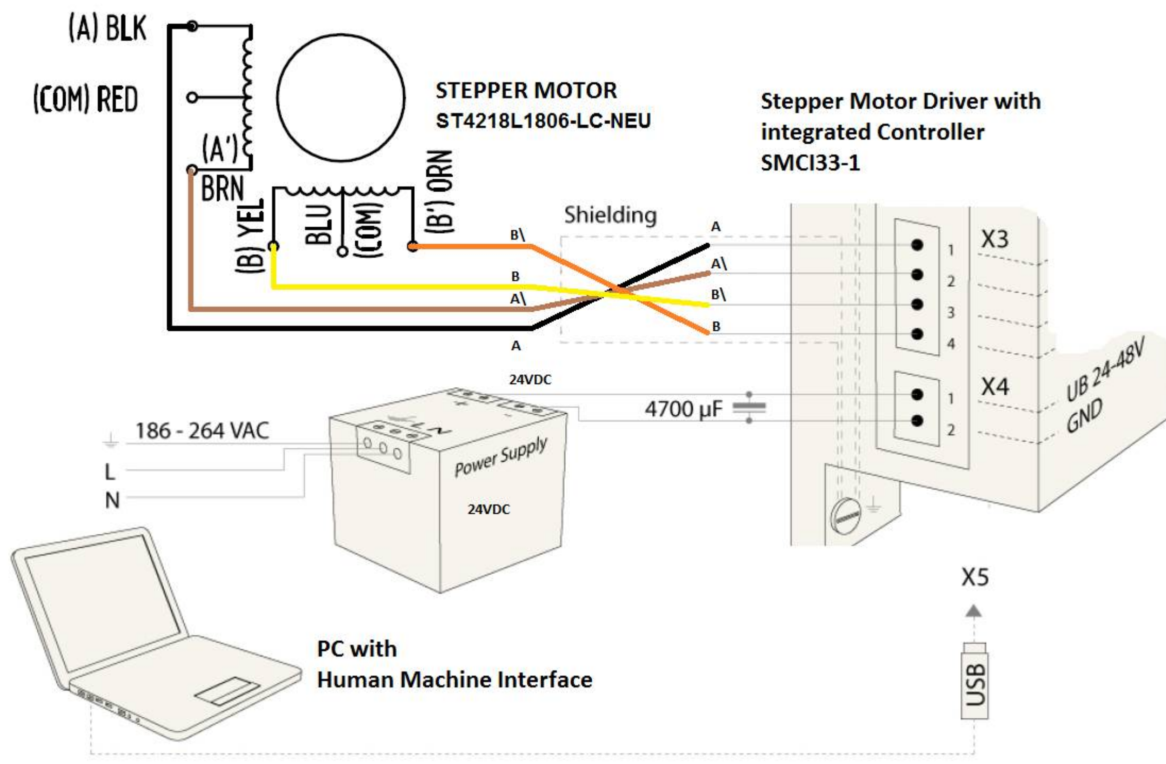

Figure 5-8: Schematic diagram showing the wiring of the stepper motor as well as its interface with the HMI.

5.4. Electrical cabinet

The electrical cabinet (Figure 5-9) is located in a ‘drawer’ under the base of the machine. It contains all the electrical components necessary to operate the machine. Each of these components will be detailed in the following sections.

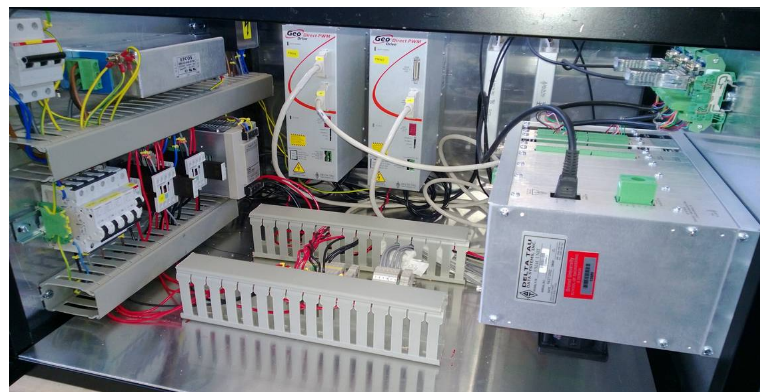

Figure 5-9: Picture of the electrical cabinet

5.4.1. Control components

5.4.1.1. Power PMAC motion controller

The control system is the one of the most innovative part of the machine. As special process control algorithms need to be developed, a controller with an open architecture should be chosen is order to facilitate the development. The Delta Tau Power PMAC suits perfectly to the requirement: it can run PLCs and programs which are either written in C or in PMAC script language (which is a proprietary programming language from Delta Tau).

The Power PMAC is actually a computer on a single board which can be interfaced to an extensive range of compatible Delta Tau motion control, analogue input/output and digital input/output boards. The Power PMAC runs a Linux Debian distribution whose kernel has been patched with the open-source real time extension Xenomai to give real time capabilities to the operating system (Barbalace et al., 2008).

It is very important for a control system to be real-time in order to ensure a deterministic behaviour in cases where hazardous events could occur.

The Delta Tau Power PMAC CPU board is placed into a UMAC rack (Figure 5-10) and interfaced with the following boards.

Figure 5-10: A picture representing the UMAC rack as a modular system.
Source: http://www.heason.com/catalogue/74/umac.html

5.4.1.2. ACC24E-2 4 axes interface board

This motion control board allows the Power PMAC to control up to 4 axes. The inputs of this board are the encoders and the hall sensors of the X, Y and Z axes (Figure 5-11 and Figure 5-12).

The connections between the encoders and the Acc24E-2 are made via a Ziplink DB15 to Terminal Block adapters using the following connection list:

- TB1 Pin1 => Pin 14 (A+)
- TB1 Pin 2 => Pin 6 (A-)
- TB1 Pin 3 => Pin 13 (B+)
- TB1 Pin 4 => Pin 5 (B-)
- TB1 Pin 5 => Pin 12 (Reference mark Z+ = C+)
- TB1 Pin 6 => Pin 4 (Reference mark Z- = C-)
- TB1 Pin 7 => Pin 7,8 (+5V)
- TB1 Pin 8 => Pin 2,9 (0V, GND)

The Hall sensors are connected the following way:

- RED = HALL +5V => TB7
- BLACK = GND => TB8
- WHITE= S1 = Phase U => TB9
- BLUE = S2 = Phase V => TB10
- ORANGE = S3 = Phase W => TB11

TTL Level Inputs and Outputs

Quadrature Encoders

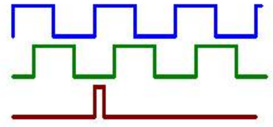

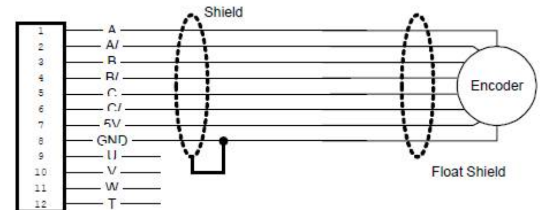

Figure 5-11: Electrical schematic of the encoder wired to the Acc24E-2 (Delta Tau Data Systems, 2009)

This board is also interfaced with the direct PWM amplifiers: the outputs of this board are the PWM control signals that switch the power semiconductors in the drive.

The Acc-24E2 allows the use of sinking or sourcing position limits and flags to the controller. The opto-isolator IC used is a PS2705-4NEC-ND quad photo-transistor output type. This IC allows the current to flow from return to flag (sinking) or from flag to return (sourcing) (Delta Tau Data Systems, 2009). In the current setup, the flag inputs are not wired.

TTL Hall Effect Sensors

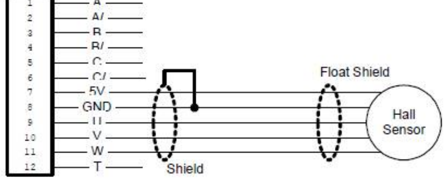

Figure 5-12: Electrical schematic of the Hall effect sensor wired to the Acc24E-2 (Delta Tau Data Systems, 2009)

5.4.1.3. ACC36UK 16bit Analogue input board

This analogue input board is made of 16 analogue inputs which have a 16bit resolution. Analogue signals can be acquired at a frequency of 1 kHz for all channels and 16 kHz on a

single channel. This board is used to acquire the peak value of the measured machining current.

The ACC36UK is a special card and is therefore not detected automatically by the Power PMAC. Even though it does not have automatic detection hardware, their outputs can still be cleared at start-up using a custom programme written in C. The base addresses the I/O cards occupy must be known. The base addresses correspond to which jumper settings (or SW1 if a newer card) are used on the I/O card; for example, E1-E4, shown on page 15 of the ACC-11E manual, set the base address for ACC-11E (Delta Tau Data Systems, 2011).

The address of the board is set using the DIP switch configuration shown in Table 5-3.

Chip select	Base address (Turbo PMAC)	8	7	6	5	4	3	2	1
CS14	Y:$78E00	ON	OFF	OFF	OFF	ON	OFF	OFF	OFF

Table 5-3: Table of the DIP switch configuration used to set the address of the Acc36UK

$78E00 ⇔ $C00000 for Power PMAC, index of the board will be 1.

Each card's manual will describe how to set the jumpers or SW1 setting for various base addresses. A document correlating Turbo PMAC base addresses to the Power I/O base address offsets needed for Power PMAC was used to access to the data acquired in each channel of the ACC36UK.

To point to the card, piom (pointer to I/O memory) must be added to the value given in the Power PMAC I/O Base Address Offset, divided by 4, and point thereto using a volatile unsigned int pointer.

To access an undetected card the definitions of the pointers toward the ACC36UK memory must be made. For the base address of $78E00 ($C00000 on Power PMAC), the following pointer configuration is obtained (Figure 5-13).

The defined pointers are then used in the C function GetAcc36UKValue() in the programme bgcplc0.c (Figure 5-14).

```
// ACC36UK (ADC board) pointers
ptr ADC1->s.io:$C00694.8.16;  // ADC input 01  (78ED5 converted to ppmac) in differential mode
ptr ADC2->s.io:$C00698.8.16;  // ADC input 02  (78ED6 converted to ppmac) in differential mode
ptr ADC3->s.io:$C0069C.8.16;  // ADC input 03  (78ED7 converted to ppmac) in differential mode
ptr ADC4->s.io:$C006C0.8.16;  // ADC input 04  (78ED8 converted to ppmac) in differential mode
ptr ADC5->s.io:$C006C4.8.16;  // ADC input 05  (78ED9 converted to ppmac) in differential mode
ptr ADC6->s.io:$C006C8.8.16;  // ADC input 06  (78EDA converted to ppmac) in differential mode
ptr ADC7->s.io:$C006CC.8.16;  // ADC input 07  (78EDB converted to ppmac) in differential mode
ptr ADC8->s.io:$C006D0.8.16;  // ADC input 08  (78EDC converted to ppmac) in differential mode
ptr ADC9->s.io:$C006D4.8.16;  // ADC input 09  (78EDD converted to ppmac) in differential mode
ptr ADC10->s.io:$C006D8.8.16;  // ADC input 10  (78EDE converted to ppmac) in differential mode
ptr ADC11->s.io:$C006DC.8.16;  // ADC input 11  (78EDF converted to ppmac) in differential mode
ptr ADC12->s.io:$C00700.8.16;  // ADC input 12   (78EE0 converted to ppmac) in differential mode
ptr ADC13->s.io:$C00704.8.16;  // ADC input 13   (78EE1 converted to ppmac) in differential mode
ptr ADC14->s.io:$C00708.8.16;  // ADC input 14   (78EE2 converted to ppmac) in differential mode
ptr ADC15->s.io:$C0070C.8.16;  // ADC input 15   (78EE3 converted to ppmac) in differential mode
ptr ADC16->s.io:$C00710.8.16;  // ADC input 16   (78EE4 converted to ppmac) in differential mode
```

Figure 5-13: ACC36UK memory pointers setup in the global definitions.pmh file of the Power PMAC IDE

```
double GetAcc36UKChValue(int channel){
    volatile unsigned int *pACC36UK; // pointer for ACC36UK
    short ADC_Result = 0;
    double CurrentVal;
    switch(channel){
            case 1:
                // Point to Address of Ch. 1 of ACC-36UK Card
                pACC36UK = (piom + 0xC00694/4);
                // 0xC00694  <=> $78ED5 (turbo) <=> A/D Ch. 1 16 bit signed value from ACC36UK datasheet
                break;
            case 2:
                // Point to Address of Ch. 2 of ACC-36UK Card
                pACC36UK = (piom + 0xC00698/4);
                // 0xC00698  <=> $78ED6 (turbo) <=> A/D Ch. 2 16 bit signed value from ACC36UK datasheet
                break;
             [DONE FOR EACH CHANNEL]
            case 16:
                // Point to Address of Ch. 16 of ACC-36UK Card
                pACC36UK = (piom + 0xC00710/4);
                // 0xC00710  <=> $78EE4 (turbo) <=> A/D Ch. 16 16 bit signed value from ACC36UK datasheet
                break;
            default:
                fisError((char *)"ACC36UK Channel number is out of bound!");
                pshm->P[gRTIPLCmode] = SOFTSTOP; //terminate algo
    }
    if(pACC36UK != NULL){
    // shift right 8 bits, bits 8-23 (16 bits), then mask the to get the first 16 bits
    // to obtain ADC Result for Channel 1
     ADC_Result = (short)(((*pACC36UK)>> 8 )& 0x0000FFFF );
     // ADC_Result is a short int (need to keep polarity ADC in bipolar mode)
     CurrentVal = (double) (10.0)*ADC_Result/30000.0;
     // gives the ADC value in Volts
     return CurrentVal;
    }else{
    return pshm->P[gParamsOptimalCurrent+1];
    // return optimal value, which does not trigger any move and leaves time to stop the programme
    }
}
```

Figure 5-14: The function GetAcc36UKValue() using pointers to access the data acquired by the ACC36UK in C.

5.4.1.4. ACC65E digital input/output board

This digital input/output board is used to receive logic signals from the pulse power supply and all the safety related components. Its outputs are used to switch on relays and enable/disable features on the pulse power supply.

The controller is the UMAC rack containing the Delta Tau Power PMAC and its control boards, which will be described later on.

5.4.1. GeoDrive direct PWM amplifiers

The GeoDrive direct PWM amplifiers are controlled by the PWM logic signals coming from the ACC24E-2. The model used is the GPL052 and its characteristics are summarized in Table 5-4. Each amplifier has two control inputs (with 36-pin mini-D connectors) and is able to power two motors. Therefore two amplifiers are needed to control the 3 motors for the X, Y and Z axis. The first drive 'PWM1' powers axes X and Y whereas the second one 'PWM2' is used for the Z axis.

Main input power: • Nominal Input voltage: 230VAC • Rated input voltage: 97-265VAC • Rated Continuous input current: 6.6 AAC(rms) • Rated input Power: 2629W • Frequency: 50Hz • Phase requirements: 3 • Main bus capacitance: 3380µF Output power: • Rated output voltage: 138V • Rated continuous output current per axis: 5A • Peak output current for (2 seconds): 10A • Rated output power per axis: 1195W Bus protection : • Nominal DC bus 325 • Over-voltage trip level (VDC): 410 • Under-voltage Lockout level (VDC): 10	Shunt regulator ratings: • Turn-On Voltage (VDC) : 392 • Turn-Off Voltage (VDC) : 372 • Delta Tau Recommended Load Resistor (300 W Max.) : GAR78 Control logic power: • Input Voltage (VDC): 20-27 • Input Current (A): 2A • Inrush Current (A): 4A Current feedback: • Resolution (bits) : 12 • Full-scale Signed Reading (±A) : 16.26 Transistor Control: • Delta tau recommended PWM frequency (kHz) : 12 • Minimum Dead Time (µs): 1 • Charge Pump Time (% of PWM period): 5

Table 5-4: Summary of the specifications of the direct PWM drive GPL052 (Delta Tau Data Systems, 2006)

The amplifiers also need a 24VDC source to supply their logic unit which controls the power semiconductors chopping the rectified 138VDC voltage. The installation manual claims that *'This [24VDC] power can remain on, regardless of the main AC input power, allowing the signal electronics to be active while the main motor power control is inactive.'* (Delta Tau Data Systems, 2006).

The rated input voltage is 230VAC and therefore each amplifier is power by 1 phase. The 3rd phase 'L3' is connected to 'PWM1' and the 2nd phase 'L2' powers 'PWM2' (Figure 5-15).

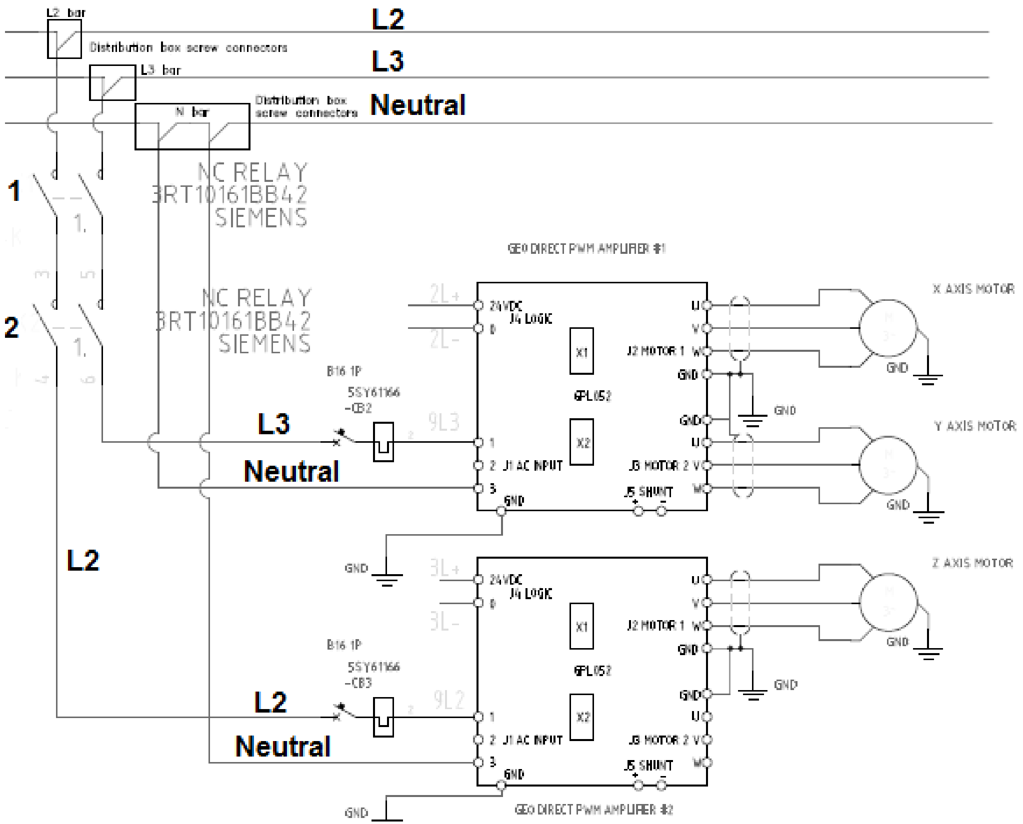

Figure 5-15: Electrical schematic of the wiring of the amplifiers

5.4.2. 24V logic and electrical Safety components

5.4.2.1. 24V logic components

The ACC65E uses logic signals with voltages in the 12-24V range and therefore an external 24V DC power supply is needed. A 24VDC signal is produced by an Omron S8VS-18024 power supply.

Two Siemens 3-phase contacts relays (3RT10161BB42) are placed between the AC voltage supply and the inputs of the GeoDrive amplifiers (Figure 5-15). The first is controlled by the Power PMAC and is used to enable/disable the amplifiers for safety purposes.

A 3RT19161DG00 suppression diode is added to the relays to avoid any damage when releasing the current of coil at turn-off.

An emergency stop button is connected to one of the contact relays in order to cut-off the power to the drives quickly and reliably in case of dangerous situation.

A relay is also used to turn on/off the pump. The 24V logic of the relay is connected to the digital output 'DO2' of the board ACC65E.

5.4.2.2. Circuit breakers

To protect the controller, a 6A circuit breaker with a B curve has been selected (B6).

For the 24VDC PSU, a C6 circuit breaker was chosen. The direct PWM amplifiers are protected by B16 circuit breakers.

For the PC running the HMI, a B6 circuit breaker was initially chosen, but it seemed like the in rush current of its power supply was too high and made the circuit breaker trigger at power up. Therefore, it was replaced by a C6 circuit breaker.

5.4.3. Filtering and shielding

The 3-phase + neutral line filter FN256-16-46 from Schaffner is a general purpose filter which acts as an EMI filter and improves the power quality.

It helps reducing noise and prevents the machine from being affected by other events on the network (voltage spikes, etc...).

The cables connecting the drives to the linear DC motors are shielded to reduce the emission of noise linked to the switching power conductors.

5.5. Electrochemical machining cell and electrical connections

The electrochemical machining cell has been designed to machine workpieces which have the shape of a coin. These parts were provided by the company Delphi (UK) and used in the fuel injection system of diesel engines. The electrochemical cell has 3 holes: 1 electrolyte inlet delivering the fresh electrolyte to the working zone and 2 electrolyte outlets taking the already used electrolyte to the filtering station.

The part to be machined is clamped using a cap that is bolted on the top of the cell. This cap not only maintains the workpiece in position, but it is also made of conductive material to connect the workpiece to the pulse PSU.

In electrochemical machining the electrical connections must not be exposed to the effect of the working electrolyte. The part to be machined is clamped using a cap that is bolted on

the top of the cell (Figure 5-16, Figure 5-17). This cap not only maintains the workpiece in position, but it is also made of conductive material (stainless steel) and connects the workpiece to the pulse PSU.

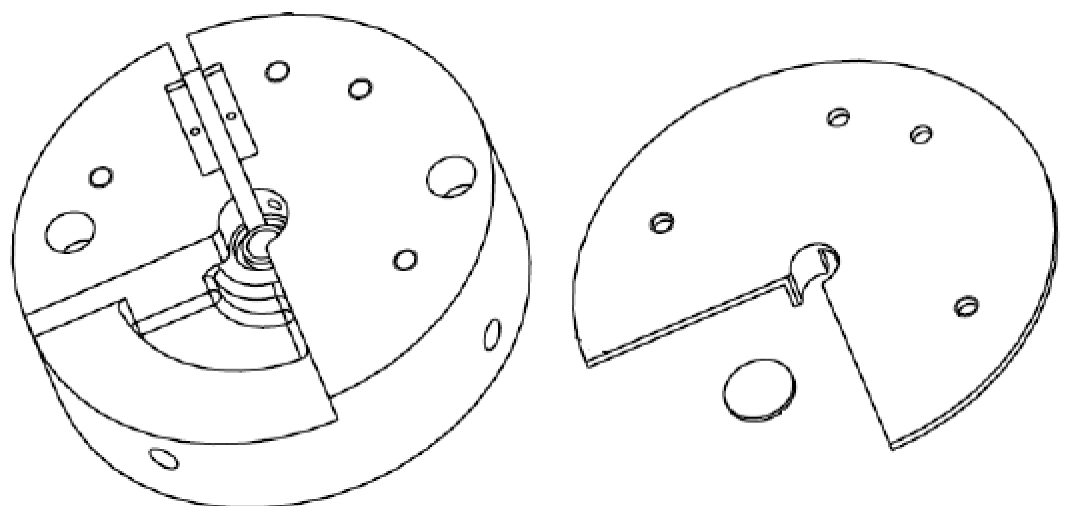

Figure 5-16: CAD View of the machining cell with the base, the workpiece and the cap

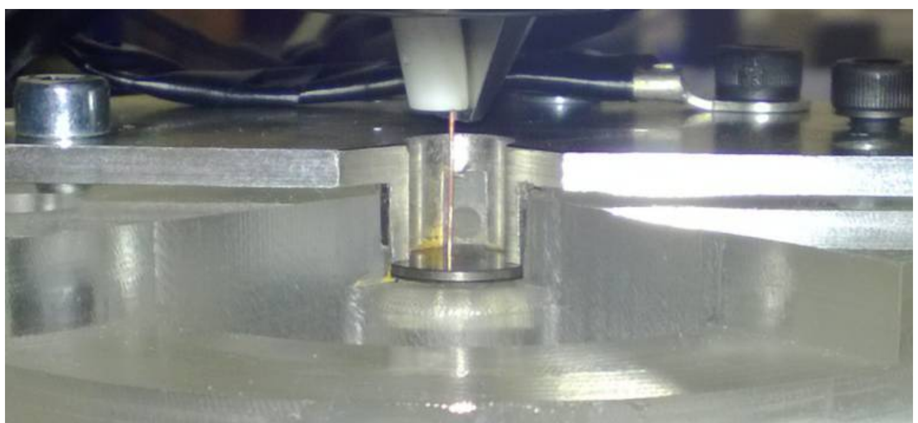

Figure 5-17: Picture of the workpiece (coin) being clamped by the cap and making electrical contact with a copper electrode.

As mentioned in the literature review, one of the critical parameters of the µECM process circuitry is the inductance of the cables connecting the PSU to the electrodes (Burkert et al., 2009). The parasitic cable inductance increases the rise time of the voltage pulses especially for pulse durations below 1µs. At high frequency, the impedance of the cables becomes so big that only a portion of the output power is delivered to the IEG and the pulses are distorted. The cabling therefore limits the frequency at which machinining can occur and problems have been reported above 1MHz (Fan, Hourng and Lin, 2012).

To solve this issue, special low inductance cables should be used and their length must be minimised. The use of coaxial cables to minimise cable inductance have also been reported

(Park, Kim and Chu, 2006). This would mean that the PSU has to *'be positioned as close as possible at the gap connection'* (Burkert et al., 2009).

The solution adopted by the author to minimize the cable length was to mount the pulse PSU directly on the Z axis, very close to the spindle.

The machining cell also allows the installation of a wire to perform the machining of micro-tools and micro-probes. Metallic washers assure the wire fixture and electrical connection (Figure 5-18).

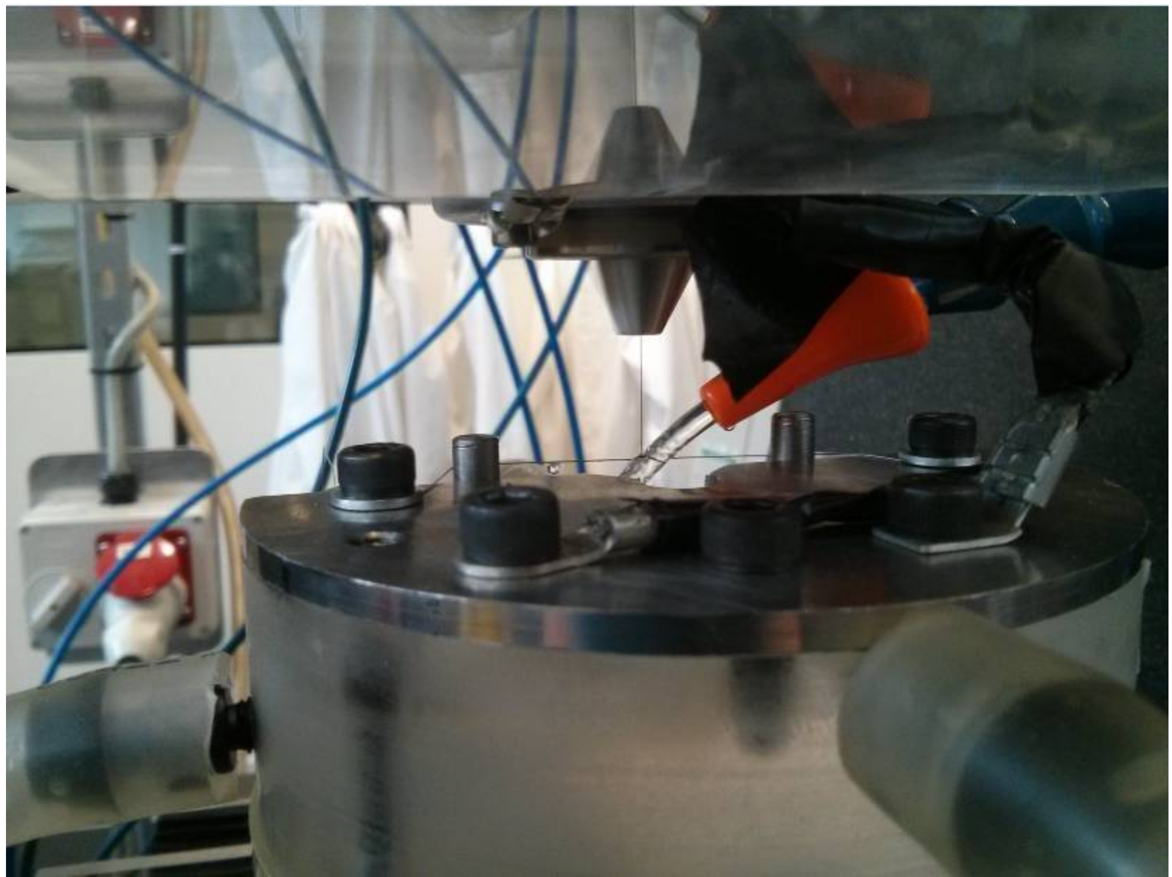

Figure 5-18: Picture of the electrochemical cell with a wire installed for micro-probe machining

5.6. Electrolyte circuit

Figure 5-19: Picture of the 2 filters and the pump

- Pump: The pump is a single phase Iwaki Magnet Pump model MD-20RZM-220N. It has 2 poles and has power consumption of 45-57W. It works directly from the mains electrical supply (220V/50Hz) and is protected by a 1A circuit breaker. The chamber of the pump is made of chemical resistant material, allowing the use of corrosive electrolyte such as aqueous solutions of sulphuric acid or hydrochloric acid.
- Filters: Two inline filters made of spun polypropylene (of the type used for micro-EDM machining) with a fineness of 5µm and 1µm were chosen to accomplish the electrolyte filtration task (Figure 5-19). The filter cartridges are of 2.5 inch dia. and 10 inch length and fit into a housing bowl. The inlet and outlet ports of the housing bowls have a 3/4inch diameter.
- Valves: A system of valves allows the user to select the electrolyte path. The user can either supply the workpiece clamped in the electrochemical cell or supply the wire-µECM process through a nozzle (Figure 5-18).
- Flexible pipes: The flexible pipes (Cole-Palmer C-Flex clear, EW-06422-16 – 7 metres length approx.) will carry the electrolyte supply system to the machining cell. Their flexibility allows the positioning and motion of the cell at different locations.
- Electrolyte container: The electrolyte is stored in a tank located in a thermally controlled container. The chosen container is the Waeco Tropicool TC-35FL-AC Container.

Temperature control is an important factor within the machining process. As the temperature increases, the conductivity increases which can influence the MRR. Therefore the electrolyte container helps maintaining the temperature of the electrolyte constant. Holes had to be drilled where the electrolyte is piped to and from the container.

5.7. Conclusions

In this chapter, the machine integration and the interfaces between its different subsystems were presented. State of the art components were selected in order to meet the required specifications identified after an in-depth research and analysis.

The presented machine provides outstanding capabilities in terms of programmability and precision motion thanks to the Delta Tau Power PMAC control system interfaced with 2nm resolution encoders.

The unique cell configuration allows the fabrication of micro-tools and the machining of parts on a single setup and in a sequential manner.

This research and development can lead to various applications such as the drilling of micro-holes in hard to machine material for the automotive and aerospace sectors. Each of these applications will require the design of an adapted workpiece clamping system which should meet the electrical and spatial requirements for an optimal machining performance (short current path for high frequency, chemical resistant fixtures…).

Chapter 6: PROCESS CONTROL AND SUPERVISION

6.1. Servo loop tuning of the X, Y and Z axes

The servo algorithm controlling the position and the velocity of the X, Y and Z axes is a PID with velocity and acceleration feed forward loops.

The proportional (Kp), integral (Ki), derivative (Kd), velocity feed forward (Kvff) and acceleration feed forward (Kaff) have to be accurately tuned for each axis in order to achieve an optimum performance.

The tuning of the control loop is done using the interactive tuning feature of the Power PMAC Suite software.

At the beginning, the step response test is made: A voltage step is applied to the motor and the velocity and position are plotted over time. Kp is progressively increased until the rise time is short enough and an overshoot is reached. The derivative gain Kd can then be adjusted to reduce the overshoot and damp the system response (Figure 6-1).

The role of Ki is to eliminate the steady state error, it must be high enough to reduce it rapidly but increasing it also increases the overshoot of the step response.

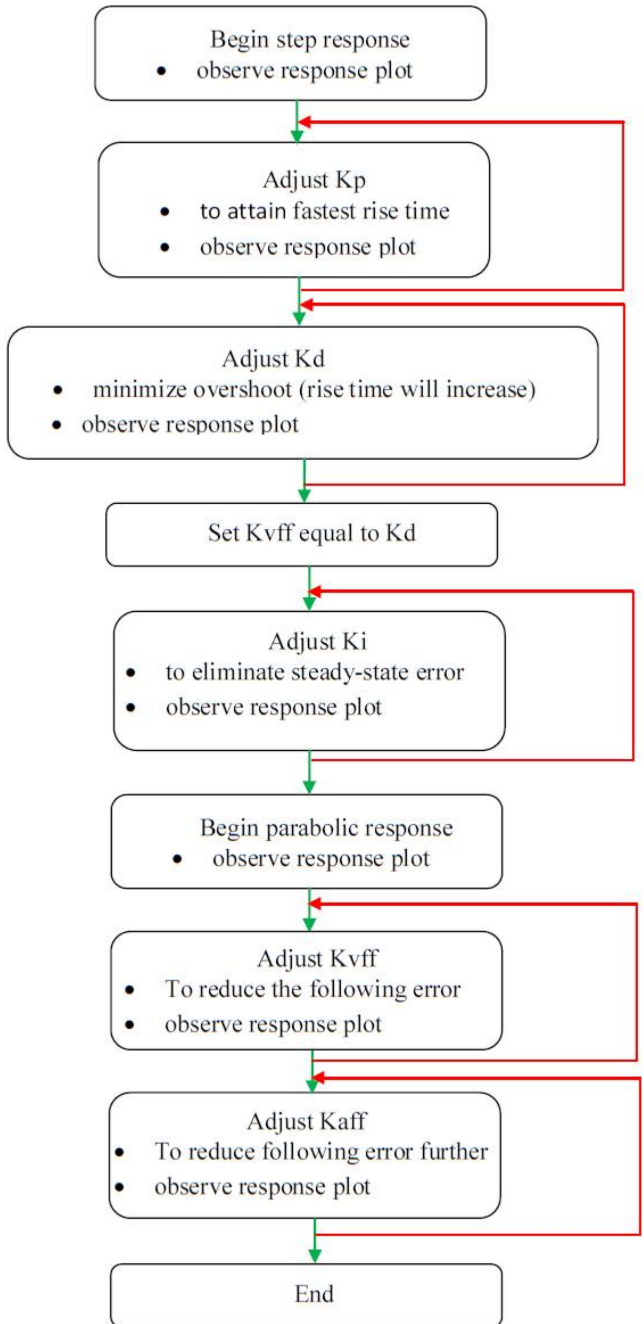

Figure 6-1: Flow chart of the PID tuning method (Nor, 2010).

Once the PID gains have been set properly and the desired step response is obtained (Figure 6-2), a parabolic velocity curve response can be plotted in order to setup the velocity and the acceleration feed forward curves (Figure 6-3).

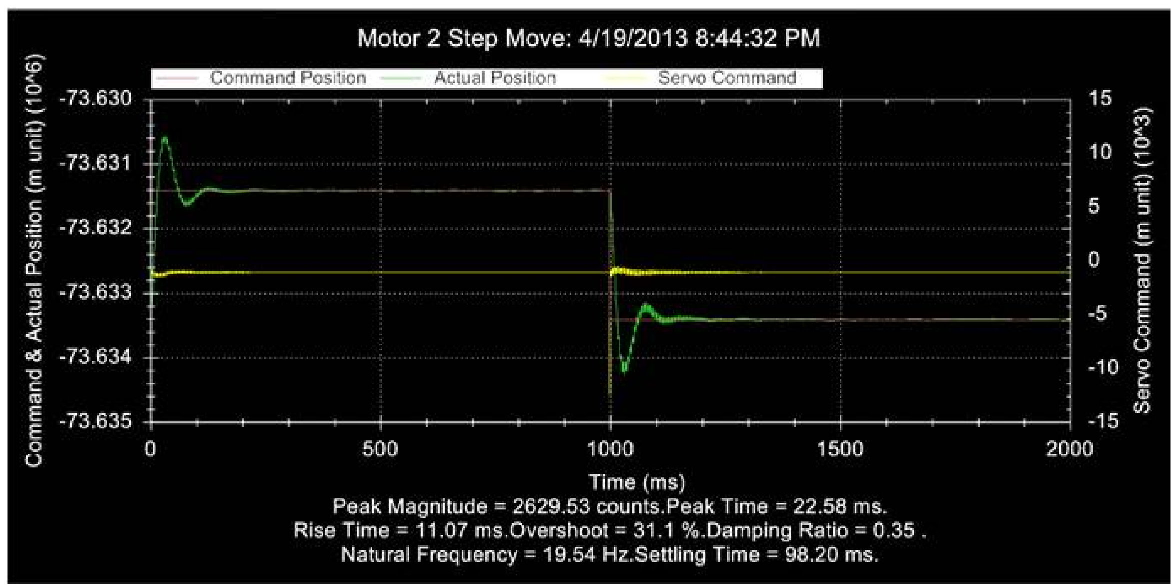

Figure 6-2: Plot of a step response step used to setup the PID gains of motor 2.

The position following error can be used as a criterion to determine the precision at which the motion is being performed. In Figure 6-3 it can be seen that the maximum following error is approximately 34 motor units. Motor units correspond to encoder counts so 1 count represents 2nm. The following error of the Y axis is therefore 68nm on a parabolic move, which is an acceptable amount of error and better than most of the ultra-precision motion linear stages available on the market which usually have a 0.1µm accuracy.

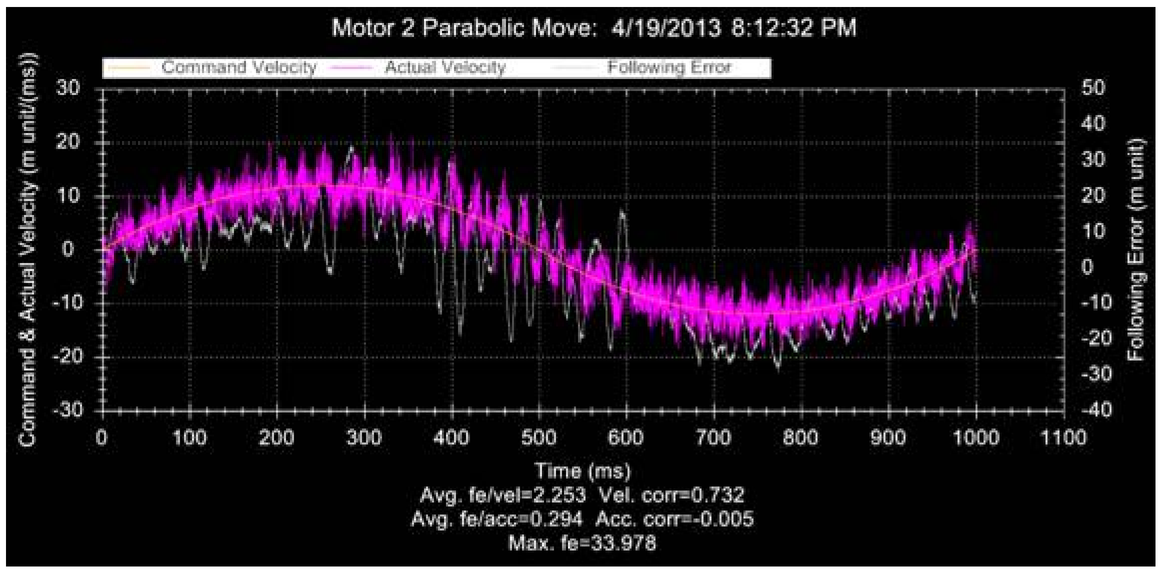

Figure 6-3: Plot of a parabolic move used to setup the feed forward gains of motor 2.

The following configurations are currently used for each motor and guarantee a very precise motion with following errors below 0.1µm for all axes. The values of the parameters are specific to the cycle time of the servo loop of the controller. If the servo cycle time is changed, these coefficients are not suitable anymore and the motors have to be tuned again:

Motor 1 (X):

```
Motor[1].Servo.Kp = 0.80000007;
Motor[1].Servo.Kvfb = 12;
Motor[1].Servo.Ki = 0.0070000001;
Motor[1].Servo.Kvff = 12;
Motor[1].Servo.Kaff = 15;
```

Motor 2 (Y) (implemented with a Notch filter to improve stability):

```
Motor[2].Servo.Kc1=-1.67232439712759
Motor[2].Servo.Kc2=0.90811731417569
Motor[2].Servo.Kc3=0
Motor[2].Servo.Kc4=0
Motor[2].Servo.Kc5=0
Motor[2].Servo.Kc6=0
Motor[2].Servo.Kc7=0
Motor[2].Servo.Kd1=-0.904859562345772
Motor[2].Servo.Kd2=0.277998561498207
Motor[2].Servo.Kd3=0
Motor[2].Servo.Kd4=0
Motor[2].Servo.Kd5=0
Motor[2].Servo.Kd6=0
Motor[2].Servo.Kd7=0
Motor[2].Servo.SwPoly7=0
Motor[2].Servo.Kp=0.332322052212607
Motor[2].Servo.Kvfb = 5;
Motor[2].Servo.Ki = 0.005;
Motor[2].Servo.Kvff = 5;
Motor[2].Servo.Kaff = 0;
```

Motor 3 (Z):

```
Motor[3].Servo.Kp = 0.8;
Motor[3].Servo.Kvfb =  12;
Motor[3].Servo.Ki = 0.006;
Motor[3].Servo.Kvff = 12;
Motor[3].Servo.Kaff = 12;
```

6.2. Orbiting motion

A function allowing the orbiting of the tool electrode has been developed to allow the machining of features bigger than the tool diameter using the ‘electrochemical micro milling’ technique.

The X and Y positions of the stages have been recorded for 10seconds when the orbiting motion program was started. The following chart (Figure 6-4) displays the trajectory of the tool. It can be seen that even at a small scale, the reproducibility of the motion is very acceptable, with very small position differences.

The program needs to be given an orbiting radius, the centre of the orbiting movement and the feed rate.

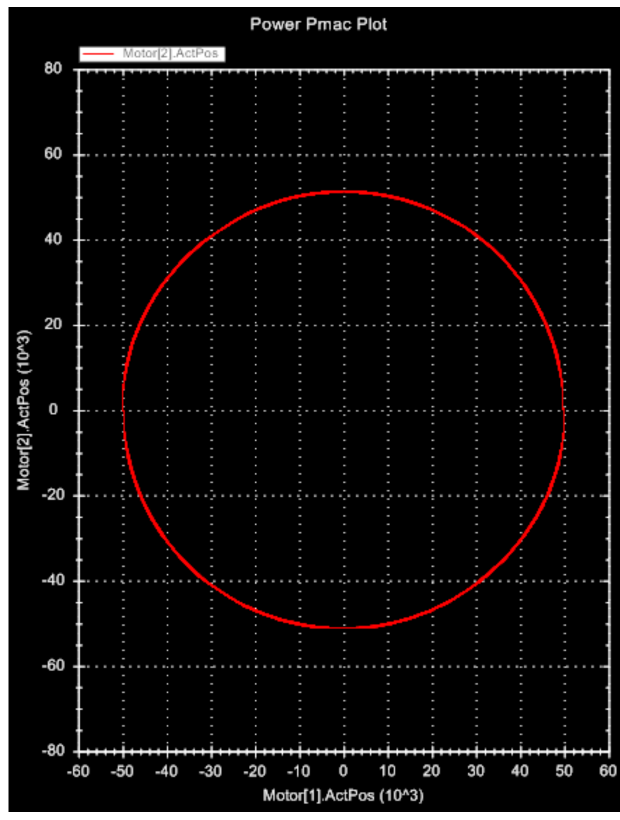

Figure 6-4: Plot of the tool trajectory in the X, Y plane when the orbiting motion program is executed, the position is in motor units, corresponding to 2nm/unit. The radius of the orbiting movement was therefore 100µm.

This program only affects the X and Y axis, which means the Z axis can be controlled independently in another program like the fuzzy control state machine. In case of OCP, the orbiting motion program should be able to stop the motion immediately to avoid the tool electrode from being damaged.

6.3. Machine initialization algorithms

At power up, the absolute position of each of the axes is unknown. Therefore, before beginning any operation, all the axes much find their home position. For this purpose, special programs have been written for each motor:

- Plc 2: Does the setup of the X axis
- Plc 3: Does the setup of the Y axis
- Plc 4: Does the setup of the Z axis

These programs follow the same structure and their logic has been summarized in the flow chart in Figure 6-5.

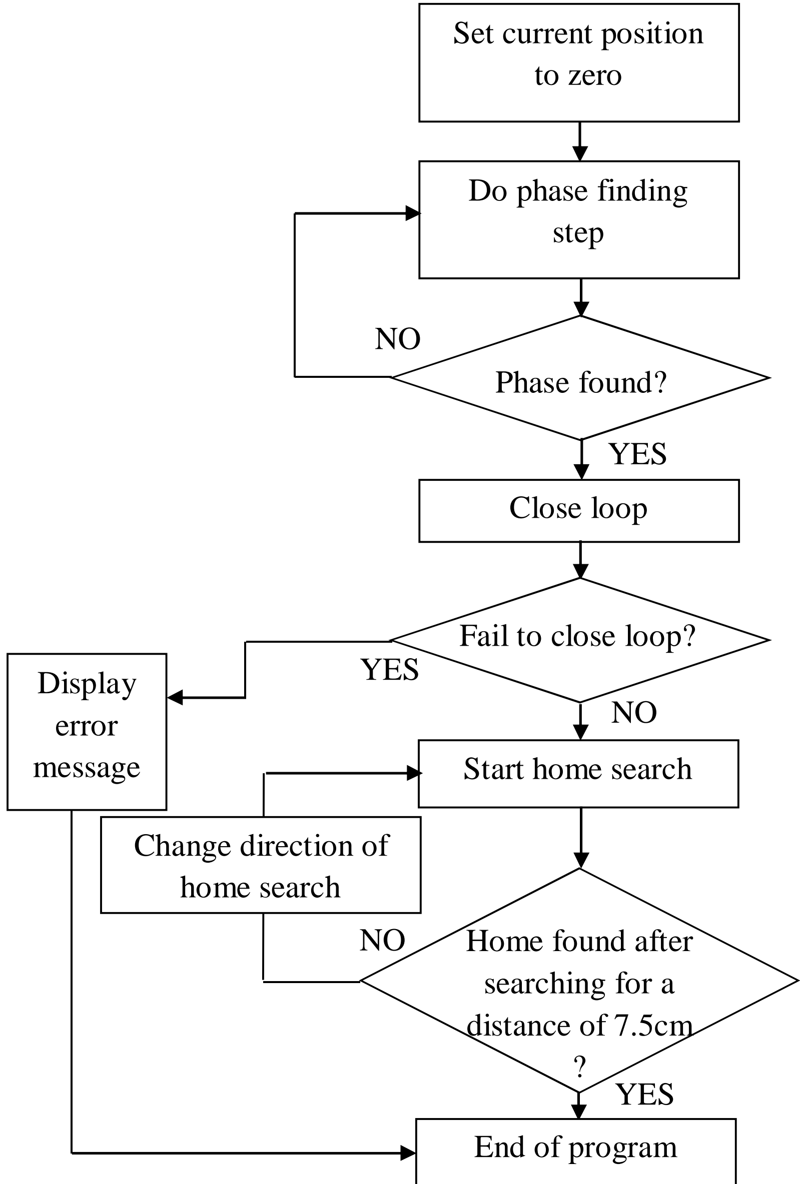

Figure 6-5: Flowchart describing the program to setup the motors at the power up of the machine

6.4. Process control algorithms

The dimension of the gap can vary from a few µm to 100µm depending on the application and has a dramatic influence on the machining accuracy. During the machining process, the motion control logic mainly depends on the variation of the interelectrode gap (IEG) size. The different issues influencing the IEG size such as variation in local anodic current efficiency, short circuits and variation of electrolyte conductivity in the IEG can be met during the ECM or µECM process (Wei, 1994; Kozak, Rajurkar and Makkar, 2004a; Shin, Kim and Chu, 2008). These events influence the material removal rate and therefore create a non-desired variation of the IEG.

The process control algorithm is made of steps executed in a particular sequence programmed using a state machine.

6.4.1. The state machine

The program running in the Power PMAC is a state machine containing all the different actions necessary for the proper operation of the machine.

The state machine has the following main states:

- SOFTSTOP: this state is triggered when a software problem happened during the execution of a program on the PPMAC. It will automatically interrupt all the programs running at the time the problem was detected.
- SETUP: this state is used to setup the different parameters according to the values sent by the HMI. It is also a stage at which all important variables are reset in order to ensure proper machine operation.
- TOUCH_N_GO: As its name suggests, in this state, a 'Touch and go' procedure is performed. It consists of an algorithm which will determine the position of the workpiece surface and then initialise the IEG.
- FIND_WIRE: This state runs an algorithm similar to the one in the TOUCH_N_GO state. The aim of this algorithm is to determine the position of the wire before performing and electrochemical turning session for micro tool fabrication.
- MEASURE_CURRENT: This state is necessary to measure the current flowing through the gap at the beginning of machining. It will help setup the current target for the fuzzy logic controller.
- MACHINING: In this state, the electrochemical machining process is being performed. This state is made of a state machine to react to unexpected events such as short-circuits.
- IDLE: The machine does not perform any task in this state, this is a 'waiting' state.
- ESTOP: The machine goes in this state when the emergency stop button is pressed. Pressing the ESTOP button will abort all programs and switch-off the power of the amplifiers, therefore stopping any dangerous motion.

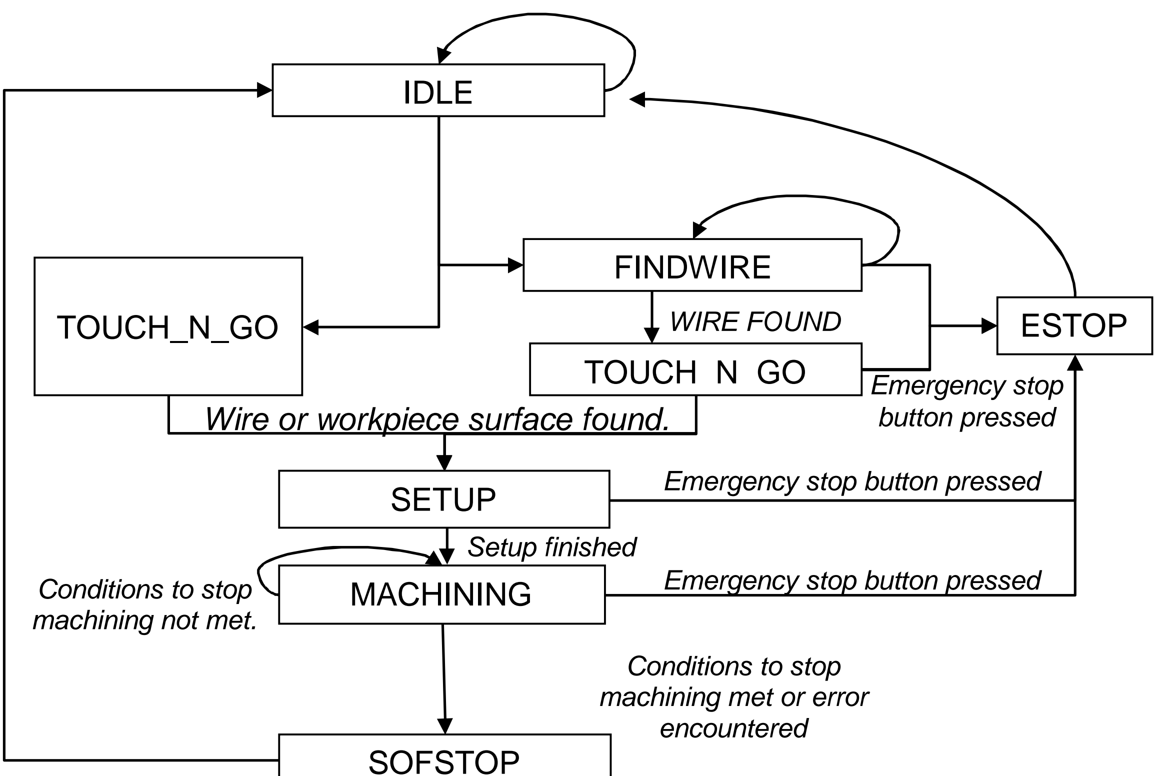

Figure 6-6: Flow chart of the main control programme running on the µECM machine

PLCs written in PMAC script language run in parallel of the main control algorithm. The roles of the PLCs nr. 2, 3 and 4 are to automate the setup of the motors, each motor is automatically setup (phase finding step, then home searching routine) when the user clicks on the button 'Motor Setup' of the human machine interface (HMI).

Another PLC (plc1) is taking care of sending relevant data to the HMI.

6.4.1. The gap initialisation algorithm

To define the inter-electrode gap the following approach is used: A small voltage is applied to the electrodes of the electrochemical cell and the tool-electrode is moved towards the workpiece until a short circuit is detected. When the short circuit occurs, the machine switches to a different mode where it will search the exact position where contact has been made. This stage is done by a state machine program which is described in the flowchart on Figure 6-7. This method helps define the position of the workpiece surface with a precision of 0.1µm or better. From this position, the tool is retracted by the initial gap distance, which is set to 5µm by default but it could be user specified.

The gap initialization method is reliable only on dry surfaces. Therefore, a major challenge comes from cleaning the surfaces of the workpiece and removing the electrolyte drops from the electrodes.

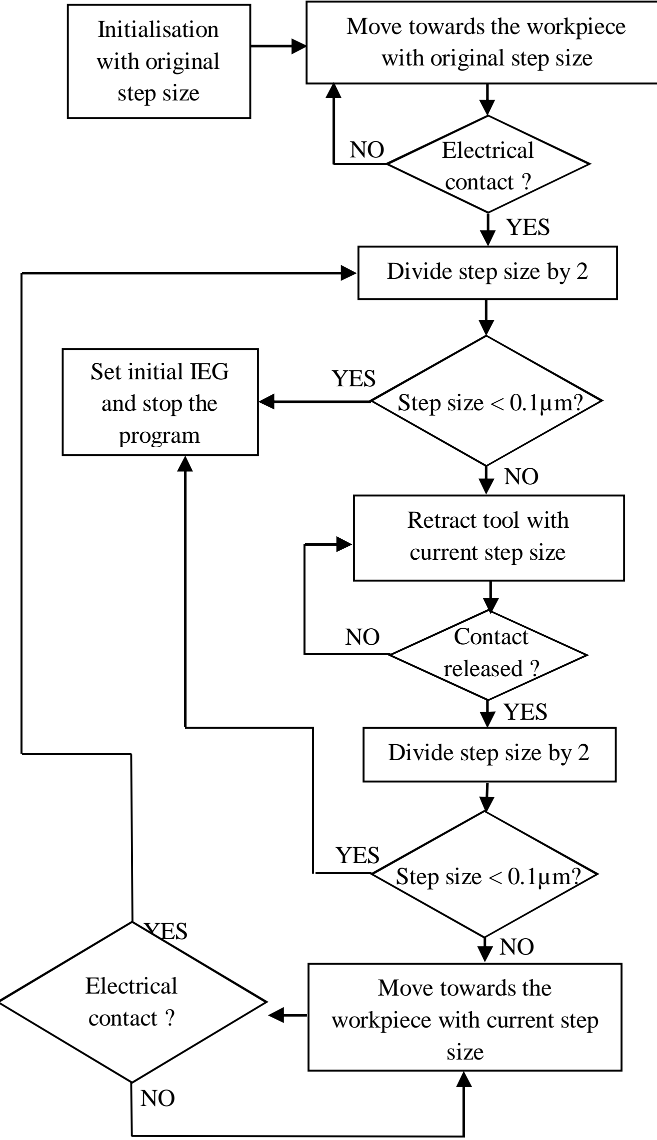

Figure 6-7: Flowchart describing the program to set the initial IEG

Figure 6-8 shows the tool trajectory during gap initialisation. This screenshot of the HMI has been taken in Germany and the Z axis direction is inverted to represent the depth of the hole. Therefore when the tool goes down, the position increases positively. It can be observed that during gap initialisation the tool position behaves as expected: the tool goes down step by step until electrical contact is made, it is then retracted for a distance that is half of the original step size and then stepped forward again until another electrical contact is made. Each time an electrical contact in made, the step size is halved and a back and forth

motion is done. This process takes place until the step size reaches 0.1μm, giving a sufficient degree of precision for the workpiece surface position. After the surface position has been determined, the tool is moved backwards for a distance corresponding to the gap size.

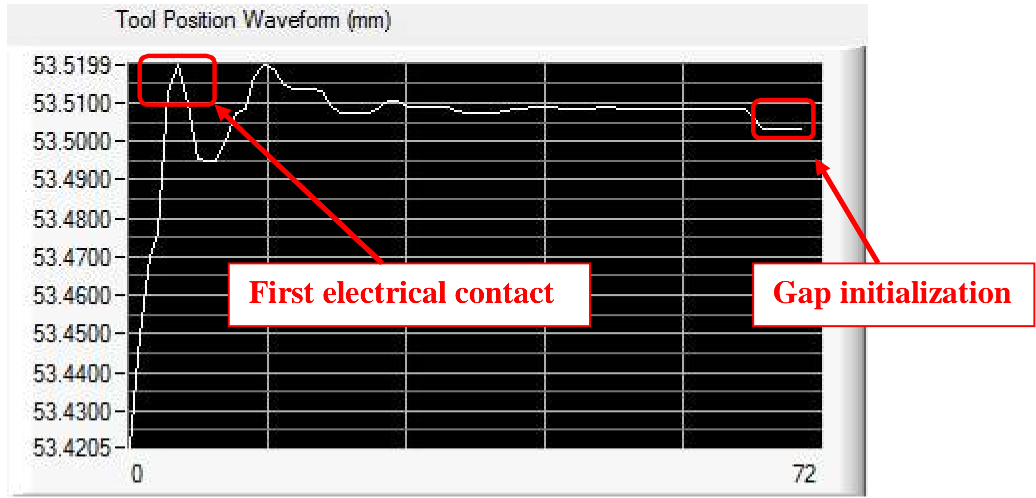

Figure 6-8: Gap initialization, tool trajectory in Z axis

6.4.2. Machining process control algorithms

Different control approaches have been experimented in the past (Spieser and Ivanov, 2013) and for this project 2 control strategies have been developed.

The machining process control algorithm is executed when the MACHINING state of the main state machine described in section 6.4.1.

This algorithm also consists of a state machine in which two different control methods are embedded.

6.4.2.1. IEG control using fuzzy logic

The first control algorithm consists of the use of a fuzzy controller to adjust the IEG according to a desired machining current. The use of this approach for the ECM processed was pointed out by Labib et al. (2011) who highlighted the necessity for the controller to have decision making capabilities. Since the PECM process is very hard to mathematically model, conventional control approaches such as proportional-integral-derivative (PID) or state space controllers are limited and based on the linearisation of the process function (and therefore approximation). They observed that the occurrence of sparking was efficiently prevented when fuzzy logic control (FLC) was applied to the ECM process and encouraged further research to develop FLCs for the EMM process. Moreover, it is worth mentioning that fuzzy logic was also used to control the process in EDM, Wire-EDM (Çaydaş, Hasçalık

and Ekici, 2009; Lin, Chung and Huang, 2001) and Electro-Chemical Discharge Machining (ECDM) (Mediliyegedara et al., 2005; Skrabalak, Zybura-Skrabalak and Ruszaj, 2004).

Fuzzy logic has been introduced in the 1960's and allows nonlinear functions to be modeled. The fuzzy logic concept is based on the fact that in the real world something might not be entirely TRUE or entirely FALSE as suggested by Boolean Logic.

The control algorithm consists of a fuzzy logic algorithm embedded in a state-machine allowing it to react to unexpected events such as short circuits. The logic of the algorithm is based on monitoring and maintaining a constant current through the inter-electrode gap. The position of the tool electrode is controlled with respect to the variation between the desired value of the machining current and its actual value. The type of the developed fuzzy logic control algorithm is Takagi-Sugeno.

The input of the fuzzy logic controller is 'mapped' into different sub-levels. The membership of the input variable with respect to these sub-levels is defined thanks to functions called 'membership functions' that will help the controller determine to which of the sub-levels the input belongs to. Therefore, a fuzzy logic controller deals with the degrees of memberships of the variables it has to control (Labib et al., 2011). The output variable is then adjusted according to the degree of membership of the input variable thanks to a rule-based process. The definition of the rules is based on human knowledge and experience. This provides the controller with a human decision-making capability.

The controller has two inputs:

1. The value of the measured current
2. The state of the PSU: pulsing (ON) or not pulsing (OFF)

The state of the over current protection signal is not taken into account here because a special retraction routine has been implemented to handle short circuits and tool protection.

The fuzzy logic functions were developed in C and are based on a heavily modified version of the Matlab fuzzy.c standalone fuzzy inference system. Indeed, the original C programme reads parameters from a text file, which is not suitable for our application since the Power PMAC does not run the HMI programme via which the user inputs their data. The way the developed programme handles the fuzzy parameters has been made very dynamic, allowing it to change its fuzzy rules on the fly.

The fuzzy logic inference system is fully integrated in the main routine controlling the process; constantly monitoring the current at a sample rate of 1 kHz and adjusting the tool position every 0.4s.

Input membership functions

For illustration purposes, the fuzzy logic controller was first simulated using Matlab's Fuzzy logic Toolbox.

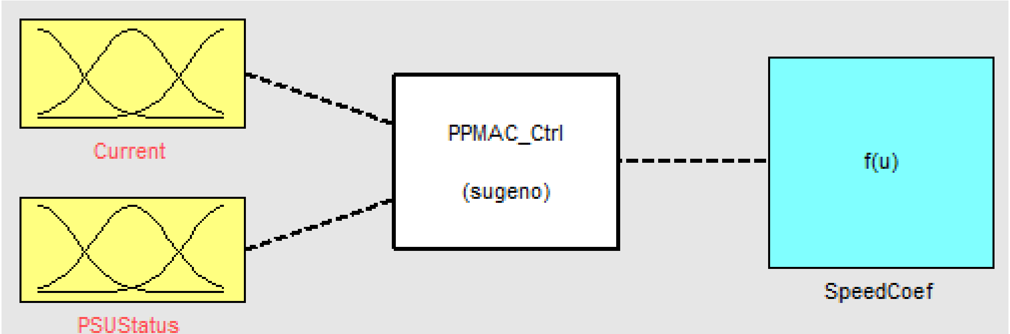

Figure 6-9: Block diagram representation of the fuzzy logic controller on Matlab

The membership functions for the input variables have to be defined. Two types of membership functions are used to define the input variables:

1. **Trapezoidal membership function**

The trapezoidal membership is configured thanks to 4 parameters: a, b, c and d.

a and d are used to define the 'base' of the trapezoid whereas b and c are used to define the 'shoulders' (Figure 6-10).

The formula of the trapezoidal membership function trapmf(x, a, b, c, d) is (Mathworks, 2014a):

$$\text{trapmf}(x, a, b, c, d) = \max\left(\min\left(\frac{x-a}{b-a}, 1, \frac{d-x}{d-c}\right), 0\right) \qquad (6\text{-}1)$$

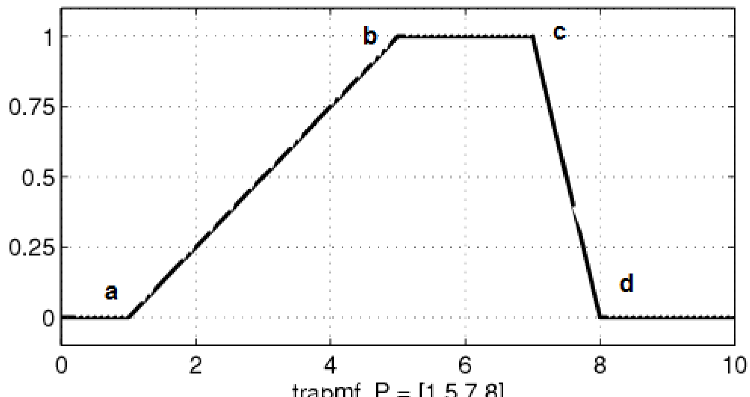

Figure 6-10: Example of trapezoidal membership function (Mathworks, 2014a)

2. **Triangular membership function**

The trapezoidal membership is configured thanks to 3 parameters: a, b and c.

a and c are used to define the ‘base’ of the trapezoid whereas b is used to define the ‘summit’ (Figure 6-11).

The formula of the trapezoidal membership function trimf(x, a, b, c) is (Mathworks, 2014b):

$$\mathrm{trimf}(x,a,b,c) = \max\left(\min\left(\frac{x-a}{b-a},\frac{c-x}{c-b}\right),0\right) \tag{6-2}$$

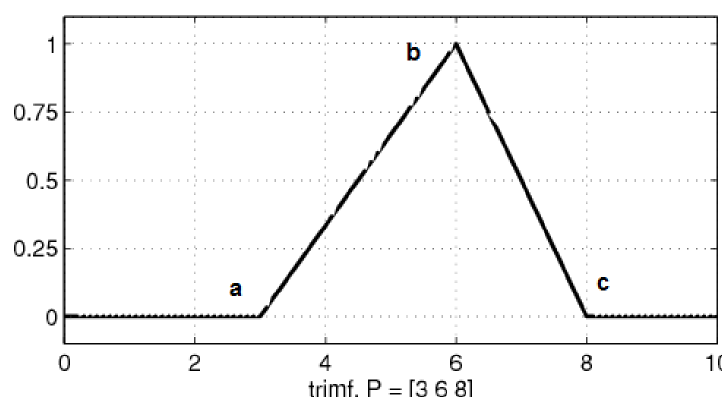

Figure 6-11: Example of triangular membership function (Mathworks, 2014b)

The value of the input variable ‘Current’ is divided into 3 ‘levels’ represented by 3 membership functions:

1. LowCurrent: this membership function is trapezoidal
2. OptimalCurrent: this membership function is triangular
3. HighCurrent: this membership function is trapezoidal

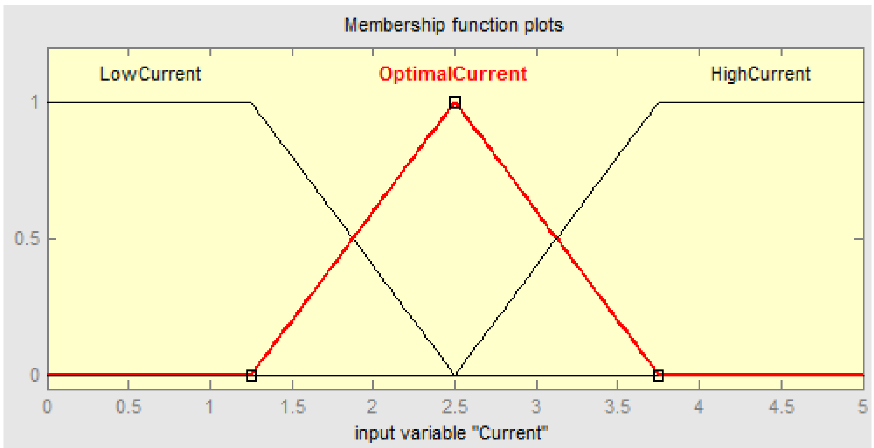

Figure 6-12: Defined membership functions for the input variable 'Current'

The value of the input variable 'PSUStatus' is divided into 2 'levels' represented by 2 membership functions:

1. ON: this membership function is triangular with [a,b,c] = [1,1,1]
2. OFF: this membership function is triangular with [a,b,c] = [0,0,0]

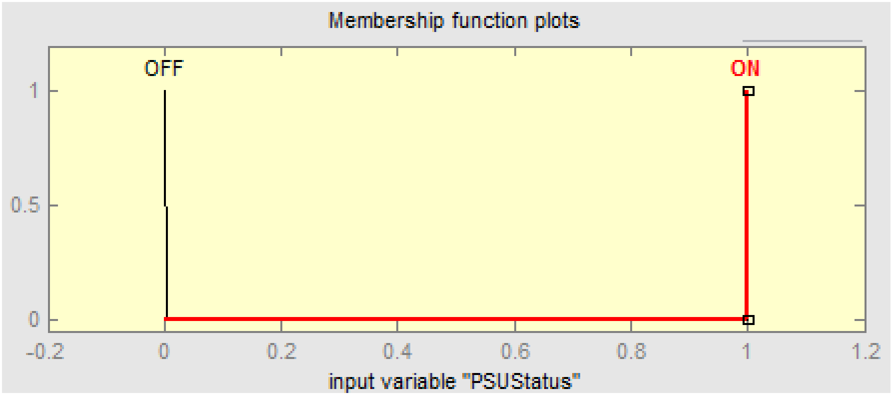

Figure 6-13: Defined membership functions for the input variable 'PSUStatus'

Output membership function

Once the inputs have been defined, the output has to be configured. The output of the fuzzy logic controller is called 'SpeedCoef', it is a coefficient of which the value is ranging from -1 to 1. 'SpeedCoef' is multiplied by the maximum step length that can be achieved by the controller in one step.

Definition of the membership functions for the output variable SpeedCoef: 'SpeedCoef' determines the direction and amplitude of the step move that will be performed.

In the Sugeno-type fuzzy controller, the output is defined by constant membership functions:

1. Reverse: SpeedCoef is set to -1
2. Optimal: SpeedCoef is set to 0
3. Forward: SpeedCoef is set to 1

The rules determining the behaviour of the fuzzy logic controller can be seen below:

- RULE #1: If current is 'low' AND Psu is 'ON' then Relative position is 'forward'
- RULE #2: If current is 'low' AND Psu is 'OFF' then Relative position is 'nochange'
- RULE #3: If current is 'optimal' AND Psu is 'ON' then Relative position is 'nochange'
- RULE #4: If current is 'optimal' AND Psu is 'OFF' then Relative position is 'nochange'
- RULE #5: If current is 'high' AND Psu is 'ON' then Relative position is 'backwards'
- RULE #6: If current is 'high' AND Psu is 'OFF' then Relative position is 'nochange'

There are two ways of configuring the fuzzy logic controller and setting up the membership function parameters:

1. Manually entering the values of the Maximum, Minimum and Optimal machining current in the HMI:

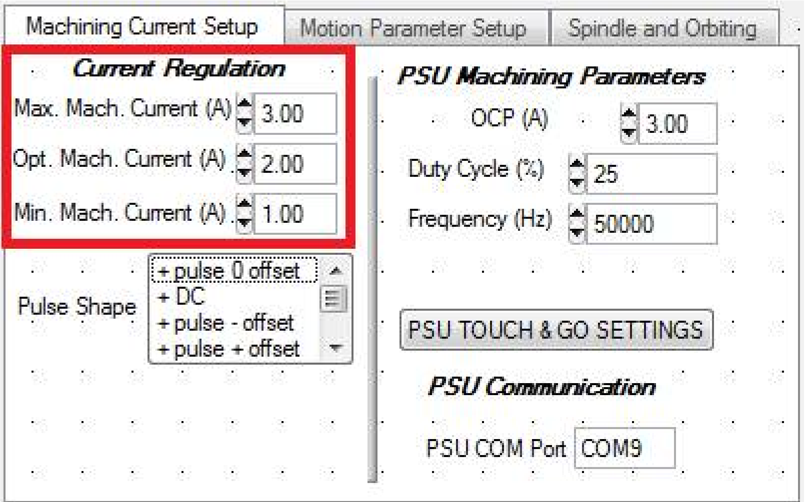

Figure 6-14: The machining current setup tab in which the current parameters can be entered

2. Waiting for the gap to be initialized, start the electrolyte supply by turning on the pump and pressing the button 'MEASURE CURRENT'.
   Pressing this button will make the PSU pulse for a short time during which the current will be measured by the Power PMAC. The value of the measured current will be assigned to the Optimal Current value (Opt_Current_Val) because it corresponds to the current flowing through the gap at the initial gap. From this value

the maximum and minimum machining current values ($Min_Current_Val$ and $Max_Current_Val$) are computed as follows:

$$
\begin{aligned}
Min_Current_Val &= Opt_Current_Val \times 0.5 \\
Max_Current_Val &= Opt_Current_Val \times 1.5
\end{aligned}
\tag{6-3}
$$

6.4.2.2. Adaptive feed rate algorithm

This control algorithm has been developed in order to adapt the tool feed rate according to parameters calculated throughout the machining time:

- Number of OCP events
- Times and positions at which the OCP events occurred
- Overall feed rate of the tool (calculated by using the start position, the current position and the elapsed machining time)
- Instantaneous feed rate (calculated after each step)
- Approximation of MRR using the OCP times and positions

When the adaptive feed rate algorithm has enough data to influence the feed rate, it activates itself.

This algorithm assumes that the positions and times at which the short circuits occur can be used to calculate and adapt the feed rate. In the following illustration Figure 6-15, the positions and times at which the short circuits occurred are stored in the Power PMAC.

Not all the short-circuits can be used to calculate the new feed rate of the tool: a filtering mechanism is used to filter out and ignore the consecutive short-circuits positions and times in order to only use representative data.

As soon as two representative short circuits have been gathered, the first feed rate can be calculated using the formula:

$$
\text{OCPFeed rate}_n = \frac{\text{Short circuit position}_n - \text{Short circuit position}_{n-1}}{\text{Short circuit time}_n - \text{Short circuit time}_{n-1}} \tag{6-4}
$$

All the calculated feed rates are stored in an array and the average of all the feed rates is computed in order to obtain a more reliable result.

$$
\text{AvgOCPFeed rate} = \frac{\sum_{i=0}^{n-1} \text{OCPFeed rate}_i}{n} \tag{6-5}
$$

The ratio between the current feed rate and the computed feed rate is calculated and the feed rate is adjusted by the following operation:

$$\mathrm{FRCoef} = \frac{((1-\alpha)\times \mathrm{InitialFR} + \alpha \times 0.5 \times \mathrm{AvgOCPFR} + \alpha * 0.5 * \mathrm{Last3OCPFR})}{\mathrm{InitialFR}} \qquad (6\text{-}6)$$

Where $\alpha = \frac{\beta}{10}$ if $\beta < 10$ or $\alpha = 1$ otherwise. β represents the number of representative short-circuits. The above expression considers that after 10 short circuits the value of AvgOCPFR enables precise calculation of the desired feed rate and therefore the influence of the initial feed rate can be neglected. This expression prevents the feed rate from being reduced too quickly and assumes an increasing degree of confidence when more data is gathered. This expression also takes into account the feed rate values calculated for the last 3 short circuits through the use of Last3OCPFR. It can be seen that the weight of Last3OCPFR is the same as AvgOCPFR. Since the μECM process is long, providing the controller with recent data is important and this is why Last3OCPFR has been integrated into the formula.

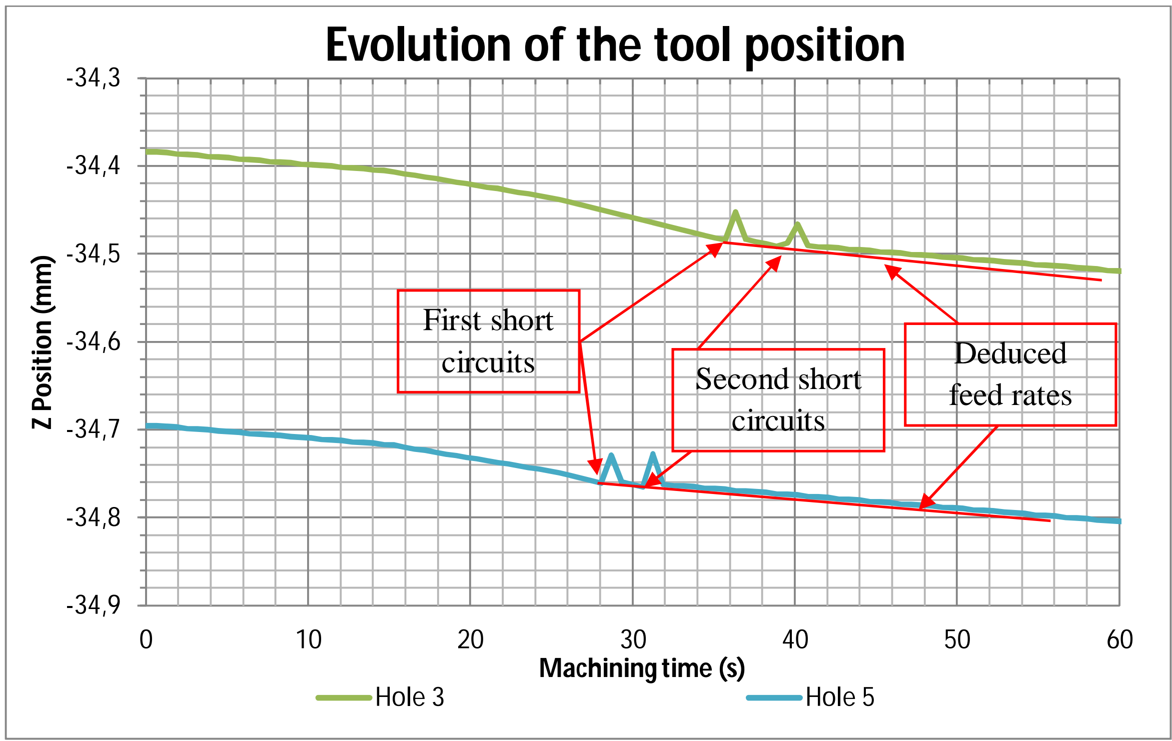

Figure 6-15: Illustration of the adaptive feed rate algorithm

6.4.2.3. *Escape strategy*

The process control algorithm consists of a state machine which reacts to the unpredictable occurrence of short circuits during machining. In normal operation, the values of the signals 'OCP' and 'PSU ON' are checked to verify that no problem has been encountered. If everything is fine (when the PSU is pulsing and the OCP has not been triggered), the controller reads the value of the current on one of the channels of the data acquisition board and computes the appropriate step size necessary to maintain the interelectrode gap to a constant value. Controller constantly loops into that step unless an over current protection signal is triggered or the PSU stops pulsing. If the PSU stops pulsing, the controller interrupts the program and displays an error message on the HMI.

On the other hand, if an OCP event occurs (short circuit situation), the controller will switch to a state which retracts the tool, restarts the power supply and goes back to the state of fuzzy logic or adaptive control.

The retraction of the tool can be simple or in two steps according to the value of the global variable gRetractBackNForward:

- If the Power PMAC motion controller is configured for the simple tool retraction (gRetractBackNForward set to 0), the tool will be retracted by a distance of which the value is stored in the variable DesRetractDistance.
- If gRetractBackNForward is set to 1 then the tool will be retracted by the user-defined distance DesRetractDistance and then repositioned at a relative position – creating a zone of turbulence in the electrolyte - defined by ResetPosition, defined by:

ResetPosition = DesRetractDistance - (Consecutive_OCP_Counter+1) × InitialGap;

Consecutive_OCP_Counter represents the amount of short circuits that have occurred consecutively. Short circuits are considered as consecutive if the time period between their occurrences is less than 5seconds. According to the above formula, the bigger the number of consecutive short circuits, the further away from the surface the tool is repositioned. This algorithm has proven to be very efficient in decreasing the number of short-circuits. The first retraction of the tool creates some local electrolyte turbulence which eases the renewal of the electrolyte in the area

where the short circuit occurred. Replacing the tool at distances that are multiples of the gap size enables a better gap control and more efficient machining than with the simple retraction previously described.

The retraction code and graph illustrations can be seen in Figure 6-16.

Since the Power PMAC did not have the necessary drivers to communicate with the microcontroller on the PSU, the communication between the PSU and the Power PMAC is achieved via the HMI. However, when the over current protection is triggered and the pulsing parameters do not need to be changed, the Power PMAC can trigger a restart of the PSU using the 4 digital I/O ports that have been implemented on the PSU.

The communication protocol to reset the PSU is as follows:

The Power PMAC detects the OCP signal is high, so it retracts the tool for a predetermined distance. Once the retraction move is performed, it sets one of the outputs connected to the PSU inputs to a HIGH state. The PSU detects this action via one of its inputs and sets one of its outputs to HIGH as an acknowledgment sign. The power PMAC then sets his output to LOW to confirm it has received the signal. The PSU now resets the over current protection and sets its output to LOW. The controller then carries on the machining program until another unexpected event occurs.

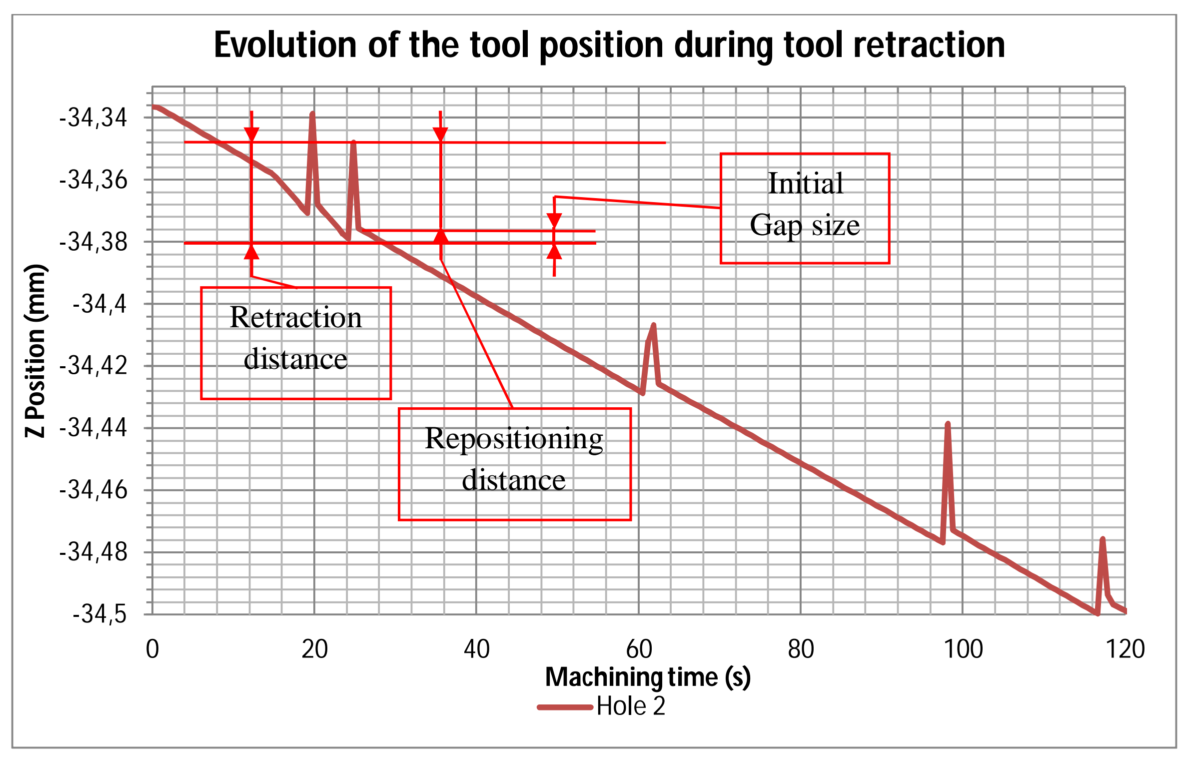


```
if(pshm->P[gRetractBackNForward] > 0){
//TWO-STEP RETRACTION MODE

        if(JogRelAndWaitUntilFinished(3, RetractPosition, JOGTIMEOUT)!=0){
        SpecialSend((char*)'error when jogging');
        pshm->P[gRTIPLCmode] = SOFTSTOP;
        }

        if((ResetPosition>0) && (ResetPosition<(250000))){
                if(JogRelAndWaitUntilFinished(3, ResetPosition, JOGTIMEOUT)!=0){
                SpecialSend((char*)'error when jogging');
                pshm->P[gRTIPLCmode] = SOFTSTOP;
                }
        }

}else{
//SIMPLE RETRACTION MODE
        if(JogRelAndWaitUntilFinished(3, RetractPosition, JOGTIMEOUT)!=0){
        SpecialSend((char*)'error when jogging');
        pshm->P[gRTIPLCmode] = SOFTSTOP;
        }
}
```

Figure 6-16: Graph and code illustrating the tool retraction followed by the repositioning to reset the IEG

6.5. An intelligent Human Machine Interface (HMI)

A self-developed HMI connects directly to the motion controller (Power PMAC) and the pulse PSU and allows the user to setup and monitor the machining current, tool position and other essential machining parameters (Figure 6-17). This program has been written in C using the CVI/LabWindows IDE from National Instruments. The communication protocol used to connect with the Power PMAC is Telnet and the HMI is communicating to the PSU via USB using a virtual COM port. The refresh time period of the displayed values has been set to 150ms. The HMI also communicated with the spindle drive to set the rotation speed.

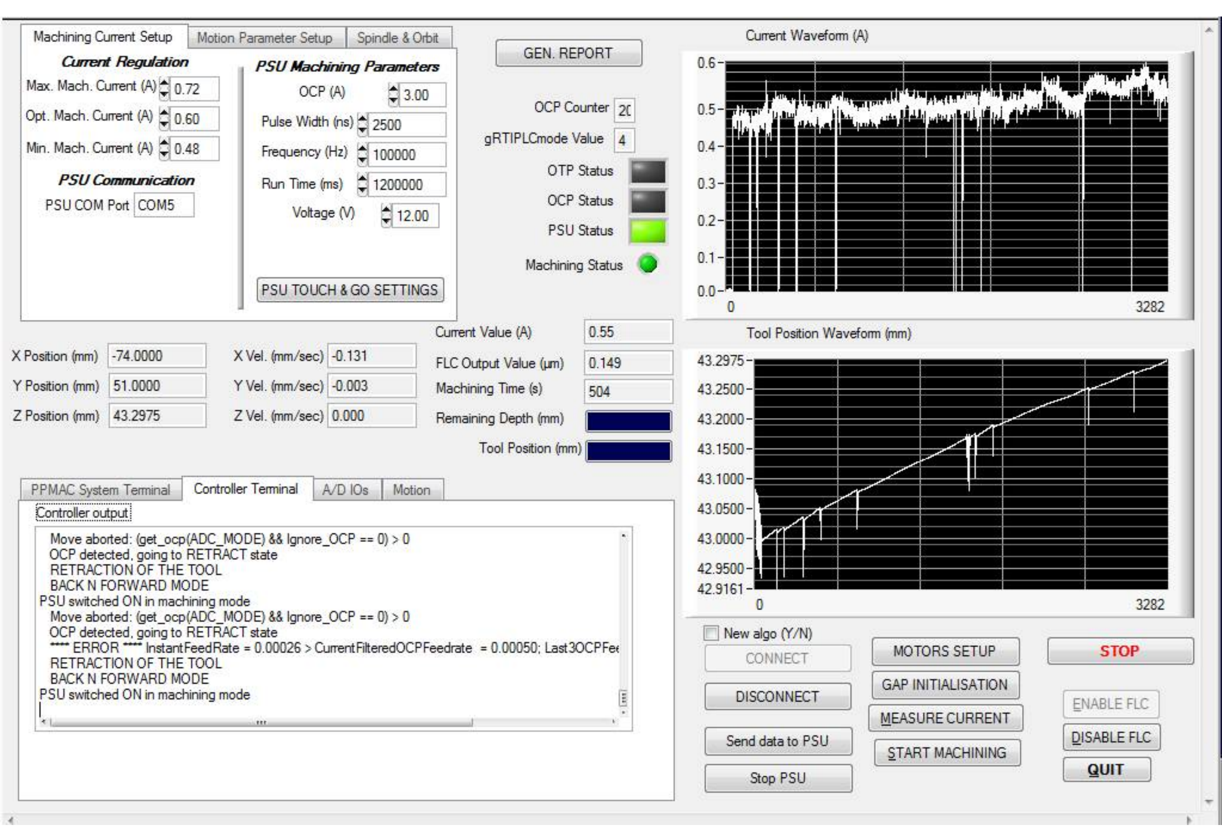

Figure 6-17: Screenshot of the self-developed HMI of the µECM machine

The HMI is a very important aspect of the machine: It not only displays relevant information to the user, but also communicates with the PSU and the drive of the spindle.

Because of software driver issues, the Power PMAC cannot communicate with the PSU and the spindle drive directly. Therefore the HMI is charged of communicating with these components when the Power PMAC requests it.

The HMI reacts to some specific values that are sent by the Power PMAC, for example if the controller wants to switch on the PSU, the global variable 'gPSUCom' is set to 1 and sent to the HMI. The Power PMAC then waits for the PSU to switch within a certain time

lapse. If the elapsed time is too long, then the function times out and the Power PMAC puts itself in a fail-safe mode by aborting any running program.

Also, if the connection between the HMI and the Power PMAC is interrupted for more than 2 seconds during machining, the Power PMAC stops instantly the ongoing programs.

After each machining session, the program automatically generates a machining report containing all the parameters used for this particular session as well as all the current and tool position values. These reports can also be generated at any time by pressing the 'GEN. REPORT' button.

The HMI is made out of different Tabs which focus on particular aspects of the machine:

- The Power PMAC (PPMAC) System Terminal: this tab (Figure 6-18) allows the user to interact with the firmware of the Power PMAC motion controller. This is an integrated Telnet client which allows the user to send commands to the controller.

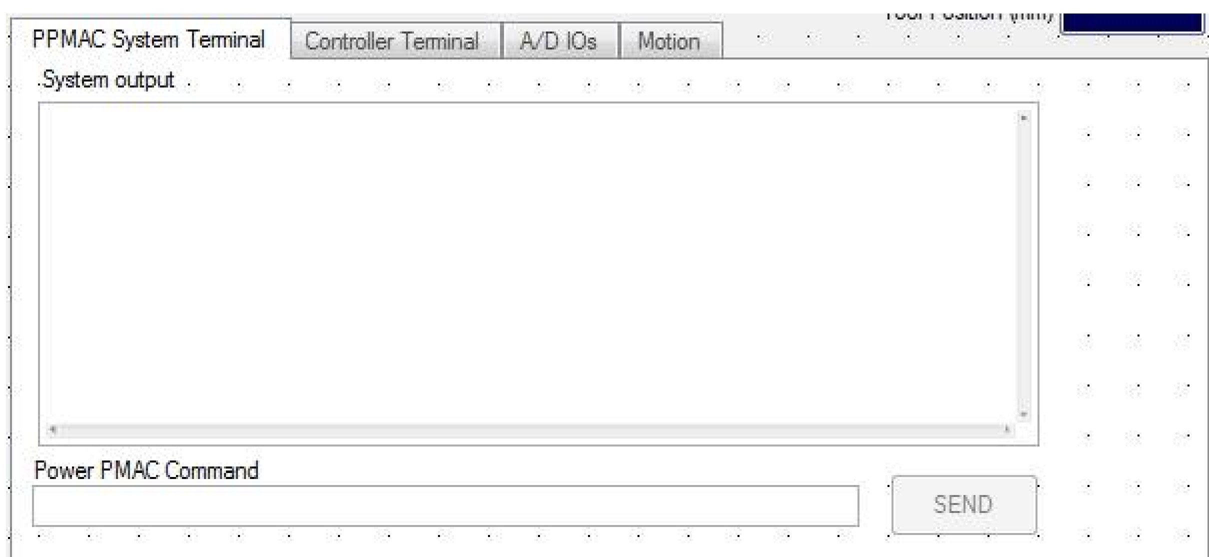

Figure 6-18: Picture of the 'PPMAC System Terminal' tab of the HMI

- The Controller Terminal: this tab (Figure 6-19) allows the user to see what actions that the programs on the machine are currently executing. For example, if an OCP event occurs, this will be printed out in this dialog box.

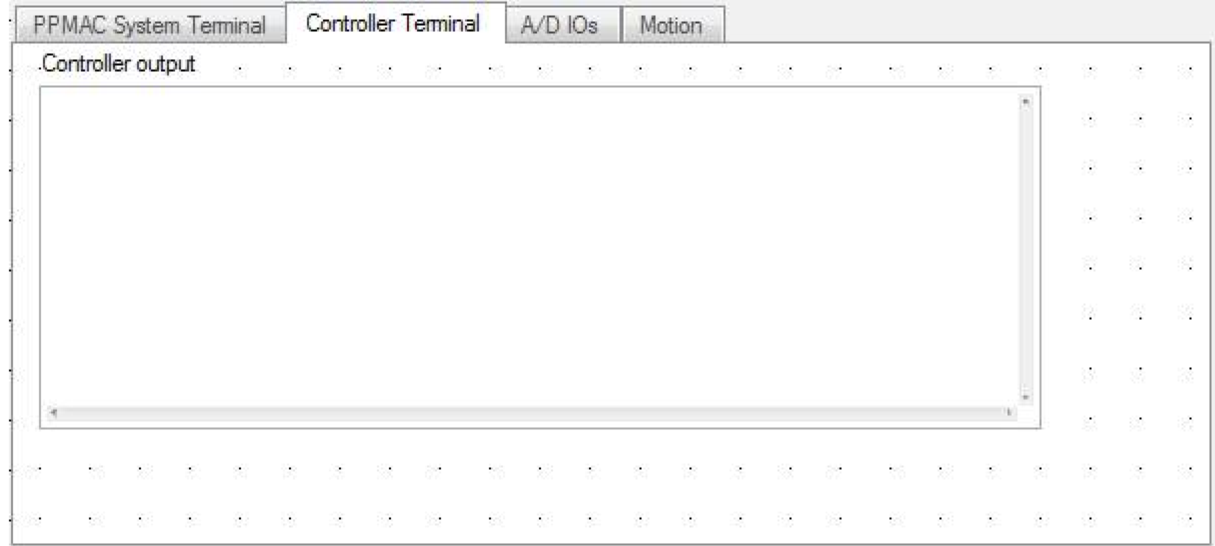

Figure 6-19: Picture of the 'Controller Terminal' tab of the HMI

- The Analog/Digital Inputs/Outputs (A/D I/Os): this tab (Figure 6-20) reports the status and voltage values acquired by the digital I/O board (ACC65E) and analogue input board (ACC36UK). The ACC65E is configured so that it has 24 digital inputs and 24 digital outputs. On the other hand the ACC36UK features 16 acquisition channels.

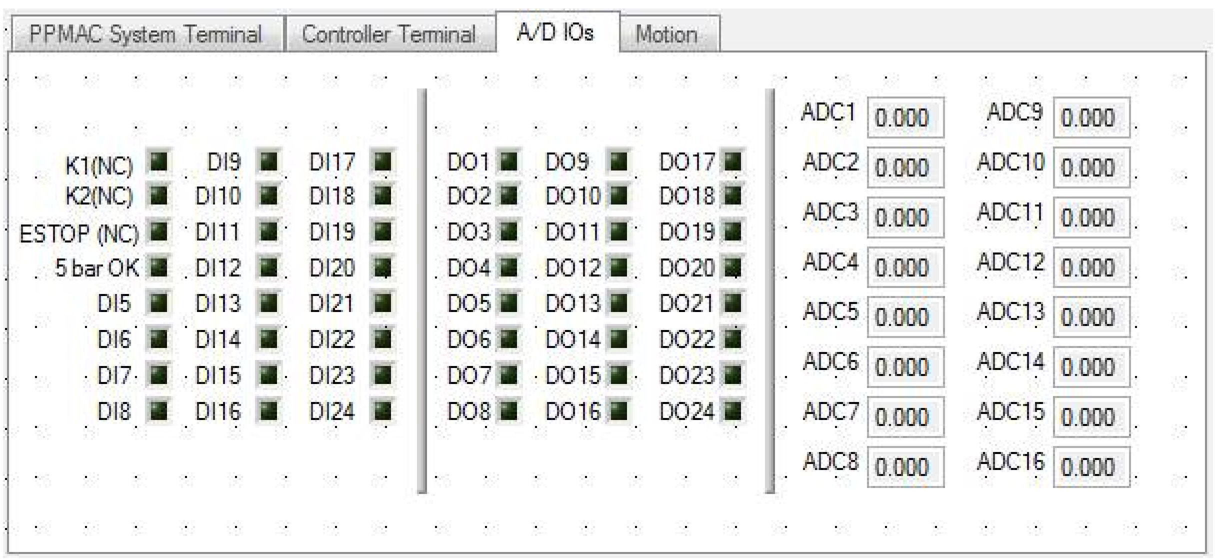

Figure 6-20: Picture of the 'A/D IOs' tab of the HMI

- The Motion tab: this tab (Figure 6-21) focuses of the motion aspects of the machine, it contains information regarding the status of each motors and allows the user to reset, start homing search and jog for each of the 3 linear motors of the machine.

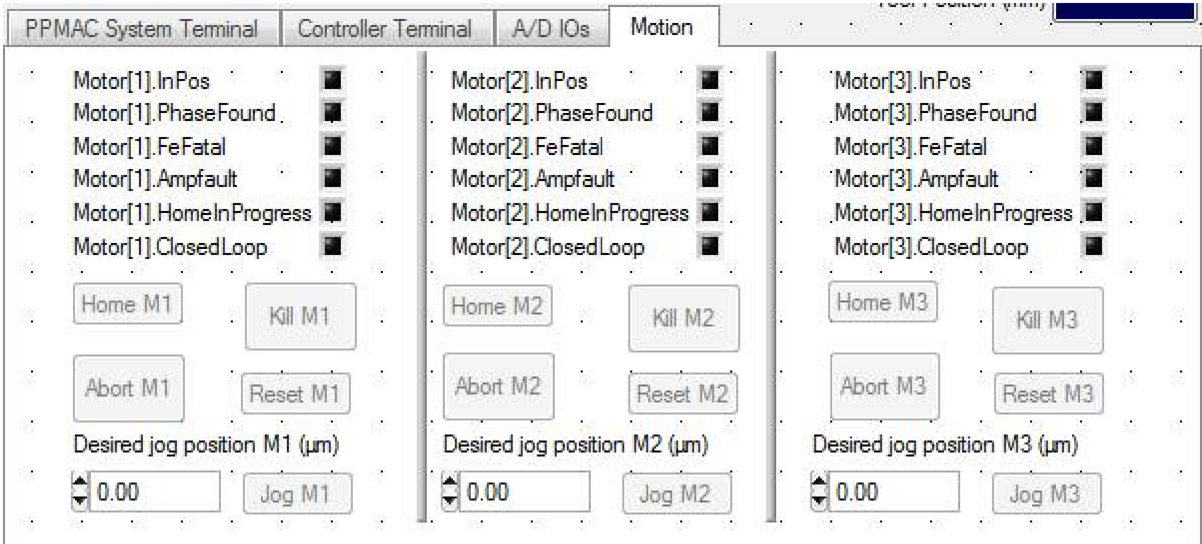

Figure 6-21: Screenshot of the 'Motion' tab of the HMI

- Machining Current Setup: this tab (Figure 6-22) enables the user to configure the fuzzy logic controller in the 'Current Regulation' side of the tab. The operator sets the maximum machining current, the optimal machining current and the minimum machining current by inputting numerical values in the corresponding fields. These values are used to calculate the membership functions necessary for the fuzzy logic controller to operate.

  The other parameters are related to the programming of the pulse PSU. From this panel, the user can set the pulse shape (8 different choices available), the over current protection (OCP), the duty cycle and the frequency. The button 'PSU TOUCH & GO SETTINGS' makes another window appear to set the parameters of the PSU used for the gap initialisation procedure.

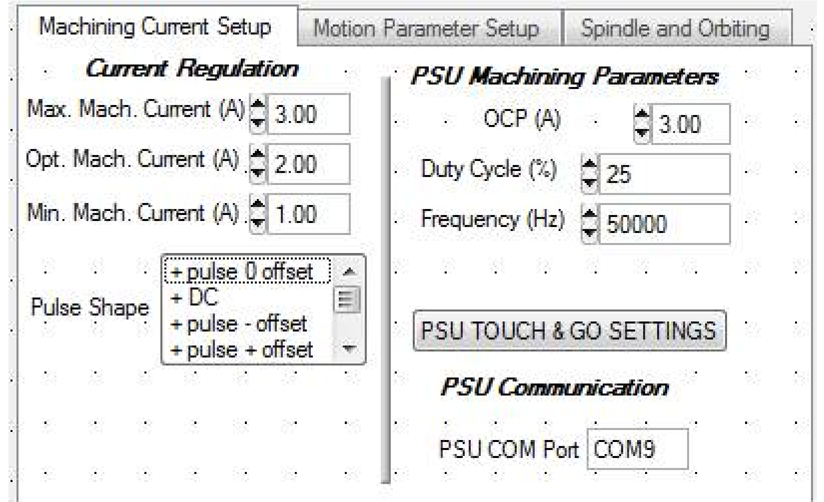

Figure 6-22: Picture of the 'Machining Current Setup' tab of the HMI

- Motion Parameter Setup: The user can set up the parameters for tool feed rate and tool retraction using this tab (Figure 6-23).

  The 'maximum negative step' as well as the 'maximum positive step' input field are used to set the boundaries of the fuzzy logic controller's output.

  The value entered for the 'OCP Retraction' sets the distance for which the tool is retracted when the over current protection is triggered.

  The 'Desired Depth' parameter corresponds to the desired depth of the hole to be machined and the feed rate of the tool will be set to 0 when the difference between the 'start' and 'stop' positions reaches this value.

  The parameters on the right hand side are related to the gap initialisation and determine the initial speed at which the tool is being fed to touch the workpiece (Forward length Gap Ini.) as well as the initial distance for which the tool is retracted when electrical contact has been made (Retraction length at Gap Ini).

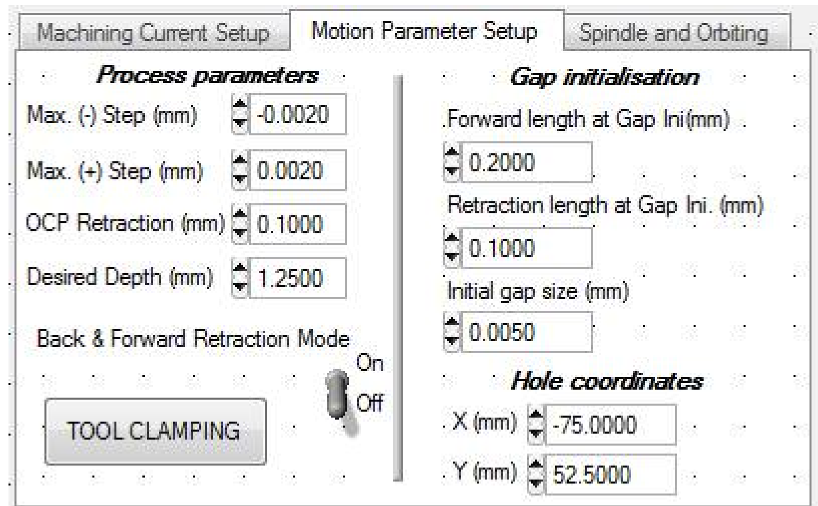

Figure 6-23: Picture of the 'Motion Parameter Setup' tab of the HMI

- Spindle and Orbiting: this tab (Figure 6-24) contains parameters related to the spinning and orbiting of the tool. The user can set the rotational speed of the spindle as well as the spindle modes. The orbiting motion of the tool during machining can be enabled and configured using the 'Start Orbiting' toggle switch and the Orbiting radius/feed rate input fields respectively.

  From this tab it is also possible to enable the adaptive feed rate algorithm which changes the feed rate value according to the number of times the over current protection is triggered.

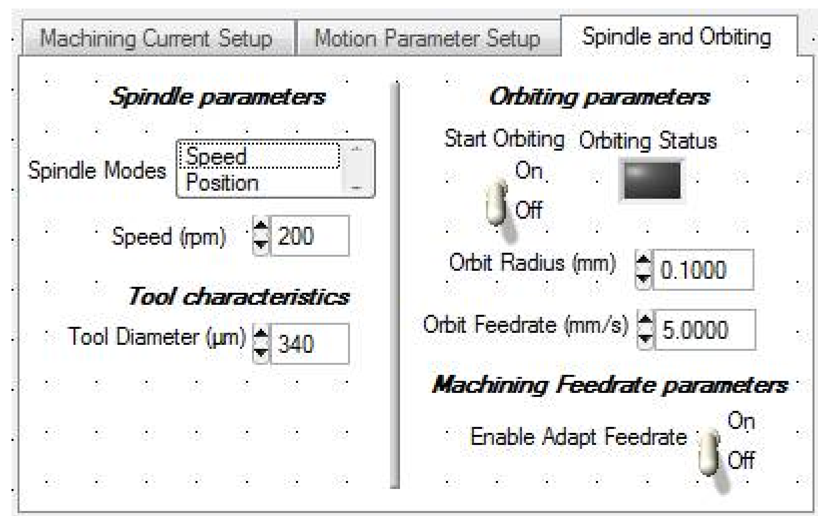

Figure 6-24: Picture of the Spindle and Orbiting tab of the HMI

6.6. Conclusions

In this Chapter, the control system programme was described in detail. The main challenge was to setup the communication protocols between the different subsystems the PSU, the Power PMAC and the PC running the HMI.

With the developed escape strategy the machine is able to control the interelectrode gap very reliably and during long machining sessions. The different control strategies have been explained and their efficiency was assessed in the experiments described in the next chapter.

Precise and detailed information about the control strategies used in ECM and µECM are very hard to find in the literature. This chapter can therefore be regarded as a useful contribution by providing insights and analysing what needs to be taken into consideration when developing a control strategy for µECM.

The development of a custom-made HMI from scratch can also be considered as an achievement and the source code that was written can be used as a framework for further development with Power PMAC systems.

Chapter 7: EXPERIMENTAL WORK AND RESULTS

This chapter presents the experimental work achieved during two different projects:

- Experiments performed in Micro ECM project funded by the European commission (work achieved in Sonplas)
- Experiments performed at Brunel University in the frame of the European research project MIDEMMA.

Preliminary drilling experiments with a test-bench can be read in 0.

The work presented in this chapter has been therefore performed on two different machines: the machine at Sonplas uses components developed by other research partners such as the pulse PSU from VOX Power. The author was responsible of the HMI and control systems design on the machine in Sonplas.

On the other hand, the experiments at Brunel were performed using the machine described in 'Chapter 5: Machine system integration' which has been developed by the author.

7.1. Experimental work at Sonplas GmbH on the machine developed in 2013 (Germany)

7.1.1. Discussion on the setup

A series of tests have been undertaken to study the efficiency of the fuzzy logic control strategy. The machined parts were made of the following materials: copper, 18NiCr6, stainless steel, iron, chromium based alloys.

The HMI developed for the machine at Sonplas had to be adapted to the pulse PSU developed by VOX Power. The research partners decided the use a round PCB with spring probes to connect to PSU to the workpiece (Figure 7-1). The aim of this configuration was to reduce the noise and the inductance of the connections by providing a Faraday cage.

The tool holder was then connected to the PSU using a slip ring in a conductive bath made of galinstan. Galinstan is a liquid conductive metal and it was chosen instead of mercury for safety reasons.

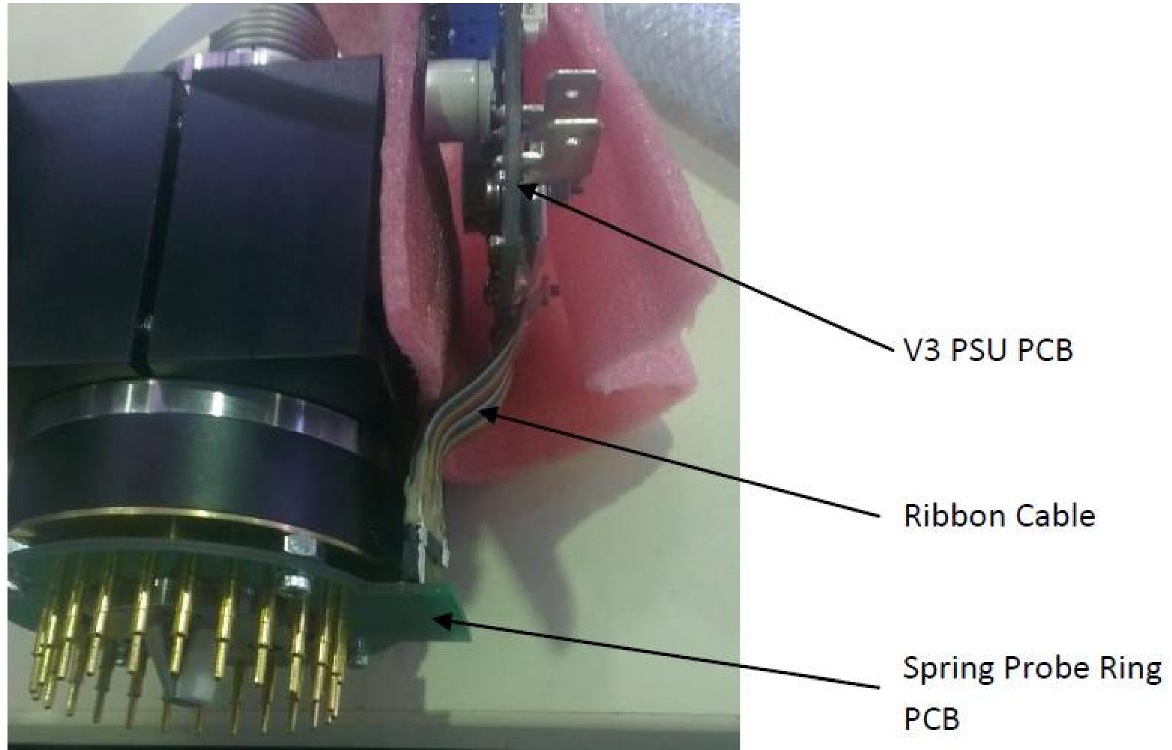

Figure 7-1: Pulse PSU mounting and connection to the PCB ring with spring probes

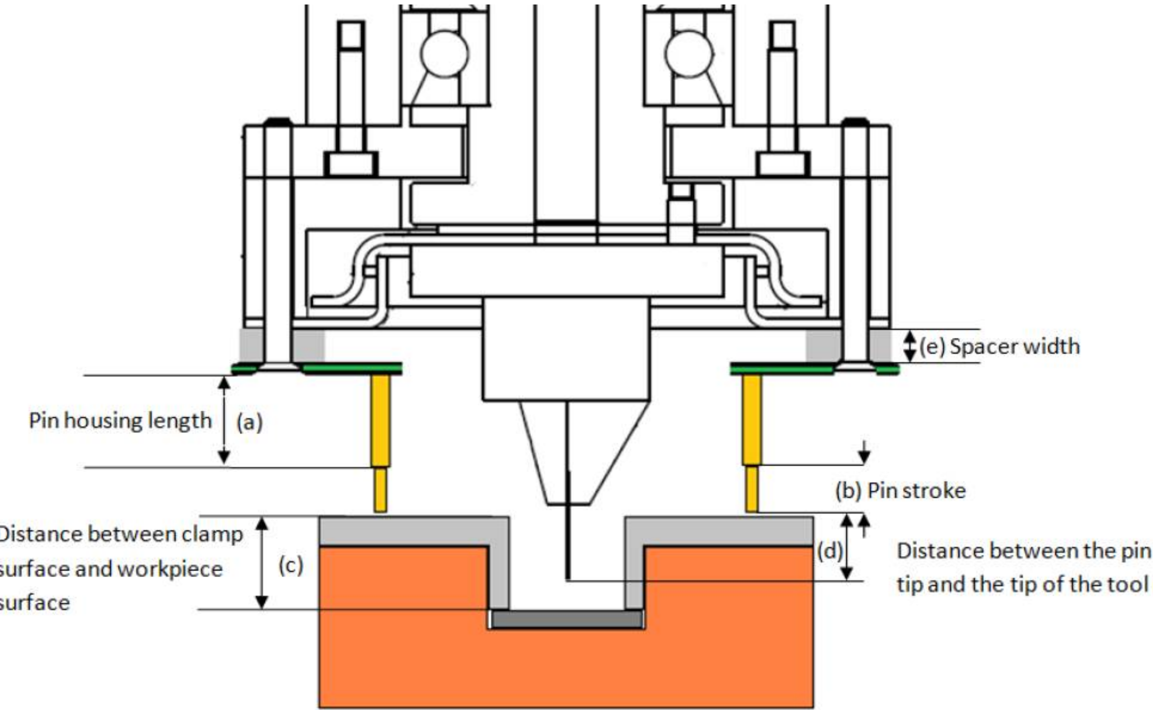

Figure 7-2: Electrochemical cell configuration used at Sonplas and the different dimensions of each element.

However, this solution turned out to be preventing any motion of the X and Y axes during machining, but also limiting the motion in the Z direction because of the pin stroke.

The spindle had a significant run-out, so it was decided to replace the tool-holder with a Sarix one.

7.1.2. Experiments and results

7.1.2.1. Effect of frequency on the hole shape

The aim of this experiment was to investigate the influence of frequency on the machining process, and in particular on the shape of the hole. Holes were drilled in a workpiece made of 18NiCr6 using a $NaNO_3$ electrolyte with a conductivity of 12S/m. The cathode used was made of tungsten carbide (WC) and had a diameter of 340μm.

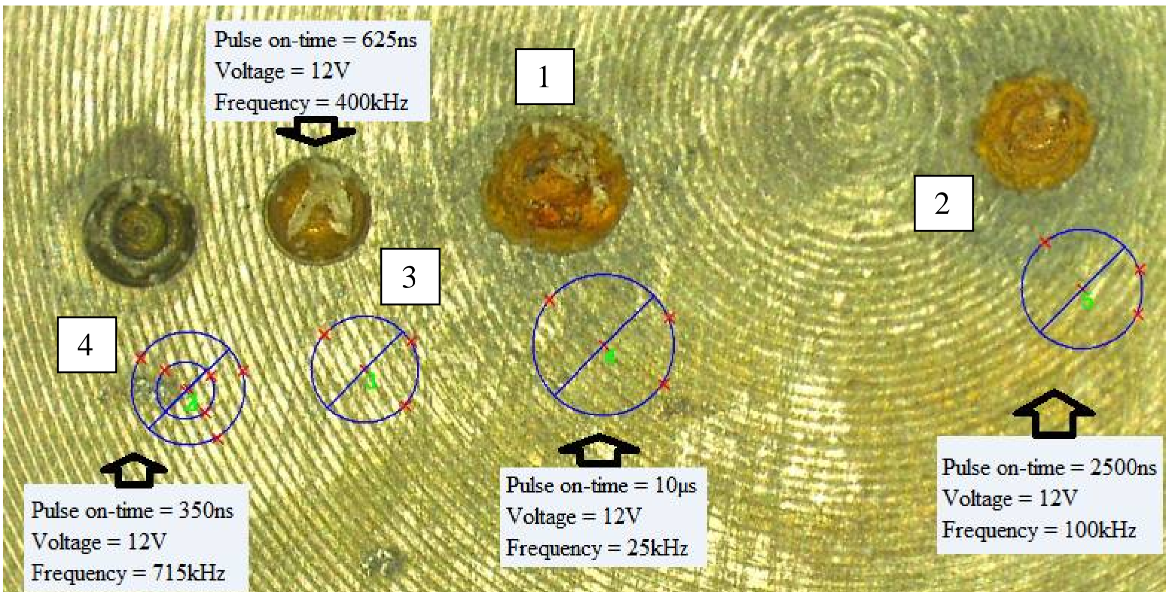

Figure 7-3: Pictures of the holes machined, only the frequency and the pulse width were varied, to preserve the same duty cycle value (25%), electrolyte $NaNO_3$.

The influence of the frequency can be clearly seen on Figure 7-3, the area affected and surface finish are clearly better when high frequency pulses are applied to the gap. This therefore confirms the theory that the electrical double layer effect restricts the affected zones at greater frequencies.

It can be seen on the fourth hole that the bottom of the hole is not flat (Figure 7-4). This phenomenon has been report by Thanigaivelan et al. who suggested that *'the inner portion of the workpiece is not machined properly due to insufficient flow rate'* when flat tip tool electrodes were used and recommended the use of cone tip electrodes for a higher machining rate and better machinability of the workpiece (Thanigaivelan and Arunachalam, 2010).

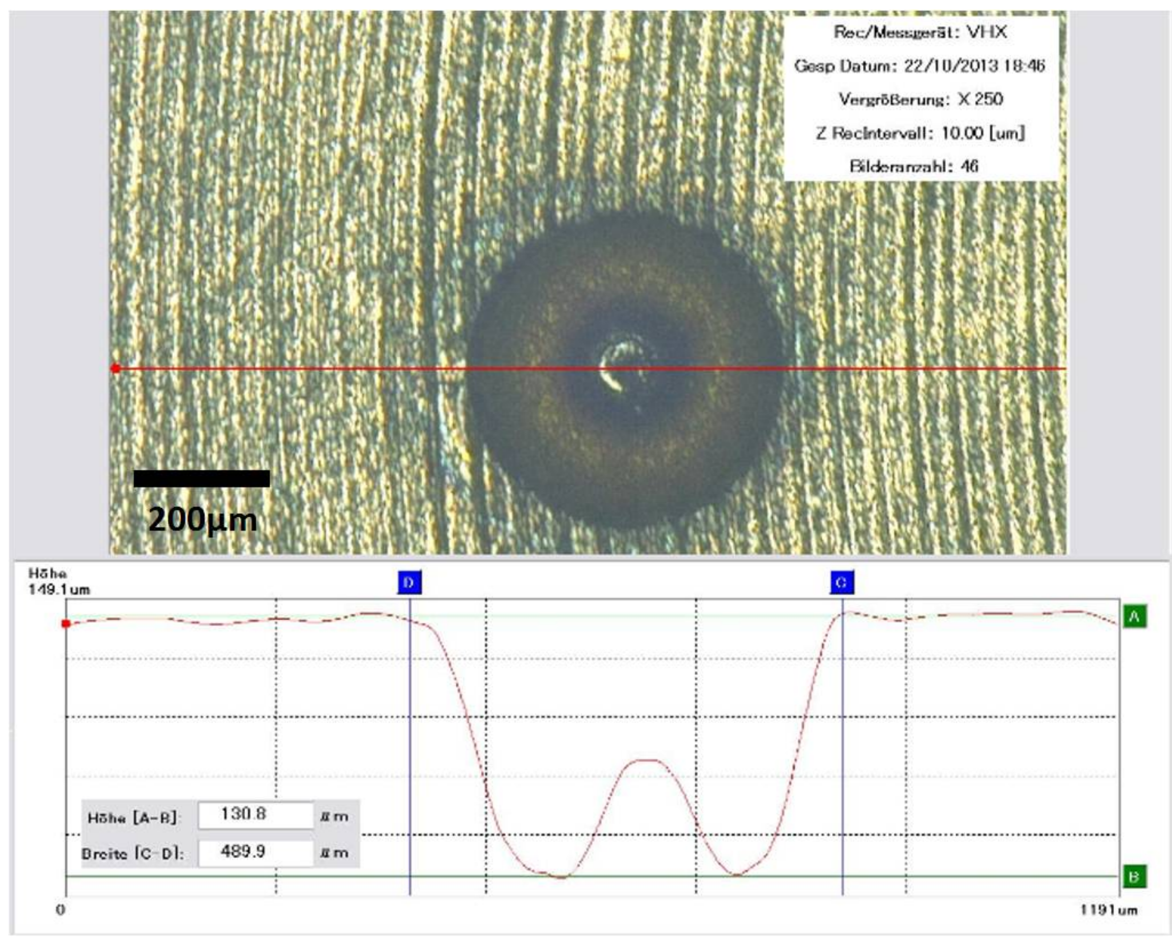

Figure 7-4: Profile of hole 4

7.1.2.2. Drilling with orbiting electrode

For these experiments, a 340µm-diameter WC tool-electrode was used. The electrolyte was $NaNO_3$ with a conductivity of 12S/m.

Our initial tests focused on determining the effect of different orbiting diameters. In all instances the cathode was also rotating on its own axis as well orbiting.

The parameters were 12V pulse amplitude with a 500ns pulse on time and 500kHz (25% duty cycle).

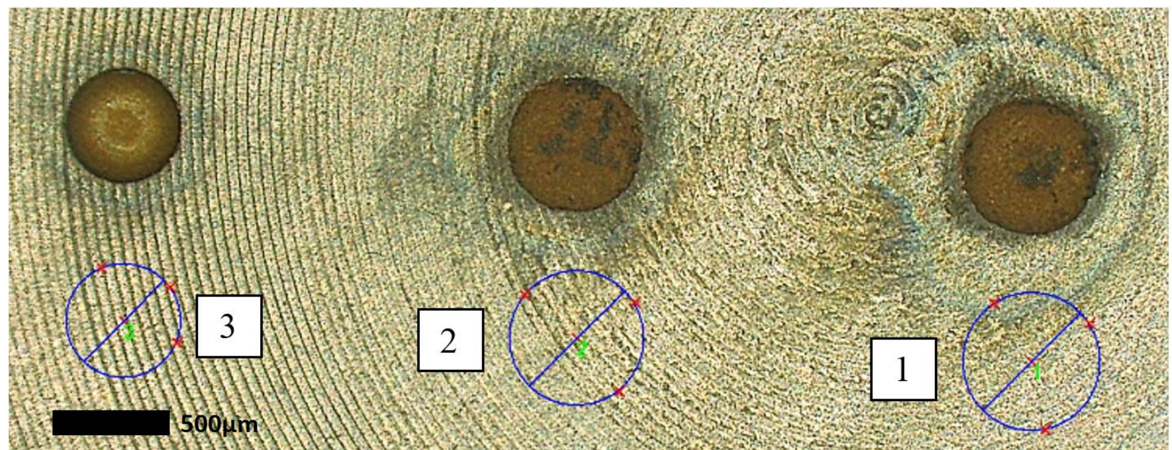

Figure 7-5: 1) 607µm ∅ (right hole); 2) 596µm ∅ (middle hole); 3) 505µm ∅ (left hole)

Holes 1 and 2 had a 100µm orbiting radius set and hole 3 had an orbiting radius of 50µm. The hole shape on 3 has a much better definition.
Hole 1 and 2 same parameters orbiting at 0.1mm similar depth and diameter. Process was stable.

Although hole 3 was left to machine for a longer time, it can be seen that reducing the orbiting offset from 0.1mm to 0.05mm resulted in a deeper hole and a smaller external diameter (3 times deeper 178.4µm compared to 65.6µm and 60.4µm deep in 1 and 2 respectively).

This can be explained by the fact that when the tool is orbiting at a greater radius, the amount of material to remove is bigger, so holes 1 and 2 are logically less deep than hole 3.

The value of the side gap at the top surface for each hole is:

- (607-340-200)/2 = 33.5µm overcut for hole 1
- (596-340-200)/2 = 28µm overcut for hole 2
- (505-340-100)/2 = 32.5µm overcut for hole 3

If we approximate the volume of each tapered hole with the volume of a truncated cone, the approximated volume of removed material for each hole is:

- 13615521.19 μm^3 for hole 1, corresponding to a MRR of 0.0138mm^3/min
- 12686968.96 μm^3 for hole 2, corresponding to a MRR of 0.0147mm^3/min
- 20611297.99 μm^3 for hole 3, corresponding to a MRR of 0.0164mm^3/min

The MRR was calculated by dividing the amount of volume removed by the machining time displayed in Figure 7-7.

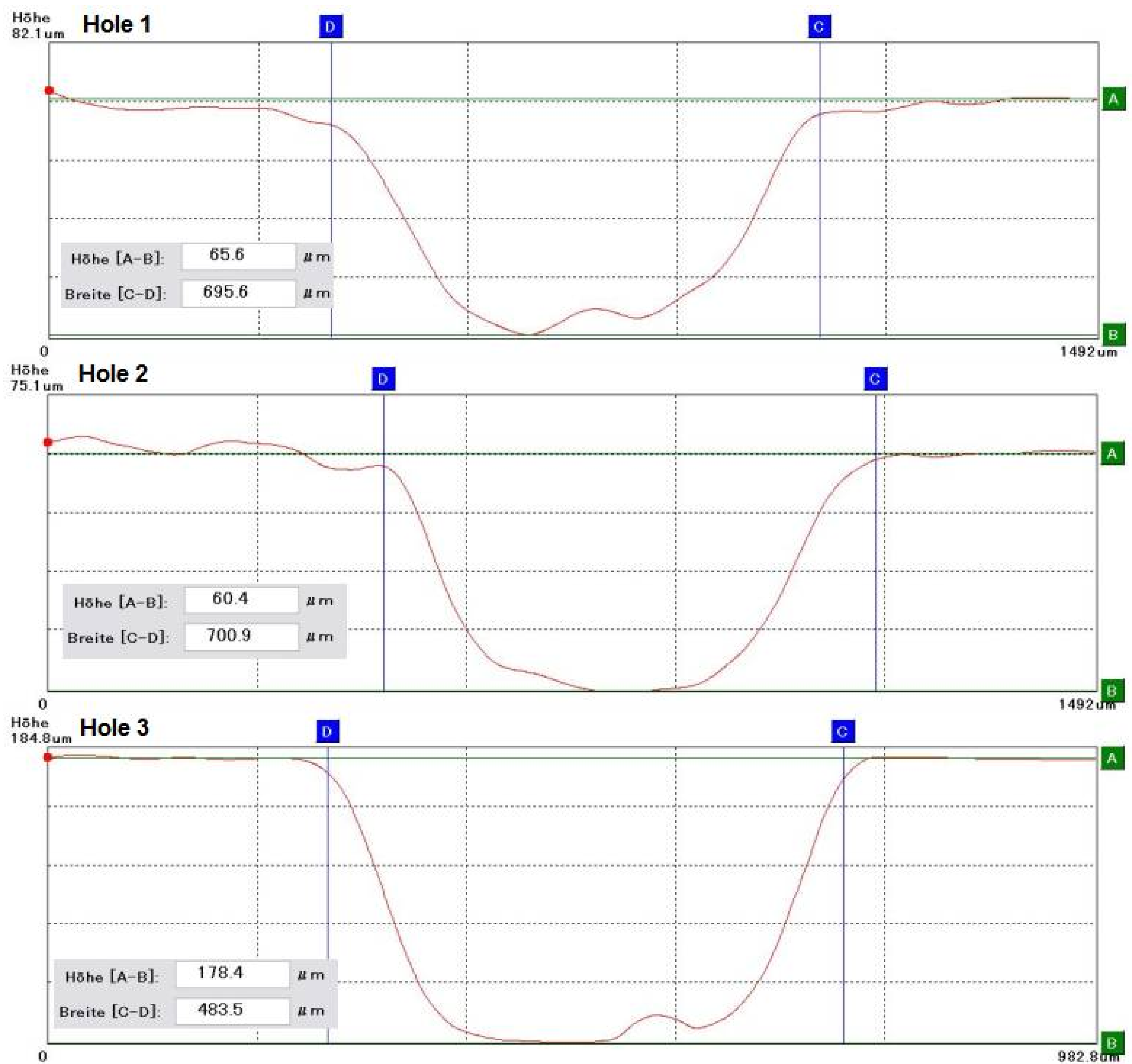

Figure 7-6: Profiles of the holes 1, 2 and 3

The MRR of the hole with a 0.05mm orbiting radius seems to be greater than those of the holes with 0.1mm orbiting radius.

From the charts, the average machining current was 0.8A and the progression of the tool was linear. The step size of the fuzzy control algorithm was kept constant for these three tests. Since the amount of surface machined is bigger for holes 1 and 2, the tool was progressing more slowly and more short-circuits occurs than for hole 3 (Figure 7-7).

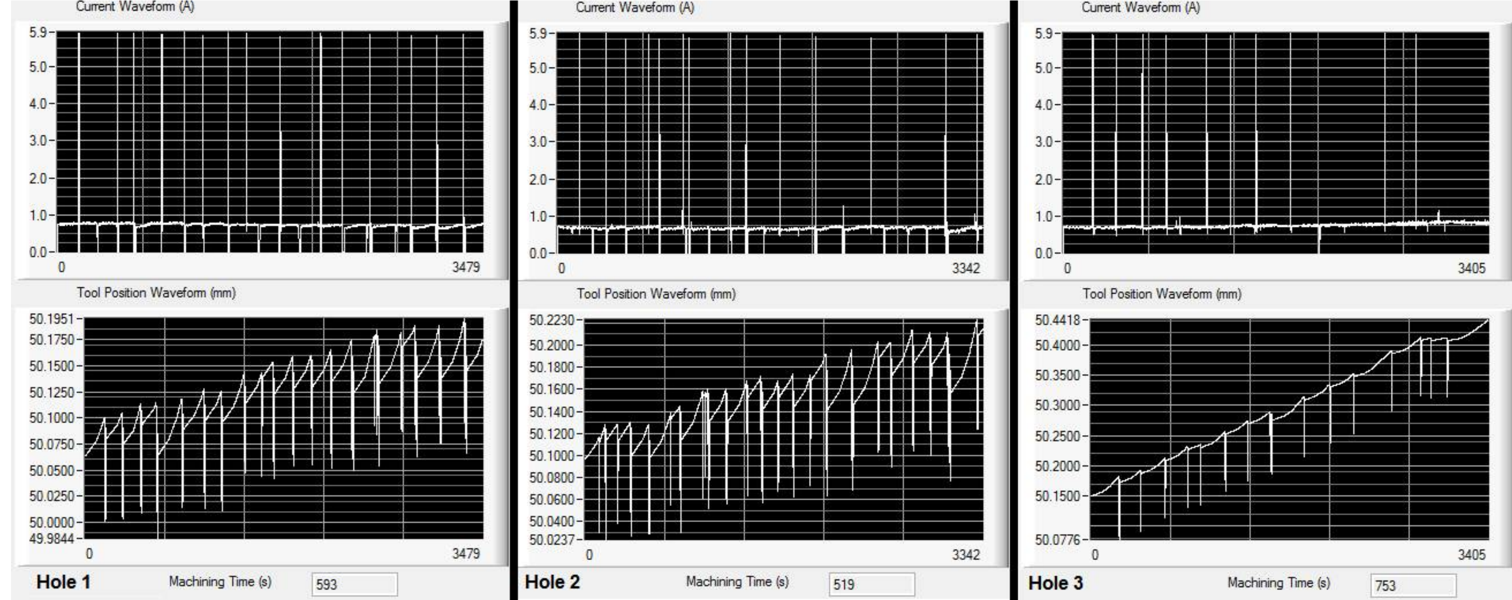

Figure 7-7: Current and position charts for each of the holes drilled.

The short circuits occurred in a rather periodical pattern, which means that the MRR was constant but that the feed rate set by the fuzzy logic controller was too high. This highlighted the need for an adaptive feed rate algorithm to be developed.

Experiments showed that reducing the orbiting diameter has a clear impact on the hole diameter and that rotation of the cathode as well as orbiting improves flushing and provides a better hole shape.

7.1.2.1. Gasoline injector drilling

Tests were made on gasoline injectors provided by Magneti Marelli (Figure 7-9). These parts are made of a chromium-based alloy which has an electrochemical behaviour similar to the previously studied 18NiCr6 alloy. Holes were drilled using $NaNO_3$ electrolyte and 12V pulses with a duty cycle of 25% and a frequency of 120 kHz.

The holes drilled in this experiment have a tapered shape due to the fact that the tool was not side insulated and not orbiting during the machining process (Figure 7-10). Indeed, the fact that the tool was not orbiting increased the number of short-circuits which slowed down the progression of the tool.

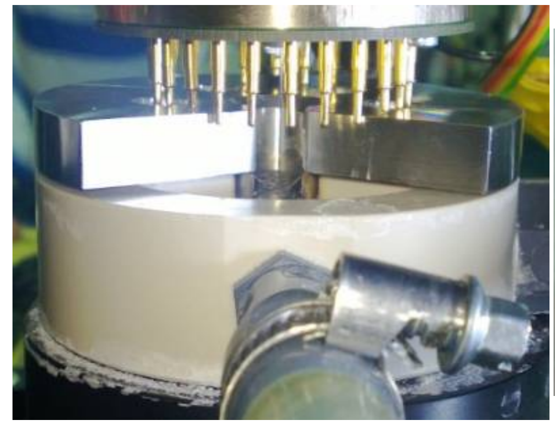

Figure 7-8: Picture of a part being machined

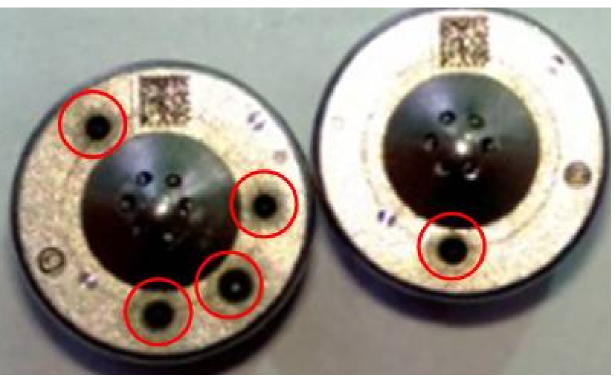

Figure 7-9: Picture of holes drilled in gasoline injectors (chromium-based alloy)

The surface finish on these parts was very good, but the machining time was as long as for 18NiCr6 disks.

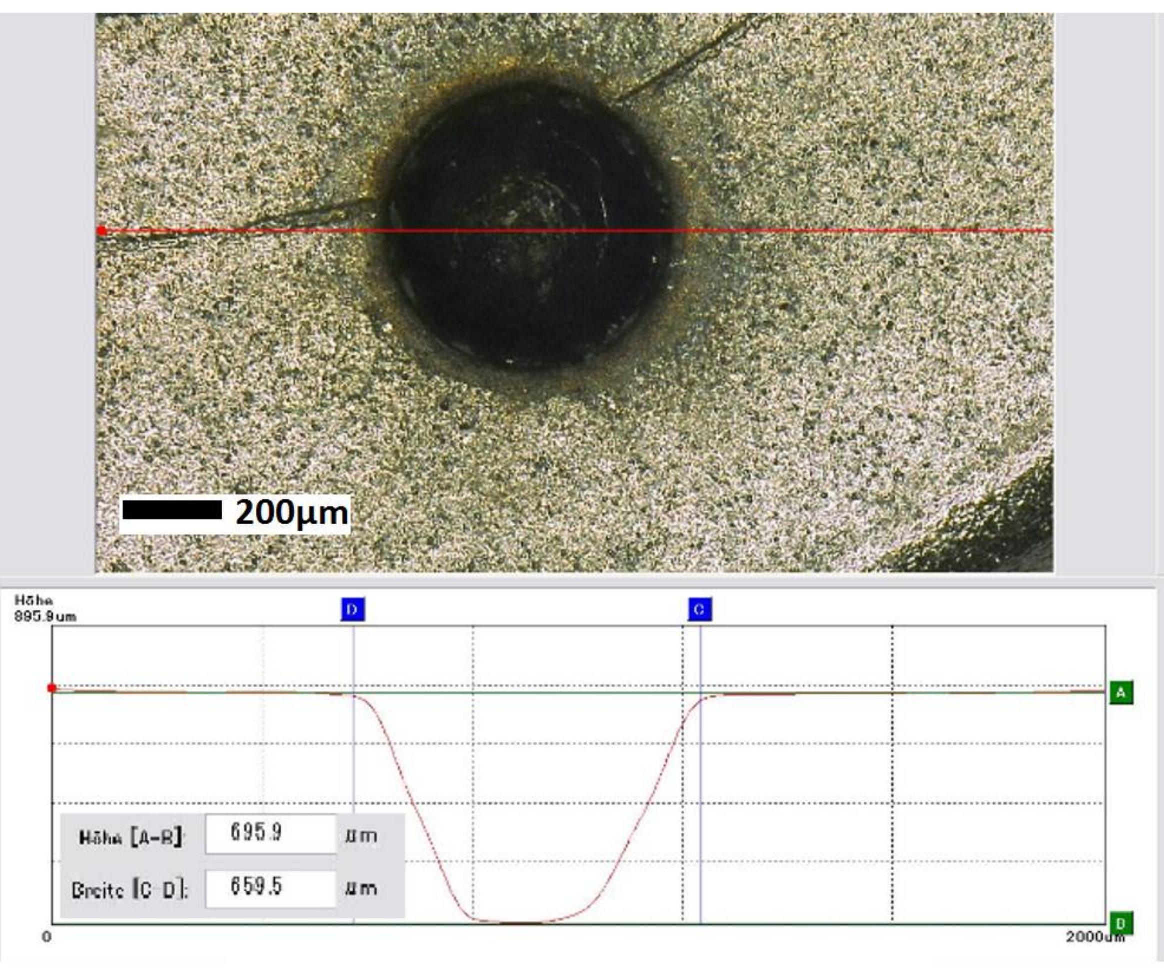

Figure 7-10: Picture and profile of a hole machined in a fuel injector with the sidewalls of the tool non-insulated.

7.1.2.1. Damaged electrodes due to sparking

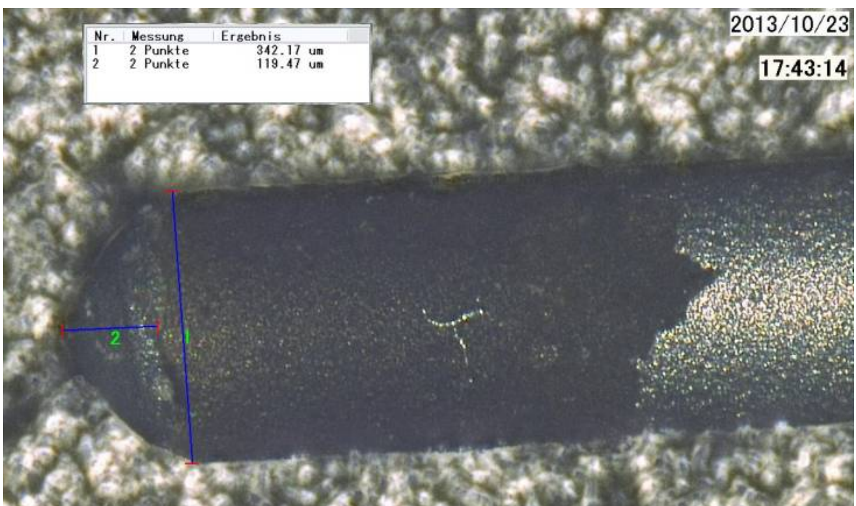

Figure 7-11: A case of extreme tool-electrode wear when machining at 12V

It was often observed that during the drilling process the travel distance of the electrode would not match the depth of the hole. An investigation concluded that pulses above 10V would generate sparks and would damage the tool (Figure 7-11). The machining trials therefore suggested that the machining voltage shall not be greater than 8V.

7.1.3. Process behaviour with the fuzzy logic control algorithm

The fuzzy logic algorithm behaved as expected: the algorithm was told to reach a target value for the machining current and maintain it throughout the machining process.

However most of the machining tests were performed using non-insulated tool-electrodes, so the sidewalls of the tool were conductive and taking part in the reaction. Since the process was hole drilling, the active area of the tool would increase when the tool was fed. This meant that the overall resistance of the machining gap was progressively reduces and that more current was drawn by the IEG.

This resulted in the target current being reached very quickly, so the fuzzy logic controller would reduce the feed rate to adapt to the change in current. Figure 7-12 illustrates perfectly this phenomenon: at the beginning of the process, the tool progresses very quickly towards the workpiece. Machining is taking place and the tool is fed forward, but then the current increases because the side-walls are taking part in the reaction. The fuzzy logic controller who had a machining current target of 1.5A would then reduce the feed rate of the tool when

the current value would reach 1.5A. On the picture it can be observed that the machining current is very well regulated, with only a few short-circuits at the beginning of the process.

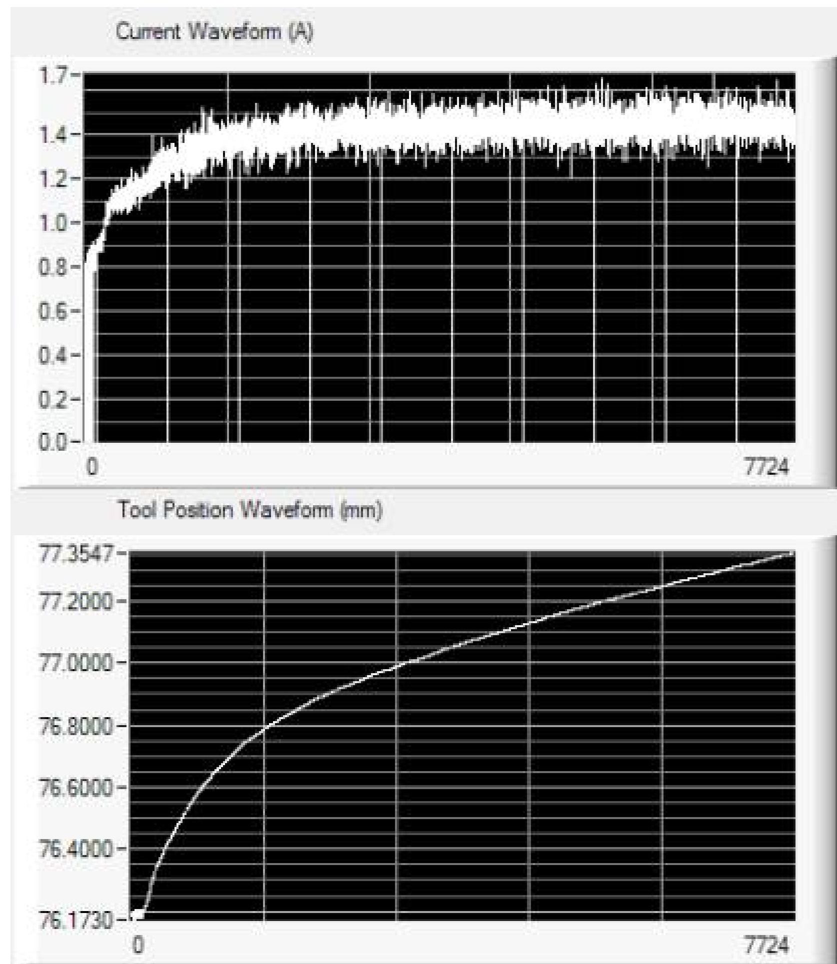

Figure 7-12: Machining result with the fuzzy logic control algorithm. Machining current and tool position (Z) plotted over time (150ms per count)

The fuzzy logic controller regulated efficiently the machining current, but at the expense of the machining feed rate, the cycle time was therefore not optimal. The machining was not localized, because the tool was fed too slowly and the current passing through the side-walls was increasing the side gap. This resulted in a long machining time with a big overcut.

7.2. Drilling experiments with orbiting tool-electrode

Machining tests have been performed on workpieces made of 18NiCr6 alloys used in the automotive industry which is hard to machine with conventional machining processes. The machined part was a disk provided by the automotive component manufacturer Delphi UK. The disk had a diameter of 1cm and was 1.1mm thick.

The use of many different types of electrolytes was reported in electrochemical machining. For the experiments, $NaNO_3$ mixed with a small amount of HCl was used as electrolyte. HCl was combined with other chemicals in many papers (Lee, Baek and Cho, 2007; Sen and Shan, 2005; Kirchner et al., 2001; Bilgi, Jain, Shekhar and Kulkarni, 2006; Trimmer et al., 2003; Zemann et al., 2012; Mukherjee, Kumar and Srivastava, 2005; Mithu, Fantoni and Ciampi, 2011a; Haisch, 2002; Zhang et al., 2007; Lu, Liu and Zhao, 2010; Cagnon et al., 2003) in concentrations varying from 0.01M HCl (Trimmer et al., 2003) up to 3M HCl (Cagnon et al., 2003). In this trial, the concentration of $NaNO_3$ was 0.27mol/L, the measured conductivity of the electrolyte was of 24.3mS/cm and its pH was 2.54, which corresponds to 0.00284M HCl.

In this experiment, the reproducibility of the drilling process and the effect of orbiting tool-electrode was evaluated. Nine holes were machined in the workpiece (Figure 7-13) and in 8 out of 9 trials the tool went through the workpiece. Hole number 4 is blind because of a communication problem between the HMI and the PSU which stopped the machining process. The adaptive feed rate algorithm was initialized at the beginning of the machining session and the initial feed-rate was set to 0.5µm per sec. Moreover, in all those trials the spindle was rotating at 600rpm. After machining all the holes, the workpiece was unclamped for inspection. A thick and sticky black film seemed to have formed all over the workpiece surface. It seemed like the overall surface was affected by the applied voltage.

The parameters for the machining process can be summarized in Table 7-1.

Hole number	Parameters in the following order: Voltage, Frequency, Duty cycle, PSU Mode, Orbiting (Y/N)
1	6V, 1MHz, 15%, 2.3A, Mode 1, No
2	6V, 1MHz, 15%, 2.3A, Mode 1, No
3	6V, 1MHz, 15%, 2.3A, Mode 1, No
4	6V, 1MHz, 15%, 2.3A, Mode 1, No
5	6V, 1MHz, 15%, 2.3A, Mode 1, No
6	6V, 1MHz, 15%, 2.3A, Mode 1, No
7	6V, 50kHz, 15%, 2.3A, Mode 1, Yes: 50µm radius
8	6V, 1MHz, 15%, 2.3A, Mode 1, Yes: 50µm radius
9	6V, 1MHz, 15%, 2.3A, Mode 1, Yes: 50µm radius

Table 7-1: The different pulse PSU parameters and their respective range of values

It can be said from these results that the drilling charts (Figure 7-15) are very similar in behaviour: at the beginning of the drilling process, it seemed difficult to remove material, as a lot of short circuits took place (short circuits provoked the rapid tool retractions which can be observed on the position chart), short circuits also occurred at this moment because

the adaptive feed rate algorithm was initialized and therefore had a limited effect. After a few minutes, an optimal feed-rate was found by the algorithm and a linear progression was observed. The algorithm resets itself periodically to verify if the optimal feed-rate has been found and therefore some short circuits happen periodically until the feed-rate reaches an appropriate value.

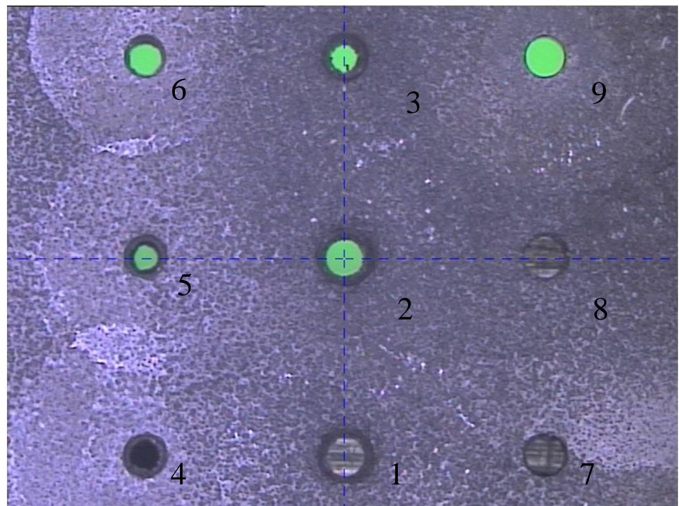

Figure 7-13: Picture of the workpiece after the electrochemical drilling process (taken with a TESA Visio)

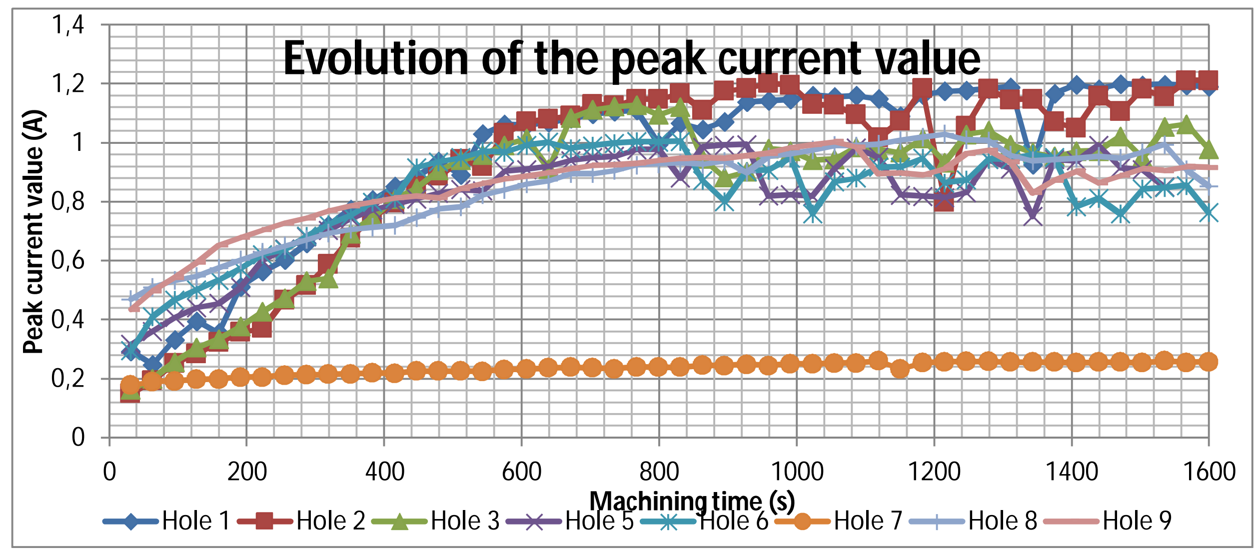

Figure 7-14: Evolution of the current peak value during the machining process. Each point represents an average of 50 data points.

In almost all cases, when the depth of the hole approached 0.9mm it became more difficult to remove material debris and a lot of short circuits were detected. The time necessary to break through the work-piece seems to vary considerably from one workpiece to another.

Moreover, it can be observed that the current is increasing when the hole becomes deeper (Figure 7-14). This phenomenon can be explained by the fact that the sides of the tool-electrode are not insulated so when the tool is moved down to maintain the IEG the distance between the inner surface of the hole and the side wall of the tool electrode becomes shorter. Therefore the amount of active surface increases when the tool-electrode goes down.

The low value of the peak current when machining the hole 7 (Figure 7-14) is explained by the limited bandwidth of the peak detector of the pulse PSU which has been designed to operate at frequencies above 250 kHz.

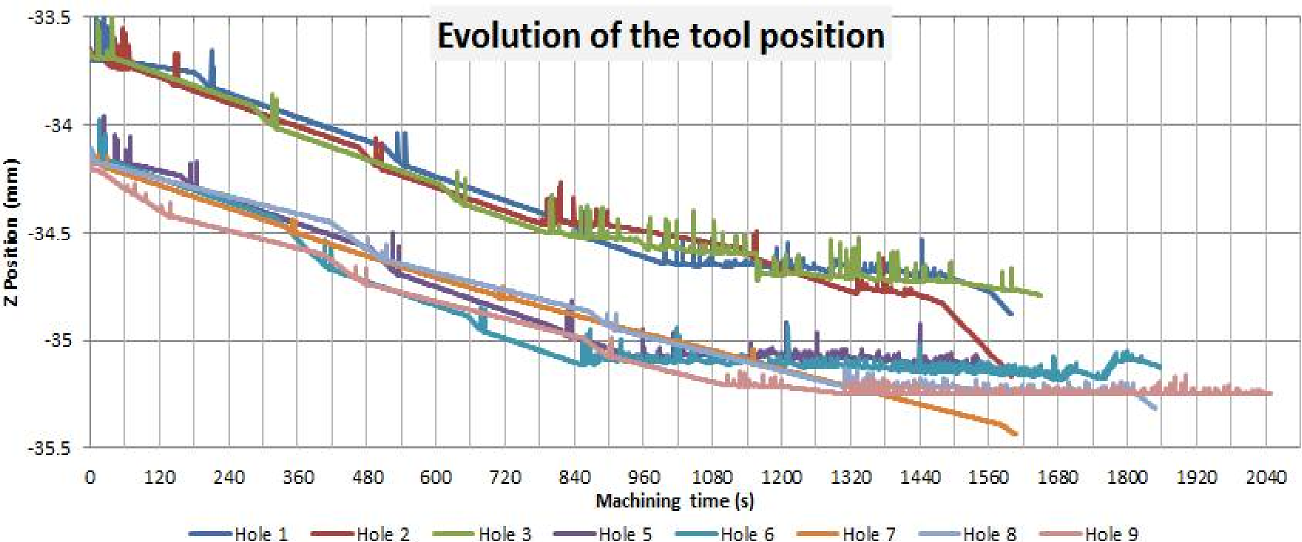

Figure 7-15: Evolution of the tool position during the machining process

Regarding the holes machined without tool orbiting, a significant difference between the entrance and exit diameters can be observed (Figure 7-13 & Figure 7-16).

For the machining of the holes 7, 8 and 9 the electrode tool was orbiting above the workpiece surface with an orbit radius of 50µm and a velocity of 0.4mm/s. It has been observed that orbiting the tool-electrode during machining would improve the quality of the drilled holes (smaller tapper effect and more homogeneous shape at the exit of the hole). Also it can be seen that when machining at 50 kHz (hole 7) the tool-electrode would progress more linearly, even when approaching the 0.9mm depth where short circuits were more likely to occur.

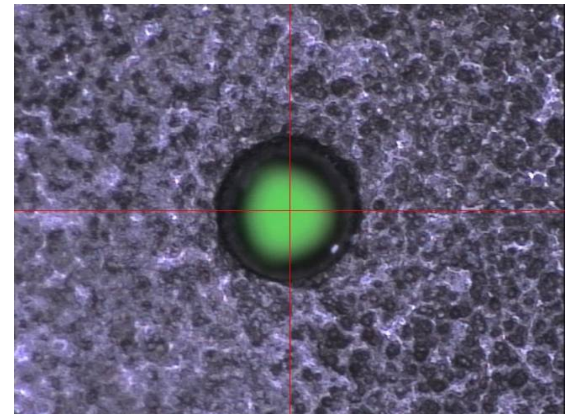

Figure 7-16: Hole 5 diameter: Top: 0.432mm, Bottom: 0.221mm

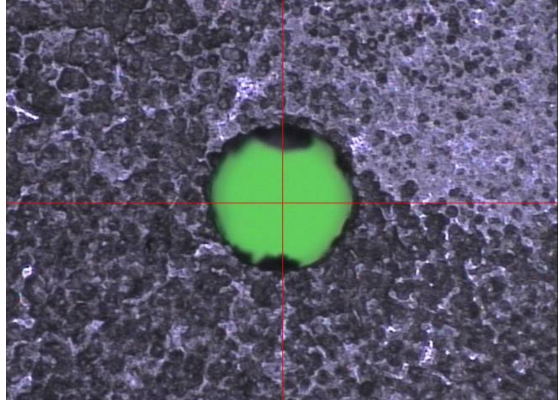

Figure 7-17: Hole 7 diameter: 0.472mm

The tool electrode used in this experiment has a diameter of 170µm (Figure 7-19) and is made of tungsten carbide (WC +5% Co). The best machining performance obtained in the experiment is the hole nr. 9 (Figure 7-18) using the following machining parameters: 1MHz, 15% duty cycle, 2.3A OCP, orbiting of the tool with a 50µm orbit radius with a pulse amplitude of 6V. The following pictures and diameter measurements have been taken with a Tesa-Visio 200GL.

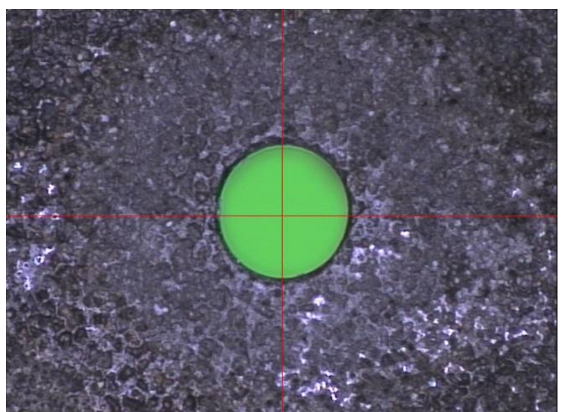

Figure 7-18: Hole 9, diameter: 0.394mm

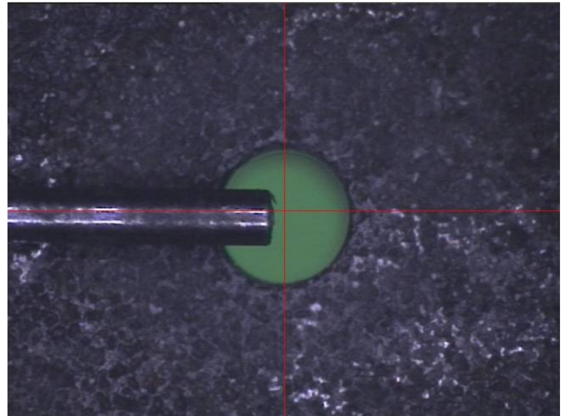

Figure 7-19: Picture of the hole nr. 9 and the tool-electrode of a diameter of 175µm orbiting with 50µm radius

It can also be observed in Table 7-2 that the machining time of the hole number 9 was the longest and resulted in a better result. The diameter for hole nr. 9 is 394µm. If we include the orbiting radius and neglect the misalignment and run-out of the tool, the effective diameter covered by the orbiting movement of the tool-electrode is 275µm, which represents a 43% overcut. Moreover, the comparison between hole 7 (Figure 7-17) and hole 9 (Figure 7-18) shows that the use of lower frequency results in a less precise machining and a rougher surface.

Hole number	Entrance dia. (mm)	Exit dia. (mm)	Freq.	Machining time (s)	Orbiting
1	0.567	0.37	1MHz	1602	No
2	0.591	0.366	1MHz	1600	No
3	0.475	0.255	1MHz	1667	No
4	0.445	0.301	1MHz	N/A	No
5	0.432	0.221	1MHz	1536	No
6	0.451	0.317	1MHz	1855	No
7	0.472	0.472	50kHz	1602	Yes
8	0.44	0.44	1MHz	1843	Yes
9	0.394	0.394	1MHz	2043	Yes

Table 7-2: The different pulse PSU parameters and their respective range of values

7.3. Investigation on the effect of pulse frequency, duty cycle and voltage on the machining performance

7.3.1. Methodology

The aim of this set of experiments was to analyse the influence of the machining parameters (pulse frequency, duty cycle, and voltage) on the machining time and the side gap created during the drilling of deep holes in 18NiCr6. The tool-electrode was made of WC-Co with a diameter of 170µm and the electrolyte used was the same as in section 6.3: $NaNO_3$ mixed with a small amount of HCl with a conductivity of 24.3mS/cm.

The selected parameters are the following:

Level	**1**	**2**	**3**
Frequency Value (KHz)	250	500	1000
Duty Cycle (%)	15	30	45
Voltage (V)	5	7	9

Table 7-3: Selected parameter values for the experiment

3 main parameters have been identified and 3 different levels will be tested for most of them, which results in an average number of levels close to 3.

According to the following array provided by Peter Woolf (Woolf, 2014), the array for this experiment should be an L9 one.

Number of Levels	Number of Parameters (P)					
	2	3	4	5	6	7
2	L4	L4	L8	L8	L8	L8
3	L9	L9	L9	L18	L18	L18
4	L'16	L'16	L'16	L'16	L'32	L'32
5	L25	L25	L25	L25	L25	L50

Figure 7-20: Array used to determine which type of experimental array to use (Woolf, 2014)

Experiment	Frequency (kHz)	Duty Cycle (%)	Voltage (V)
1	250	15	5
2	250	30	7
3	250	45	9
4	500	15	7
5	500	30	9
6	500	45	5
7	1000	15	9
8	1000	30	5
9	1000	45	7

Table 7-4: L9 Table of experiments to evaluate the influence of frequency

7.3.2. Results

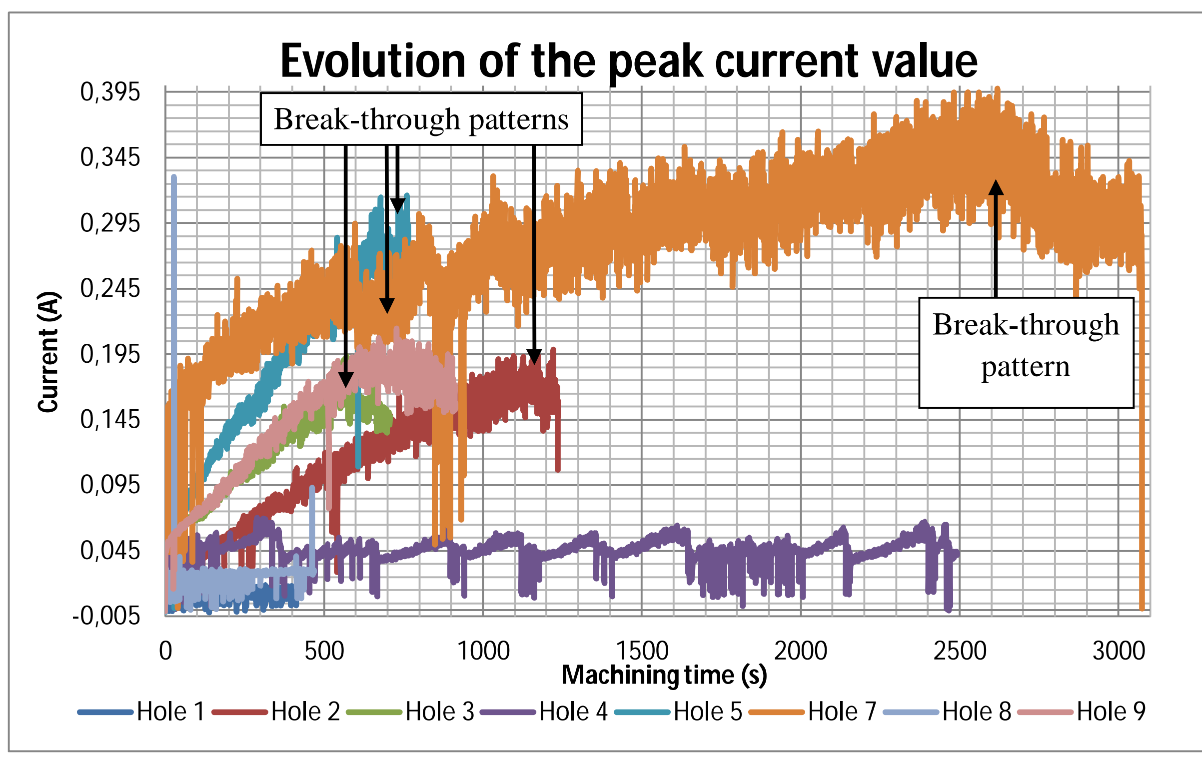

Figure 7-21: Graph representing the evolution of the peak value of the current during machining time

A break-through pattern can be observed in the graphs Figure 7-21 and Figure 7-22: the current decreases when the tool drills through the surface. This decrease in current can be explained by the fact that the front face of the cathode is no longer active because the bottom of the hole has been dissolved, so the only remaining active surfaces are the side walls. The amount of active surface has therefore decreased so less current is flowing through the system. Moreover, machining of the inner walls of the hole is still happening despite off the tool having gone through because the sidewalls of the tool is not insulated; since the tool is not moving in the X and Y directions, the side gap is increasing, which makes the current decrease over time.

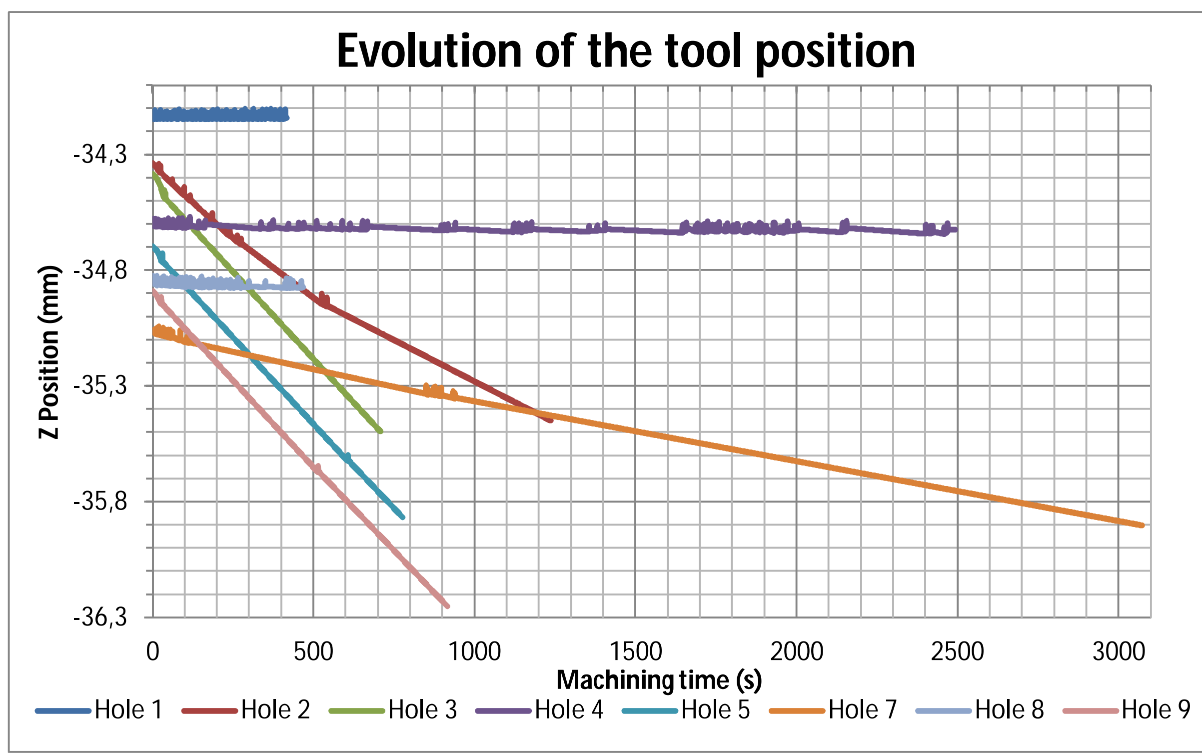

Figure 7-22: Graph representing the evolution of the tool position during machining

An overview of the resulting holes in the 18NiCr6 can be seen in Figure 7-23.

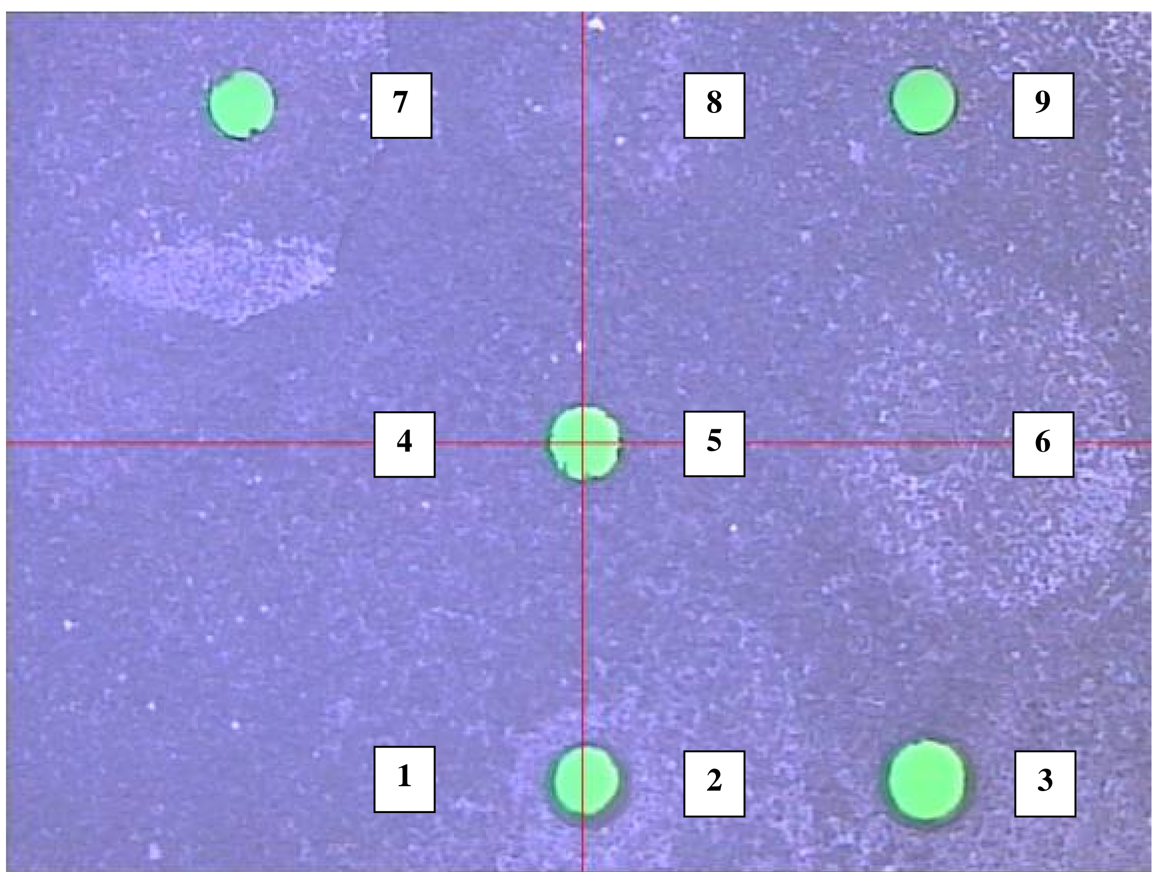

Figure 7-23: Overall picture of the workpiece used for the experiment

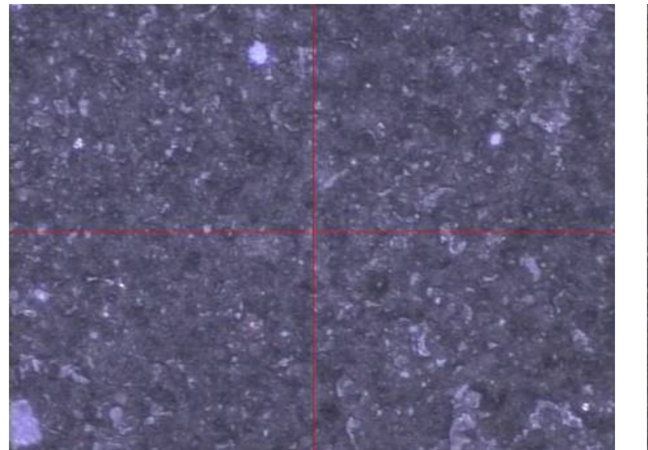

Figure 7-24: Experiment 1

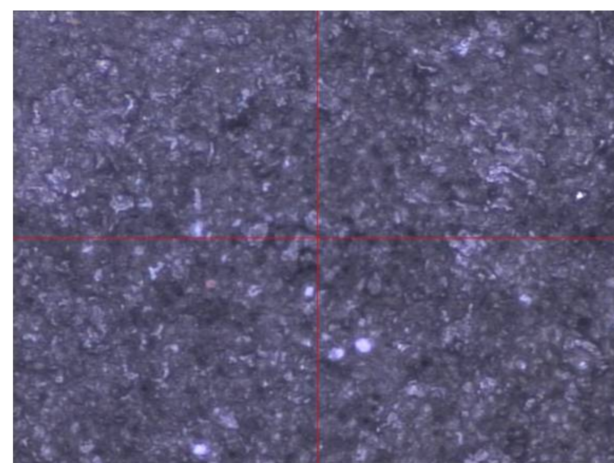

Figure 7-25: Experiment 4

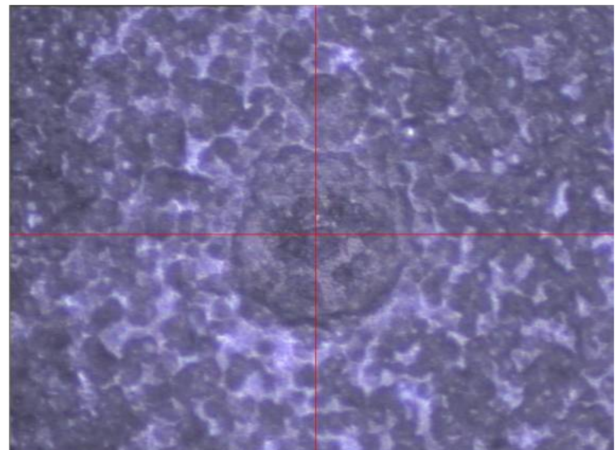
Figure 7-26: Experiment 6

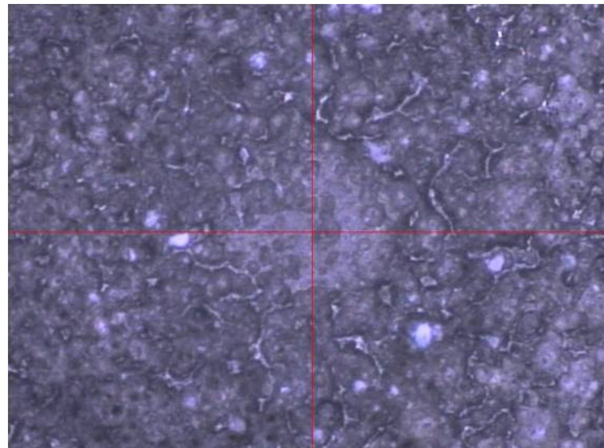
Figure 7-27: Experiment 8

From the results of the experiments and by observing the above figures, it can be seen that poor machining performance was observed for the following combination of parameters:

Experiment	Frequency (kHz)	Duty Cycle (%)	Voltage (V)
1	250	15	5
4	500	15	7
6	500	45	5
8	1000	30	5

Table 7-5: Table of the parameters considered as non-optimal for the drilling of 18NiCr6 under the test conditions

It can be observed that all the experiments with a voltage set to 5V resulted in poor results and therefore the voltage has a very important influence on the material removal rate.

Experiments 3, 5 and 9 presented the best results, the machining time was optimal and the process resulted in well-shaped holes (Figure 7-28 to Figure 7-33). The influence of the frequency can be observed by making a comparison between holes 3 and 9: hole 9 presents sharper features, and almost no taper shape.

Experiment	Frequency (kHz)	Duty Cycle (%)	Voltage (V)
3	250	45	9
5	500	30	9
9	1000	45	7

Table 7-6: Table of the parameters considered as optimal for the drilling of 18NiCr6 under the test conditions.

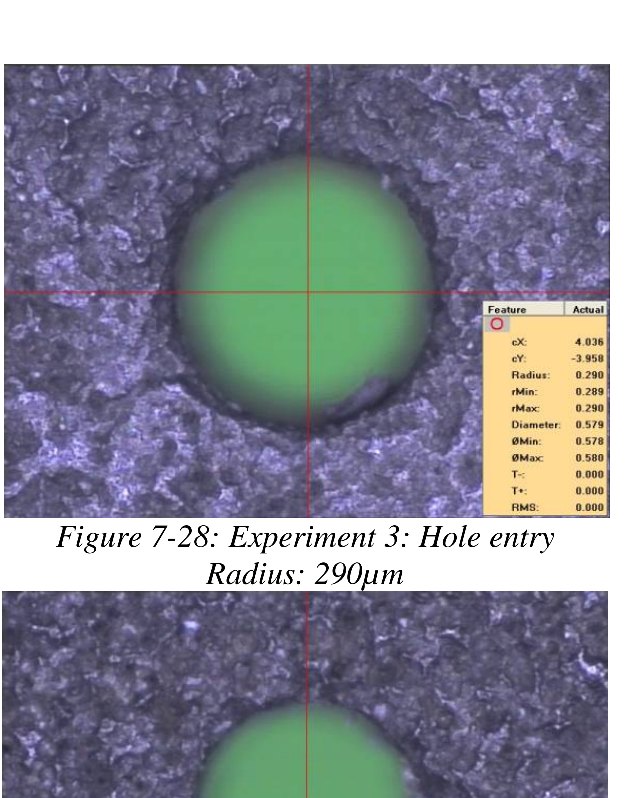

Figure 7-28: Experiment 3: Hole entry
Radius: 290µm

Figure 7-29: Experiment 3: Hole exit
Radius: 223µm

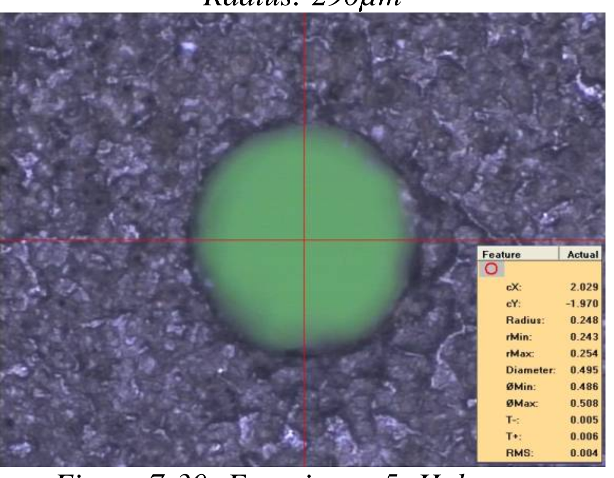

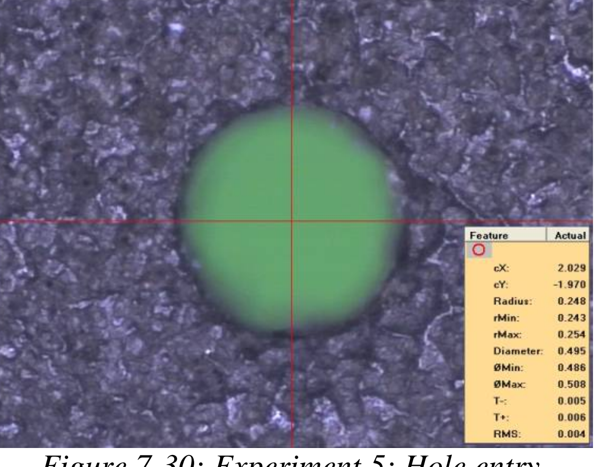

Figure 7-30: Experiment 5: Hole entry
Radius: 248µm

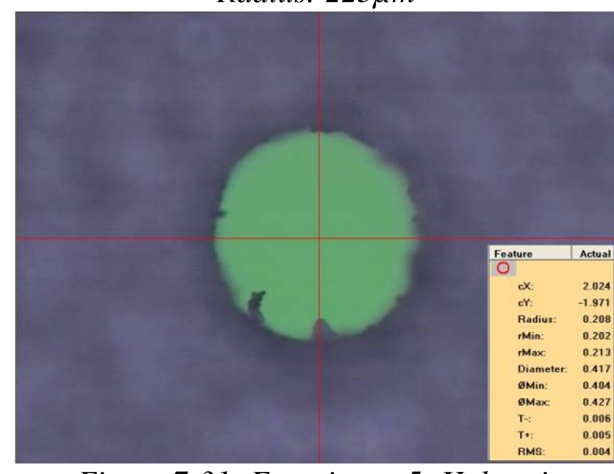

Figure 7-31: Experiment 5: Hole exit
Radius: 208µm

Figure 7-32: Experiment 9: Hole entry
Radius: 193µm

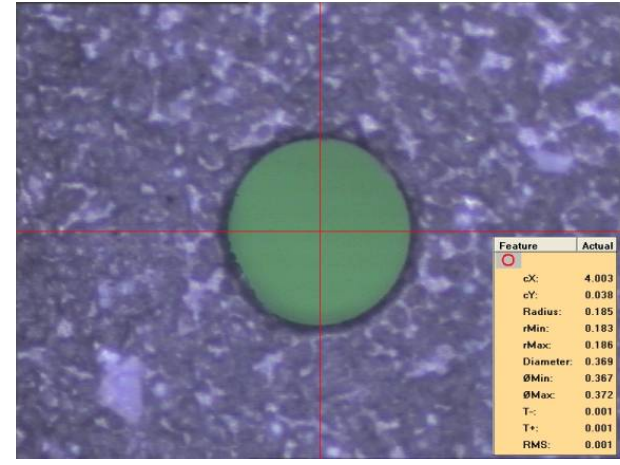

Figure 7-33: Experiment 9: Hole exit
Radius: 185µm

Regarding the holes nr 2 and 7, the progression of the tool was slower than for holes 3, 5 and 9. However, the hole nr 7 showed very sharp edges and no taper shape. This is mainly due to the high frequency and low duty cycle of the pulses.

Experiment	Frequency (kHz)	Duty Cycle (%)	Voltage (V)
2	250	30	7
7	1000	15	9

Table 7-7: Table of the parameters considered as medium for the drilling of 18NiCr6 under the test conditions.

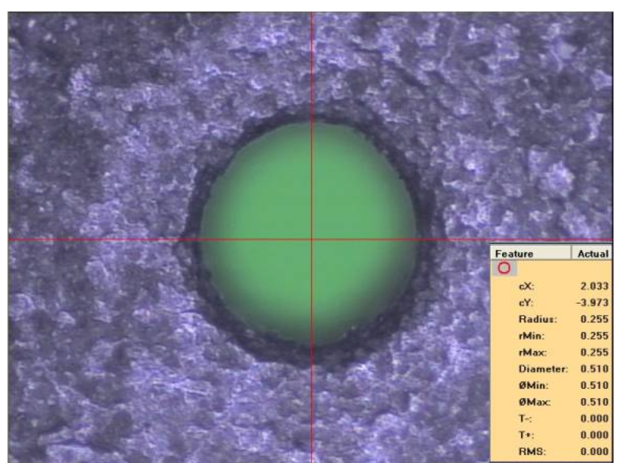

Figure 7-34: Experiment 2: Hole entry
Radius: 255µm

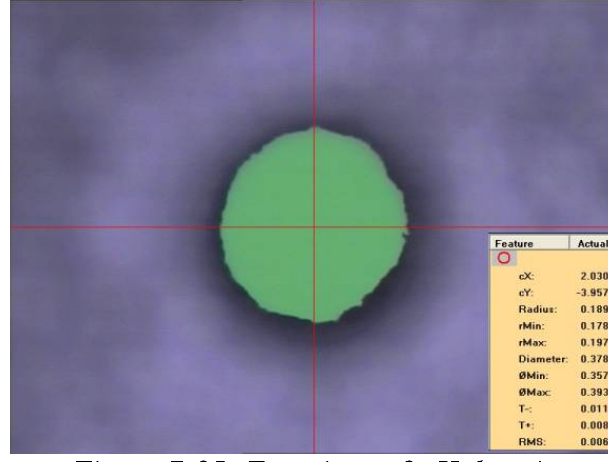

Figure 7-35: Experiment 2: Hole exit
Radius: 189µm

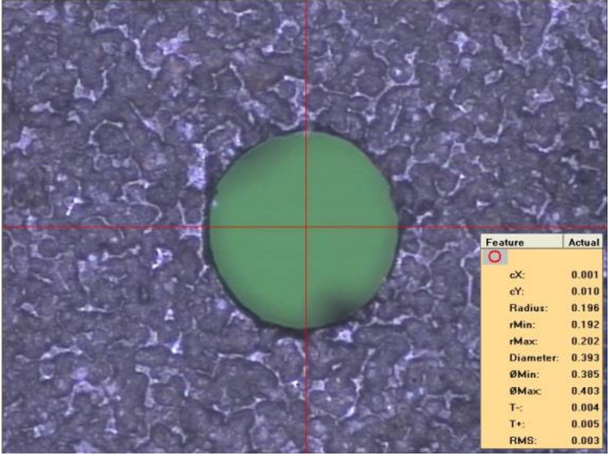

Figure 7-36: Experiment 7: Hole entry
Radius: 196µm

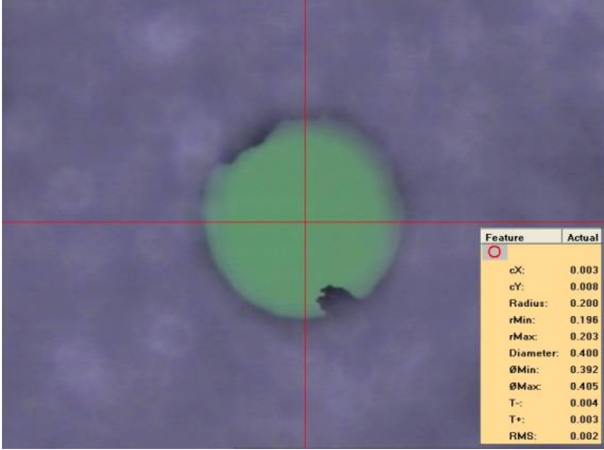

Figure 7-37: Experiment 7: Hole exit
Radius: 200µm

7.3.3. Discussion on the effect of pulse frequency, duty cycle and voltage on the machining performance

From the above results, it can be seen that the voltage has the strongest influence of the process: no machining occurred below 7V, and 7V with 15% duty cycle was not enough to remove material efficiently. The second most influential parameter is the duty cycle: the combinations of parameter resulting in the fastest machining session had a duty cycle above 30%. The frequency had an influence on the resolution and the shape of the hole, but did not influence the material removal rate as much as the duty cycle did.

The overcut presented in the results is not representative of the machining resolution: the run-out of the spindle tool-holder is too significant to be ignored and was still visible despite several attempts to reduce it. The same problems were observed on the machine developed in Germany but it could be replaced by a Sarix precision tool-holder. The author suggests the tool-holder to be changed in order to reduce the run-out.

7.3.4. Verification of the μECM LabVIEW simulation model

This section is a comparison between simulated and experimental results in section 3.6 'Investigation on the effect of pulse frequency, duty cycle and voltage on the machining performance'.

In order to assess if the results coming from the developed simulation programme were realistic, the values of the simulated and actual material removal rates for the experiments in section 3.6 were compared and the error between the two was calculated.

The volume of material removed during the simulation could be approximated to the volume of a cylinder with the following expression:

$$V_{removed} = (\pi r_{hole}{}^{2}) \times h_{hole} \tag{7-1}$$

Where $V_{removed}$ is the volume of material removed in mm^3.

r_{hole} is the radius (in mm) of the hole and h_{hole} is the depth of the hole at the end of the machining session (in mm).

The MRR is then calculated as follows:

$$MRR = \frac{V_{removed}}{T_{mach}} \tag{7-2}$$

Where T_{mach} is the total machining time (in s).

Machining parameters used for all simulations:

- Current efficiency : 70% (when using NaNO3 electrolyte with current densities higher than 20A/cm² according to Haisch, Mittemeijer and Schultze (2004).
- Activation potential : 0.92V (Fe),
- EDL capacitance : $1E^{-7}F/mm^2$,
- Kv : $0.0281 mm^3/(A.s)$,

- Conductivity : 0.00243 S/mm (NaNO3 electrolyte)

Experiment	Frequency (kHz)	Duty Cycle (%)	Voltage (V)	Simulated MRR (mm³/s)	Actual MRR (mm³/s)	Error (%)
1	250	15	5	$1.010\,E^{-4}$	NA	NA
2	250	30	7	$2.008E^{-4}$	$1.5642E^{-4}$	28%
3	250	45	9	$2.933E^{-4}$	$3.213E^{-4}$	-8.71%
4	500	15	7	$1.088E^{-4}$	NA	NA
5	500	30	9	$1.931E^{-4}$	$2.032E^{-4}$	-4.97%
6	500	45	5	$1.741E^{-4}$	NA	NA
7	1000	15	9	$9.565E^{-5}$	$3.517E^{-5}$	171%
8	1000	30	5	$1.022E^{-4}$	NA	NA
9	1000	45	7	$1.583E^{-4}$	$1.502E^{-4}$	5.39%

Table 7-8: Comparison of the material removal rates (MRR) between the process simulations and the actual experiments

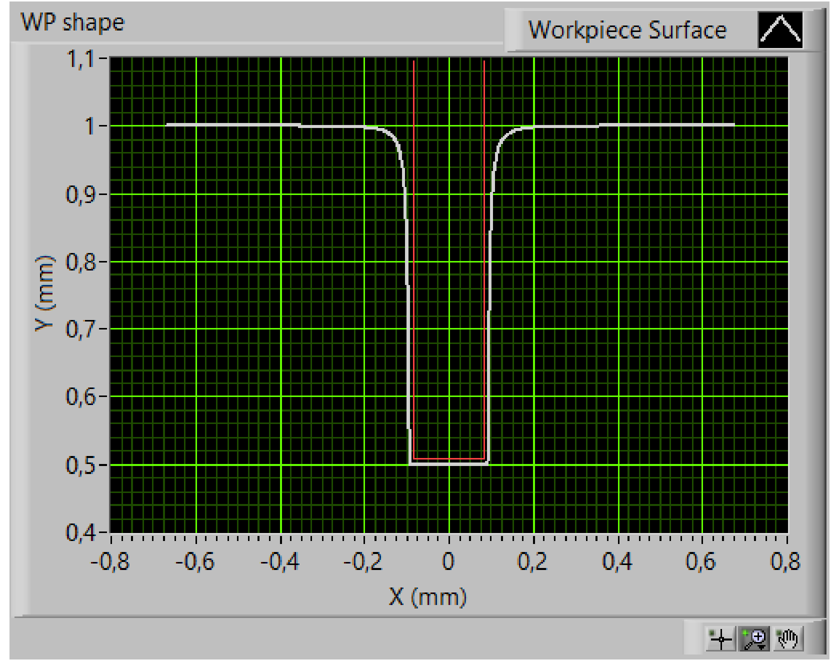

Figure 7-38: Screenshot of the resulting workpiece shape after the simulations.

In the experiments where the parameters were optimal for machining, the model error of the simulation programme was below 10%.

When the parameters were not optimal and short-circuits occurred, the actual process took longer than in the simulation and the material removal rate was reduced.

It can be concluded than when short-circuits occur, it is very hard to predict what the material removal rate is going to be using the simulation software.

The simulation software can however be used to provide some insights to the operator and the control system. The predictions are particularly accurate when the pulse duration is above 450ns and the voltage is higher than 7V.

7.4. On-line tool fabrication followed by workpiece drilling

In these machining trials, a mixture of 0.1M H_2SO_4 and 0.5M $NaNO_3$ solutions has been used as electrolyte.

The tool-electrode has a diameter of 170µm and is made of WC-Co alloy (WC +5% Co).

The workpiece was one disk made of 18NiCr6 alloy which was provided by the automotive company Delphi UK. The disk is 1.1mm thick.

The positions of the surfaces of the wire and workpiece were determined by using the OCP of the PSU. Setting the OCP to a very low threshold level allows the detection of the electrical contact necessary to localize the surface and initialize the interelectrode gap.

The tool was first etched to a diameter of 105µm via Wire µECM (Figure 7-39) with the following parameters: -7V pulses with no offset (pulse shape n°5), at a frequency of 2MHz and 10% duty cycle (50ns pulses). Over current protection was set to 1A. The micro-tool was spinning at 600rpm during the etching process and was slowly fed down towards the wire while ultrashort pulses were delivered to the IEG. The wire was produced by Agie/Charmilles and is commonly used for EDM, it had a diameter of 200µm and was made of zinc.

The following pictures and diameter measurements have been taken with a Tesa-Visio 200GL.

After the tool was fabricated, a hole was drilled in the workpiece by reversing the polarity of the pulses. A black film can be observed on the workpiece because of the carbide compounds created during the machining of the 18NiCr6 alloys. This phenomenon is well-known and was reported by Haisch et al. (Haisch, Mittemeijer and Schultze, 2004).

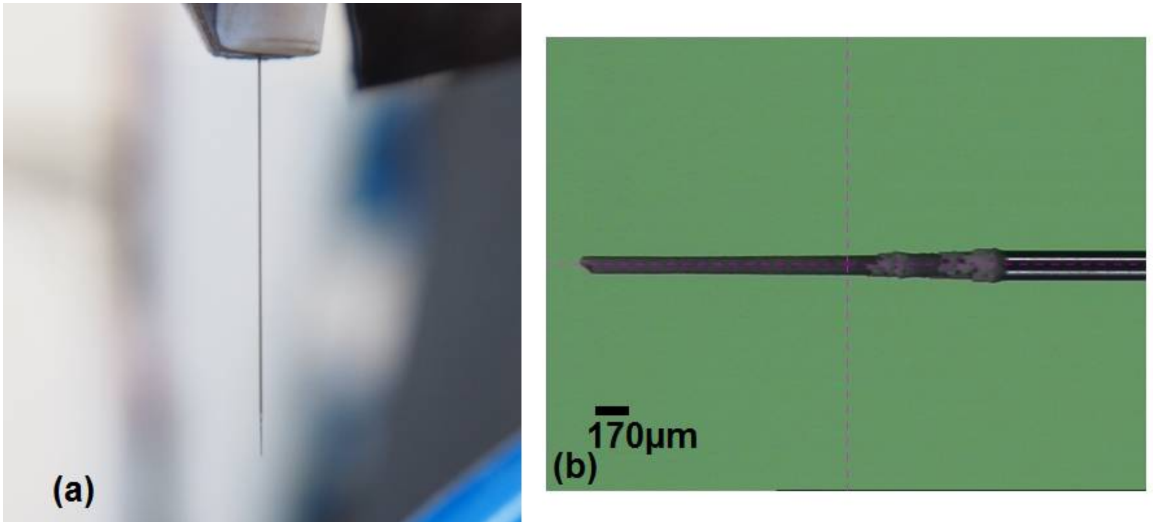

Figure 7-39: (a) Tool in the tool holder (b) Picture of the micro tip etched via Wire µECM (electrochemical turning), a $NaNO_3$ salt layer can be observed along the tool surface (WC-Co alloy, electrolyte 0.5M $NaNO_3$+ 0.1M H_2SO_4, pulse amplitude: -7.5 V, pulse duration: 50 ns, pulse period: 500ns, feed rate: 0.3µm/s, diameter: 95µm).

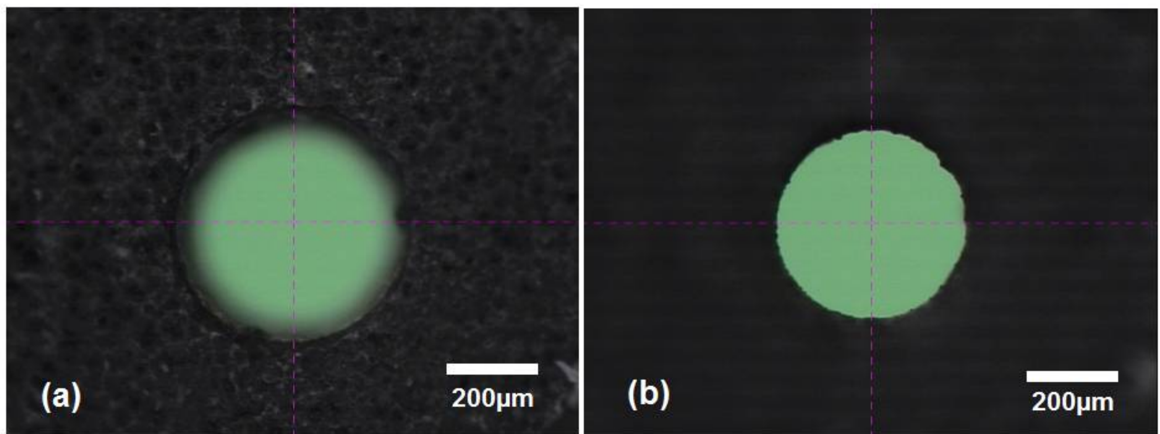

Figure 7-40: Picture of the hole fabricated by ECM with the WC-Co etched tool. (a) hole entrance, (b) hole exit (18NiCr6 alloy, depth: 1.1mm, hole entrance diameter: 517µm, hole exit diameter: 414µm, electrolyte 0.5M $NaNO_3$+ 0.1M H_2SO_4, pulse amplitude: 8V, pulse duration: 250 ns, pulse period: 1 µs, feed rate: 0.3µm/s).

From the chart (Figure 7-41) it can be seen that the progression was rather linear, with a lot of OCP retractions during the first half of the machining tests. This caused the current to drop for a short amount of time, as it can be seen on the current chart. The process is controlled by an algorithm which adapts the feed-rate of the tool according to the positions and times at which the short circuits have occurred. The machining time was 3748s.

Evolution of the current peak value of the pulses (A)

Peak Current Value(A)

0,3
0,25
0,2
0,15
0,1
0,05
0

0 400 800 1200 1600 2000 2400 2800 3200 3600

Time (s)

Current drops because of OCP triggering

Evolution of Tool position (mm)

0 400 800 1200 1600 2000 2400 2800 3200 3600

Tool position (mm)

-27,65
-27,85
-28,05
-28,25
-28,45
-28,65
-28,85

Time (s)

Tool retractions because of short-circuits

Figure 7-41: Graphs representing (a) the evolution of the current peak value of the pulses (in A) and (b) the evolution of the tool position (in mm) throughout the machining time (in s)

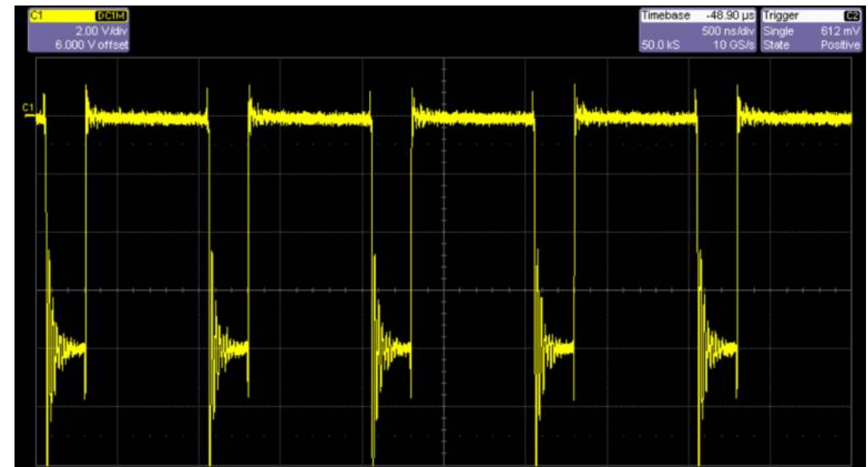

Figure 7-42: Oscilloscope screenshot of the measured pulses at the IEG during workpiece machining, 1MHz frequency, duty cycle of 25%, pulse amplitude of 8V and no offset during off-time 500ns/div.

7.5. Micro-Tool fabrication

The pulse PSU was also used to machine micro-tools from WC-Co electrodes (170µm diameter) via electrochemical turning.

A very sharp tool (Figure 7-43) was fabricated by repetitively scanning the surface of the wire at a fixed gap. The tip of the tool measures 5µm. The machining of this tool was very fast and took only 350 seconds.

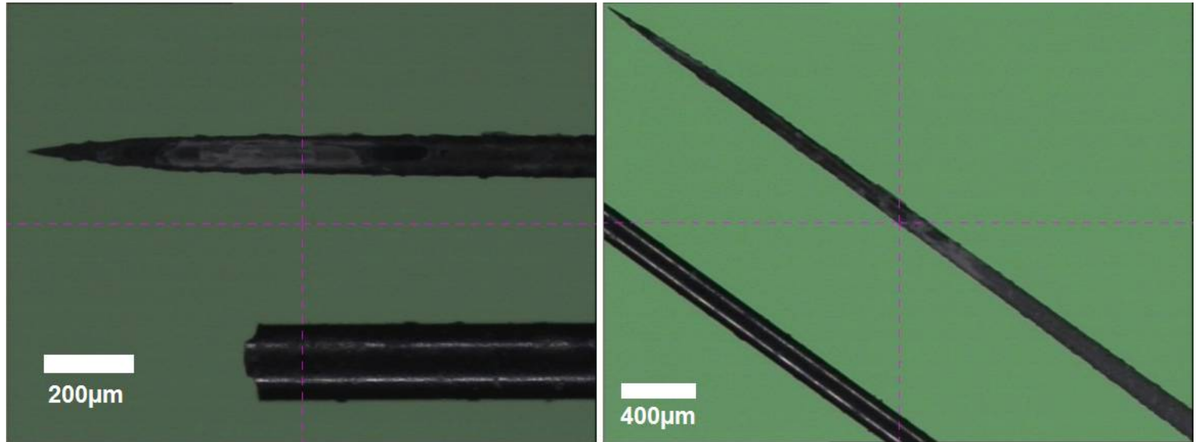

Figure 7-43: Tool of the shape of a needle made by micro electrochemical turning. A non-machined tool-electrode of 170µm is placed next to it for size comparison. (WC-Co alloy, electrolyte 0.5M $NaNO_3$+ 0.1M H_2SO_4, pulse amplitude: -7.5 V, pulse duration: 50 ns, pulse period: 500ns, feed rate: 0.3µm/s, diameter: 95µm)

Another technique was applied to produce the tool seen in Figure 7-44. The smallest diameter measured on that micro-tool is 46µm. The tip of the tool is slightly bigger and measures 57µm. The side gap between the micro-tool and the wire was varied during the machining process to achieve this curved tool shape. The aim of this experiment was to fabricate a tool looking like a micro-probe used in CMM machines.

The surface was observed using optical equipment with the help of the National Physics Laboratory (NPL). It was determined that the roughness of the machined WC-Co shaft in Figure 7-44 was 120nm. In Figure 7-45 it can also be observed that the surface texture is very uniform.

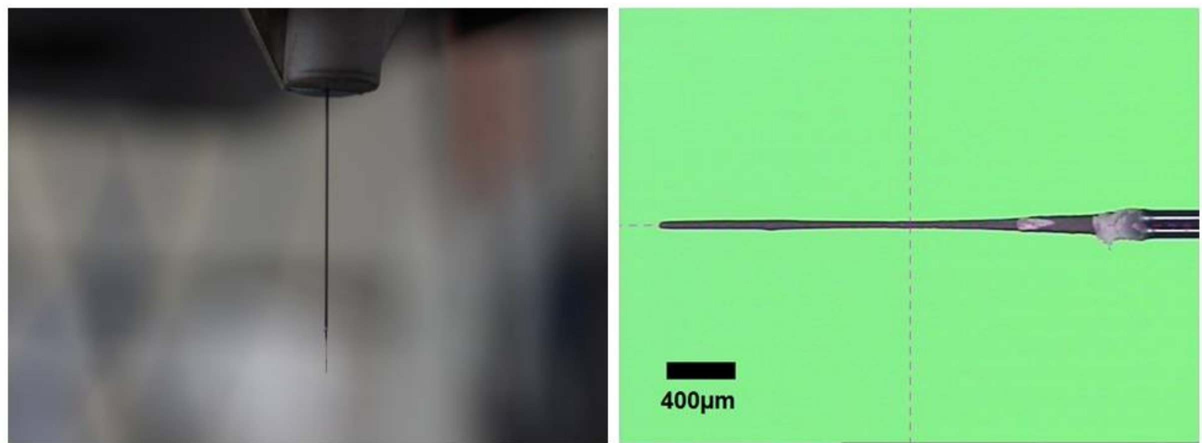

Figure 7-44: Micro-tool made by micro electrochemical turning. (WC-Co alloy, electrolyte 0.5M $NaNO_3$+ 0.1M H_2SO_4, pulse amplitude: -7.5 V, pulse duration: 50 ns, pulse period: 500ns, feed rate: 0.2µm/s, diameter of tip: 57µm, smallest diameter measured: 46µm)

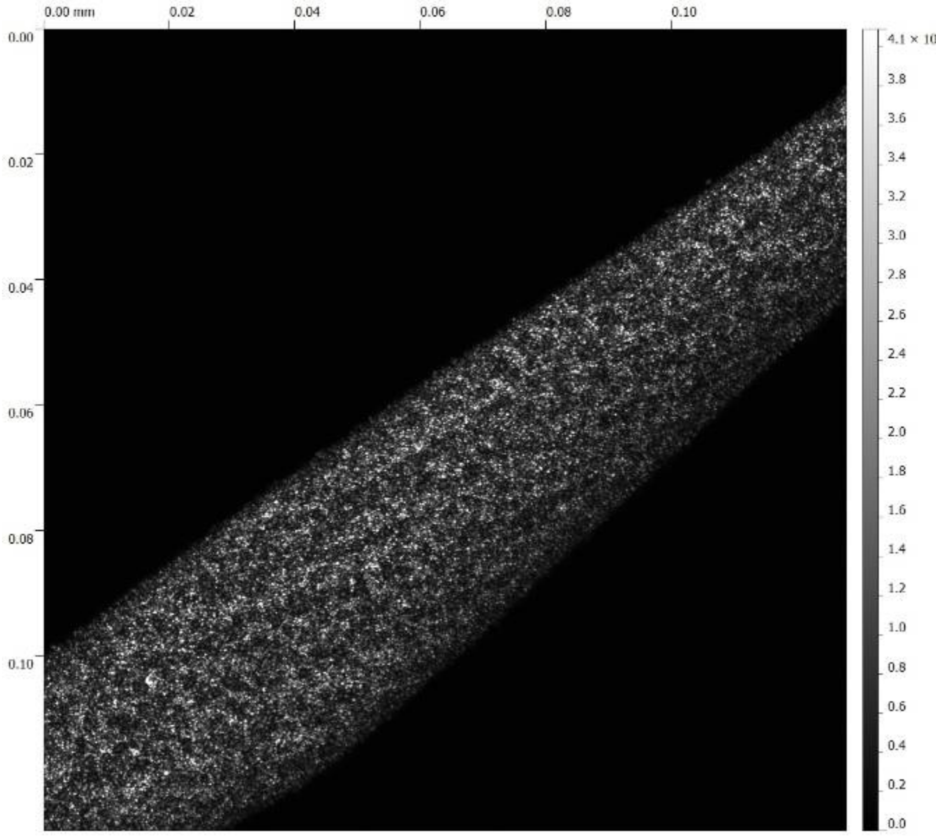

Figure 7-45: Shaft surface picture Ra = 120nm.

In Figure 7-46 (a) a micro-styli made of tungsten carbide with very high aspect ratio was fabricated using the same technique. In Figure 7-46 (b) a micro-shaft with a diameter of 95µm was fabricated by ‘scanning’ the workpiece along the wire at a fixed machining gap.

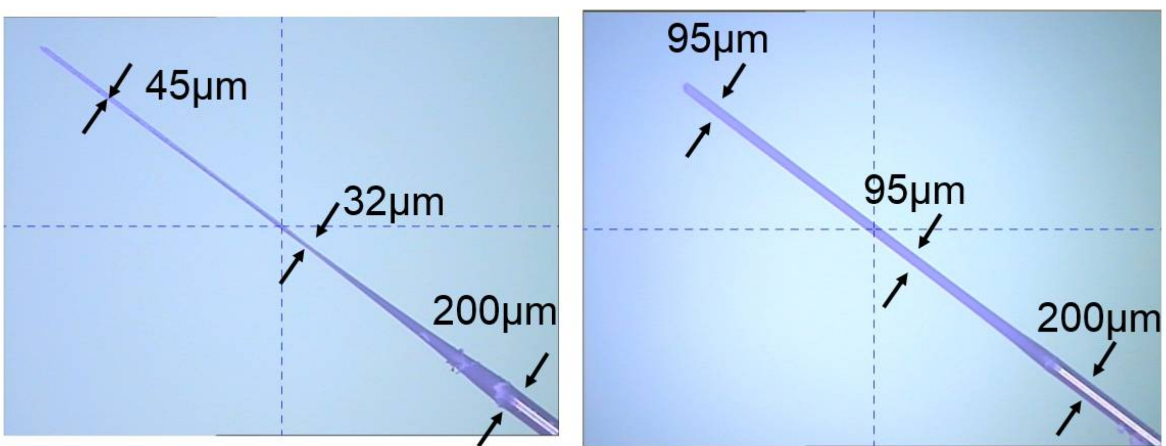

Figure 7-46: (a) Micro-styli, diameter of tip: 45μm, smallest diameter measured: 32μm (b) Micro-shaft of 95μm diameter. (both made of WC-Co alloy with electrolyte 0.5M $NaNO_3$+ *0.1M* H_2SO_4*, pulse amplitude: -7.5 V, pulse duration: 50 ns, pulse period: 500ns, feed rate: 0.2μm/s)*

Chapter 8: CONCLUSIONS AND FUTURE WORK

8.1. Conclusions

In this work, a fully operational electrochemical micromachining machine was designed and developed. The objectives defined at the beginning of this work have all been met.

(1) An extensive literature review provided insights on the state of the art development in µECM and its research gaps.

The machine requirements for ultraprecision motion were identified, and it was found that the use of air-bearings combined with DC brushless linear moter was essential to achieve ultraprecision motion. A granite base was selected for its low thermal expansion and a gantry configuration provided a very stable mechanical structure.

For the motion control system, a 2-nm resolution encoder system was installed and interfaced with the high-performance motion controller Delta Tau Power PMAC to control the direct PWM drives.

This research concluded that the design and assembly of an innovative power supply capable of delivering ultrashort pulses and providing enough power to the IEG was needed in order to progress in the development of µECM equipment. Furthermore, it implied that an ultrafast overcurrent protection should be integrated into the power supply.

The trend in control systems for µECM seemed to go towards fuzzy logic and neural networks, allowing manufacturers to put their knowledge into the system. Therefore a special fuzzy logic control algorithm embedded in a state machine was first developed to control the tool position during machining.

(2) The behaviour of the µECM process and the influence of the electrical double layer have been modelled and simulated. The presented work is built over models found in the literature review and provided an enhanced version of what was achieved so far. The simulation programme provided realistic results and can be used to determine optimum machining parameters.

The influence of conductivity and frequency on the localisation and the machining time were analysed. It was concluded that for a same frequency, the lower

conductivity electrolyte exploited at best the EDL effect, providing an improved localization.

However, a lower electrolyte conductivity and a higher pulse frequency would increase the machining time. Therefore, a trade-off had to be made between the localization of the machining and the cycle time.

(3) The design of a programmable power supply capable of delivering ultra-short pulses and providing enough power to the IEG is essential in order to progress in the development of μECM equipment.

In this work, a review for the pulse PSU requirements in μECM has been done and a device meeting those requirements has been developed and tested. An ultra-fast (50ns time delay) over current protection (OCP) system has been designed to protect the tool against undesired events occurring within the interelectrode gap during machining. The pulse PSU provides the control system with signals such as the current peak value as well as the OCP signal, in order to quickly react and adapt the motion of the tool. It is able to supply pulse with duration of 50ns at a frequencies ranging from 1kHz to 5MHz, although it was found at above 2MHz, the material removal rate dropped significantly.

The developed pulse PSU is also able to reverse its pulse polarity and add a positive/negative biases during pulse off-time. This means that the μECM machine is able to perform on-line tool fabrication as well as workpiece machining without any intervention on the hardware (no need to change any cable connection). Pulse PSUs with similar performance and functionalities have not been reported.

(4) A quick communication protocol between the power supply and the control system was essential for the successful control of the μECM process. A special fuzzy logic control algorithm embedded in a state machine was first developed to control the tool position during machining.

With the developed escape strategy the machine is able to control the interelectrode gap very reliably and during long machining sessions. The different control strategies have been explained and their efficiency was assessed in the experiments. The main findings resulting from the machining trials using the fuzzy logic strategy were:

- The occurrence of sparking is efficiently prevented when fuzzy logic control (FLC)
- There is a need to constantly update the rules to change the targeted machining current when drilling with a tool-electrode of which the sidewalls are not insulated.
- For the first time, fuzzy logic has been successfully applied to control a μECM process.

The main findings resulting from the machining trials using the adaptive feed rate control strategy were:

- The occurrence of sparking is efficiently prevented when the optimum tool-electrode feed rate in reached.
- There is no machining underperformance linked to the tool feed rate, resulting in a more efficient machining process.

The adaptive feed rate adapted rapidly the feed rate of the tool-electrode in order to match the material removal rate. This resulted in a shorter machining time with respect to the fuzzy logic control strategy. The progression of the tool-electrode was linear and the occurrences of short-circuits were decreasing over time.

The adaptive feed rate algorithm provided with the most encouraging results. The results presented show that fuzzy logic is a viable control method for maintaining the inter-electrode gap throughout machining time although it is preferable to use side-insulated cathode when using this control strategy.

(5) An intelligent of HMI to allow inexperienced users to communicate with the machine was developed. The HMI allows the user to setup and monitor the machining current, tool position and other essential machining parameters. The HMI was fully integrated into the control system and was also responsible for communicating with the spindle drive and pulse PSU on behalf of the controller. Its source code can be used as a framework for further development with Power PMAC systems. The HMI also reacts intelligently to values sent by the Power PMAC, and suggests parameter values to the user for the fuzzy logic control system configuration.

(6) The machine capabilities and applications have been investigated through machining experiments including:

- Drilling hole in 18NiCr6 disks
- Fabricating micro styli and micro shafts
- Fabricating micro needles

From these experiments it can be deduced that the shape of the hole is strongly influenced by the drilling time, the tool spinning, the conductivity of the electrolyte and the pulse frequency. The drilling time will have an influence on the diameter of the hole but also on the tapper effect. It has been observed that orbiting of the tool electrode with a small radius would enhance the machine performance and improve the shape of the hole substantially.

It has been confirmed that a fine tuning of the pulse width and the scanning ratio would ensure the localization of the dissolution process. The developed pulse PSU was used to produce micro-tools and drill deep holes in 18NiCr6 with an on-line fabricated tool. The results from the drilling in 18NiCr6 show that μECM is not suitable for drilling applications in the automotive sector because of its long cycle time compared to EDM. Nevertheless, the μECM process can be used as a post-process step in order to improve the surface finish on parts machined by EDM.

On the other hand, the use of this μECM machine for the fabrication of micro-probes targeting the CMM sector looks very promising.

The presented machine provides outstanding capabilities in terms of programmability and motion precision. This research and development can lead to various applications such as the drilling of micro-holes in hard to machine material for the metrology and medical sectors.

8.2. Contributions to knowledge

The development of this machine is associated by the following contributions to knowledge in the μECM sector:

1) A thorough background research showing that the problems limiting full scale ECM are the same as those being identified for μECM. This work contributed to the overall knowledge by analysing the research challenges the μECM and ECM industries are facing today and by identifying the gaps where further research in needed.

2) The developed LabVIEW simulation programme provides the µECM sector with a greater understanding of the process and is a step towards the development of an on-the-machine simulation step before machining.
3) The innovative pulse PSU provides not only tens nanosecond order pulse duration, but also plus and minus biases and a polarity switching functionality as well. It fulfils the requirements of tool preparation with reversed ECM on the machine easily. The careful design and implementation, integration with MCU, are of good references to the researchers and engineers who work in micro ECM.
4) The machine configuration and PSU integration enabled an innovated and industry-capable machining strategy consisting of a 2-step sequential method: a fully automated on-line tool preparation followed by workpiece machining.
5) Two innovative interelectrode gap (IEG) control strategies were developed. Both of these control approaches required the use of the developed pulse PSU featuring an ultra-fast Over Current Protection (OCP):
   i. The first one is the use of a fuzzy controller to adjust the IEG according to a desired machining current.
   ii. The second control strategy consists in the use of an adaptive machining algorithm decreasing the tool-electrode feed rate according to the times and positions at which short circuits are detected.
6) The experimental work in 'Chapter 7: Experimental work and results' described µECM drilling trials in 18NiCr6 alloys, which were never published before. The fabrication of micro-tools in tungsten carbide using wire µECM complements the rare the literature describing this process.

This development can lead to various applications such as the drilling of micro-holes in hard to machine material for the automotive and aerospace sectors. Each of these applications will require the design of an adapted workpiece clamping system which should meet the electrical and spatial requirements for an optimal machining performance (short current path for high frequency, chemical resistant fixtures…).

Moreover, the machine can be used to fabricate micro-tools and micro-probes for the micro coordinate measuring machine (micro-CMM) sector.

The author also strongly encourages the use of the µECM machine on hard to machine materials such as indium antimonite (InSb).

8.3. Recommendations for future work

This machine presents the first µECM prototype ever built in the UK. The author suggests the following future work to be undertaken:

- Improvement of the control system to allow the tool retraction when short-circuit occurs during 3-axis motions.
- Improvement of the tool clamping system to reduce the run-out and make the tool-changing operation easier.
- Development of a machine learning algorithm and comparison of performance with the already existing control strategy.
- Setup of a database to assist the operator in choosing the machining parameters depending on the materials of the electrodes
- Work on the pulse PSU to reduce the noise generated by the power semiconductors during the turn-on and turn-off times.
- Improvement of the workpiece clamping system to allow the installation of a piezo-actuated machining cell in order to make the cell vibrate during machining.

REFERENCES

Abuzied, H.H., 2012. Prediction of Electrochemical Machining Process Parameters using Artificial Neural Networks. 4(01), pp.125–132.

Ahn, S.H., Ryu, S.H., Choi, D.K. and Chu, C.N., 2004. Electro-chemical micro drilling using ultra short pulses. *Precision Engineering*, 28(2), pp.129–134.

Altena, H.S.J., 2004. EDM and ECM for mass production Philips DAP. *Journal of Materials Processing Technology*, 149(1-3), pp.18–21.

Altera, 2001. Application note 75: High-Speed Board Designs. (November), pp.1–18.

Analog Devices, 2010. *Datasheet: AD8402: 2-Channel Digital Potentiometer*. [online] Available at: <http://www.analog.com/static/imported-files/data_sheets/AD8400_8402_8403.pdf> [Accessed 19 Apr. 2012].

Analog Devices, 2012. *Datasheet: ADuM110 - iCoupler Digital Isolator*. [online] Available at: <http://www.analog.com/static/imported-files/data_sheets/ADUM1100.pdf> [Accessed 17 Apr. 2013].

Anorad Linear Motor Division, U.S.. A., 1999. *LE SERIES Motor Integration Manual LEA, LEB, LEC & LEM Linear Motors*.

Ardizzoni, J., 2005. *A Practical Guide to High-Speed Printed-Circuit-Board Layout*. [online] Analog Dialog. Available at: <http://www.analog.com/library/analogdialogue/archives/39-09/layout.pdf> [Accessed 14 Apr. 2013].

Asokan, P., Ravi Kumar, R., Jeyapaul, R. and Santhi, M., 2008. Development of multi-objective optimization models for electrochemical machining process. *The International Journal of Advanced Manufacturing Technology*, 39(1-2), pp.55–63.

Bähre, D., Weber, O. and Rebschläger, A., 2013. Investigation on Pulse Electrochemical Machining Characteristics of Lamellar Cast Iron using a Response Surface Methodology-Based Approach. *Procedia CIRP*, 6, pp.363–368.

Balogh, L., 2001. Design And Application Guide For High Speed MOSFET Gate Drive Circuits. In: *Proc. Power Supply Design Seminar (SEM 1400)*. Texas Instruments.

Barbalace, A., Luchetta, A., Manduchi, G., Moro, M., Soppelsa, A. and Taliercio, C., 2008. Performance comparison of VxWorks, Linux, RTAI, and Xenomai in a hard real-time application. In: *IEEE Transactions on Nuclear Science*. pp.435–439.

Bhattacharyya, B., Doloi, B. and Sridhar, P.S., 2001. Electrochemical micro-machining: new possibilities for micro-manufacturing. *Journal of Materials Processing Technology*, 113(1-3), pp.301–305.

Bhattacharyya, B., Malapati, M. and Munda, J., 2004. Advancement in electrochemical micro-machining. *International Journal of Machine Tools and Manufacture*, 44(15), pp.1577–1589.

Bhattacharyya, B., Malapati, M. and Munda, J., 2005. Experimental study on electrochemical micromachining. *Journal of Materials Processing Technology*, 169(3), pp.485–492.

Bhattacharyya, B., Malapati, M., Munda, J. and Sarkar, A., 2007. Influence of tool vibration on machining performance in electrochemical micro-machining of copper. *International Journal of Machine Tools and Manufacture*, 47(2), pp.335–342.

Bhattacharyya, B. and Munda, J., 2003. Experimental investigation on the influence of electrochemical machining parameters on machining rate and accuracy in micromachining domain. *International Journal of Machine Tools and Manufacture*, 43(13), pp.1301–1310.

Bignon, C., Bédrin, C. and Weill, R., 1982. Application of Eddy Currents to the In-Process Measurement of the Gap in E.C.M. *CIRP Annals - Manufacturing Technology*, 31(1), pp.115–118.

Bilgi, D.S., Jain, V.K., Shekhar, R. and Kulkarni, A. V., 2006. Hole quality and interelectrode gap dynamics during pulse current electrochemical deep hole drilling. *The International Journal of Advanced Manufacturing Technology*, 34(1-2), pp.79–95.

Burkert, S., Schulze, H., Gmelin, T. and Leone, M., 2009. THE PULSE ELECTROCHEMICAL MICROMACHINING (PECMM) - SPECIFICATIONS OF THE PULSE UNITS -. *International Journal of Material Forming*, 2(1), pp.645–648.

Cagnon, L., Kirchner, V., Kock, M., Schuster, R., Ertl, G., Gmelin, W.T. and Kück, H., 2003. Electrochemical Micromachining of Stainless Steel by Ultrashort Voltage Pulses. *Zeitschrift für Physikalische Chemie*, 217(4-2003), pp.299–314.

Campbell, D., Harper, J., Natham, Vinodhkumar, Xiao, F. and Sundararajan, R., 2008. A Compact High Voltage Nanosecond Pulse Generator. In: *Proc. ESA Annual Meeting on Electrostatics 2008*. pp.1–12.

Çaydaş, U., Hasçalık, A. and Ekici, S., 2009. An adaptive neuro-fuzzy inference system (ANFIS) model for wire-EDM. *Expert Systems with Applications*, 36(3), pp.6135–6139.

Chang, D.-Y., Shen, P.-C., Hung, J.-C., Lee, S.-J. and Tsui, H.-P., 2011. Process Simulation–Assisted Fabricating Micro-Herringbone Grooves for a Hydrodynamic Bearing in Electrochemical Micromachining. *Materials and Manufacturing Processes*, 26(12), pp.1451–1458.

Cheng, K., 2008. *Machining dynamics: Fundamentals, applications and practices*. London: Springer.

Choi, S.H., Kim, B.H., Shin, H.S., Chung, D.K. and Chu, C.N., 2013. Analysis of the electrochemical behaviors of WC–Co alloy for micro ECM. *Journal of Materials Processing Technology*, 213(4), pp.621–630.

Choi, S.H., Ryu, S.H., Choi, D.K. and Chu, C.N., 2007. Fabrication of WC micro-shaft by using electrochemical etching. *The International Journal of Advanced Manufacturing Technology*, 31(7-8), pp.682–687.

Clark, W.G. and McGeough, J. a., 1977. Temperature distribution along the gap in electrochemical machining. *Journal of Applied Electrochemistry*, 7(4), pp.277–286.

Clifton, D., Mount, A., Alder, G. and Jardine, D., 2002. Ultrasonic measurement of the inter-electrode gap in electrochemical machining. *International Journal of Machine Tools and Manufacture*, 42(11), pp.1259–1267.

Van Damme, S., Hotoiu, E.L., Albu, C., Weyns, G., Deconinck, D. and Deconinck, J., 2011. Double Layer Effects in Computational Electrochemistry. In: *The 219th ECS meeting*.

Danilovic, M., Chen, Z., Wang, R., Luo, F., Boroyevich, D. and Mattavelli, P., 2011. Evaluation of the switching characteristics of a gallium-nitride transistor. In: *2011 IEEE Energy Conversion Congress and Exposition*. IEEE, pp.2681–2688.

Data Delay Devices, 2008. *Selection Guide - Pulse Generator & Oscillators*. [online] Available at: <http://www.datadelay.com/datasheets/3d7622.pdf> [Accessed 15 Jul. 2014].

Datta, M. and Landolt, D., 1981. Electrochemical machining under pulsed current conditions. *Electrochimica Acta*, 26(7), pp.899–907.

Datta, M. and Landolt, D., 2000. Fundamental aspects and applications of electrochemical microfabrication. *Electrochimica Acta*, 45(15-16), pp.2535–2558.

Davydov, a. D., Volgin, V.M. and Lyubimov, V. V., 2004. Electrochemical machining of metals: Fundamentals of electrochemical shaping. *Russian Journal of Electrochemistry*, 40(12), pp.1230–1265.

Deconinck, D., Van Damme, S. and Deconinck, J., 2012a. A temperature dependent multi-ion model for time accurate numerical simulation of the electrochemical machining process. Part I: Theoretical basis. *Electrochimica Acta*, 60, pp.321–328.

Deconinck, D., Van Damme, S. and Deconinck, J., 2012b. A temperature dependent multi-ion model for time accurate numerical simulation of the electrochemical machining process. Part II: Numerical simulation. *Electrochimica Acta*, 69, pp.120–127.

Deconinck, J., 1992. *Current Distributions and Electrode Shape Changes in Electrochemical Systems*. Berlin, Heidelberg/New York: Springer-Verlag.

Delta Tau Data Systems, 2006. *Installation Manual: Geo Direct PWM Amplifiers*. pp.1–78.

Delta Tau Data Systems, 2009. USER MANUAL: Acc24E2 - Axis Expansion Board. (818).

Delta Tau Data Systems, 2011. User manual: Acc11E. (818).

ECMTEC GmbH, 2012. *ECMTEC Website*. [online] Available at: <http://www. ecmtec.com/> [Accessed 6 Aug. 2014].

EMAG, 2012. *MicroECM Machine brochure EMAG*. [online] Available at: <http://www.interempresas.net/FeriaVirtual/Catalogos_y_documentos/1163/EMAG-MicroECM-ingles.pdf> [Accessed 6 Aug. 2014].

EMAG GmbH, 2014. *EMAG Website - ECM / PECM Machines*. [online] Available at: <http://www.emag.com/machines/ecm-pecm-machines/cs-ci.html> [Accessed 6 Aug. 2014].

Fairchild-Semiconductor, 2009. *FDMS7578 Power Trench N-MOSFET*. [online] Available at: <http://www.fairchildsemi.com/ds/FD/FDMS7578.pdf> [Accessed 12 May 2013].

Fan, Z.-W. and Hourng, L.-W., 2011. Electrochemical micro-drilling of deep holes by rotational cathode tools. *The International Journal of Advanced Manufacturing Technology*, 52(5-8), pp.555–563.

Fan, Z.-W., Hourng, L.-W. and Lin, M.-Y., 2012. Experimental investigation on the influence of electrochemical micro-drilling by short pulsed voltage. *The International Journal of Advanced Manufacturing Technology*, 61(9-12), pp.957–966.

Floridor, G., Van den Bossche, B., Nelissen, G., Bortels, L. and Deconinck, J., 2004. Numerical investigation of transient current density distributions for multi-ion electrolytes at a rotating disk electrode. *Analytical chemistry*, 76(18), pp.5579–90.

Fujii, Y., Muramoto, Y. and Shimizu, N., 2010. Analysis of electric double layer in aqueous solutions of sodium chloride. *2010 Annual Report Conference on Electrical Insulation and Dielectic Phenomena*, pp.1–4.

Gao, W., Arai, Y., Shibuya, A., Kiyono, S. and Park, C.H., 2006. Measurement of multi-degree-of-freedom error motions of a precision linear air-bearing stage. *Precision Engineering*, 30(1), pp.96–103.

Haisch, T., 2002. *High rate electrochemical dissolution of iron- based alloys in NaCl and NaNO3 electrolytes*. Max-Planck-Institut für Metallforschung Stuttgart.

Haisch, T., Mittemeijer, E. and Schultze, J.W., 2001. Electrochemical machining of the steel 100Cr6 in aqueous NaCl and NaNO3 solutions: microstructure of surface films formed by carbides. *Electrochimica Acta*, 47(1-2), pp.235–241.

Haisch, T., Mittemeijer, E.J. and Schultze, J.W., 2004. High rate anodic dissolution of 100Cr6 steel in aqueous NaNO3 solution. pp.997–1005.

Hocheng, H., Sun, Y.H., Lin, S.C. and Kao, P.S., 2003. A material removal analysis of electrochemical machining using flat-end cathode. *Journal of Materials Processing Technology*, 140(1-3), pp.264–268.

Hotoiu, E.L., Van Damme, S., Deconinck, D., Albu, C., Weyns, G. and Deconinck, J., 2011. Development of simulation software package for nano-pulsed electrochemical micro machining. In: *The 219th ECS meeting*.

Hotoiu, L., Van Damme, S. and Deconinck, J., 2011. Progress report PECMM simulations WP3-M4. pp.1–18.

Huang, S.H., Huang, F.Y. and Yan, B.H., 2004. Fracture strength analysis of micro WC-shaft manufactured by micro-electro-discharge machining. *The International Journal of Advanced Manufacturing Technology*, 26(1-2), pp.68–77.

Hui, C., Wang, Y.-K., Wang, Z.-L. and Zhao, W.-S., 2011. Effects of Complexing Agent on Electrochemical Micro Machining of Stainless Steel. *American Journal of Nanotechnology*, 2(1), pp.100–105.

Huo, D. and Cheng, K., 2008. A dynamics-driven approach to the design of precision machine tools for micro-manufacturing and its implementation perspectives. *Proceedings of the Institution of Mechanical Engineers, Part B: Journal of Engineering Manufacture*, 222(1), pp.1–13.

Huo, D., Cheng, K. and Wardle, F., 2010a. Design of a five-axis ultra-precision micro-milling machine-UltraMill. Part 1: Holistic design approach, design considerations and specifications. *International Journal of Advanced Manufacturing Technology*, 47, pp.867–877.

Huo, D., Cheng, K. and Wardle, F., 2010b. Design of a five-axis ultra-precision micro-milling machine-UltraMill. Part 2: Integrated dynamic modelling, design optimisation and analysis. *International Journal of Advanced Manufacturing Technology*, 47, pp.879–890.

IIT Kharagpur, 2014. *Lesson 38. Electro Chemical Machining - Non-conventional Manufacturing processes*. [online] Available at: <http://nptel.iitm.ac.in/courses/Webcourse-contents/IIT Kharagpur/Manuf Proc II/pdf/LM-38.pdf> [Accessed 22 Sep. 2014].

Indec, 2014. *Indec 'ET' ECM Machines*. [online] Available at: <http://www.indec-ecm.com/en/equipment/ekp/ekp/ET500-1&ET1000-1/> [Accessed 26 Aug. 2014].

Intersil, 2010. *Datasheet: EL5166 - 1.4GHz Current Feedback Amplifiers with Enable*. [online] Available at: <http://www.intersil.com/content/dam/intersil/documents/el51/el5166-67.pdf> [Accessed 12 Apr. 2013].

Jain, V.K. and Pandey, P.C., 1981. Tooling Design for ECM—A Finite Element Approach. *Journal of Engineering for Industry*, 103(2), p.183.

Jauregui, D., 2009. *Reducing Ringing Through PCB Layout Techniques*. Texas Instruments, pp.1–6.

Jo, C.H., Kim, B.H., Shin, H.S., Chung, D.K., Kwon, M.H. and Chu, C.N., 2008. Micro Electrochemical Machining for Complex Internal Micro Features. *Internal Conference on Smart Manufacturing Application*, pp.247–250.

Kamaraj, A.B. and Sundaram, M.M., 2013. Mathematical modeling and verification of pulse electrochemical micromachining of microtools. *The International Journal of Advanced Manufacturing Technology*.

Kamaraj, A.B., Sundaram, M.M. and Mathew, R., 2013. Ultra high aspect ratio penetrating metal microelectrodes for biomedical applications. *Microsystem Technologies*, 19(2), pp.179–186.

Kenney, J. a., Hwang, G.S. and Shin, W., 2004. Two-dimensional computational model for electrochemical micromachining with ultrashort voltage pulses. *Applied Physics Letters*, 84(19), p.3774.

Kim, B., Na, C., Lee, Y., Choi, D. and Chu, C., 2005a. Micro Electrochemical Machining of 3D Micro Structure Using Dilute Sulfuric Acid. *CIRP Annals Manufacturing Technology*, 54(1), pp.191–194.

Kim, B.H., Ryu, S.H., Choi, D.K. and Chu, C.N., 2005b. Micro electrochemical milling. *Journal of Micromechanics and Microengineering*, 15(1), pp.124–129.

Kirchner, V., Cagnon, L., Schuster, R. and Ertl, G., 2001. Electrochemical machining of stainless steel microelements with ultrashort voltage pulses. *Applied Physics Letters*, 79(11), p.1721.

Kock, M., Kirchner, V. and Schuster, R., 2003. Electrochemical micromachining with ultrashort voltage pulses–a versatile method with lithographical precision. *Electrochimica Acta*, 48(20-22), pp.3213–3219.

Kozak, J., 2001. Computer simulation system for electrochemical shaping. *Journal of Materials Processing Technology*, 109(3), pp.354–359.

Kozak, J., Dabrowski, L., Lubkowski, K., Rozenek, M. and Søawin, R., 2000. CAE-ECM system for electrochemical technology of parts and tools. *Journal of Materials Processing Technology*, 107(1-3), pp.293–299.

Kozak, J., Gulbinowicz, D. and Gulbinowicz, Z., 2008. The Mathematical Modeling and Computer Simulation of Pulse Electrochemical Micromachining. In: *IAENG TRANSACTIONS ON ENGINEERING TECHNOLOGIES VOLUME 2: Special Edition of the World Congress on Engineering and Computer Science*. San Francisco (CA): AIP Conf. Proc., pp.174–185.

Kozak, J., Rajurkar, K.P. and Makkar, Y., 2004a. Selected problems of micro-electrochemical machining. *Journal of Materials Processing Technology*, 149(1-3), pp.426–431.

Kozak, J., Rajurkar, K.P. and Makkar, Y., 2004b. Study of Pulse Electrochemical Micromachining. *Journal of Manufacturing Processes*, 6(1), pp.7–14.

Kozak, J., Rajurkar, K.P. and Ross, R.F., 1991. Computer Simulation of Puse Electrochemical Machining (PECM). *Journal of Materials Processing Technology*, 28, pp.149–157.

Labib, A.W., Keasberry, V.J., Atkinson, J. and Frost, H.W., 2011. Expert Systems with Applications Towards next generation electrochemical machining controllers : A fuzzy logic control approach to ECM. *Expert Systems With Applications*, 38(6), pp.7486–7493.

Landolt, D., Chauvy, P.-F. and Zinger, O., 2003. Electrochemical micromachining, polishing and surface structuring of metals: fundamental aspects and new developments. *Electrochimica Acta*, 48(20-22), pp.3185–3201.

Lee, E.S., Baek, S.Y. and Cho, C.R., 2007. A study of the characteristics for electrochemical micromachining with ultrashort voltage pulses. *The International Journal of Advanced Manufacturing Technology*, 31(7-8), pp.762–769.

Lee, E.S., Park, J.W. and Moon, Y.H., 2002. A Study on Electrochemical Micromachining for Fabrication of Microgrooves in an Air-Lubricated Hydrodynamic Bearing. *International Journal of Advanced Manufacturing Technology*, 20(10), pp.720–726.

Li, Z. and Ji, H., 2009. Machining Accuracy Prediction of Aero-engine Blade in Electrochemical Machining Based on BP Neural Network. In: *Proceedings of the 2009 International Workshop on Information Security and Application (IWISA 2009) ISBN 978-952-5726-06-0*. Qingdao, China: ACADEMY PUBLISHER, pp.9–12.

Lin, C.-T., Chung, I.-F. and Huang, S.-Y., 2001. Improvement of machining accuracy by fuzzy logic at corner parts for wire-EDM. *Fuzzy Sets and Systems*, 122(3), pp.499–511.

Linear Technology, 2014. *LTC6903/LTC6904 - 1kHz to 68MHz Serial Port Programmable Oscillator*. [online] Available at: <http://cds.linear.com/docs/Datasheet/69034fc.pdf> [Accessed 15 Jul. 2014].

Liu, Y., Zhu, D., Zeng, Y. and Yu, H., 2011. Development of microelectrodes for electrochemical micromachining. *The International Journal of Advanced Manufacturing Technology*, 55(1-4), pp.195–203.

Liu, Y., Zhu, D. and Zhu, L., 2012. Micro electrochemical milling of complex structures by using in situ fabricated cylindrical electrode. *The International Journal of Advanced Manufacturing Technology*, 60(9-12), pp.977–984.

Lu, X. and Leng, Y., 2005. Electrochemical micromachining of titanium surfaces for biomedical applications. *Journal of Materials Processing Technology*, 169(2), pp.173–178.

Lu, Y., Liu, K. and Zhao, D., 2010. Experimental investigation on monitoring interelectrode gap of ECM with six-axis force sensor. *The International Journal of Advanced Manufacturing Technology*, 55(5-8), pp.565–572.

Luo, X., Cheng, K., Webb, D. and Wardle, F., 2005. Design of ultraprecision machine tools with applications to manufacture of miniature and micro components. *Journal of Materials Processing Technology*, 167(2-3), pp.515–528.

Marla, D., Joshi, S.S. and Mitra, S.K., 2008. Modeling of electrochemical micromachining: comparison to experiments. *Journal of Micro/Nanolithography, MEMS and MOEMS*, 7(3), p.033015.

Masuzawa, T., Fujino, M., Kobayashi, K., Suzuki, T. and Kinoshita, N., 1985. Wire Electro-Discharge Grinding for Micro-Machining. *CIRP Annals - Manufacturing Technology*, 34(1), pp.431–434.

Mathew, R. and Sundaram, M.M., 2012. Modeling and fabrication of micro tools by pulsed electrochemical machining. *Journal of Materials Processing Technology*, 212(7), pp.1567–1572.

Mathworks, 2014a. *Trapezoidal-shaped membership function*. [online] Available at: <http://www.mathworks.co.uk/help/fuzzy/trapmf.html> [Accessed 14 Nov. 2013].

Mathworks, 2014b. *Triangular-shaped membership function*. [online] Available at: <http://www.mathworks.co.uk/help/fuzzy/trimf.html> [Accessed 14 Nov. 2013].

Maxim, 2007. *Datasheet: MAX038, High-Frequency Waveform Generator*. [online] Available at: <http://datasheets.maximintegrated.com/en/ds/MAX038.pdf> [Accessed 19 Apr. 2012].

McGeough, J.A., 1974. *Principles of Electrochemical Machining*. London: Chapman and Hall.

Mediliyegedara, T.K.K.R., Silva, a. K.M. De, Harrison, D.K. and McGeough, J. a., 2005. New developments in the process control of the hybrid electro chemical discharge machining (ECDM) process. *Journal of Materials Processing Technology*, 167(2-3), pp.338–343.

Meijer, J. and Veringa, J.C.M., 1984. Characteristic numbers to describe the detail transfer quality of electro-chemical machining. *Precision Engineering*, 6(2), pp.79–82.

Mithu, M. a. H., Fantoni, G. and Ciampi, J., 2011a. The effect of high frequency and duty cycle in electrochemical microdrilling. *The International Journal of Advanced Manufacturing Technology*, 55(9-12), pp.921–933.

Mithu, M.A.H., Fantoni, G. and Ciampi, J., 2011b. A step towards the in-process monitoring for electrochemical microdrilling. *The International Journal of Advanced Manufacturing Technology*, 57(9-12), pp.969–982.

Mithu, M.A.H., Fantoni, G., Ciampi, J. and Santochi, M., 2012. On how tool geometry, applied frequency and machining parameters influence electrochemical microdrilling. *CIRP Journal of Manufacturing Science and Technology*, 5(3), pp.202–213.

Muetze, A. and Oh, H.W., 2008. Design Aspects of Conductive Microfiber Rings for Shaft-Grounding Purposes. *IEEE Transactions on Industry Applications*, 44(6), pp.1749–1757.

Muir, R.N., Curry, D.R., Mill, F., Sherlock, A. and Mount, a R., 2007. Real-time parameterization of electrochemical machining by ultrasound measurement of the interelectrode gap. *Proceedings of the Institution of Mechanical Engineers, Part B: Journal of Engineering Manufacture*, 221(4), pp.551–558.

Mukherjee, S.K., Kumar, S. and Srivastava, P.K., 2005. Effect of Over Voltage on Material Removal Rate During Electrochemical Machining. 8(1), pp.23–28.

Mukherjee, S.K., Kumar, S. and Srivastava, P.K., 2007. Effect of electrolyte on the current-carrying process in electrochemical machining. *Proceedings of the Institution of Mechanical Engineers, Part C: Journal of Mechanical Engineering Science*, pp.1415–1419.

Narayanan, O.H., Hinduja, S. and Noble, C.F., 1986. The prediction of workpiece shape during electrochemical machining by the boundary element method. *International Journal of Machine Tool Design and Research*, 26(3), pp.323–338.

Nor, M.K.M., 2010. *Development of the UMAC-Based Control System with Application to 5-Axis Ultraprecision Micromilling Machines*. Brunel Univeristy.

NXP, 2014. *UM10204 - I2C-bus specification and user manual*. [online] Available at: <http://www.nxp.com/documents/user_manual/UM10204.pdf> [Accessed 21 Apr. 2013].

Oh, K.S., 2000. MOSFET Basics, Application Note AN9010. *Fairchild Semiconductor*, pp.1–37.

Owlad, M., Aroua, M.K., Daud, W.A.W. and Baroutian, S., 2009. Removal of Hexavalent Chromium-Contaminated Water and Wastewater: A Review. *Water, Air, and Soil Pollution*, 200(1-4), pp.59–77.

Ozkeskin, F.M., 2008. *Feedback controlled high frequency electrochemical micromachining*. Texas A&M University.

Park, B.J., Kim, B.H. and Chu, C.N., 2006. The Effects of Tool Electrode Size on Characteristics of Micro Electrochemical Machining. *CIRP Annals - Manufacturing Technology*, 55(1), pp.197–200.

Pathak, B.A.D., 2001. *APPLICATION NOTE AN0002: MOSFET/IGBT DRIVERS THEORY AND APPLICATIONS*. pp.1–28.

Pattavanitch, J., Hinduja, S. and Atkinson, J., 2010. Modelling of the electrochemical machining process by the boundary element method. *CIRP Annals - Manufacturing Technology*, 59(1), pp.243–246.

pECM Systems, 2014. *pECM Systems Website*. [online] Available at: <http://pecmsystems.co.uk/> [Accessed 6 Aug. 2014].

Pham, D.T., Dimov, S.., Bigot, S., Ivanov, A. and Popov, K., 2004. Micro-EDM—recent developments and research issues. *Journal of Materials Processing Technology*, 149(1-3), pp.50–57.

Purcar, M., Bortels, L., Vandenbossche, B. and Deconinck, J., 2004. 3D electrochemical machining computer simulations. *Journal of Materials Processing Technology*, 149(1-3), pp.472–478.

Rajurkar, K.P., Kozak, J., Wei, B. and McGeough, J.A., 1993. Study of Pulse Electrochemical Machining Characteristics. *CIRP Annals - Manufacturing Technology*, 42(1), pp.231–234.

Rajurkar, K.P., Levy, G., Malshe, A., Sundaram, M.M., McGeough, J., Hu, X., Resnick, R. and DeSilva, A., 2006. Micro and Nano Machining by Electro-Physical and Chemical Processes. *CIRP Annals - Manufacturing Technology*, 55(2), pp.643–666.

Rajurkar, K.P., Schnacker, C.L. and Packard, H., 1988. Some Aspects of ECM Performance and Control. *Annals of the CIRP*, 37(1), pp.183–186.

Rajurkar, K.P., Wei, B., Kozak, J. and McGeough, J.A., 1995. Modelling and Monitoring Interelectrode Gap in Pulse Electrochemical Machining. *CIRP Annals - Manufacturing Technology*, 44(1), pp.177–180.

Ruszaj, a, Zybura, M., Żurek, R. and Skrabalak, G., 2003. Some aspects of the electrochemical machining process supported by electrode ultrasonic vibrations optimization. *Proceedings of the Institution of Mechanical Engineers, Part B: Journal of Engineering Manufacture*, 217(10), pp.1365–1371.

Schulze, H., Borkenhagen, D. and Burkert, S., 2008. Demands on process and process energy sources for the electro-erosive and electrochemical micro machining. *Journal of Materials*, 1, pp.1383 – 1386.

Schulze, H.-P., 2009. Problems of the processing accuracy for electro-erosion and electro-chemical machining processes. *International Journal of Material Forming*, 2(S1), pp.641–644.

Schuster, R., 2007. Electrochemical microstructuring with short voltage pulses. *Chemphyschem A European Journal Of Chemical Physics And Physical Chemistry*, 8(1), pp.34–39.

Schuster, R. and Kirchner, V., 2004. *Method for electrochemically processing material.* [online] US 6689269 B1. Available at: <http://ip.com/pdf/patent/US6689269.pdf>.

Schuster, R., Kirchner, V., Allongue, P. and Ertl, G., 2000. Electrochemical Micromachining. *Science*, 289(5476), pp.98–101.

Schuurman, A. and Faber, J., 1997. *(WO1997035810) A method of removing iron compounds and chromium compounds from an aqueous electrolytic soultion as well as the use of this method in electrochemical machining*. WO/1997/035810.

Sen, M. and Shan, H.S., 2005. A review of electrochemical macro- to micro-hole drilling processes. *International Journal of Machine Tools and Manufacture*, 45(2), pp.137–152.

Shin, H.S., Kim, B.H. and Chu, C.N., 2008. Analysis of the side gap resulting from micro electrochemical machining with a tungsten wire and ultrashort voltage pulses. *Journal of Micromechanics and Microengineering*, 18(7), p.075009.

De Silva, A.K.M., Altena, H.S.J. and McGeough, J.A., 2000. Precision ECM by Process Characteristic Modelling. *CIRP Annals - Manufacturing Technology*, 49(1), pp.151–155.

De Silva, A.K.M., Altena, H.S.J. and McGeough, J.A., 2003. Influence of Electrolyte Concentration on Copying Accuracy of Precision-ECM. *CIRP Annals - Manufacturing Technology*, 52(1), pp.165–168.

Skrabalak, G., Zybura-Skrabalak, M. and Ruszaj, A., 2004. Building of rules base for fuzzy-logic control of the ECDM process. *Journal of Materials Processing Technology*, 149(1-3), pp.530–535.

Spieser, A., 2011. *Master Thesis: Investigation of the interelectrode gap behavior and its controllability in Pulsed Electrochemical Micromachining (μPECM).* Brunel University, pp.1–115.

Spieser, A. and Ivanov, A., 2013. Recent developments and research challenges in electrochemical micromachining (μECM). *The International Journal of Advanced Manufacturing Technology*.

Spieser, A. and Ivanov, A., 2014a. Design of a Pulse Power Supply Unit for Micro ECM. *International Journal of Advanced Manufacturing Technology*.

Spieser, A. and Ivanov, A., 2014b. Design of an electrochemical micromachining machine. *The International Journal of Advanced Manufacturing Technology*.

Stanev, P.T., Wardle, F. and Corbett, J., 2004. Investigation of grooved hybrid air bearing performance. *Proceedings of the Institution of Mechanical Engineers, Part K: Journal of Multi-body Dynamics*, 218(2), pp.95–106.

STMicroelectronics, 2004. *74V1G08 SINGLE 2-INPUT AND GATE Datasheet*. [online] Available at: <http://www.st.com/st-web-ui/static/active/en/resource/technical/document/datasheet/CD00001409.pdf> [Accessed 25 Feb. 2013].

Swain, A. k., 2010. *Preparation of Coated Microtools for Electrochemical Machining Applications*. University of Nebraska.

Tang, T. and Burkhart, C., 2009. Hybrid MOSFET/driver for ultra-fast switching. *IEEE Transactions on Dielectrics and Electrical Insulation*, 16(4), pp.967–970.

Taylor, R. and Manack, R., 2012. *Controlling switch-node ringing in synchronous buck converters*. *Analog Applications Journal*.

Technologyuk.net, 2011. *The characteristic voltage and current curve for a Zener diode*. [online] Available at: <http://www.technologyuk.net/electronics/electrical_principles/the_diode.shtml> [Accessed 21 Jul. 2014].

Thanigaivelan, R. and Arunachalam, R., 2010. Experimental Study on the Influence of Tool Electrode Tip Shape on Electrochemical Micromachining of 304 Stainless Steel. *Materials and Manufacturing Processes*, 25(10), pp.1181–1185.

TI, 2008. *Datasheet: UCC27200/1 - 120-V Boot , 3-A Peak , High Frequency , High-Side / Low-Side Driver*. [online] Available at: <http://www.ti.com/lit/ds/symlink/ucc27201.pdf> [Accessed 17 Apr. 2014].

Trimmer, A.L., Hudson, J.L., Kock, M. and Schuster, R., 2003. Single-step electrochemical machining of complex nanostructures with ultrashort voltage pulses. *Applied Physics Letters*, 82(19), p.3327.

Tsui, H.-P., Hung, J.-C., You, J.-C. and Yan, B.-H., 2008. Improvement of Electrochemical Microdrilling Accuracy Using Helical Tool. *Materials and Manufacturing Processes*, 23(5), pp.499–505.

Wang, M., Zhu, D., Qu, N.S. and Zhang, C.Y., 2007. Preparation of Turbulated Cooling Hole for Gas Turbine Blade Using Electrochemical Machining. *Key Engineering Materials*, 329, pp.699–704.

Wang, M.H. and Zhu, D., 2009. Fabrication of multiple electrodes and their application for micro-holes array in ECM. *The International Journal of Advanced Manufacturing Technology*, 41(1-2), pp.42–47.

Wang, Y., Chen, H., Wang, Z., Zhou, Z. and Shan, D., 2010. Development of a Soft-Computer Numerical Control System for Micro - Electrochemical Machining. 1(2), pp.51–55.

Wardle, F.P., Bond, C., Wilson, C., Cheng, K. and Huo, D., 2010. Dynamic characteristics of a direct-drive air-bearing slide system with squeeze film damping. *International Journal of Advanced Manufacturing Technology*, 47, pp.911–918.

Wei, B., 1994. *Modeling and analysis of pulse electrochemical machining*. The University of Nebraska – Lincoln.

Wei, B., Li, W. and Lamphere, M.S., 2005. *Electrochemical machining tool assembly and method of monitoring electrochemical machining*. US 6968290.

Wei, B., Rajurkar, K.P. and Talpallikar, S., 1996. On-line identification of interelectrode gap sizes in pulse electrochemical machining (PECM). In: *Proceedings of the symposium on HighRate Metal Dissolution Processes*. p.248.

Winbro Group Technologies, 2012. *Winbro Group - Systems*. [online] Available at: <http://www.winbrogroup.com/systems/> [Accessed 6 Aug. 2014].

Woolf, P., 2014. *Design of Experiments: Taguchi Methods*. [online] Available at: <https://controls.engin.umich.edu/wiki/images/0/0b/Lecture.25.pdf> [Accessed 3 Feb. 2014].

Yang, I., Park, M.S. and Chu, C.N., 2009. Micro ECM with ultrasonic vibrations using a semi-cylindrical tool. *International Journal of Precision Engineering and Manufacturing*, 10(2), pp.5–10.

Yong, L., Di, Z., Yongbin, Z., Shaofu, H. and Hongbing, Y., 2010. Experimental Investigation on Complex Structures Machining by Electrochemical Micromachining Technology. *Chinese Journal of Aeronautics*, 23(5), pp.578–584.

Yong, L., Yunfei, Z., Guang, Y. and Liangqiang, P., 2003. Localized electrochemical micromachining with gap control. *Sensors and Actuators A: Physical*, 108(1-3), pp.144–148.

Yonghua, L. and Kai, L., 2010. Fuzzy Controlling Interelectrode Gap of ECM Based on 6 Dimensional Forces and Machining Current. In: *2010 International Conference on Intelligent System Design and Engineering Application*. Ieee, pp.775–779.

Zare Chavoshi, S., 2011. Analysis and predictive modeling of performance parameters in electrochemical drilling process. *The International Journal of Advanced Manufacturing Technology*, 53(9-12), pp.1081–1101.

Zemann, R., Reiss, P.W., Schörghofer, P. and Bleicher, F., 2012. *Cutting Edge Research in New Technologies - Chapter 1: Some Contributions at the Technology of Electrochemical Micromachining with Ultra Short Voltage Pulses*. InTech, pp.3–29.

Zhang, Y.J., Tang, Y.J., Liu, X.K., Guo, Z.N. and Li, F., 2009. Development of Ultra-Short Pulse Power Supply Applicable to Micro-ECM. *Materials Science Forum*, 626-627, pp.369–374.

Zhang, Z., Wang, Y., Chen, F. and Mao, W., 2011. A Micro-machining system based on electrochemical dissolution of material. *Russian Journal of Electrochemistry*, 47(7), pp.819–824.

Zhang, Z., Zhu, D., Qu, N. and Wang, M., 2007. Theoretical and experimental investigation on electrochemical micromachining. *Microsystem Technologies*, 13(7), pp.607–612.

Zhu, D. and Xu, H.Y., 2002. Improvement of electrochemical machining accuracy by using dual pole tool. *Journal of Materials Processing Technology*, 129(1-3), pp.15–18.

LIST OF FIGURES IN APPENDICES

Appendix 3

Appendix 3 Figure 1: Picture of the ChipKIT Max32 development board 211
Appendix 3 Figure 2: Typical application of the I2C bus in a system (NXP, 2014) 212
Appendix 3 Figure 3: The Structure of an Enhancement Type MOSFET and its Operation; (a) When VGS (Gate-source voltage) is not supplied; (b) When VGS (Gate-source voltage) is supplied (Oh, 2000)....213
Appendix 3 Figure 4: Symbol and equivalent circuit of a MOSFET (Pathak, 2001) 214
Appendix 3 Figure 5: MOSFET Turn-On and Turn-Off procedures 215
Appendix 3 Figure 6: Functional block diagram of the magnetocoupler ADuM1100(Analog Devices, 2012) 217
Appendix 3 Figure 7: Basic resistive current sensing amplifier 218
Appendix 3 Figure 8: Typical op amp circuit, as designed (a) and with parasitics (b) (Ardizzoni, 2005)....220
Appendix 3 Figure 9: Illustration of stripline routing (Altera, 2001)....220

Appendix 4

Appendix 4 Figure 1: Schematic diagram of the first PSU prototype and its interfaces 221
Appendix 4 Figure 2: Waveform selection using inputs A0 and A1 (Maxim, 2007) 222
Appendix 4 Figure 3: MAX038 pin configuration (Maxim, 2007) 223
Appendix 4 Figure 4: Chart representing the output frequency as a function of IIN, for different CFvalues (Maxim, 2007)....223
Appendix 4 Figure 5: Schematic diagram of the MAX038 signal generator 223
Appendix 4 Figure 6: Electrical schematic of the circuitry used to set VDADJ 226
Appendix 4 Figure 7: Electrical schematic of the potentiometer AD840 setting up the IIN and DADJ 226
Appendix 4 Figure 8: Schematic diagram of the two ultrafast comparators LT1719 converting the MAX038 output signal to a 5V logic level....227
Appendix 4 Figure 9: Electrical schematic of the control circuitry part 228
Appendix 4 Figure 10: Picture of the printed circuit board layout of the control circuitry....229
Appendix 4 Figure 11: Picture of the control board of the first prototype 229
Appendix 4 Figure 12: Simplified diagram of the power part connect to the interelectrode gap ..230
Appendix 4 Figure 13: Diagram representing the timing of the 2 signals controlling the MOSFETs SW1 and SW2....231
Appendix 4 Figure 14: Schematic diagram of the dead-time circuitry of the first prototype....232

Appendix 4 Figure 15: CAD Model of the package (Power 56) and representation of the MOSFET FDMS7578 (Fairchild-Semiconductor, 2009) 233
Appendix 4 Figure 16: Schematic diagram of the MOSFETs and their drivers 234
Appendix 4 Figure 17: Picture of the printed circuit board layout of the control circuitry 235
Appendix 4 Figure 18: Picture of the power board of the first prototype 235
Appendix 4 Figure 19: Electrical schematic of the current sensing circuitry featuring the amplifier EL5166ISZ...236
Appendix 4 Figure 20: Schematic of the OCP circuitry..237
Appendix 4 Figure 21: Peak detector circuitry 238
Appendix 4 Figure 22: Flowchart describing the firmware workflow running on the first PSU prototype 239
Appendix 4 Figure 23: the digitalPotWrite() function used to communicate with the AD8402 digital potentiometer 240
Appendix 4 Figure 24: Picture of the fully assembled first PSU prototype 241
Appendix 4 Figure 25: C1 (yellow): current measured from external current sensor (1V/div.,1V/A); C2 (pink): voltage measured across the load, after the cables (2V/div.); C3 (cyan): voltage measured at the output of the pulse PSU, on the board connectors (2V/div.). Frequency: 2.5MHz duty cycle: 20%. 242
Appendix 4 Figure 26: C1 (yellow): current measured from external current sensor (1V/div.,1V/A); C2 (pink): voltage measured across the load, after the cables (2V/div.); C3 (cyan): voltage measured at the output of the pulse PSU, on the board connectors (2V/div.). Frequency: 800kHz duty cycle: 20%...243
Appendix 4 Figure 27: Signals on the current sensing board 243

Appendix 5

Appendix 5 Figure 1: Model of the second prototype of the pulse PSU.....................................245
Appendix 5 Figure 2: Simulation result: evolution of the IEG voltage (V) over time (s) in steady state..246
Appendix 5 Figure 3: Electrical schematic diagram of the power stage used in the Simulink simulation 247
Appendix 5 Figure 4: Simulation result: evolution of the IEG voltage (V) over time (s) in steady state when the parasitics have been added 247

Appendix 6

Appendix 6 Figure 2: Electrical schematic diagram of the oscillator and the pulse generator......248

Appendix 6 Figure 3: Control circuitry of the second PSU prototype 250

Appendix 6 Figure 4: Drawing representing the 4 different control signal used to change the pulse shape when Channel A is selected...250

Appendix 6 Figure 5: Drawing representing the 4 different control signal used to change the pulse shape when Channel B is selected 251

Appendix 6 Figure 6: Drawing of the different pulse shapes that can be obtained in the different configuration 252

Appendix 6 Figure 7: Electrical schematic of the dead time circuitry used in the PSU................252

Appendix 6 Figure 8: Measurement of the dead time between the control signals to the 2 low side switches of the H-bridge; frequency: 5MHz, duty cycle: 25% 253

Appendix 6 Figure 9: Schematic of the MOSFETs switching between the PULSE and OFFSET voltages to be applied to the H-bridge 254

Appendix 6 Figure 10: Schematic of the MOSFETs in the H-bridge 255

Appendix 6 Figure 11: Output of the second PSU prototype without any snubber circuitry, in mode 3, 3V pulse and 1V negative offset, 2MHz with 25% Duty cycle, no load. 256

Appendix 6 Figure 12: Output of the second PSU prototype with snubber circuitry in mode 3, 3V pulse and 1V negative offset, 2MHz with 25% Duty cycle, no load...................................256

Appendix 6 Figure 13: Picture of the second PSU prototype being tested with a 1Ω load. 257

Appendix 6 Figure 14: C1: current (1V/A), C2: voltage; PSU in pulse mode 1: 3V pulse, no offset; 750kHz 25% duty cycle 257

Appendix 6 Figure 15: C2: voltage; PSU in pulse mode 2: 2VDC (positive) 258

Appendix 6 Figure 16: C1: current (1V/A), C2: voltage; PSU in pulse mode 3: 3V pulse, 1 V negative offset; 750kHz 25% duty cycle 258

Appendix 6 Figure 17: C1: current (1V/A), C2: voltage; PSU in pulse mode 4: 3V pulse, 1 V positive offset; 750kHz 25% duty cycle 259

Appendix 6 Figure 18: C1: current (1V/A), C2: voltage; PSU in pulse mode 5: 3V negative pulse, no offset; 750kHz 25% duty cycle 259

Appendix 6 Figure 19: C2: voltage; PSU in pulse mode 6: 2VDC (negative) 260

Appendix 6 Figure 20: C1 current (1V/A), C2: voltage; PSU in pulse mode 7: negative 3V pulse, 1 V positive offset; 750kHz 25% duty cycle 260

Appendix 6 Figure 21: C1 current (1V/A), C2: voltage; PSU in pulse mode 8: negative 3V pulse, 1 V negative offset; 750kHz 25% duty cycle 261

Appendix 6 Figure 22: Electrical diagram of the current sensing part on the OCP stage of the second prototype 262

Appendix 6 Figure 23: Picture of the OCP stage being tested and refined. 262
Appendix 6 Figure 24: C1: OCP threshold (380mV/A); C2: comparator output; C3: OCP signal (latched output); C4: current (380mV/A); 1MHz 25% duty cycle......................................263
Appendix 6 Figure 25: C1: OCP threshold (380mV/A); C2: comparator output; C3: OCP signal (latched output); C4: current (380mV/A); 1MHz 25% duty cycle (20ns/div) 263

Appendix 7

Appendix 7 Figure 1: Schematic diagram of the experimental setup 264
Appendix 7 Figure 2: Flowcharts of the different states of the programme controlling the test bench developed at Brunel...267
Appendix 7 Figure 3: Formula block in the LabVIEW programme of the test bench 267
Appendix 7 Figure 4: Screenshot of the tool approach performed on the test bench....................268
Appendix 7 Figure 5: Surface of the workpiece in trial 1 269
Appendix 7 Figure 6: Surface of the workpiece in trial 2 269
Appendix 7 Figure 7: Hole in the workpiece in trial 3...270
Appendix 7 Figure 8: Hole in the workpiece in trial 4..270
Appendix 7 Figure 9: Hole in the workpiece in trial 5...271
Appendix 7 Figure 10: Hole in the workpiece in trial 6...272
Appendix 7 Figure 11: Hole in the workpiece in trial 7...272
Appendix 7 Figure 12: Hole in the workpiece in trial 8...273

LIST OF TABLES IN APPENDICES

Appendix 2

Appendix 2 Table 1: Composition of the 100Cr6 alloy and calculation of $Kv\ alloy$ 210

Appendix 4

Appendix 4 Table 1: Value of RWB for different D values 224
Appendix 4 Table 2: Value of $VW2$ for different D values...225
Appendix 4 Table 3: Table summarizing the main characteristics of the MOSFET FDMS7578 .233
Appendix 4 Table 4: Description of the signals measured in Appendix 4 Figure 27....................244

Appendix 5

Appendix 5 Table 1: Table summarizing the parameters of the N-Channel MOSFET Simulink component used in the simulation 245

Appendix 1. LIST OF PUBLICATIONS

The outcome of this work was published in three different articles:

- Spieser A, Ivanov A (2013) Recent developments and research challenges in electrochemical micromachining (µECM). Int J Adv Manuf Technol. doi: 10.1007/s00170-013-5024-8
- Spieser A, Ivanov A (2014) Design of a Pulse Power Supply Unit for Micro ECM,. Int. J. Adv. Manuf. Technol. doi: 10.1007/s00170-014-6322-5
- Spieser A, Ivanov A (2014) Design of an Electrochemical Micromachining, Int. J. Adv. Manuf. Technol. doi: 10.1007/s00170-014-6332-3

Appendix 2. CALCULATION OF $K_{v\,alloy}$ FOR 100CR6

The workpiece that will be machined is made of 100Cr6 steel. Therefore the coefficient of electrochemical machinability $K_{v\,100Cr6}$ for this material has to be calculated. The composition of the alloy 100Cr6 is the following:

100Cr6 composition		F=	96500									
Material	C	Si	Mn	P	S	Cr	Mo	Al	Cu	On	Fe	**Total**
$\alpha_i(\%)$	0,99	0,25	0,35	0,00	0,02	1,48	0,10	0,05	0,30	0,00	96,47	**100,00**
A_i (g)	12,01	28,09	54,94	30,97	4,00	51,90	95,94	26,98	63,55	16,00	55,85	
z_i	4,00	4,00	4,00	3,00	32,07	6,00	4,00	3,00	2,00	2,00	2,33	
$\frac{A}{Fz} = k_i$	3,11E-05	7,28E-05	1,42E-04	1,07E-04	1,29E-06	8,96E-05	2,49E-04	9,32E-05	3,29E-04	8,29E-05	2,48E-04	
$\frac{\rho\alpha_i}{100}$	7,72E-02	1,95E-02	2,73E-02	1,95E-04	1,17E-03	1,15E-01	7,80E-03	3,90E-03	2,34E-02	1,17E-04	7,52	**7,80**
$\frac{\rho\alpha_i}{100k_i}$	2,48E+03	2,68E+02	1,92E+02	1,82E+00	9,05E+02	1,28E+03	3,14E+01	4,18E+01	7,11E+01	1,41E+00	3,03E+04	**3,56E+04**
$K_{v\,alloy} = \frac{1}{\rho\sum(\frac{\alpha_i}{100k_i})}$	2,81E-05											

Appendix 2 Table 1: Composition of the 100Cr6 alloy and calculation of $K_{v\,alloy}$

The density of the material ρ is equal to $7800\text{kg} / \text{m}^3 = 7.8 \times 10^{-3}\text{g} / \text{cm}^3$

So $K_{v\,100Cr6} = \eta \frac{1}{\rho\sum(\frac{\alpha_i}{k_i})} = 2.81 \times 10^{-5}\ \text{cm}^3/\text{As} = 2.81 * 10^{-2}\ \text{mm}^3/\text{As} = 1.686\ \text{mm}^3/\text{Amin}$ at $\eta = 100\%$

Appendix 3. POWER ELECTRONICS FUNDAMENTALS

Appendix 3.1. Structure of a pulse power supply unit

Power electronics devices are generally made of 2 parts:

- The control part: this part sends control signals to the power parts. The voltage levels of the signals in the control circuit is low (ranging from 3.3V to 24V). The control part generally contains a microcontroller which controls the electrical components of the power parts.
- The power part: the power part contains the electrical components designed to handle electrical power, such as power semiconductors. The voltage levels and current intensities on the power part are much higher than in the control part.

Appendix 3.1.1. Microcontroller

The power supply units use the same model of microcontroller for their operations. They are controlled via an Arduino compatible Max32 ChipKIT development board having an 80MHz 32bit PIC microprocessor (from Microchip) (Appendix 3 Figure 1).

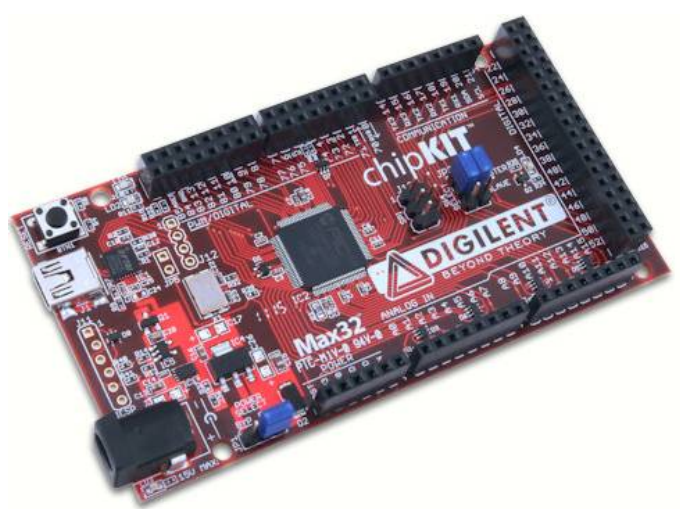

Appendix 3 Figure 1: Picture of the ChipKIT Max32 development board

The Max32 development board is directly interfaced with the control circuitry of the pulse power supply unit.

Appendix 3.1.1.1. On-board I2C communication

I2C is a simple bidirectional 2 wire bus for efficient inter-IC control developed by Philips Semiconductors (now NXP Semiconductors) in the 1990's. Only two bus lines are required: a serial data line (SDA) and a serial clock line (SCL) (NXP, 2014). Both SDA and SCL lines have to be connected to the 5V rail through pull-up resistors.

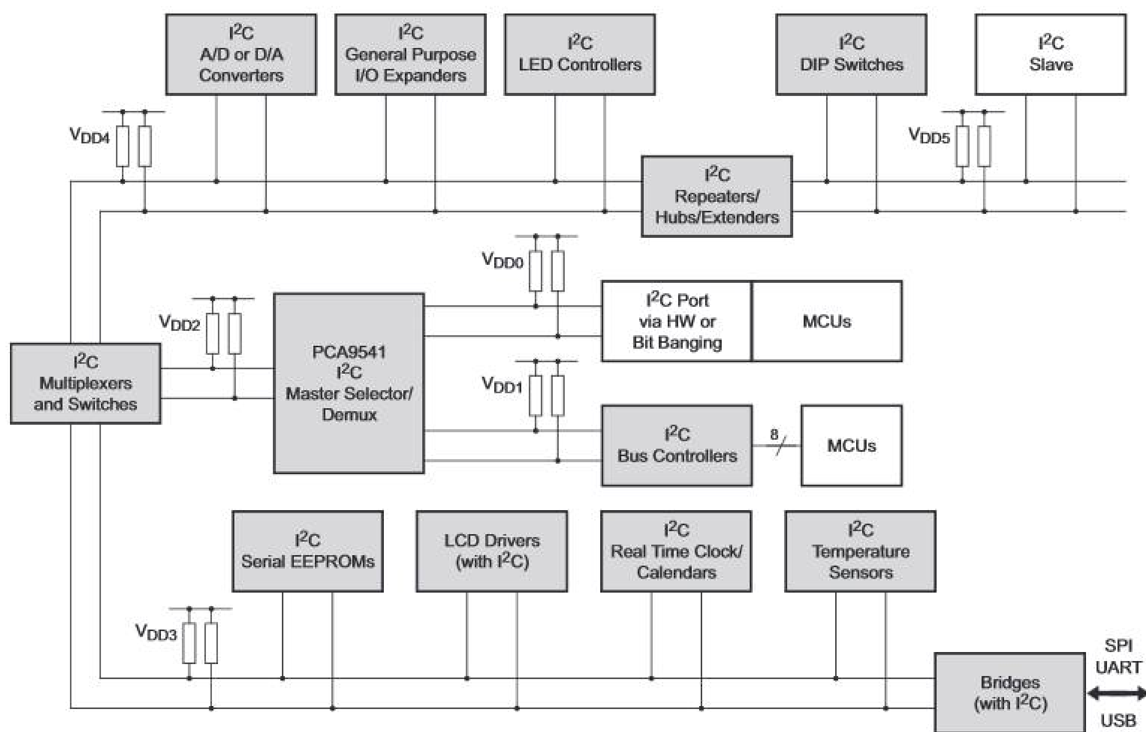

Appendix 3 Figure 2: Typical application of the I2C bus in a system (NXP, 2014)

Appendix 3.1.1.2. On-board SPI communication

The SPI (Serial Peripheral Interface) bus was created by Motorola to allow microcontroller unit to communicate with other components is a system. The SPI bus is made out of 4 lines: SCK (clock) SS (slave select) MOSI (master out slave in) and MISO (master in slave out).

In the case of the pulse generator SCK is pin SC, SS corresponds to pin AE and MOSI is pin SI. Pin MISO is SO but it is not used in this configuration since the pulse generator does not send data back to the microcontroller. SPI is therefore implemented with 3 lines in the prototype.

Appendix 3.1.1.3. Modulation

Modulation is the process of varying one or more properties of a high-frequency periodic waveform called the carrier signal to indicate or control some secondary state change, often given as a change in a modulating signal. Pulse width modulation, or PWM, uses a rectangular pulse wave whose pulse width is modulated, changing the relative t_{on} and t_{off} times, thus altering the duty cycle.

A pulse generator can either be an internal circuit or piece of electronic test equipment used to generate pulses. Simple pulse generators allow the control of parameters such as: pulse repetition rate (frequency), pulse width, delay with respect to an internal or external trigger and the high- and low-voltage levels of the pulses.

Appendix 3.1.2. The power part of a pulse power supply unit

As previously mentioned, the main components of the power part are power semiconductors. These semiconductors have two states:

- conducting (the current can pass through the component) or in 'ON state'
- not conducting (the current is blocked) or in 'OFF state'

Appendix 3.1.2.1. MOSFET basics

Due to the high switching frequencies at which the pulse power supply is expected to work, it has been decided to use MOSFETs as power switches.

MOSFET stands for Metal Oxide Semiconductor Field Effect Transistor. The power MOSFET is used in many power electronics devices, such as switched mode power supplies, computer peripherals, automotive and motor control.
An enhancement type (or N-type) MOSFET is normally off, which means that the drain to source current increases as the voltage at the gate increases (Oh, 2000) (Appendix 3 Figure 3).

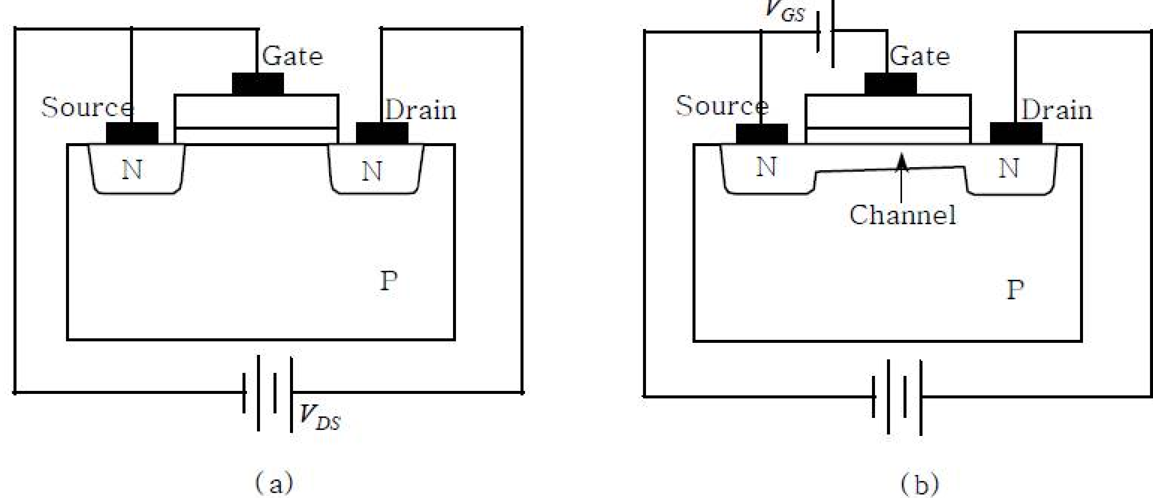

Appendix 3 Figure 3: The Structure of an Enhancement Type MOSFET and its Operation; (a) When VGS (Gate-source voltage) is not supplied; (b) When VGS (Gate-source voltage) is supplied (Oh, 2000)

The electrical symbol of an N-Type MOSFET can be seen in Appendix 3 Figure 4. To turn an N-type MOSFET 'ON', the capacitance at its gate C_{GS} must be charged by applying a voltage between its source (S) and its gate (G) so that $V_{GS} > 0$.

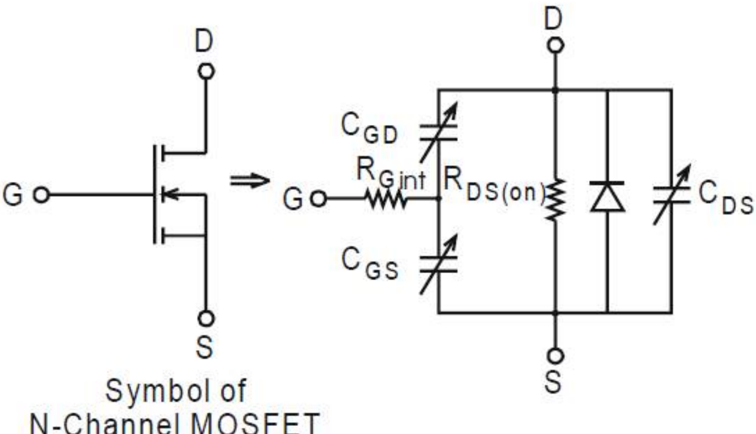

Appendix 3 Figure 4: Symbol and equivalent circuit of a MOSFET (Pathak, 2001)

In order to quickly switch ON and OFF the MOSFET, a driving circuit called 'driver' is necessary. A driver outputs high current pulses in order to speed up the charging time of the C_{GS} capacitance, therefore reducing the turn-on time of the MOSFET and making it possible to reaching higher switching frequencies. A resistor is often added to the gate of the MOSFET in order to increase the charging time of the gate capacitance and reduce the noise generated when the device is switched ON.

During the turn-on procedure (Appendix 3 Figure 5 (a)), the output of the driver is connected to the supply voltage V_{DRV}, the current flows through the external gate resistor R_{GATE} and the internal gate resistor $R_{G,I}$ and charges the gate capacitance C_{GS}. Once C_{GS} is fully charged, the MOSFET is conducting and allowing current to pass from its Drain to its Source.

During the turn-off procedure (Appendix 3 Figure 5 (b)), the output of the driver is connected to the ground, this discharges the gate capacitance C_{GS} through R_{GATE} and $R_{G,I}$. Once C_{GS} is fully discharged, the MOSFET stops conducting and prevents current from flowing from its Drain to its Source.

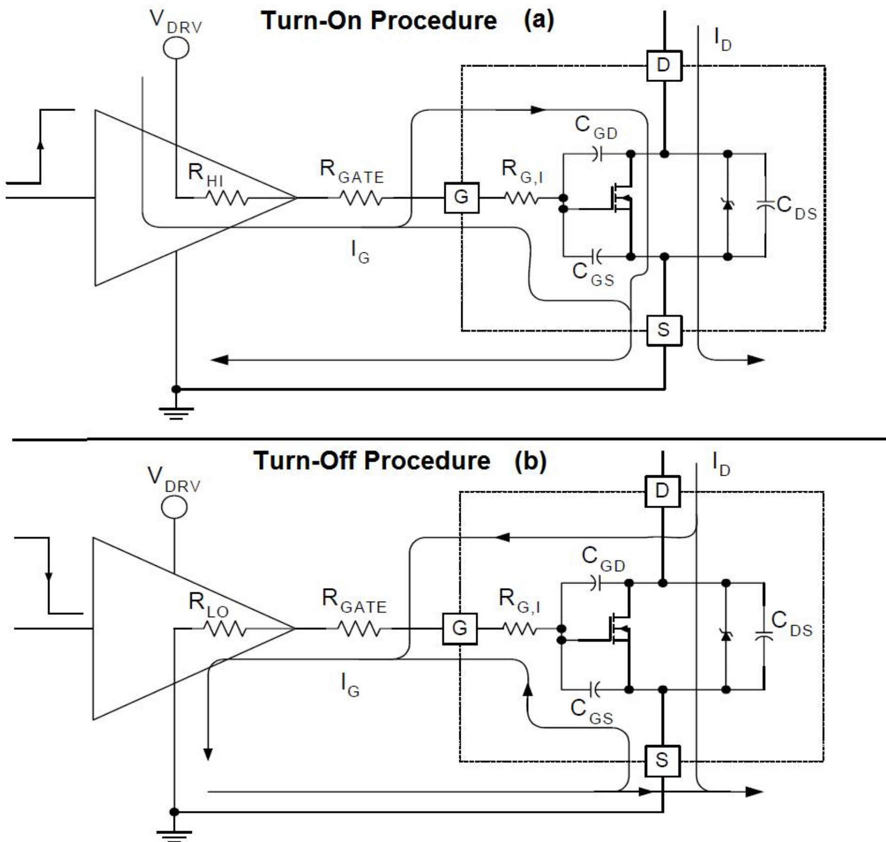

Appendix 3 Figure 5: MOSFET Turn-On and Turn-Off procedures

Appendix 3.1.2.2. Reducing ringing at the MOSFET switch nodes using snubbers

A so-called ringing effect is caused by the parasitic inductance and capacitance of the copper traces as well as the components packages. When a switching device changes its state from ON-state to OFF-state, the impedance of the device abruptly jumps to a very high level, blocking the current. But the current still tends to keep flowing through the switch, which induces a high voltage across the switch. The faster the current decreases, the higher the induced voltage becomes. It may reach to sufficiently high level to destroy the switch. If the switch is unable to withstand the high induced voltage, it will be destroyed, and can no longer block the current as an OFF-state switch.

Conversely, when a switching device changes its state from OFF-state to ON-state, the impedance of the device abruptly goes down to nearly zero, allowing current to flow freely. The problem in this case is that the current does not start to flow uniformly through the switch. This is because the switch does not recover its conductivity over the whole of its cross-sectional area simultaneously. Some part of the area may be open first, and the current flow is concentrated to this relatively small portion of the switch, which may cause overheating and eventually failure.

When a sudden voltage transient occurs - for example when a MOSFET is turned on/off - the association of the parasitic inductance and capacitance of the circuit creates an overshoot followed by an oscillation whose resonant frequency is equal to $1/(2\pi\sqrt{LC})$. Where L and C are respectively the parasitic inductance and capacitance of the circuit and the MOSFET

packages. This frequency is usually very high (around 200MHz) and creates disturbances which can damage nearby components.

To reduce the ringing a snubber circuitry can be implemented between the drain and the source of the MOSFET. This snubber circuit consists of a capacitor in series with a resistor which both need to be dimensioned precisely (Taylor and Manack, 2012). Snubbers are simple, efficient and cost effective open loop equalizers for SMPS. The purpose of a snubber is to control the balance between the rate of rise and the overshoots of transient switching in waveforms, in order to optimise the efficiency and reliability of a power supply. Snubbers can do many things:

- Reduce or eliminate voltage or current spikes
- Limit dI/dt or dV/dt. Shape the load line to keep it within the safe operating area
- Transfer power dissipation from the switch to a resistor or a useful load.
- Reduce total losses due to switching
- Reduce EMI by damping voltage and current ringing
    - Dimensioning the snubber capacitor:

To be able to dimension the capacitor properly, the ringing frequency (F1) must be determined by measuring the frequency of the signal at the switch node.

$$F1 = \frac{1}{2\pi\sqrt{L1C1}} \quad (1)$$

To find L1 and C1, a capacitor C2 is added to the circuit and placed in parallel with C1 - between the drain and the source of the MOSFET. The value of C2 should be adjusted so that the ringing frequency F2 is half of F1:

$$F2 = \frac{1}{2 \times F1} = \frac{1}{2\pi\sqrt{L1(C1 + C2)}} \quad (2)$$

Since C2, F1and F2 are known, C1 can be calculated this way:

$$(1) \quad \left(\frac{F1}{F2}\right)^2 = \frac{C1 + C2}{C1}$$

$$(2) \quad C1 = \frac{C2}{\left(\left(\frac{F1}{F2}\right)^2 - 1\right)} \quad (3)$$

Solving C1 allows L1 to be calculated using equation (2). The value of the snubber capacitor must be at least 3 times higher than C1 (i.e. $C_s \geq 3C1$).

- Dimensioning the snubber resistor:

The role of the snubber resistor is to dissipate the energy stored in the capacitor. The lower the resistor value, the better the damping of the ringing will be. However, the amount of energy to dissipate increases for lower resistor values, so the resistor wattage should be considered. The value of the resistor can be calculated with the following expression:

$$R_{snub} = \sqrt{L1/C1} \quad (4)$$

The power to dissipate is also depending on the switching frequency and the snubber capacitor value.

Appendix 3.1.3. Isolation between control and power parts

Most of the time - because of the power difference between those two parts – the control part is electrically isolated from the power part. This isolation is done by using optocouplers or magnetocouplers and protects the control part from any problem occurring in the power part.

On all the prototypes, the electrical isolation is guaranteed using an ADuM1100 100Mbps bus isolator from Analog Devices (Appendix 3 Figure 6). According to the datasheet, the ADuM1100 operates with a voltage supply ranging from 3.0 V to 5.5 V and boasts a propagation delay of <18 ns (Analog Devices, 2012). This component is perfectly suited for transmitting the high frequency control signals to the power part of the PSU.

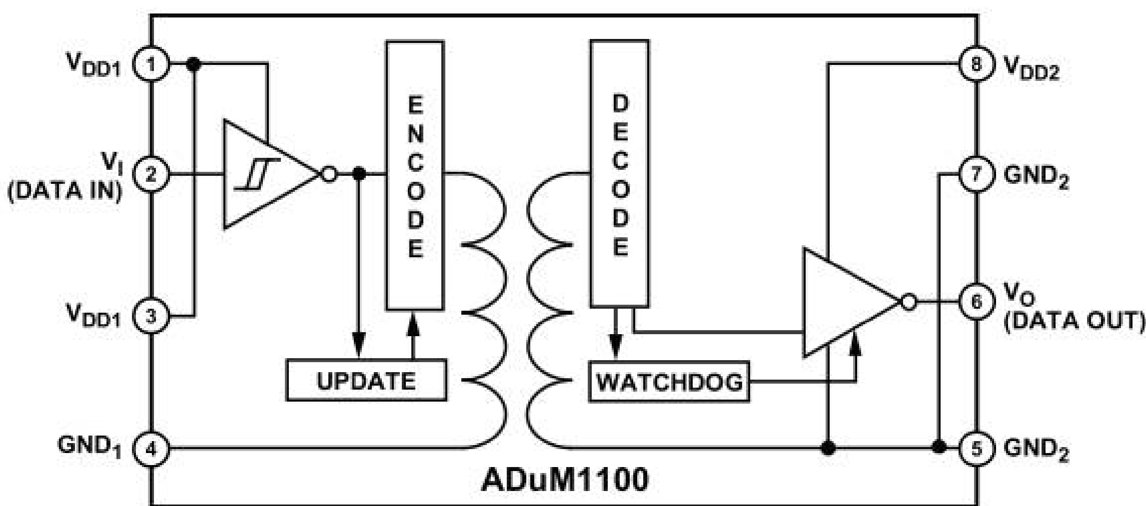

Appendix 3 Figure 6: Functional block diagram of the magnetocoupler ADuM1100(Analog Devices, 2012)

Appendix 3.1.4. Current sensing for over-current protection

The resistive current sensing technique is the most commonly used technique for measuring electrical current on PCB assemblies at low or moderate current level. The amplifier best suited for this is the instrumentation amplifier.

In the drawing below (Appendix 3 Figure 7) the instrumentation amplifier amplifies the differential voltage (V_S) to a usable level. To minimize voltage drop across the sense resistor, the resistor value is often sized to deliver a sense voltage of a few tens of millivolts at the maximum current level so as not to adversely affect I_L.or V_{LOAD}.

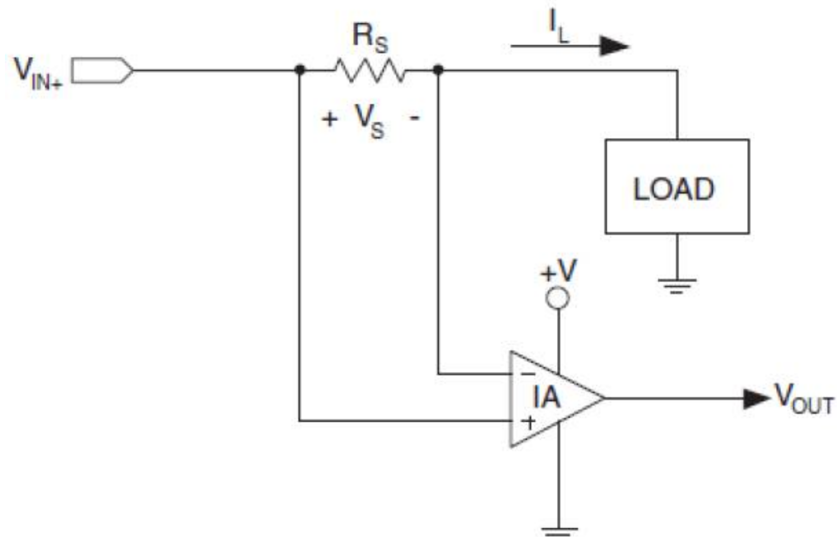

Appendix 3 Figure 7: Basic resistive current sensing amplifier

For example the circuit can use a 0.01ohm (10mohm) R_S resistor value which produces a V_S value equal to 10mV for every 1A (i.e. 10mV/A) of load current across the resistor. For measuring the current over the range of 0 – 5A, a maximum voltage of 50mV will be developed.

An instrumentation amplifier gain of 30 can provide a reasonable amplification 300mV = 1A which will best suit the needs that are estimated. These needs are that the circuit will have to measure up to 20A and give a V_{OUT} between 0 and 5v.

One of the major trade-offs in the resistive current measurement technique is that of selecting a resistor value. The larger the voltage V_S drop the easier it is to measure, and reduces the offset voltage and common-mode rejection requirement of the amplifier used, but a smaller drop affects the load voltage (V_{LOAD}) less.

When working at high frequency care needs to be taken with many amplifier parameters:

- Common mode rejection ratio (input voltage range)
- Temperature drift
- Input offset voltage
- Gain bandwidth product
- Slew rate

Appendix 3.1.5. Board design considerations and assembly

The printed circuit board was designed using the software EAGLE CAD and was etched with the machine available at Brunel University.

The components of the PSU were off-the-shelf and ordered to suppliers such as RS Online, Farnell and Arrow.

All the components were placed and soldered by hand.

Certain rules and considerations must be taken into account when placing and routing the components in high-speed circuits (Ardizzoni, 2005; Altera, 2001):

- The output of the driver must be as close as possible to the gate of the MOSFET, in order to minimize the inductance of the trace through which the high current is passing.
- Whenever possible the low power components shall be grounded with a trace that is not common with the ground of the drivers. This mainly due to the fact that a high return current is flowing in the ground trace of the drivers, this creates noise and could make the low power components unstable.
- Add bypass or decoupling capacitors for as many power supply traces as possible (Altera, 2001). The bypass capacitors shall be placed as close as possible to the power pins of the device in order to reduce the length of the high frequency current loop. This aspect is critical in high-speed board design.
- All the unused input pins shall be tied to the ground whenever possible. The output pins shall be driven to a low state; this can be done by using pull down resistors connected to ground. A resistor value of 3600Ohms was used in the prototypes for this purpose.
- Eliminate sockets whenever possible, sockets add parasitics.
- The number of outputs that can switch simultaneously shall be reduced and/or they shall be spread across the board to make sure their influence is reduced.
- A ground plane shall be used whenever possible. The ground planes provides the return current with a low-impedance path to ground, therefore reducing the influence of parasitic inductors and capacitors on the signal.
- Power and ground pins shall be placed to each other, this reduces the overall inductance since the current from the supply pin (Vcc) flows in the opposite direction of the return current flowing in the ground (GND) pin.
- Parasitics are hidden stray capacitors and inductors that must be considered when designing high-speed circuits (Appendix 3 Figure 8). They are created by the package leads and trace length, vias, pad to trace capacitors and many other elements in the circuit (Ardizzoni, 2005). Surface mount components shall be used to reduce the inductance of the leads and wide and short traces shall be used to connect vias to the devices (Altera, 2001).

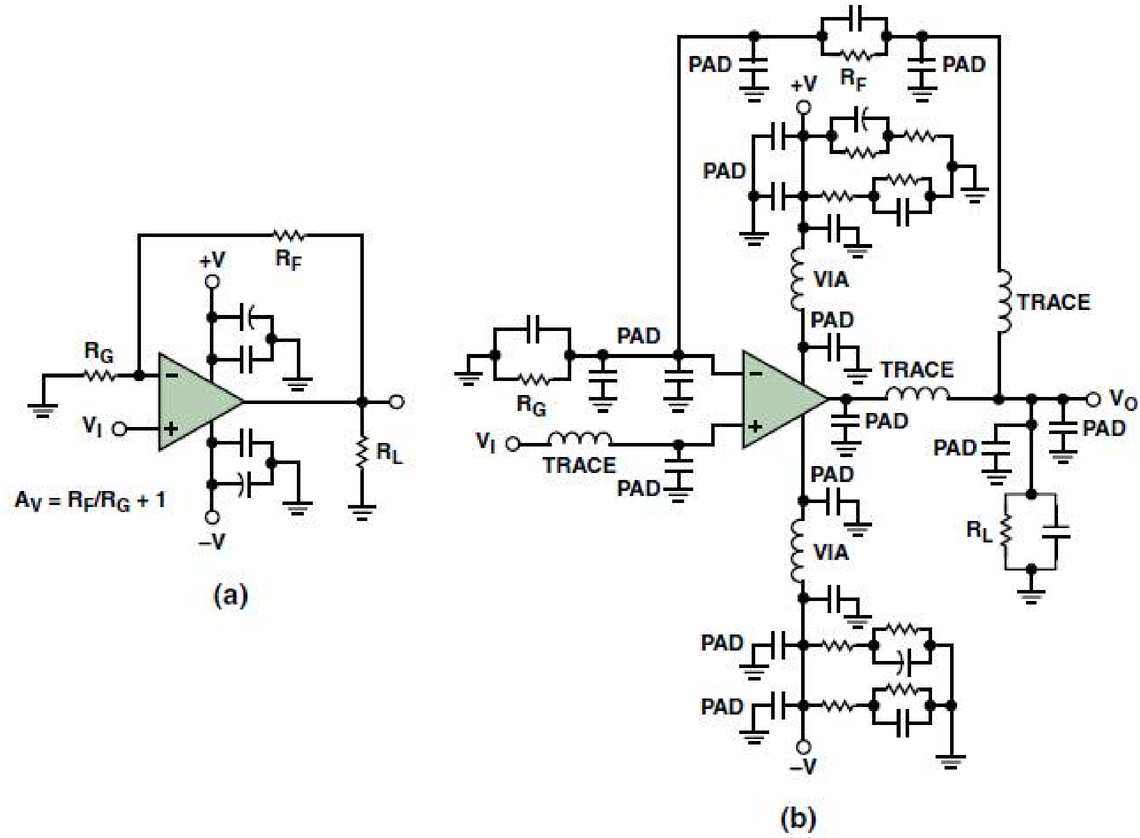

Appendix 3 Figure 8: Typical op amp circuit, as designed (a) and with parasitics (b) (Ardizzoni, 2005)

- *'Cross-talk is the unwanted coupling of signals between parallel traces'*- (Altera, 2001). Signal coupling can result in unexpected component behaviour and a malfunctioning circuit. To reduce the influence of cross-talk on the traces, the center-to-center separation between the two traces should be at least 4 times the trace width (Altera, 2001).

All these considerations have been taken into account whenever possible. The use of 4-layer boards is optimum for reducing parasitics because it provides the possibility to have a power plane and two ground planes. Those planes can be used for stripline routing: surrounding the high-frequency trace in a 'sandwich' configuration as shown in Appendix 3 Figure 9.

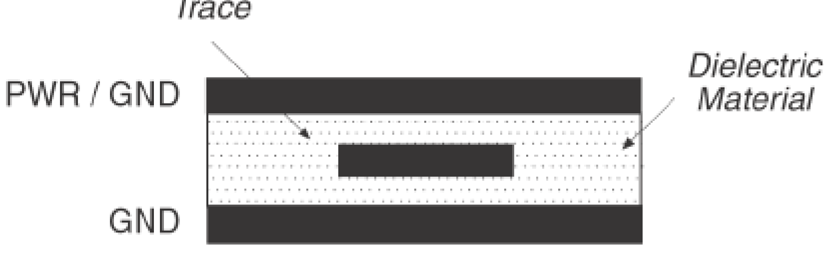

Appendix 3 Figure 9: Illustration of stripline routing (Altera, 2001)

The fact that the prototypes were made on dual layer boards made it challenging to follow the routing guidelines and some trade-offs had to be made to make the assembly of the board feasible.

Appendix 4. DEVELOPMENT OF THE FIRST PULSE PSU PROTOTYPE

Appendix 4.1. First prototype: General presentation

This first prototype demonstrated the critical influence of the inductance of the circuitry in high frequency applications. The successful design of the power supply unit not only resides in the choice of the components but also in the layout of the PCB. The schematic diagram of the first PSU prototype and its interface can be seen on the figure below:

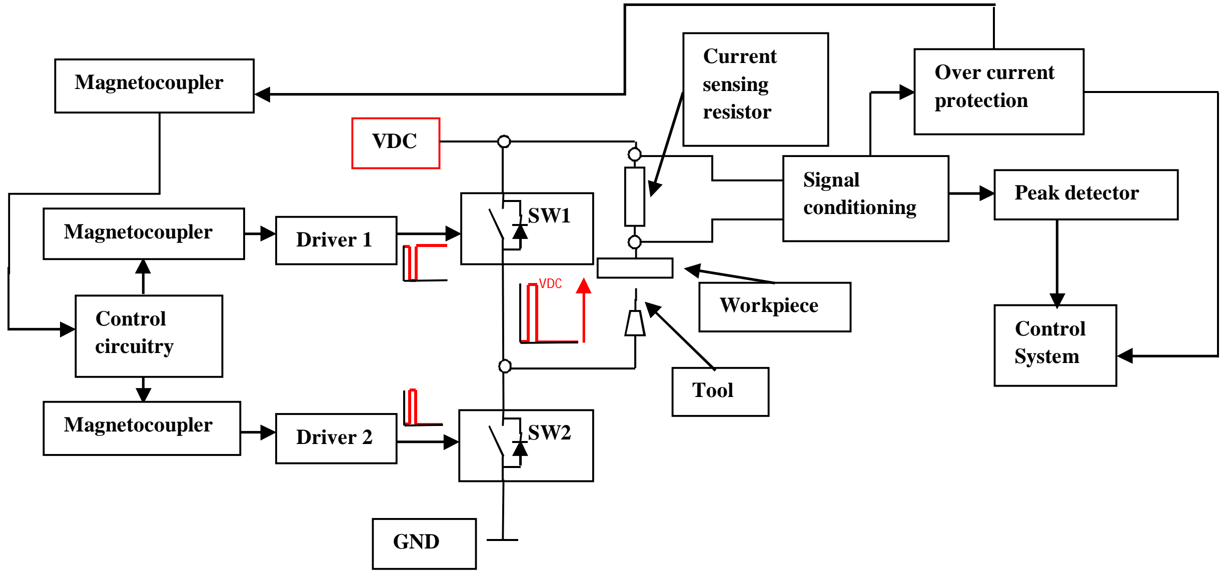

Appendix 4 Figure 1: Schematic diagram of the first PSU prototype and its interfaces

Appendix 4.2. First prototype: The control circuitry

The most critical component is the pulse generator; this device generates the logic signal that will actuate the MOSFETs on the power stage.

This control circuitry has been designed on a shield that is pin-to-pin compatible with the Max32 board so that it can be stacked on top of it. This modular approach makes the development on the prototypes easier, since each of the boards can be tested individually. Moreover, if a board fails to perform a function, a new board can be designed, without having to redesign and reassemble the other working parts.

Appendix 4.2.1. Pulsing circuitry for Pulse Width Modulated control

In the first prototype, the pulse generating function is performed by a MAX038. The MAX038 is a high-frequency precision function generator producing accurate waveforms at frequencies up to 20MHz such as:

- triangle
- sine
- square

The type of waveform can be selected using inputs A0 and A1 with the combinations shown in the table below (Maxim, 2007):

A0	A1	WAVEFORM
X	1	Sine wave
0	0	Square wave
1	0	Triangle wave

X = Don't care.

Appendix 4 Figure 2: Waveform selection using inputs A0 and A1 (Maxim, 2007)

The frequency and the duty cycle can be adjusted independently using 3 inputs, allowing the generation of sawtooth and PWM signals. The inputs control the oscillator inside the MAX038, which is a relaxation type that operates by alternately charging and discharging the capacitor C_F connected to the COSC input:

- IIN: Current input for frequency control which sets the nominal frequency of the output. IIN is used to control the charging and discharging current of the oscillator inside the MAX038. IIN can vary from 2µA to 750µA, producing more than two decades of frequency for any value of C_F .
- DADJ: Duty-cycle adjust input. Applying ±2.3V to DADJ controls the duty cycle from 10% to 90%.
- FADJ: Frequency adjust input. Applying ±2.4V to FADJ changes the nominal frequency (with VFADJ = 0V) by ±70%)

The frequency and the duty cycle of the output are controlled using an internal voltage reference (REF) of 2.5V. REF can furnish a stable current to IIN and can also be used to bias DADJ and FADJ.

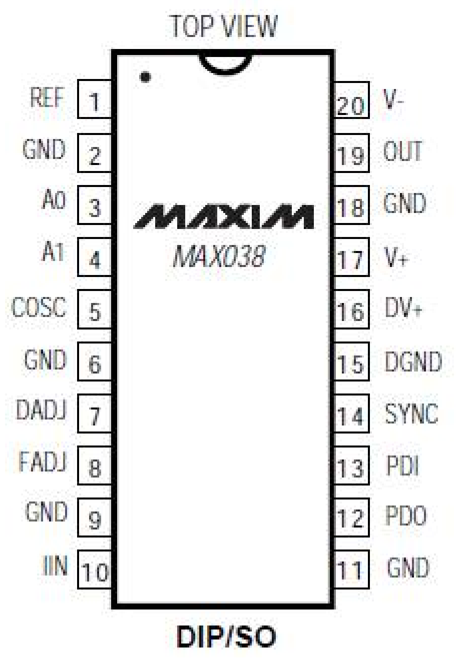

Appendix 4 Figure 3: MAX038 pin configuration (Maxim, 2007)

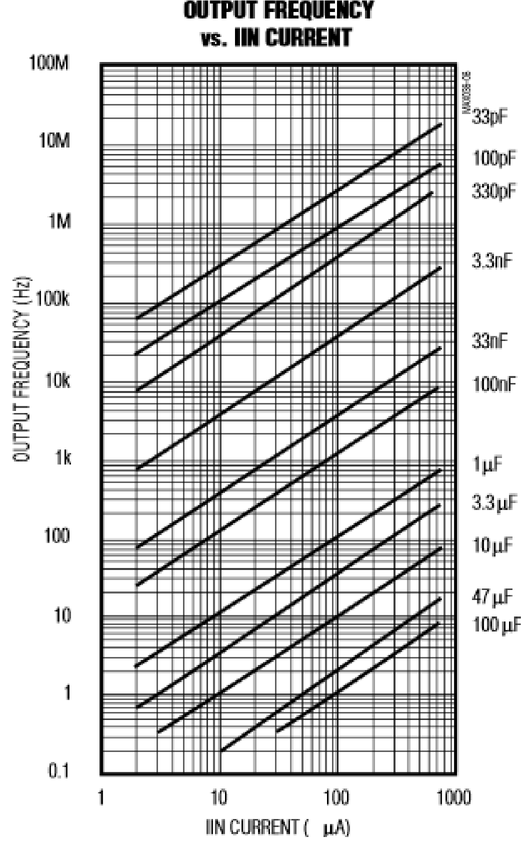

Appendix 4 Figure 4: Chart representing the output frequency as a function of IIN, for different C_F values (Maxim, 2007)

The control circuitry of the first PSU prototype uses IIN and DADJ to vary the frequency and duty cycle of a square waveform. FADJ is disabled by being connected to ground though a 12kΩ resistance.

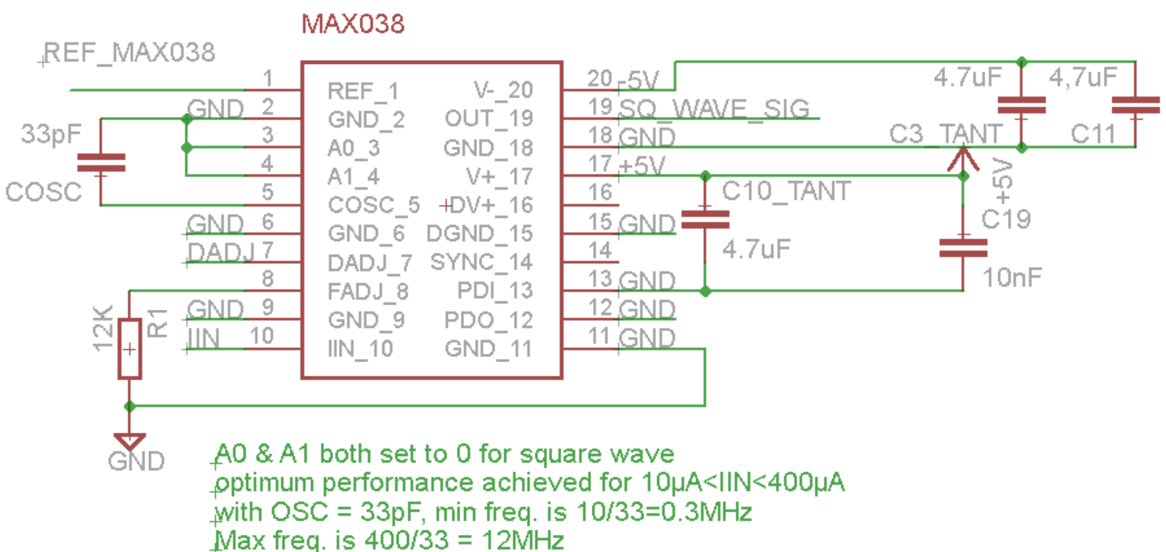

Appendix 4 Figure 5: Schematic diagram of the MAX038 signal generator

Appendix 4.2.2. Adjusting the frequency

According to the chart presented in Appendix 4 Figure 4, 33pF is a suitable value of C_F for µECM: it allows the output frequency of be controlled within a range of 60kHz to 20MHz. The nominal frequency $F_O$is adjusted according to the following expression(Maxim, 2007):

$$F_O(MHz) = \frac{IIN\ (\mu A)}{C_F\ (pF)} \quad (1)$$

With IIN ranging from 2µA to 750µA, the frequency can theoretically be varied from 60.6kHz to 22MHz. The datasheet however suggests that *'optimum performance is achieved with IIN between 10µA and 400µA'* (Maxim, 2007). IIN can be varied using a potentiometer with a resistance R_{POT} connected to the 2.5V reference voltage. The expression of F_O would then become:

$$F_O(MHz) = \frac{VREF\ (V)}{R_{POT}C_F\ (pF)} \quad (2)$$

The required range of values for R_{POT} is then calculated using the IIN values:

For IIN = 750µA, $R_{POT} = \frac{2.5(V)}{750.10^{-6}} = 3333\Omega$

For IIN = 2µA, $R_{POT} = \frac{2.5(V)}{2.10^{-6}} = 1.25M\Omega$

This means that ideally a potentiometer with a resistance ranging from 3kΩ to 1.25MΩ is needed to cover the whole range of output frequencies. Unfortunately potentiometers providing such an extended range of resistance are not available on the market. A digital potentiometer model AD8402ARZ50 of a maximum resistance value of 50kΩ has therefore been chosen to set IIN. The AD8402ARZ50 has an 8 bit resolution allowing its nominal resistance R_{AB} to be set using 256 contact points accessible by the wiper terminal (Analog Devices, 2010). Its typical wiper resistance R_W is equal to 50Ω.

Two resulting resistances can be measured:

- R_{WB} across the wiper and the B terminal
- R_{WA} across the wiper and the A terminal

The resistance R_{WB}will be used to control IIN, and therefore REF is connected to both A1 and W1 in Appendix 4 Figure 5. The value of R_{W1B1} is varied according to the following expression (Analog Devices, 2010):

$$R_{W1B1}(D) = \frac{D}{256} \times R_{A1B1} + R_{W1} \quad (3)$$

Where D is the decimal data loaded into the 8-bit register.

The variation of $R_{W1B1}(D)$ for different D values is summarised in Appendix 4 Table 1: Value of R_{WB} for different D values

below:

D(Dec)	$R_{W1B1}(\Omega)$	Output state
255	49,854	Full scale
128	25,050	Midscale
1	245	1LSB
0	50	Zero-scale (wiper contact resistance)

Appendix 4 Table 1: Value of R_{WB} for different D values

F_O should vary from 20MHz to 1.5MHz, which is restricting access to frequencies in the kHz range. The capacitance C_F was then changed to 246pF, allowing the frequencies to be varied from 201 KHz to 2.68 MHz.

The AD8402ARZ50 has a 3-wire SPI-compatible serial data input allowing the resistance R_{W1B1} to be programmed.

Appendix 4.2.3. Adjusting the duty cycle

The value of V_{DADJ} (in V) needed to produce a particular duty cycle can be calculated thanks to the formula(Maxim, 2007):

$$V_{DADJ}(duty) = \left(\frac{50}{100} - duty\right) \times 0.0575 \quad (4)$$

Where duty is the value of the desired duty cycle in %.
The second potentiometer is used the set the voltage V_{DADJ} applied to DADJ. This time, the AD8402ARZ50 is wired as a potential divider with A2 connected to a voltage $V_{A2} = -2.5V$ and B2 connected to $V_{B2} = 2.5$. Therefore a voltage $V_{A2B2} = V_{A2} - V_{B2} = -5V$ is applied to the potentiometer, as shown in Appendix 4 Figure 6.
A general purpose dual operational amplifier LF353DRG4 is used to invert the voltage of the REF to produce the accurate -2.5V voltage connected to A2. W2 is connected to a second amplifier which is configured in a follower mode to provide a reliable voltage VDADJ.
According to the datasheet of the AD8402ARZ50, the voltage V_{W2} applied to the wiper can be calculated as follows (Analog Devices, 2010):

$$V_{W2}(D) = \frac{D}{256} \times V_{A2B2} + V_{B2} \quad (5)$$

The variation of $V_{W2}(V)$ for different D values is summarised in Appendix 4 Table 2: Value of V_{W2} for different D values Appendix 4 Table 2 below:

D(Dec)	$V_{W2}(V)$	Output state
255	-2.48	Full scale
128	0	Midscale
1	+2.48	1LSB
0	+2.5	Zero-scale (wiper contact resistance)

Appendix 4 Table 2: Value of V_{W2} for different D values

Resistors R9 and R12 provide safety limits by preventing the voltage VDADJ to swing beyond +/- 2.31V.

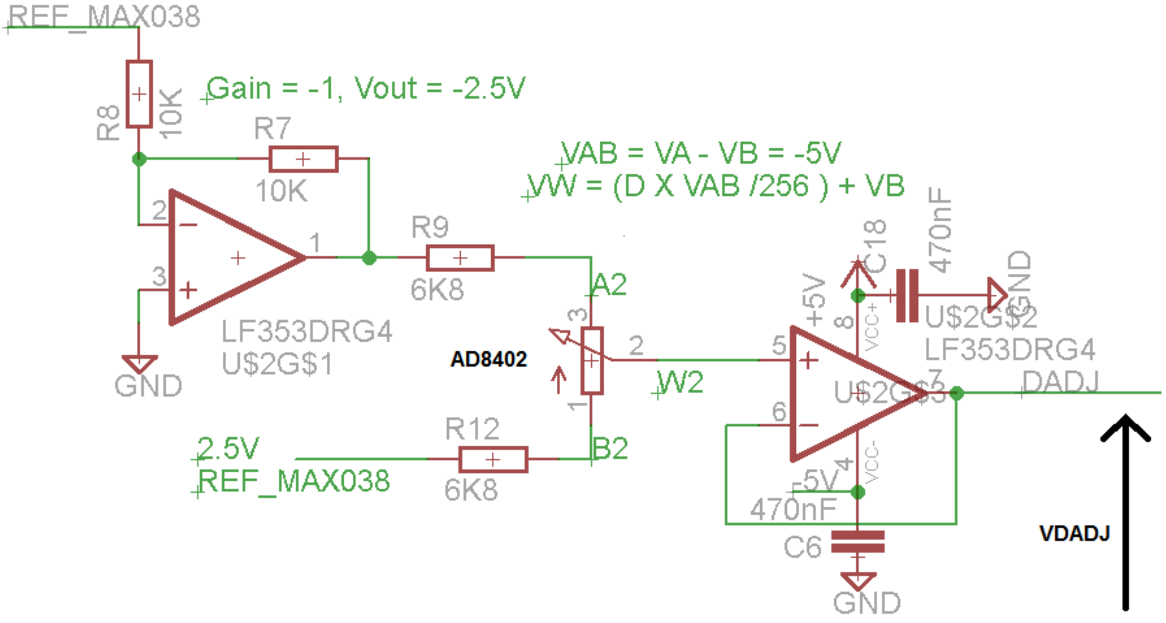

Appendix 4 Figure 6: Electrical schematic of the circuitry used to set VDADJ

The resulting duty cycle can be calculated thanks to the following expression (Maxim, 2007):

$$\text{duty}\left(V_{DADJ}\right) = \frac{50}{100} - \left(V_{DADJ} \times 17.4\right) \qquad (6)$$

In this configuration, the duty cycle can therefore theoretically be varied from 9.8% (with $V_{DADJ} = 2.31V$) to 90.2% (with $V_{DADJ} = -2.31V$).

The overall conditioning of the AD8402ARZ50 can be seen in Appendix 4 Figure 7.

The Max32 board sends data via the SPI communication protocol to a digital potentiometer (AD840) in order to set the appropriate resistance values to obtain the right frequency and duty cycle at the output of the function generator.

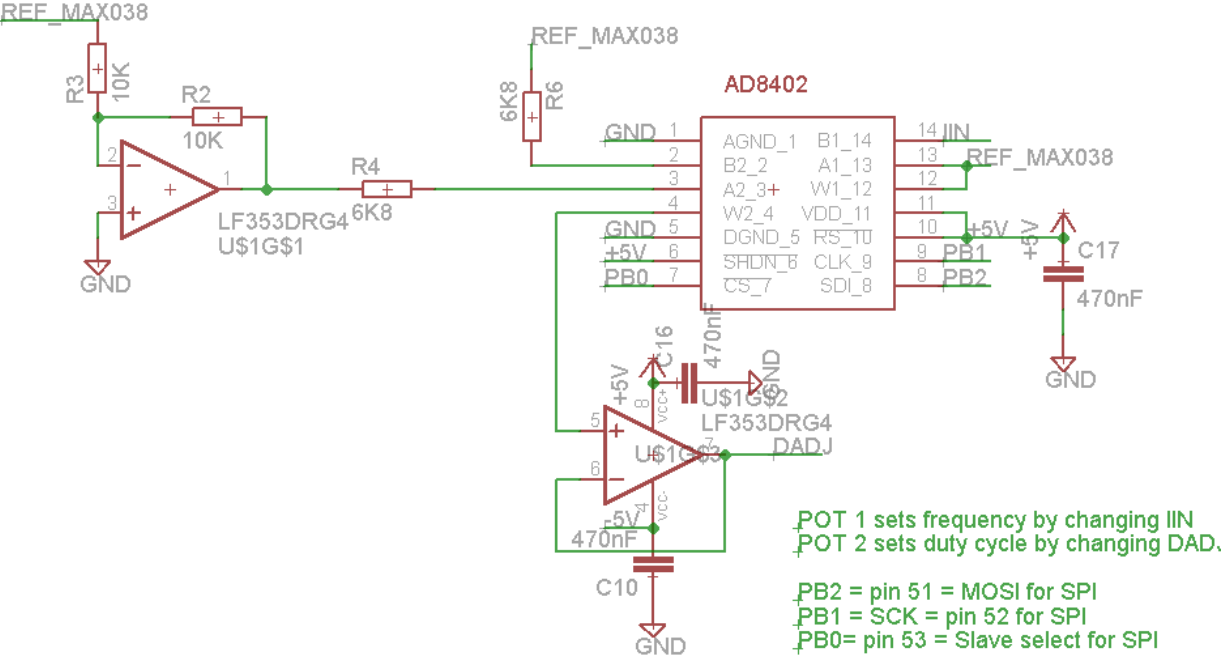

Appendix 4 Figure 7: Electrical schematic of the potentiometer AD840 setting up the IIN and DADJ

Appendix 4.2.4. Conversion of the square wave signal to TTL signal

Since the output of the generator is a square wave, it needs to be converted to a 5V logic level signal. Two ultra-fast comparators (LT1719 from Linear Technologies) assure this task (Appendix 4 Figure 8), the first one compares the pulse voltage with the ground reference so its output goes to a 'High' state each the signal is positive. The other comparator is configured so that the output goes to a 'High' state each time the output of the function generator is negative, it is therefore the inverted signal from the other comparator. The first comparator will control the low side MOSFET of the half bridge and the second one will control the high side.

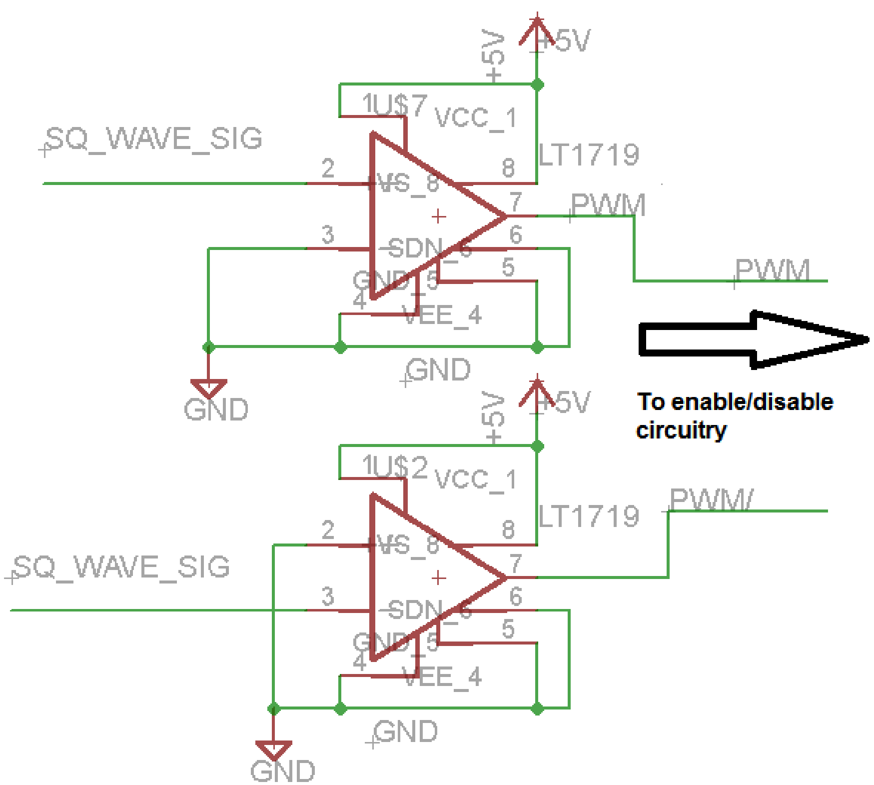

Appendix 4 Figure 8: Schematic diagram of the two ultrafast comparators LT1719 converting the MAX038 output signal to a 5V logic level

Appendix 4.2.5. Enabling and disabling the signals

The control signals are then sent to quad AND logic gate which allows the enabling/disabling of the control signals, the enabling/disabling function is simply done by changing the logic level a pin of the microcontroller from ‘Low’ to ‘High’.

The enabled signals are then sent to other AND gates but this time they are compared with the over current protection (OCP) logic signal. If the OCP signal is ‘High’, it means that it has not been triggered and the signals at the outputs of the AND gates can be sent to the MOSFETs.

If the over current protection is triggered, the OCP signal goes ‘Low’ which stops the sending of the control signal to the power stage and prevents the MOSFETs from being turned on when the output of the pulse power supply is short-circuited.

Therefore, the control signals are sent to the power stage only when the enable and OCP signals are both ‘High’ (Appendix 4 Figure 9).

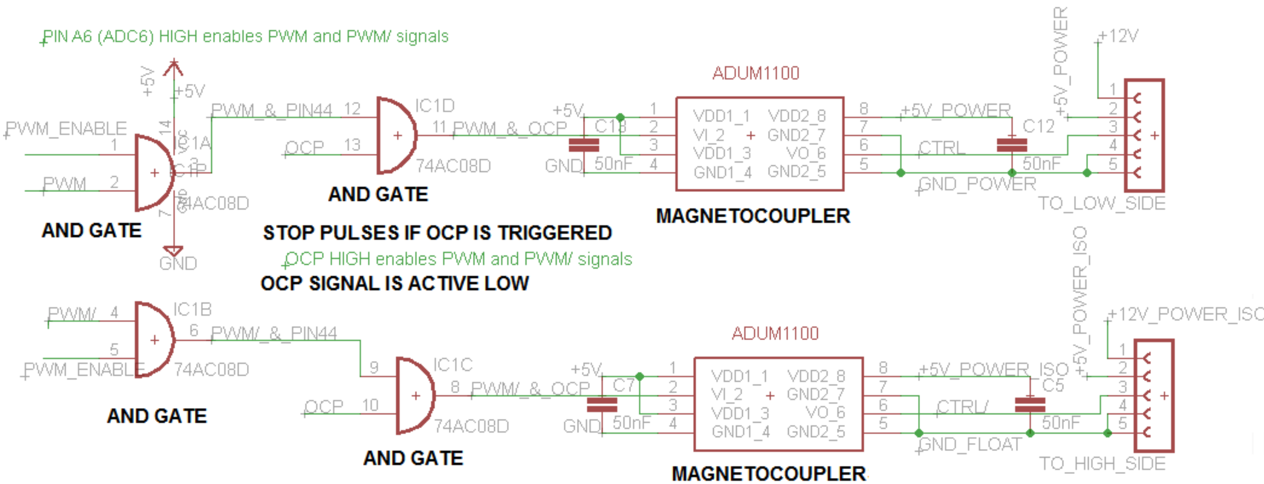

Appendix 4 Figure 9: Electrical schematic of the control circuitry part

Appendix 4.2.6. Control Board power requirements and layout

The control board of the first prototype is bigger than the power and over current protection boards. This is mainly due to the fact that all the isolated power supplies for the power parts are soldered on this board to reduce the current path irregularities on the power and over-current protection boards. This board therefore contains the 12V isolated DC-DC converter supplying the high-side driver as well as the 12VDC to +/- 5V isolated converter supplying the over current protection board. Those converters can be seen on Appendix 4 Figure 10.

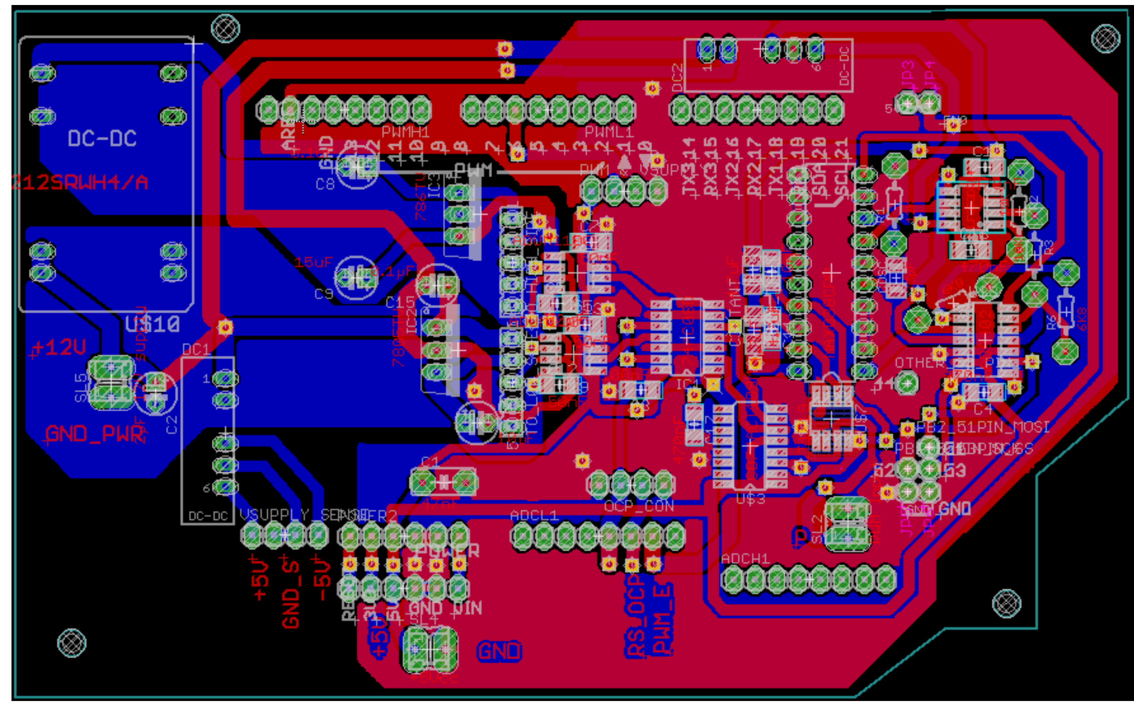

Appendix 4 Figure 10: Picture of the printed circuit board layout of the control circuitry

The control board is supplied by the linear voltage regulator on the Max32 board providing 5V and up to 500mA in current. However this current value is not achievable because the Max32 is powered only via the USB cable of the computer.

A picture of the fully assembled control board can be seen on Appendix 4 Figure 11.

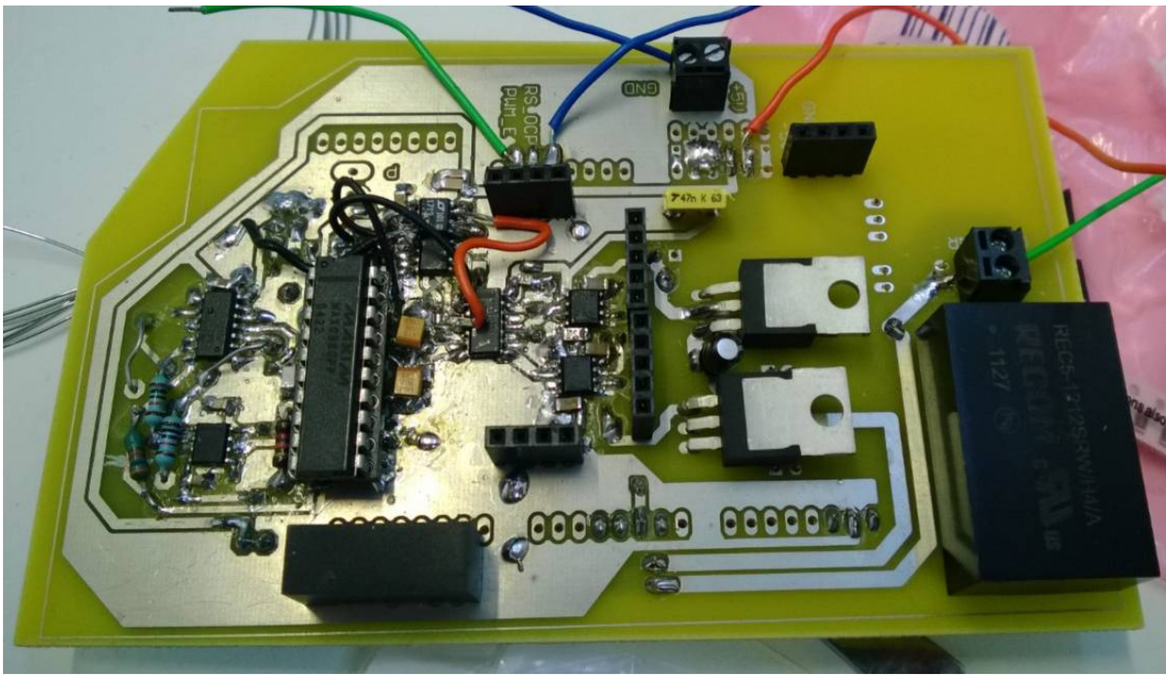

Appendix 4 Figure 11: Picture of the control board of the first prototype

Appendix 4.3. First prototype: The power stage

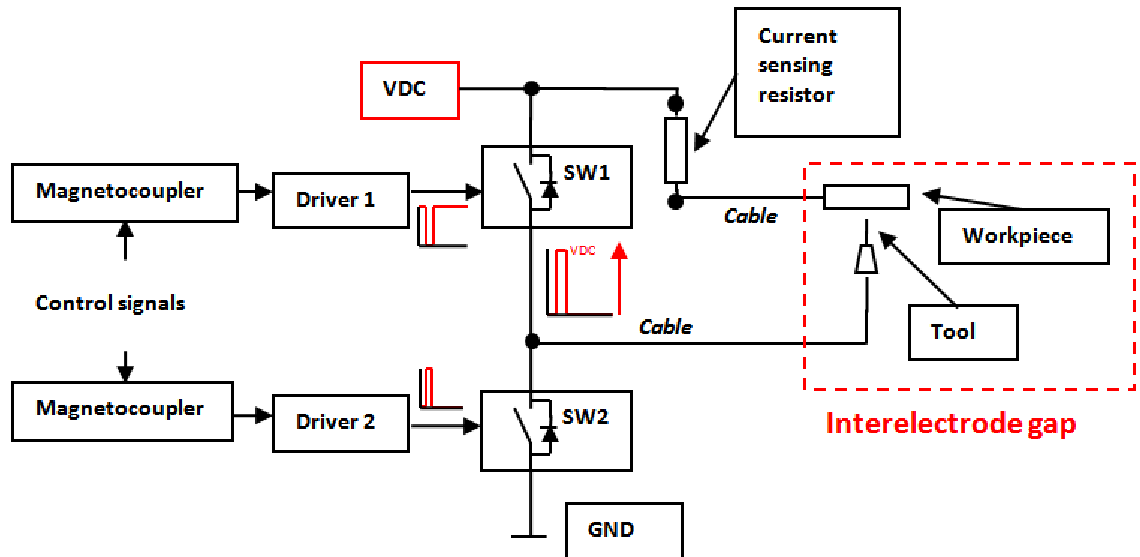

Appendix 4 Figure 12: Simplified diagram of the power part connect to the interelectrode gap

The power stage contains the MOSFET that will turn on/off to create the voltage pulses and can be represented by the simplified schematic below (Appendix 4 Figure 12).

Appendix 4.3.1. Timing aspects of the control signals

SW1 and SW2 are controlled according to the signals showed in Appendix 4 Figure 13.

When SW2 is turned ON and SW1 is turned OFF (situation number 1), the voltage VDC is applied to the IEG and machining occurs: this is the pulse on-time.

When SW1 is turned ON and SW2 is turned OFF (situation number 3), the IEG gap is in short circuit situation: this is the pulse off-time.

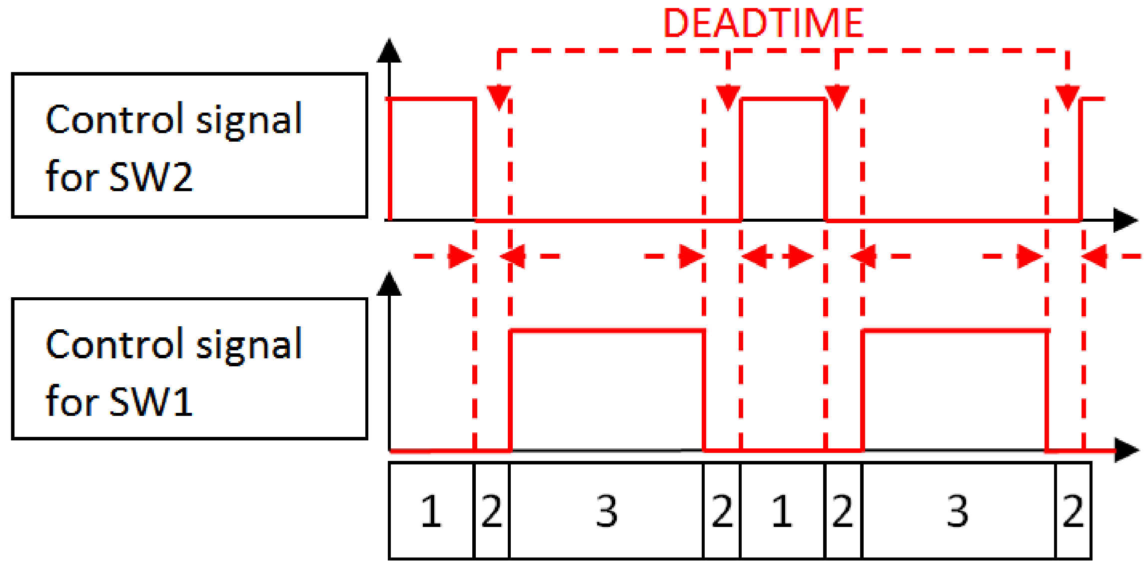

Appendix 4 Figure 13: Diagram representing the timing of the 2 signals controlling the MOSFETs SW1 and SW2

It is very important that SW1 and SW2 are not turned ON at the same time, which would short circuit the power supply VDC. For this reason, a dead-time generating circuit (Appendix 4 Figure 14) must control the dead-time between the ON and OFF signals actuating SW1 and SW2 (2).

The dead time circuitry ensures there is no cross-conduction of the MOSFETs which would short-circuit the output of the power supply. It is made of an AND logic gate, a resistor, a diode and a capacitor. The aim of the resistor-capacitor (RC) network is to delay the signal before it arrives at the input B, so that the output Y stays low during this time. The duration of the dead time is set to match the turn-on and turn-off times of the MOSFET in order to avoid having two conducting MOSFETs at the same time. According to the datasheet of the FDMS7578 (Fairchild-Semiconductor, 2009), the typical turn-on delay time is 8ns, whereas the typical turn-off delay time is 20ns. This means that there is a possibility for both MOSFETs to conduct at the same time for 12ns, which can damage the PSU at high switching frequencies.

The AND logic gate is a 74V1G08 from STMicroelectronics which has a 'High Level Input Voltage' of $0.7 \times \mathrm{Vcc}$ (STMicroelectronics, 2004). Since the 74V1G08 has a 3.3V supply, the input is detected as 'HIGH' when it reaches 2.31V. The RC time constant of the RC network constant is defined as the time it takes for the voltage across the capacitor to reach 63% of its maximum value. Since the logic voltage on the board is 3.3V, with a capacitor value of 33pF and a resistor of 360Ω the voltage at the input B should theoretically reach 2.08V in 11.88 ns ($\mathrm{i.e.}\ 360 \times 33 \times 10^{-12} = 11.88 \times 10^{-9}$).

This delay should therefore ensure a reliable operation of the pulse PSU.

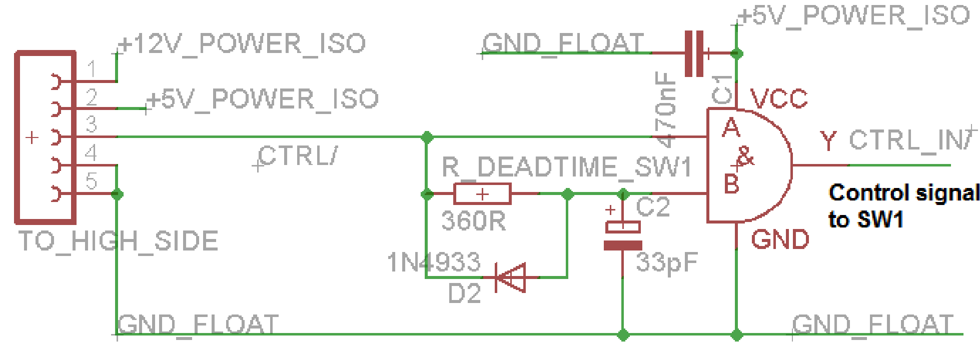

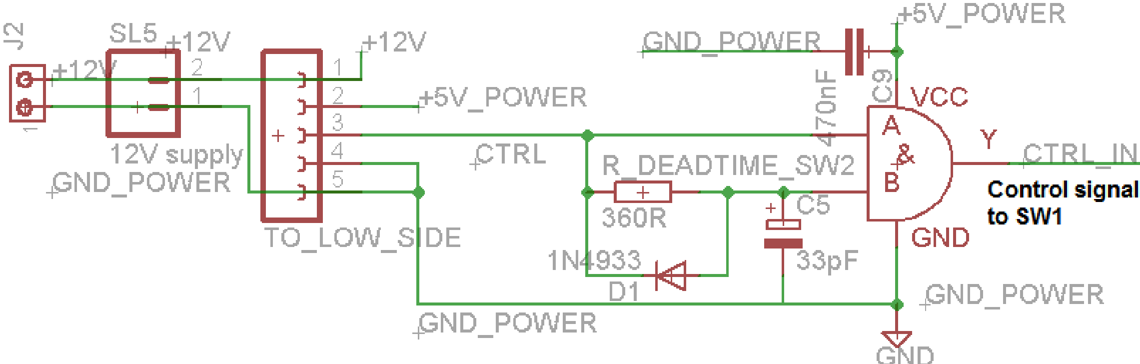

Appendix 4 Figure 14: Schematic diagram of the dead-time circuitry of the first prototype

The role of the diode is to provide a quick discharge path for the current in the capacitor in order to have a quick signal transition from the HIGH to the LOW state. This prevents the turn-off command from being delayed by the RC network.

Appendix 4.3.2. MOSFET selection

The MOSFETs have been selected to the following criteria:

- Operating voltage
- Operating current
- Turn-on and turn off-time
- Package shall allow soldering by hand

The selected MOSFET is a FDMS7578 from Fairchild Semiconductors (Appendix 4 Figure 15). This N-Channel MOSFET has been designed specifically to improve the overall efficiency and to minimize switch node ringing of DC/DC converters using either synchronous or conventional switching PWM controllers. It has been optimized for low gate charge, low ON resistance ($R_{DS(ON)}$), fast switching speed and body diode reverse recovery performance (Fairchild-Semiconductor, 2009).

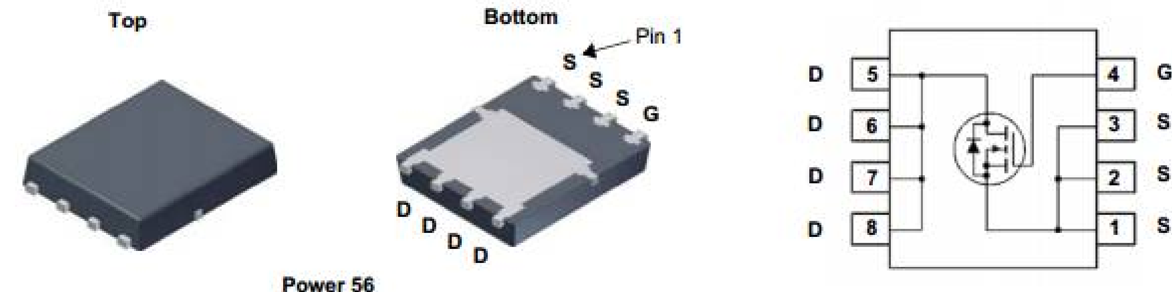

Appendix 4 Figure 15: CAD Model of the package (Power 56) and representation of the MOSFET FDMS7578 (Fairchild-Semiconductor, 2009)

The main characteristics of the FDMS7578 are summarised below (Appendix 4 Table 3):

Parameters	**Value**	**Unit**
Maximum drain to source voltage V_{DS}	25	V
Maximum drain current I_D	17 continuous 60 pulsed	A
Drain-source on resistance, $R_{DS(ON)}$:	0.0058	Ω
Typical Turn-On Delay time	8	ns
Typical Rise Time	2.6	ns
Typical Turn-Off Delay time	20	ns
Typical Fall Time	2.2	ns
Maximum Gate-source voltage, V_{GS}:	+/-20	V
Gate-source threshold voltage V_{TH}:	1.6	V
Source ohmic resistance:	0.0025	Ω
Drain ohmic resistance:	0.0025	Ω
Input capacitance C_{iss}:	1221	pF
Reverse transfer capacitance C_{rss}:	54	pF

Appendix 4 Table 3: Table summarizing the main characteristics of the MOSFET FDMS7578

Appendix 4.3.3. Driver selection

The UCC27201DG4 high frequency N-Channel MOSFET driver includes a high-side/low-side driver with independent inputs for maximum control flexibility. This allows for N-Channel MOSFET control in half-bridge or full-bridge converters. The low-side and the high-side gate drivers are independently controlled and matched to 1-ns between the turn-on and turn-off of each other (TI, 2008).

In most cases, controlling the high-side MOSFET requires the use of a bootstrap diode and a bootstrap capacitor to create a floating reference at its source - allowing a gate-source voltage V_{GS} to be applied. However the desired switching frequency of the pulse power supply is too high to use such configuration. The high-side gate driver is therefore not used and each MOSFET will have its own driver. A floating ground (GND_FLOAT) is provided to the high-side driver using an isolated 12V DC-DC converter (Appendix 4 Figure 16).

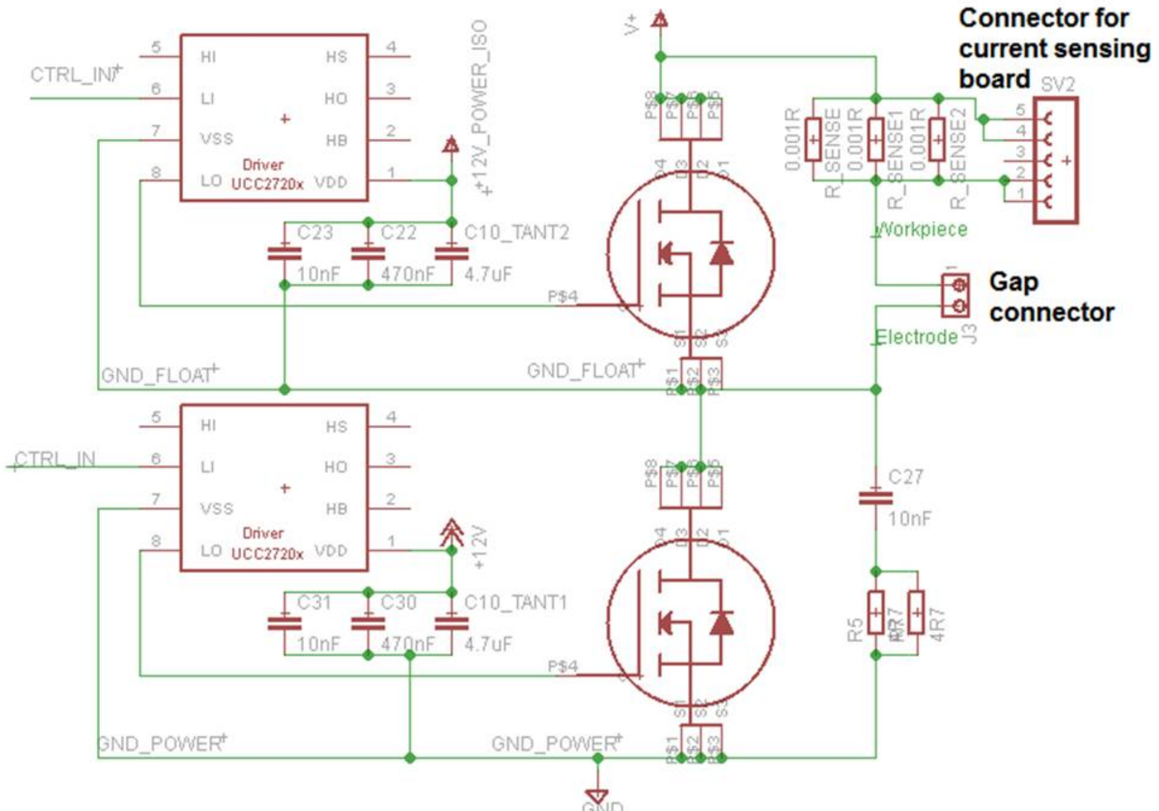

Appendix 4 Figure 16: Schematic diagram of the MOSFETs and their drivers

Appendix 4.3.4. Power electronics board layout

The layout of the power board is important in order to reduce the noise generated by the board and the recommendations mentioned in section 'Appendix 3.1.5 Board design considerations and assembly' were followed whenever possible.

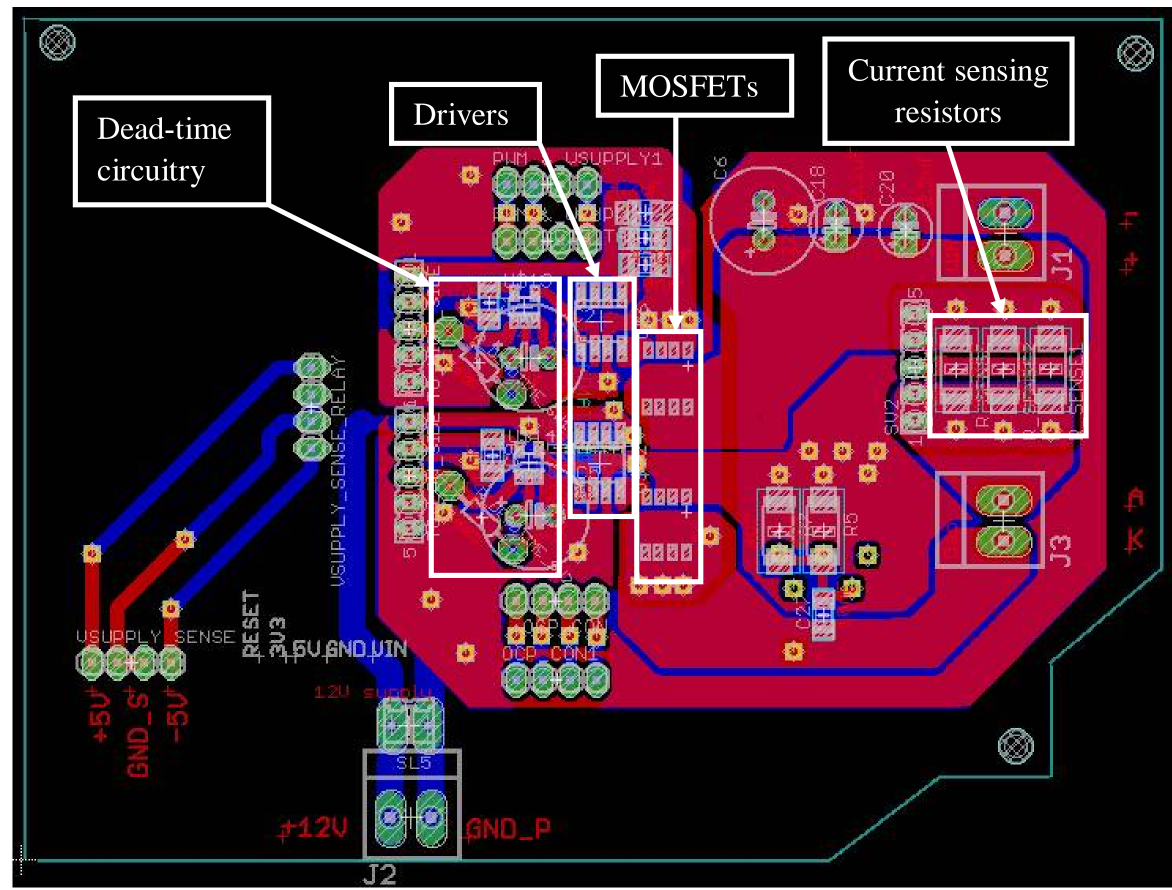

Appendix 4 Figure 17: Picture of the printed circuit board layout of the control circuitry

A picture of the fully assembled power board can be seen on Appendix 4 Figure 18.

Appendix 4 Figure 18: Picture of the power board of the first prototype

Appendix 4.4. First prototype: The current sensing board

The current flowing through the IEG is measured via a sensing resistor in series with the gap. The voltage across this resistor is amplified and sent to both the over current protection (for power supply safety purposes) and the control system –via a peak detector– (for gap control purposes).

According to Ohm's law, the voltage across this resistor is an image of the current flowing through the system. This voltage is measured using a current feedback amplifier EL5166ISZ which has a very high bandwidth of 1.4GHz and a 6000V/µs slew rate (Intersil, 2010). It is therefore suitable for the detection and amplification of small high frequency signals similar to the signal across the current sensing resistor.

The output of the differential amplifier goes to 2 different parts: 1) the over current protection (OCP) and 2) the peak detector.

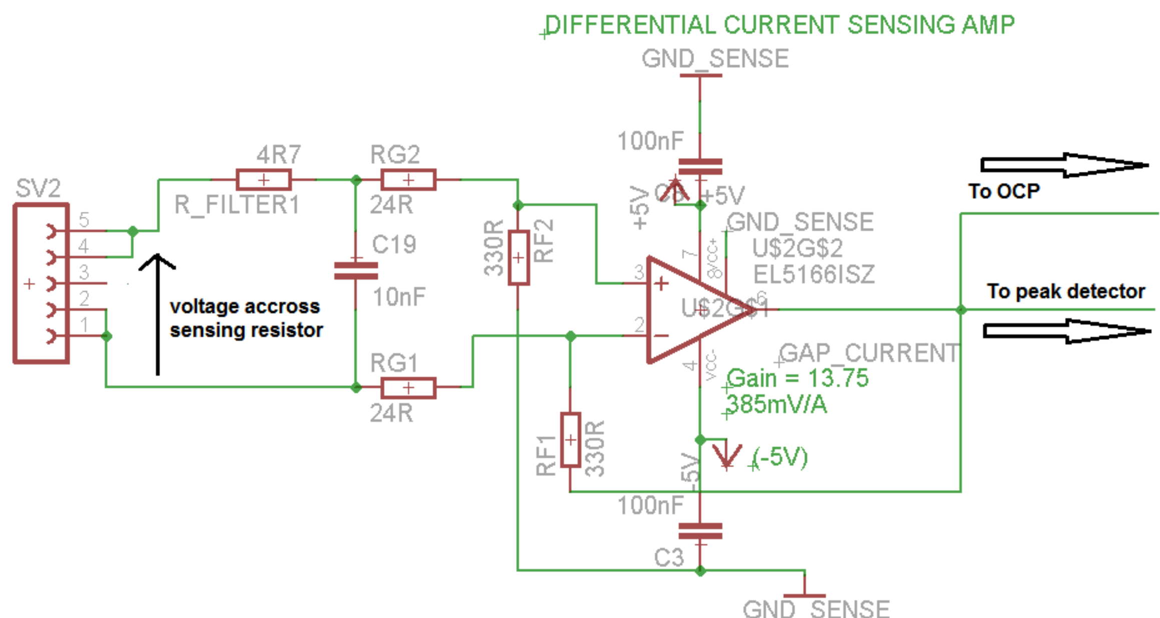

Appendix 4 Figure 19: Electrical schematic of the current sensing circuitry featuring the amplifier EL5166ISZ

The current sensing resistor has value of 25mΩ, which means that a measured voltage of 25mV corresponds to 1A. The differential amplifier has a gain of 13.75 and is set using the equation:

$$G = RF1/RG1 = RF2/RG2 \tag{7}$$

The on-board current scale is therefore $0.025 \times 13.75 = 0.344$ V/A.

Due to the low precision of the resistors setting the gain, the actual scale is 0.385V/A.

Appendix 4.4.1. Over current protection (OCP)

The OCP circuitry (Appendix 4 Figure 20) is made of a comparator which will compare the output of the differential amplifier with the OCP level set by the microcontroller. The

comparator used for this application is very fast: it is a LT1719 from linear technology and features a very short 4.5ns propagation delay.

The OCP threshold level is set by filtering one of the PWM outputs of the microcontroller with an RC filter. If the measured current is higher than the defined threshold level, the output of the comparator will go HIGH. The signal is its HIGH state will then go through a magnetocoupler (which ensures the isolation between the OCP circuitry and the control circuitry) and will then set the S/R latch gate to HIGH as well. The S/R latch gate will remain in a latched state until it is reset by the Max32 microcontroller board sending a 1ms pulse to the RES_R pin.

The OCP signal connected to the AND gates in the previously seen control circuitry actually corresponds to the OCP_LATCH/ signal, as the signal needs to go LOW to stop the PSU from pulsing. On the other end, the OCP_LATCH signal is connected to a red LED (not presented in the schematic) which will light up to signal to the operator that the PSU has been stopped because of an OCP event.

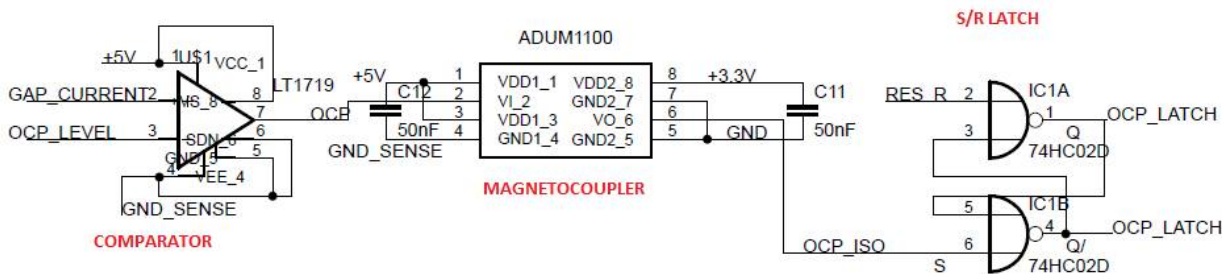

Appendix 4 Figure 20: Schematic of the OCP circuitry

Appendix 4.4.2. The peak detector

The peak detector plays a very important role as it delivers the peak value of the current to the motion controller. It is used to control the interelectrode gap as an input variable for the control algorithm. This peak detector circuitry uses a transistor (Q1) instead of a diode in order to reduce the rise time of the pulse (Appendix 4 Figure 21). When a pulse is detected, the operational amplifier LM7171 will charge the capacitor CDECAY via the resistor R_RISE – which sets the charging time of CDECAY. During the pulse off time the voltage across CDECAY decreases slowly as this latter is discharging itself through the resistor R_DECAY. The role of the transistor is to control the discharging current of CDECAY.

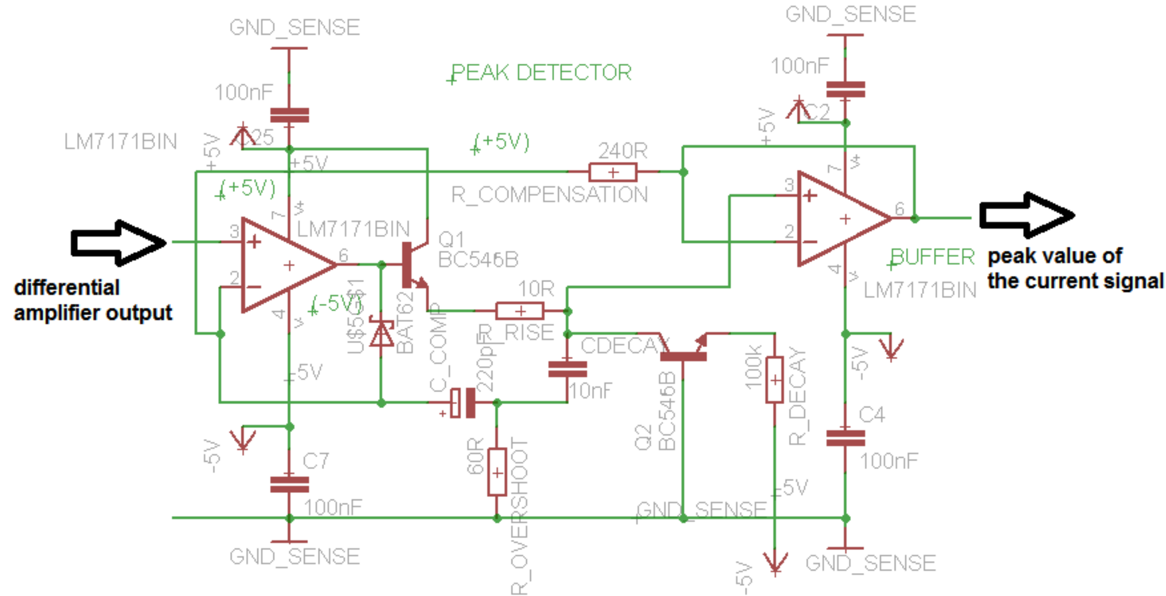

Appendix 4 Figure 21: Peak detector circuitry

Appendix 4.4.3. First prototype: firmware programming

The firmware of the PSU has been programmed using the MPIDE developing environment. This programme allows you to write a programme, compile it and the download it to the Max32 development board via an USB cable. The programme will start executing as soon as the Max32 is powered up, allowing it to run in standalone mode and its execution workflow is summarised in Appendix 4 Figure 22.

If no data is received, the programme stays in 'idle' mode and disables the pulses if the OCP is triggered.

The programme starts a sequence of instructions as soon as it receives data. The data is extracted from a character buffer and each parameter is converted from a string to a long integer using the standard atol() C function.

When all the data is received, the OCP is reset by the microcontroller which send a 50ms pulse to the reset pin of the S/R latch.

The controller then starts calculating the value of IIN using the formula:

$$\text{IIN}\ (\mu\text{A}) = \frac{C_F\ (\text{pF}) \times F_O(\text{Hz})}{1000000} \tag{8}$$

Then the controller checks if the condition $2\mu A < IIN < 750\mu A$ is satisfied, if that is not the case it aborts and returns to its 'idle' mode.

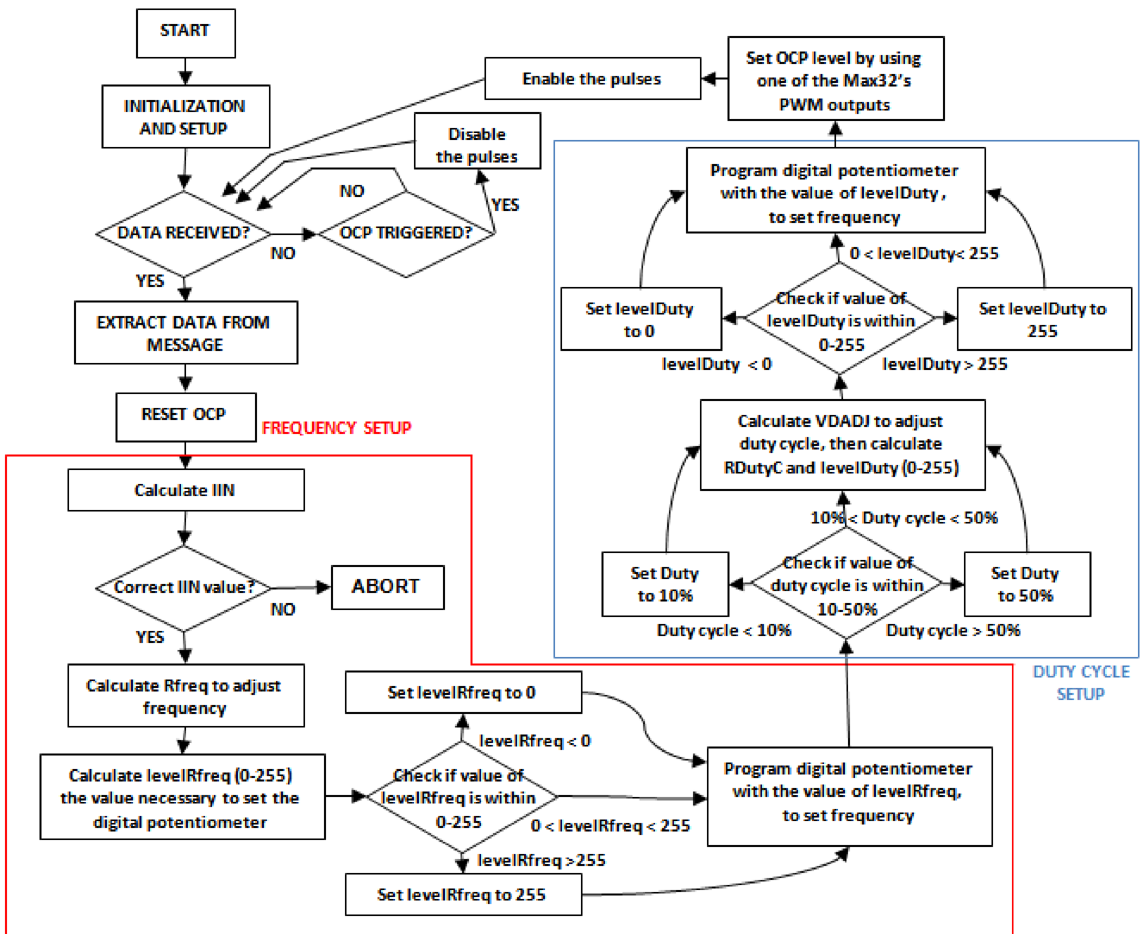

Appendix 4 Figure 22: Flowchart describing the firmware workflow running on the first PSU prototype

If IIN has a correct value, the resistance R_{Freq} is calculated. R_{Freq} corresponds to R_{W1B1}, the resistance of the potentiometer AD8402 connecting REF to IIN.

$$R_{Freq} = R_{W1B1} = \frac{REF}{IIN} \tag{9}$$

R_{Freq} is then used to calculate the value of levelRfreq which is the decimal value ranging from 0 to 255 needed to programme the AD8402:

$$levelRfreq = round\left(\frac{(R_{Freq} - R_{W1}) \times 256}{R_{A1B1}}\right) \tag{10}$$

The value of levelRfreq is then assessed to prevent the digital potentiometer from being configured with wrong values:

- If levelRfreq > 255, then levelRfreq is set to 255
- If levelRfreq < 0, then levelRfreq is set to 0

The value of levelRfreq is then to the digital potentiometer using the SPI communication protocol. The programme uses the standard SPI library provided by mpide. The function of

the SPI library were wrapped in the function digitalPotWrite() presented in Appendix 4 Figure 23.

```
int digitalPotWrite(int address, int value) {
  // take the SS pin low to select the chip:
  digitalWrite(slaveSelectPin,LOW);
  //  send in the address and value via SPI:
  SPI.transfer(address);
  SPI.transfer(value);
  // take the SS pin high to de-select the chip:
  digitalWrite(slaveSelectPin,HIGH);
}
```

Appendix 4 Figure 23: the digitalPotWrite() function used to communicate with the AD8402 digital potentiometer

The same approach was used for setting up the duty cycle:

1- The value of the duty cycle is checked and readjusted if necessary
2- The voltage VDADJ needed to reach the desired duty cycle is calculated
3- The resistance R_{W2B2} value of the potentiometer needed to adjust VDADJ is calculated
4- The decimal value levelDuty (0-255) is calculated using the value of R_{W2B2} and readjusted if it is out of the 0 and 255 boundaries
5- The decimal value levelDuty is sent to the digital potentiometer using the function digitalPotWrite()

Once both potentiometers have been configured, the controller will set the OCP trigger threshold by using one of its pulse width modulated (PWM) outputs. Pin 5 outputs the PWM signal with a frequency of 500Hz and is connected to the input of a ADUM1100 magnetocoupler. The output of the magnetocoupler is connected to a low-pass filter (on the OCP board) which is itself connected to the – input of the ultrafast LT1719 comparator.

The function SoftPWMServoPWMWrite() controls the PWM signal and is a standard function of the SoftPWMServo library.

Finally, after the OCP threshold is setup, the pulses are enabled. This operation is done by setting the pin A6 to a HIGH state which satisfying the AND condition of the AND gate on the circuit board.

Appendix 4.5. Tests and conclusion on first prototype

In the following tests, the 3 boards were assembled (Appendix 4 Figure 24) and the output of the pulse PSU was connected to a 1Ω resistor having a 50W power rating.

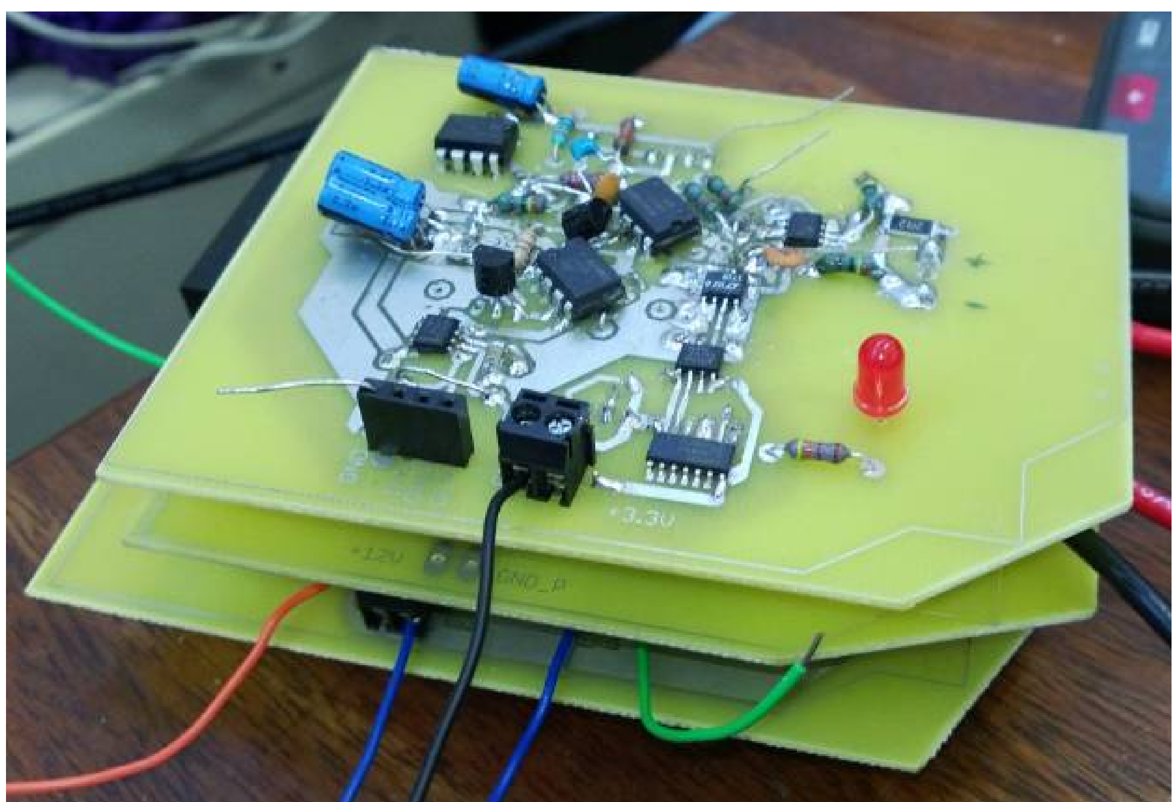

Appendix 4 Figure 24: Picture of the fully assembled first PSU prototype

Appendix 4.5.1. Measuring the PSU output and the influence of cabling

It can be seen on Appendix 4 Figure 25 that there is a big difference between the amplitude of the pulses measured on-board at the output of the PSU (C3) and their amplitude measured at the load, after the cabling. This highlights the influence of the cabling, showing that their length shall be minimized to reduce their parasitic inductance. Parasitic inductance is an important issue when working at high-frequencies (typically above 1MHz), it increases the impedance of the cable, which will distort the pulses and decrease the amount of current able to flow through the system.

The frequency was set to 2.5MHz and the duty cycle was 20%. The pulse voltage was adjusted manually to 6V.

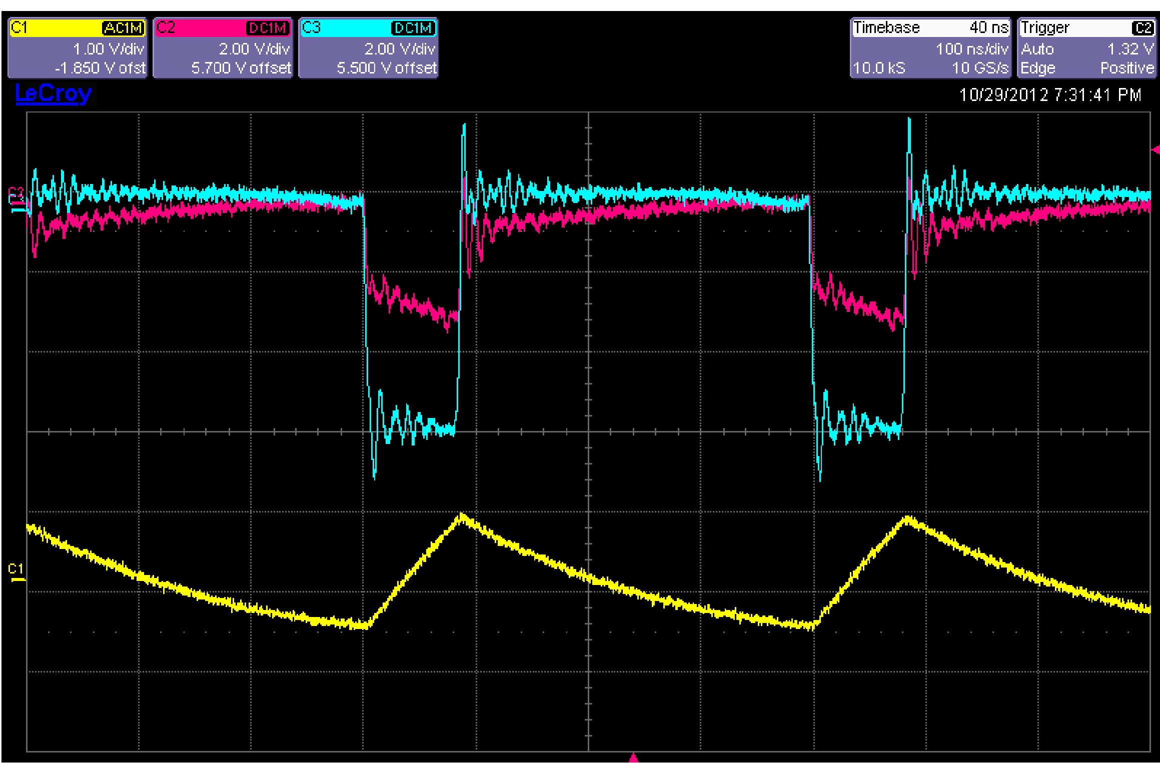

Appendix 4 Figure 25: C1 (yellow): current measured from external current sensor (1V/div.,1V/A); C2 (pink): voltage measured across the load, after the cables (2V/div.); C3 (cyan): voltage measured at the output of the pulse PSU, on the board connectors (2V/div.). Frequency: 2.5MHz duty cycle: 20%.

The frequency was then lowered to 800kHz and the voltage was set to 5V to prevent the load from heating up too much. It can be seen on Appendix 4 Figure 26 that the voltage at the load is much higher than when it was at 2.5MHz. Moreover, the amplitude of the current pulses is much high also, reaching 2.5A. This confirms the necessity for a low impedance cables to be used in µECM.

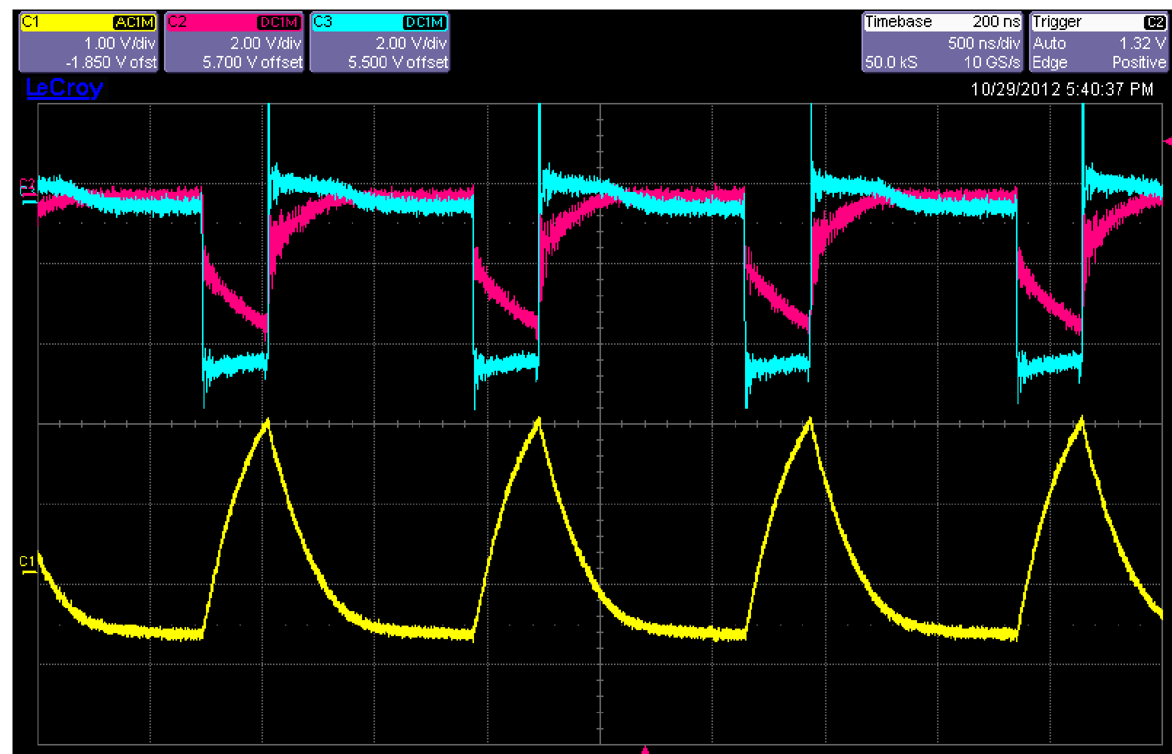

Appendix 4 Figure 26: C1 (yellow): current measured from external current sensor (1V/div.,1V/A); C2 (pink): voltage measured across the load, after the cables (2V/div.); C3 (cyan): voltage measured at the output of the pulse PSU, on the board connectors (2V/div.). Frequency: 800kHz duty cycle: 20%.

Appendix 4.5.2. On-board signal measurement

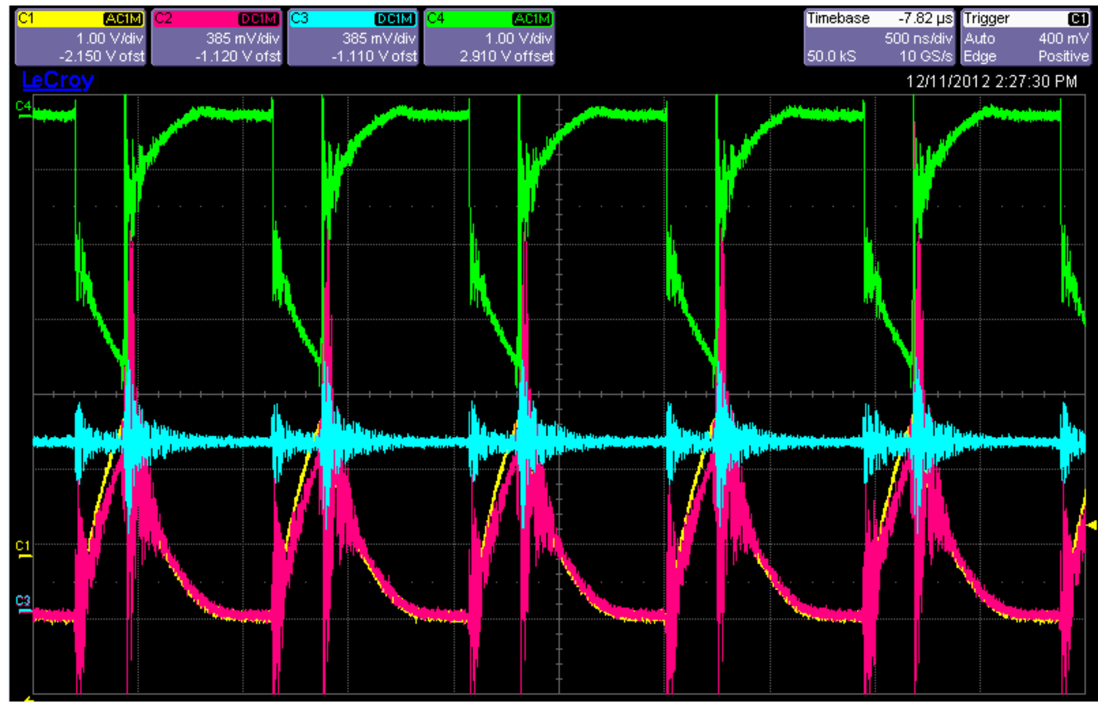

Appendix 4 Figure 27: Signals on the current sensing board

Channel	Description	Scaling
C1	Measured gap current via commercial current sensor	1V/div., 1V/A
C2	Measured gap current via on-board current sensing circuitry	380mV/div., 380mV/A
C3	OCP threshold level	380mV/div., 380mV/A
C4	Measured voltage across the resistance (inverted to avoid short circuits)	380mV/div., 380mV/A

Appendix 4 Table 4: Description of the signals measured in Appendix 4 Figure 27

On Appendix 4 Figure 27 it can be seen that the shape of the current measured with the on-board circuitry (C2) is very similar to the one measured with the commercially available current sensor (C1). The peak detector is working as expected and its output signal can be seen in channel C3. However, the presence of noise on channel C2 and C3 can be observed. This noise is generated when the MOSFETs are switched ON and OFF.

Appendix 4.5.3. Conclusions regarding the first PSU prototype

The first prototype delivered the expected results despite off the noise present in the sensing circuitry. However, some limitations have been observed:

- The way the MAX038 function generator is configured prevents a wide range of frequency to be reached because the C_F capacitance used to the oscillator cannot be changed automatically.
- There is no possibility to reverse to polarity is a programmed way. The only way to do so is to swap the cable connections.
- It is not possible to apply a negative or positive voltage offset voltage during the pulse of time
- The size of the board is too big and the footprint of the board shall be optimized.

This prototype was mainly considered as a proof of concept to validate the choice for the core components and the 3-board modular architecture. It has been deduced that this concept would be a viable way to develop the other prototypes.

Appendix 5. PULSE PSU SIMULATION WITH MATLAB/SIMULINK

Appendix 5.1. Basic model (ideal)

To simulate the behaviour of the pulse PSU prototype, a model of the circuitry has been realised using MATLAB/Simulink.

The MOSFET switches used in the pulse PSU design are FDMS7578 N-channel MOSFETs from Fairchild Semiconductor. They have been chosen because of their very fast turn-on and turn-off times (respectively 8 and 20ns).

The behaviour of the MOSFET is simulated by the Simulink library component 'N-Channel MOSFET' and its parameters (Appendix 5 Table 1) have been set according to the values available in the datasheet of the FDMS7578 (Fairchild-Semiconductor, 2009).

Parameters	Value	Unit
Drain-source on resistance, R_DS(on):	0.0058	Ω
Drain current, Ids, for R_DS(on):	17	A
Gate-source voltage, Vgs, for R_DS(on):	10	V
Gate-source threshold voltage Vth:	1.6	V
Source ohmic resistance:	0.0025	Ω
Drain ohmic resistance:	0.0025	Ω
Input capacitance Ciss:	1221	pF
Reverse transfer capacitance Crss:	54	pF

Appendix 5 Table 1: Table summarizing the parameters of the N-Channel MOSFET Simulink component used in the simulation

The pulse PSU model used in the simulation is represented in Appendix 5 Figure 1:

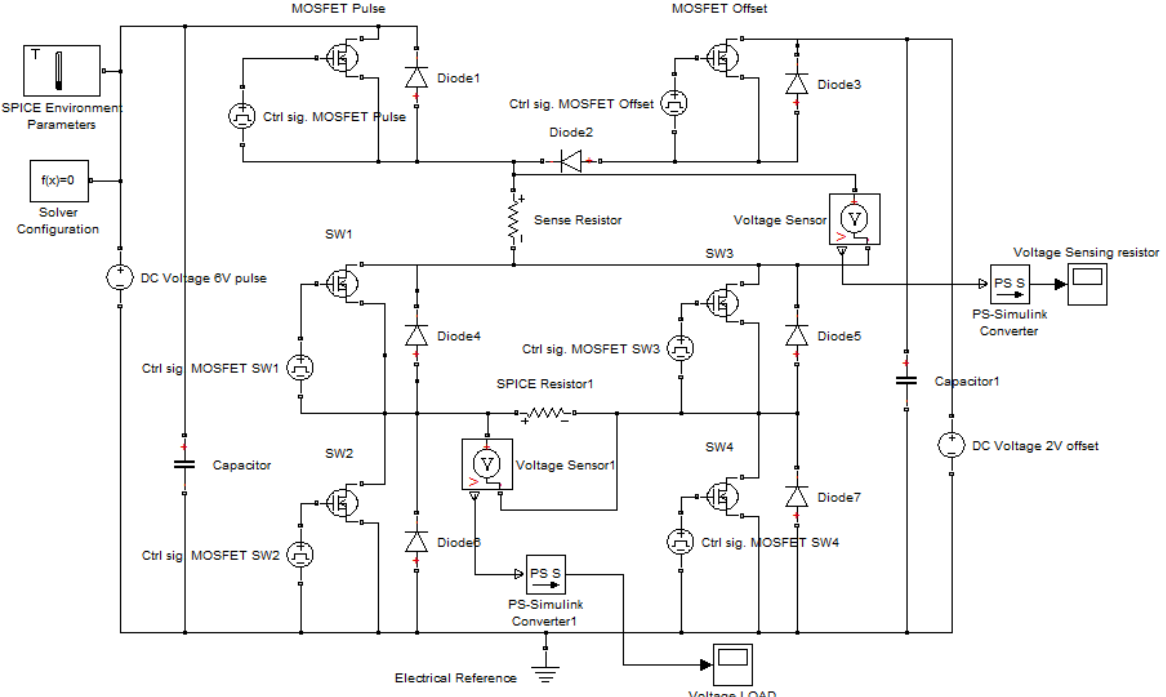

Appendix 5 Figure 1: Model of the second prototype of the pulse PSU

The value of the DC voltage source for pulses was set to 6V, whereas the DC source for the offset was set to 2V. The load is represented by a resistor of 1Ω.

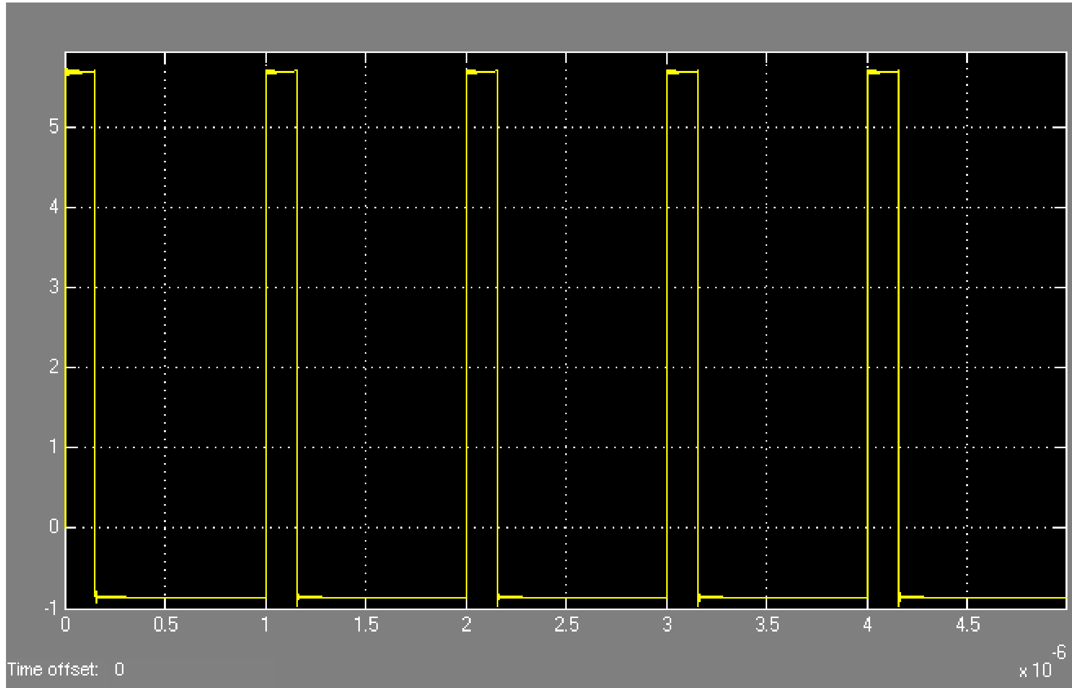

Appendix 5 Figure 2: Simulation result: evolution of the IEG voltage (V) over time (s) in steady state

Diode forward voltage has been set to 1V, therefore the negative Offset during the pulse off-time is closer to -1V instead of -2V (which is the value of the source).

Appendix 5.2. Realistic model (including parasitics)

The following model has been modified by adding parasitic inductance and snubber capacitors. Cables have a parasitic inductance of 75nH and to model its influence on the pulses, inductors have been added to the circuit.

It can be observed that the inductance of the cables decreases the rise time of the pulses and will therefore be an issue when sending high frequency pulses to the IEG. On the other hand, a negative kick can be observed after each pulse. Changing the values of the snubber resistors and capacitors affects the shape of this negative transient signal. Conclusions for second PSU prototype

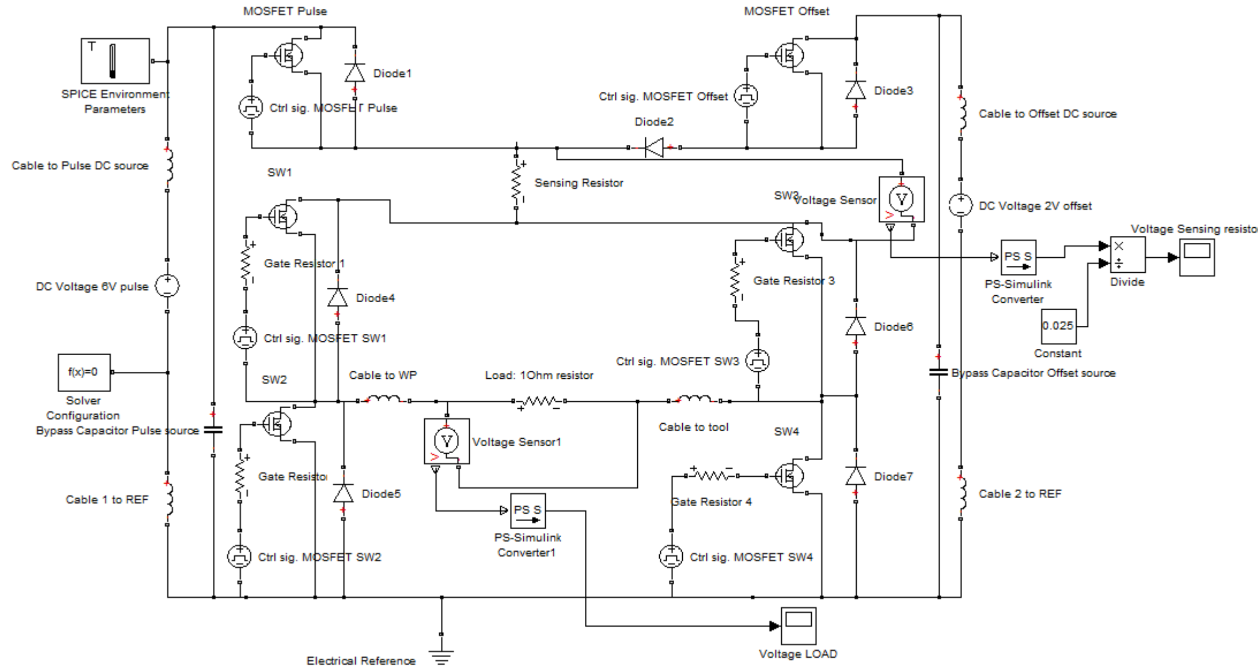

Appendix 5 Figure 3: Electrical schematic diagram of the power stage used in the Simulink simulation

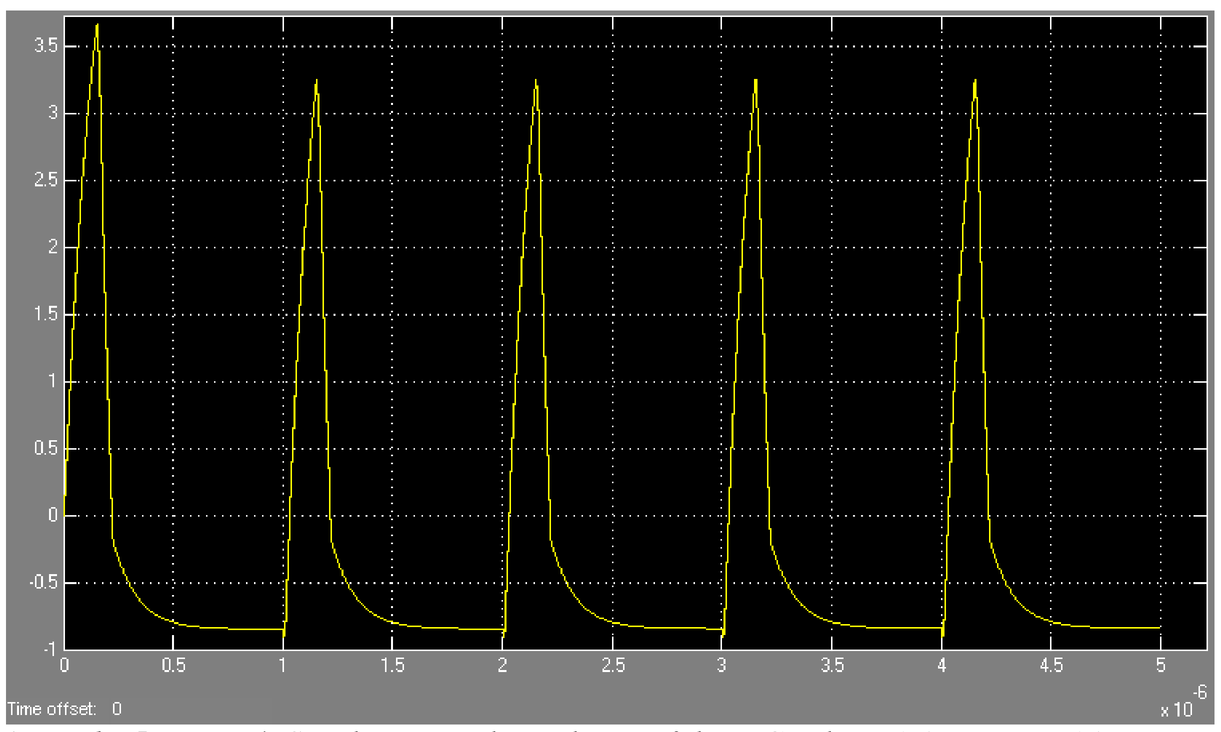

Appendix 5 Figure 4: Simulation result: evolution of the IEG voltage (V) over time (s) in steady state when the parasitics have been added

Appendix 6. SECOND PULSE PSU PROTOTYPE

The second PSU was designed according to the simulation results from the previous appendix.

Appendix 6.1. Second PSU prototype: control circuitry

Appendix 6.1.1. Pulse generating module

This module generates the signal controlling the MOSFETs. The frequency needs to be variable over a range, 1 kHz to 5MHz, with a duty cycle changing from 5% to 100% (DC).

The solution adopted is shown in **Error! Reference source not found.** and uses two components: an oscillator and a pulse generator.

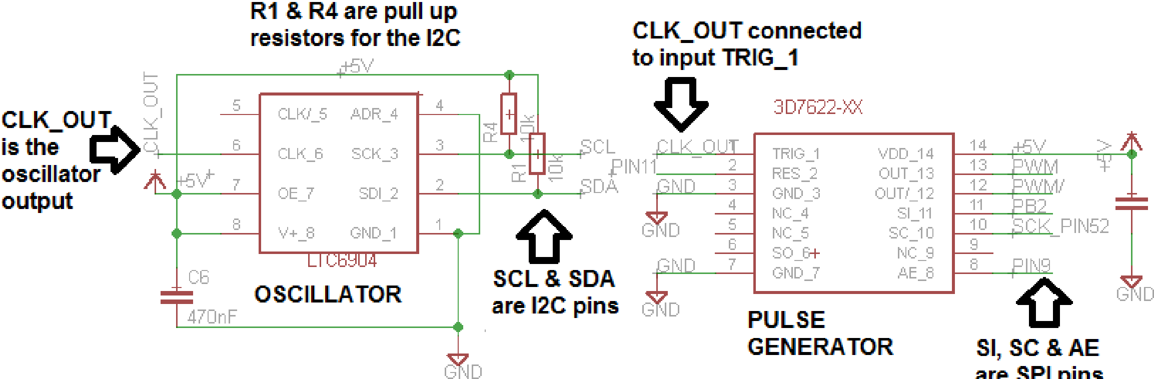

Appendix 6 Figure 1: Electrical schematic diagram of the oscillator and the pulse generator

- **Oscillator**

The LTC6904 is a low power self-contained digital frequency source providing a precision frequency from set through a serial port. This programmable oscillator is capable of generating a 5V logic signal at a frequency varying from 1kHz to 68MHz. The LTC6904 requires no external components other than a power supply bypass capacitor, and it operates over a single wide supply range of 2.7V to 5.5V.

The frequency of the oscillator is set according to the following equation (Linear Technology, 2014):

$$f = 2^{OCT} \cdot \frac{2078(Hz)}{\left(2 - \frac{DAC}{1024}\right)} \qquad (1)$$

OCT is a four-bit digital code and DAC is a ten-bit digital code. Evaluating this formula to calculate OCT and DAC from a required frequency f, gives the following statements:

$$\mathrm{OCT} = 3.22\log_{10}\left(\frac{f}{1039}\right),$$
$$\mathrm{DAC} = \mathrm{round}\left(2048 - \frac{2078(\mathrm{Hz}).\,2^{(10+\mathrm{OCT})}}{f}\right) \quad (2)$$

The output of the programmable oscillator LTC6904 is connected to the trigger input of the programmable pulse generator 3D7622-0.25 (**Error! Reference source not found.**Figure 4-2). The pulse generator will therefore output pulses at each rising edge of the signal coming from the LTC6904, thus creating a pulse train with adjustable frequency and duty cycle.

- **Modulation component**

The Data Delay Devices 3D7622-0.25 device is a twenty two bit serial programmable pulse generator that operates with either CMOS or TTL logic levels (Data Delay Devices, 2008).

A rising edge on the trigger input (TRIG) initiates a pulse, which is presented on the output pins (OUT, OUTB) and ends at a time determined by the address loaded into the device via SPI serial interface. The pulse width, programmed via the serial interface, can be varied over 4,194,303 equal steps of 0.25ns. The 3D7622-0.25 has a minimum pulse width of 14.0ns and a maximum pulse width of 1.05ms. The pulse width can be varied according to the formula (Data Delay Devices, 2008):

$$t_{PW} = t_{inh} + \mathrm{addr} + t_{inc} \quad (3)$$

Where addr is the programmed address, t_{inc} is the pulse width increment (equal to 0.25ns) and t_{inh} inherent pulse width (equal to 14ns). The device also offers a reset input (RES) to terminate the pulse before the programmed pulse duration has expired.

The Arduino compatible Max32 development board is directly interfaced with the human machine interface (HMI), which sends all the data necessary to configure the pulse PSU: frequency, duty cycle, over current protection threshold and desired pulse shape. The microcontroller then sets the frequency by communicating with the programmable oscillator via I2C and also sets the duty cycle thanks to the pulse generator using the SPI communication protocol.

Appendix 6.1.2. Pulse shape selection

A multiplexer defines the polarity of the pulsed voltage. Signals PWM and PWM/ correspond respectively to outputs OUT and OUTB of the pulse generator. OUT and OUTB generate signals that are logically inverted from each other: if OUT is HIGH (5V) then OUTB is LOW (0V) and vice versa.

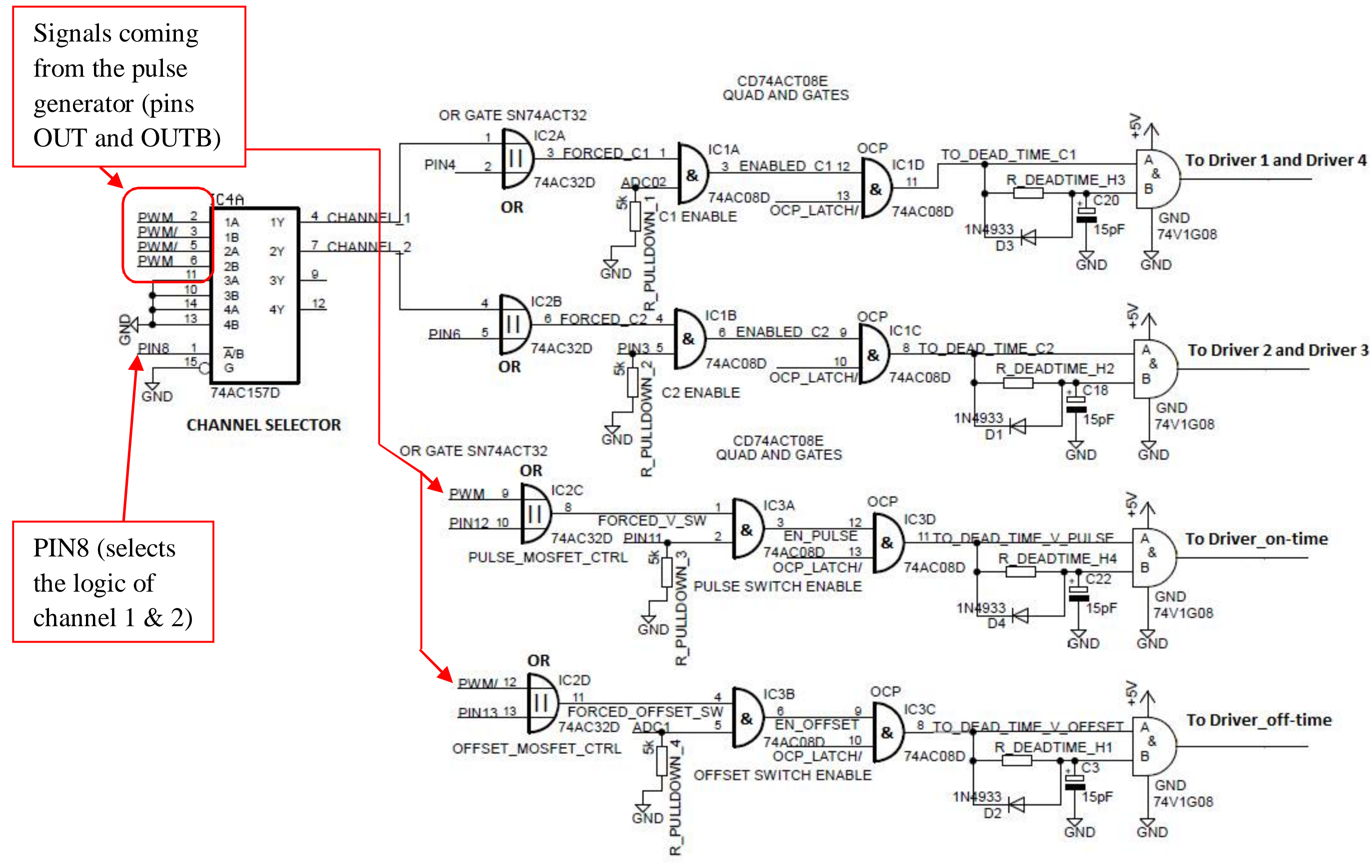

Appendix 6 Figure 2: Control circuitry of the second PSU prototype

If PIN8 is LOW (0V), Channel A is selected, so SW1 and SW4 are synchronized with SW_pulse whereas SW2 and SW3 are synchronized with SW_offtime. This results in the following configuration (Appendix 6 Figure 3):

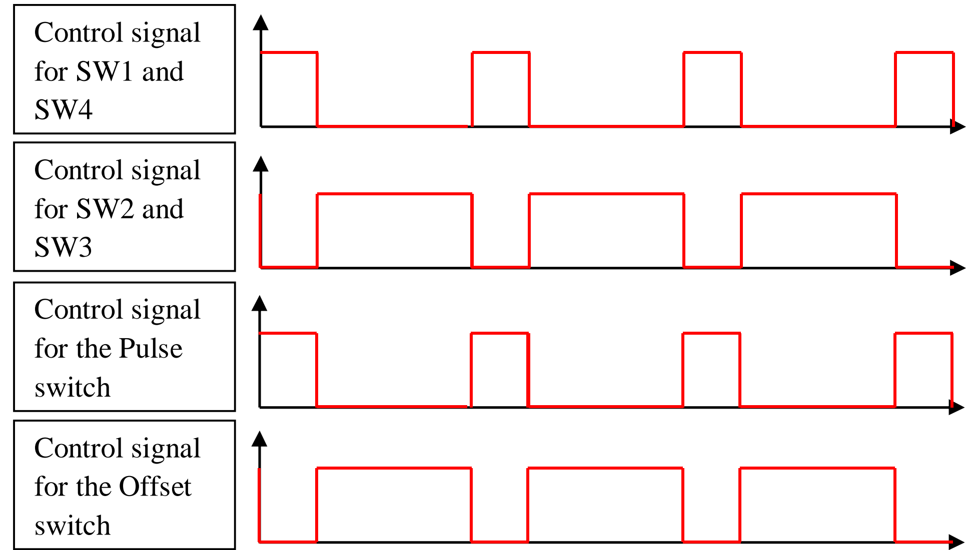

Appendix 6 Figure 3: Drawing representing the 4 different control signal used to change the pulse shape when Channel A is selected.

If PIN8 is HIGH (5V), Channel B is selected, so SW2 and SW3 are synchronized with SW_pulse whereas SW1 and SW4 are synchronized with SW_offtime. The following signals are obtained (Appendix 6 Figure 4):

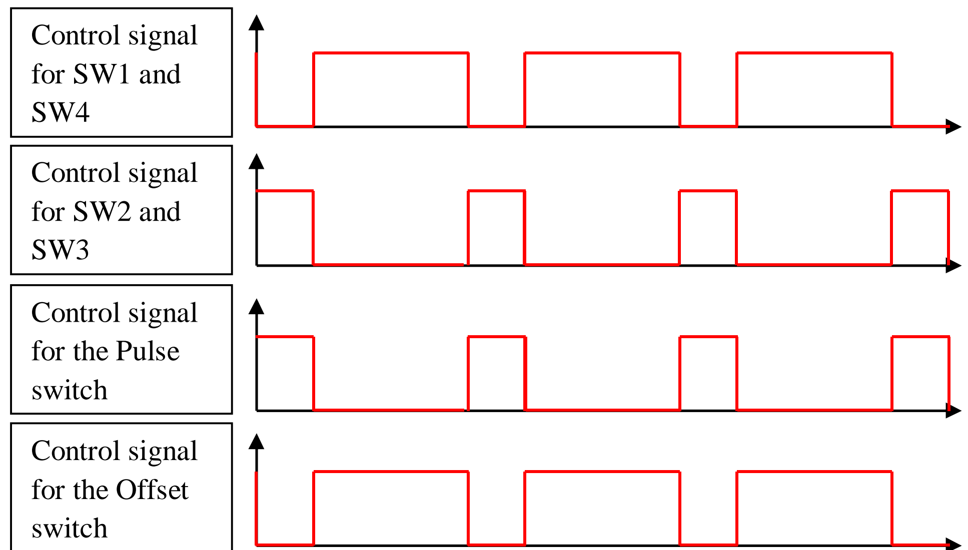

Appendix 6 Figure 4: Drawing representing the 4 different control signal used to change the pulse shape when Channel B is selected

The following drawing (Appendix 6 Figure 5) describes the different pulse shapes that can be obtained with the developed power supply:

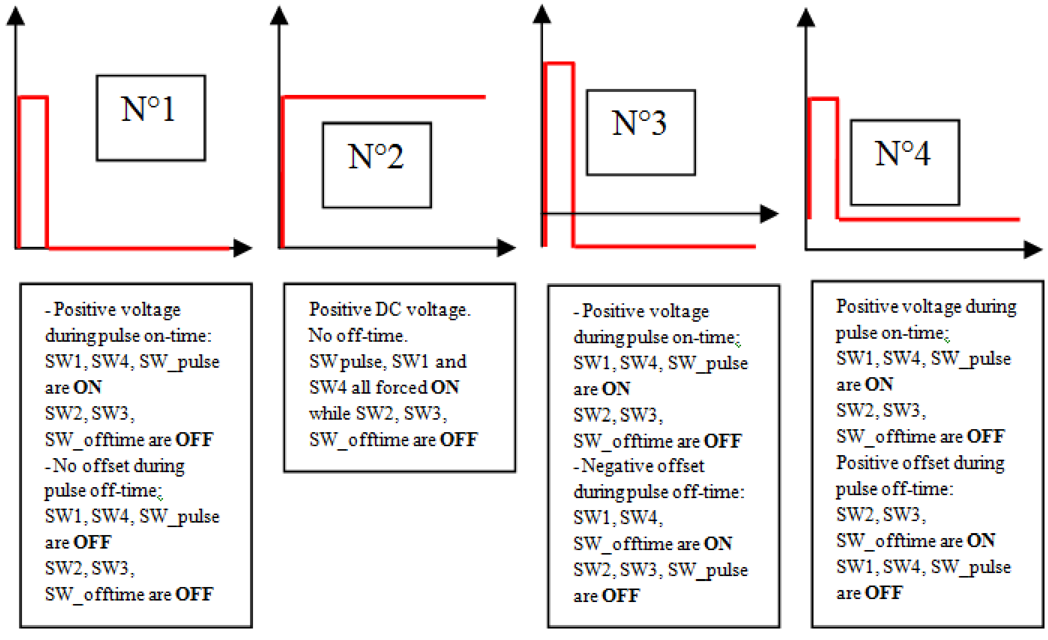

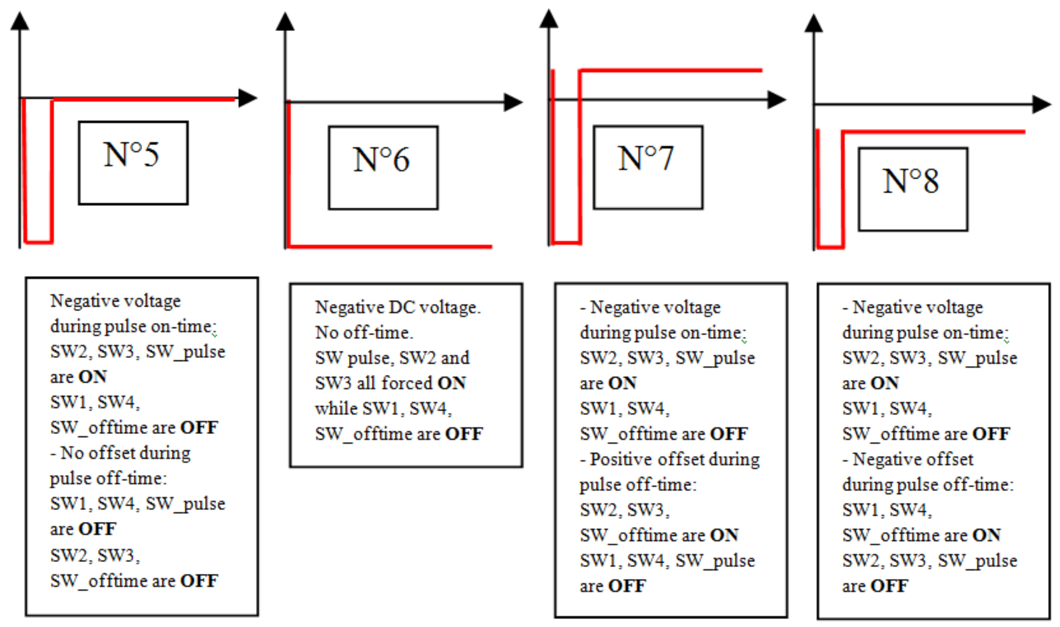

Appendix 6 Figure 5: Drawing of the different pulse shapes that can be obtained in the different configuration

Appendix 6.1.3. Avoiding MOSFET cross conduction

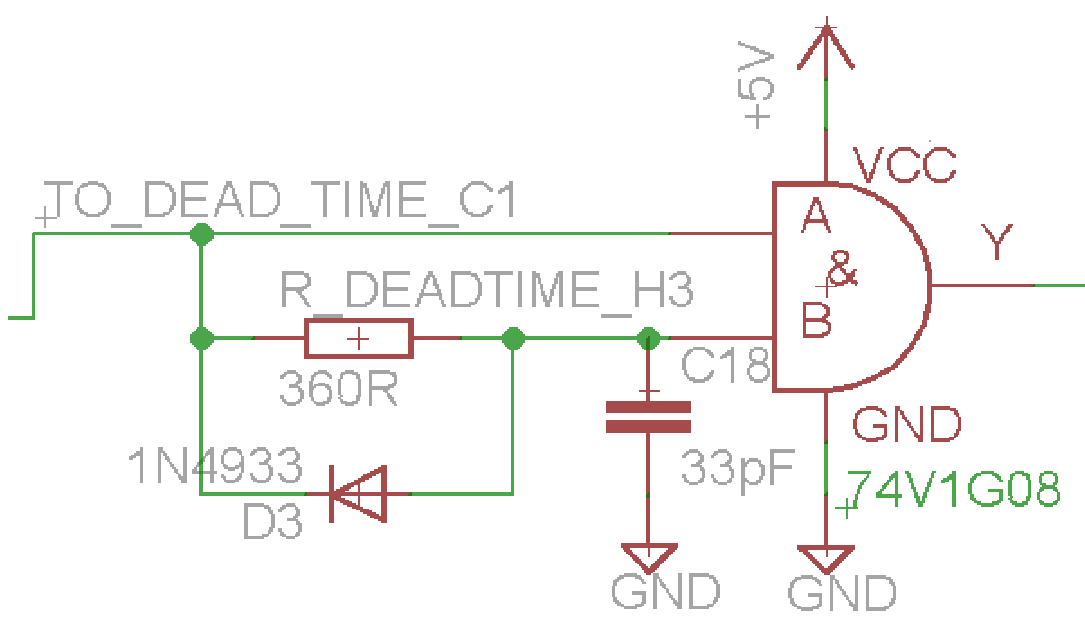

Appendix 6 Figure 6: Electrical schematic of the dead time circuitry used in the PSU

The dead time circuitry ensures there is no cross-conduction of the MOSFETs which would short-circuit the output of the power supply. It is made of an AND logic gate, a resistor, a diode and a capacitor (Appendix 6 Figure 6). The aim of the resistor-capacitor (RC) network is to delay the signal before it arrives at the input B, so that the output Y stays low during this time. The duration of the dead time is set to match the turn-on and turn-off times of the MOSFET in order to avoid having two conducting MOSFETs on the same side of the H Bridge (which would create a short circuit situation). According to the datasheet of the FDMS7578 (Fairchild-Semiconductor, 2009), the typical turn-on delay time is 8ns, whereas

the typical turn-off delay time is 20ns. This means that there is a possibility for both MOSFETs to conduct at the same time for 12ns, which can damage the PSU at high switching frequencies.

To reduce the noise generated by the MOSFETs during their turn-on and turn-off transitions, a resistor of 4.7Ω is added in series between the output of the MOSFET driver and the gate of the MOSFET. The aim of this resistor is to reduce the value of di/dt by increasing the charging time of the input capacitance C_{iss} of the MOSFET. The datasheet mentions typical values of C_{iss} = 1221pF for the gate capacitance and an internal gate resistance of 1.2Ω. Adding an external gate resistor of 4.7 therefore sets the charging of the gate capacitor to 7.2ns ($(4.7 + 1.2) \times 1221.10^{-12} = 7.2 \times 10^{-9}$).

The AND logic gate is a 74V1G08 from STMicroelectronics which has a 'High Level Input Voltage' of $0.7 \times Vcc$ (STMicroelectronics, 2004). Since the 74V1G08 has a 3.3V supply, the input is detected as 'HIGH' when it reaches 2.31V. The RC time constant ($\tau = RC$) of the RC network constant is defined as the time it takes for the voltage across the capacitor to reach 63% of its maximum value. Since the logic voltage on the board is 3.3V, with a capacitor value of 33pF and a resistor of 360Ω the voltage at the input B should theoretically reach 2.08V in 11.88 ns ($360 \times 33 \times 10^{-12} = 11.88 \times 10^{-9}$).

This delay should therefore ensure a reliable operation of the pulse PSU.

The role of the diode is to provide a quick discharge path for the current in the capacitor in order to have a quick signal transition from the HIGH to the LOW state. This prevents the turn-off command from being delayed by the RC network.

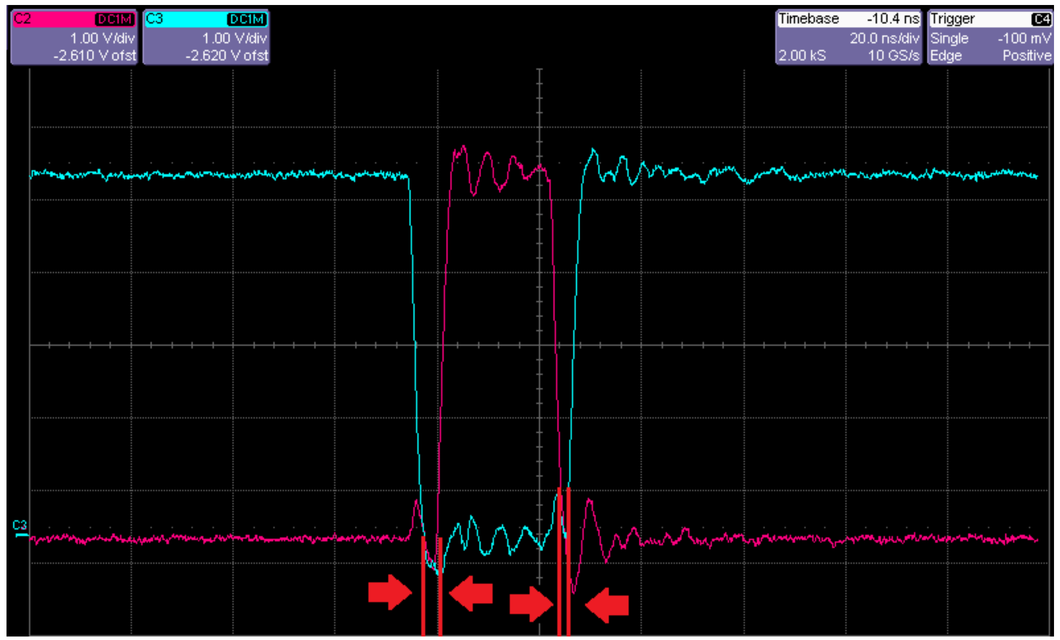

Appendix 6 Figure 7: Measurement of the dead time between the control signals to the 2 low side switches of the H-bridge; frequency: 5MHz, duty cycle: 25%

Appendix 6.2. Second PSU prototype: power stage

Different voltages can be applied to the H-bridge thanks to two MOSFETs, allowing to apply a lower voltage during the pulse off-time. A Schottky barrier prevents current from

flowing from V_PULSE to V_OFFSET (because V_PULSE is greater than V_OFFSET and the MOSFETs have built-in parallel diodes).

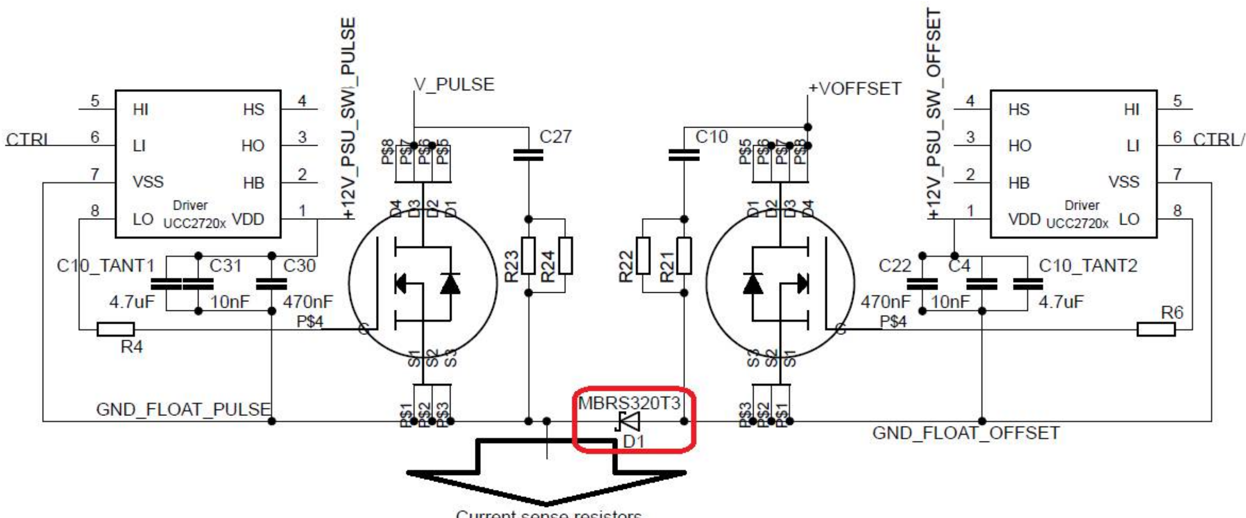

Appendix 6 Figure 8: Schematic of the MOSFETs switching between the PULSE and OFFSET voltages to be applied to the H-bridge

The drivers of the MOSFETs SW_pulse, SW_offset, SW1 and SW3 are isolated from the ground thanks to 4 individual isolated DC-DC converters. This allows driving the MOSFETs at a very wide range of frequencies and duty cycles.

To optimise the layout of the power stages, it has been decided that the drivers would be powered by the control circuitry board. The isolated DC-DC converters are therefore not present on the power stage, but on the control stage.

A pin connector placed close to the current sensing resistors allows the current sensing circuitry board to be plugged onto the power stage. The output of the current sensing circuitry board is interfaced with the control stage in order to interrupt the pulsing when the over current protection is triggered.

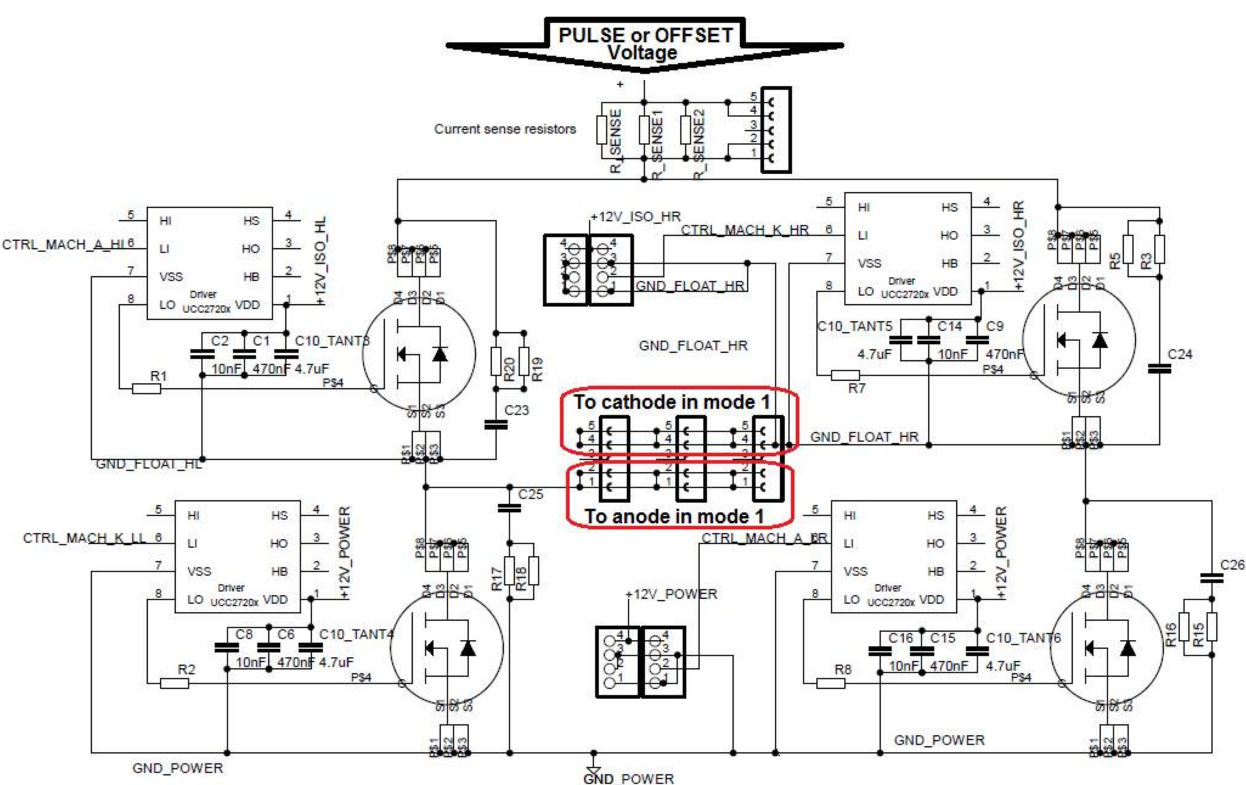

Appendix 6 Figure 9: Schematic of the MOSFETs in the H-bridge

- Configuration of the snubbers

Each of the switches on the power board has its own snubber circuitry which is made of a 10nF capacitor in series with two 500mW 10Ω resistors in parallel (equivalent resistance 5Ω). The snubbers damp the ringing which occurs when the switches are turned ON or OFF.

The following figures illustrate the improvement in pulse shape when the snubber circuitry is mounted of the power stage: it can be seen that the ringing is significantly reduced thanks to the snubbers, resulting in a better pulse shape.

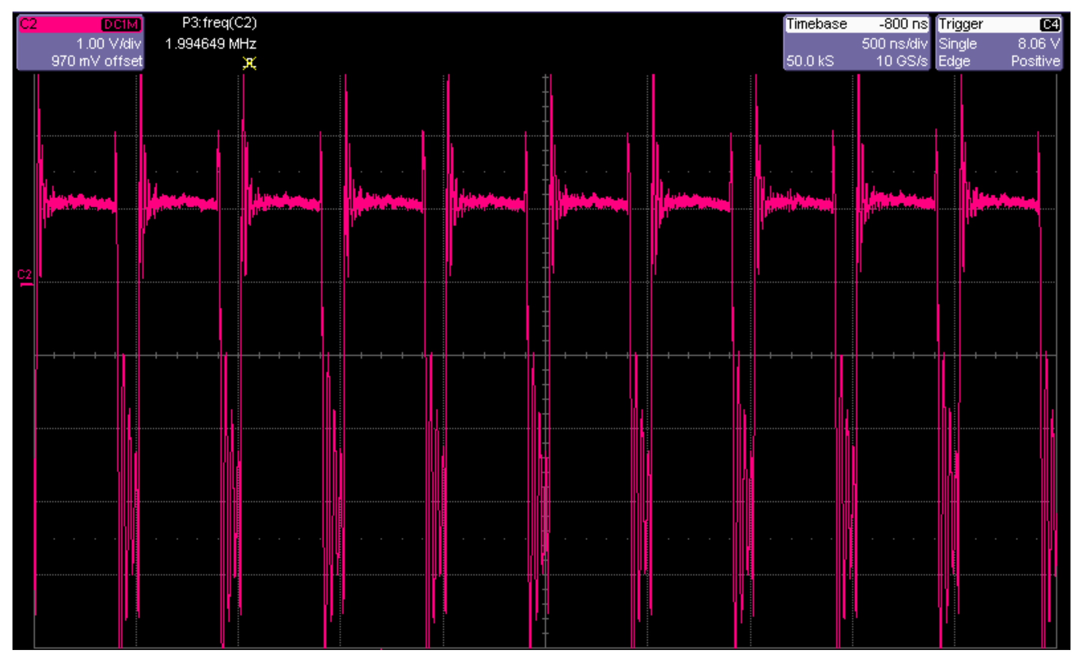

Appendix 6 Figure 10: Output of the second PSU prototype without any snubber circuitry, in mode 3, 3V pulse and 1V negative offset, 2MHz with 25% Duty cycle, no load.

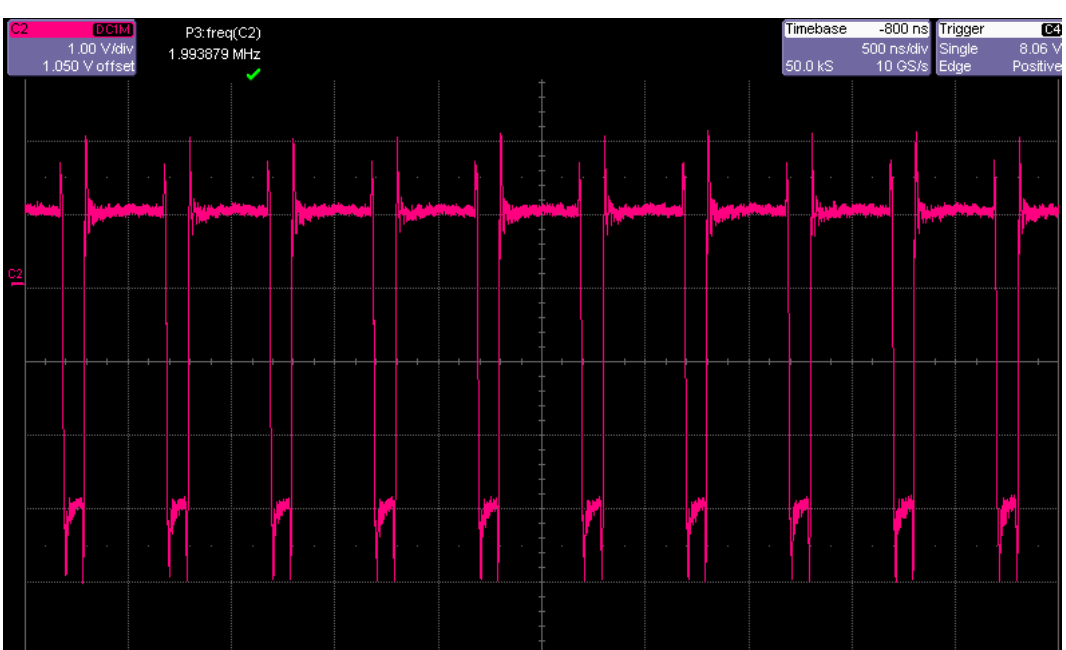

Appendix 6 Figure 11: Output of the second PSU prototype with snubber circuitry in mode 3, 3V pulse and 1V negative offset, 2MHz with 25% Duty cycle, no load.

Some heat sinks have been placed on the MOSFETs and their drivers to help them cool down when the pulse PSU is switching at high frequencies.

- Testing of the PSU output

In this section, the output of the PSU is connected to a 1Ω 50W resistor which simulates the gap and allows high current to flow through the PSU (as shown on the figure below).

Commands are then sent to the PSU via the developed HMI and the obtained pulse shapes are visualized with a scope. The current flowing though the resistor is measured thanks to a current transformer.

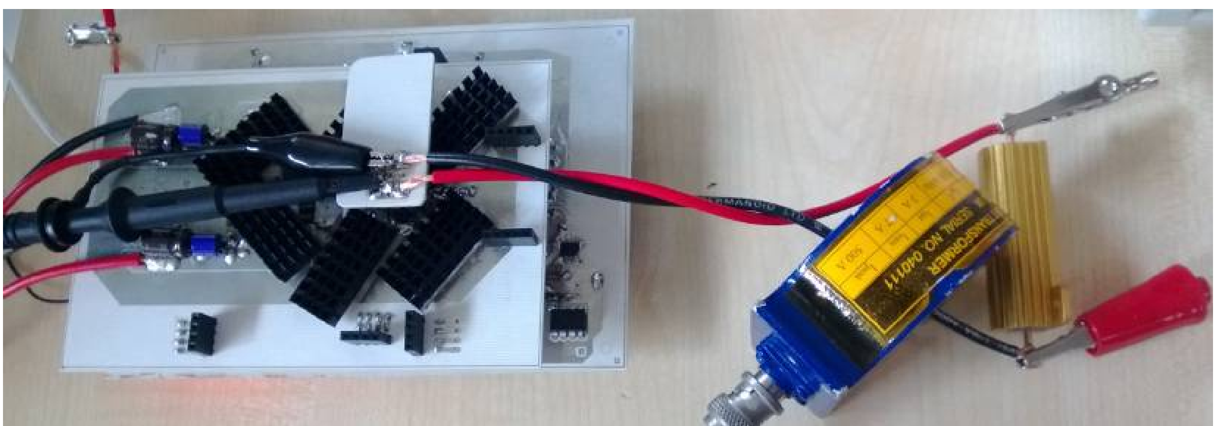

Appendix 6 Figure 12: Picture of the second PSU prototype being tested with a 1Ω load.

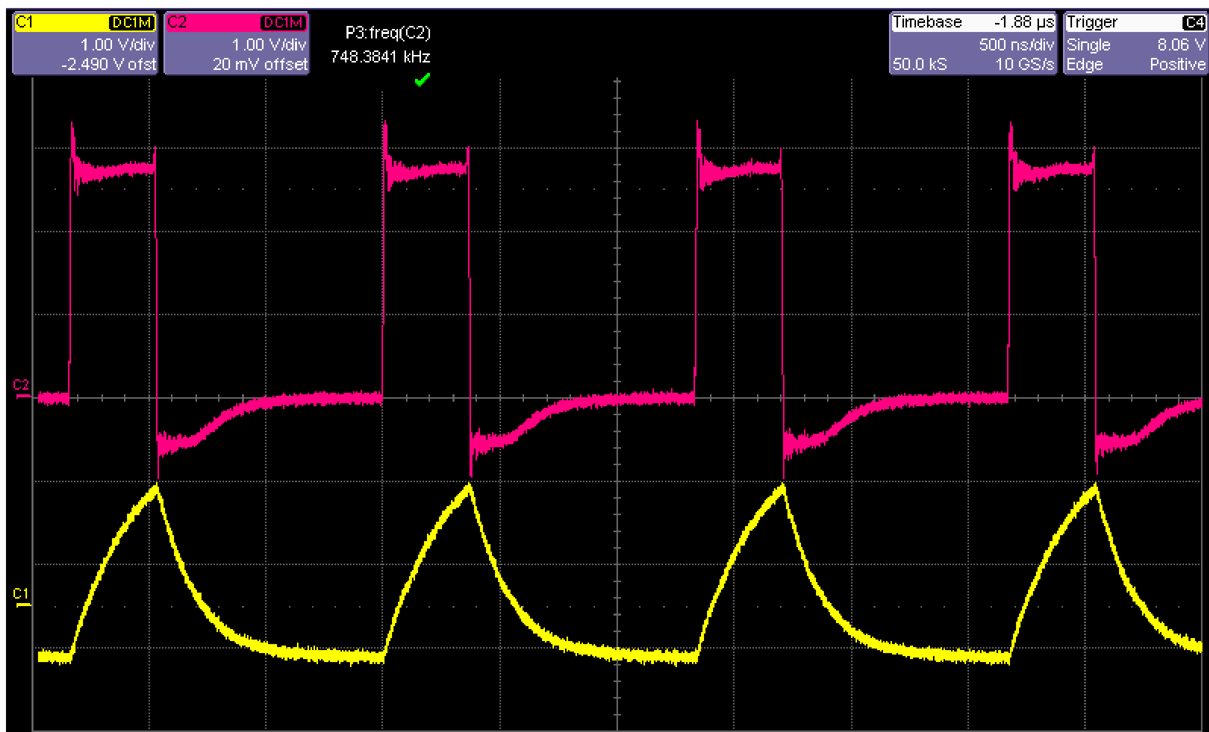

Appendix 6 Figure 13: C1: current (1V/A), C2: voltage; PSU in pulse mode 1: 3V pulse, no offset; 750kHz 25% duty cycle

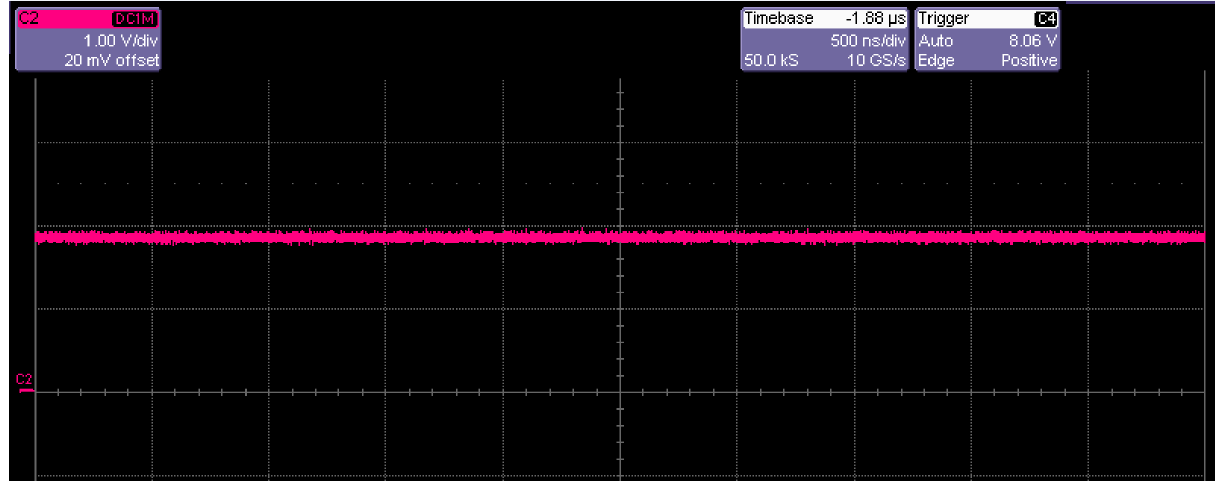

Appendix 6 Figure 14: C2: voltage; PSU in pulse mode 2: 2VDC (positive)

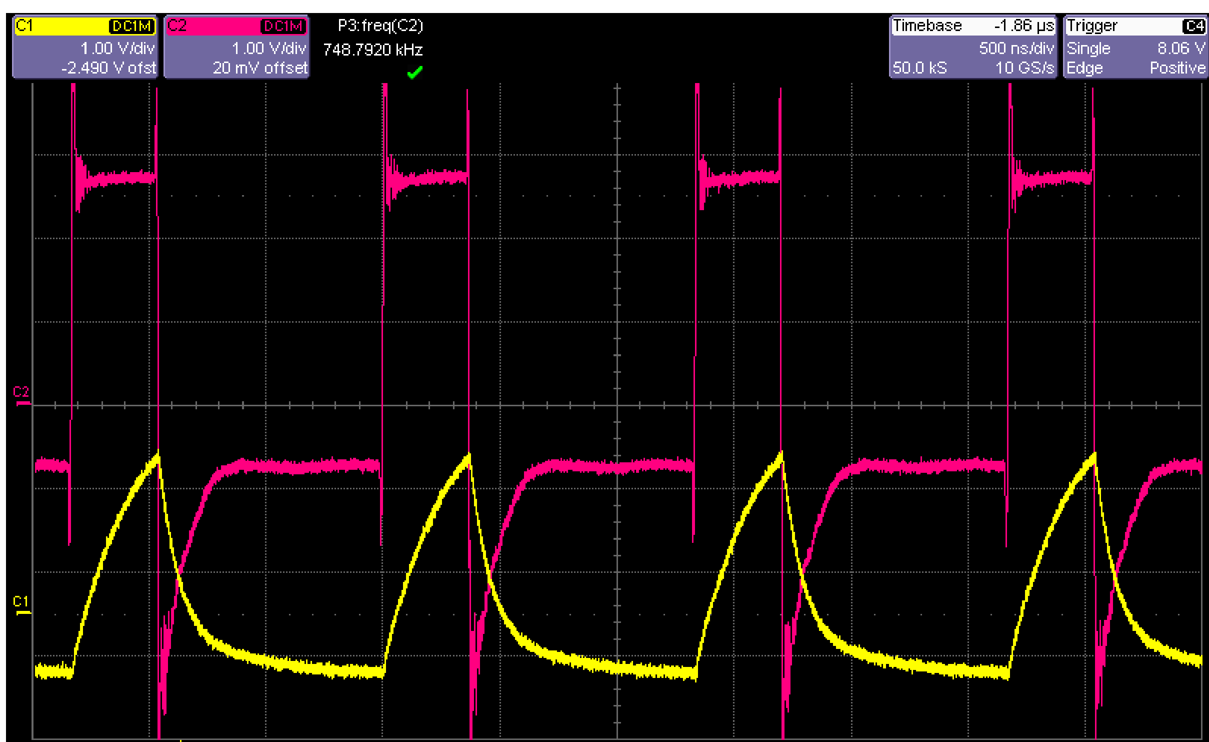

Appendix 6 Figure 15: C1: current (1V/A), C2: voltage; PSU in pulse mode 3: 3V pulse, 1 V negative offset; 750kHz 25% duty cycle

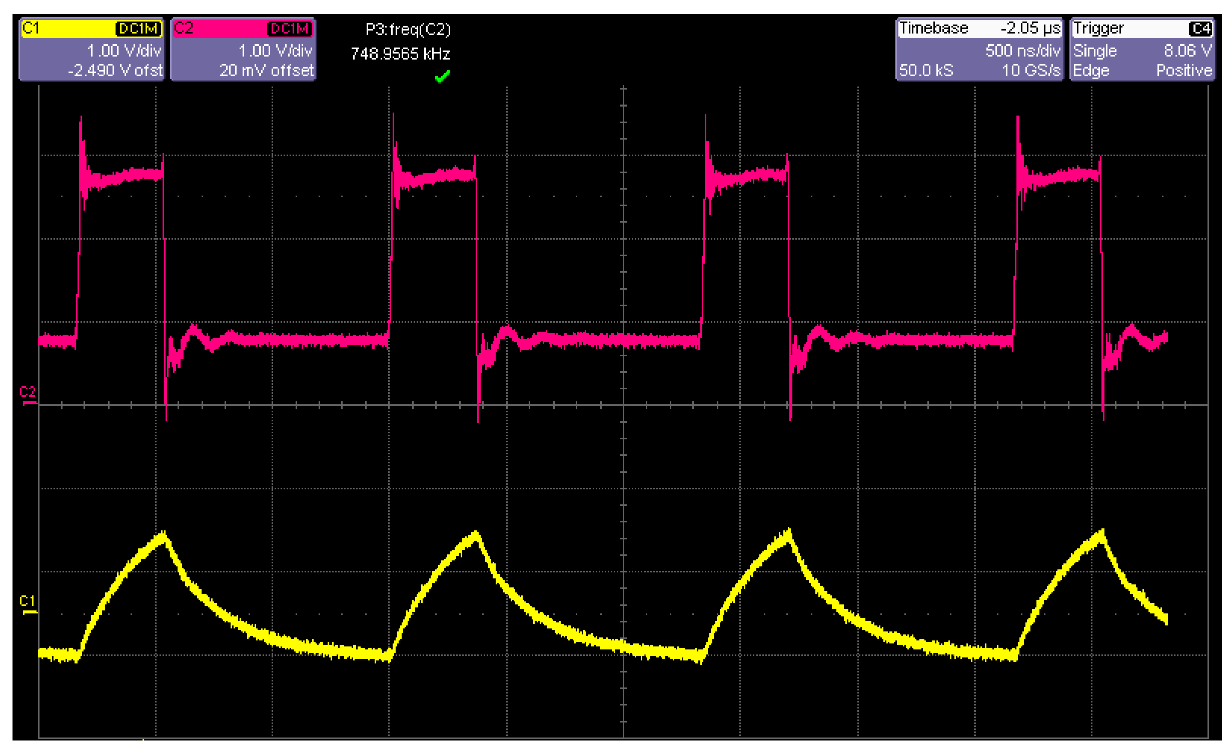

Appendix 6 Figure 16: C1: current (1V/A), C2: voltage; PSU in pulse mode 4: 3V pulse, 1 V positive offset; 750kHz 25% duty cycle

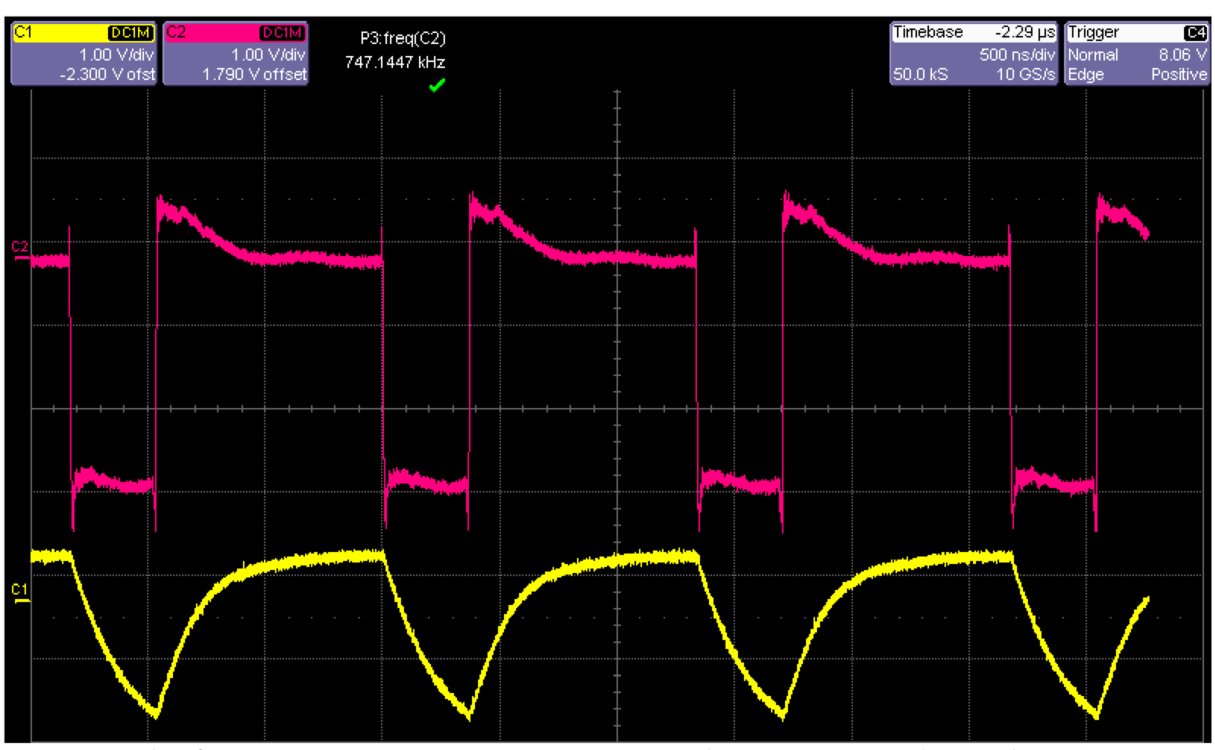

Appendix 6 Figure 17: C1: current (1V/A), C2: voltage; PSU in pulse mode 5: 3V negative pulse, no offset; 750kHz 25% duty cycle

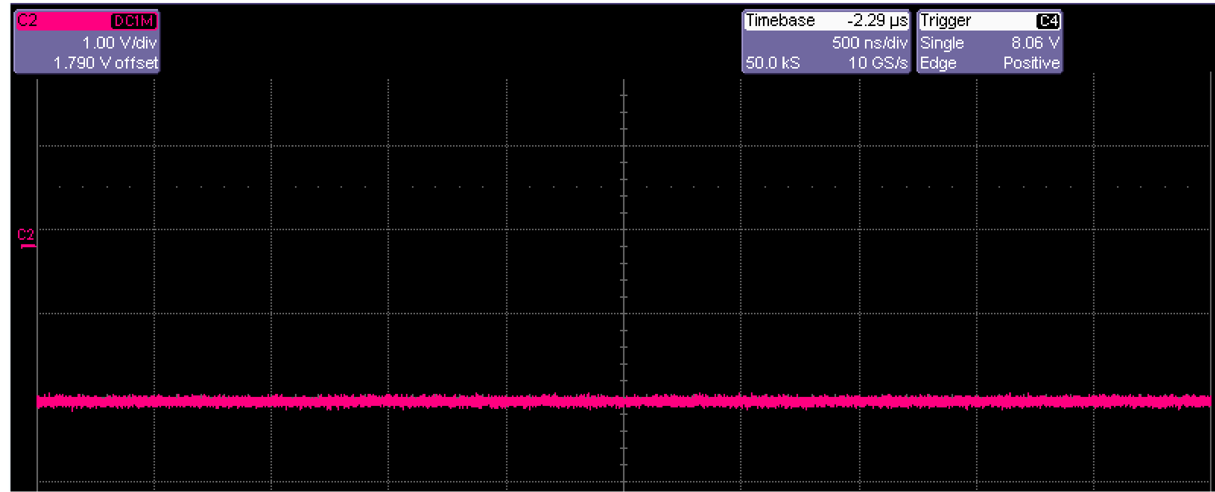

Appendix 6 Figure 18: C2: voltage; PSU in pulse mode 6: 2VDC (negative)

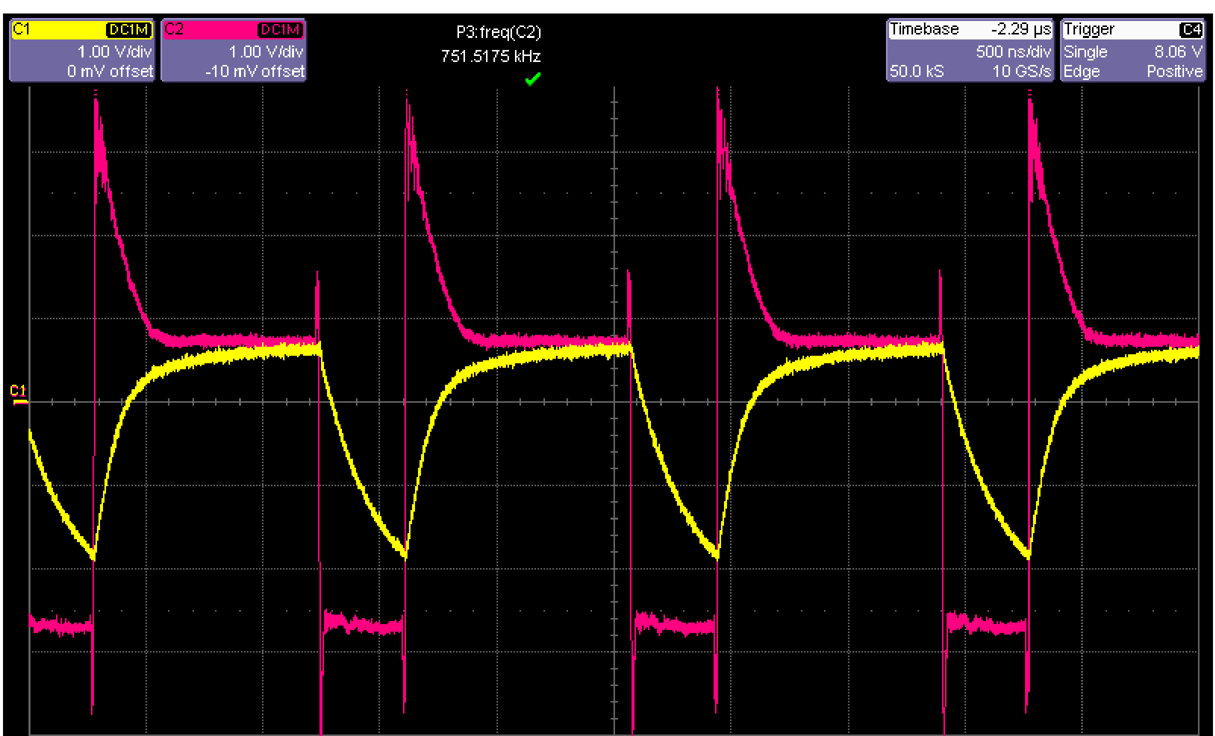

Appendix 6 Figure 19: C1 current (1V/A), C2: voltage; PSU in pulse mode 7: negative 3V pulse, 1 V positive offset; 750kHz 25% duty cycle

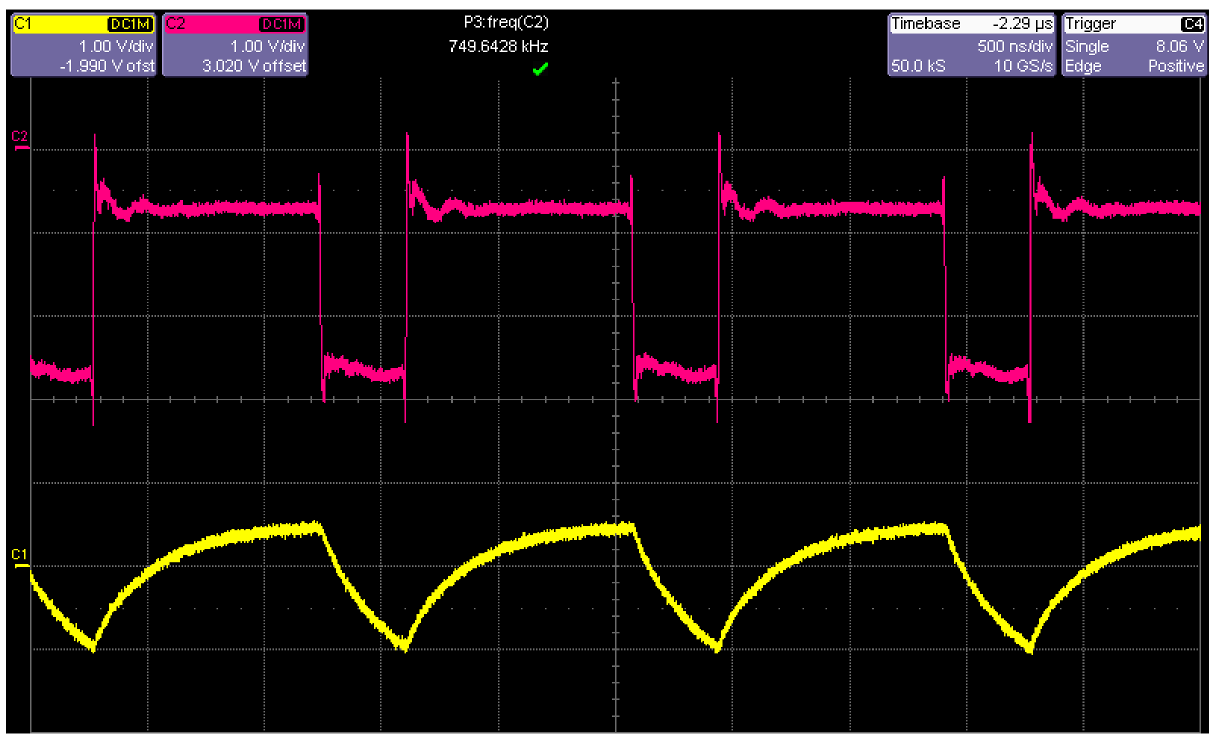

Appendix 6 Figure 20: C1 current (1V/A), C2: voltage; PSU in pulse mode 8: negative 3V pulse, 1 V negative offset; 750kHz 25% duty cycle

- Conclusion from tests with standard power cables

From the previous results, it can be seen that the parasitic inductance of the standard cables is quite high as we can observe – particularly in mode 3 and 7 – a significant reverse voltage peak after each pulse. This highlights the fact that low inductance cabling should be used to improve the pulse shape.

The developed pulse PSU will enable to experiment the effects of the offset voltage during the pulse off-time. Some papers advised a positive off-set during the pulse off time, which would maintain the EDL constantly charged, whereas other papers mentioned that a negative pulse off-time would enhance the machining process by accelerating the unloading/reloading process of the EDL.

Appendix 6.3. Second PSU prototype: over current protection (OCP) stage

The over current protection (Appendix 6 Figure 21) on the second prototype is similar to the one on the first prototype: the current is measured via a sensing resistor and sent to a comparator as well as a peak detector. The comparator compares the measured current with a threshold set by the microcontroller. On the other hand, the peak detector provides the control system with a reliable current value.

Appendix 6 Figure 21: Electrical diagram of the current sensing part on the OCP stage of the second prototype

- Testing of the OCP stage

The OCP stage is mounted on the top of the power stage, as shown on the picture below. The output of the PSU is connected to a 1Ω load.

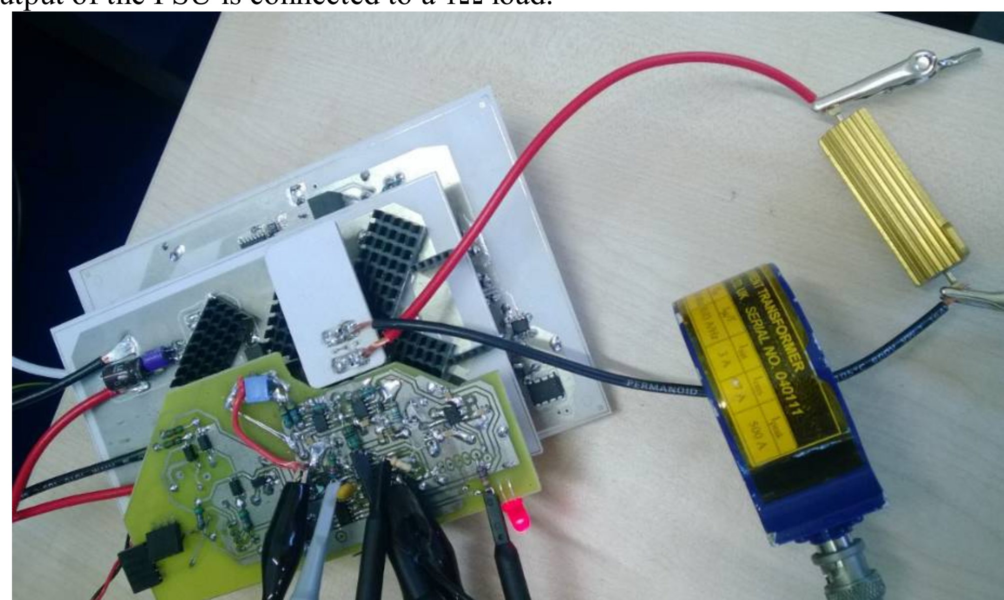

Appendix 6 Figure 22: Picture of the OCP stage being tested and refined.

On Appendix 6 Figure 23, the OCP can be seen triggering when the current goes above 3A. The comparator output goes HIGH for a very short amount of time, but this time is sufficient to make the SR flip-flop latch and stop the pulses.

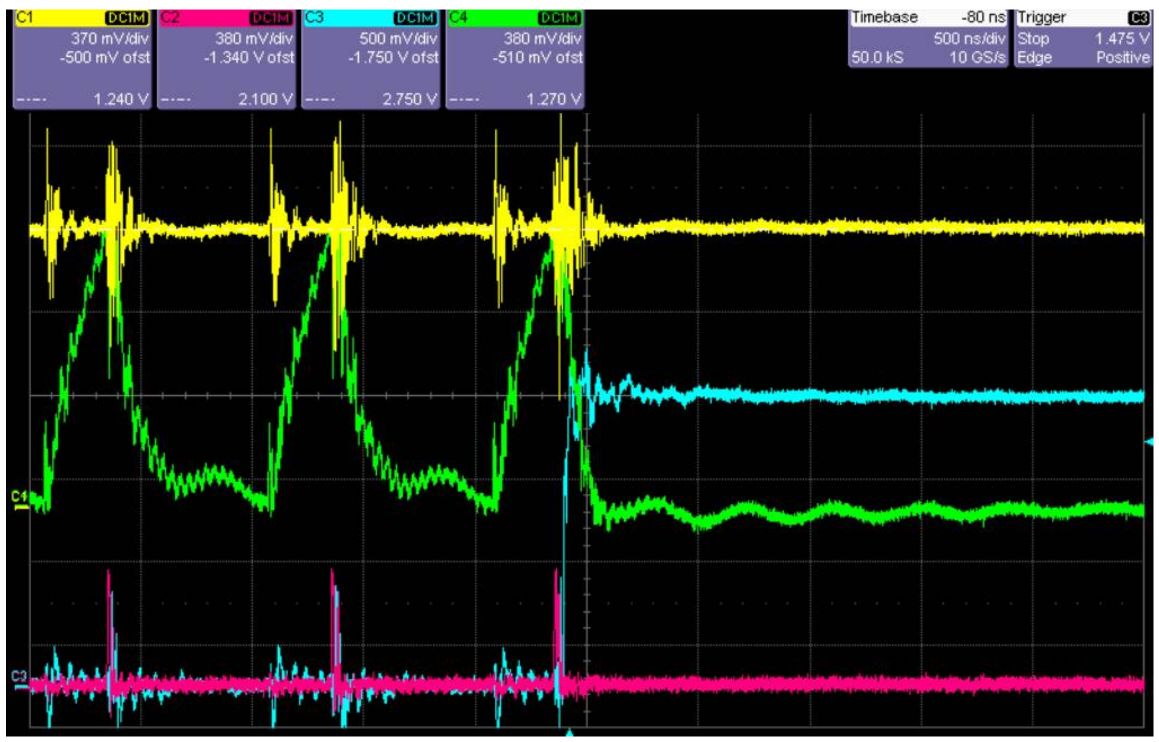

Appendix 6 Figure 23: C1: OCP threshold (380mV/A); C2: comparator output; C3: OCP signal (latched output); C4: current (380mV/A); 1MHz 25% duty cycle

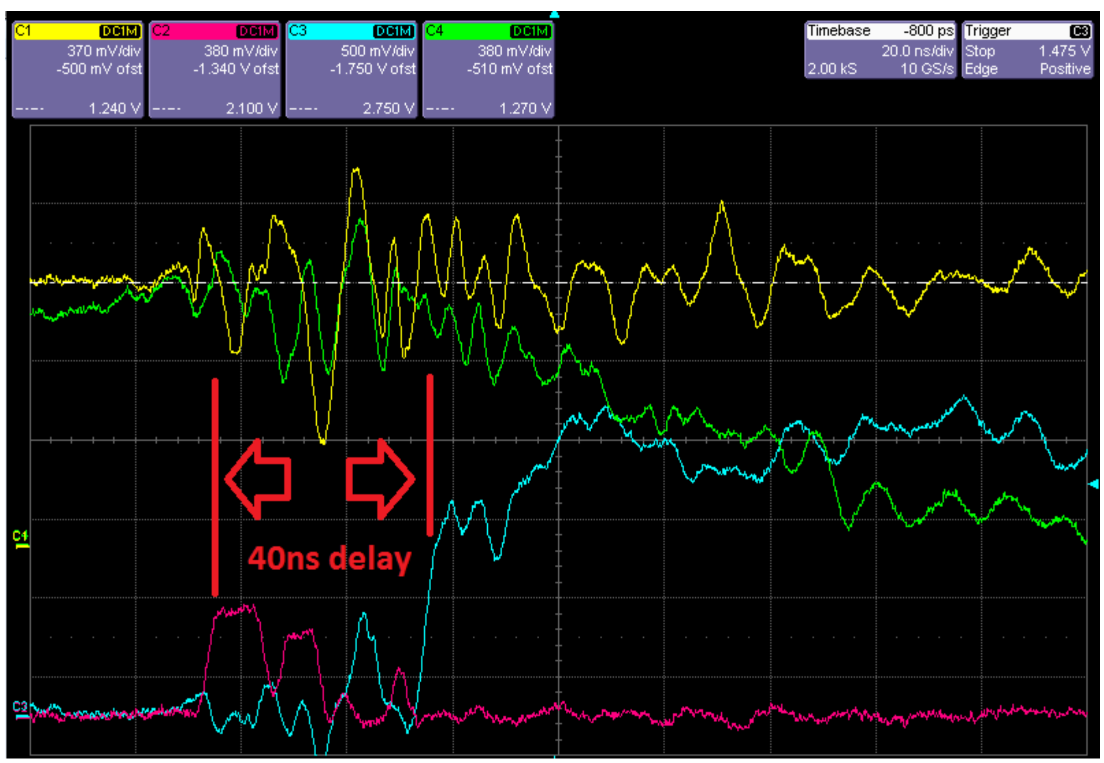

Appendix 6 Figure 24: C1: OCP threshold (380mV/A); C2: comparator output; C3: OCP signal (latched output); C4: current (380mV/A); 1MHz 25% duty cycle (20ns/div)

From a timing perspective, the pulses are stopped approximately 40ns after the comparator triggers the over current protection signal (Appendix 6 Figure 24).

Appendix 7. EXPERIMENTAL WORK AT BRUNEL USING A TEST STAND

This section details the trials carried out in Brunel from the 27th of February until the 2nd of March 2012 in the frame of the FP7 Micro-ECM project.

The objectives of this set of experiments were:

- To investigate the machining of Iron and Nickel Chrome (18NiCr6) discs.
- To test the PSU developed by VOX Power and IT Sligo

Appendix 7.1. Planning of experiment and experimental setup

A fuzzy logic control system was implemented on a test rig to verify the viability of this control approach. A control program was developed using LabVIEW running on a desktop PC. The PC was interfaced with:

- The motion controller (controlling the position of the tool-electrode)
- The power supply (applying short voltage pulses at high frequency)
- A data acquisition module

The control algorithm consisted of a fuzzy logic algorithm embedded in a state-machine allowing it to react to unexpected events such as short circuits. The logic of the algorithm was based on monitoring and maintaining constant current through the inter-electrode gap. The position of the tool electrode was controlled with respect to the variation between the desired value of the machining current and its actual value.

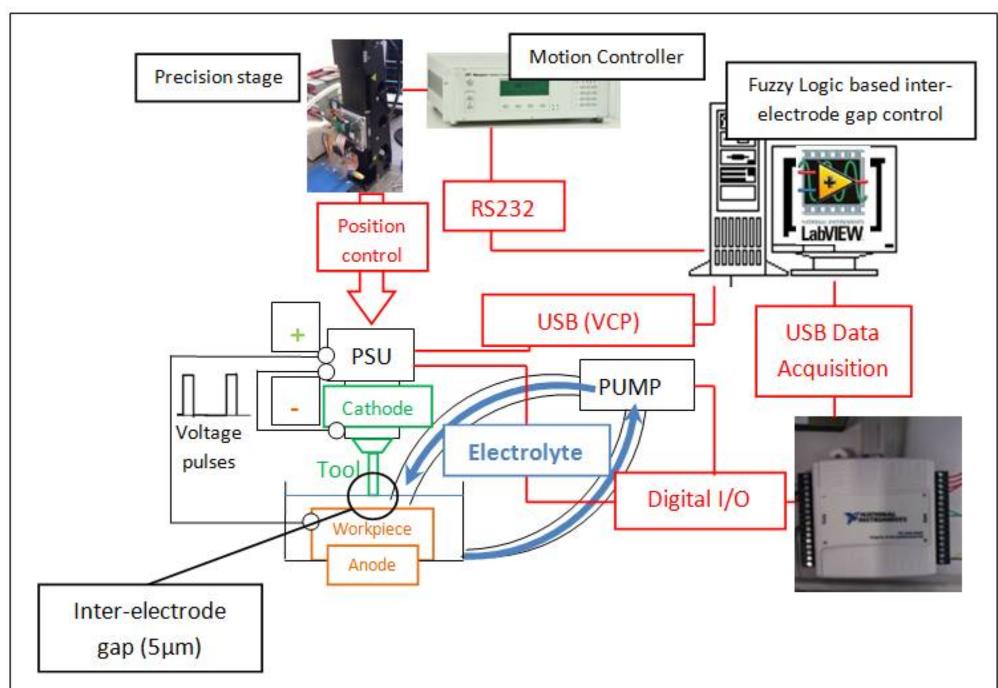

Appendix 7 Figure 1: Schematic diagram of the experimental setup

Appendix 7.1.1. Materials and equipment used

- **Controller MM4006, produced by Newport SA**

The controller controls the stage movements. It can be used in two different modes, manual mode and program mode. The controller is programmed using a proprietary programming language developed by Newport. The position of the tool is set by sending commands to this controller, using the RS232 communication protocol.

- **Linear stage 462-XY-M, produced by Newport SA**

The linear stage is powered by a DC electrical motor. This servo-controlled stage makes use of a linear encoder with a resolution of 0.1µm. The stage is controlled by the Newport Controller MM4006.

- **Plastic basin**

A purpose-designed plastic basin was manufactured at Brunel University. The workpiece can be clamped using plastic cap screwed to the bottom of the basin. The electrolyte is supplied to the basin via two apertures: one inlet and one outlet. The basin also allows the power supply unit (PSU) to be connected to the workpiece.

- **Current probe 13G1000 produced by Lilco LTD**

The probe can measure pulses with a rise time of 7 ns. It was placed between the tool and the PSU.

- **Power supply unit (PSU)**

In these tests the PSU prototype was produced by ITSligo. It is powered by two DC generators (5V and 8V). The PSU can be used to send the pulses for the process with frequency 2 MHz and a maximum voltage amplitude of about 12 Vpp.

- **Workpieces**

Iron discs 0.3mm thick and 16mm diameter

18NiCr6 discs 1.1mm thick 14mm diameter

- **Cathodes**

Copper tubes 1.0 mm outside diameter and 0.3mm internal diameter

Tungsten carbide tubes 0.5mm outside diameter and 0.2-0.3mm internal diameter

Coated Tungsten carbide tubes 0.5mm outside diameter and 0.2-0.3mm internal diameter

Coated solid Tungsten Carbide 0.4mm outside diameter.

The coated cathodes only had the front face clear of insulation.

- **Electrolyte**

$NaNO_3$ – Sodium Nitrate was used; a recommendation was made by VUB to use a concentration of 200g/l.

Appendix 7.1.2. Interelectrode gap (IEG) initialization

The interelectrode gap size is a very important parameter in electrochemical micromachining and must therefore be defined precisely. To do so, a LabVIEW programme has been developed according to the following flowchart:

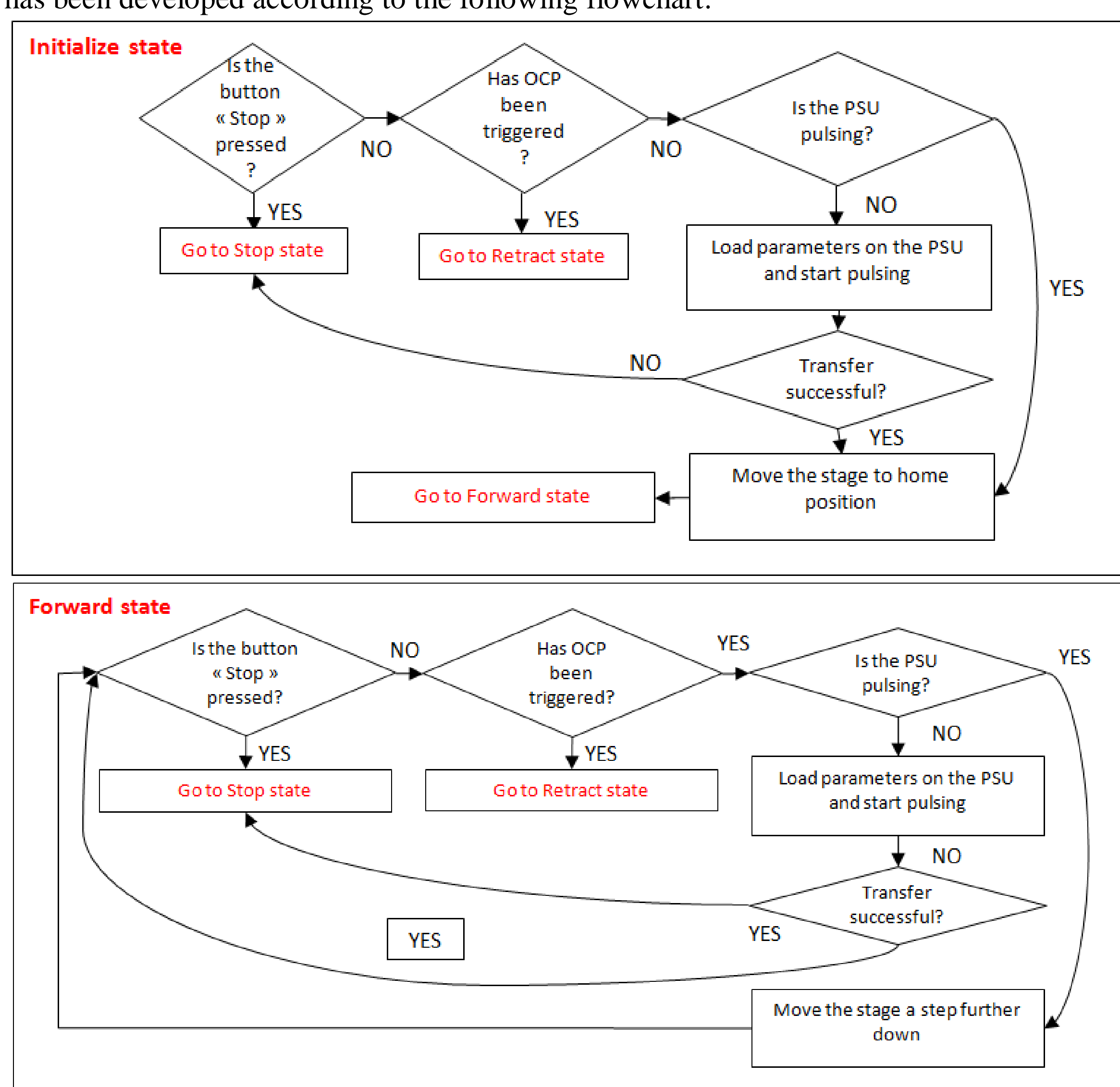

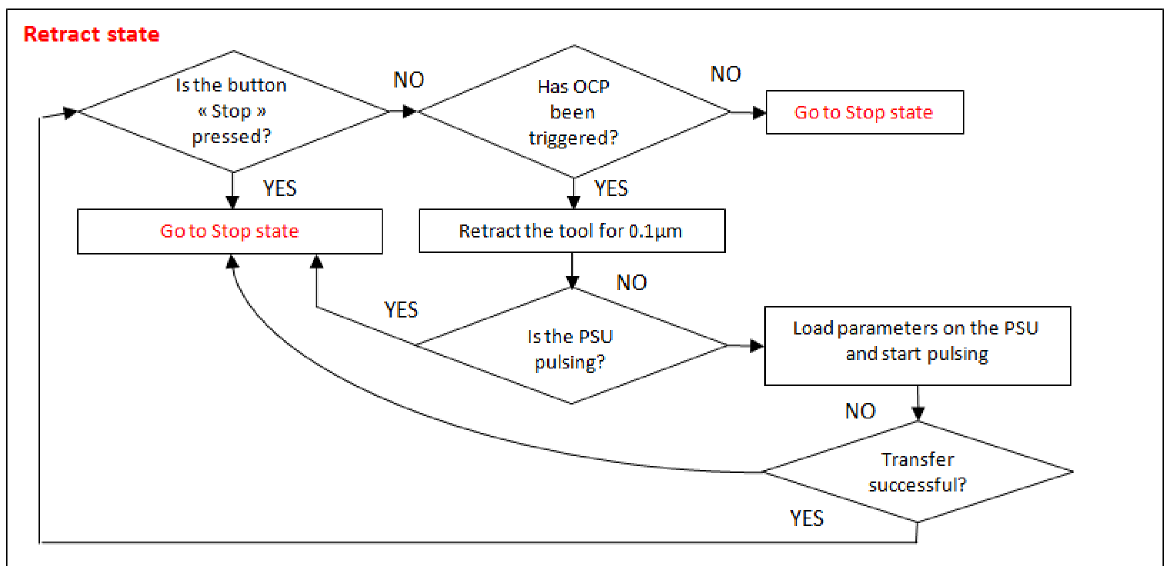

Appendix 7 Figure 2: Flowcharts of the different states of the programme controlling the test bench developed at Brunel

Appendix 7.1.3. Tool approach and gap initialization on the test stand

When the approach programme is started, the stage moves down step by step. The step length gradually decreases according to the distance the stage has travelled, to gain some time and to reach a better step resolution just before contact is made. At each iteration of the loop, a new step length is calculated according to the following formula:

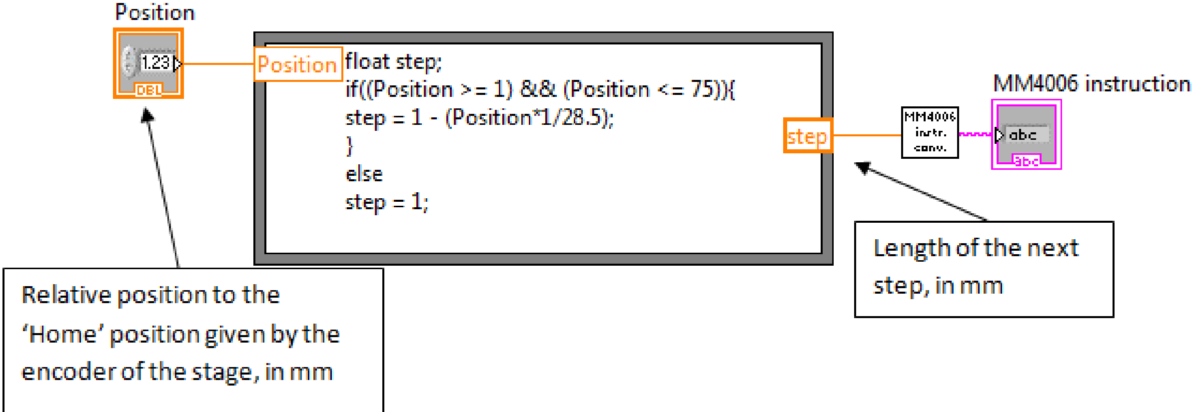

Appendix 7 Figure 3: Formula block in the LabVIEW programme of the test bench

28.5 mm corresponds to the approximate distance between the tip of the electrode and the expected touching point (= the surface of the workpiece).

With this algorithm implemented, the following evolution of the stage position is observed (Appendix 7 Figure 4):

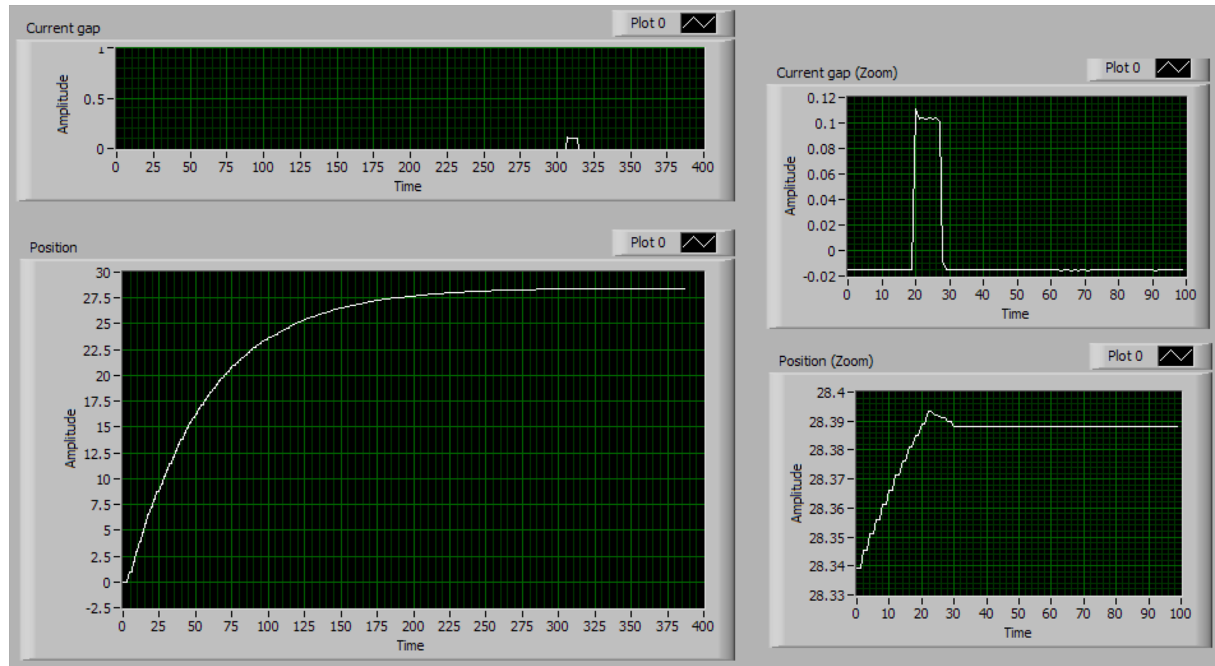

Appendix 7 Figure 4: Screenshot of the tool approach performed on the test bench

The parameters of the power supply during the gap initialization are the following:

Pulse amplitude: 3V, Frequency: 200000 Hz, Pulse Width: 500 ns, Runtime: 120 sec, Over current protection threshold: 10%, maximal board temperature: 50°C.

When contact is made, the over current protection is triggered and the power supply stops pulsing. Signals are sent to the PC to get the state of the over current protection (OCP) (i.e. triggered (ON) or not triggered (OFF)) and the status of the power supply (i.e. pulsing (ON) or not pulsing (OFF)). When the PC receives the ON signal from the OCP, it stops moving the tool forward and retracts it step by step - with a 0.1µm steps length - until the electrical contact between the tool and the surface of the workpiece disappears.

Appendix 7.2. Preliminary Experiments

Experiments were carried out on this test bench. Iron and nickel chrome discs and were used during the trials.

Appendix 7.2.1. Trials 1 & 2

The aim of these two trials was to verify the fundamental concepts of electrochemical machining. Using pure iron (Fe) as workpiece material would make the dissolution reaction easy to trigger. Experiments were stopped as soon as a visible result was achieved. A solution of $NaNO_3$ with a conductivity of 19.4S/m was used as electrolyte.

These trials used a hollow copper (Cu) cathode with an internal diameter of 300µm and a 1mm outer diameter. It was decided to flush the electrolyte through the cathode. The pulse amplitude was set to 5V and the on-time was 500ns, the frequency was 150kHz.

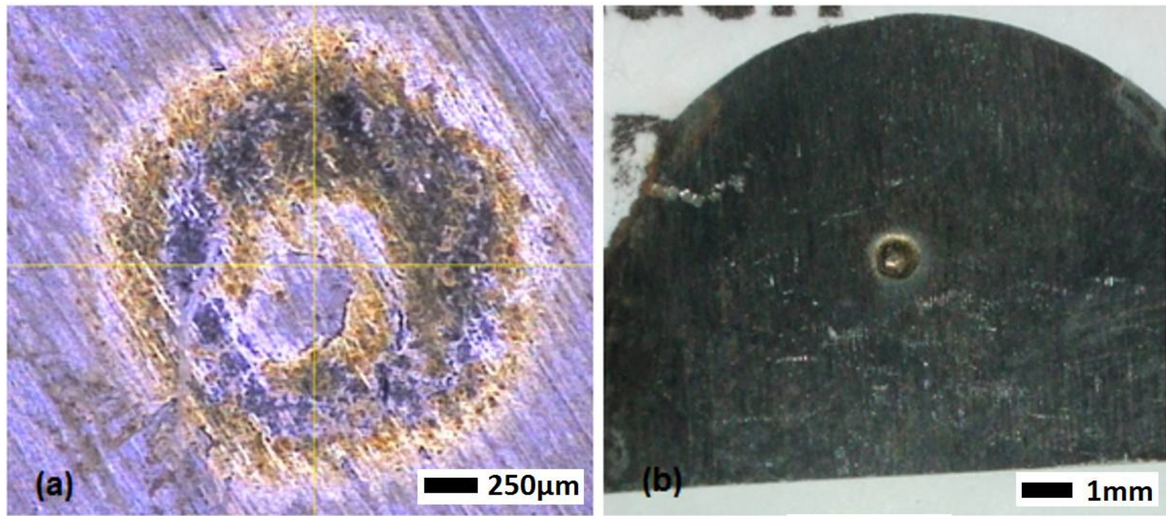

Appendix 7 Figure 5: Surface of the workpiece in trial 1

Machining around the annulus of the cathode was clearly visible (Appendix 7 Figure 6). There was a central portion that had less machining as this was the area in the centre of the tube and hence the gap to the active portion of the cathode is larger.

The microscope measurements showed that the external diameter of the machined area was 1.030mm and the internal diameter was 0.248mm

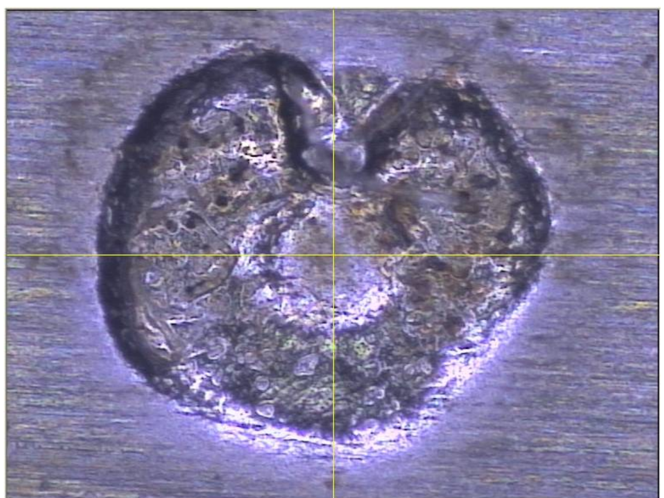

Appendix 7 Figure 6: Surface of the workpiece in trial 2

A similar result was achieved with this part when compared to what was achieved in Trial 2. The measurements taken from the microscope images gave an external diameter of 1.093mm and an internal diameter of 0.354mm. The depth of machining was measured as 0.492mm with the microscope. As it can be seen on the images there is a portion of the circle that was not machined, this may have been due to cathode damage.

Appendix 7.2.2. Trials 3 & 4

These trials used a material expected to be more difficult to machine: the workpiece material was 18NiCr6, which contains chromium. Chromium is known for creating a passivation layer which prevents the electro-dissolution reaction from occurring.

In Trial 3 an attempt was made to achieve a breakthrough. $NaNO_3$ electrolyte was used at 200g/l concentration and the conductivity was measured at 17.4S/m. The cathode had an external diameter of 1.0mm and an internal diameter of 0.3mm. The electrolyte was injected through the cathode (internal flushing). The pulse on time was set at 95µs and 10kHz which is a 95% on-time. In this trial breakthrough was achieved, it took 15mins and 53seconds to drill through the 1.1mm thickness of the 18NiCr6 disc. The surface finish was good, the hole had a large taper and the surface of the disc was affected with black staining. The localization was poor however, the diameter of the hole on the top surface was measured at 2.7mm and the breakthrough hole had a diameter of 1mm.

In trial 4 side flushing was attempted instead of internal flushing which was used in the previous experiment. There was a significant improvement in cycle time to reach breakthrough, in this trial it took 4mins 30seconds compared to 15mins 53seconds in the previous trial. The edge is quite well defined apart from a specific area, this may be due to the direction of the side flushing.

The diameter on the top edge was measured 3.015mm and the breakthrough diameter was measured at 1.230mm. The SEM image shows the defined edge and also the area of the hole where the definition was poor.

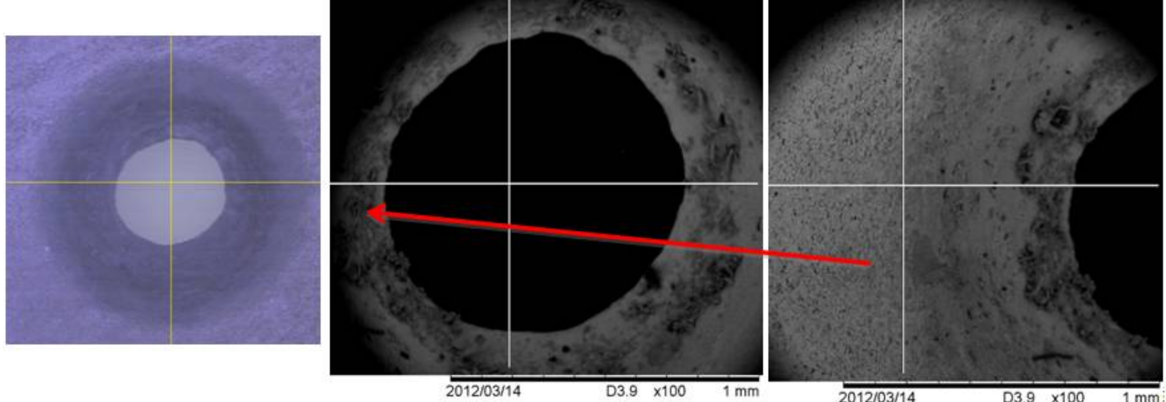

Appendix 7 Figure 7: Hole in the workpiece in trial 3

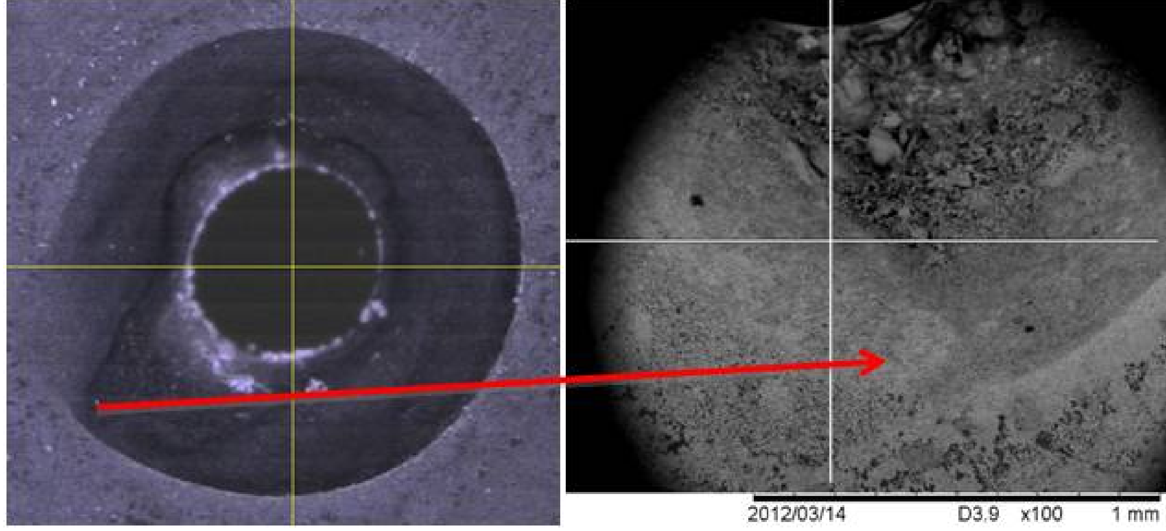

Appendix 7 Figure 8: Hole in the workpiece in trial 4

Appendix 7.2.3. Trial 5

In this trial a Tungsten Carbide cathode was used instead of the Copper tube that was used in the previous trials. The external diameter was 0.5mm with an internal diameter of 0.2mm. The electrolyte was $NaNO_3$ at a concentration of 200g/l. The processing parameters were the same as those used in trial 4. Side flushing was used.

Breakthrough was achieved in a cycle time of 6minutes 29seconds. The process was allowed to run for a further minute to attempt to have a cleaner breakthrough. The microscope image below clearly shows that the extended time at breakthrough definitely improved the quality of the exit hole. The hole is also less tapered as there was time to open out the bottom of the hole. The diameter of the hole was measured at 1.269mm which gives a radial gap of 0.38mm. The SEM image shows the hole produced and it is clear that the walls are vertical, there is very little taper in comparison to some of the previous trials. The SEM image (Appendix 7 Figure 9) below shows a view of the hole to the right hand side of the hole shown in the first SEM image. It shows very little taper and a smooth radius at the edge of the hole.

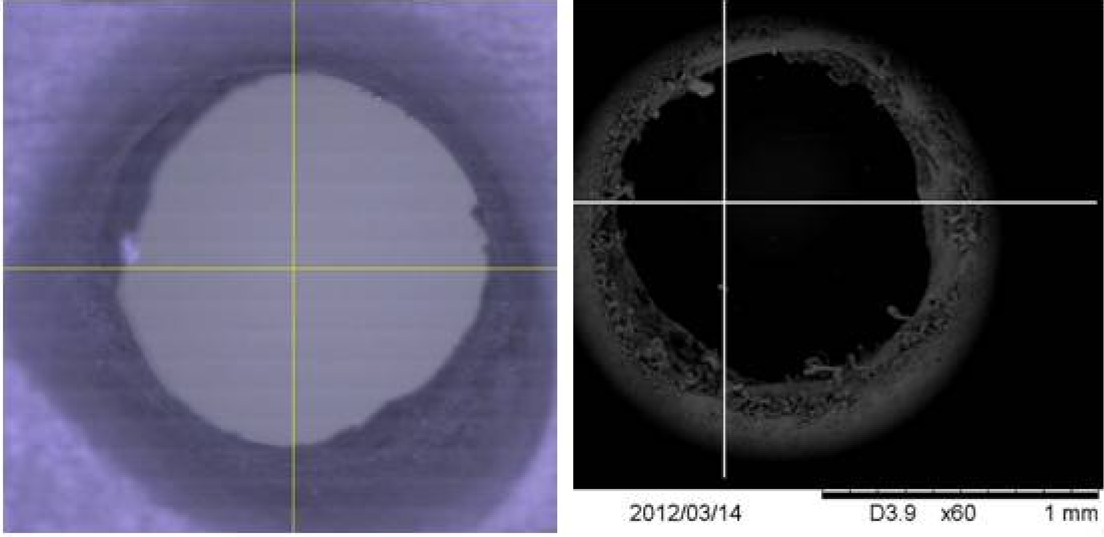

Appendix 7 Figure 9: Hole in the workpiece in trial 5

Appendix 7.2.4. Trial 6

In this trial a solid Tungsten Carbide cathode with 0.4mm external diameter was used. This was a repeat of the previous trial but with a solid cathode. The trial was allowed to run for 11minutes 50 seconds and side flushing was used, breakthrough was achieved however the quality of the exit hole is quite poor. The hole was very well defined the process control showed that approximately 0.2Amps were being used during the process. The external diameter of the defined edge of the hole on the top surface was measured at 0.903mm. This gives a radial gap of approximately 250µm. The SEM image also shows that the hole was well defined and that there was very little taper. Appendix 7 Figure 10 shows the shape of the breakthrough hole and the scale in this image is 200µm. SEM shows that the quality of ECM is good from the appearance of the quality of the machined surface. There is some debris present in the hole, this occurred post process.

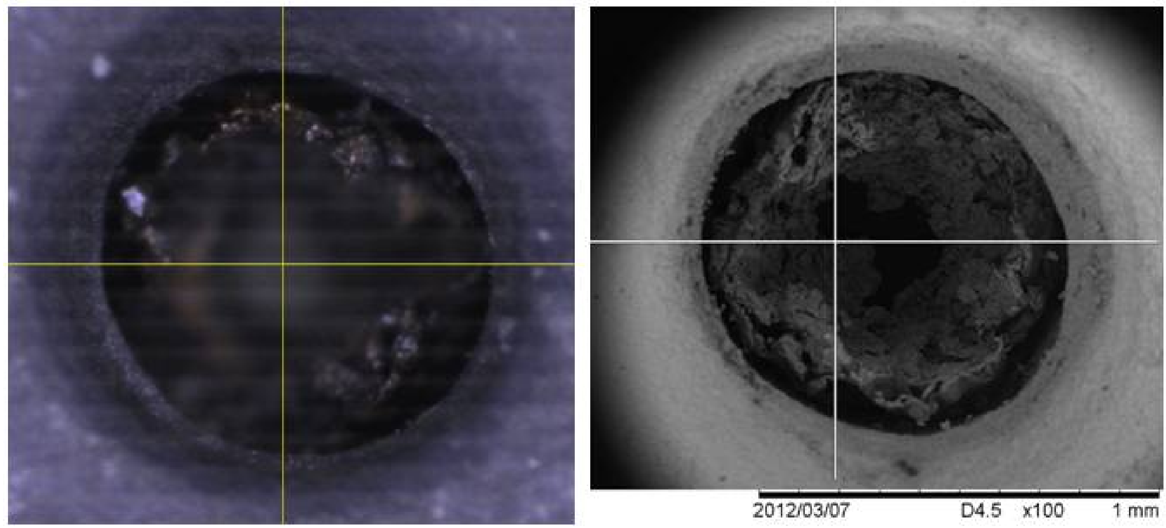

Appendix 7 Figure 10: Hole in the workpiece in trial 6

Appendix 7.2.5. Trial 7

In this trial the duty cycle was reduced from 95% to 25%. The pulse on time was set at 95µs and the frequency was set at 2.6kHz. The cathode was changed back to the Tungsten Carbide tube with 0.5mm external diameter and 0.2-0.3mm internal diameter with internal flushing. The supply voltage was 10V and the starting gap was 20µm. The process was allowed to run for 11minutes and 34seconds.

The microscope image shows that a high level of polishing was achieved, this should be a result of the pulsing at 25% duty cycle. Breakthrough was not achieved, which was expected since it should have theoretically taken four times longer than for the other trials which were done at 95% duty cycle.

The images show that the surface finish achieved is of a good level, there is evidence of tapering of the hole however this may seem pronounced as the hole is blind. Diameter measurements taken via the microscope show that the diameter on the top surface was 2.331mm at the extremes of the polished surface and 0.912mm at the top of the hole.

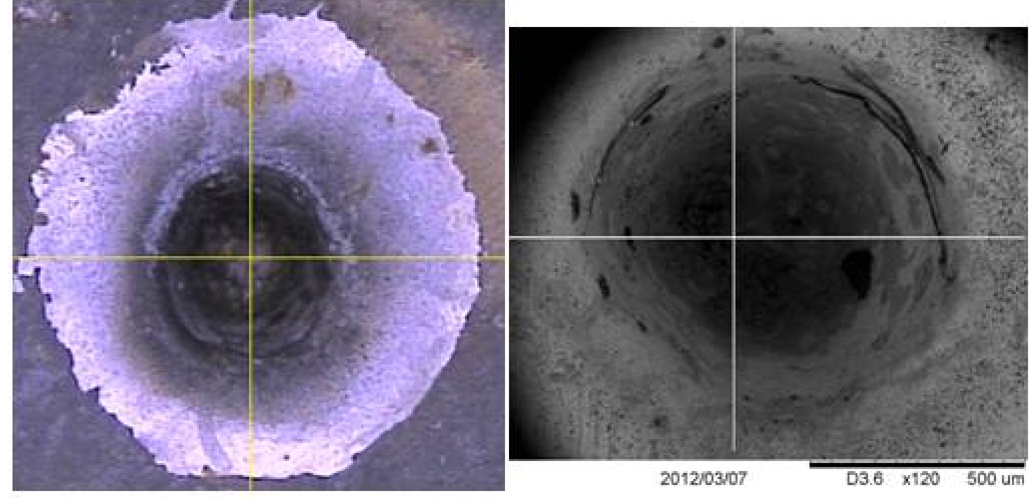

Appendix 7 Figure 11: Hole in the workpiece in trial 7

Appendix 7.2.6. Trial 8

This trial was run in the same way as trial 7 and the goal was to achieve breakthrough, however this was not possible to achieve it. The process monitoring software showed good depth progress up until 12minutes, after that the process was struggling to achieve more depth. It would move forward trigger OCP then step back and then move forward again. The microscope image shows a well-defined hole, the diameter measurement indicates that the diameter was between 1.240mm and 1.067mm and the cathode had an external diameter of 0.5mm. The SEM image shows a well-defined hole, the surface finish is at an acceptable level, the degree of taper does not seem too large.

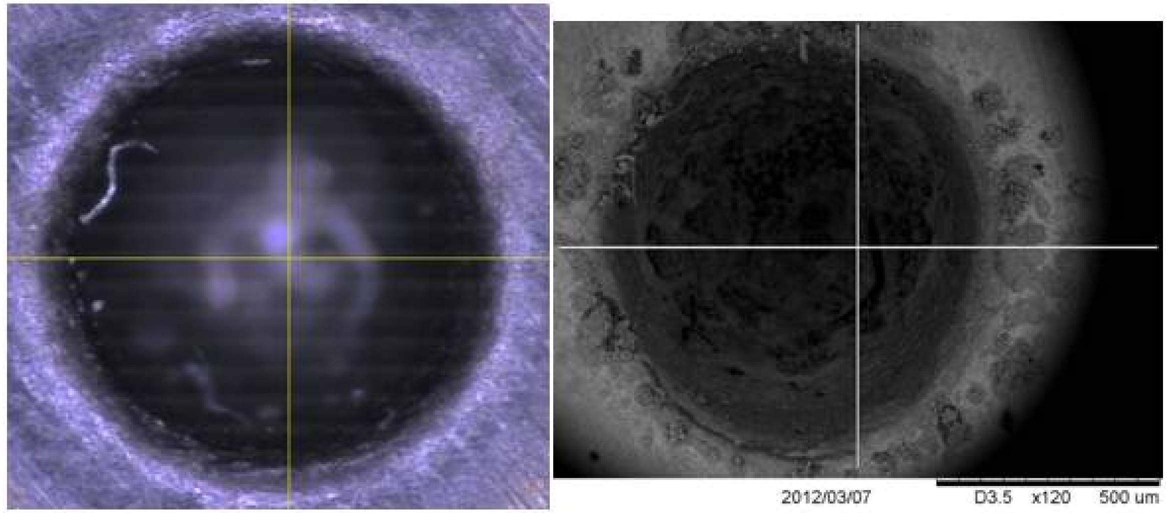

Appendix 7 Figure 12: Hole in the workpiece in trial 8

Appendix 7.2.7. Conclusions and discussion for the preliminary experimental work at Brunel

The work carried out has shown that it is possible to remove material using nanosecond and microsecond pulses using the PSU developed by VOX-power and IT Sligo. Three different electrolytes were used in the experimental work, Sodium Chloride, Sodium Nitrate, and Phosphoric Acid in all instances material removal was observed, however Sodium Nitrate appeared to work quite well.

Through holes were produced in NiCr discs using $NaNO_3$ electrolyte at 10kHz. Cycle time increases significantly when we go from a duty cycle of 95% (close to DC) to 25%. In our examples it appeared to go from about 3 minutes to 12 minutes for the same depth reached. This makes sense since the temporal mean value of the current supplied to the gap is approximately 4 times smaller at 25% duty cycle than at 95%.

The quality of the machining process was quite good from a surface finish point of view. However there were issues around localisation as the side gap between the cathode diameter and the workpiece hole was in the region of 200-350 µm. This can be explained by the fact that the voltage applied was close to DC and that the frequency was very low with respect to what was found in the literature. Coating of the cathodes should result in improved localization and less tapering of the holes. It could also be confirmed that when using a voltage higher than 8V, the cathode would start to wear.

Passivation issues were observed and needed to be investigated further to understand how these could be overcome. The work also highlighted that rotation of the cathode may also have a significant impact on the process as it will aid flushing and will therefore reduce the chances for OCP to occur. The process showed that for a 25% duty cycle and a tubular cathode with an external diameter of 0.5mm and an internal diameter of 0.2-0.3mm and internal flushing that it was difficult to machine to a depth greater than 0.8mm. This could be explained by the pressure building up the deeper the tool is fed.

The trials showed that it Fe reacts better than NiCr to the process when nanosecond pulses are used. We found that internal flushing appeared to give better localization and allowed material removal, however we also saw with NiCr parts that side flushing was quite effective also especially at 95% duty cycles when using $NaNO_3$. Coating of the cathode is expected to give better localization and to reduce the tapering effect of the process, it should also result in a more defined hole edge.

The process has highlighted that there is a need to understand how NiCr parts react to nanosecond pulses and at what frequency and duty cycle the process starts to remove material. It is necessary to understand the electrochemistry of the process for the set-up where 18NiCr6 workpieces are used with $NaNO_3$ electrolyte and Tungsten Carbide cathodes.

Sodium Chloride, Sodium Nitrate, and Phosphoric acid were used during the trials. $NaNO_3$ appeared to work quite well for the 18NiCr6 and Fe parts. The quality of the ECM was quite good on the 18NiCr6 parts with $NaNO_3$.

It has also been observed that allowing the process to run after breakthrough allows a better shape of the breakthrough hole.

Fe discs appear to react better than 18NiCr6 discs when nanosecond pulses are used (e.g. 500ns 150kHz) in that there is visible evidence of machining.

Control board of PSU prototype 1

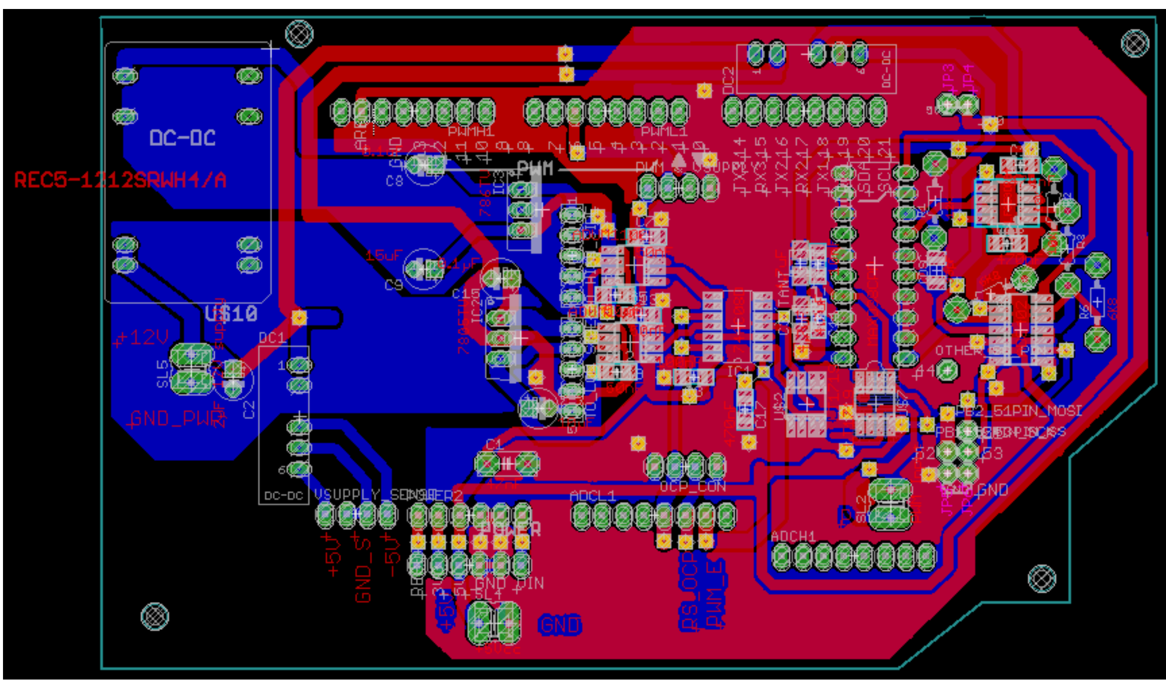

Power board of PSU prototype 1

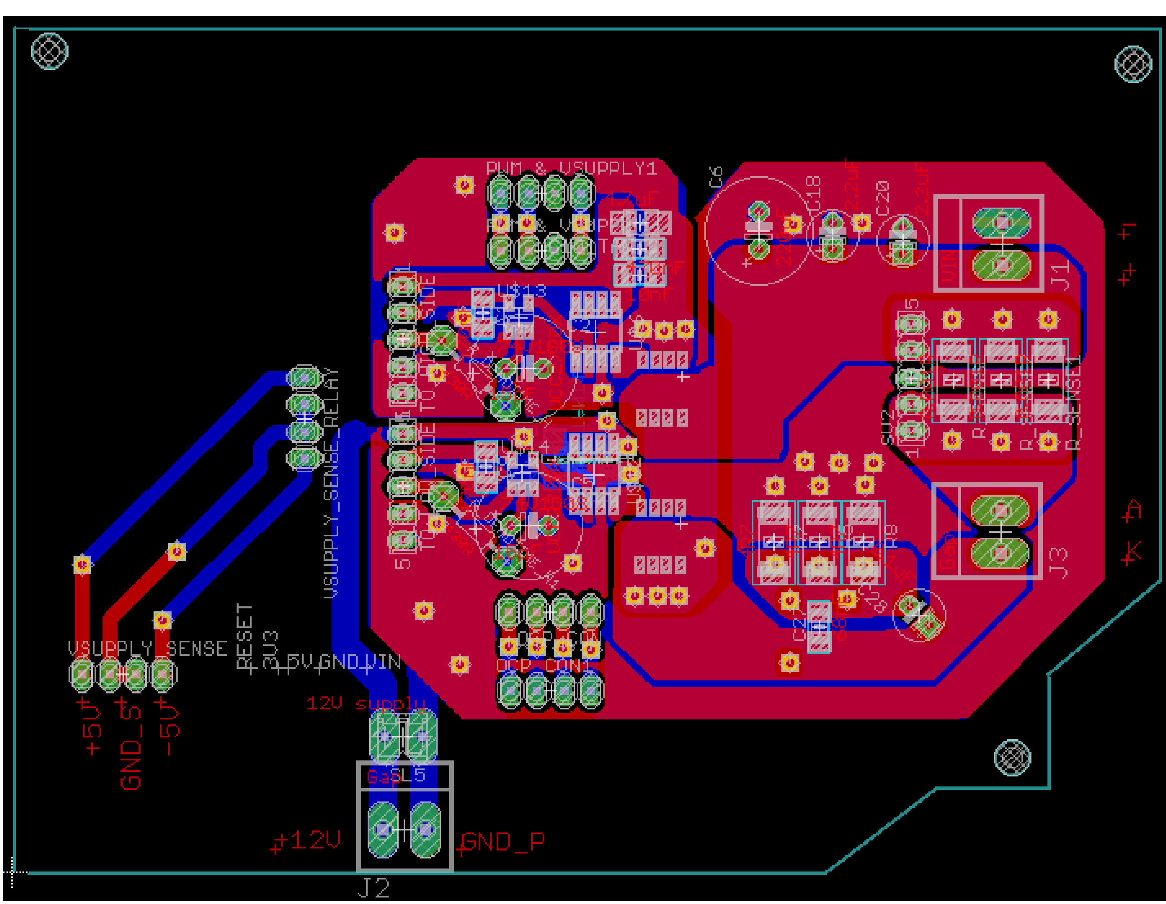

OCP board of PSU prototype 1

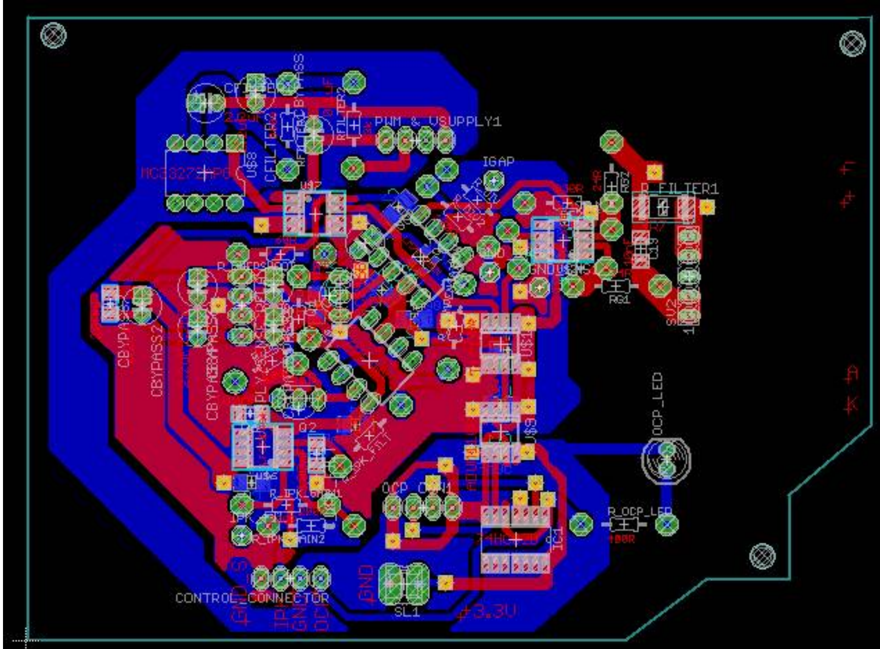

Control board of PSU prototype 2

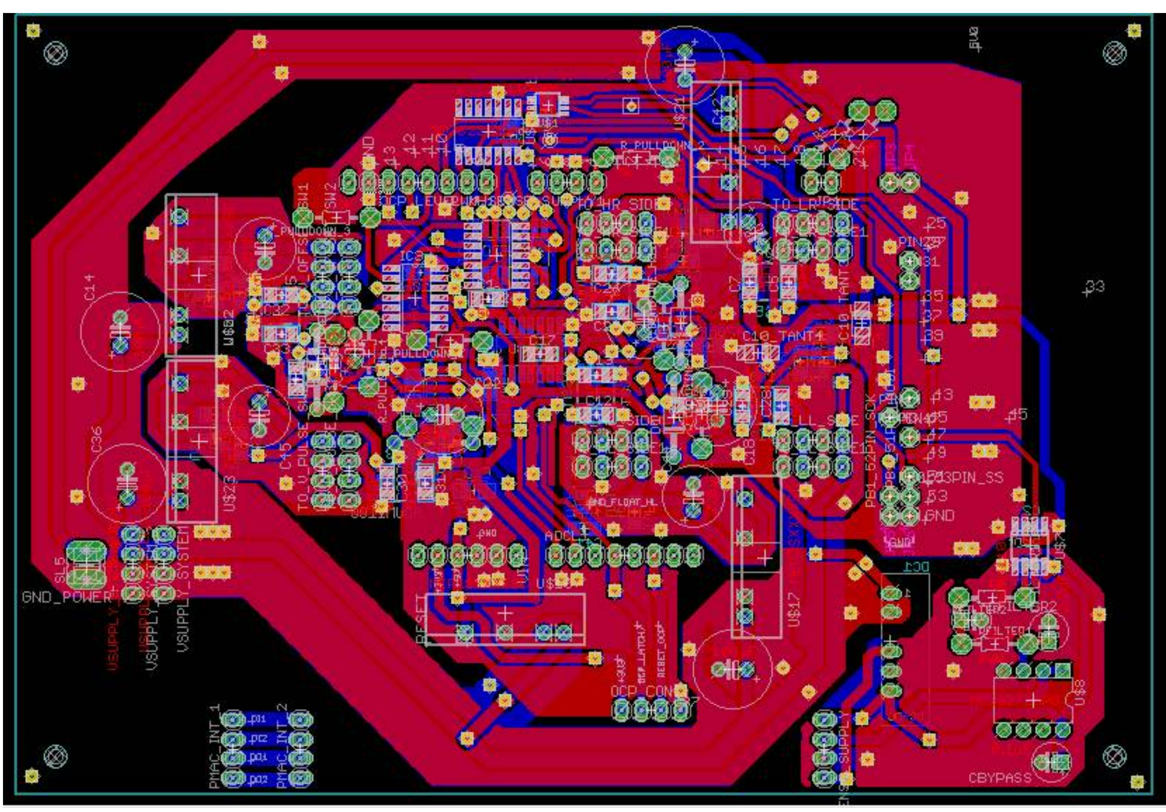

Power board of PSU prototype 2

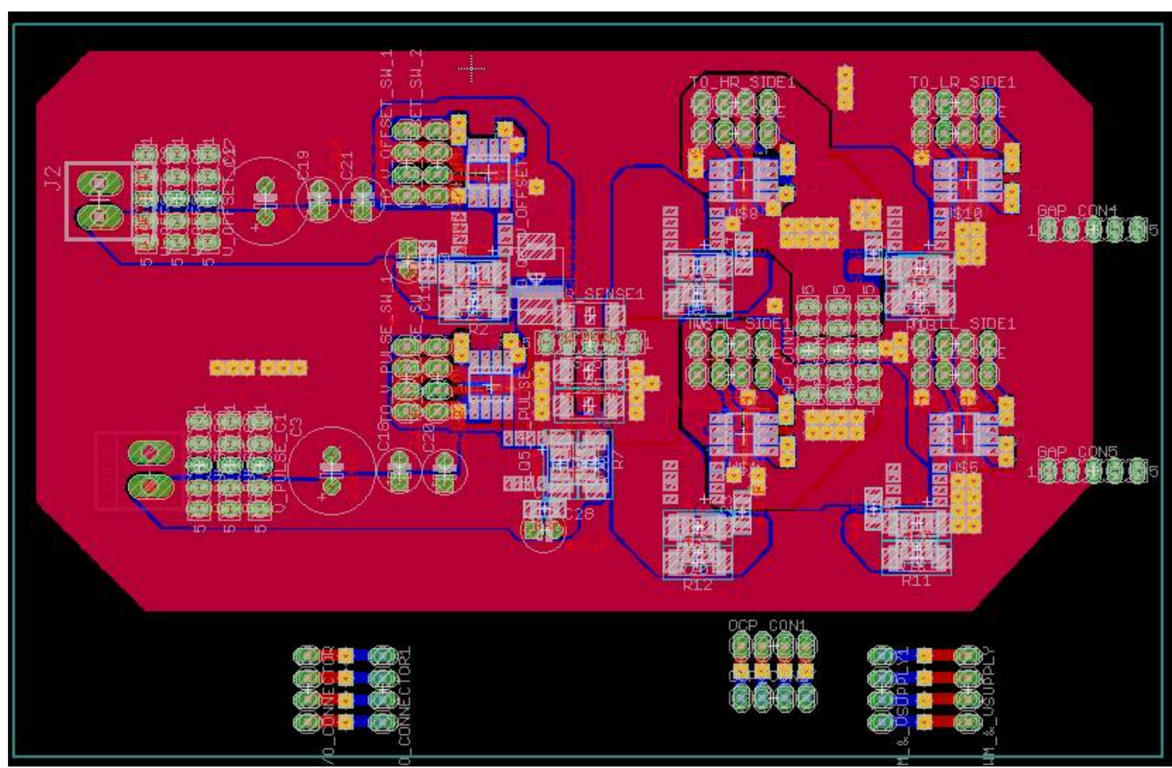

OCP board of PSU prototype 2

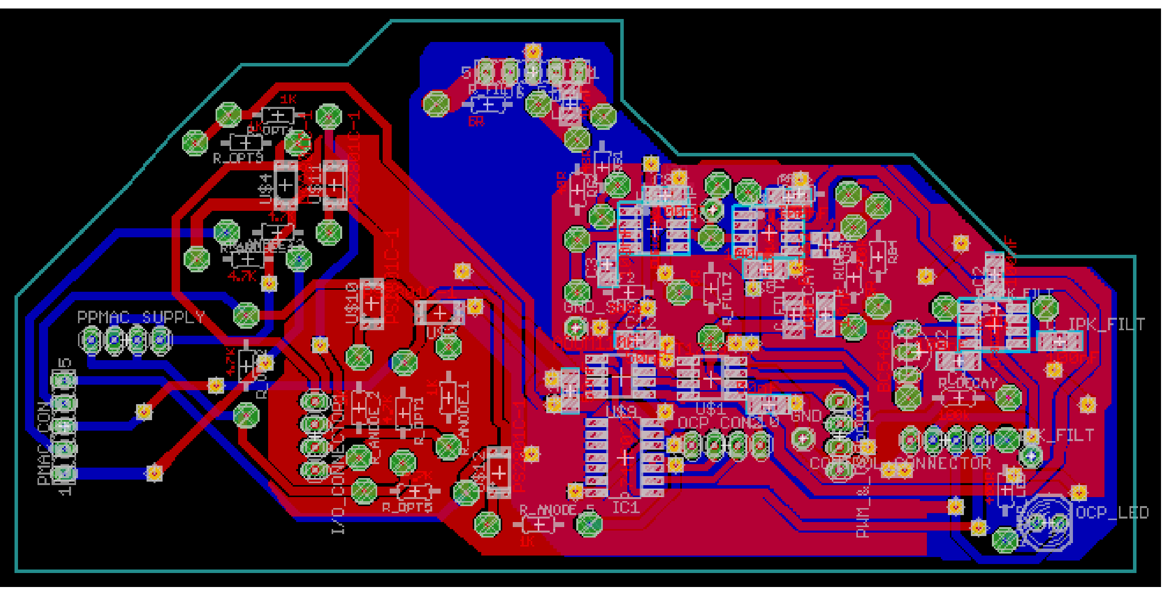

Control board of PSU prototype 3

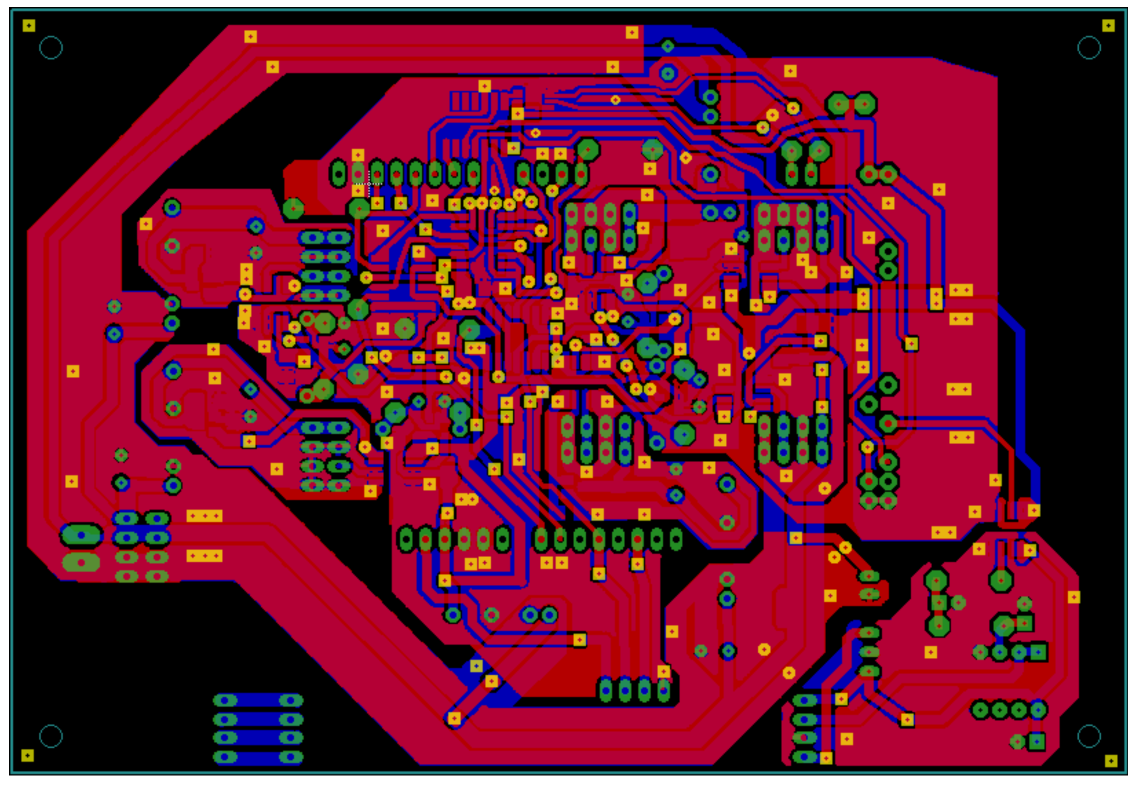

Power board of PSU prototype 3

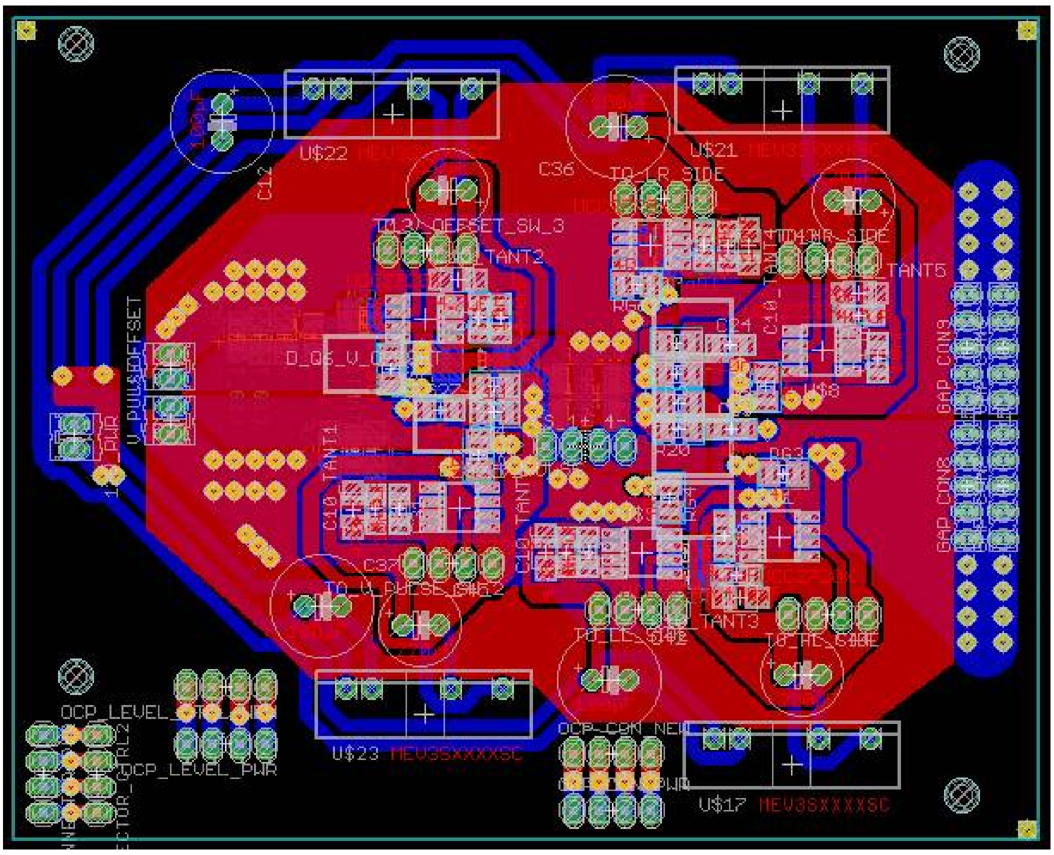

OCP board of PSU prototype 3

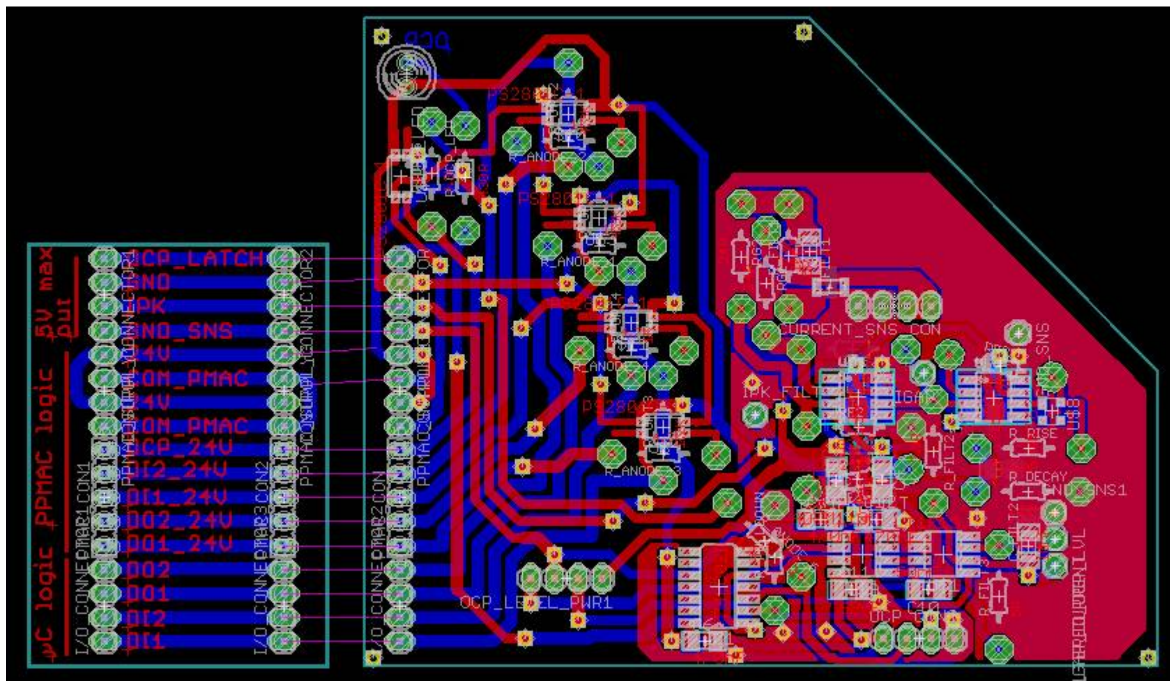

Appendix 8. PSU Modes

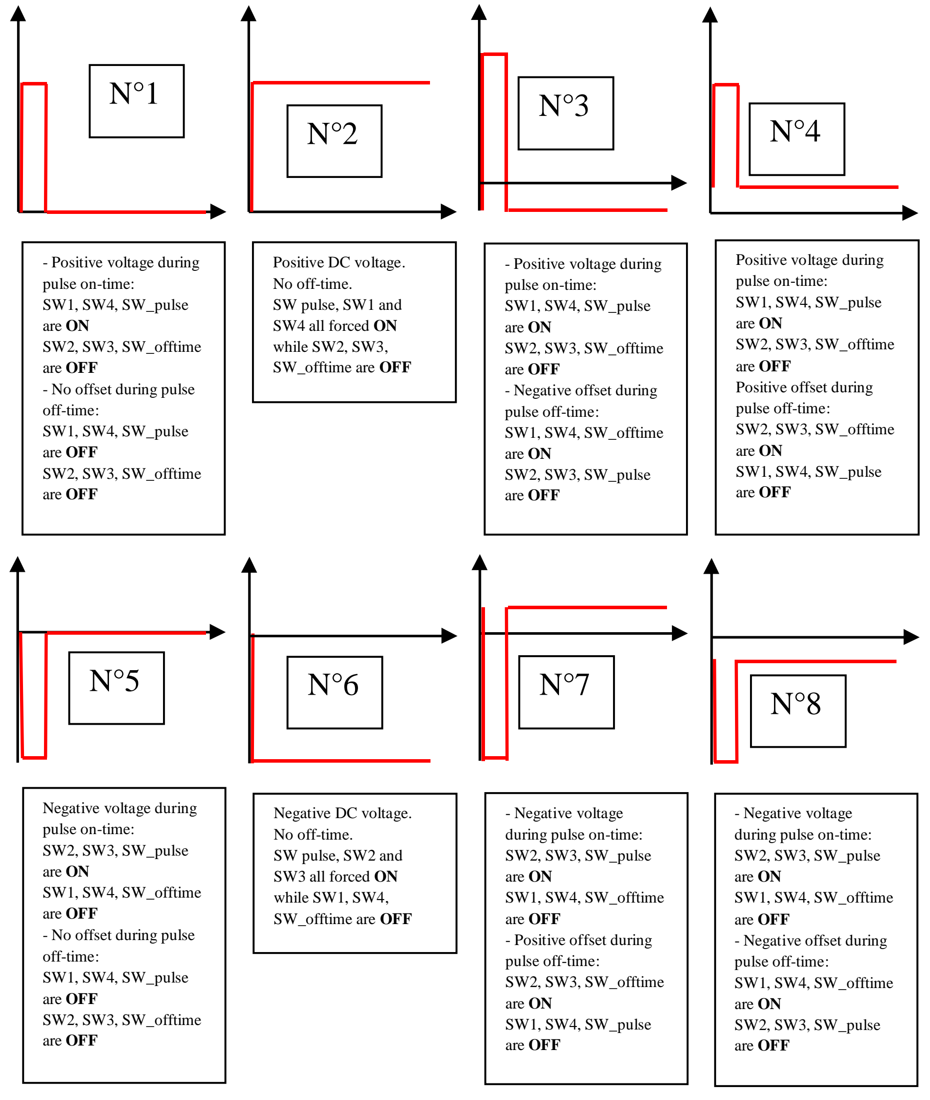

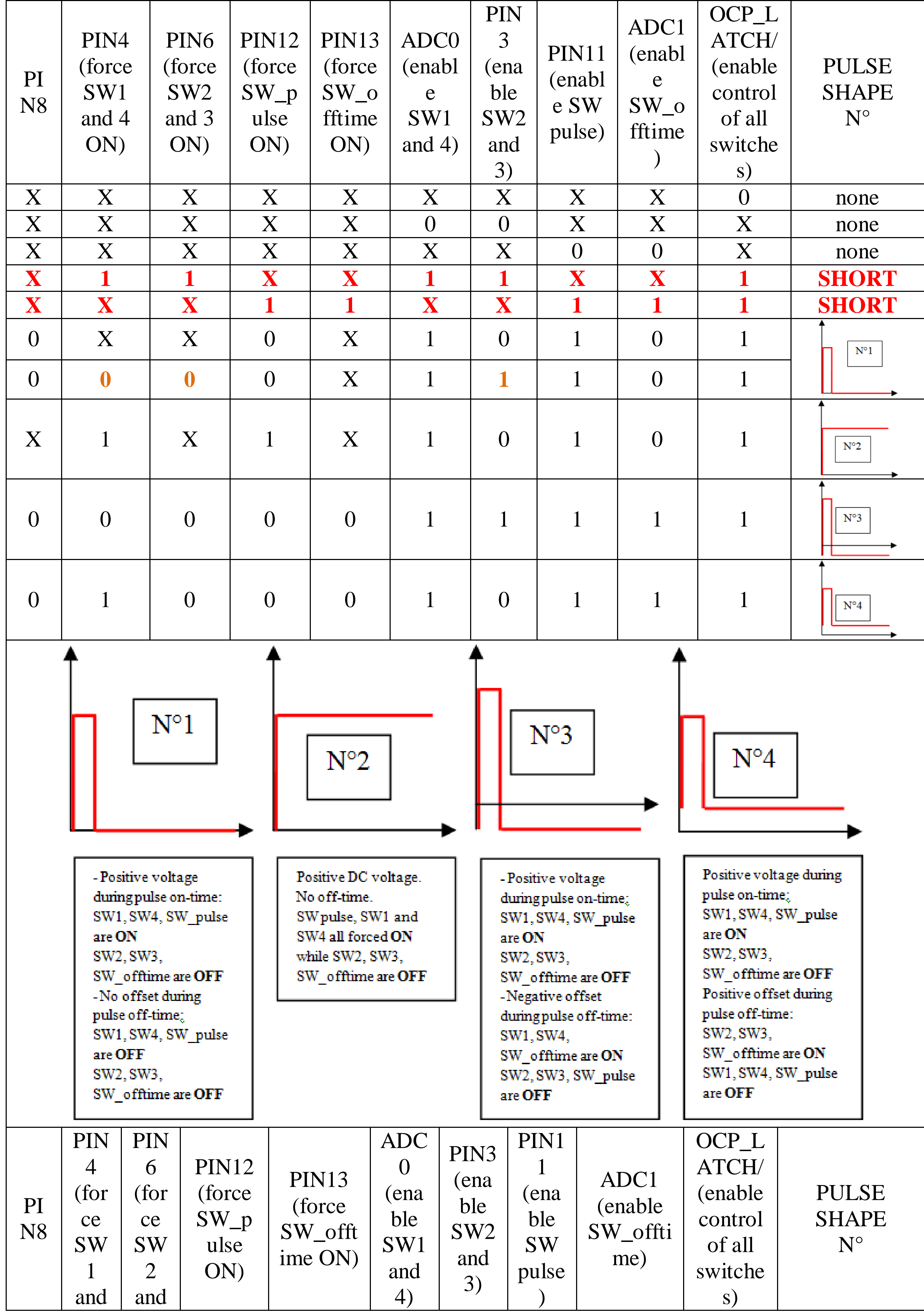

PIN8	PIN4 (force SW1 and 4 ON)	PIN6 (force SW2 and 3 ON)	PIN12 (force SW_pulse ON)	PIN13 (force SW_offtime ON)	ADC0 (enable SW1 and 4)	PIN3 (enable SW2 and 3)	PIN11 (enable SW pulse)	ADC1 (enable SW_offtime)	OCP_LATCH/ (enable control of all switches)	PULSE SHAPE N°
X	X	X	X	X	X	X	X	X	0	none
X	X	X	X	X	0	0	X	X	X	none
X	X	X	X	X	X	X	0	0	X	none
X	1	1	X	X	1	1	X	X	1	**SHORT**
X	X	X	1	1	X	X	1	1	1	**SHORT**
0	X	X	0	X	1	0	1	0	1	N°1
0	0	0	0	X	1	1	1	0	1	
X	1	X	1	X	1	0	1	0	1	N°2
0	0	0	0	0	1	1	1	1	1	N°3
0	1	0	0	0	1	0	1	1	1	N°4

PIN8	PIN4 (force SW1 and	PIN6 (force SW2 and	PIN12 (force SW_pulse ON)	PIN13 (force SW_offtime ON)	ADC0 (enable SW1 and 4)	PIN3 (enable SW2 and 3)	PIN11 (enable SW pulse)	ADC1 (enable SW_offtime)	OCP_LATCH/ (enable control of all switches)	PULSE SHAPE N°

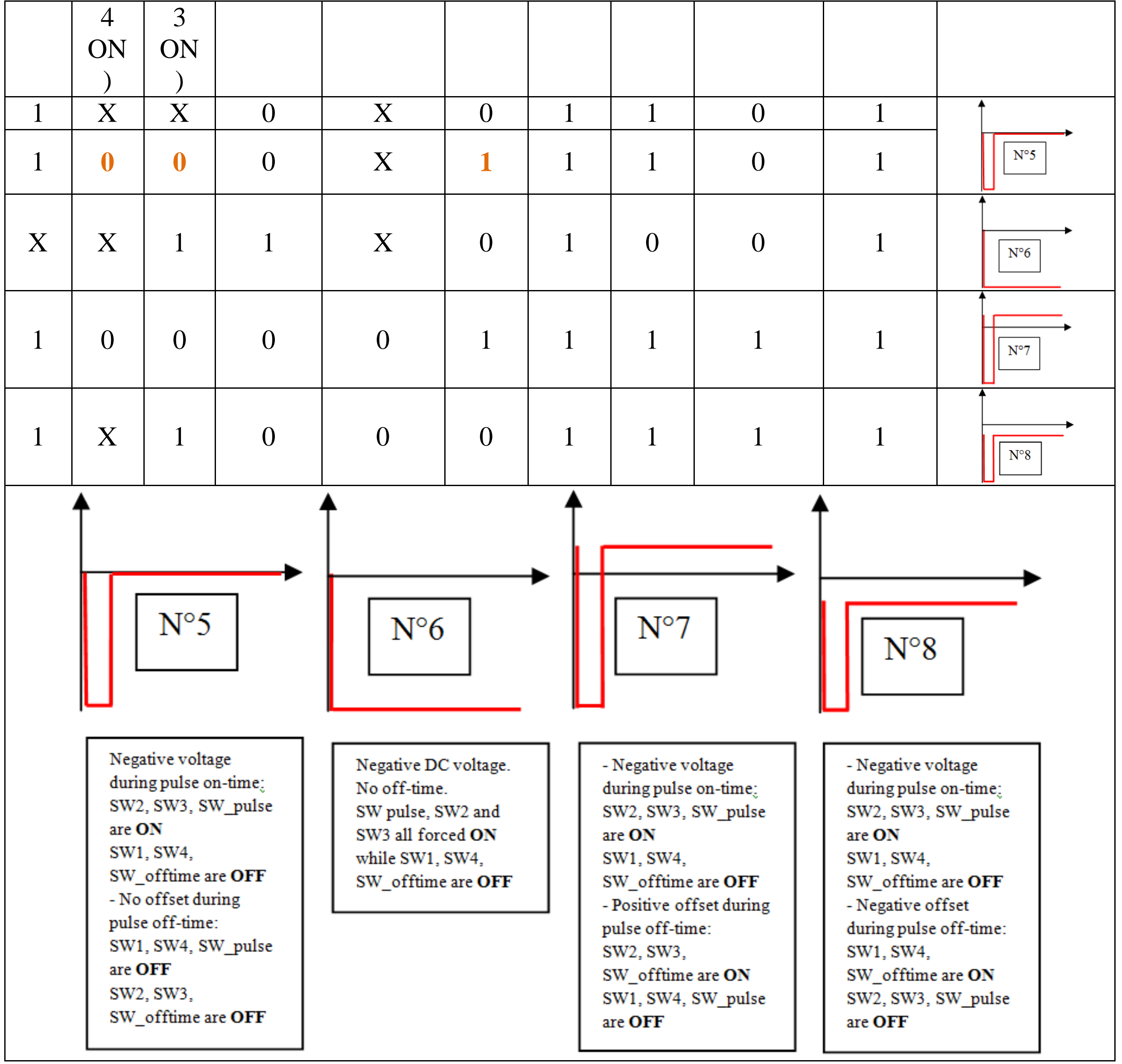

	4 ON)	3 ON)								
1	X	X	0	X	0	1	1	0	1	
1	0	0	0	X	1	1	1	0	1	N°5
X	X	1	1	X	0	1	0	0	1	N°6
1	0	0	0	0	1	1	1	1	1	N°7
1	X	1	0	0	0	1	1	1	1	N°8

Negative voltage during pulse on-time: SW2, SW3, SW_pulse are **ON** SW1, SW4, SW_offtime are **OFF** - No offset during pulse off-time: SW1, SW4, SW_pulse are **OFF** SW2, SW3, SW_offtime are **OFF**

Negative DC voltage. No off-time. SW pulse, SW2 and SW3 all forced **ON** while SW1, SW4, SW_offtime are **OFF**

- Negative voltage during pulse on-time: SW2, SW3, SW_pulse are **ON** SW1, SW4, SW_offtime are **OFF**
- Positive offset during pulse off-time: SW2, SW3, SW_offtime are **ON** SW1, SW4, SW_pulse are **OFF**

- Negative voltage during pulse on-time: SW2, SW3, SW_pulse are **ON** SW1, SW4, SW_offtime are **OFF**
- Negative offset during pulse off-time: SW1, SW4, SW_offtime are **ON** SW2, SW3, SW_pulse are **OFF**